A Multi-Scale Approach to Process Development: Laboratory to Pilot Scaling of Methanol Synthesis from CO_2-Rich Synthesis Gas with Promoted Carrier Catalysts

Von der Fakultät für Georessourcen und Materialtechnik der
Rheinisch-Westfälischen Technischen Hochschule Aachen

zur Erlangung des akademischen Grades eines

Doktors der Ingenieurwissenschaften

genehmigte Dissertation

vorgelegt von

Friedrich Carl Fritsch, M.Sc.

Berichter: Univ.-Prof. Dr.-Ing. Peter Quicker
Univ.-Prof. Dr.-Ing. habil. Thomas Wintgens

Tag der mündlichen Prüfung: 18.05.2026

Diese Dissertation ist auf den Internetseiten der Universitätsbibliothek online verfügbar.

Acknowledgments

This Thesis is the result of multiple laboratory- and pilot-scale testing campaigns that could not have been conducted without the relentless support of colleagues, friends, and mentors. I would like to thank everybody who contributed to this thesis as the support was essential to its outcome and remains highly appreciated.
I want to thank Prof. Dr. Peter Quicker and Prof Dr. Thomas Wintgens for taking me on as Doctoral-Candidate, and supporting me through the years of work.
I would like to thank my fiance, partner and best friend Dr. Katharina Schäfer. She set the standard for my persistence, supported me in the most difficult times and cheered me towards completion of this work. Without her example in work ethic and persistence, her support, her advice and her motivation, this thesis would have been considerably more difficult.
I would like to thank Dr. Jürgen Dornseiffer of Forschungszentrum Jülich GmbH and CCD Chemical Consulting GbR for his continued support of this matter. His ideas, tips, input and his work in producing the catalysts tested in this thesis were a constant corner stone of orientation for designing the experiments and setting my goals. He remains a constant partner in development of ideas and novel research approaches and I am looking forward to continuing our collaboration in the future!
I would like to thank my family, especially my mother and sister who have been scientific role models for and supported me constantly through all the small wins and desperate failures. My continued interest and passion for science would not have come to fruition without your inspiration and encouragement.
I would like to thank the entire team at FiW, who have grown to become more than colleagues. Without the unique atmosphere in UVT, the hardship of finishing this thesis would have been a lot less bearable. Thank you for all the ups and downs. I am looking forward to our shared future.
Herein, I would like to thank Jule Blankenstein specifically, whose ideas laid the foundations for this future thesis and who shared many of the hardships associated with decentralized operation of laboratory and pilot plants.
I want to thank the team of Kläranlage Emschermündung, who supported the operation of our methanol pilot plant relentlessly. Without the support of Christoph and Frank, many experiments would not have been possible in our limited time frame and with the limited resources.
Thank you to all students who played a role in carrying out the experiments, honing the scientific goals and their modeling and data evaluation expertise. Thank you especially to Chris Groteklaes, Andy Serwe and Moritz Haep, who were essential to carrying out the large amount of experiments that we conducted.

Contents

List of Figures **x**

List of Tables **xii**

List of Symbols and Abbreviations **xiv**

1. Introduction **1**
1.1. Methanol Production and Use 1
1.2. Outline, Objectives and Structure of this Work 3

2. Theoretical Background and State of the Art **8**
2.1. Synthesis Gas Production 9
2.1.1. Gasification Processes 10
2.1.2. Reforming Processes 11
2.2. Process Technology for Thermo-catalytic Production of Methanol 14
2.3. Contemporary Approaches and Limitations in Regenerative Methanol Synthesis 18
2.3.1. Direct Production of Methanol from CO_2 18
2.3.2. Biomass and Biogas derived Methanol 20
2.4. Catalysts Systems for Heterogeneous Synthesis of Methanol 22
2.4.1. Working Mechanism of the Commercial Catalyst 22
2.4.2. Catalyst Manufacturing and Deployment 25
2.4.3. Enhanced Catalysts for Efficient Production of MeOH from CO and CO_2 27
2.5. Kinetic Modeling of Methanol Synthesis 34
2.6. Parameter Estimation in Methanol Reaction Kinetics 36

3. Experimental Setups and Methods **52**
3.1. Research Track 1: Development, Characterization and Testing of Carrier Catalysts for Conversion of CO_2-rich Synthesis Gas to Methanol 52
3.1.1. Manufacturing of Catalyst samples 53
3.1.2. Physio-chemical characterization of catalyst samples 54
3.1.3. Laboratory Setup for Performance Evaluation and Kinetic Studies 55
3.1.4. Parameter Optimization for Reaction Kinetics 58
3.2. Research Track 2: Methanol Synthesis from Biogas 60

4. Results of the Catalyst Screening **64**

5. CO_2-to-Methanol over Cu/ZnO Infiltration Composites **69**
5.1. Introduction 71

5.2. Results and Discussion . . . 72
5.2.1. Results Sample Characterization . . . 72
5.2.2. Catalyst Performance . . . 78
5.3. Conclusions . . . 84
5.4. Experimental . . . 85
5.4.1. Catalyst Preparation . . . 85
5.4.2. Sample Characterization . . . 86
5.4.3. Catalyst Performance . . . 86

6. Industrial Methanol Synthesis over Cu/ZnO Infiltration Composites 93
6.1. Introduction . . . 96
6.2. Experimental Section . . . 98
6.2.1. Catalyst preparation . . . 98
6.2.2. Physical characterization of the samples . . . 99
6.2.3. Activity Testing . . . 101
6.2.4. Reaction Kinetics . . . 103
6.3. Results . . . 111
6.3.1. Material characterization . . . 111
6.3.2. Catalyst Performance in Mixed Carbon-Oxide Synthesis Gas . . . 117
6.3.3. Results of the Parameter Fitting . . . 122
6.4. Conclusion . . . 128

7. Integrated H_2/O_2-Enhanced Biogas-to-Methanol Process 137
7.1. Introduction . . . 140
7.2. State-of-the-Art, Pilot plant Design and Set-Up . . . 142
7.2.1. Design and Setup of the Autothermal Reforming Unit . . . 143
7.2.2. Design and Setup of the Methanol Synthesis System . . . 145
7.2.3. Integrated System and System Control . . . 146
7.3. Experimental . . . 147
7.3.1. System Parameters and Performance Indicators . . . 147
7.3.2. System Start-Up and Determination of Steady-State . . . 150
7.3.3. Combined operation of ATR and MeOH Synthesis . . . 151
7.4. Results . . . 151
7.4.1. System Start-Up of ATR . . . 151
7.4.2. Operation of the Biogas ATR . . . 152
7.4.3. Operation of MeOH-Synthesis Loop . . . 153
7.4.4. Combined System Operation . . . 156
7.5. Conclusion and Outlook . . . 159

8. Conclusion, Discussion and Outlook 166
8.1. Summary . . . 166
8.2. Discussion of Research Questions . . . 167
8.3. Limitations . . . 168

8.4. Outlook and Recommendations for future research 170

Appendices **171**

A. Supplementary Materials Publication 1 **172**

B. Supplementary Materials Publication 2 **188**

B.1. Physio-chemical Characterization 188

B.2. Reaction kinetics 196

B.2.1. Test conditions for each catalyst 196

B.2.2. Constrained Optimization Problem 203

B.2.3. Test for mass transfer limitations 204

B.2.4. Results of the Statistical analysis 212

C. Supplementary Materials Publication 3 **215**

List of Figures

1.1. Applications and associated percentages of global methanol use (2024). Own representation, data taken from [8]. 2
1.2. General pathways for the production of both fossil and regenerative MeOH. Own representation, adapted from [14] 3
1.3. Structure of this work and how the different research approaches relate to each other. 5

2.1. SynGas production pathways and expected COR for conventional and selected regenerative pathways. Own representation, adapted from [9] 9
2.2. Schematic image of different gasification reactors. a) Updraft fixed bed gasifier b) Entrained bed gasifier c) Fluidized bed gasifier. Own representation, contents adapted from [10, 11] . . 11
2.3. Schematic image of different NG reforming approaches. a) Steam Methane Reforming b) Partial Oxidation Reforming c) Dry Methane Reforming d) Autothermal Reforming. Own representation, flow sheets adapted from [21, 22]. 13
2.4. Schematic representation of a MeOH synthesis plant utilizing coal as carbon feedstock. 1) Air separation unit 2) Gasifier 3) Water Gas Shift (WGS) Reactor 4) Product Gas Scrubbing 5) Methanol Reactor 6) Gas Liquid Separator 7) Low pressure separation and Distillation. Own representation, based on flowsheet by [43, 9, 44] 15
2.5. Schematic representation of a MeOH synthesis plant utilizing NG as carbon feedstock. 1) Sulfur Removal 2) Reformer with partial feed combustion 3) Gas Liquid Separator 4) Methanol Reactor 5) Gas Liquid Separator 6) Low pressure separation and Distillation. Own representation, based on flowsheet by [9, 45, 46] 15
2.6. Equilibrium conversion of different CO- and CO_2-based reactant feeds under varying pressure and temperature. Used with permission from [40]. 16
2.7. Common reactor Types in industrial MeOH Synthesis and their technology suppliers. Own representation, contents adapted from [40] and [56]. a] Lurgi tubular reactor (AirLiquide today), b] Counter flow isothermal with steam cooling (applied by Mitshbishi Chemical) c] Adiabatic reactor design with intermediate SynGas mediated cooling (Applied in principle by Toyo and Clariant) d] Quasi-isothermal with internal cooling (Linde). 18
2.8. Schematic comparison of a conventional MeOH-synthesis process with a CO_2 based approach. Associated gas compositions and process parameters are given in the schematic for each process. a) Conventional MeOH-Synthesis flow sheet b) CO_2 based E-MeOH-production scheme. Compositions calculated based upon [9, 55, 59, 60]. Own representation. 19
2.9. Schematic of possible reaction pathways for MeOH formation. a) Formate pathway for CO_2 hydrogenation b) Carboxyl pathway for CO_2 hydrogenation, c) RWGS and CO hydrogenation pathway for for CO_2 hydrogenation d) CO hydrogenation e) RWGS. Own representation based upon mechanistic data from [48, 57, 61]. 24

2.10. In-situ imagining of Cu/ZnO structures during reduction in H_2 at different temperatures in the reduction temperature ramp. Reproduced under creative commons license from [85]. 26
2.11. Schematic representation of CeO_2s ability to act both as a chemical (left) as well as an electronic promoter (right), generating highly active oxygen vacancies for CO_2 adsorption as well as electronically induced H_2-spillover, creating charge differentials in the metal lattice that actively promote adsorption. Own representation, adapted mechanistically from [61, 77]. 29
2.12. Types of catalyst materials reported for MeOH production from CO_2 or CO_2-rich SynGas. Percentages are calculated based on more than 200 journal articles identified from scopus search by [106]. Own representation, graphic reproduced under creative commons license agreement (CC-BY-NC-ND). 30
2.13. Comparison of reported CO_2-conversion performance of different, promoted catalyst samples from recent literature [107, 108, 109, 110, 111, 112]. 31

3.1. Flowsheet representation of the catalyst manufacturing protocol applied in the thesis. 1) Specified amount of distilled water 2) Precursors according to final molar composition 3) Adding Carrier Spheres under stirring 4) Drying Catalyst 5) Calcination. 54
3.2. Images of the laboratory single-reactor test setup applied for catalyst screening and testing. 1) total plant. 2) gas dosing and reactor section 3) User Interface for plant operation. a) Gas dosing H_2 b) Gas dosing CO c) Coriolis gas dosing CO_2 d) Reactor with connectors for thermal oil heating/cooling e) Counter current product gas cooling f) Oil thermostat setup g) Pressure regulating valves. 56
3.3. P&ID of the laboratory test plant. 1) Gas supply from high pressure containers 2) Pressure regulators 3) Shut-off valves and mass flow controllers 4) Reactor Coupling 5) Thermal oil control unit 6) GC unit 7) High pressure counter current heat exchanger and flash 8) Online IR gas analysis 9) Inline gas analysis. 58
3.4. Basic sketch of the designed biogas-to-methanol plant 1) Biogas / Sewage Gas Plant 2) Electrolysis Unit 3) Reformer 4) Gas Mixer 5) Methanol Reactors 6) raw product separator. . 61
3.5. Image of the pilot plant control user interface implemented in WinCC. 61
3.6. Foto of the pilot plant setup. a) Activated carbon filter b) Siloxane filter c) Reformer in insulation enclosure d) Gas chromatography unit e) Heat exchanger for make up gas preheating f) Double reactor setup g) Oil thermostat heater/cooler h) Gas buffering/make up gas mixing i) Three stage gas compressor. 62

4.1. Results of the catalyst screening applying CO_2-only SynGas. MeOH STY and CO_2 conversion (left) and selectivity towards MeOH, CO, Ethanol, Formaldehyde and Water (right). All tests conducted at SN = 3, 25 bar reactor pressure, 250 °C reactor temperature and GHSV of 10.000 h^{-1}. 65
4.2. Results of the catalyst screening applying lower COR SynGas. All tests conducted at SN = 3, 20 bar reactor pressure, 250 °C reactor temperature and GHSV of 10.000 h^{-1} 66

5.1. Powder X-ray diffraction patterns of the different catalysts in comparison to the reference and the used alumina spheres. The diamond icon is used for identification of distinctive Cu-diffraction peaks, while star and triangle identify CeO_2 and ZnO respectively. 73

5.2. Highly magnified SEM-images of the catalyst surfaces. Two SEM-images for each catalyst sample are used, to demonstrate the inhomogeneous catalyst structures, both in the reference and in the carrier catalysts. Image sections used for EDX analyses are marked by yellow boxes. Corresponding EDX mappings are presented in figure 5.3. 74

5.3. EDX mapping overlays for all metal components in the herein presented catalyst samples. Each mapping corresponds to an image section presented in figure 5.2. 75

5.4. H_2-TPR profiles of the catalysts compare to the industrial reference. TO marks onset reduction temperature. α, β and γ are used for marking the three distinctive reduction peaks. T_o - Onset reduction for first reduced, small and widely dispersed CuO particles, α - Onset reduction peak at around 190-220 °C, β - Main reduction peak at around 200-225 °C, γ - Shoulder peak at around 240-280 °C caused by more strongly interacted CuO species 76

5.5. NH_3-TPD profiles of the catalysts compare to the industrial reference. Magnitude for TCD signal is increased fivefold for better identifiability of desorption peaks. Br: Brønsted acid cites for weakly acidic surface acid components, Le: Lewis acid cites – more strongly interacted with NH_3 in testing 78

5.6. a] CO_2 conversion over reactor pressure for the catalyst samples at 250°C reactor temperature, GHSV at 10,000 h^{-1} b] CO_2 conversion over GHSV at 250°C reactor temperature and 5 MPa reactor pressure, c] methanol production rate over reactor pressure for the catalyst samples at 250 °C reactor temperature, GHSV at 10,000 h^{-1} and gas composition SN = 3 for H_2/CO_2 . 79

5.7. a] CO_2 conversion and Methanol STY for different reactor temperatures b] Selectivity for MeOH, CO, CH_4 and DME generation at different temperatures. Catalyst performance was tested at 3.5 MPa reaction pressure, GHSV of 10,000 h^{-1} and H_2/CO_2 of SN = 3. 81

5.8. Schematic of the lab test bench for catalyst sample performance. 1: Pressure control valves 2: Mass flow control (MFC) and check valves 3: Double valve coupling for reactor removal 4: Reactor with three temperature measurements 5: Electro-thermal oil heating/cooling 6: Product cooling and flash 7: Liquid sample 8: Flow control and expansion valve 9: Exhaust. 87

6.1. Basic Setup for catalyst activity testing and kinetic performance measurements. 102

6.2. Detail HAADF-STEM-images of the FIB-Lamellae cross sections for all four herein presented infiltration composite catalysts. a1-a4) HAADF-STEM-images of the catalyst cross sections at 200 nm b1-b4) STEM-EDX-spectrum mappings for Cu ad Zn c1-c4) 10 nm and 5 nm magnification of the lamellae cross sections d1-d4) Integrated STEM-EDXS line profiles for the detected elements over the 2 µm FIB lamellae radial cross sections. 112

6.3. Raman and XPS surface characterization of the catalyst samples: a1)-a3) Raman surveys for 100-1350 cm^{-1} shift (a1) and for 380-520 cm^{-1} (a2) and 500-720 cm^{-1} shift respectively (a3). Reference Raman-spectra for the individual metal oxides used in the infiltration composites (a4). b1)-b3) XPS survey spectrum for all four infiltration composite catalysts (b1). Detailed spectra for 950-930 eV (b2 - CuO) and 1060-1010 eV (b3 - ZnO). 113

6.4. a) CO_2-desorption measurements for the carrier and reference catalysts b) H_2-desorption curves 115

6.5. Conversion-equilibria of the presented catalyst samples at 225 °C, 250 °C and 275 °C as well as performance figures for the determined conversion equilibria at 20 bar and 50 bar reactor pressure 118

6.6. Conversion performance of the Samples under different COR influent compositions (35 bar reactor pressure, 250 °C reactor temperature, 10.000 h^{-1} GHSV). 118
6.7. Correlation of metallic Cu surface area and CO_2-adsorption properties to catalyst performance measured at COR = 0.71, p = 50 bar, T = 250 °C and GHSV = 10,000 h^{-1}. 119
6.8. Parity Plots for measured vs. predicted effluent partial pressures for a) CO and CO_2 and b) MeOH and H_2O in the four catalyst samples. 124
6.9. Calculated concentration profiles inside the test reactor for three different inlet gas compositions. Top to bottom: 1) COR = 0.81, SN = 3; 2) COR = 1, SN = 3; 3) COR = 0.36, SN = 3. 126

7.1. Piping and Instrumentation Diagram (P&ID) of the Autothermal Reforming unit for oxygen-added conversion of Biogas to SynGas. 1) Gas-dosing lines for synthetic biogas and oxygen. 2) Biogas-gas pump. 3) Siloxane Filter. 4) Activated Carbon Filter. 5) Reforming Reactor with radial oxygen injection. 6) Combined heat exchanger for water evaporation and biogas preheating. 7) Feed water demineralization unit. 8) Feed water dosing pump. 144
7.2. P&ID of the Methanol Synthesis Loop for Conversion of Reformate from Autothermal Reforming. 1) Gas dosing lines for synthesis gas dosing from gas cylinders. 2) Three-stage synthesis gas compressor with intermediate stage cooling and condensation. 3) Gas mixer, combined heat exchanger and pulsation dampener for synthesis gas. 4) Thermal oil thermostat for system tempering in start-up and reactor cooling in steady-state operation. 5) Double heat-exchanger arrangement for synthesis gas pre-conditioning. 6) Double tubular quasi-isothermal methanol reactors. 7) Combined raw-product condensation and recycling gas conditioning unit. 8) Heat exchanger for product-gas cooling/recycling gas pre-heating. 9) Recycling gas compressor. 145
7.3. a) Outside view of the plant in operation. 1 - Sewage gas line. 2 - Activated. charcoal filter. 3 - Gas storage for Helium and Calibration Gas (GC). 4 - Gas Storage for O_2, H_2, CO_2 and CH_4. b) Inside view of the operational process. 1 - Three-stage reformate compressor. 2 - Siloxane filter. 3 - Reforming unit encased in mantle. 4 - tubular MeOH reactors. 5 - Gas mixer/pulsation dampener. 6 - Thermostat heating and cooling unit. 7 - Heat exchanger for SynGas-preheating and energy recuperation. 147
7.4. Reformer Start-Up after preheating of the catalytic chamber and the combined heat exchanger and start of O_2-injection for autothermal operation. a) Reformate composition after reformer start-up. Steady-state gas composition is reached after 10 minutes. b) Record of feed injection into reformer for the depicted start-up procedure. c) λ and S/C for the presented start-up protocol. 151
7.5. Operational Results for separate ATR-operation under different GHSV and λ at S/C = 1.3 . . 152
7.6. Φ and η_{el} of the different tested operational setpoints for the ATR 153
7.7. Recycle Loop Gas Composition after System Start-Up (t = 0:00) of the Methanol Synthesis Unit. Depicted COR reflects the COR of injected SynGas into the system over the period of system start-up and equilibration. Times used in x-axes refer to test dureation from the beginning of the recording. 154
7.8. STY_{MeOH}, $X_{C_{sp}}$ and resulting reactor influent COR for four different SynGas COR used in separate MeOH testing 155

7.9. MeOH-unit STY, $X_{C_{sp}}$ and resulting reactor influent COR in CO_2-only operation at different temperatures and SN = 2 . . . 156
7.10. Sankey Diagram of the balanced steady state system for the combined operation of ATR and MeOH synthesis with molar and energy flux given for each compounded process stream. Bar thickness correlates to molar flux. . . . 158

A.1. N_2-adsorption isotherm for the γ-Al_2O_3 carrier spheres . . . 172
A.2. N_2-adsorption isotherm for the 20% CZ catalyst sample . . . 173
A.3. N_2-adsorption isotherm for the 20% CZC catalyst sample . . . 173
A.4. N_2-adsorption isotherm for the 20% CZCZ catalyst sample . . . 174
A.5. N_2-adsorption isotherm for the 20% CZCZC catalyst sample . . . 174
A.6. EDX-Analysis of the first SEM-image supplied for REF . . . 175
A.7. EDX-Analysis of the second SEM-image supplied for REF . . . 175
A.8. EDX-Analysis of the first SEM-image supplied for 20% CZ . . . 176
A.9. EDX-Analysis of the second SEM-image supplied for 20% CZ . . . 177
A.10. EDX-Analysis of the first SEM-image supplied for 20% CZC . . . 177
A.11. EDX-Analysis of the second SEM-image supplied for 20% CZC . . . 178
A.12. EDX-Analysis of the first SEM-image supplied for 20% CZCZ . . . 179
A.13. EDX-Analysis of the second SEM-image supplied for 20% CZCZ . . . 179
A.14. EDX-Analysis of the first SEM-image supplied for 20% CZCZC . . . 181
A.15. EDX-Analysis of the second SEM-image supplied for 20% CZCZC . . . 181
A.16. Single Element EDX Mapping for Reference Catalyst Image 1 . . . 182
A.17. Single Element EDX Mapping for Reference Catalyst Image 2 . . . 183
A.18. Single Element EDX Mapping for 20% CZ SEM Image 1 . . . 183
A.19. Single Element EDX Mapping for 20% CZ SEM Image 2 . . . 184
A.20. Single Element EDX Mapping for 20% CZC SEM Image 1 . . . 184
A.21. Single Element EDX Mapping for 20% CZC SEM Image 2 . . . 185
A.22. Single Element EDX Mapping for 20% CZCZ SEM Image 1 . . . 185
A.23. Single Element EDX Mapping for 20% CZCZ SEM Image 2 . . . 186
A.24. Single Element EDX Mapping for 20% CZCZC SEM Image 1 . . . 186
A.25. Single Element EDX Mapping for 20% CZCZC SEM Image 2 . . . 187

B.1. STEM-Images of 20% CZ for scoping areas suitable for FIB-milling . . . 189
B.2. EDX-analysis of the radial lamellae cross sections for each catalyst sample. l.t.r.: 20% CZ, 20% CZC, 20% CZCZ, 20% CZCZC . . . 190
B.3. STEM EDX-analysis of the radial lamellae cross sections for 20% CZ . . . 191
B.4. STEM EDX-analysis of the radial lamellae cross sections for 20% CZC . . . 192
B.5. STEM EDX-analysis of the radial lamellae cross sections for 20% CZCZ . . . 192
B.6. STEM EDX-analysis of the radial lamellae cross sections for 20% CZCZC . . . 193
B.7. Additional bright and dark field TEM images at very high magnification of the FIB-lamella of 20% CZ . . . 194
B.8. Additional bright and dark field TEM images at very high magnification of the FIB-lamella of 20% CZC . . . 194

B.9. Additional bright and dark field TEM images at very high magnification of the FIB-lamella of 20% CZCZ 195
B.10. Additional bright and dark field TEM images at very high magnification of the FIB-lamella of 20% CZCZC 195
B.11. FFT and IFFT analysis of a HAADF STEM Image of the lamella of 20% CZCZC. Four different areas (Regions of Interest) are investigated. 196

C.1. Influence on applied GHSV on Methanol Synthesis Performance 215

List of Tables

2.1. Overview of catalyst promoter properties, their effects, and methods to probe them. 28
2.2. Classification of selected MeOH synthesis catalysts by their primary mechanisms of action (Part 1) 32
2.3. Classification of selected MeOH-synthesis catalysts by their primary mechanisms of action (Part 2) 33
2.4. Summary of kinetic models (Part 1) 38
2.5. Summary of kinetic models (Part 2) 39

4.1. Target composition of reference and synthesized catalysts (mol.%) 64

5.1. Specific surface areas (A_{BET}) and corresponding pore volumes of the catalysts in comparison to the supporting Al_2O_3 spheres and the reference. 73
5.2. Onset catalyst reduction temperature (T_{o}) and temperature peaks for the three distinctive reduction peaks for each catalyst (α, β, γ). 77
5.3. Conditions with best methanol space time yield (STY) and CO_2 turnover for the coated catalyst in comparison with the reference. 82
5.4. Comparison of catalyst performance with literature data. 83
5.5. Molar composition of the catalyst fractions within the infiltration composites. 85

6.1. Catalyst composition for the tested samples. 98
6.2. Mechanism on the catalyst surface with kinetic model driving forces 106
6.3. CO_2-TPD analysis results for supported copper catalysts. Catalyst masses for 20% CZ - 20% CZCZC are reduced to weight of coating (20% of total catalyst weight) 116
6.4. H_2-TPD Part 1: H_2-TPD experimental results for the catalyst samples 116
6.5. H_2-TPD Part 2: Derived parameters from H_2-TPD analysis 116
6.6. Comparison of catalyst performance with selected literature values. 120
6.7. Mass transfer analysis results for the catalyst samples. 122
6.8. Kinetic parameters for novel 20% catalyst systems. 123
6.9. Kinetic parameters for methanol synthesis catalysts. 125
6.10. Normalized sensitivity of key model outputs towards the variation of selected model parameters. Sensitivity is given as compounded value for first order single parameters impact and higher order cross sensitivities. 127

7.1. Performance Data for Combined Operation Series at moderate system loads 158

A.1. eZAF quantitative analysis results for elemental composition REF 1 175
A.2. eZAF quantitative analysis results for elemental composition REF 2 176
A.3. eZAF quantitative analysis results for elemental composition 20% CZ1 176

A.4. eZAF quantitative analysis results for elemental composition 20% CZ2 177
A.5. eZAF quantitative analysis results for elemental composition 20% CZC1 178
A.6. eZAF quantitative analysis results for elemental composition 20% CZC2 178
A.7. eZAF quantitative analysis results for elemental composition 20% CZCZ1 179
A.8. eZAF quantitative analysis results for elemental composition 20% CZCZ2 180
A.9. eZAF quantitative analysis results for elemental composition 20% CZCZC1 181
A.10. eZAF quantitative analysis results for elemental composition 20% CZCZC2 182

B.1. Experimental Conditions - 20% CZ Catalyst 198
B.2. Experimental Conditions - 20% CZC Catalyst 199
B.3. Experimental Conditions - 20% CZCZ Catalyst 200
B.4. Experimental Conditions - 20% CZCZC Catalyst 201
B.5. Experimental Conditions - 20% CZCZC Catalyst (continuation) 202
B.6. Kinetic Parameter Constraints for Methanol Synthesis Optimization 203
B.7. Mass Transfer Analysis - 20% CZ Catalyst 206
B.8. Mass Transfer Analysis - 20% CZC Catalyst 207
B.9. Mass Transfer Analysis - 20% CZCZ Catalyst 208
B.10. Mass Transfer Analysis - 20% CZCZC Catalyst - Part 1 209
B.11. Mass Transfer Analysis - 20% CZCZC Catalyst - Part 2 210
B.12. Fitted kinetic and adsorption parameters with 95% confidence bounds for 20% catalyst systems 212

List of Symbols and Abbreviations

Abbreviations

ATR	Autothermal reforming
BASF	Badische Anilin- und Sodafabrik
BECCS	Bioenergy with carbon capture and storage
BET	Brunauer-Emmett-Teller (surface area analysis)
BJH	Barrett-Joyner-Halenda (pore size analysis)
CCC	Concordance correlation coefficient
CCU	Carbon capture and utilization
COR	Carbon oxide ratio
Cov	Covariance
CZA	$CuO/ZnO/Al_2O_3$ catalyst
DAC	Direct air capture
DME	Dimethyl ether
DMR	Dry methane reforming
DRIFTS	Diffuse reflectance infrared Fourier transform spectroscopy
EDXS	Energy-dispersive X-ray spectroscopy
E-MeOH	Methanol from electrochemically produced hydrogen and CO_2
EPR	Electron paramagnetic resonance
EtOH	Ethanol
FAD	Formaldehyde
GHG	Greenhouse gas emissions
GHSV	Gas hourly space velocity
HAADF-STEM	High-angle annular dark-field scanning transmission electron microscopy
ICI	Imperial Chemical Industries
ID	Inner diameter
IWI	Incipient wetness impregnation
LHHW	Langmuir-Hinshelwood-Hougen-Watson
LSBGS	Least-Squares Block-Gradient Search
MAPE	Mean absolute percentage error
Mears	Mears criterion for external mass transfer limitations
MeOH	Methanol
MTBE	Methyl-tert-butyl ether
MUG	Make-up gas
MVA	Müllverbrennungsanlage (waste incineration plant)
NG	Natural gas
NLP	Nonlinear programming
NRMSE	Normalized root mean square error

Abbreviations (continued)

P2M	Power-to-methanol
PFR	Plug-flow reactor
POX	Partial oxidation reforming
Re	Reynolds number
Ref	Reference catalyst sample
RSC	Royal Society of Chemistry
RWGS	Reverse water-gas shift
Sc	Schmidt number
SE	Standard error
SEM	Scanning electron microscopy
Sh	Sherwood number
SMR	Steam methane reforming
SMSI	Strong metal-support interaction
SN	Stoichiometric number
STY	Space-time yield
SynGas	Synthesis gas
TCD	Thermal conductivity detector
TEM	Transmission electron microscopy
TGA	Thermogravimetric analysis
TOT	Total
TPD	Temperature-programmed desorption
TPR	Temperature-programmed reduction
Var	Variance
WGS	Water-gas shift
WP	Weisz-Prater
WPI	Weighted performance index
XAS	X-ray absorption spectroscopy
XPS	X-ray photoelectron spectroscopy
XRD	X-ray diffraction
UPS	Ultraviolet photoelectron spectroscopy
20% CZ	20 wt.% coated CuO/ZnO catalyst
20% CZC	20 wt.% coated CuO/ZnO/CeO_2 catalyst
20% CZCZ	20 wt.% coated CuO/ZnO/CeO_2/ZrO_2 catalyst
20% CZCZC	20 wt.% coated CuO/ZnO/CeO_2/ZrO_2/CaO catalyst
α-Al_2O_3	Alpha-alumina (corundum, hexagonal crystalline phase)
α-peak	Low-temperature reduction peak in TPR
β-peak	Medium-temperature reduction peak in TPR
γ-Al_2O_3	Gamma-alumina (cubic defect spinel structure)
γ-peak	High-temperature reduction peak in TPR
θ-Al_2O_3	Theta-alumina (monoclinic crystalline phase)

Symbols

α	Significance level
a_i	Pre-exponential factor in Van't Hoff equation for species i
A_i	Pre-exponential factor for reaction i [mol/(kg_{cat}·s·Pa^n)]
b_i	Pre-exponential factor in Arrhenius equation
Br	Brønsted acid site
B_i	Pre-exponential factor for adsorption of species i (Van't Hoff) [Pa^{-1}]
ξ	Parameter vector
$\hat{\xi}$	Best-fit parameter vector
θ_i	Individual kinetic parameter
ξ	Kinetic parameter vector
ξ^*	Optimal kinetic parameter vector
C_{surface}	Surface concentration of species
$C_{\theta,ii}$	Diagonal element of covariance matrix
$\mathbf{C}_\theta$	Covariance matrix of parameters
D	Diameter; Denominator (context-dependent)
D_{AB}	Binary diffusivity [m^2/s]
D_{eff}	Effective diffusivity [m^2/s]
D_K	Knudsen diffusivity [m^2/s]
d_p	Particle diameter
d_{pore}	Pore diameter
E_a	Activation energy
$E_{a,i}$	Activation energy for reaction i [kJ/mol]
ε	Porosity
f_i	Fugacity of species i
F_{obj}	Objective function
$\mathbf{H}$	Hessian matrix
$H_{i,j}$	Element of Hessian matrix
ΔH_{ads}	Adsorption enthalpy
$\Delta H_{\text{ads},i}$	Adsorption enthalpy for species i [kJ/mol]
k_1	Reaction rate constant for CO hydrogenation to MeOH
k_2	Reaction rate constant for RWGS reaction
k_3	Reaction rate constant for CO_2 hydrogenation to MeOH
k_c	Mass transfer coefficient
K_i	Adsorption constant for species i
$K_{\text{eq},i}$	Reaction equilibrium constant for reaction i
Le	Lewis acid site
m	Mass
$\dot{m}$	Mass flow rate
M	Molar mass
M_i	Molar mass of species i
μ_g	Gas dynamic viscosity

Symbols (continued)

n	Number of data points; Kinetic model parameter (reaction order)
N	Number of data points
ν	Degrees of freedom
P	Pressure
p_i	Partial pressure of species i
Φ_{WP}	Weisz-Prater parameter
q_i	Weighting factor for species i
R	Universal gas constant
R^2	Coefficient of determination (R-squared)
R^2_{combined}	Combined R-squared for multiple variables
R^2_{rates}	R-squared for reaction rates
$R^2_{\text{pressures}}$	R-squared for partial pressures
$\mathbf{r}(\xi)$	Residual vector
ρ_b	Bulk density
ρ_g	Gas density
ρ_p	Particle density
r_i	Reaction rate for species or reaction i
r_{obs}	Observed reaction rate
r_{pore}	Average pore radius
R_p	Particle radius
$S(\theta)$	Sum of squared residuals
$S(\xi)$	Sum of squared residuals (optimization context)
$S_w(\xi)$	Weighted sum of squared residuals
S_i	Selectivity for product i
$\text{SE}(\theta_i)$	Standard error of parameter θ_i
σ^2	Variance of residuals
σ^2_{calc}	Variance of calculated values
σ^2_{exp}	Variance of experimental values
$\sigma_{\text{exp,calc}}$	Covariance of experimental and calculated values
Σv_i	Sum of atomic diffusion volumes for species i
$t_{(1-\alpha/2,\,\nu)}$	Student's t value
τ	Tortuosity
u_s	Superficial velocity
$\dot{V}$	Volumetric flow rate
V	Volume
w_i	Weighting factors
X_i	Conversion of species i
y_i	Molar concentration of species i

Symbols (continued II)

y_i^{calc}	Calculated value for species i
y_i^{exp}	Experimental value for species i
y_i^{mod}	Model-predicted value for species i
$\bar{y}^{\text{calc}}$	Calculated stream pressure
$\bar{y}^{\text{exp}}$	Experimental stream pressure
λ	Oxygen equivalence ratio
S/C	Steam-to-carbon ratio
T	Temperature [K/°C]

1. Introduction

The continued high volume use of non-renewable feedstock for production of value-added fuels, chemicals and materials continues to impact the environment due to the high green house gas (GHG) emissions associated with their extraction, conversion and application [1]. Methanol (methyl alcohol - MeOH) is the most simple organic alcohol and one of the most important petrochemical products from fossil feedstock on the market today, with over 100 Mt being produced and traded every year, most of which from natural gas (NG) [2]. Additionally, large parts of the global MeOH supply are produced from coal (mainly in China), with associated GHG-emissions for this production route exceeding those from NG-based MeOH two- to three-fold [3]. MeOH is used in various applications ranging from solvents and fuels to base chemicals and feedstock for polymerization to plastics [4]. In an effort to de-fossilize heavily carbon-reliant sectors, various approaches for regenerative MeOH production have been explored scientifically with some preliminary commercial applications being demonstrated in recent years [5]. Still, the effective production of MeOH from renewable sources or from carbon dioxide (CO_2) directly poses some process challenges and limitations. These limitations complicate the use of alternative feedstock and the efficient catalytic conversion of CO_2-rich synthesis gas (SynGas) to MeOH [6, 7]. In the process of defossilization of carbon-reliant sectors, catalyst- and process-strategies have to be applied to valorize alternative MeOH feedstock effectively for possible future commercialization of regenerative production routes.
This thesis comprises two research tracks that address different aspects and scales of process development for regenerative MeOH production on an industrial scale. In the first track, adapted γ-alumina (Al_2O_3)-sphere supported catalysts, for the heterogeneous catalytic conversion of high CO_2-content SynGas to MeOH are developed, investigated and proven. An array of different catalyst promoters is selected and tested for enhancing the activation properties of commercial catalyst compositions in hydrogenation of CO_2 towards MeOH formation. Catalyst samples are produced and deployed on a laboratory scale, characterizing both physical and chemical properties of the prototype catalysts as well as the conversion performance of the novel catalyst formulations. The results for research track one are included as two previously published contributions to international journals.
In the second research track of this thesis, an adapted process for converting high CO_2-content biogas towards SynGas with subsequent conversion to MeOH and water (H_2O) is designed and a test plant for demonstration and piloting of the integrated process is operated. The process applies a highly promoted prototype catalyst sample, which has previously been developed in part 1 of the thesis. The results of this chapter are included as a third, previously published journal article.

1.1. Methanol Production and Use

MeOH is primarily produced from NG (66%) and coal (33%) in multistage processes, with the conversion of SynGas to MeOH carried out in heterogeneous catalytic reactors exclusively at the current commercial scale [5]. It serves a wide range of industrial applications, with most MeOH being processed into downstream

products. The main uses include the production of formaldehyde (FAD), acetic acid, methyl-tert-butyl ether (MTBE), and dimethyl ether (DME).

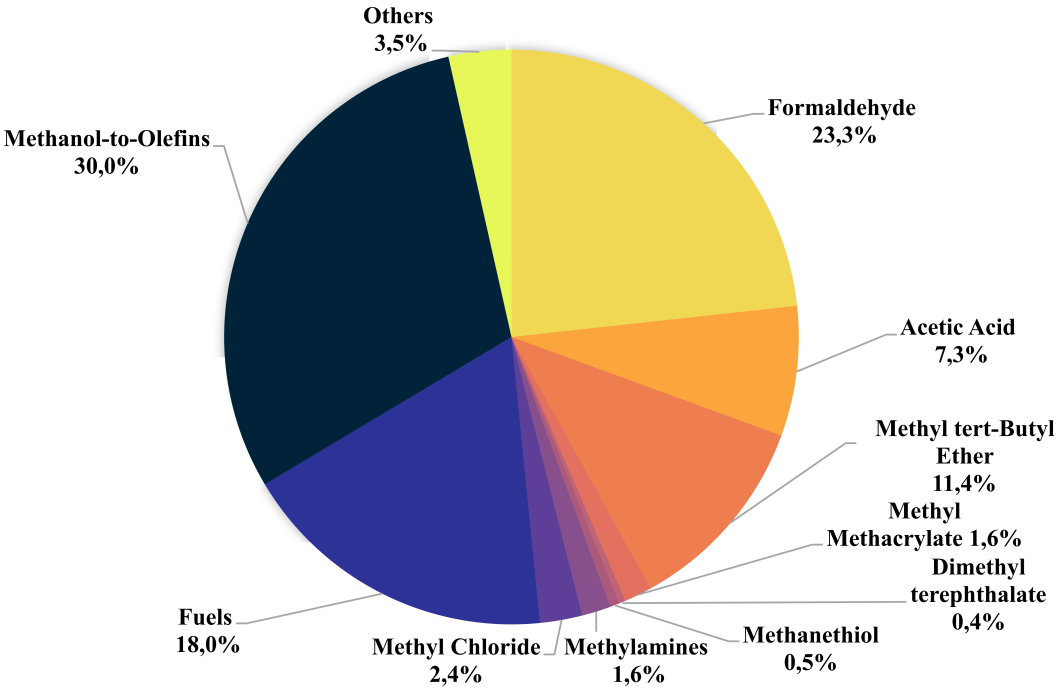

Figure 1.1.: Applications and associated percentages of global methanol use (2024). Own representation, data taken from [8].

The current global distribution of MeOH applications by weight for downstream products and applications is shown in Figure 1.1 [8]. Owing to its broad application spectrum and the increasing maturity of regenerative production pathways, MeOH has emerged as a pivotal element in the de-fossilization of energy- and resource-intensive sectors . Its global production network, established transport infrastructure, and flexibility as both a fuel and a substitute chemical feedstock render MeOH a key enabler for de-fossilization processes [9].
The simple single-carbon (C1)-molecule can be synthesized through a variety of adapted processes using regenerative or reclaimed carbon feedstocks, making it an attractive candidate as an alternative platform chemical and fuel, particularly for hard-to-abate sectors such as heavy-duty transport and advanced chemical production [10]. An overview of both traditional fossil and current as well as possible future regenerative production pathways is presented in Figure 1.2.
Thus, processes converting CO_2-rich SynGas streams from regenerative sources such as biomass or captured CO_2 directly to MeOH have gained increasing attention. Unlike conventional fossil-based processes, which utilize SynGas mainly comprised of carbon monoxide (CO) and hydrogen (H_2), CO_2 hydrogenation to MeOH requires adapted process conditions though, facilitating the effective activation of CO_2 through temperature adaptions, flow-rate control and deployment of enhanced catalysts. Valorization of alternative feedstock such as biomass and its derivatives for SynGas production is also under active development, while only few examples of commercial implementation have been realized to date [11]. Application of high CO_2-content, regenerative SynGas for MeOH production poses significant challenges for process design, as adaptations on multiple process levels are needed to accommodate for regenerative feedstocks. Moreover, many commercial catalysts—commonly based on copper oxide (CuO), zinc oxide (ZnO), and alumina (Al_2O_3) (CZA-catalysts)—are not sufficiently effective for large-scale CO_2 conversion to MeOH due to lacking activity

towards CO_2 conversion and long term stability [12].
Given these limitations, numerous development approaches have emerged in recent years. In the pursuit of a regenerative international "Methanol Economy," research has increasingly focused on advancing both processes and catalysts for the efficient utilization of CO_2-rich SynGas [13].

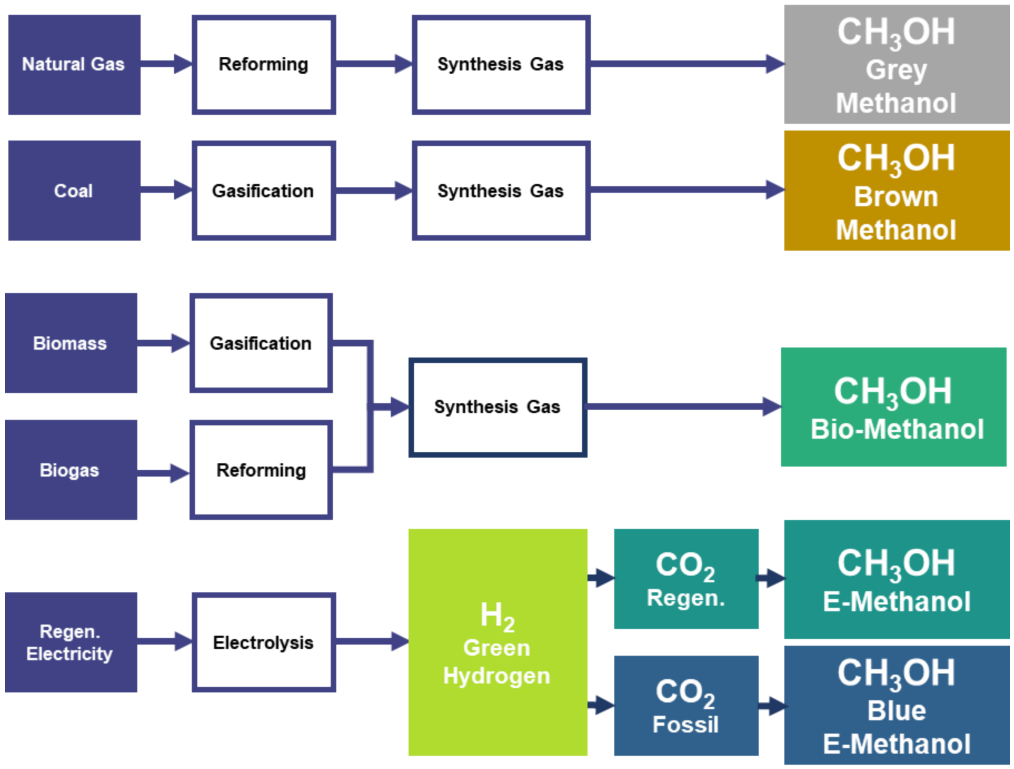

Figure 1.2.: General pathways for the production of both fossil and regenerative MeOH. Own representation, adapted from [14]

Progress hinges on catalyst innovations that improve both activation of the stable CO_2 molecule for hydrogenation to MeOH and catalyst resistance against oxidation, sintering and deactivation. While many studies report novel catalyst formulations or process-design models for regenerative MeOH production, few integrate catalyst development with real-world deployment in novel MeOH-synthesis approaches. Consequently, knowledge on the practical efficiency of new catalysts, as well as operational constraints and implementation hurdles in regenerative MeOH-production processes and the linking of multiple applications scales in MeOH synthesis, remains very limited.

1.2. Outline, Objectives and Structure of this Work

Based upon the identified knowledge gaps in current research and application, the present thesis addresses two interconnected challenges in sustainable MeOH synthesis in two linked research tracks: The first research track focuses on the development of efficient Cu/ZnO-based carrier catalysts for the hydrogenation of CO_2 and mixed CO_2/CO streams to MeOH. The catalyst formulations are prepared via incipient wetness impregnation (IWI) on high–surface-area γ-alumina supports. This approach aims to reduce the required quantity of catalytically active material for large-scale operation while maintaining, or surpassing, the performance of conventional co-precipitated catalysts. Comprehensive physico-chemical characterization, performance

testing, and kinetic investigation are carried out to establish quantitative links between catalyst formulation, structure, and mechanistic behavior over a broad range of operating conditions. In contrast to many recent studies that examine CO_2-only feeds, the present work explicitly evaluates catalyst performance in mixed CO_2/CO gas streams, representative of thermochemical processes and recycling-based synthesis systems close to carbon conversion equilibria.

The second research track develops a novel process for decentralized conversion of biogas to MeOH. The concept integrates autothermal biogas reforming (ATR) with subsequent catalytic synthesis of MeOH. A pilot plant is designed, constructed, and commissioned to demonstrate the process under industrially relevant conditions. The optimized catalyst formulation identified in research track one is implemented in the synthesis section of the pilot plant, enabling direct assessment of catalyst applicability in a regenerative biogas-to-MeOH system while linking the microscopic catalyst devolvement scale to real world condition, demonstration-scale process deployment.

Overall, this thesis aims to: (i) determine whether targeted promoter incorporation into supported Cu/ZnO coatings can yield catalysts with performance comparable to, or exceeding, commercial materials; (ii) elucidate structure–performance relationships governing CO_2- and CO conversion; (iii) quantify mechanistic effects through kinetic modeling with predictive capability; and (iv) evaluate the suitability of the developed catalyst system within an integrated, renewable biogas-to-MeOH-process. Following the aims and goals, several research questions are introduced that follow the previously introduced research track logic, relating either to the development and testing of supported catalyst formulations (track one, 1.1 - 1.3) or to the development and deployment of the biogas-to-MeOH process plant (track two, 2.1 and 2.2):

Question 1.1: To what extent can novel CuO/ZnO catalyst formulations, developed through controlled promoter selection and tailored preparation protocols, improve MeOH yield and selectivity from regenerative CO_2-rich SynGas compared to conventional co-precipitated CZA-catalysts?

Question 1.2: Which chemical and physical properties characterize these novel catalyst samples, and how do these properties quantitatively influence catalytic performance in CO_2 and mixed CO_2/CO-hydrogenation?

Question 1.3: Are the mechanistic effects of promoter incorporation quantifiable through kinetic reaction modeling, and do the resulting models provide predictive capability for MeOH-synthesis reactor performances?

Question 2.1: How can a technically viable process be designed for decentralized conversion of biogas to renewable MeOH, based on reforming and catalytic synthesis?

Question 2.2: How do the developed carrier catalysts perform when implemented under industrially relevant conditions in a biogas-to-MeOH pilot and what operational insights can be derived regarding their applicability in decentralized renewable MeOH production?

To address these research questions, the thesis is structured into eight chapters:

1. **Introduction** — Provides an overview of the research area, outlines the motivation and objectives, and presents the structure of the thesis.

2. **Theoretical Background and State of the Art** — Summarizes the scientific and technical foundations relevant to MeOH synthesis, biomass and biogas conversion, catalyst design, and reactor modeling. Reviews the current state of research and identifies the knowledge gaps addressed in this work.

3. **Experimental Setups and Methods** — Describes the preparation methods for catalyst samples, characterization techniques, laboratory reactors for CO_2 and CO_2/CO hydrogenation, kinetic evaluation procedures, and the design and operation of the biogas-to-MeOH pilot plant.

4. **Results of the Catalyst Screening** — Presents the results of the catalytic screening campaign, comparing the performance of a broad range of catalyst formulations and identifying the most promising promoted Cu/ZnO-based carrier catalyst for further study.

5. **"CO_2-to-Methanol over Cu/ZnO Infiltration Composites"** — Reproduces a peer-reviewed publication in *ChemCatChem*, reporting the fundamental physico-chemical properties of the selected catalyst system and its performance in CO_2 hydrogenation as well as selectivity and water-gas-shift behavior.

6. **"Industrial Methanol Synthesis over Cu/ZnO Infiltration Composites"** — Reproduces a peer-reviewed publication in *Applied Catalysis A: General*, extending the structural characterization extensively, evaluating performance in mixed CO_2/CO feeds, and deriving kinetic models to investigate mechanistic behavior and reactor-level implications.

7. **"Integrated H_2/O_2-Enhanced Biogas-to-Methanol Process"** — Reproduces a peer-reviewed publication in *Sustainable Energy & Fuels*, detailing the process concept, engineering design, commissioning and piloting of the integrated biogas-to-MeOH system, applying the optimized catalyst formulation previously characterized.

8. **Conclusion, Discussion and Outlook** — Synthesizes the findings of both research tracks, discusses scientific and practical implications, limitations of the presented findings and protocols and provides an outlook on future developments in catalyst and process design for renewable MeOH synthesis.

The structure of the thesis and the relation between the two research tracks are illustrated schematically in Figure 1.3.

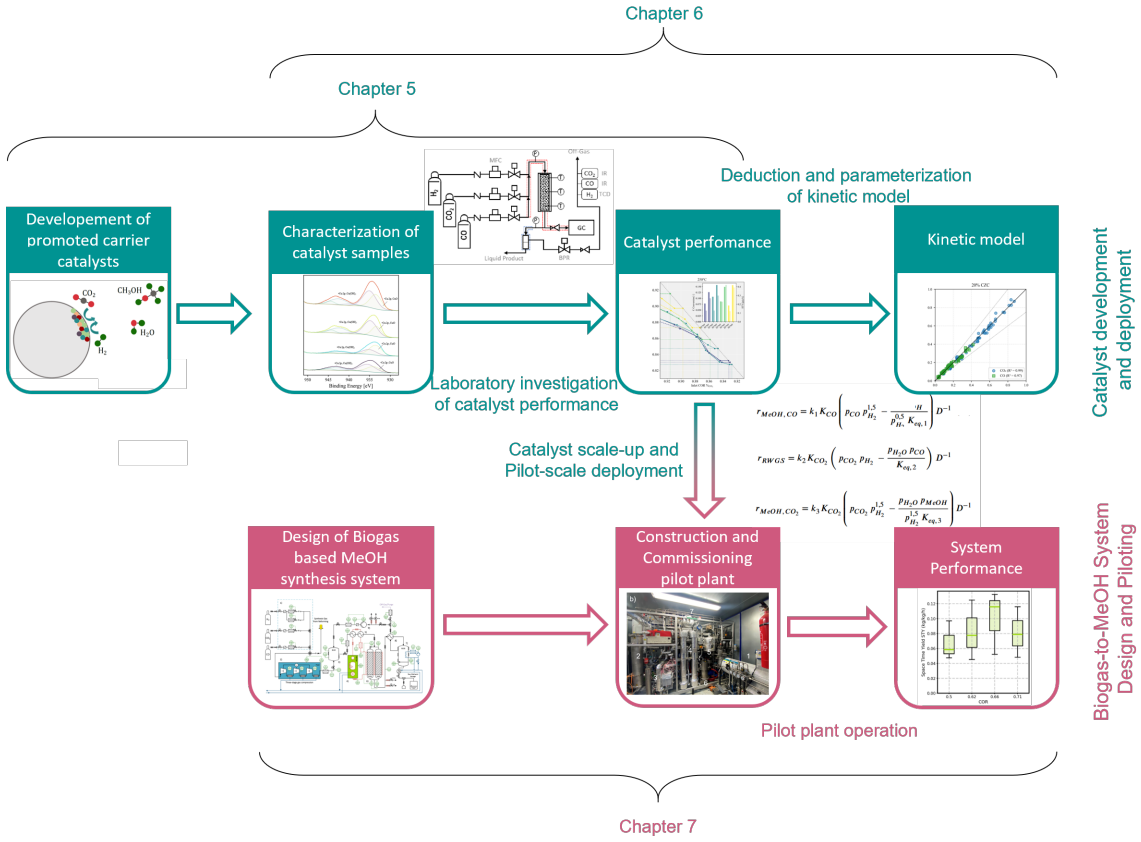

Figure 1.3.: Structure of this work and how the different research approaches relate to each other.

References

[1] Matthew W. Jones et al. “National contributions to climate change due to historical emissions of carbon dioxide, methane, and nitrous oxide since 1850”. In: *Scientific data* 10.1 (2023), p. 155. DOI: 10.1038/s41597-023-02041-1.

[2] Nathan Barrow et al. “Doubling the life of Cu/ZnO methanol synthesis catalysts via use of Si as a structural promoter to inhibit sintering”. In: *Science advances* 10.3 (2024), eadk2081. DOI: 10.1126/sciadv.adk2081.

[3] Seyed Shayan Tabibian and Mahdi Sharifzadeh. “Statistical and analytical investigation of methanol applications, production technologies, value-chain and economy with a special focus on renewable methanol”. In: *Renewable and Sustainable Energy Reviews* 179 (2023), p. 113281. ISSN: 13640321. DOI: 10.1016/j.rser.2023.113281.

[4] Mahdi Fasihi and Christian Breyer. “Global production potential of green methanol based on variable renewable electricity”. In: *Energy & Environmental Science* 17.10 (2024), pp. 3503–3522. ISSN: 1754-5692. DOI: 10.1039/D3EE02951D.

[5] Vincent Dieterich et al. “Power-to-liquid via synthesis of methanol, DME or Fischer–Tropsch-fuels: a review”. In: *Energy & Environmental Science* 13.10 (2020), pp. 3207–3252. ISSN: 1754-5692. DOI: 10.1039/D0EE01187H.

[6] Mads Valentin Bram et al. “Challenges in Power-to-X: A perspective of the configuration and control process for E-methanol production”. In: *International Journal of Hydrogen Energy* 76 (2024), pp. 315–325. ISSN: 03603199. DOI: 10.1016/j.ijhydene.2024.05.273.

[7] Hamilton Varela et al. “Renewable methanol and the energy challenge: The role of electrocatalysis”. In: *Current Opinion in Electrochemistry* 46 (2024), p. 101539. ISSN: 24519103. DOI: 10.1016/j.coelec.2024.101539.

[8] Methanol Market Services Asia. *Methanol Supply/Demand*. Ed. by Methanol Insitute. Washington D.C., 2024. URL: https://www.methanol.org/methanol-price-supply-demand/.

[9] Phillip Nathrath et al. “Methanol production in a sustainable, mild and competitive process: concept launch and analysis”. In: *Green Chemistry* 27.30 (2025), pp. 9268–9279. ISSN: 1463-9262. DOI: 10.1039/D5GC01307K.

[10] Felix Schorn et al. “Methanol as a renewable energy carrier: An assessment of production and transportation costs for selected global locations”. In: *Advances in Applied Energy* 3 (2021), p. 100050. ISSN: 26667924. DOI: 10.1016/j.adapen.2021.100050.

[11] Ephraim Bonah Agyekum, Paul C. Okonkwo, and Farhan Lafta Rashid. “Research on biomass energy and CO2 conversion to methanol: a combination of conventional and bibliometric review analysis”. In: *Carbon Research* 4.1 (2025). DOI: 10.1007/s44246-024-00179-0.

[12] M. B. Fichtl. “Efficient Methanol Synthesis Catalysts: Long-Term Stability and Deactivation Phenomena”. Dissertation. Munich: TUM, 8.12.2024. URL: https://mediatum.ub.tum.de/doc/1232028/1232028.pdf.

[13] Ujjal Mondal and Ganapati D. Yadav. “Methanol economy and net zero emissions: critical analysis of catalytic processes, reactors and technologies”. In: *Green Chemistry* 23.21 (2021), pp. 8361–8405. ISSN: 1463-9262. DOI: 10.1039/D1GC02078A.

[14] K. Seungwoo et al. *Irena Innovation Outlook: Renewable Methanol*. Ed. by Methanol Insitute. Masdar, 2021. URL: https://www.methanol.org/wp-content/uploads/2020/04/IRENA_Innovation_Renewable_Methanol_2021.pdf.

2. Theoretical Background and State of the Art

Catalytic MeOH production through hydrogenation of CO and CO_2 is based on the generation of SynGas from carbon feedstock, with multiple processes necessary for its effective conversion. These process steps often include feedstock pretreatment, SynGas generation, enhanced SynGas treatment and subsequent catalytic MeOH synthesis in single or multi-reactor setups following three major hydrogenation routes for the involved carbon oxides (equations 2.1 - 2.3) [1]. The complete hydrogenation reactions of CO and CO_2 (2.1 and 2.2) to MeOH are linked by the reverse water gas shift reaction (RWGS) (2.3), where CO and H_2O are generated in partial hydrogenation of CO_2:

$$CO + 2H_2 \rightleftharpoons CH_3OH \quad \Delta_r H^O = -90.8 \frac{kJ}{mol} \tag{2.1}$$

$$CO_2 + 3H_2 \rightleftharpoons CH_3OH + H_2O \quad \Delta_r H^O = -49.5 \frac{kJ}{mol} \tag{2.2}$$

$$CO_2 + 2H_2 \rightleftharpoons CO + H_2O \quad \Delta_r H^O = 41.2 \frac{kJ}{mol} \tag{2.3}$$

Originally, MeOH synthesis was carried out on a large scale applying zinc/chromium oxide (Zn/CrO_3)-catalysts utilizing SynGas fabricated from coal in a proprietary process by BASF (Badische Anilin und Soda Fabrik - 1920s) [2]. As early commercial catalysts applied in this process showed relatively low activity in SynGas conversion, very high pressures of about 300 bar and high synthesis temperatures of up to 400 °C were applied to achieve economically viable yields [3]. While known and available at the time, more active Cu/ZnO-based MeOH catalysts only became applicable after the later introduction of CH_4-reforming and advancements in gas scrubbing technologies, which allowed for the introduction of purified CO/H_2 mixtures into the MeOH synthesis process [4]. The application of these more active catalyst formulations, lead to the realization of much milder reaction conditions of approx. 100 bar and 300 °C, with higher reactor temperatures also leading to premature catalyst deactivation of the then deployed Cu/ZnO-formulations [5]. This low-pressure, low-temperature, high-yield process was introduced by ICI (Imperial Chemical Industries) in the 1960s. Shortly after, Lurgi introduced an optimized process approach, utilizing even lower temperatures and pressures (250 °C, 50 bar) laying the groundwork for today's commercial low-pressure MeOH-synthesis processes [5].

Commercial production plants today still utilize Cu/ZnO-based catalyst formulation, mostly produced through co-precipitation processes and pelleted for application in the solid bed reactors [6]. Industrial MeOH-production plants can reach nameplate capacities of up to 5.000 t/d today, resulting in single plant production volumes of up to 1,8 Mt/a at full load [7]. In de-fossilization attempts, further development focuses on the utilization of alternative and regenerative feedstock or CO_2 directly for the production of SynGas and process adaptions for the more effective conversion of CO_2-rich SynGas to MeOH.

The following section covers the state of the art in SynGas generation from different feedstocks and the

conversion of different SynGases to MeOH in greater detail. Conventional catalyst systems are introduced and the necessity for further process and catalyst development as well as their linking is deduced. Mathematical models for description of kinetic phenomena over catalysts are outlined and modeling of compounded production processes is described.

2.1. Synthesis Gas Production

SynGas for MeOH synthesis is usually produced from NG or coal in reforming or gasification processes [8]. Different production methods for the $CO/CO_2/H_2$ mixture yield varying compositions and inherently produce varied impurities or inert gas fractions, that are able to impact the subsequent conversion to MeOH. SynGas for MeOH synthesis is characterized by two major indicators, that describe the proportions of CO and CO_2 to each other (COR - carbon oxide ratio) and the stoichiometric availability of H_2 (SN - stoichiometric number), with SN = 2.0 indicating perfectly stoichiometric availability of H_2:

$$SN = \frac{y_{H_2} - y_{CO_2}}{y_{CO_2} + y_{CO}} \tag{2.4}$$

$$COR = \frac{y_{CO_2}}{y_{CO_2} + y_{CO}} \tag{2.5}$$

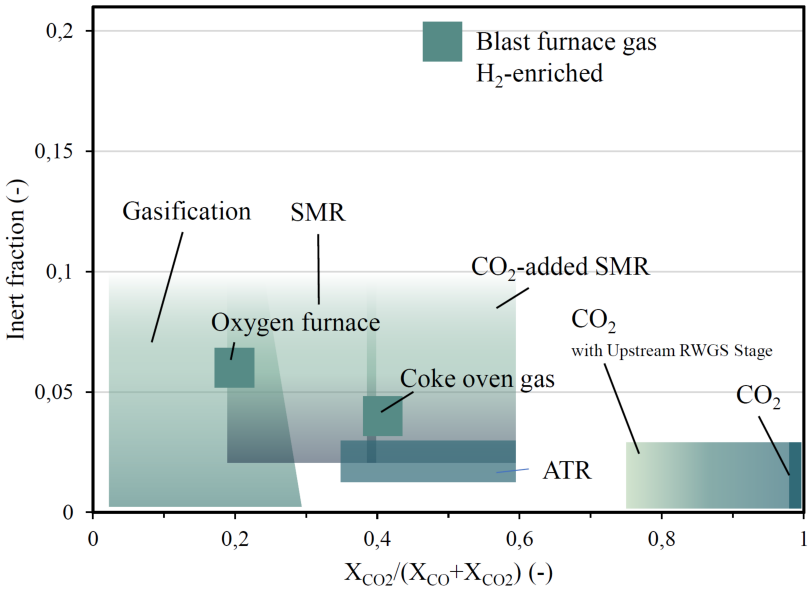

Figure 2.1.: SynGas production pathways and expected COR for conventional and selected regenerative pathways. Own representation, adapted from [9]

The wide possible range of applications for conventional SynGas-production, contemporary approaches for regenerative MeOH production and the direct use of CO_2 as carbon feedstock lead to a wide possible array of COR as well as multiple pathways for introduction of unwanted inert gas fractions into contemporary MeOH-synthesis systems. This can necessitate further upgrading of SynGas or the introduction of additional H_2 into the MeOH-synthesis process to adapt gas compositions towards suitable conditions [9]. A general overview

over different gas compositions and possible inert gas fractions yielded by common SynGas applications is given in figure 2.1.

Conventional approaches for conversion of fossil feedstock to SynGas such as coal gasification or steam methane reforming (SMR) of NG yield low COR, high CO-content SynGas. Applications for the recycling of CO_2 and partially or fully renewable feedstock conversion such as CO_2-added steam methane reforming (SMR) or the direct application of sequestrated CO_2 deliver high COR, with CO_2 representing the major carbon-oxide source for MeOH formation, necessitating process adaptions and catalyst optimization. An overview over common SynGas-applications, process design and inherent application properties of conventional gasification or reforming processes are described in the following sections 2.1.1 and 2.1.2.

2.1.1. Gasification Processes

Coal gasification for SynGas generation is especially common in China and is generally carried out in three competing gasifier types: Fixed Bed, fluidized Bed and entrained bed gasifiers [10]. Decomposition of carbon containing feedstock and reactions thereof with steam or O_2 is usually conducted at high temperatures of 800-1.200 °C and atmospheric pressure in one of these reactor types [11]. Coal or other carbon containing feed stock is fed into the reactor with steam and/or an oxidative agent and reacts at high temperatures and forced convection to form a CO- and H_2-containing product gas. Basic schematic illustrations of gasification reactors for industrial production of SynGas from coal are given in figure 2.2. Recently, plasma gasification has additionally been under investigation for energy efficient hydration of elementary carbon and possible future process addition in converting alternative feedstock to SynGas.

On a microscopic level, coal gasification involves the thermal breakdown of solid carbonaceous material into a mixture of gases, primarily CO and H_2, through a series of heterogeneous reactions between solid carbon and gaseous reactants. When coal is exposed to the high temperatures common in industrial gasification as well as controlled amounts of O_2 and H_2O-steam, its complex organic structure decomposes.

Initially, pyrolysis releases volatile compounds, leaving behind char in the reaction complex. This char then reacts with steam (equation 2.8) and CO_2 (equation 2.9), while partial oxidation of the involved carbon (equation 2.6) provides supplementary heat for the endothermic reactions. At the atomic scale, these reactions predominantly take place on the surface of carbon particles, where adsorbed species dissociate and recombine, progressively converting the solid feedstock particles into gaseous products and ultimately generating SynGas [12]. The overall reaction scheme includes oxidation (equations 2.6 and 2.7) and hydration of elementary carbon (equation 2.7) contained in coal, the reaction of carbon with CO_2 to form CO (equation 2.9) as well the the water gas shift reaction (WGS) (previously introduced in equation 2.3):

$$2C + O_2 \rightleftharpoons 2CO \quad \Delta_r H^O = -110.6 \frac{kJ}{mol} \tag{2.6}$$

$$C + O_2 \rightleftharpoons CO_2 \quad \Delta_r H^O = -393.8 \frac{kJ}{mol} \tag{2.7}$$

$$C + H_2O \rightleftharpoons CO + H_2 \quad \Delta_r H^O = 131.3 \frac{kJ}{mol} \tag{2.8}$$

$$C + CO_2 \rightleftharpoons 2CO \quad \Delta_r H^O = 172.5 \frac{kJ}{mol} \tag{2.9}$$

The introduced gasifier types aim to maximize intermixing and contact of the different phases as well as stratification of educt-product layers inside the reactors, for optimal generation and separation of produced SynGas from the educt streams. Current efforts in de-fossilization of SynGas reliant processes concentrate on reactor adaption towards the use of sustainable feedstock in gasification. Especially lignocellulosic biomass is herein being discussed as possible base for large-scale applications [13]. As most biomass has higher hydrogen to carbon ratios than coal and water content is usually elevated, gasification or pyrolysis of it can produce more suitable SynGas compositions than coal gasification processes, while feedstock impurities and irregularities in regenerative feedstock composition challenge downstream processes through introduction of volatile SynGas contaminants [14].

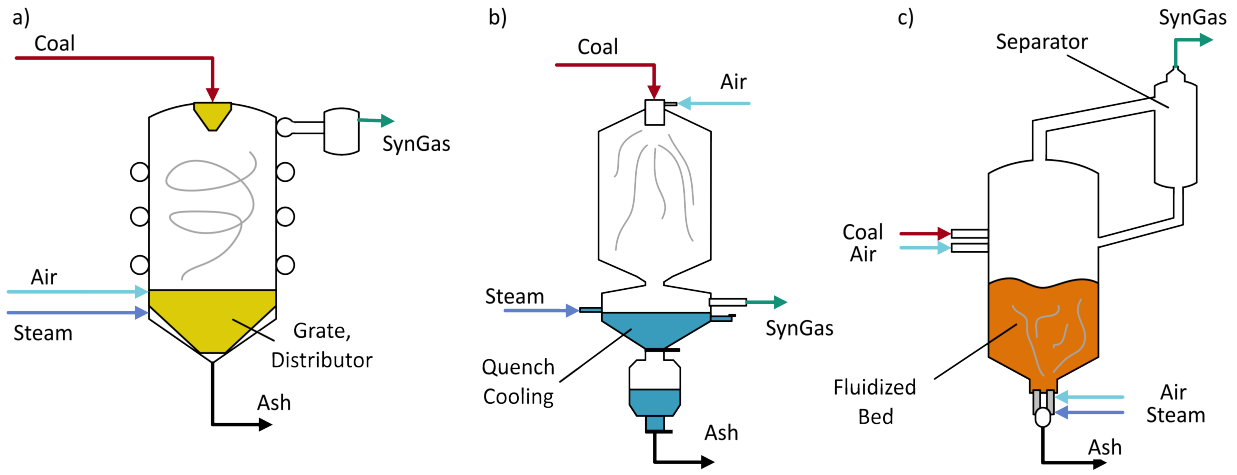

Figure 2.2.: Schematic image of different gasification reactors. a) Updraft fixed bed gasifier b) Entrained bed gasifier c) Fluidized bed gasifier. Own representation, contents adapted from [10, 11]

2.1.2. Reforming Processes

Most of the MeOH produced on an industrial scale today originates from production plants utilizing SynGas from NG reforming. In industrial application, NG can be converted to high H_2-content SynGas through several different reforming processes, utilizing Nickel (Ni) or noble metal catalysts, often supported on alumina [15]. On a commercial scale, different variations of methane reforming (MR) are applied, that can be distinguished by their use of different methods of CH_4-dehydration or oxidation for obtaining SynGas. Four common variation of MR are illustrated in figure 2.3. Reforming of CH_4-containing gases follows a scheme of four different general reactions, depending on the involvement of H_2O in SMR-reactions or O_2 in (partial-) oxidation of CH_4 (2.10 - 2.13):

$$CH_4 + H_2O \rightleftharpoons CO + 3H_2 \quad \Delta_r H^O = 206.0 \frac{kJ}{mol} \tag{2.10}$$

$$2CH_4 + O_2 \rightleftharpoons 2CO + 4H_2 \quad \Delta_r H^O = -71.0 \frac{kJ}{mol} \tag{2.11}$$

$$CO + H_2O \rightleftharpoons CO_2 + H_2 \quad \Delta_r H^O = -41.2 \frac{kJ}{mol} \tag{2.12}$$

$$CO_2 + CH_4 \rightleftharpoons CO + 2H_2 \quad \Delta_r H^O = 247.0 \frac{kJ}{mol} \tag{2.13}$$

The effectiveness of NG conversion to SynGas depends on a variety of different process parameterizations, with feed-composition, the ratio of dosed steam to gas (steam to carbon ratio, S/C (equation 2.14), the involvement of O_2 or air as oxidizing agent and the fuel to oxygen ratio (λ, equation 2.15) as well as applied catalysts, gas velocities and pressures applied to the process [16].

$$S/C = \frac{\dot{n}_{H_2O,feed}}{\dot{n}_{CH_4,feed}} \tag{2.14}$$

$$\lambda = \frac{\dot{n}_{O_2,feed}}{2\,\dot{n}_{CH_4,feed}} \tag{2.15}$$

The most commonly applied processes for conversion of NG to SynGas are listed below, all of which are available commercially in different versions of their application:

1. Steam Methane Reforming (SMR) is the most widely applied industrial process for large-scale H_2 and SynGas production [17]. The process utilizes the endothermic catalytic reaction of CH_4 with steam at elevated temperatures (700–1100 °C) and moderate to high pressures (typically 1–3 MPa) over nickel-based catalysts [18]. Heat required for the strongly endothermic reforming step is typically supplied by burning additional fuel in external furnaces. SMR is usually carried out in tubular fixed bed reactors and utilizes high S/C ratios above 2 and up to 4.5, thus necessitating the additional combustion of large amounts of fuel for production of high pressure, critical steam [19]. Gas velocities through the reforming reactor are commonly set above 10.000 h^{-1} and up to 50.000 h^{-1}, with lower GHSV contributing to more complete conversion ratios of educt hydrocarbons, while higher GHSV generally achieving better hourly SynGas yield [20]. GHSV can be balanced with SN and reactor pressure to achieve high conversion ratios while maintaining high reactor throughput in industrial setups. SMR of NG usually yields favorable SynGas compositions, with achievable SN often times above 2.0 and COR optimal for efficient conversion of SynGas to downstream value-added products like MeOH. For enhanced performance, Ni-catalysts are often doped with noble metals to improve catalyst stability and its reactivity towards decomposition of CH_4 [19]. SMR is highly efficient but also carbon-intensive, as significant CO_2-emissions are inherent to the process due to the necessity of the auxiliary fuel firing for temperature and steam management [16].

2. Partial oxidation reforming (POX) can be conducted as catalytic or auto-catalytic process in which CH_4 reacts with a sub-stoichiometric amount of O_2 to produce SynGas. It is carried out either in cooled, fixed bed reactors (catalytic) or in entrained flow reactor types (auto-catalytic) [23]. The principal reaction is highly exothermic and is operated at high temperatures (typically 1100–1500 °C), with nickel- or noble-metal-based catalysts employed in catalytic POX to improve selectivity and enable lower operating temperatures [24]. Compared to SMR, POX usually requires no external heat supply due to its intrinsic exothermicity, enabling compact reactor designs and rapid startup. It typically yields lower H_2/CO (1.8 - 2.2) ratios than SMR, due to the missing involvement of H_2O in the reaction scheme [25]. Oxygen is usually dosed as an effective oxidation agent of CH_4, with λ usually set in a range of 0.2 - 0.4 in POX of NG and CH_4 [21]. POX is usually carried out utilizing high GHSV with effective temperature control of the oxidative reaction scheme relying on high throughput. Pilot and industrial scale applications of POX have been reported to apply GHSV of up to 400.000 h^{-1}, with some commercial plants utilizing GHSV well above 100.000 h^{-1} [26, 27].

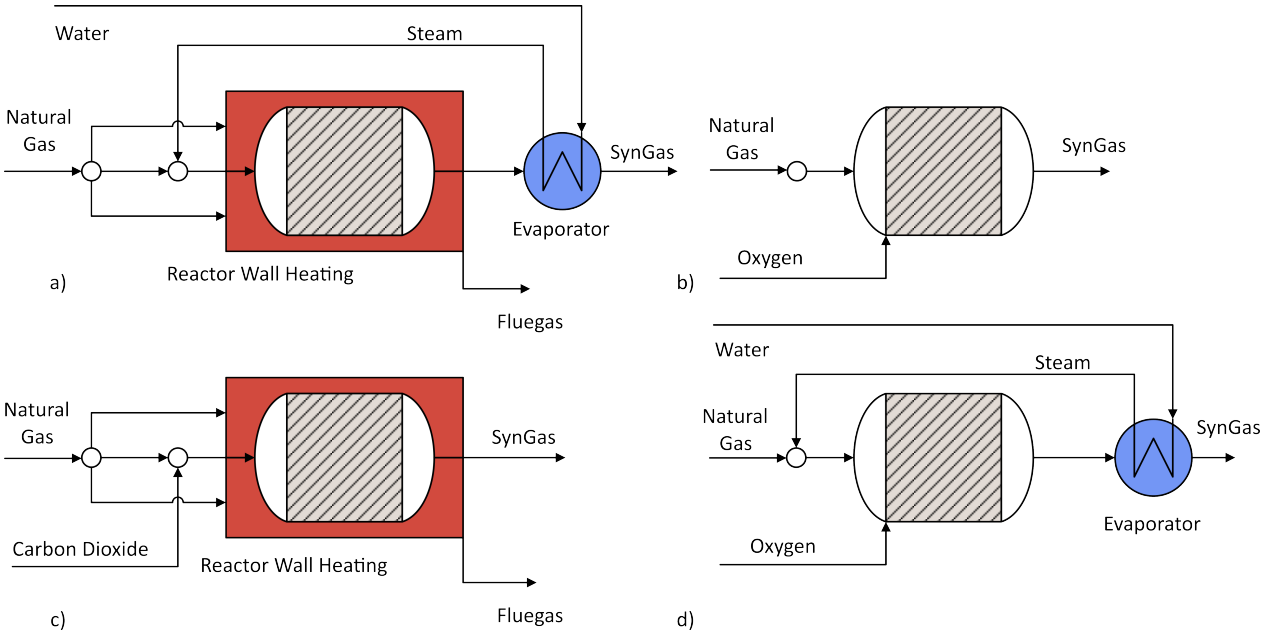

Figure 2.3.: Schematic image of different NG reforming approaches. a) Steam Methane Reforming b) Partial Oxidation Reforming c) Dry Methane Reforming d) Autothermal Reforming. Own representation, flow sheets adapted from [21, 22].

Due to the high process temperatures and the predisposition of the oxidative reactions of O_2 with CH_4 to occur without additional catalyst involvement, hot-spot generation in the catalyst bed and soot formation are common obstacles in stable catalytic system operation, as they challenge catalyst stability and subsequent SynGas conversion processes [28]. Additionally, the introduction of pure O_2 instead of air is necessary when coupled to downstream processes, as introduction of N_2 into the process when applied with air as oxidizing agent negatively effects energy efficiency of these [25]. This represents an additional economical hurdle in large-scale system viability.

3. Dry Methane Reforming (DMR) involves the direct reaction of CH_4 with CO_2 to produce SynGas with low H_2/CO ratios. The main reaction is strongly endothermic, requiring high operating temperatures (700–950 °C) and typically employing Ni-based catalysts in tubular fixed bed reactors [29]. DMR simultaneously utilizes two greenhouse gases for generation of SynGas, opening up possible future environmental applications for conversion of both molecules to higher value SynGas. The use of biogas, a mixture of regeneratively produced CO_2 and CH_4 from biomass, as direct feedstock for DMR constitutes a possible sustainable path for SynGas generation. The process suffers greatly from thermodynamic limitations compared to SMR as well as strong tendencies for carbon deposition and soot generation, leading to challenges in catalyst stability and lifetime [30]. DMR is carried out at reactor pressures up to 20 bar to improve throughput and SynGas yield [31]. Concerning gas velocity, GHSV above 10.000 h^{-1} and up to 120.000 h^{-1} are applied to balance kinetic limitations of the DMR reaction [32]. The produced SynGas (H_2/CO approx. 1) is particularly suitable for certain downstream applications such as Fischer–Tropsch synthesis of long-chain hydrocarbons, but doesn't contain sufficient H_2 for direct use in MeOH synthesis [33].

4. Autothermal Reforming of CH_4 (ATR) combines the approaches of SMR and POX. It is carried out in fixed bed reactors utilizing doped or promoted Ni- or noble metal catalysts. The required heat for the

endothermic catalytic reaction of CH_4 and H_2O to H_2 and CO is generated through in-situ catalytic partial oxidation of some of the feed CH_4, making external heat supply to the process obsolete. This benefits overall energy efficiency of the process greatly, but poses significant challenges in process design and control [34]. It is carried out at temperatures between 700 - 900°C with higher temperatures resulting in increased soot formation and decreased stability of steady state reaction schemes. GSHV above 10.000 are usually applied and effective conversion ratios can be achieved at up to 100.000 h^{-1}, with reactor pressure commonly elevated above atmospheric and pressures of up to 30 bars applied industrially [35, 36]. Effectiveness of ATR is additionally affected by S/C as well as the λ chosen, making system control challenging as the resulting system contains a multitude of inter-dependent variables that are able to influence yield and system stability. Common applications of commercial ATR plants have S/C ranging between 1.5 and 3.5 and λ between 0.15 and 0.4 [36]. Due to the involvement of O_2 as oxidizing agent for CH_4, the resulting SynGas contains increased amounts of CO_2, influencing the suitability of the produced SynGas for downstream processes such as MeOH synthesis [37].

Current research focuses mainly on the adaption of reforming processes and the development of advanced catalysts to accommodate for the application of bio-methane or biogas. This poses a number of different obstacles, as the idle, hard to activate and high heat capacity molecule CO_2 is introduced into the reforming system and has to be accounted for on a process as well as catalytic level [38, 39].

2.2. Process Technology for Thermo-catalytic Production of Methanol

Conventional, industrial MeOH synthesis is carried out utilizing SynGas made up of mainly CO and H_2. Conversion of the make-up gas (MUG) is achieved through application of efficient catalyst systems, usually applied in fixed bed tubular reactors. Still, single reactor-pass conversion of the MUG usually does not exceed 30-50%, necessitating the application of SynGas recycling loops [40]. Product gas exiting the reactor set-up is therefore cooled, liquid product condensed and discharged in a high pressure flash and unconverted SynGas recycled through compression, heating and introduction back into the synthesis system in most industrial applications [41]. Here, recycled gas is mixed with fresh SynGas from the upstream processes such as gasification of reforming, usually achieving ratios of $\frac{\dot{V}_{recycle}}{\dot{V}_{feed}}$ 2:1 to 5:1 [9]. Schematic representations of commercial MeOH applications utilizing both coal and NG as feedstock with essential common system components are given in figures 2.4 and 2.5. Generation of MeOH relies on the hydrogenation of both CO_2 and CO contained in the MUG. Both reactions require catalysts (usually CZA) for the effective and controlled conversion towards MeOH, as chemical equilibria favor other stable molecules such as CH_4 without the agency of tuned catalyst systems under the reaction conditions applied in commercial MeOH production [42]. Effectiveness of MeOH synthesis from SynGas over CZA-catalysts depends on a variety of operational parameters that balance thermodynamic constraints, kinetic limitations and economic considerations, all of which influence conversion on a microscopic level as well as system effectiveness on a process level. The most important process variables and tuneable operational parameters are listed below with short introductions into their effects on MeOH synthesis on both levels.

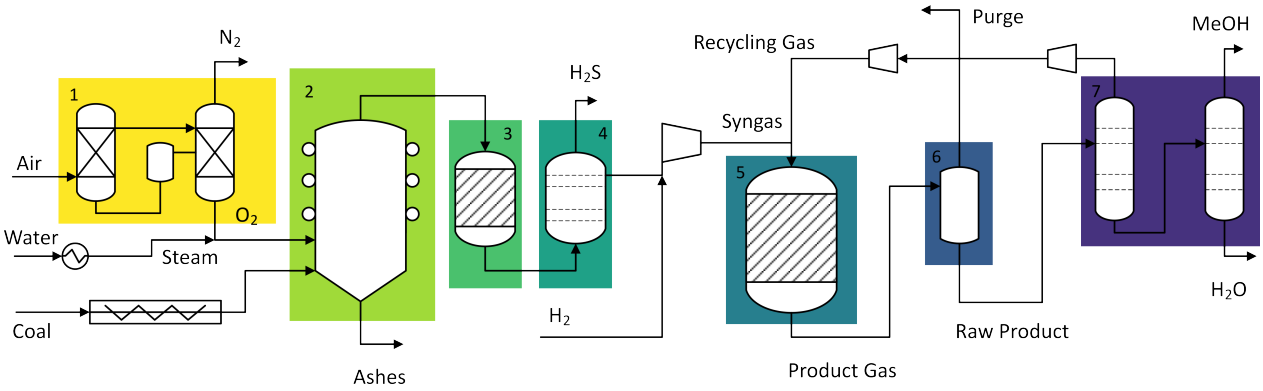

Figure 2.4.: Schematic representation of a MeOH synthesis plant utilizing coal as carbon feedstock. 1) Air separation unit 2) Gasifier 3) Water Gas Shift (WGS) Reactor 4) Product Gas Scrubbing 5) Methanol Reactor 6) Gas Liquid Separator 7) Low pressure separation and Distillation. Own representation, based on flowsheet by [43, 9, 44]

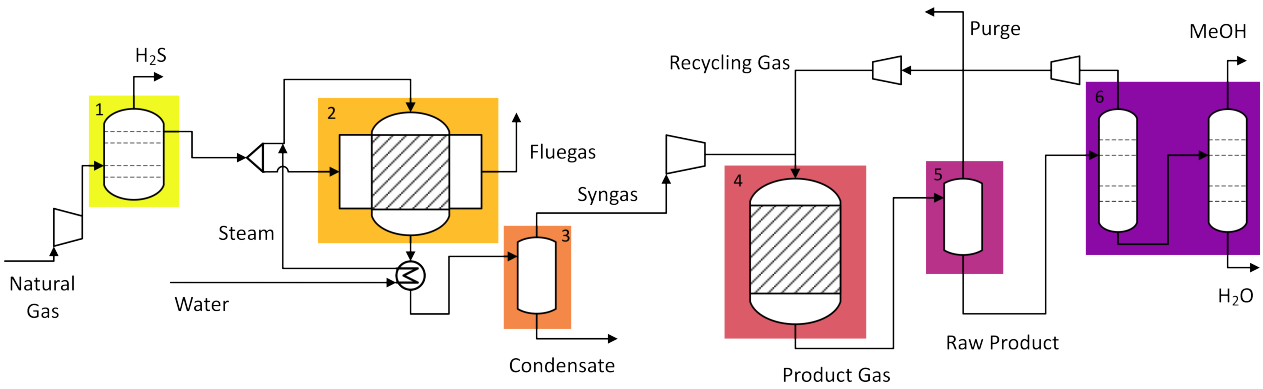

Figure 2.5.: Schematic representation of a MeOH synthesis plant utilizing NG as carbon feedstock. 1) Sulfur Removal 2) Reformer with partial feed combustion 3) Gas Liquid Separator 4) Methanol Reactor 5) Gas Liquid Separator 6) Low pressure separation and Distillation. Own representation, based on flowsheet by [9, 45, 46]

Stoichiometric Number

H_2 supply or SN (equation 2.4) for complete conversion of all carbon oxides equals 2.0, but industrial operations typically employ values of 2.05-2.20 to ensure slight H_2 excess. This ensures full catalyst reduction (especially CuO-reduction to metallic Cu-species) and maintains optimal selectivity while minimizing additional H_2 costs [40]. Values significantly above 2.2 can reduce carbon efficiency due to the volumetric reactor occupation of H_2 and reduced CO/CO_2 partial pressures, while SN below 2.0 limit conversion and promote water-gas shift activity [9]. The management of SN poses a major economic obstacle in MeOH synthesis based upon regenerative and CO_2-rich SynGas applications, as these approaches typically produce MUG with substoichiometric SN and high COR and additional H_2 has to be supplied to the process for realization of stoichiometric or slightly super stoichiometric SynGas compositions.

Carbon oxide ratio

SynGas COR significantly affects MeOH synthesis on different levels:
Catalyst activity and stability in CZA-formulations is significantly impacted by COR, as it influences the preferred mechanistic route and thus requires different concentration of active sites for effective conversion of the different reactants [47]. While the detailed reaction mechanisms and the influence of different metal active

sites in MeOH formation for both CO and CO_are still disputed, CO_2 is mostly considered to be the primary carbon source in industrial synthesis lately [48]. Conventional, fossil MeOH-synthesis process designs usually maintain 2-10% CO_2, with pure CO_2 sometimes being dosed into high CO-content SynGas streams for enhanced conversion efficiency and COR balancing [49].
The presence of CO_2 is assumed to kick-start multiple reaction mechanisms, with some active sites oxidized through the excess oxygen in CO_2 functioning as pivotal points in CO adsorption and its efficient, stable conversion to MeOH [48]. However, excessive CO_2 concentrations lead to stoichiometric co-production of H_2O, which accelerates catalyst deactivation through crystallite growth, zinc migration and oxidization of metallic active sites, posing a number of catalytic and process constraints in converting regenerative, high CO_2-content SynGas to MeOH over conventional CZA-catalysts [41]. CO_2-rich SynGas streams thus also challenge industrial processes economically, as the high H_2O content liquid product necessitates energy intensive separation and product upgrading.

Reactor pressure

Reactor pressure influences both equilibrium conversion and reaction kinetics. Industrial processes operate at 50-100 bar today, and modern plants typically employ 50-80 bar to optimize the trade-off between comprressor capital costs, operational costs and MeOH yield [50]. Higher pressures shift the equilibrium toward MeOH formation according to Le Chatelier's principle, as the synthesis involves a net reduction in molar volume. Additionally, elevated reactant partial pressure increases the concentration of said reactants over the catalyst surface, enhancing reaction rates kinetically. Pressure in MeOH plants is controlled through feed compressor exit pressure in SynGas- and MUG-compression as well as gas-purge regulation. Latter is necessary for controlling the accumulation of excess inert components such as CH_4, N_2, DME and Formaldehyde (FAD) in the recycle gas stream stemming from byproduct formation in the reactors as well as partial stream introduction through upstream processes [1]. The typical equilibrium conversion of SynGas over CZA-based catalyst over different temperature and pressure ranges is represented in figure 2.6.

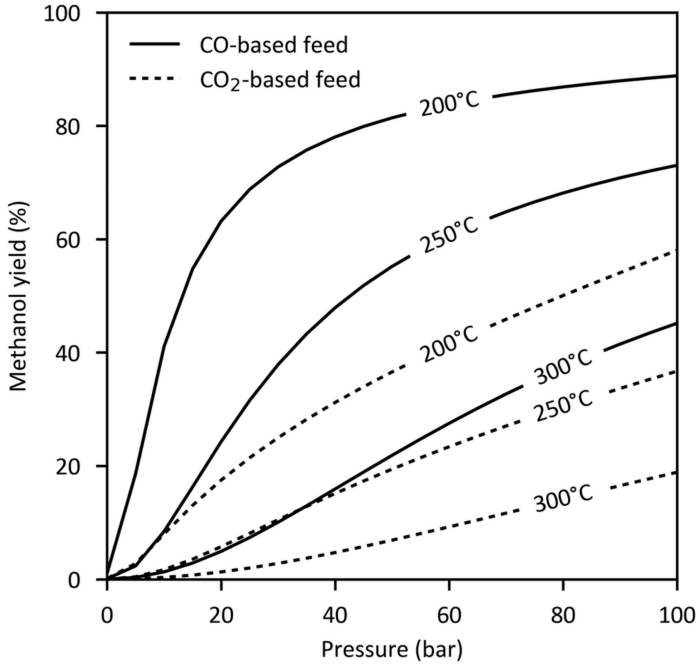

Figure 2.6.: Equilibrium conversion of different CO- and CO_2-based reactant feeds under varying pressure and temperature. Used with permission from [40].

Gas velocity

Gas Hourly Space Velocity (GHSV) and residence time are inverse parameters that determine the contact time between reactants and catalyst and the hold-up duration of reactant gas in the reactor.

$$GHSV = \frac{\dot{V}_{Syngas}}{V_{Reactor}} \tag{2.16}$$

Industrial reactors typically operate at GHSV values of 3,000-15,000 h^{-1}, corresponding to residence times of a few seconds to small fractions of a second [40]. In commercial MeOH synthesis, lower GHSV (longer residence time) increases per-pass conversion but reduces overall productivity and increases the risk of longer chain byproduct formation such as ethanol (EtOH) and DME, while excessive GHSV can lead to incomplete conversion and reduced selectivity [51]. Additionally, high GHSV is penalized through equally high pressure losses in tubular reactors [52]. In industrial MeOH synthesis, GHSV is a compounded value, relating to both fresh SynGas compression into the MeOH loops as well as the gas recycling rate. In modern process applications, where single-pass reactor conversions reach 30-50%, recycling ratios of $\dot{V}_{Syngas}/\dot{V}_{Recycling} = 0.2 - 0.5$ are common with overall GHSV often set close to 10.000 h^{-1} [9].

Temperature management

Temperature plays a crucial role in MeOH synthesis and is typically maintained between 200-300°C in modern, low-pressure process approaches. Lower temperatures favor MeOH formation over byproducts thermodynamically and mechanistically, as the synthesis reactions are exothermic and Cu/ZnO-based catalysts tend to produce CO, CH_4 and higher alcohols at elevated temperatures. However, temperatures below 200 °C result in reaction rates insufficient for commercial production of MeOH, while temperatures exceeding 300°C accelerate catalyst sintering [53]. For temperature control of the exothermic reaction scheme, different approaches for reactor design are applied to manage reactor temperature across the entire reactor length and to harness excess thermal energy from the exothermic MeO -formation reactions for application in other related processes such as raw product distillation or SynGas pretreatment. Modern reactors for SynGas conversion to MeOH are dominated by quasi-isothermal fixed bed designs, that utilize boiling water or steam cooling for thermal management [40].

Reactor Design

Reactor temperature and GHSV through the reactor bed are both controlled by reactor design and proportions, with different process approaches applying various, proprietary reactor designs for different technology providers on the market.

In fixed bed reactor types using multiple, parallel single reactor tubes in one combined reactor setup and where catalyst is usually loaded as pellet bulk, the ratio between reactor diameter and catalyst pellet diameter play a crucial role in ensuring homogeneous flow, minimizing transport limitations in reactant adsorption and product desorption as well as ensuring sufficient reactor cooling for temperature management. Industrial reactor designs usually apply pellet diameter (D_{Pellet}) to reactor inner diameter ($D_{R,inner}$) ratios of 1:7 - 1:10 [54, 55]. For temperature management, different approaches for reactor temperature control are applied. Most commonly multi-tubular-reactors utilizing boiling water reactor wall cooling are applied, initially introduced in Lurgi's proprietary process design (figure 2.7 a]) [40]. In current industrial MeOH synthesis, different alternative reactor designs are common, applying quasi-isothermal or adiabatic reactor concepts. An overview

over the common reactor types and their respective applicators and marketers is given in figure 2.7.

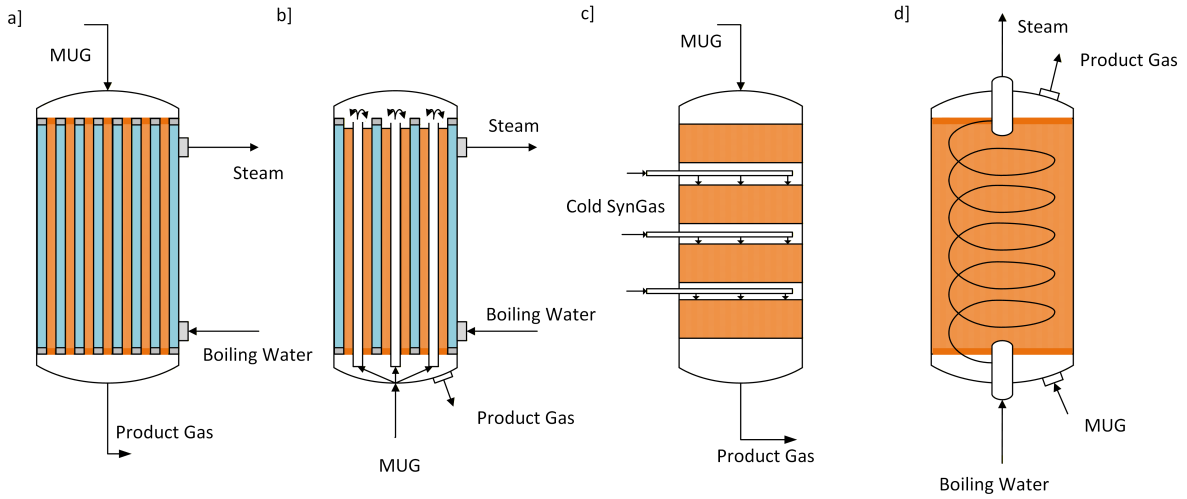

Figure 2.7.: Common reactor Types in industrial MeOH Synthesis and their technology suppliers. Own representation, contents adapted from [40] and [56]. a] Lurgi tubular reactor (AirLiquide today), b] Counter flow isothermal with steam cooling (applied by Mitshbishi Chemical) c] Adiabatic reactor design with intermediate SynGas mediated cooling (Applied in principle by Toyo and Clariant) d] Quasi-isothermal with internal cooling (Linde).

2.3. Contemporary Approaches and Limitations in Regenerative Methanol Synthesis

Recent research around regenerative MeOH production can be divided into two parallel streams that occasionally overlap: the direct hydrogenation of CO_2 with renewable H_2, commonly called “power-to-methanol” (P2M) or e-methanol, and routes that derive MeOH from biomass, biogas or other biogenic/waste carbon via gasification or reforming and downstream synthesis. Both approaches aim to replace fossil carbon in the MeOH value chain, but they differ in their feedstock characteristics, process requirements, and practical limitations. In both cases, the literature mainly discusses catalyst performance under ideal feed conditions, the equilibria and heat-management limits of the relevant reactions, the cost and availability of clean H_2 and carbon sources, and the system-level impacts of operating dynamically with variable availability and price of renewable electricity.

2.3.1. Direct Production of Methanol from CO_2

Direct CO_2 hydrogenation remains the most widely studied, alternative production route, linking large-scale CO_2-capture and electrolytically generated H_2. CO_2 is obtained either through separation from industrial CO_2-rich process streams such as flue gases, biogas or filtered directly from air (direct air capture - DAC), compressed and mixed with appropriate amounts of H_2 to form a synthetic SynGas stream for subsequent conversion to MeOH. As current CZA-catalysts favor the generation of CH_4 and other hydrocarbons at elevated temperatures, low reaction temperatures and high pressures are favored in early industrial applications. A major obstacle in direct CO_2 conversion is the activity of catalysts towards the RWGS reaction, reducing single pass reactor conversion to MeOH and elevating H_2O partial pressure along the reactor length [9]. For effective conversion of CO_2, a compromise is therefore necessary on both a process as well as a catalyst/kinetic level

(moderate temperatures, elevated pressures), which relies on efficient recycle gas and process or utility stream heat integration to achieve acceptable overall carbon conversion and sustainable catalyst longevity [57]. A scheme comparing the process streams of CO_2 hydrogenation plants to common industrial production facilities and the associated differences in operational parameters and gas compositions are given in figure 2.8. The common industrial CZA-catalyst family continues to be the foundation for most CO_2-based MeOH studies and early industrial applications, but its limitations in conversion of CO_2-rich SynGas are widely documented [58]. H_2O produced during CO_2 hydrogenation participates in site oxidation and sintering of Cu particles; long-term deactivation by sintering and oxidation under realistic $CO_2/H_2/H_2O$ atmospheres has also been shown to significantly shorten the working lifetime of standard CZA-catalysts, prompting intensive work on mitigation strategies and alternative formulations. Recent experimental studies therefore pursue two complementary directions: (i) engineering the CZA family to increase water tolerance, reduce CO_2-reduction activity to CO and stabilize the copper phase through promoters and supports and (ii) developing fundamentally different active phases that are inherently more tolerant to CO_2/H_2O environments.

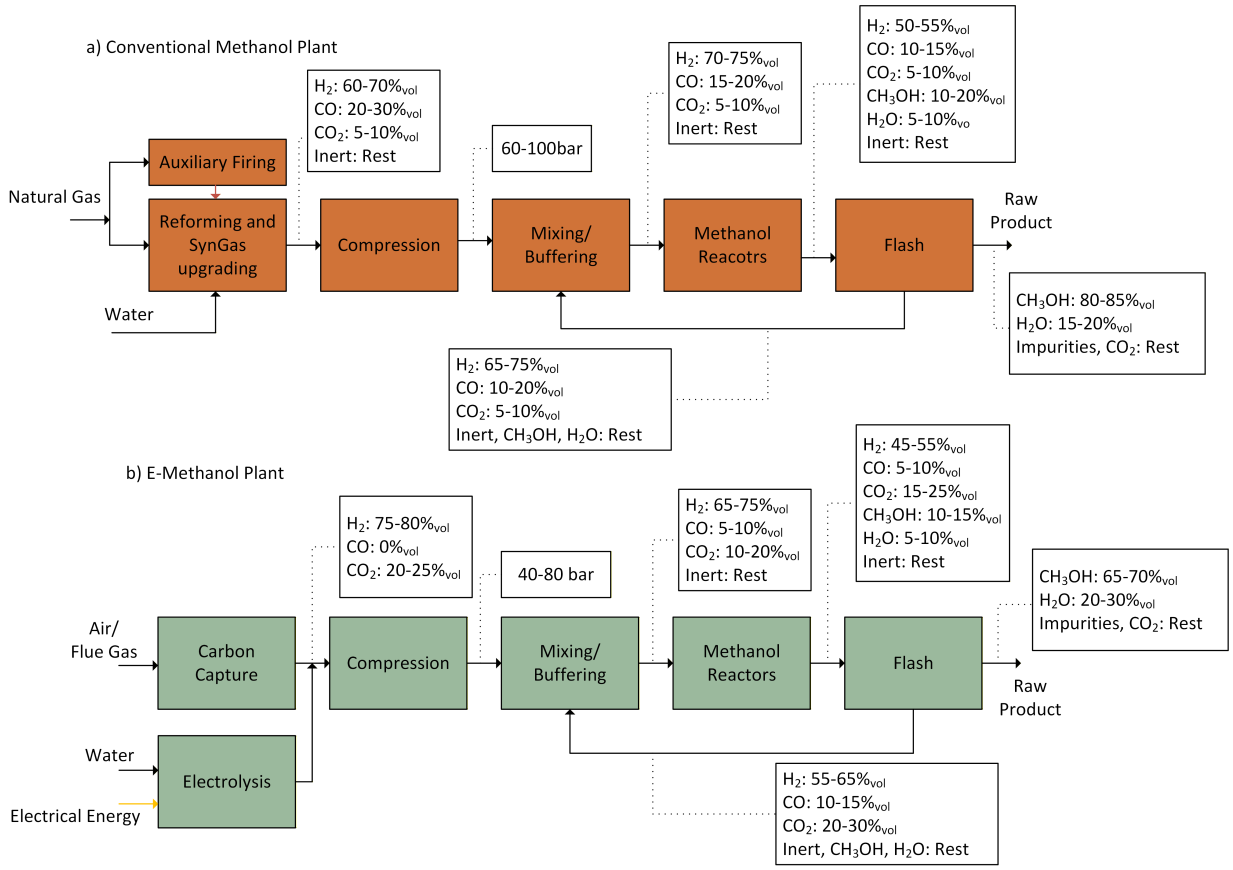

Figure 2.8.: Schematic comparison of a conventional MeOH-synthesis process with a CO_2 based approach. Associated gas compositions and process parameters are given in the schematic for each process. a) Conventional MeOH-Synthesis flow sheet b) CO_2 based E-MeOH-production scheme. Compositions calculated based upon [9, 55, 59, 60]. Own representation.

Different metal oxide catalysts and certain inter metallic catalyst combinations have attracted particular interest because they are able to enhance stable elementary reaction pathways and can show higher intrinsic selectivity to MeOH under CO_2-rich feed compositions in many laboratory studies. These materials often function via formate or oxygen-vacancy mediated activation steps that are less sensitive to the oxidative deactivation inhibit metallic Cu, and many have demonstrated promising selectivities at typical testing conditions (200-300 °C

and 1-5 MPa pressures) in recent literature reports [61].
At the reactor and process level, two major limitations dominate the development of processes. The first is reaction equilibrium: CO_2 conversion produces H_2O and reduces molar volume, single-pass conversion is therefore strictly limited thermodynamically, especially at mild temperatures that favor selectivity towards MeOH formation compared to RWGS (compare figure 2.6) [48]. Practically, this necessitates large internal recycles or multi-stage reactor systems with intermediate reactor stage cooling to reach high overall conversion, which, on an application level, in turn raises capital costs and compression energy demand as well as complicating overall plant balance and effective heat management [62].
The second limitation is the cost and availability of low-carbon H_2. Contemporary techno-economic studies consistently find that H_2-supply — both capital costs for electrolyzers and operational electricity costs for electrolysis itself — constitutes the main cost element in CO_2-based P2M applications [63]. Additionally, availability of regenerative electricity and its associated CO_2-impact in production and procurement influence effectiveness of P2M-approaches heavily in reducing emissions associated with the produced MeOH heavily, with only pure regenerative electricity applied for CO_2 extraction and electrolysis being able to significantly reduce overall associated emissions [64].

2.3.2. Biomass and Biogas derived Methanol

The use of biomass as a renewable carbon-oxide sources for chemical- and specifically MeOH synthesis is being re-evaluated as part of the broader shift towards regenerative chemical production. Two main process routes have emerged: gasification of solid biomass and reforming of biogas. Both approaches aim to deliver a sustainable SynGas suitable for MeOH production through adaption of known SynGas production routes, but each presents distinct advantages and challenges regarding SynGas quality, possible process integration, and scalability.
Gasification of solid biomass occurs at 700–1000 °C under limited addition of oxygen and/or steam [65]. Typically wood residues, agricultural waste, or lignocellulosic materials are utilized in these processes. The raw SynGas produced generally contains 30–40 % H_2, 20–25 % CO, and 25–35 % CO_2, along with CH_4 and light hydrocarbons [13]. This composition deviates from the ideal SN for MeOH synthesis, requiring extensive conditioning through additional water–gas shift process-stages, CO_2-removal from SynGas and additional H_2-supplementation [14]. Moreover, impurities stemming from biomass gasification such as tars, metal-residues and metaloxide-compounds as well as different sulfur species can deactivate Cu/ZnO-based MeOH catalysts, making advanced gas cleaning after gasification stages crucial. While biomass gasification offers broad flexibility of possible feedstock and proven potential for negative emissions associated with the products if coupled to carbon capture technologies (Bioenergy with Carbon Capture and Storage [BECCS]), its economic viability is limited by high cost of gas purification and low carbon efficiency [13].
Biogas reforming represents a more direct and potentially modular pathway, as it can be integrated directly into existing biogas-production facilities. Biogas, composed mainly of CH_4 and CO_2 from anaerobic digestion, can be converted to SynGas applying the same methods as for NG conversion through steam, dry or autothermal reforming [39]. The process generally benefits from more uniform feedstock, simplifying reactor design and process control compared to the gasification of more heterogeneous biomass feedstocks for SynGas generation. However, the high CO_2 fraction leads to a SynGas with insufficient SN for subsequent MeOH synthesis, requiring co-feeding of regeneratively produced H_2. Alternatively steam and dry reforming in autothermal configurations or sequestration of part of the CO_2 prior to, or after reforming of the gas can be

applied for producing appropriate SynGas [66]. Carbon deposition and catalyst deactivation are common issues for biogas reformers, especially under CO_2-rich conditions with limited H_2 supply through the reduced CH_4 content in biogas. The smaller scale of biogas facilities also limits possible economies of scale compared to centralized gasification plants often times also posing additional infrastructural and automation-related challenges for decentralized operation of technically complex, high-temperature catalytic processes [39].
From a systems perspective, both the biomass gasification route as well as biogas reforming highlight the importance of process adaptation toward sustainable feedstock. Integrating renewable H_2-production offers a viable means to adjust SynGas composition while enhancing carbon utilization. The key bottlenecks on the path to global commercialization of the regenerative MeOH-synthesis approaches remain the control of SynGas composition and impurities, catalyst tolerance under variable gas feeds, and economic up scaling of small, distributed biomass or biogas sources. Recent studies have demonstrated the technical viability of biogas reforming and renewable MeOH synthesis as separate process steps, providing valuable insights into potential integrated concepts combining the two process steps [67, 68]. Several investigations have also shown that biogas reforming can serve as an effective route for SynGas-production, and the well-known limitations of conventional SMR have inspired the development of alternative reforming strategies, in some cases incorporating electrolysis [69]. Nevertheless, no pilot-scale demonstration combining electrolysis, autothermal oxygen-based biogas reforming with additional H_2-injection into the SynGas with subsequent bio-MeOH-synthesis has been reported yet, highlighting a significant gap in current research towards complex system integration of several regenerative energy process systems. Rau et al.for example demonstrated ATR on semi-industrial scale, though using air for partial oxidation, which introduces large amounts of inert N_2 and is unfavorable for subsequent MeOH synthesis [70, 9]. Laboratory studies by Rathod & Bhale (2014), Guerrero et al. (2020) and Hou et al. (2007)confirmed the general feasibility of (ATR) biogas reforming and highlighted key sensitivities such as S/C ratio, oxygen demand, catalyst stability, temperature windows, and space velocity [71, 72]. These works collectively demonstrate that biogas reforming can reach high CH_4 and CO_2 conversion, though risks such as soot formation, catalyst oxidation, or excessive water dosing must be addressed. Only few studies address upstream biogas reforming directly for MeOH production. DTU's bio-reforming approach (BIO-ReFuel) combines different reforming stages to generate H_2-rich SynGas, but requires multiple reforming stages and does not exploit O_2 from electrolysis for process synergies. Small-scale three-phase MeOH synthesis from biogas was also demonstrated by Schipek et al. (2021) [73], though with significantly higher reactor complexity. While biogas reforming for H_2-production is well established in research and early commercial adaption, integrated biogas reforming with direct MeOH synthesis is still rarely reported on in practical, pilot, demonstration or commercial applications. This highlights the relevance and novelty of the combined pilot-scale process investigated in this thesis. As both strategies for regenerative MeOH-production yield CO_2-rich SynGas with inherently reduced SN compared to commercial SynGas-production routes, adaptions to the commercial catalysts are central to advancing the commercial applicability of regenerative MeOH systems. The next chapter will therefore cover catalysts, their working mechanisms and strategies for catalyst adaption towards future CO_2-based production of MeOH.

2.4. Catalysts Systems for Heterogeneous Synthesis of Methanol

For more than five decades, the ternary metal-oxide CZA-catalyst system has represented the industrial standard for MeOH synthesis. Despite its long-standing commercial application and its well documented conversion efficiency, the exact nature of the active sites and the fundamental surface interactions determining its catalytic performance remain the subjects of ongoing research and dispute [58]. The CZA-system exhibits high stability, activity, and selectivity under industrial conditions, yet the complex interplay of metal dispersion, inter-metal and metal-oxide effects and interactions as well as dynamic surface restructuring under reaction conditions continue to challenge a complete and unambiguous mechanistic understanding of the phenomena influencing heterogeneous MeOH formation [74].

Variations in catalyst preparation routes, operating conditions, and reaction environments are known to significantly affect the performance of Cu-based catalysts in both CO- and CO_2-hydrogenation pathways. Consequently, optimization of catalyst production protocols and investigation of modified or novel catalyst recipes represent major strategies for enhancing MeOH productivity and catalyst longevity, especially in regenerative, CO_2-rich process environments. A deeper understanding of the reaction mechanisms, surface chemistry, and structure–activity relationships in these systems is therefore essential for future catalyst design and targeted improvement.

While CZA-catalysts work very well under industrial low COR-reaction conditions, their activity and stability fall short of common industrial performance when applied in higher COR or CO_2-only process conditions. This can be attributed to several different effects, which include the higher activation energies for CO_2 adsorption, kinetic favorability of CO_2-reduction to CO and H_2O over direct MeOH formation, challenging intermediate stability of CO_2-surface intermediates and inherent catalytic limitations originating from elevated H_2O partial pressures in MeOH reactors for CO_2 hydrogenation [75]. For targeted catalyst design in regenerative, CO_2-based synthesis approaches, the catalytic properties and their resulting mechanistic effects in conversion of CO and CO_2 have to be studied in detail.

Additionally, structural improvements of catalyst designs have to be correlated carefully to the activity-measurements for heterogeneous catalyst systems. Lastly, catalyst developments in highly controlled laboratory environments need to be proven in system scale-up, providing insights into the possible transferability of laboratory assumptions and results to commercial application. The following section therefore introduces the commercial catalyst system and the known kinetic phenomena in application of these. Current catalyst optimization approaches are introduced and associated to the catalytic mechanisms contributing to MeOH formation.

2.4.1. Working Mechanism of the Commercial Catalyst

In commercial CZA-catalysts, active catalyst surface species for both the hydrogenation of CO and CO_2 are mostly associated with partially or fully reduced Cu^0 species in synergistic contact with ZnO or partially reduced ZnO_x-phases [1]. The catalytic activity of Cu in MeOH synthesis is strongly correlated with its surface structure, oxidation state, and dispersion as well as interactions with other catalyst materials. Metallic Cu^0 sites are generally regarded as the primary adsorption centers for CO and H_2, while partially oxidized Cu^+ species at metal–oxide interfaces between reduced metallic Cu and metal-oxides have been proposed to play an important role in CO_2-activation in the commercial CZA-catalysts [48]. The coexistence of multiple

oxidation states of Cu (Cu^0 and Cu^+)-species thus creates a dynamic redox environment that promotes multiple reactant adsorption and facilitates intermediate stabilization during the reaction sequence following adsorption, enabling CZAs catalytic effectiveness.

Looking more closely at the reaction sequence of carbon-oxides and adsorbed H_2 to MeOH, it is widely accepted that H_2 adsorbs dissociatively on the catalyst surface, while adsorption mechanisms for CO and CO_2 are more openly disputed [76]. While metallic Cu in its self is not necessarily an efficient catalyst for H_2-dissociation compared to noble metals for example, it can activate H_2 under MeOH-reaction conditions through a homolytic dissociation mechanism at Cu lattice defects or step sites, which are promoted, enhanced and dispersed through other metal oxide catalyst additives like ZnO ($H_{2(g)} \rightarrow H^*_{2,ads} \rightarrow 2H^*_{ads}$) [77]. The two resulting surface H^* atoms then participate in the sequential hydrogenation of adsorbed CO or CO_2 and their reaction intermediates. The topological proximity of reduced Cu to reducible metal oxide species such as ZnO is then able to facilitate H^*-spillover, enhancing H^* availability at the boundaries between reduced Cu and surface metal oxides [78]. Heterolytic adsorption of H_2 has also been shown to occur in CZA systems and for example in Cu-ZrO_2 catalyzed MeOH synthesis at metal-metal-oxide borders. Here anion vacancy sites in the metal-oxide lattice stabilize adsorbed H^*-pairs, that are later both involved in formation of MeOH intermediates [57]. Thus, reduction of Cu into different oxidation states, dispersion of different metallic Cu-species and their interactions with other metal-oxides play pivotal roles in the activity of Cu-based MeOH catalysts.

The exact mechanisms contributing to CO adsorption and the formation of its reaction intermediates on CZA-catalysts and other promoted or adapted formulations are more openly disputed. Generally, CO adsorption appears to occur primarily at metallic Cu sites and at Cu–ZnO interfacial regions through electron bonding interactions involving carbon, forming linear or bridge-bound CO species [79]. While CO can adsorb molecularly, both experimental and kinetic studies have shown it to be less reactive toward the direct hydrogenation than CO_2. Current studies suggest instead, that its main mechanistic role in MeOH formation is as a surface intermediate or a scavenger of adsorbed O^* atoms generated during adsorption of CO_2 or H_2O on metal-oxide sites or on oxygen defects at metal-oxide boundaries on the catalyst surface [57]. This can lead to removal of adsorbed O^* as CO_2 through the reaction mechanism $CO^* + O^* \rightarrow CO^*_2 \rightarrow CO_{2(g)}$.

Following CO adsorption, a series of different surface intermediates can form under hydrogenation conditions, including formyl (HCO^*), formate- ($HCOO^*$), hydroxymethyl- (CH_2OH^*) and methoxy- (CH_3O^*)species. Among these, formate and methoxy intermediates are most commonly detected by in-situ spectroscopy and associated TPD-studies, indicating that these are the most common direct reaction routes for MeOH formation from CO [61]. The formate species typically adopts a bridging configuration between Cu and adjacent ZnO or other metal-oxide O-atoms at the metal–oxide interfaces [76]. Successive hydrogenation of these intermediates leads to the formation of surface MeOH (CH_3OH^*), which subsequently desorbs once the surface oxygen balance is restored, either through H_2O formation or CO-oxidation reactions that remove O^*- or OH^*-species from oxidized catalyst surface species [47].

Consequently, CO adsorption serves a dual role in MeOH synthesis: it acts as both a hydrogenation-intermediate and a redox-active species that helps maintain the catalyst's metal-oxide stoichiometry [61]. This highlights the role of metal-oxide catalyst promoters, that are able to form highly active interfaces with metallic Cu and influence catalyst surface O-balance while also generating interfacial effects for H^*-spillover, O-scavenging through adsorbed CO-species and facilitate the adsorption of CO via C^* through interfacial fluctuation of catalyst surface charge and electrons [76].

CO_2-activation in industrial CZA-catalysts involves several coordinated steps at different possible active sites. CO_2 primarily adsorbs onto ZnO and Al_2O_3 surface sites, forming weakly bound carbonate (CO_3^{2-*}) and bicarbonate (HCO_3^{-*}) species through interactions with surface O^*- or OH^*- groups [8].

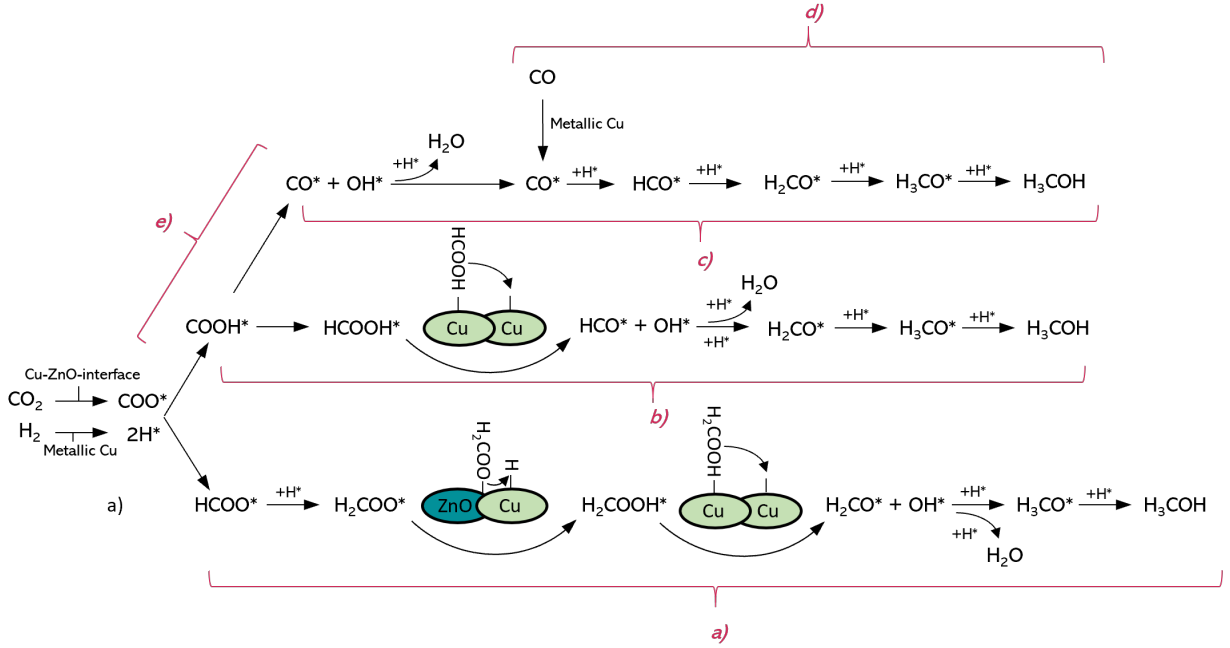

Figure 2.9.: Schematic of possible reaction pathways for MeOH formation. a) Formate pathway for CO_2 hydrogenation b) Carboxyl pathway for CO_2 hydrogenation, c) RWGS and CO hydrogenation pathway for for CO_2 hydrogenation d) CO hydrogenation e) RWGS. Own representation based upon mechanistic data from [48, 57, 61].

In the formation of CO_2-intermediates for MeOH production, highly dispersed Cu particles also play a central role, as proximity of H^* to adsorbed CO_2^* species is necessary in providing H-atoms that migrate to the oxide interface where they can reduce and hydrogenate adsorbed CO_2 [80]. Upon CO_2 adsorption, several surface intermediates can be formed. Most current research is in agreement, that the formate species is the most stable intermediate in CO_2 hydrogenation to MeOH [74]. Development of specialized catalyst formulations, that promote the formate-route through lowering kinetic boundaries on a molecular level have thus found great attention in recent literature.

The formate species ($HCOO^*$) is formed from the primary hydrogenation of surface CO_3^{2-*}-species at interfaces between metallic Cu and metal-oxides. Alternatively, it can also be formed on reduced or partially reduced Zn-sites directly adjacent to Cu, offering metal lattice defects that are able to supply active sites for effective CO_2 binding via O, highlighting the importance of ZnO in conventional catalyst systems [81].

In a comparable manner to CO hydrogenation, the formate-species is then stabilized by positively charged ions on the catalyst surface. In CZA-catalysts, these are common within the ZnO lattice or incorporated into mixed oxide structures involving both Al_2O_3 and ZnO [82]. Formate then undergoes stepwise hydrogenation through formation of hydroxy-formyl (H_2COOH^*), CH_3O^* or CH_2OH^* intermediates adsorbed directly on Cu-sites, ultimately forming MeOH, which desorbs from the catalyst surface. In formation of MeOH from CO_2, H_2O forms and desorbs after the decomposition of H_2COOH^*, which produces formaldehyde (H_2CO) and a surface hydroxyl group (OH^*). This OH^* species subsequently reacts with H^* to yield H_2O^* [74]. The cooperative interaction between Cu, which efficiently dissociates the H_2 reactant, and ZnO, which stabilizes and activates

CO_2 and $HCOO^*$, is fundamental to the high MeOH yield and selectivity achieved in CZA-catalysts in both conventional as well as regenerative MeOH synthesis. Next to the hydrogenation reactions of CO and CO_2 to MeOH, the reduction of CO_2 to CO and H_2O via RWGS play a central role in defining catalyst efficiency and MeOH yield in modern and especially CO_2-based MeOH applications. In CZA-catalysts, RWGS is catalyzed through the partial reduction of CO_2 by H^* at the Cu–ZnO interface. Current research suggests, that CO_2 first forms a carboxyl intermediate ($COOH^*$) via H^* addition, which then decomposes to CO^* and surface OH^* in RWGS. The hydroxyl groups can subsequently react with additional H^* adsorbed on Cu to yield H_2O^*, that desorbs from the surface and leaves CO^*. MeOH formation through the caboxyl group through stepwise hydrogenation of the intermediate is possible in principle, but carboxyl has been shown to have much weaker adsoprtion than formate for instance, which can lead to its decomposition and premature desorption as CO, the most common byproduct in single-pass CO_2 hydrogenation to MeOH [61].

2.4.2. Catalyst Manufacturing and Deployment

As performance of catalysts depends on the dispersion of active sites, proximity of adsorbed species to each other and accessibility of active sites for reactants, it is heavily structure-sensitive and thus strongly influenced by catalysts synthesis parameters, thermal treatment, and reduction protocols [83]. Even subtle variations in these steps can alter the Cu–ZnO interfacial structure, surface composition, and lattice defect or step density, thereby affecting the number and nature of active sites available for CO- and CO_2 hydrogenation. While different approaches for manufacturing exist, some selected have shown to produce catalysts with the desired properties while exhibiting high structural density and rigidity necessary for multi-year deployment, as is common in industrial MeOH synthesis settings [84]. Although some examples of Cu/ZnO carrier catalysts for industrial MeOH synthesis exist and some sources explicitly (and falsely) refer to commercial CZA-catalysts as supported catalysts systems, the vast majority of industrially applied MeOH catalysts is produced through co-precipitation [1]. Conventionally, these catalysts are synthesized via a three-step co-precipitation method [61, 66]. In the first step, mixed aqueous solutions of copper, zinc, and aluminum salts are co-precipitated, typically using carbonate, nitrate or hydroxide ions to form hydroxycarbonate precursors such as malachite-like or aurichalcite-like phases [1]. The composition and crystallinity of these precursors critically determine the later dispersion and catalytic interaction between the metal-oxides in the final catalyst.

During the second step, calcination of the hydroxy carbonates under controlled conditions decomposes the precursors to yield highly dispersed CuO–ZnO-Al_2O_3 composite oxides under emission of CO_2. Some residual carbonate are often retained, which contribute to maintaining a high specific surface area and mesoporosity by inhibiting sintering and phase separation during heat treatment [83]. Calcined metal-oxide mixtures are then pelleted for application as bulk in fixed bet reactors. In the final step, the catalyst is transferred to its active, reduced state. Here, CuO and some ZnO or other readily reducible metal-oxide catalyst promoters are reduced in a H_2- or CO-containing atmosphere to generate the highly active, (partially) reduced Cu^0 and Cu^+ species. This leads to a reduction of Cu particle size and to fragmentation of Cu sites and copper lattices over the catalyst surface. These metallic and partially oxidized Cu sites usually distribute themselves widely over ZnO or partially reduced ZnO_x particle surfaces, establishing very long interfacial regions that serve as the primary active centers for CO_2-activation [48, 85]. The degree of reduction and the strength of interactions between Cu and other metal oxides developed during this stage are very important for the overall catalytic activity and stability [61, 83]. A visual representation of the reduction process of precipitated Cu/ZnO mixtures under H_2 at different points in the reduction process is given in figure 2.10 [85].

The formation of small copper fragments and their distribution during the reduction process is clearly exhibited in the images. These smaller copper particles can distribute themselves well over ZnO, Al_2O_3 as well as additional active catalyst promoters or supports, enhancing surface area and interfacial site distances for both CO and CO_2-activation [86].

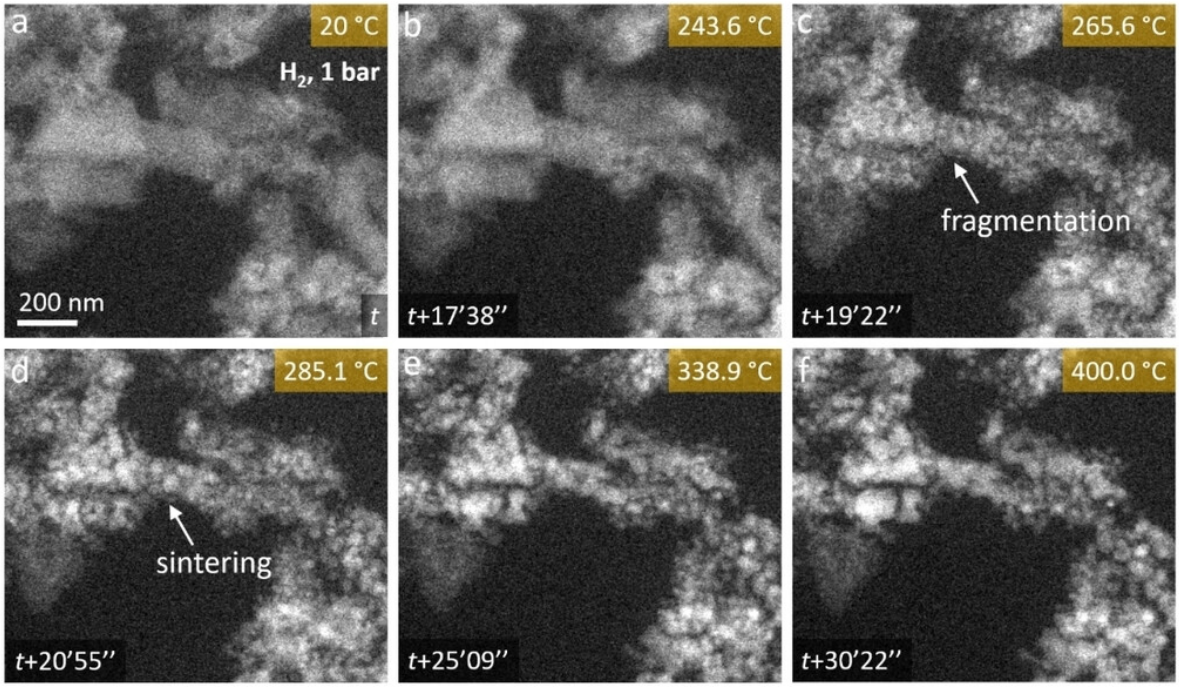

Figure 2.10.: In-situ imagining of Cu/ZnO structures during reduction in H_2 at different temperatures in the reduction temperature ramp. Reproduced under creative commons license from [85].

Impregnation methods involve impregnating porous supports like alumina or ZnO with catalyst precursor solutions, followed by drying and calcination [87]. Although the coating of porous carriers often times yields catalysts less homogeneous than their counterparts from co-precipitation, it enables precise control of metal loading and catalyst surface composition. Although co-precipitation yields very effective CZA-catalysts, some alternative production approaches have been reported in recent years, with single commercial applications seen recently. The precise metal loading allows for the detailed control of phase formation on the carrier surface. Additionally, catalyst-support interactions can be tuned to produce very high surface area boundaries, that can act as active centers in MeOH formation [87]. In recent literature, Sol-gel routes for effective catalyst production routines have increasingly been reported [88]. Sol-Gel precipitation creates catalysts by hydrolysis and poly condensation of metal alk-oxides, providing catalysts with controlled textural properties and metal dispersion [89]. This method is far more complex than co-precipitation or impregnation and has thus not yet found much application in the commercial production of MeOH catalysts. It is currently being reviewed as an emerging alternative for tailored catalyst synthesis.

Hydrothermal synthesis of MeOH catalysts involves aging aqueous precursor solutions under high temperature and pressure to promote crystallinity, highly controlled particle size, and uniform phase formation after drying and calcination. This method allows for the tailoring of catalyst properties by adjusting parameters such as pH, temperature, mineralizers, and precursor aging time, but is uncommon for the production of industrial catalyst bulk [90].

2.4.3. Enhanced Catalysts for Efficient Production of MeOH from CO and CO_2

To enhance the performance of CZA-catalysts in conventional SynGas-operation or for regenerative or CO_2-based MeOH production, various strategies have been explored, many of which are reflected in recent commercial systems representing selected key advances. In adapting CZA towards more sustainable SynGas feedstocks, two primary challenges are being addressed: Firstly, CO_2 adsorption follows a distinct mechanism compared to CO adsorption. While CO_2 adsorbs readily at Cu-ZnO interfaces, incorporating additional or mixed metal-oxides has shown potential to overcome kinetic barriers in CO_2-activation and its subsequent hydrogenation to MeOH [91, 92]. Second, H_2O acts as a major kinetic and stability-limiting factor during CO_2 conversion. It influences both the surface H^* and O^* balances and competes with other adsorbates for active sites, while its continuous co-production can degrade catalyst structure and active centers under continuous exposure to it [93, 94].
Current approaches to catalyst adaptation focus on modifying the CZA-system by incorporating additional metal promoters or replacing individual components (Cu, ZnO, or Al_2O_3) with alternative metals and metal-oxides that enhance activity, selectivity, or stability. The resulting effects can be classified into several categories: electronic, chemical, textural, interfacial, and stability-related. Each classification can herein operate at different structural and functional scales to improve overall catalytic performance. Catalysts and their promoters and additives can influence catalytic activity, selectivity, and long-term stability through several distinct mechanisms.

- Structural promoters (e.g., Al_2O_3, SiO_2) enhance surface area, dispersion, and crystal-phase stability, thereby improving the accessibility of active sites and preventing metal sintering during reaction [95, 96].
- Electronic promoters (e.g., alkali metals, CeO_2) modify the local electron density of metal sites and tune the position of the d-band center and work function, thereby influencing adsorption strength and catalytic turnover rates [97, 98, 99].
- Chemical promoters (e.g., ZnO, ZrO_2) adjust surface acid–base and redox characteristics and form interfaces that facilitate reactant adsorption and hydrogenation to MeOH. Their interaction with the active phase can stabilize intermediates such as formate and methoxy-species [97, 96, 100].
- Textural promoters and supports determine pore structure, diffusion pathways, and the distribution of active sites. High surface area and mesoporosity minimize concentration gradients and enhance the uniformity and durability of the catalytic phase [95, 101]. The precise metal loading allows for the detailed control of phase formation on the carrier surface. Additionally, catalyst-support interactions can be tuned to produces very high surface area boundaries, that can act as active centers in MeOH formation [87].
- Interface or synergistic promoters (e.g., Ga_2O_3, ZnO) generate highly active metal–oxide junctions that improve charge transfer and stabilize key intermediates. Their precise interfacial structure governs the balance between reducibility and catalytic selectivity [102, 103].
- Finally, stability promoters (e.g., CrO_3, MgO) reinforce metal–support interactions and inhibit sintering, segregation, and deactivation by poisoning. They maintain structural integrity under thermal and reactive stress, ensuring long-term MeOH productivity [104].

Figure 2.11 shows a schematic mechanistic overview, of how CeO_2 can act as both a chemical and as electronic promoter. It does this, through generating oxygen vacancies in the metal-oxide lattice, that are able to induce stable adsorption of CO_2 from the gas phase [77]. On the other hand, charge differences at metal oxide interfaces involving CeO_2 are able to induce hydrogen spillover of dissociatively adsorbed H_2 in metallic reduced Cu particles, generating charged hydroxyl groups, that can act as active centers for CO_2 adsorption through interchanging positions under the influence of additional charge interchange in H^+ and e^- on the catalyst surface. A summary of these promoter effects, their functional roles, and representative characterization methods is provided in Table 2.1.

Table 2.1.: Overview of catalyst promoter properties, their effects, and methods to probe them.

Property Type	**Description / Function**	**Typical Characterization Methods**
Structural	Increase surface area, particle dispersion and phase stability; prevent sintering (e.g., Al_2O_3, SiO_2), adapt catalyst surface structure and macroscopic form [95, 96].	BET[1], XRD[2], TEM[3], SEM[4], H_2-TPR[5]
Electronic	Modify electronic density and d-band position; tune adsorption and reaction kinetics (e.g., alkali metals, CeO_2) through availability of surplus electrons or surface electron deficiency [97, 98, 99].	XPS[6], UPS[7], DRIFTS[8], EPR[9], DFT[10]
Chemical	Alter surface composition, acid–base and redox behavior; create multi catalyst interfacial sites, supply active centers through lattice steps/defects and oxygen vacancies [97, 96, 100].	XPS[6], TPD[11], TPR[5], in-situ/operando XAS[12]
Textural / Supports	Control porosity, diffusion space, and dispersion of catalysts; improve accessibility and thermal stability [95, 101].	N_2 adsorption (BET/BJH)[1,13], TEM[3], Hg-porosimetry[14]
Interface / Synergistic	Create active multi-metal or metal–oxide interfaces; enhance charge transfer and intermediate stabilization; facilitate spillover phenomena [102, 103].	STEM–EDS[15], XPS[6], operando XAS[12], in-situ DRIFTS[8]
Stability	Prevent sintering and deactivation; strengthen metal–support interaction (e.g., CrO_3, MgO) [104].	TGA[16], XRD (after cycling)[2], TEM[3], long-term catalytic testing[17]

[1]BET: Brunauer–Emmett–Teller surface area analysis. [2]XRD: X-ray diffraction. [3]TEM: Transmission electron microscopy. [4]SEM: Scanning electron microscopy. [5]TPR: Temperature-programmed reduction. [6]XPS: X-ray photoelectron spectroscopy. [7]UPS: Ultraviolet photoelectron spectroscopy. [8]DRIFTS: Diffuse reflectance infrared Fourier transform spectroscopy.[9]EPR: Electron paramagnetic resonance. [10]DFT: Density functional theory calculations. [11]TPD: Temperature-programmed desorption. [12]XAS: X-ray absorption spectroscopy. [13]BJH: Barrett–Joyner–Halenda pore-size analysis.[14]Hg porosimetry: Mercury intrusion porosimetry. [15]STEM–EDS: Scanning transmission electron microscopy with energy-dispersive X-ray spectroscopy. [16]TGA: Thermogravimetric analysis. [17]Long-term catalytic testing: Time-on-stream performance evaluation.

The discussed effects in catalysis can be achieved both through promoting catalyst formulas or by applying the discussed catalytically active materials as catalyst carriers and supports. When supported catalysts or carrier catalysts are applied, the choice of carrier material, form and wash coating protocols are indicative in determining catalytic performance. The choice of carrier material and its form can influence catalytic performance in the same ways as active components, additives, or promoters.

Appropriate carrier materials help improve the dispersion and stability of the active catalyst coating and

can modify its electronic properties. They can also prevent sintering and promote beneficial metal–support interactions, which enhance reactant adsorption and increase hydrogenation efficiency. Common carrier materials discussed today include metal oxides such as zinc oxide (ZnO), alumina (Al_2O_3), zirconia (ZrO_2), ceria (CeO_2) and silica (SiO_2).

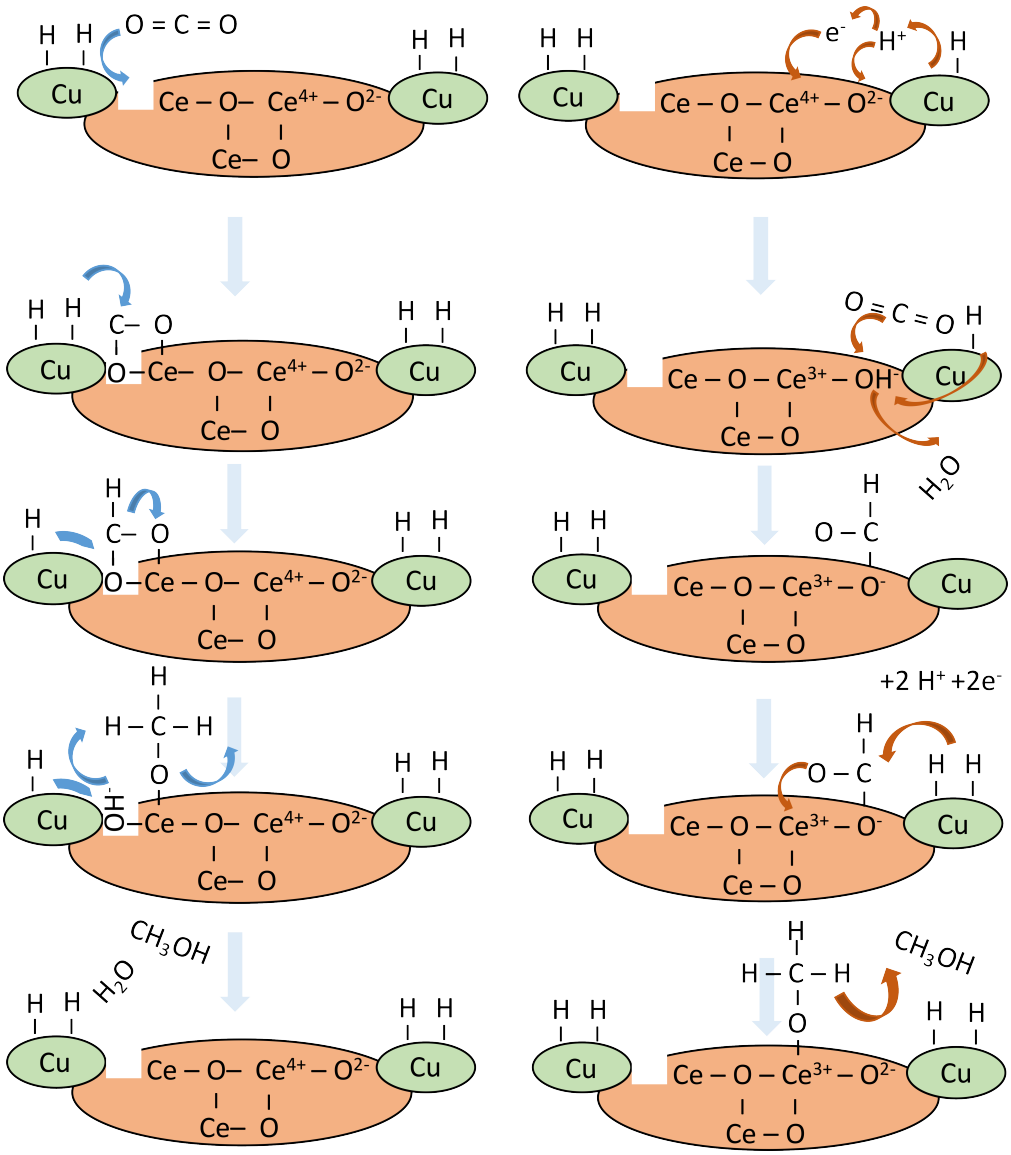

Figure 2.11.: Schematic representation of CeO_2s ability to act both as a chemical (left) as well as an electronic promoter (right), generating highly active oxygen vacancies for CO_2 adsorption as well as electronically induced H_2-spillover, creating charge differentials in the metal lattice that actively promote adsorption. Own representation, adapted mechanistically from [61, 77].

ZnO is considered essential in Cu-based MeOH catalysts for its role in dispersing and stabilizing copper particles, enabling the formation of thin Cu films over its particles, thus promoting the formation of interfacial active cites as well as facilitating adsorption of CO_2 and intermediates directly [105]. Alumina often serves as a physical spacer that increases catalyst lifetime and surface area without directly participating in the reaction mechanism [47]. Zirconia and ceria are noted for their oxygen storage capacity and ability to create oxygen vacancies, promoting CO_2-activation through enhanced metal-support interactions. Titania and silica are also applied as both promoters or supports, impacting catalyst surface area and copper dispersion favorably [1].

A literature based overview over the prevalence of active metal compounds discussed for MeOH synthesis is given in figure 2.12. CZA-catalysts and their working mechanisms still dominate the discussion, with promoters such as ZrO_2, CeO_2, Ga_2O_3 or SiO_2 often taken into account as additive in ternary and quaternary catalyst systems or as active replacement of ZnO.

Alternatively, precious metals and transitions metal such as Pd (or Pt for instance) are discussed as catalysts, replacing CZA altogether, with the previously mentioned promoters also regularly investigated in combination with them. Additionally, bimetallic formulations used in co-precipitated catalysts or in catalyst-support combinations are common in recent literature, with Cu, Ni and Ga investigated most commonly [106].

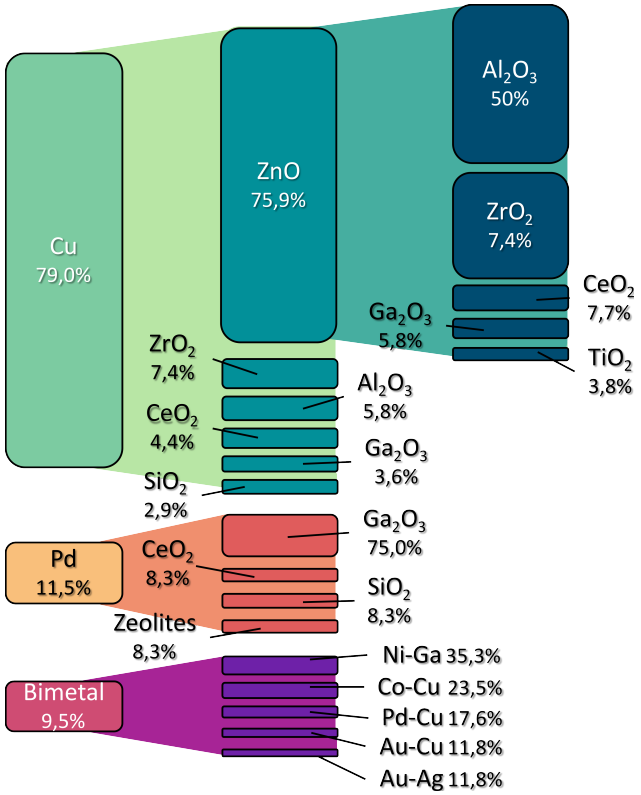

Figure 2.12.: Types of catalyst materials reported for MeOH production from CO_2 or CO_2-rich SynGas. Percentages are calculated based on more than 200 journal articles identified from scopus search by [106]. Own representation, graphic reproduced under creative commons license agreement (CC-BY-NC-ND).

pH control through the addition of alkali metals, as well as adjustment of the synthesis pH, has also been identified as a major determining factor in influencing catalyst performance for MeOH synthesis. While single active promoters or supports are commonly discussed in an isolated fashion, the effects of multi-metal oxide interactions as well as combinations of several enhancement strategies are only very seldomly discussed in literature. This leaves room for the investigation of highly promoted catalysts, utilizing more than one strategy in enhancing conversion performance for CO_2. In this thesis, several mechanistic effects discussed in literature were therefore transferred to novel carrier-based catalysts.

A comparison of recent studies shows that γ-Al_2O_3 spheres coated with Cu/ZnO/ZrO_2 achieve high CO_2 conversion at moderate temperatures and pressures, while work by Shi *et al.* (2020) demonstrates that the relative proportions of CeO_2 and ZrO_2 strongly affect the activity of ternary and quaternary catalysts [107]. Tungsten-doped catalysts exhibit enhanced conversion relative to binary Cu/ZnO, and both synthesis- and surface-pH modified recipes are able to further influence performance in CO_2 hydrogenation.

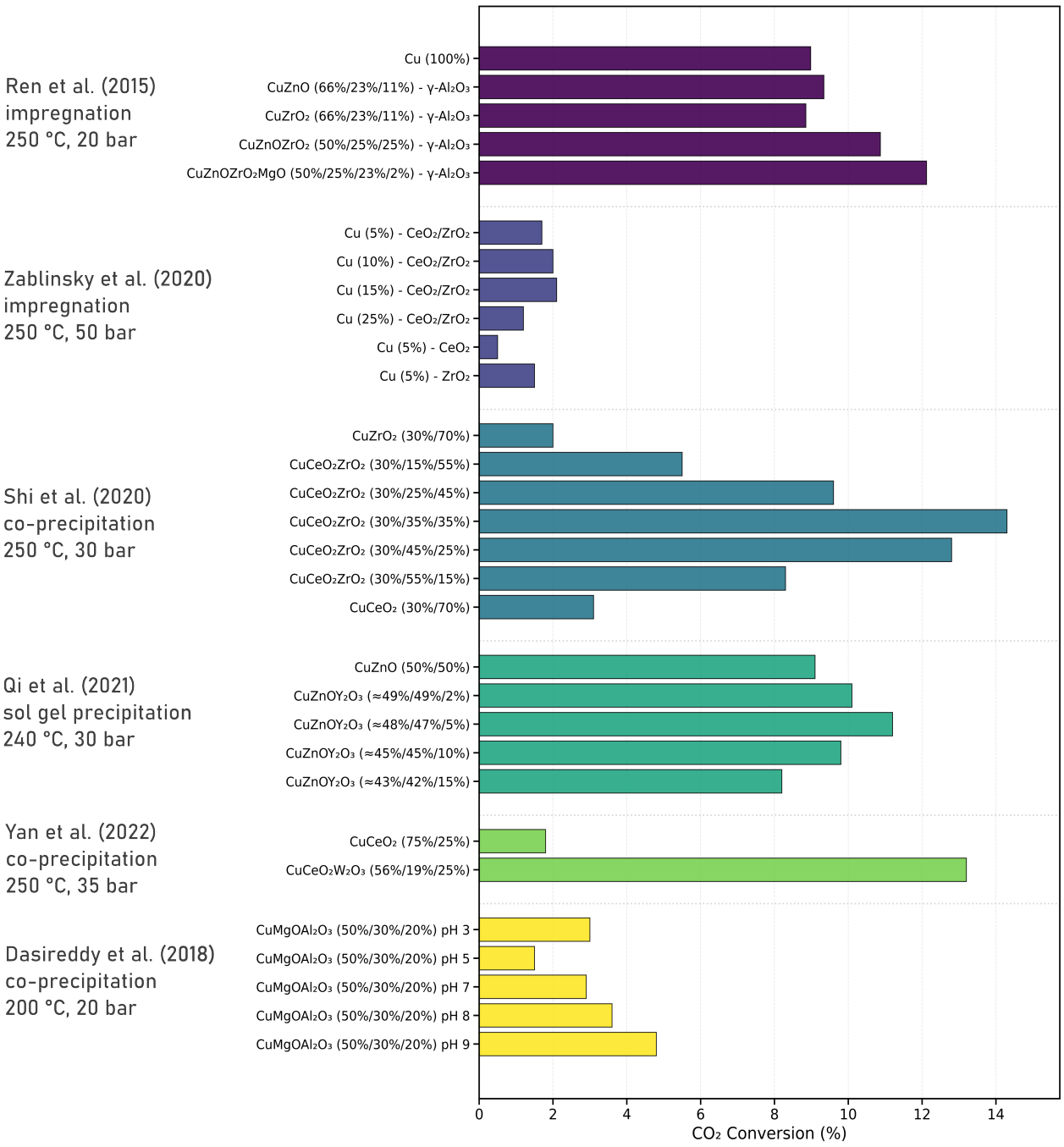

Figure 2.13.: Comparison of reported CO_2-conversion performance of different, promoted catalyst samples from recent literature [107, 108, 109, 110, 111, 112].

The results of this meta-analysis are shown in figure 2.13. The performance comparison highlights the effects of pH and multi-metal-oxide interactions in W_2O_3, Y_2O_3, CeO_2, ZrO_2, ZnO, MgO promoted Cu-catalyst formulations. The possible role of carriers and the choice of high surface area support with possible support-catalyst interactive properties are highlighted. Based upon the recent findings from literature, 13 different catalyst formulations were chosen for coating highly porous Al_2O_3 carrier spheres. Herein, an optimized Cu/ZnO surface ratio was applied [113], applying yttria [114, 108], ceria [115], zirconia [109, 116], tungsten [111], the alkali metal CaO [109] and adapted mixtures and combinations thereof [110] for advanced CO_2-activation and its subsequent conversion to MeOH.

Table 2.2.: Classification of selected MeOH synthesis catalysts by their primary mechanisms of action (Part 1)

Catalyst	**Electronic**	**Chemical/ Compositional**	**Morphological/ Structural**	**Textural**	**Interface/ Synergistic**	**Stability**	**Refs**
Noble Metal Catalysts							
Pd	• Modifies d-band center • Alters work function		• Reduces particle size • Improves Cu-dispersion		• Forms Pd-Cu sites • Enhances H_2-spillover	• Prevents agglomeration • Sintering resistance	[6, 117, 118, 119]
Pt	• Tunes electronic density • Modifies CO/CO_2 adsorption		• Controls crystal faces • Optimizes particle size		• Creates Pt-Cu interfaces • Facilitates H-activation	• Boosts sintering resistance • Thermal stability	[6, 118, 119]
Au	• Alters d-band center • Weakens CO-binding		• Stabilizes nanoparticles • Controls morphology		• Au-Cu alloy formation • Promotes selective CO_2-activation	• Inhibits particle growth • Maintains dispersion	[6, 118, 120, 121]
Transition Metal/Rare Earth Metal Oxide Catalysts							
CeO_2	• Creates O-vacancies • Facilitates e^- transfer • Redox cycling	• Enhances CO_2-activation • Stabilizes Cu^+/Cu^0	• Maintains Cu-dispersion		• Ce-Cu interfaces • Redox active sites	• Inhibits deactivation • Water tolerance	[48, 118, 122]
ZrO_2	• Creates O vacancies • Modifies electronic structure	• Tunes acid-base balance • Improves Cu-reducibility	• Stabilizes Cu-phases • Prevents over-reduction	• Creates mesoporosity • Enhances accessibility	• Forms Cu-ZrO_2 sites • Stabilizes intermediates	• Prevents sintering • Maintains dispersion	[118, 123, 86]
TiO_2	• Modifies SMSI • Changes work function		• Promotes Cu-nanoparticle stability	• High surface area • Reduces transport limits	• Ti-Cu interfaces • Enhances CO_2-binding	• Structural support	[124, 125]
MnO_x	• Induces variable oxidation states	• Redox active centers • Facilitates O transfer			• Mn-Cu synergy	• Prevents Cu oxidation • Stabilizes active states	[118, 126, 127]
Y_2O_3	• Modifies e^- density	• Basic sites for CO_2	• Controls crystallite size • Stabilizes Cu structure		• Suppresses phase segregation	• Thermal stability • Phase segregation inhibitor	[118, 128]
ZnO	• Modifies work function • d-band center tuning	• Forms Cu-Zn alloy • Creates ZnO_x overlayer	• Defective structure • Amorphous phases	• Textural promoter • Surface stabilization	• Cu-ZnO interfaces • Builds primary active sites	• Prevents sintering • Maintains Cu-dispersion	[6, 47, 61]

Table 2.3.: Classification of selected MeOH-synthesis catalysts by their primary mechanisms of action (Part 2)

Catalyst	Electronic	Chemical/ Compositional	Morphological/ Structural	Textural	Interface/ Synergistic	Stability	Refs
Transition Metal/ Rare Earth Metal Oxide Catalysts (continued)							
Co_3O_4	• Modifies redox properties • Has mixed valence states (Co^{2+}/Co^{3+})	• Forms Co-X alloys • Creates active Co-X sites	• Controls particle morphology		• Co-Cu interfaces • Enhances CO_2-activation	• Maintains structural integrity under reaction conditions	[129, 130]
Fe_2O_3	• Electronic modification • Tunes surface redox	• Improves Cu-Fe interaction • Cu-Fe active sites	• Reduces particle size distribution		• Fe-Cu-interfaces • FeO_x facilitates CO_2-adsorption	• Good thermal stability • Prevents sintering	[131, 132]
La_2O_3	• Modifies e^- density • Basic character	• Strong CO_2 adsorption • Basic active sites	• Controls Cu-particle size		• La-Cu interfaces • Enables CO_2 activation	• High thermal stability and water tolerance	[118]
ZnO		• Forms Cu-Zn alloy • Creates ZnO_x overlayer	• Defective structure • Amorphous phases		• Cu-ZnO interfaces • Primary active site	• stabilizes and disperses particles	[95, 97, 133]
Main Group Metal Oxide Catalysts							
SiO_2			• Prevents sintering • Maintains dispersion	• High specific surface area • Mesoporous structure		• Structural support • Mechanical robustness	[100, 101]
Al_2O_3		• Improves acid-base properties	• Improves Cu-dispersion • Reduces particle size	• Enhances BET-area • Distributes uniformly	• Strong metal-support interaction	• Thermally stable • Prevents agglomeration	[47, 58]
Alkaline Earth Oxide Catalysts							
CaO	• Basic sites • e^- donation	• Modulates surface basicity • CO_2-chemisorption • Promotes carbonate formation and reversible adsorption				• Inhibits Zn migration • Structural reinforcement	[134]
MgO	• Tunes surface basicity • Modifies adsorption	• Facilitates HCOO* pathway		• Maintains Cu dispersion		• Prevents sintering • Phase stability	[109, 134]
Other Metal Promoters							
In	• Electronic modification	• Forms In-Cu alloy • Modifies active sites					[117]

2.5. Kinetic Modeling of Methanol Synthesis

The development of kinetic models for MeOH synthesis has evolved in parallel with advances in catalytic science, experimental methodology and advancements in availability of computational performance. Very early investigations, primarily conducted up until the 1990s, were based on empirical correlations of reaction rates obtained under varying conditions using steady state spinning basket or Berty reactors. This ensured negligible mass and heat transfer limitations, allowing for intrinsic, true catalytic kinetics to be measured directly. However, such experiments typically neglect the spatial variations in gas composition and temperature or pressure that arise under industrial fixed-bed and tubular reactor conditions with vertical reactor flow [94]. Consequently, while these models were valuable for mechanistic interpretation, they can exhibit challenges in predictive applicability to larger scale tubular or fixed bed reactor systems, if not adapted or otherwise adjusted to account for these limitations.

With improving capacity for modern computing and in-situ characterization techniques, kinetic modeling has increasingly transitioned toward reactor-integrated and spatially resolved approaches, where rate expressions are embedded into one-dimensional (or multi-dimensional) plug flow reactor (PFR) models. These models account for axial concentration and temperature gradients, enabling the determination of kinetic parameters that are representative of more realistic catalytic environments as they may be found in industrial application. This paradigm shift has been crucial to more direct coupling of proposed kinetic models with their ability to predict reactor performance and catalyst behavior under industrially relevant conditions. Additionally, the correlation of more detailed knowledge of the involved reaction mechanisms, concerning, for example, intermediates and carbon sources in MeOH synthesis, has led to adaptation of macro kinetic models to the physical micro kinetic foundations upon which they are often based [56].

Most mechanistic models of MeOH synthesis employ the Langmuir-Hinshelwood-Hougen-Watson (LHHW) formalism, derived from classical Langmuir–Hinshelwood (LH) surface reaction theory [94]. These models are based upon the fundamental assumption, that the overall rate is controlled by a single rate-determining surface reaction step (RDS), while all other surface reactions and adsorption-desorption phenomena are assumed to be in quasi-equilibrium. Coverage of the catalyst surface with reactants and intermediates is expressed in terms of partial pressures and adsorption equilibrium constants, leading to an algebraic rate expression of the general form

$$r_i = \frac{k_i \cdot \prod_i p_i^{v_i} - k_r \cdot \prod_j p_j^{v_j} / K_{eq}}{(1 + \sum_i K_i \cdot p_i)^n} \tag{2.17}$$

where k_i is the reaction isotherm, p_i are partial pressures of the involved reactants, p_j are partial pressures of the products of reaction i over the catalyst surface, k_r is a reaction constant for the reverse reaction, K_i are adsorption/and desorption isotherms and K_{eq} is the reaction equilibrium isotherm. v_i herein represent exponents, that are determined by the position in the overall reaction scheme, usually resulting from the amount of reactant i still having to be adsorbed/to react until product j is formed.

The denominator represents the fractional surface-coverage correction and is influenced by partial pressures of the reactants and their respective adsorption/desorption isotherms. The overall expression is derived by solving a system of algebraic equations describing surface species balances under the quasi-steady-state approximation, identifying which of the mechanistically involved reaction steps is rate determining (RDS) through optimization of several models accounting for the different surface reactions taking place. In modern approaches the RDS can also be identified through advanced mechanistic analysis (based on Density

Functional Theory (DFT) -caluclations or spectroscopic data) [135]. For calculation of these kinetic models, a set of rate equations representing the involved macro-kinetic reaction scheme is formulated. Important differentiation between competing reaction models can be made by the assumption of different active sites on the catalyst surface for adsorption of reactants and their intermediates, which in turn influences the formulation of the underlying equations. Especially the denominator, which mathematically balances the coverage of the catalyst surface with reactants and reaction intermediates is thus influenced by these assumptions. Historically, most models assumed CO and CO_2 adsorb on the same active centers, while H_2 and H_2O share another type of active site [136].

Generally, the distinction for involvement of different active sites for adsorption can lead to the formulation of four different types of kinetic models in MeOH synthesis: Those that consider a single active site for the adsorption of all involved reactant (single-site mechanism, SS), those considering two active sites (double-site mechanism, DS) and those considering three different active sites, one for CO, one for CO_2 and one for H_2 and H_2O (triple-site mechanisms, TS) [56].

Contemporary models, such as the one by Seidel et al. (2018) can also account for dynamic structural changes on the catalyst surface, modifying the quantity of available active sites with a mathematical factor fitted to the test data used for parameter optimization. This phenomenon has been experimentally observed, and is explained by metal-oxide species mobility at typical MeOH synthesis conditions in CZA-catalysts. This can cause dynamic changes in the catalyst structure, especially in dynamic operation of MeOH reactors [56, 137]

Within this framework, the rate-determining step (RDS) was typically assumed to be either the hydrogenation of CO^* or the hydrogenation of formate intermediates $HCOO^*$ in early studies, as CO hydrogenation from low COR SynGas seemed to be the main reaction in forming MeOH. Thus, Villa et al. (1985) developed one of the first mechanistic LHHW-type models for MeOH synthesis, which incorporated only the hydrogenation of CO and the WGS/RWGS reaction scheme. They identified the hydrogenation of surface formate to methoxy (CH_3O^*) as the RDS for the model. Their work introduced quasi-equilibrium relationships for adsorption and desorption processes, leading to an algebraic rate expression consistent with observed inhibition by CO and H_2O [138].

Later, Graaf et al. (1988) advanced this approach by imposing thermodynamic consistency and explicitly coupling the CO_2 hydrogenation and RWGS. Their model demonstrated mathematically that the experimentally observed dependence of MeOH formation rate on CO_2 partial pressure could only be reproduced if CO_2, rather than CO, served as the dominant carbon source for MeOH. This provided one of the first quantitative indications that MeOH primarily originates from CO_2 hydrogenation, with CO formation arising from the RWGS equilibrium [139]. Additionally, they introduced a mathematical basis for the assumption, that H_2 adsorbed dissociation over CZA-catalysts, comparing mechanistic approaches for both in detail [139]. Vanden Bussche and Froment (1996) refined Graaf et al.s understanding by developing a model that simultaneously describes MeOH synthesis and RWGS in a plug flow reactor framework, accounting for composition and temperature gradients along the catalyst bed. Assuming the formate-hydrogenation step as the RDS, their model incorporated competitive adsorption of CO, CO_2, H_2O, and CH_3OH in a single active site, yielding good agreement with reactor-scale experimental data [140]. This holistic kinetic approach derived from Graaf's model can be seen as the basis for most modern kinetic models in MeOH synthesis. In recent years, the mechanistic focus has shifted decisively toward CO_2-derived MeOH synthesis, supported by in-situ spectroscopy, isotopic labeling, and DFT-calucations. Modern models by Park et al. (2014), Seidel et al (2018)., or Nestler et al. (2020) link micro kinetic reaction networks with reactor models, resolving axial

concentration and temperature profiles, utilizing significantly enhanced data sets for deriving models with very good statistical fit to experimental data [137, 141, 142]. These approaches confirm that MeOH is formed predominantly through the successive hydrogenation of adsorbed CO_2 to formate, methoxy, and then MeOH, while CO formation as well as CO consumption arise as a parallel WGS/RWGS process. Tables 2.4 and 2.5 showcase some of the important kinetic model formulations from the past 40 years, highlighting the assumed active centers and reactions included in the models as well as the derived rate equations. A key research gap arises from the limited understanding of how catalyst-specific properties, in particular promoter-induced changes in surface chemistry, can affect the applicability, parameterization, and mechanistic validity of kinetic models, requiring systematic evaluation of model performance, rate expressions, and fitted parameters. The comparison across different catalyst formulations can highlight shifts in rate-determining steps and to quantify how such variations translate into differences in reactor concentration profiles, conversion behavior in mixed reactant streams and overall catalytic functionality induces by the applied catalyst enhancements.

2.6. Parameter Estimation in Methanol Reaction Kinetics

Parameter estimation and optimization in chemical kinetics aim to determine sets of kinetic parameters ξ (e.g., pre-exponential factors, activation energies, adsorption constants (compare tables 2.4 and 2.5) that allow a kinetic rate model or a rate models embedded into a reactor model to reproduce experimentally measured data as closely as possible. Given a set of measured quantities y_i^{exp} (usually as partial pressures, conversions, or reaction rates) and corresponding model predictions from the kinetic model $y_i^{\text{mod}}(\xi)$, a parameter fitting procedure is then formulated, often as a multi-parameter optimization problem [143]. In reaction kinetics, one of the most commonly applied methods is nonlinear programming (NLP) and nonlinear least-squares minimization herein, where an optimized parameter set ξ^* minimizes the sum of the squared residuals of the kinetic model output compared to recorded test data values in laboratory setups [143]:

$$\xi^* = \min_{\xi} S(\xi) \tag{2.18}$$

with

$$S(\xi) = \sum_{i=1}^{N} \left(y_i^{\text{exp}} - y_i^{\text{mod}}(\xi)\right)^2 \tag{2.19}$$

The residual vector is defined as

$$\mathbf{r}(\xi) = \begin{bmatrix} y_1^{\text{exp}} - y_1^{\text{mod}}(\xi) \\ \vdots \\ y_N^{\text{exp}} - y_N^{\text{mod}}(\xi) \end{bmatrix} \tag{2.20}$$

and the optimization problem is typically solved using algorithms such as the simplex and downhill simplex algorithms or quasi-Newton-methods [144]. In cases where gradients are difficult to compute, derivative-free optimization strategies can be applied and today empirical models are commonly utilized in generating models with good statistical fit, thus omitting the models relation to physio-chemical foundations though [143]. In modern MeOH-synthesis kinetics, parameter fitting involves the linking of the mathematical rate expressions based on LHHW-mechanisms to a reactor-model such as a plug-flow reactor (PFR) [141]. The objective function includes partial pressures or fugacities of CO_2, CO, H_2, H_2O, and MeOH, sometimes including

other byproducts such as DME as well and overall reaction rates for CO/CO_2 hydrogenation, the RWGS and possible rate equations for byproducts [137]. In contemporary literature, weighted least squares

$$S_w(\xi) = \sum_{i=1}^{N} w_i \left(y_i^{\text{exp}} - y_i^{\text{mod}}(\xi)\right)^2 \tag{2.21}$$

are often applied to account for measurement uncertainties and to influence model accuracy towards specific species and optimization targets [93]. Here, global optimization algorithms such as differential evolution, genetic algorithms, or particle swarm optimization are particularly useful because MeOH-synthesis kinetic models are highly nonlinear and often exhibit multiple local minima that depend on applied reaction pressures, temperatures, catalyst design and reactor type as well as transfer limitations and other observed non-optimal factors [143]. These approaches are able to deliver robust estimation of kinetic parameters that ensure accurate reproduction of test data and reliable extrapolation to reactor-scale simulations.

Table 2.4.: Summary of kinetic models (Part 1)

Authors	Reactions	Active Sites	Conditions	Rates	Eq.
Villa et al. (1985) [138]	R1: CO-Hyd. R3: RWGS	A: H_2, CO, CO_2	30–95 bar 215–245 °C	$r_{CO} = \frac{f_{CO} \cdot f_{H_2}^2 - f_{CH_3OH} \cdot K_P^0}{A_1 + A_2 \cdot p_{CO} + A_3 \cdot p_{H_2} + A_4 \cdot p_{CO_2}}$	(2.22)
				$r_{RWGS} = \frac{f_{CO_2} \cdot f_{H_2} - f_{CO} \cdot f_{H_2O} \cdot K_P^0}{A_6}$	(2.23)
Graaf et al. (1988) [139]	R1: CO-Hyd. R2: CO_2-Hyd. R3: RWGS	A: CO, CO_2 B: H_2, H_2O	15–50 bar 210–245 °C	$r_{CO} = \frac{k_{CO} \cdot K_{CO} \cdot (f_{CO} \cdot f_{H_2}^{0.5} - f_{CH_3OH} \cdot f_{H_2}^{0.5} \cdot K_{Eq,CO})}{(1 + K_{CO} \cdot f_{CO} + K_{CO_2} \cdot f_{CO_2}) \cdot [f_{H_2}^{0.5} + (K_{H_2O} \cdot k_{H_2O}^{-0.5}) \cdot f_{H_2O}]}$	(2.24)
				$r_{CO_2} = \frac{k_{CO_2} \cdot K_{CO_2} \cdot (f_{CO_2} \cdot f_{H_2}^{1.5} - f_{CH_3OH} \cdot f_{H_2O} \cdot f_{H_2}^{-1.5} \cdot K_{Eq,CO_2})}{(1 + K_{CO} \cdot f_{CO} + K_{CO_2} \cdot f_{CO_2}) \cdot [f_{H_2}^{0.5} + (K_{H_2O} \cdot k_{H_2O}^{-0.5}) \cdot f_{H_2O}]}$	(2.25)
				$r_{WGSR} = \frac{k_{RWGS} \cdot K_{CO_2} \cdot (f_{CO_2} \cdot f_{H_2} - f_{H_2O} \cdot f_{CO} \cdot K_P^0)}{(1 + K_{CO} \cdot f_{CO} + K_{CO_2} \cdot f_{CO_2}) \cdot [f_{H_2}^{0.5} + (K_{H_2O} \cdot k_{H_2O}^{-0.5}) \cdot f_{H_2O}]}$	(2.26)
V. Bussche & Froment (1996) [140]	R2: CO_2-Hyd. R3: RWGS	A: H_2, H_2O	15–51 bar 180–280 °C	$r_{CO_2} = \frac{k_{CO_2} \cdot [p_{CO_2} \cdot p_{H_2} - p_{CH_3OH} \cdot p_{H_2O} \cdot p_{H_2}^{-2} \cdot K_{Eq,CO_2}^{-1}]}{(1 + K_{H_2O} \cdot p_{H_2O} \cdot (K_8 \cdot K_9 \cdot K_{H_2} \cdot p_{H_2})^{-1} + (K_{H_2} \cdot p_{H_2})^2 + K_{H_2O} \cdot p_{H_2O})^3}$	(2.27)
				$r_{RWGS} = \frac{k_{RWGS} \cdot [p_{CO_2} - p_{CO} \cdot p_{H_2O} \cdot (K_{Eq,WGSR} \cdot p_{H_2})^{-1}]}{(1 + K_{H_2O} \cdot p_{H_2O} \cdot (K_8 \cdot K_9 \cdot K_{H_2} \cdot p_{H_2})^{-1} + (K_{H_2} \cdot p_{H_2})^{0.5} + K_{H_2O} \cdot p_{H_2O})}$	(2.28)
Lim et al. (2009)	R1: CO-Hyd. R2: CO_2-Hyd. R3: RWGS	A: CO B: CO_2 C: H_2, H_2O	50 bar 250–280 °C	$r_{CO} = \frac{k_{CO} \cdot K_{CO} \cdot K_{H_2}^2 \cdot K_{CH,CO} \cdot (p_{CO} \cdot p_{H_2}^2 - p_{CH_3OH} \cdot K_{Eq,CO}^{-1})}{(1 + K_{CO} \cdot f_{CO}) \cdot (1 + K_{H_2}^{0.5} \cdot p_{H_2}^{0.5} + K_{H_2O} \cdot p_{H_2O})}$	(2.29)
				$r_{CO_2} = \frac{k_{CO_2} \cdot K_{CO_2} \cdot K_{H_2} \cdot K_{CH_3O} \cdot (p_{CO_2} \cdot p_{H_2} - p_{CH_3OH} \cdot p_{H_2O} \cdot p_{H_2}^{-2} \cdot K_{Eq,CO_2}^{-1})}{(1 + K_{CO_2} \cdot p_{CO_2}) \cdot (1 + K_{H_2}^{0.5} \cdot p_{H_2}^{0.5} + K_{H_2O} \cdot p_{H_2O})}$	(2.30)
				$r_{RWGS} = \frac{k_{RWGS} \cdot K_{CO_2} \cdot K_{H_2}^{0.5} \cdot (p_{CO_2} \cdot p_{H_2}^{0.5} - p_{H_2O} \cdot p_{CO} \cdot p_{H_2}^{-0.5} \cdot K_{Eq,RWGS}^{-1})}{(1 + K_{CO_2} \cdot p_{CO_2}) \cdot (1 + K_{H_2}^{0.5} \cdot p_{H_2}^{0.5} + K_{H_2O} \cdot p_{H_2O})}$	(2.31)

Table 2.5.: Summary of kinetic models (Part 2)

Authors	Reactions	Active Sites	Conditions	Rates	Eq.
Park et al. (2014) [141]	R1: CO-Hyd. R2: CO_2-Hyd. R3: RWGS	A: for CO B: for CO_2 C: for H_2 and H_2O	50–90 bar 230–340 °C	$r_{CO} = \frac{k_{CO} \cdot K_{CO} \cdot (f_{CO} \cdot f_{H_2}^{0.5} - f_{CH_3OH} \cdot f_{H_2}^{-0.5} \cdot K^0_{CO,hyd.})}{(1 + K_{CO} \cdot f_{CO}) \cdot (1 + K_{H_2}^{0.5} \cdot f_{H_2}^{0.5} + K_{H_2O} \cdot f_{H_2O})}$	(2.32)
				$r_{CO_2} = \frac{k_{CO_2} \cdot K_{CO_2} \cdot (f_{CO_2} \cdot f_{H_2}^{1.5} - f_{CH_3OH} \cdot f_{H_2O} \cdot f_{H_2}^{-0.5} \cdot K^0_{CO_2,hyd.})}{(1 + K_{CO_2} \cdot f_{CO_2}) \cdot (1 + K_{H_2}^{0.5} \cdot f_{H_2}^{0.5} + K_{H_2O} \cdot f_{H_2O})}$	(2.33)
				$r_{RWGS} = \frac{k_{RWGS} \cdot K_{CO_2} \cdot (f_{CO_2} \cdot f_{H_2} - f_{H_2O} \cdot f_{CO} \cdot K^0_{P,RWGS})}{(1 + K_{CO_2} \cdot f_{CO_2}) \cdot (1 + K_{H_2}^{0.5} \cdot f_{H_2}^{0.5} + K_{H_2O} \cdot f_{H_2O})}$	(2.34)
Seidel et al. (2018) [137]	R1: CO-Hyd. R2: CO_2-Hyd. R3: RWGS	A: for CO B: for H_2, CO_2, H_2O C: for H_2	30–70 bar 230–260 °C	$r_{CO} = \frac{(1 - \varphi_{zn}) k_{CO} \cdot (f_{CO} \cdot f_{H_2}^0 - f_{CH_3OH} \cdot K^0_{CO,hyd.})}{(1 + K_{CO} \cdot f_{CO}) \cdot (1 + k_{H_2}^{0.5} \cdot f_{H_2}^{0.5})}$	(2.35)
				$r_{CO_2} = \frac{\varphi_{Zn}^2 \cdot k_{CO_2} \cdot (f_{CO_2} \cdot f_{H_2}^{1.5} - f_{CH_3OH} \cdot f_{H_2O} \cdot f_{H_2}^{-1} \cdot K^{-1}_{Eq,CO_2,hyd.})}{[1 + (K_{H_2O} \cdot K_o \cdot K_{H_2}^2) \cdot f_{H_2O} \cdot f_{H_2}^{-1} + K_{CO} \cdot f_{CO} + K_{H_2O} \cdot f_{H_2O}] \cdot (1 + k_{H_2}^{0.5} \cdot f_{H_2}^{0.5})}$	(2.36)
				$r_{RWGS} = \frac{\varphi_{zn} \cdot (1 - \varphi_{zn})^{-1} \cdot k_{RWGS} \cdot (f_{CO_2} - f_{H_2O} \cdot f_{CO} \cdot f_{H_2}^{-1} \cdot K^{-1}_{Eq,RWGS})}{[1 + (K_{H_2O} \cdot K_o \cdot K_{H_2}^{-2}) \cdot f_{H_2O} \cdot f_{H_2}^{-1} + K_{CO} \cdot f_{CO} + K_{H_2O} \cdot f_{H_2O}] \cdot (1 + K_{CO} \cdot f_{CO})}$	(2.37)
Nestler et al. (2020) [142]	R2: CO_2-Hyd. R3: RWGS	Not specified	50–90 bar 230–340 °C	$r_{CO_2} = \frac{k_{CO_2} \cdot K_{CO_2} \cdot f_{CO_2} \cdot f_{H_2}^{1.5} \cdot \left(1 - f_{CH_3OH} \cdot f_{H_2O} \cdot f_{CO_2}^{-1} \cdot f_{H_2}^{-1.5} \cdot K^{-1}_{Eq,CO_2}\right)}{(1 + K_{CO} \cdot f_{CO} + K_{CO_2} \cdot f_{CO_2}) \cdot (f_{H_2}^{0.5} + K_3 \cdot f_{H_2O})}$	(2.38)
				$r_{RWGS} = \frac{k_{RWGS} \cdot K_{CO_2} \cdot f_{CO_2} \cdot f_{H_2} \cdot \left(1 - f_{CO} \cdot f_{H_2O} \cdot f_{CO_2}^{-1} \cdot f_{H_2}^{-1} \cdot K^{-1}_{eq,2}\right)}{(1 + K_{CO} \cdot f_{CO} + K_{CO_2} \cdot f_{CO_2}) \cdot (f_{H_2}^{0.5} + K_3 \cdot f_{H_2O})}$	(2.39)

References

[1] Maryam Ebrahimzadeh Sarvestani et al. “From catalyst development to reactor Design: A comprehensive review of methanol synthesis techniques”. In: *Energy Conversion and Management* 302 (2024), p. 118070. ISSN: 01968904. DOI: 10.1016/j.enconman.2024.118070.

[2] Daniel Sheldon. “Methanol Production – A Technical History”. In: *Johnson Matthey Technology Review* 61.3 (2017), pp. 172–182. ISSN: 2056-5135. DOI: 10.1595/205651317X695622.

[3] M. B. Fichtl. “Efficient Methanol Synthesis Catalysts: Long-Term Stability and Deactivation Phenomena”. Dissertation. Munich: TUM, 8.12.2024. URL: https://mediatum.ub.tum.de/doc/1232028/1232028.pdf.

[4] Giulia Bozzano and Flavio Manenti. “Efficient methanol synthesis: Perspectives, technologies and optimization strategies”. In: *Progress in Energy and Combustion Science* 56 (2016), pp. 71–105. ISSN: 03601285. DOI: 10.1016/j.pecs.2016.06.001.

[5] Mohammad Malakootikhah. “Deactivation of methanol catalysts; A comparison of a dynamic modeling study with an industrial water-cooled methanol reactor”. In: *International Journal of Hydrogen Energy* 114 (2025), pp. 221–228. ISSN: 03603199. DOI: 10.1016/j.ijhydene.2025.02.456.

[6] Malte Behrens et al. “Understanding the complexity of a catalyst synthesis: Co-precipitation of mixed Cu,Zn,Al hydroxycarbonate precursors for Cu/ZnO/Al2O3 catalysts investigated by titration experiments”. In: *Applied Catalysis A: General* 392.1-2 (2011), pp. 93–102. ISSN: 0926860X. DOI: 10.1016/j.apcata.2010.10.031.

[7] Sirous Motahari, Sadegh Froud Moorjani, and Mohammad Reza Rahimpour. “Methanol Production: A Comprehensive Review of Processes, Catalysts, and Reactors”. In: *Comprehensive Methanol Science* (2025), pp. 518–541. DOI: 10.1016/B978-0-443-15740-0.00067-7. URL: https://www.sciencedirect.com/science/article/abs/pii/B9780443157400000677?via%3Dihub.

[8] Dongliang Wang et al. “Novel coal-to-methanol process with near-zero carbon emission: Pulverized coal gasification-integrated green hydrogen process”. In: *Journal of Cleaner Production* 339 (2022), p. 130500. ISSN: 09596526. DOI: 10.1016/j.jclepro.2022.130500.

[9] Florian Nestler et al. “Methanol Synthesis – Industrial Challenges within a Changing Raw Material Landscape”. In: *Chemie Ingenieur Technik* 90.10 (2018), pp. 1409–1418. ISSN: 0009-286X. DOI: 10.1002/cite.201800026.

[10] Fei Dai et al. “Recent Progress on Hydrogen-Rich Syngas Production from Coal Gasification”. In: *Processes* 11.6 (2023), p. 1765. DOI: 10.3390/pr11061765.

[11] Adnan Midilli et al. “A comprehensive review on hydrogen production from coal gasification: Challenges and Opportunities”. In: *International Journal of Hydrogen Energy* 46.50 (2021), pp. 25385–25412. ISSN: 03603199. DOI: 10.1016/j.ijhydene.2021.05.088.

[12] Nabila Aprianti et al. “Gasification kinetic and thermodynamic parameters of fine coal using thermogravimetric analysis”. In: *Energy* 268 (2023), p. 126666. ISSN: 03605442. DOI: 10.1016/j.energy.2023.126666.

[13] Atefeh Akbarian et al. “Challenges and opportunities of lignocellulosic biomass gasification in the path of circular bioeconomy”. In: *Bioresource technology* 362 (2022), p. 127774. DOI: 10.1016/j.biortech.2022.127774.

[14] Ying-Ju Chang, Jo-Shu Chang, and Duu-Jong Lee. “Gasification of biomass for syngas production: Research update and stoichiometry diagram presentation”. In: *Bioresource technology* 387 (2023), p. 129535. DOI: 10.1016/j.biortech.2023.129535.

[15] Muhammad Usman and W. M. A. Wan Daud. “Recent advances in the methanol synthesis via methane reforming processes”. In: *RSC Advances* 5.28 (2015), pp. 21945–21972. DOI: 10.1039/C4RA15625K.

[16] Lukasz Szablowski, Malgorzata Wojcik, and Olaf Dybinski. “Review of steam methane reforming as a method of hydrogen production”. In: *Energy* 316 (2025), p. 134540. ISSN: 03605442. DOI: 10.1016/j.energy.2025.134540.

[17] Magdalena Mosinska, Malgorzata I. Szynkowska, and Pawel Mierczynski. “Oxy-Steam Reforming of Natural Gas on Ni Catalysts—A Minireview”. In: *Catalysts* 10.8 (2020), p. 896. DOI: 10.3390/catal10080896.

[18] Joshua O. Ighalo and Placidus B. Amama. “Recent advances in the catalysis of steam reforming of methane (SRM)”. In: *International Journal of Hydrogen Energy* 51 (2024), pp. 688–700. ISSN: 03603199. DOI: 10.1016/j.ijhydene.2023.10.177.

[19] Aimaro Sanna et al. “Steam reforming of methane: state of the art and novel technologies”. In: *Reaction Chemistry & Engineering* 10.9 (2025), pp. 1963–1977. DOI: 10.1039/D5RE00001G.

[20] Parham Sadooghi and Reinhard Rauch. “Experimental and modeling study of hydrogen production from catalytic steam reforming of methane mixture with hydrogen sulfide”. In: *International Journal of Hydrogen Energy* 40.33 (2015), pp. 10418–10426. ISSN: 03603199. DOI: 10.1016/j.ijhydene.2015.06.143.

[21] José Juan Bolívar Caballero, Ilman Nuran Zaini, and Weihong Yang. “Reforming processes for syngas production: A mini-review on the current status, challenges, and prospects for biomass conversion to fuels”. In: *Applications in Energy and Combustion Science* 10 (2022), p. 100064. ISSN: 2666352X. DOI: 10.1016/j.jaecs.2022.100064.

[22] Hafiz Hamza Faheem et al. “Comparative study of conventional steam-methane-reforming (SMR) and auto-thermal-reforming (ATR) with their hybrid sorption enhanced (SE-SMR & SE-ATR) and environmentally benign process models for the hydrogen production”. In: *Fuel* 297 (2021), p. 120769. ISSN: 00162361. DOI: 10.1016/j.fuel.2021.120769.

[23] Dhruv Singh, Piero Sirini, and Lidia Lombardi. “Review of Reforming Processes for the Production of Green Hydrogen from Landfill Gas”. In: *Energies* 18.1 (2025), p. 15. DOI: 10.3390/en18010015.

[24] Ruoshui Ma, Bang Xu, and Xiao Zhang. “Catalytic partial oxidation (CPOX) of natural gas and renewable hydrocarbons/oxygenated hydrocarbons—A review”. In: *Catalysis Today* 338 (2019), pp. 18–30. ISSN: 09205861. DOI: 10.1016/j.cattod.2019.06.025.

[25] Yi Herng Chan et al. “Advances in bi-reforming of methane: Syngas production for low-carbon energy solutions”. In: *Chemical Engineering Journal* 505 (2025), p. 159660. ISSN: 13858947. DOI: 10.1016/j.cej.2025.159660.

[26] K. L. Hohn and L. D. Schmidt. “Partial oxidation of methane to syngas at high space velocities over Rh-coated spheres”. In: *Applied Catalysis A: General* 211.1 (2001), pp. 53–68. ISSN: 0926860X. DOI: 10.1016/S0926-860X(00)00835-8.

[27] L. L. Makarshin et al. “Syngas production by partial oxidation of methane in a microchannel reactor over a Ni–Pt/La0.2Zr0.4Ce0.4Ox catalyst”. In: *Fuel Processing Technology* 131 (2015), pp. 21–28. ISSN: 03783820. DOI: 10.1016/j.fuproc.2014.10.031.

[28] Wenyuan Guo et al. “Simulation of non-catalytic partial oxidation and scale-up of natural gas reformer”. In: *Fuel Processing Technology* 98 (2012), pp. 45–50. ISSN: 03783820. DOI: 10.1016/j.fuproc.2012.01.019.

[29] Mohammed Mosaad Awad et al. “A critical review of recent advancements in catalytic dry reforming of methane: Physicochemical properties, current challenges, and informetric insights”. In: *International Journal of Hydrogen Energy* 76 (2024), pp. 202–233. ISSN: 03603199. DOI: 10.1016/j.ijhydene.2024.03.319.

[30] Bruno Agún and Alberto Abánades. “Comprehensive review on dry reforming of methane: Challenges and potential for greenhouse gas mitigation”. In: *International Journal of Hydrogen Energy* 103 (2025), pp. 395–414. ISSN: 03603199. DOI: 10.1016/j.ijhydene.2025.01.160.

[31] Abdulrahman Abdulrasheed et al. “A review on catalyst development for dry reforming of methane to syngas: Recent advances”. In: *Renewable and Sustainable Energy Reviews* 108 (2019), pp. 175–193. ISSN: 13640321. DOI: 10.1016/j.rser.2019.03.054.

[32] Aseel G. S. Hussien and Kyriaki Polychronopoulou. “A Review on the Different Aspects and Challenges of the Dry Reforming of Methane (DRM) Reaction”. In: *Nanomaterials (Basel, Switzerland)* 12.19 (2022). ISSN: 2079-4991. DOI: 10.3390/nano12193400.

[33] Ananda Vallezi Paladino Lino et al. “Syngas for Fischer-Tropsch synthesis by methane tri-reforming using nickel supported on MgAl2O4 promoted with Zr, Ce and Ce-Zr”. In: *Applied Surface Science* 481 (2019), pp. 747–760. ISSN: 01694332. DOI: 10.1016/j.apsusc.2019.03.140.

[34] Hui Shi, Zhikai Li, and Ming Xia. “Design and stabilization of direct autothermal methane steam reformation reactor for producing hydrogen via optimizing oxygen distributed feeding”. In: *International Journal of Hydrogen Energy* 80 (2024), pp. 1266–1276. ISSN: 03603199. DOI: 10.1016/j.ijhydene.2024.07.211.

[35] M. H. Halabi et al. “Modeling and analysis of autothermal reforming of methane to hydrogen in a fixed bed reformer”. In: *Chemical Engineering Journal* 137.3 (2008), pp. 568–578. ISSN: 13858947. DOI: 10.1016/j.cej.2007.05.019.

[36] T. A. Semelsberger, ed. *FUELS – HYDROGEN STORAGE | Chemical Carriers*. Encyclopedia of Electrochemical Power Sources. 2009. DOI: 10.1016/B978-044452745-5.00331-2. URL: https://www.sciencedirect.com/science/article/abs/pii/B9780444527455003312.

[37] Matheus Henrique Silva Cavalcante et al. “Autothermal Reforming of Methane: A Thermodynamic Study on the Use of Air and Pure Oxygen as Oxidizing Agents in Isothermal and Adiabatic Systems”. In: *Methane* 2.4 (2023), pp. 389–403. DOI: 10.3390/methane2040026.

[38] Sergio Nogales-Delgado et al. “A Review on the Use of Catalysis for Biogas Steam Reforming”. In: *Catalysts* 13.12 (2023), p. 1482. DOI: 10.3390/catal13121482.

[39] Ravindra Kumar and Anil Kumar. “Recent advances of biogas reforming for hydrogen production: Methods, purification, utility and techno-economics analysis”. In: *International Journal of Hydrogen Energy* 76 (2024), pp. 108–140. ISSN: 03603199. DOI: 10.1016/j.ijhydene.2024.02.143.

[40] Vincent Dieterich et al. “Power-to-liquid via synthesis of methanol, DME or Fischer–Tropsch-fuels: a review”. In: *Energy & Environmental Science* 13.10 (2020), pp. 3207–3252. ISSN: 1754-5692. DOI: 10.1039/D0EE01187H.

[41] Guanfu Liu, Helena Hagelin-Weaver, and Bruce Welt. “A Concise Review of Catalytic Synthesis of Methanol from Synthesis Gas”. In: *Waste* 1.1 (2023), pp. 228–248. DOI: 10.3390/waste1010015.

[42] Shangkun Li et al. “Methane to Methanol through Heterogeneous Catalysis and Plasma Catalysis”. In: *Catalysts* 11.5 (2021), p. 590. DOI: 10.3390/catal11050590.

[43] Haiquan An, Zhen Liu, and Shujun Mu. “Process analysis of a novel coal-to-methanol technology for gasification integrated solid oxide electrolysis cell (SOEC)”. In: *International Journal of Hydrogen Energy* 48.26 (2023), pp. 9805–9811. ISSN: 03603199. DOI: 10.1016/j.ijhydene.2022.11.300.

[44] Ying-jie Zhao et al. “A multi-dimensional feasibility analysis of coal to methanol assisted by green hydrogen from a life cycle viewpoint”. In: *Energy Conversion and Management* 268 (2022), p. 115992. ISSN: 01968904. DOI: 10.1016/j.enconman.2022.115992.

[45] Shinje Lee et al. “Scenario-Based Techno-Economic Analysis of Steam Methane Reforming Process for Hydrogen Production”. In: *Applied Sciences* 11.13 (2021), p. 6021. DOI: 10.3390/app11136021.

[46] Abdulaziz Alarifi, Ali Elkamel, and Eric Croiset. “Steady-State Simulation of a Novel Annular Multitubular Reactor for Enhanced Methanol Production”. In: *Industrial & Engineering Chemistry Research* 52.44 (2013), pp. 15387–15393. ISSN: 0888-5885. DOI: 10.1021/ie4006589.

[47] Daniel Laudenschleger, Holger Ruland, and Martin Muhler. “Identifying the nature of the active sites in methanol synthesis over Cu/ZnO/Al2O3 catalysts”. In: *Nature communications* 11.1 (2020), p. 3898. DOI: 10.1038/s41467-020-17631-5.

[48] Jiadong Zhu et al. “Mechanism and Nature of Active Sites for Methanol Synthesis from CO/CO2 on Cu/CeO2”. In: *ACS Catalysis* 10.19 (2020), pp. 11532–11544. ISSN: 2155-5435. DOI: 10.1021/acscatal.0c02909.

[49] Chundong Zhang et al. “Efficient utilization of carbon dioxide in a gas-to-methanol process composed of CO2/steam–mixed reforming and methanol synthesis”. In: *Journal of CO2 Utilization* 16 (2016), pp. 1–7. ISSN: 22129820. DOI: 10.1016/j.jcou.2016.05.005.

[50] Yungpil Yoo et al. “Energy, exergy and thermoeconomic analyses for a power-to-green methanol production plant”. In: *Energy Nexus* 19 (2025), p. 100517. ISSN: 27724271. DOI: 10.1016/j.nexus.2025.100517.

[51] Rei-Yu Chein et al. “Analysis of methanol synthesis using CO2 hydrogenation and syngas produced from biogas-based reforming processes”. In: *Chemical Engineering Journal* 426 (2021), p. 130835. ISSN: 13858947. DOI: 10.1016/j.cej.2021.130835.

[52] Sofiane Arab et al. “Methanol synthesis from CO2 and H2 in multi-tubular fixed-bed reactor and multi-tubular reactor filled with monoliths”. In: *Chemical Engineering Research and Design* 92.11 (2014), pp. 2598–2608. ISSN: 02638762. DOI: 10.1016/j.cherd.2014.03.009.

[53] Sonia Sepahi and Mohammad Reza Rahimpour, eds. *Advances in Synthesis Gas : Methods, Technologies and Applications: Chapter 5 - Methanol production from syngas: Volume 3: Syngas Products and Usages*. Elsevier B.V., 2023. ISBN: 978-0-323-91878-7. DOI: 10.1016/B978-0-323-91878-7.00012-5.

[54] Emanuele Moioli and Tilman Schildhauer. "Tailoring the Reactor Properties in the Small–Scale Sorption–Enhanced Methanol Synthesis". In: *Chemie Ingenieur Technik* 95.5 (2023), pp. 631–641. ISSN: 0009-286X. DOI: 10.1002/cite.202200200.

[55] Filippo Bisotti et al. "Impact of Kinetic Models on Methanol Synthesis Reactor Predictions: In Silico Assessment and Comparison with Industrial Data". In: *Industrial & Engineering Chemistry Research* 61.5 (2022), pp. 2206–2226. ISSN: 0888-5885. DOI: 10.1021/acs.iecr.1c04476.

[56] Lacerda de Oliveira Campos, Bruno, ed. *Multiscale modeling of the methanol synthesis: from surface reaction kinetics to techno-economic analysis*. Karlsruhe: Karlsruher Institut für Technologie (KIT), 2023. DOI: 10.5445/IR/1000158433. URL: https://publikationen.bibliothek.kit.edu/1000158433.

[57] Michael Bowker. "Methanol Synthesis from CO2 Hydrogenation". In: *ChemCatChem* 11.17 (2019), pp. 4238–4246. ISSN: 1867-3880. DOI: 10.1002/cctc.201900401.

[58] Arik Beck et al. "The Enigma of Methanol Synthesis by Cu/ZnO/Al2O3-Based Catalysts". In: *Chemical reviews* 124.8 (2024), pp. 4543–4678. DOI: 10.1021/acs.chemrev.3c00148.

[59] William L. Luyben. "Design and Control of a Methanol Reactor/Column Process". In: *Industrial & Engineering Chemistry Research* 49.13 (2010), pp. 6150–6163. ISSN: 0888-5885. DOI: 10.1021/ie100323d.

[60] Mar Pérez-Fortes et al. "Methanol synthesis using captured CO2 as raw material: Techno-economic and environmental assessment". In: *Applied Energy* 161 (2016), pp. 718–732. ISSN: 03062619. DOI: 10.1016/j.apenergy.2015.07.067.

[61] R. Guil-López et al. "Methanol Synthesis from CO2: A Review of the Latest Developments in Heterogeneous Catalysis". In: *Materials (Basel, Switzerland)* 12.23 (2019). ISSN: 1996-1944. DOI: 10.3390/ma12233902.

[62] Judit Nyári et al. "Techno-economic barriers of an industrial-scale methanol CCU-plant". In: *Journal of CO2 Utilization* 39 (2020), p. 101166. ISSN: 22129820. DOI: 10.1016/j.jcou.2020.101166.

[63] Simone Mucci, Alexander Mitsos, and Dominik Bongartz. "Cost-optimal Power-to-Methanol: Flexible operation or intermediate storage?" In: *Journal of Energy Storage* 72 (2023), p. 108614. ISSN: 2352152X. DOI: 10.1016/j.est.2023.108614.

[64] Muflih A. Adnan and Md Golam Kibria. "Comparative techno-economic and life-cycle assessment of power-to-methanol synthesis pathways". In: *Applied Energy* 278 (2020), p. 115614. ISSN: 03062619. DOI: 10.1016/j.apenergy.2020.115614.

[65] Prayudi Suparmin et al. "Syngas production by biomass gasification: A meta-analysis". In: *Renewable and Sustainable Energy Reviews* 206 (2024), p. 114824. ISSN: 13640321. DOI: 10.1016/j.rser.2024.114824.

[66] Shashwata Ghosh et al. “Biogas to methanol: A comparison of conversion processes involving direct carbon dioxide hydrogenation and via reverse water gas shift reaction”. In: *Journal of Cleaner Production* 217 (2019), pp. 615–626. ISSN: 09596526. DOI: 10.1016/j.jclepro.2019.01.171.

[67] Xianhui Zhao et al. “Biogas Reforming to Syngas: A Review”. In: *iScience* 23.5 (2020), p. 101082. DOI: 10.1016/j.isci.2020.101082.

[68] Stefan Bube et al. “Power and biogas to methanol – A techno-economic analysis of carbon-maximized green methanol production via two reforming approaches”. In: *Energy Conversion and Management* 304 (2024), p. 118220. ISSN: 01968904. DOI: 10.1016/j.enconman.2024.118220.

[69] Jeongdong Kim et al. “Biogas reforming integrated with PEM electrolysis via oxygen storage process for green hydrogen production: From design to robust optimization”. In: *Energy Conversion and Management* 251 (2022), p. 115021. ISSN: 01968904. DOI: 10.1016/j.enconman.2021.115021.

[70] F. Rau et al. “Efficiency of a pilot-plant for the autothermal reforming of biogas”. In: *International Journal of Hydrogen Energy* 44.35 (2019), pp. 19135–19140. ISSN: 03603199. DOI: 10.1016/j.ijhydene.2018.04.014.

[71] Vikram Rathod and Purnanand V. Bhale. “Experimental Investigation on Biogas Reforming for Syngas Production over an Alumina based Nickel Catalyst”. In: *Energy Procedia* 54 (2014), pp. 236–245. ISSN: 18766102. DOI: 10.1016/j.egypro.2014.07.267.

[72] Fabián Guerrero et al. “Syngas Production From the Reforming of Typical Biogas Compositions in an Inert Porous Media Reactor”. In: *Frontiers in chemistry* 8 (2020), p. 145. ISSN: 2296-2646. DOI: 10.3389/fchem.2020.00145.

[73] Jenö Schipek et al. *Methanolherstellung aus Biogas mittels Dreiphasenreaktor: (COOMet)*. Ed. by GWF Gas. Freiberg, 2021. URL: https://gwf-gas.de/wp-content/uploads/2021/07/GE_07-08_2021_fb_Shipek.pdf.

[74] Noerma J. Azhari et al. “Methanol synthesis from CO2: A mechanistic overview”. In: *Results in Engineering* 16 (2022), p. 100711. ISSN: 25901230. DOI: 10.1016/j.rineng.2022.100711.

[75] Xiaojing Cui et al. “Enhancing methanol selectivity of commercial Cu/ZnO/Al2O3 catalyst in CO2 hydrogenation by surface silylation”. In: *Applied Catalysis B: Environmental* 339 (2023), p. 123099. ISSN: 09263373. DOI: 10.1016/j.apcatb.2023.123099.

[76] Jack E. N. Swallow et al. “Revealing the Role of CO during CO2 Hydrogenation on Cu Surfaces with In Situ Soft X-Ray Spectroscopy”. In: *Journal of the American Chemical Society* 145.12 (2023), pp. 6730–6740. DOI: 10.1021/jacs.2c12728.

[77] Liang Zhu et al. “Mechanistic Understanding of Dissociated Hydrogen in Cu/CeO2-Catalyzed Methanol Synthesis”. In: *ACS applied materials & interfaces* 17.4 (2025), pp. 7151–7163. DOI: 10.1021/acsami.4c18915.

[78] Chandra Chowdhury, Felix Studt, and Jelena Jelic. “Metal–Support Interactions in Metal/Oxide and Inverse Oxide/Metal Catalysts: A Case Study Using Cu/ZnO and ZnO/Cu Model Catalysts”. In: *The Journal of Physical Chemistry C* 129.12 (2025), pp. 5860–5867. ISSN: 1932-7447. DOI: 10.1021/acs.jpcc.4c08821.

[79] Runping Ye et al. “A Ce-CuZn catalyst with abundant Cu/Zn-OV-Ce active sites for CO2 hydrogenation to methanol”. In: *Nature communications* 15.1 (2024), p. 2159. DOI: 10.1038/s41467-024-46513-3.

[80] Niels D. Nielsen, Anker D. Jensen, and Jakob M. Christensen. “The roles of CO and CO2 in high pressure methanol synthesis over Cu-based catalysts”. In: *Journal of Catalysis* 393 (2021), pp. 324–334. ISSN: 00219517. DOI: 10.1016/j.jcat.2020.11.035.

[81] Letian Wang et al. “CO2 Activation and Hydrogenation on Cu-ZnO/Al2O3 Nanorod Catalysts: An In Situ FTIR Study”. In: *Nanomaterials (Basel, Switzerland)* 12.15 (2022). ISSN: 2079-4991. DOI: 10.3390/nano12152527.

[82] Yu Gao et al. “Stable CO 2 Hydrogenation to Methanol by Cu Interacting with Isolated Zn Cations in Zincosilicate CIT-6”. In: *ACS Catalysis* 15.3 (2025), pp. 1807–1818. ISSN: 2155-5435. DOI: 10.1021/acscatal.4c07496.

[83] N. Mota et al. “Highly active Cu/ZnO-Al catalyst for methanol synthesis: effect of aging on its structure and activity”. In: *RSC Advances* 8.37 (2018), pp. 20619–20629. DOI: 10.1039/C8RA03291B.

[84] Nathan Barrow et al. “Doubling the life of Cu/ZnO methanol synthesis catalysts via use of Si as a structural promoter to inhibit sintering”. In: *Science advances* 10.3 (2024), eadk2081. DOI: 10.1126/sciadv.adk2081.

[85] Xing Huang et al. “Visualizing Structural and Chemical Transformations of an Industrial Cu/ZnO/Al 2 O 3 Pre–catalyst during Activation and CO 2 Reduction”. In: *ChemCatChem* 14.24 (2022). ISSN: 1867-3880. DOI: 10.1002/cctc.202201280.

[86] Yangzhi Xu et al. “Insights into the interfacial structure of Cu/ZrO2 catalysts for methanol synthesis from CO2 hydrogenation: Effects of Cu-supported nano-ZrO2 inverse interface”. In: *Chemical Engineering Journal* 470 (2023), p. 144006. ISSN: 13858947. DOI: 10.1016/j.cej.2023.144006.

[87] Anisoara Oubraham et al. “Preparation of Copper-Based Catalysts for Obtaining Methanol by the Chemical Impregnation Method”. In: *Materials (Basel, Switzerland)* 17.4 (2024). ISSN: 1996-1944. DOI: 10.3390/ma17040847.

[88] Bing Han et al. “Sol-gel synthesis of Pt-Co-CeOx codierite catalyst for biogas reforming to methanol compatible syngas”. In: *Energy* 329 (2025), p. 136707. ISSN: 03605442. DOI: 10.1016/j.energy.2025.136707.

[89] Cheng-Zhang Yao et al. “Effect of preparation method on the hydrogen production from methanol steam reforming over binary Cu/ZrO2 catalysts”. In: *Applied Catalysis A: General* 297.2 (2006), pp. 151–158. ISSN: 0926860X. DOI: 10.1016/j.apcata.2005.09.002.

[90] Issaraporn Rakngam et al. “Hydrothermal synthesis of ZnZrO x catalysts for CO2 hydrogenation to methanol: the effect of pH on structure and activity”. In: *RSC sustainability* 2.12 (2024), pp. 3798–3805. DOI: 10.1039/d4su00522h.

[91] Mustapha Grema Mohammed et al. “Overview of the latest progress and prospects in the catalytic hydrogenation of carbon dioxide (CO2) to methanol in membrane reactors”. In: *International Journal of Hydrogen Energy* 77 (2024), pp. 936–957. ISSN: 03603199. DOI: 10.1016/j.ijhydene.2024.06.138.

[92] Denis Makhmutov et al. “Reaction Pathways of Methanol Formation in CO 2 Hydrogenation over Pd-Based Catalysts”. In: *ACS Catalysis* 15.3 (2025), pp. 2328–2341. ISSN: 2155-5435. DOI: 10.1021/acscatal.4c07462.

[93] F. Nestler et al. “A novel approach for kinetic measurements in exothermic fixed bed reactors: advancements in non-isothermal bed conditions demonstrated for methanol synthesis”. In: *Reaction Chemistry & Engineering* 6.6 (2021), pp. 1092–1107. DOI: 10.1039/D1RE00071C.

[94] S. K. Wilkinson et al. “Understanding the generation of methanol synthesis and water gas shift activity over copper-based catalysts – A spatially resolved experimental kinetic study using steady and non-steady state operation under CO/CO2/H2 feeds”. In: *Journal of Catalysis* 337 (2016), pp. 208–220. ISSN: 00219517. DOI: 10.1016/j.jcat.2016.01.025.

[95] Xiaohang Sun and Binhang Yan. “Emerging Strategies in Engineering Cu-ZnO Interfacial Sites for CO 2 -to-Methanol: Mechanistic Advances, Challenges, and Opportunities”. In: *ACS Catalysis* (2025), pp. 18282–18304. ISSN: 2155-5435. DOI: 10.1021/acscatal.5c05750.

[96] Sabar Pangihutan Simanungkalit. “Preparation and evaluation of Cu/ZnO-based catalysts for methanol synthesis from biomass pyrolysis syngas”. Dissertation. Perth: University of Western Australia, 2024. URL: https://api.research-repository.uwa.edu.au/ws/portalfiles/portal/371574958/THESIS_-_DOCTOR_OF_PHILOSOPHY_-_SIMANUNGKALIT_Sabar_Pangihutan_-_2024.pdf.

[97] Fei Chen et al. “Structure-Performance Correlations over Cu/ZnO Interface for Low-Temperature Methanol Synthesis from Syngas Containing CO2”. In: *ACS applied materials & interfaces* 13.7 (2021), pp. 8191–8205. DOI: 10.1021/acsami.0c18600.

[98] Paweł Kowalik, Wiesław Próchniak, and Tadeusz Borowiecki. “The effect of alkali metals doping on properties of Cu/ZnO/Al2O3 catalyst for water gas shift”. In: *Catalysis Today* 176.1 (2011), pp. 144–148. ISSN: 09205861. DOI: 10.1016/j.cattod.2011.01.028.

[99] Rajan Singh, Kaushik Kundu, and Kamal K. Pant. “CO2 hydrogenation to methanol over Cu-ZnO-CeO2 catalyst: Reaction structure–activity relationship, optimizing Ce and Zn ratio, and kinetic study”. In: *Chemical Engineering Journal* 479 (2024), p. 147783. ISSN: 13858947. DOI: 10.1016/j.cej.2023.147783.

[100] David Kordus et al. “Enhanced Methanol Synthesis from CO2 Hydrogenation Achieved by Tuning the Cu-ZnO Interaction in ZnO/Cu2O Nanocube Catalysts Supported on ZrO2 and SiO2”. In: *Journal of the American Chemical Society* 146.12 (2024), pp. 8677–8687. DOI: 10.1021/jacs.4c01077.

[101] Luiz H. Vieira et al. “CO2 Hydrogenation to Methanol over Mesoporous SiO2-Coated Cu-Based Catalysts”. In: *ACS nanoscience Au* 4.4 (2024), pp. 235–242. DOI: 10.1021/acsnanoscienceau.4c00016.

[102] Mohammad Sadegh Arabahmadi et al. “CO2-to-methanol conversion over promoted Cu/ZnO/Al2O3 catalysts by Ga, Zr, and Co: A comprehensive DFT and experimental study”. In: *Energy Conversion and Management: X* 28 (2025), p. 101291. ISSN: 25901745. DOI: 10.1016/j.ecmx.2025.101291.

[103] Xin Xin, Peng Gao, and Shenggang Li. “Mechanism and structure–activity relationship of H 2 and CO 2 activation at the ZnO/Cu catalyst interface”. In: *Catalysis Science & Technology* 14.18 (2024), pp. 5439–5449. ISSN: 2044-4753. DOI: 10.1039/d4cy00604f.

[104] Fei Chen et al. “Enhanced performance and stability of Cu/ZnO catalyst by introducing MgO for low-temperature methanol synthesis using methanol itself as catalytic promoter”. In: *Fuel* 315 (2022), p. 123272. ISSN: 00162361. DOI: 10.1016/j.fuel.2022.123272.

[105] Gianfranco Pacchioni. “From CO 2 to Methanol on Cu/ZnO/Al 2 O 3 Industrial Catalyst. What Do We Know about the Active Phase and the Reaction Mechanism?” In: *ACS Catalysis* 14.4 (2024), pp. 2730–2745. ISSN: 2155-5435. DOI: 10.1021/acscatal.3c05669.

[106] Andrea Álvarez et al. “Challenges in the Greener Production of Formates/Formic Acid, Methanol, and DME by Heterogeneously Catalyzed CO2 Hydrogenation Processes”. In: *Chemical reviews* 117.14 (2017), pp. 9804–9838. DOI: 10.1021/acs.chemrev.6b00816.

[107] Zhisheng Shi, Qingqing Tan, and Dongfang Wu. “Ternary copper-cerium-zirconium mixed metal oxide catalyst for direct CO2 hydrogenation to methanol”. In: *Materials Chemistry and Physics* 219 (2018), pp. 263–272. ISSN: 02540584. DOI: 10.1016/j.matchemphys.2018.08.038.

[108] Tianqinji Qi et al. “Yttria-doped Cu/ZnO catalyst with excellent performance for CO2 hydrogenation to methanol”. In: *Molecular Catalysis* 509 (2021), p. 111641. ISSN: 24688231. DOI: 10.1016/j.mcat.2021.111641.

[109] Hong Ren et al. “Methanol synthesis from CO2 hydrogenation over Cu/g-Al2O3 catalysts modified by ZnO, ZrO2 and MgO”. In: *Journal of Industrial and Engineering Chemistry* 28 (2015), pp. 261–267. ISSN: 1226086X. DOI: 10.1016/j.jiec.2015.03.001.

[110] Maxim Zabilskiy et al. “Methanol synthesis over Cu/CeO 2 –ZrO 2 catalysts: the key role of multiple active components”. In: *Catalysis Science & Technology* 11.1 (2021), pp. 349–358. ISSN: 2044-4753. DOI: 10.1039/d0cy01762k.

[111] Yong Yan et al. “CO2 hydrogenation to methanol on tungsten-doped Cu/CeO2 catalysts”. In: *Applied Catalysis B: Environmental* 306 (2022), p. 121098. ISSN: 09263373. DOI: 10.1016/j.apcatb.2022.121098.

[112] Venkata D.B.C. Dasireddy, Strah Štefančič Neja, and Likozar Blaž. “Correlation between synthesis pH, structure and Cu/MgO/Al2O3 heterogeneous catalyst activity and selectivity in CO2 hydrogenation to methanol”. In: *Journal of CO2 Utilization* 28 (2018), pp. 189–199. ISSN: 22129820. DOI: 10.1016/j.jcou.2018.09.002.

[113] Kang Xiao et al. “For Better Industrial Cu/ZnO/Al2O3 Methanol Synthesis Catalyst: A Compositional Study”. In: *Catalysis Letters* 147.6 (2017), pp. 1581–1591. ISSN: 1011-372X. DOI: 10.1007/s10562-017-2022-8.

[114] Peng Gao et al. “Yttrium oxide modified Cu/ZnO/Al 2 O 3 catalysts via hydrotalcite-like precursors for CO 2 hydrogenation to methanol”. In: *Catalysis Science & Technology* 5.9 (2015), pp. 4365–4377. ISSN: 2044-4753. DOI: 10.1039/c5cy00372e.

[115] Junxin Guo et al. “Synthesis of oxygen vacancies enriched Cu/ZnO/CeO 2 for CO 2 hydrogenation to methanol”. In: *Greenhouse Gases: Science and Technology* 11.6 (2021), pp. 1171–1179. ISSN: 2152-3878. DOI: 10.1002/ghg.2102.

[116] Kongzhai Li and Jingguang G. Chen. “CO 2 Hydrogenation to Methanol over ZrO 2 -Containing Catalysts: Insights into ZrO 2 Induced Synergy”. In: *ACS Catalysis* 9.9 (2019), pp. 7840–7861. ISSN: 2155-5435. DOI: 10.1021/acscatal.9b01943{\#}.

[117] Matthias S. Frei et al. “Atomic-scale engineering of indium oxide promotion by palladium for methanol production via CO2 hydrogenation”. In: *Nature communications* 10.1 (2019), p. 3377. DOI: 10.1038/s41467-019-11349-9.

[118] Marina A. Tedeeva et al. “Catalytic systems for hydrogenation of CO2 to methanol”. In: *Molecular Catalysis* 566 (2024), p. 114403. ISSN: 24688231. DOI: 10.1016/j.mcat.2024.114403.

[119] Soumalya Roy et al. “Advanced catalytic strategies for CO 2 to methanol conversion: noble metal-based heterogeneous and electrochemical approaches”. In: *RSC sustainability* 3.3 (2025), pp. 1303–1332. DOI: 10.1039/D4SU00749B.

[120] Guiming Xie et al. “Boosting CO2 hydrogenation to methanol by adding trace amount of Au into Cu/ZnO catalysts”. In: *Applied Catalysis B: Environmental* 324 (2023), p. 122233. ISSN: 09263373. DOI: 10.1016/j.apcatb.2022.122233.

[121] Fei Chen et al. “Alcohol Solvent Assisted Synthesis of Metallic and Metal Oxide Catalysts: As-Prepared Cu/ZnO/Al 2 O 3 Catalysts for Low-Temperature Methanol Synthesis with an Ultrahigh Yield”. In: *ACS Catalysis* 13.9 (2023), pp. 6169–6184. ISSN: 2155-5435. DOI: 10.1021/acscatal.3c00199.

[122] Pramod Sripada et al. “Investigating the dynamic structural changes on Cu/CeO2 catalysts observed during CO2 hydrogenation”. In: *Journal of Catalysis* 381 (2020), pp. 415–426. ISSN: 00219517. DOI: 10.1016/j.jcat.2019.11.017.

[123] Congyi Wu et al. “Inverse ZrO2/Cu as a highly efficient methanol synthesis catalyst from CO2 hydrogenation”. In: *Nature communications* 11.1 (2020), p. 5767. DOI: 10.1038/s41467-020-19634-8.

[124] Chaoheng Liu et al. “Methanol synthesis from CO2 hydrogenation over copper catalysts supported on MgO-modified TiO2”. In: *Journal of Molecular Catalysis A: Chemical* 425 (2016), pp. 86–93. ISSN: 13811169. DOI: 10.1016/j.molcata.2016.09.032.

[125] Aohua Feng et al. “Mechanism study on CO2 hydrogenation to methanol on Cu5/TiO2 catalyst”. In: *Molecular Catalysis* 563 (2024), p. 114259. ISSN: 24688231. DOI: 10.1016/j.mcat.2024.114259.

[126] Mengdong Nie et al. “Effect of Mn content in CuO/MnCeO x catalysts on CO 2 hydrogenation for methanol synthesis”. In: *Reaction Chemistry & Engineering* 8.6 (2023), pp. 1383–1394. DOI: 10.1039/D3RE00022B.

[127] Gustavo A. S. Alves et al. “Mn-promoted MoS2 catalysts for CO2 hydrogenation: enhanced methanol selectivity due to MoS2/MnOx interfaces”. In: *Catalysis Science & Technology* 14.5 (2024), pp. 1138–1147. ISSN: 2044-4753. DOI: 10.1039/D3CY01711G.

[128] Nils Ortner et al. “Factors affecting primary and secondary pathways in CO2 hydrogenation to methanol over CuZnIn/MZrOx (La, Ti or Y)”. In: *Catalysis Today* 387 (2022), pp. 47–53. ISSN: 09205861. DOI: 10.1016/j.cattod.2021.05.008.

[129] Alexey Pustovarenko et al. “Metal–Organic Framework-Derived Synthesis of Cobalt Indium Catalysts for the Hydrogenation of CO 2 to Methanol”. In: *ACS Catalysis* 10.9 (2020), pp. 5064–5076. ISSN: 2155-5435. DOI: 10.1021/acscatal.0c00449.

[130] Anastasiya Bavykina et al. “Turning a Methanation Co Catalyst into an In–Co Methanol Producer”. In: *ACS Catalysis* 9.8 (2019), pp. 6910–6918. ISSN: 2155-5435. DOI: 10.1021/acscatal.9b01638.

[131] Jiaming Liang et al. “CO2 hydrogenation over Fe-Co bimetallic catalysts with tunable selectivity through a graphene fencing approach”. In: *Nature communications* 15.1 (2024), p. 512. DOI: 10.1038/s41467-024-44763-9.

[132] Chao Meng et al. “InNi3C0.5/Fe3O4 catalyst for the CO2 hydrogenation to methanol: Co-precipitation preparation, performance and mechanistic insight”. In: *Fuel* 365 (2024), p. 131111. ISSN: 00162361. DOI: 10.1016/j.fuel.2024.131111.

[133] Malte Behrens and Robert Schlögl. “How to Prepare a Good Cu/ZnO Catalyst or the Role of Solid State Chemistry for the Synthesis of Nanostructured Catalysts”. In: *Zeitschrift für anorganische und allgemeine Chemie* 639.15 (2013), pp. 2683–2695. ISSN: 0044-2313. DOI: 10.1002/zaac.201300356.

[134] Shiva Kumar Saw et al. “Significance and influence of various promoters on Cu–based catalyst for synthesizing methanol from syngas: a critical review”. In: *Journal of Chemical Technology & Biotechnology* 98.5 (2023), pp. 1083–1102. ISSN: 0268-2575. DOI: 10.1002/jctb.7331.

[135] Daniyal Kiani and Israel E. Wachs, eds. *The Conundrum of "Pair Sites" in Langmuir-Hinshelwood Reaction Kinetics in Heterogeneous Catalysis*. Vol. 14. 2024. DOI: 10.1021/acscatal.4c02813.

[136] Y. Slotboom et al. “Critical assessment of steady-state kinetic models for the synthesis of methanol over an industrial Cu/ZnO/Al2O3 catalyst”. In: *Chemical Engineering Journal* 389 (2020), p. 124181. ISSN: 13858947. DOI: 10.1016/j.cej.2020.124181.

[137] C. Seidel et al. “Kinetic modeling of methanol synthesis from renewable resources”. In: *Chemical Engineering Science* 175 (2018), pp. 130–138. ISSN: 00092509. DOI: 10.1016/j.ces.2017.09.043.

[138] Pierluigi Villa et al. “Synthesis of alcohols from carbon oxides and hydrogen. 1. Kinetics of the low-pressure methanol synthesis”. In: *Industrial & Engineering Chemistry Process Design and Development* 24.1 (1985), pp. 12–19. ISSN: 0196-4305. DOI: 10.1021/i200028a003.

[139] G. H. Graaf, E. J. Stamhuis, and A.A.C.M. Beenackers. “Kinetics of low-pressure methanol synthesis”. In: *Chemical Engineering Science* 43.12 (1988), pp. 3185–3195. ISSN: 00092509. DOI: 10.1016/0009-2509(88)85127-3.

[140] K.M.Vanden Bussche and G. F. Froment. “A Steady-State Kinetic Model for Methanol Synthesis and the Water Gas Shift Reaction on a Commercial Cu/ZnO/Al2O3Catalyst”. In: *Journal of Catalysis* 161.1 (1996), pp. 1–10. ISSN: 00219517. DOI: 10.1006/jcat.1996.0156. URL: https://www.sciencedirect.com/science/article/pii/S0021951796901566.

[141] Nonam Park et al. “Kinetic modeling of methanol synthesis over commercial catalysts based on three-site adsorption”. In: *Fuel Processing Technology* 125 (2014), pp. 139–147. ISSN: 03783820. DOI: 10.1016/j.fuproc.2014.03.041.

[142] F. Nestler et al. “Kinetic modelling of methanol synthesis over commercial catalysts: A critical assessment”. In: *Chemical Engineering Journal* 394 (2020), p. 124881. ISSN: 13858947. DOI: 10.1016/j.cej.2020.124881.

[143] Magnus Fürst et al. “OptiSMOKE++: A toolbox for optimization of chemical kinetic mechanisms”. In: *Computer Physics Communications* 264 (2021), p. 107940. ISSN: 00104655. DOI: 10.1016/j.cpc.2021.107940.

[144] Åke Björck. *Numerical Methods for Least Squares Problems*. Society for Industrial and Applied Mathematics, 1996. DOI: 10.1137/1.9781611971484.

3. Experimental Setups and Methods

The following section provides an overview of the experimental methodologies and setups applied in this thesis. The research combines catalyst-synthesis, physio-chemical characterization, laboratory-scale reactivity testing, and advanced modeling in order to develop and analyze novel carrier-supported catalysts for MeOH synthesis from CO_2-rich SynGas. The methodological framework for the thesis spans the entire development chain: from the design and execution of synthesis and manufacturing protocols, through the implementation of a comprehensive characterization strategy, to the systematic evaluation of catalytic performance under relevant reaction conditions. This enables linking experimental observations with mechanistic insights for kinetic modeling, parameter estimation, and reactor-scale simulations. This section further introduces the laboratory test stand, reactor configuration, operating procedures, analytical instrumentation, and data acquisition strategy employed for catalyst evaluation. In addition, the software framework developed for numerical parameter fitting, reaction-engineering calculations, and model integration is outlined, highlighting its role in bridging experimental data with predictive modeling. Beyond laboratory-scale investigations, this thesis addresses the translation of MeOH synthesis from controlled experimental environments to a technically relevant demonstration scale. The second part of this section therefore presents the development of a pilot-scale test stand for MeOH production from biogas-derived SynGas. This includes the engineering design, integration, and commissioning of the process units required for continuous operation. The pilot facility serves to assess the feasibility of decentralized, renewables-based MeOH production and provides a platform for extended operation, process optimization, and evaluation of scale-up effects that cannot be accessed in laboratory settings. The subsequent subsections describe the conceptual plant design, key process components, gas-conditioning and feedstock-handling strategies, reactor integration, and the associated analytical and data acquisition systems.

3.1. Research Track 1: Development, Characterization and Testing of Carrier Catalysts for Conversion of CO_2-rich Synthesis Gas to Methanol

Based on recent literature, a catalyst-screening strategy was adopted to identify effective Cu/ZnO-based catalyst formulations, production routes, and activation protocols, yielding a total of 13 distinct catalyst samples for laboratory evaluation. These samples were tested in a dedicated laboratory test bed, and iterative adjustments were made according to preliminary screening results. From this screening, one catalyst formulation was selected for detailed testing and characterization. This formulation was subsequently deconstructed into its principal components and promoters, and a stepwise promotional approach was applied to investigate the individual effects of each promoter within the multi-promoter system on catalyst performance and physio-chemical properties.

The following subsection describes the manufacturing procedures of the 13 evaluated samples. Parts of the subsequent sections have been published in "CO_2-Hydrogenation to Methanol over CuO/ZnO Based

Infiltration Composite Catalyst Spheres" (ChemCatChem 16, 21, 2024) and "CO_2- and CO Conversion to Methanol over Promoted CuO/ZnO-Based Infiltration Composite Catalyst Spheres – Characterization, Experimental and Comparative Reaction Kinetics" (Applied Catalysis A: General, 2026).

3.1.1. Manufacturing of Catalyst samples

The catalyst samples investigated in this work were manufactured by coating high–surface-area, 800 µm-diameter Al_2O_3 spheres (SASOL, Hamburg, Germany) using the incipient wetness impregnation (IWI) method. For the preliminary catalyst screening, different carrier types of α-, γ-, and θ-Al_2O_3 spheres were applied and evaluated. The spheres were coated either in their as-received state or after applying an alkaline pre treatment protocol. Prior to coating, the maximum H_2O adsorption capacity of each carrier type was determined. For alkaline treatment in selected formulations, Al_2O_3 spheres were immersed in an NaOH solution for 2 h under stirring and subsequently dried for 4 h at 100 °C. Catalyst compositions were formulated on a CuO/ZnO basis and promoted with various metal oxides selected for their potential to modify surface basicity, surface chemistry, and electronic properties, thereby enhancing CO_2 adsorption and its conversion to MeOH. In total, 13 promotional catalyst formulations were designed and synthesized for screening. Compositions were chosen such that the molar ratio of CuO to ZnO remained constant across all promoted samples, in accordance with previously reported optimal ratios for CZA-based catalyst systems [1]. Promoter identity and loading were selected based on literature and were adapted, combined and extended for this study, with the basic concept for coating high surface are alumina carrier spheres based around the work of Gesmanee et al. (2017) [2].
In preparation of the samples, 100g of each sample were produced in two batches (each 50g). To prepare 50 g of the infiltration composite spheres with a catalyst content of 20 $\%_{wt}$ catalytically active coating, the nitrate salts of the respective metals were first weighed into a beaker according to their molar proportions in the catalyst (Introduced in Chapter 4, table 4.1).
Nitrate precursors were used for compounding the individual coating for the spheres. Citrate was herein applied for pH control in the synthesis process for selected recipes:

- $Cu(NO_3)_2 \cdot 3\ H_2O$ (Carl Roth GmbH, Karlsruhe Germany)
- $Zn(NO_3)_2 \cdot 4\ H_2O$ (Carl Roth GmbH, Karlsruhe Germany)
- $ZrO(NO_3)_2 \cdot 2.5\ H_2O$ (Alfa Aesar GmbH, Kandel Germany)
- $Ce(NO_3)_3 \cdot 6\ H_2O$ (Alfa Aesar GmbH, Kandel Germany)
- $Ca(NO_3)_2 \cdot 4\ H_2O$ (Roth GmbH, Karlsruhe Germany)
- $Y(NO_3)_3 \cdot 6\ H_2O$ (Alfa Aesar GmbH, Kandel Germany)
- $Mg(NO_3)_2 \cdot 6\ H_2O$ (Roth GmbH, Karlsruhe Germany)
- $W(NO_3)_6$ (Roth GmbH, Karlsruhe, Germany)
- $(NH_4)_3(C_6H_5O_7)$ (Ammonium Citrate) (Sigma-Aldrich Inc, St. Louis USA)

The catalyst compositions were selected such that the CuO : ZnO molar ratio remained constant across all promoted formulations, in accordance with previously reported ratios for CZA-based catalysts [1]. The beaker was filled with water corresponding to the maximum water absorption capacity of the Al_2O_3 carrier, and the

required nitrate salts were dissolved under continuous stirring. The solution was mixed with 40 g of alumina spheres until fully absorbed. The impregnated spheres were dried for 4 h at 100 °C and subsequently calcined for 1 h starting at 350 °C with a heating rate of 2 °C min^{-1}. Each batch yielded 50 g of catalyst spheres with a 20 wt% mixed-oxide coating. A schematic representation of the aforementioned catalyst production protocol is given in figure 3.1. Catalysts were manufactured on order by CCD Chemical Consulting GbR (Aachen, Germany). For comparison, an industrial, co precipitated CZA reference catalyst (Hutong HUC-98, 6mm) was crushed and sieved to a particle diameter of 800–900 µm from the original 6 mm pellets.

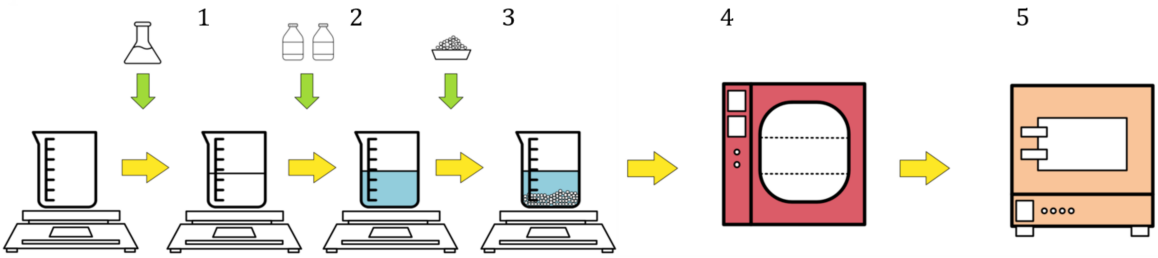

Figure 3.1.: Flowsheet representation of the catalyst manufacturing protocol applied in the thesis. 1) Specified amount of distilled water 2) Precursors according to final molar composition 3) Adding Carrier Spheres under stirring 4) Drying Catalyst 5) Calcination.

3.1.2. Physio-chemical characterization of catalyst samples

Surface Composition and Chemical State

X-ray Photoelectron Spectroscopy (XPS) measurements were performed on a Phi5000 VersaProbe II (ULVAC-Phi Inc., USA) using a monochromatic Al K-α source (1.486 keV) at 50 W and 15 kV. General surveys were recorded at 187.5 eV pass energy with 0.8 eV steps and 100 ms per step. Detailed spectra for Cu 2p (925–955 eV) and Zn 2p (1010–1060 eV) regions were acquired to determine the oxidation state and surface distribution of catalytic species on unreduced samples.

Raman spectroscopy (RS) was performed using a WITec alpha 300 R microscope (Ulm, Germany) with a 532 nm excitation laser (7 mW) and 50× magnification. For each sample, 120 accumulations with 0.5 s integration time were collected on unreduced catalyst-coated Al_2O_3 carrier spheres. Spectra were baseline-corrected using the WITec Project SIX software.

Microstructure and Morphology

Surface topography and elemental composition were investigated using Scanning Electron Microscopy (SEM) and Energy Dispersive X-ray Spectroscopy (EDX) with a JEOL JSM-IT800 microscope coupled with an EDAX Octane Elect Super EDX system (70 mm^2 chip). Unreduced catalyst samples were analyzed at room temperature to determine surface morphology and local elemental distribution.

High-Angle Annular Dark-Field Scanning Transmission Electron Microscopy (HAADF-STEM) and energy-dispersive X-ray spectroscopy (STEM-EDXS) were performed on a Talos F200i (Thermo Fisher Scientific) at 200 kV. Focused Ion Beam (FIB) lamellae were prepared from catalyst sphere surfaces at 8–9 μm depth. Fast Fourier Transformation (FFT) and inverse FFT analysis of STEM images (processed in ImageJ) were used to determine lattice spacings of metal oxide structures in the oxidized catalyst state.

Structural Characterization

X-ray Diffraction (XRD) measurements were performed using an Empyrean diffractometer (Malvern Panalytical B.V., Netherlands) with Cu Kα radiation (45 kV, 40 mA). Data were collected in Bragg–Brentano geometry

over the 2θ range of 10–90° with 0.026° step size and 250 s counting time per step using a 255-channel PIXcel detector.

Textural Properties

Specific surface areas, pore size distributions, and pore volumes were determined using Brunauer–Emmett–Teller (BET) surface area analysis on a Micromeritics ASAP 2060 analyzer. N_2-adsorption and -desorption isotherms were measured at 196 °C. Samples were pretreated under vacuum for 2 h at room temperature prior to analysis.

Redox and Adsorption Properties

Hydrogen Temperature-Programmed Reduction (H_2-TPR) was conducted on a Micromeritics 2950 MicroActive instrument using approximately 100 mg of catalyst. Samples were pretreated in-situ at 200 °C for 30 min under He flow. Reduction was performed at 10 °C/min from 35 °C to 600 °C using 5 % H_2 in Ar. Hydrogen consumption was monitored via thermal conductivity detector (TCD).

Hydrogen Temperature-Programmed Desorption (H_2-TPD) was carried out on the same device after reduction under 5 % H_2/Ar (20–300 °C). Reduced samples were flushed with 5 % H_2/Ar (20–250 °C, 10 °C/min) and subsequently desorbed under He to 700 °C at 10 °C/min. The desorbed hydrogen was quantified using TCD. Copper surface area, dispersion, and degree of reduction were determined from integrated H_2 desorption between 30–360 °C using established methodologies. The copper surface area was calculated from copper surface atom density ($\rho_{Cu} = 1.47 \times 10^{19}$ atoms m^{-2}), with dispersion defined as the ratio of surface to total copper atoms.

Carbon Dioxide Temperature-Programmed Desorption (CO_2-TPD) experiments were performed on a ChemBET Pulsar TPD/TPR instrument (Anton Paar QuantaTec, Boynton Beach, USA). Approximately 500 mg of catalyst were dried overnight at 120 °C under Ar in an outgas station, then heat-treated at 200 °C (5 min ramp) for 60 min and cooled to 50 °C under He. CO_2 adsorption was carried out at 50 °C under 5 % CO_2/He for 90 min, followed by He purging (30 min). TPD was performed from 50–600 °C at 5 °C/min under He, with detection via TCD.

Ammonia Temperature-Programmed Desorption (NH_3-TPD) was used for acid site characterization on a Micromeritics 2950 MicroActive using approximately 100 mg of catalyst. After pretreatment at 200 °C for 30 min under He, samples were exposed to 10 % NH_3/He until saturation (TCD baseline stabilization). Ammonia desorption was monitored by TCD during heating from 50–500 °C at 10 °C/min to quantify surface acid site density and distribution.

3.1.3. Laboratory Setup for Performance Evaluation and Kinetic Studies

Catalyst performance was evaluated in a laboratory test bench using a single tubular reactor (inner diameter: 25 mm, catalyst volume: 70 mL). Images of the applied laboratory plant set-up that was operated in a laboratory at MVA Müllverbrennungsanlage Bonn GmbH are given in figure 3.2.

Reactant gases (CO, H_2, CO_2) were supplied from high-pressure cylinders and regulated by mass flow controllers (Bronkhorst El-Flow C200 for CO and H_2; Bronkhorst mini CORI-Flow for CO_2). Reactor pressure was controlled via a proportional flow valve, a pressure control valve, and individual gas regulators. Temperature was maintained in counter-flow configuration using a thermo-oil cryostat.

Product gases were analyzed online by gas chromatography (Shimadzu GC2030 AT) equipped with serial Rt-U-Bond PLOT and SH MSieve 5A columns (30 m × 0.53 mm), operated with He carrier gas and thermal conductivity detection (TCD). Condensed liquids were collected in a high-pressure flash vessel and analyzed

by HPLC–MS (Shimadzu LC-MS 2020). Off-gas CO_2 and H_2 concentrations were monitored using inline sensors (BlueSense BCP-CO_2, BCP-H_2) and a redundant analyzer (Emerson NGA2000).
Catalyst samples (70 mL) were loaded into the reactor and fixed with quartz wool for uniform gas distribution. Prior to testing, each catalyst was reduced in pure H_2 flow (0.5 MPa, 5 L min^{-1}) by heating from 50 to 300°C in 10°C increments (10 min per step).

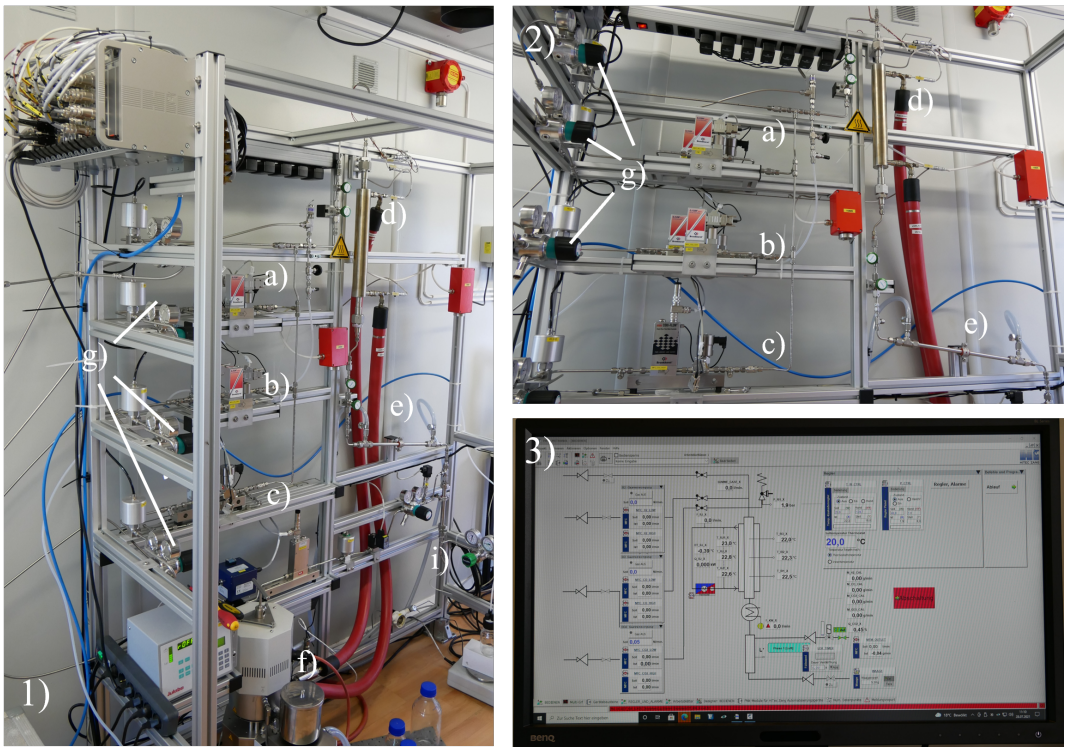

Figure 3.2.: Images of the laboratory single-reactor test setup applied for catalyst screening and testing. 1) total plant. 2) gas dosing and reactor section 3) User Interface for plant operation. a) Gas dosing H_2 b) Gas dosing CO c) Coriolis gas dosing CO_2 d) Reactor with connectors for thermal oil heating/cooling e) Counter current product gas cooling f) Oil thermostat setup g) Pressure regulating valves.

Mass and molar flow rates at the reactor outlet were determined by mass conservation:

$$\dot{m}_{\mathrm{TOT}} = \dot{m}_{\mathrm{CO_2}} + \dot{m}_{\mathrm{H_2}} + \dot{m}_{\mathrm{CO}} \tag{3.1}$$

$$M_{\mathrm{Product}} = \sum_i y_{\mathrm{Product},i} M_i \tag{3.2}$$

$$\dot{n}_{\mathrm{Product}} = \frac{\dot{m}_{\mathrm{TOT}}}{M_{\mathrm{Product}}} \tag{3.3}$$

Reaction conditions for catalyst screening included CO_2-only SynGas with SN =3 at 250°C. After selection of samples for further, detailed testing and kinetic analysis, a wide array of additional tests were included (Lists containing every test run for each selected sample are given in tables B.1 - B.4): GHSV (8 000–12 000 h^{-1}), pressure (2.0–5.0 MPa), temperature (225–275°C), and inlet gas composition defined by the stoichiometric number (SN) and carbon-oxide ratio (COR) (equations 2.4 and 2.6, described in chapter 2)
Steady-state conditions were ensured by holding each setting for 15 min followed by 20 min reaction runs. GC sampling was initiated at the end of each run. Selected experiments were repeated three times to verify

reproducibility. Catalyst performance was evaluated using CO_2 conversion, total carbon conversion, MeOH selectivity and MeOH-space-time yield (STY_MeOH) as performance metrics:

$$X_{CO_2} = \frac{\dot{n}_{CO_2,in} - \dot{n}_{CO_2,out}}{\dot{n}_{CO_2,in}} \tag{3.4}$$

$$X_C = \frac{\dot{n}_{CO_2,in} + \dot{n}_{CO,in} - \dot{n}_{CO_2,out} - \dot{n}_{CO,out}}{\dot{n}_{CO_2,in} + \dot{n}_{CO,in}} \tag{3.5}$$

$$S_{MeOH} = \frac{\dot{n}_{MeOH,out}}{\sum \dot{n}_{products,out}} \tag{3.6}$$

$$STY_{MeOH} = \frac{\dot{m}_{MeOH}}{m_{Catalyst}} \tag{3.7}$$

In early testing for catalyst screening, mass flow of the gaseous product species was taken from mass flow measurement in the off-gas stream and liquid product mass flow of the species was calculated through:

$$\dot{m}_{i,liq} = y_i \frac{\dot{m}_{in,\ gas} - \dot{m}_{out,\ gas}}{M_{tot,\ liq}} M_i, \tag{3.8}$$

$$M_{tot,\ liq} = \sum_{i,liq} y_i M_{i,liq} \tag{3.9}$$

In later, detailed testing, product species mass flow was derived from GC-data with assumption of mass conservation:

$$\dot{m}_i = y_i \frac{\dot{m}_{tot,\ in}}{M_{tot,\ GC}} M_i, \tag{3.10}$$

$$M_{tot,\ GC} = \sum_i y_i M_i \tag{3.11}$$

A P&ID scheme of the applied laboratory test plant is given in figure 3.3:

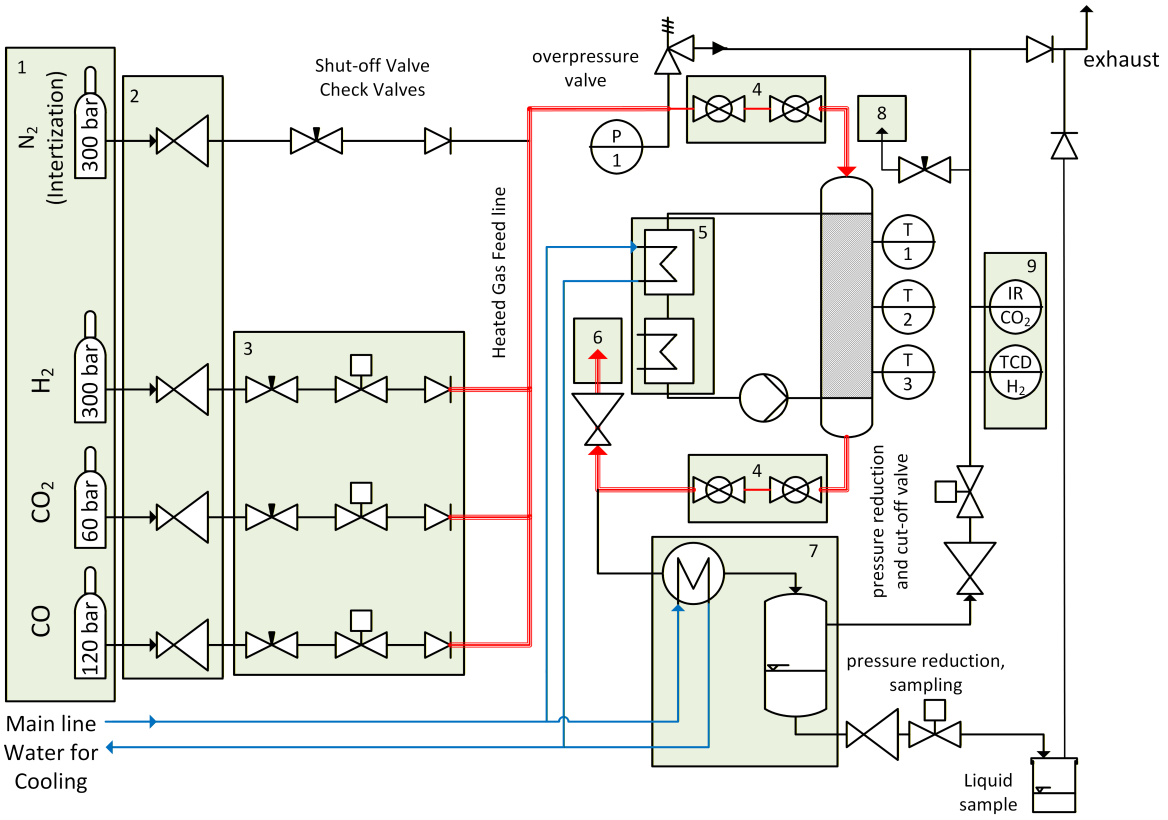

Figure 3.3.: P&ID of the laboratory test plant. 1) Gas supply from high pressure containers 2) Pressure regulators 3) Shut-off valves and mass flow controllers 4) Reactor Coupling 5) Thermal oil control unit 6) GC unit 7) High pressure counter current heat exchanger and flash 8) Online IR gas analysis 9) Inline gas analysis.

3.1.4. Parameter Optimization for Reaction Kinetics

From the cited kinetic models for MeOH synthesis from recent literature, the model published by Graaf et al. in 1988 [3] has shown to produce calculation results with good statistical fit to test setup data for both conventional CZA-catalysts as well as adapted formulations in promoted CZA systems [4]. It applies a double site adsorption mechanism (DS-AT) approach utilizing rate equation terms for all reactions (CO hydrogenation, CO_2 hydrogenation and RWGS), resulting in 13 different constants for parameter fitting to test data. Through this detailed modeling approach, it has been shown to reproduce CZA performance reliably and is thus widely applied in MeOH-synthesis reactor modeling, including refits for modified CZA and promoted catalysts [5]. Owing to its explicit treatment of both CO_2- and CO-hydrogenation pathways, the model is well suited for describing mixed $CO/CO_2/H_2$ feeds. For this thesis, the model was selected to describe the reaction kinetics of the catalyst samples introduced in the following sections. It was used to identify rate-determining steps and to simulate reactor concentration gradients and rate profiles for differently promoted catalyst samples under industrially relevant reaction conditions.

Following Graaf et al. (1988), the kinetic model assumes two types of active sites: one for CO/CO_2 adsorption and one for H_2/H_2O. From the full elementary-step scheme, only the dominant steps for each pathway are retained to minimize model complexity while preserving mechanistic relevance. This follows the general assumption in LHHW models, where all reactions that are not rate determining are assumed to be in equilibrium. The resulting rate expressions are:

$$r_{\mathrm{MeOH,CO}} = k_1 K_{\mathrm{CO}} \left(p_{\mathrm{CO}}\, p_{\mathrm{H_2}}^{1/2} - \frac{p_{\mathrm{MeOH}}}{K_{eq,1}\, p_{\mathrm{H_2}}^{1/2}} \right) D^{-1} \tag{3.12}$$

$$r_{\mathrm{RWGS}} = k_2 K_{\mathrm{CO_2}} \left(p_{\mathrm{CO_2}}\, p_{\mathrm{H_2}} - \frac{p_{\mathrm{CO}}\, p_{\mathrm{H_2O}}}{K_{eq,2}} \right) D^{-1} \tag{3.13}$$

$$r_{\mathrm{MeOH,CO_2}} = k_3 K_{\mathrm{CO_2}} \left(p_{\mathrm{CO_2}}\, p_{\mathrm{H_2}}^{3/2} - \frac{p_{\mathrm{MeOH}}\, p_{\mathrm{H_2O}}}{K_{eq,3}\, p_{\mathrm{H_2}}^{3/2}} \right) D^{-1} \tag{3.14}$$

All rates share a common denominator derived from competitive adsorption on both site types:

$$D = (1 + K_{\mathrm{CO}} p_{\mathrm{CO}} + K_{\mathrm{CO_2}} p_{\mathrm{CO_2}}) \left(p_{\mathrm{H_2}}^{1/2} + \frac{K_{\mathrm{H_2O}}}{K_{\mathrm{H_2}}^{1/2}} p_{\mathrm{H_2O}} \right) \tag{3.15}$$

Adsorption constants are modeled using a simplified van 't Hoff expression with a single pre-exponential factor which lumps the temperature dependent entropy term for adsorption and desorption into one single fitting constant a_i:

$$K_{\mathrm{ads},i} = a_i \exp\left(\frac{\Delta H_{i,\mathrm{ads}}}{RT} \right) \tag{3.16}$$

Kinetic constants follow the Arrhenius form:

$$k_i = b_i \exp\left(\frac{-E_{a,i}}{RT} \right) \tag{3.17}$$

The complete parameter set to be fitted therefore consists of the adsorption parameters a_i, $\Delta H_{i,\mathrm{ads}}$ for CO, CO_2, H_2, and H_2O, and the kinetic parameters b_i, $E_{a,i}$ for the three reaction pathways. These parameters were optimized by fitting the model within a pseudo-homogeneous plug-flow reactor (PFR) framework to experimental $CO/CO_2/H_2$ conversion and product-distribution data gathered from the kinetic studies in the laboratory test plant. A custom Python script was used to fit the kinetic parameters of the Graaf model to the experimentally measured reactor data. Parameter estimation was performed within the PFR framework. Thirteen kinetic and adsorption parameters from the original Graaf formulation were optimized by minimizing the root-mean-squared error (RMSE) between calculated and measured effluent partial pressures of MeOH and H_2O.

$$F_{\mathrm{obj}} = \sum \left[q_{\mathrm{MeOH}} \left(\frac{p_{\mathrm{MeOH,calc}} - p_{\mathrm{MeOH,exp}}}{p_{\mathrm{MeOH,exp}}} \right)^2 + q_{\mathrm{H_2O}} \left(\frac{p_{\mathrm{H_2O,calc}} - p_{\mathrm{H_2O,exp}}}{p_{\mathrm{H_2O,exp}}} \right)^2 \right] \tag{3.18}$$

Weighting factors were introduced to compensate for the higher uncertainty in H_2O prediction, typically set to $q_{\mathrm{MeOH}} = 1$ and $q_{\mathrm{H_2O}} = 3$. Alternative objective-function formulations incorporating additional species were evaluated, but optimization against MeOH and H_2O alone provided the most consistent model performance. Because each of the three reactions (CO hydrogenation, CO_2 hydrogenation, RWGS) may proceed through several possible rate-determining steps (RDS), all feasible RDS combinations were evaluated in parallel. Each RDS set was fitted independently, allowing direct comparison of competing mechanistic variants. To avoid dependence on initial guesses, three initial-guess strategies were applied for every RDS combination: (i) original Graaf-parameters (1988) [3], (ii) parameters reported by Poto et al. (2022) [6], and (iii) randomized

values within physically reasonable ranges. The best-performing preliminary result was selected as the starting point for full optimization. Parameter fitting proceeded in two sequential stages. First, the downhill simplex algorithm (Nelder–Mead) was used for preliminary minimization. Second, the resulting parameter vector was refined using the limited-memory BFGS (L-BFGS) algorithm. Both methods were run with liberal upper and lower bounds on kinetic and adsorption parameters to exclude nonphysical solutions, and each run was limited to 15 000 iterations.

3.2. Research Track 2: Methanol Synthesis from Biogas

Based upon previous work in the field, this thesis aimed to design and commission a demonstration plant for synthesizing MeOH from Biogas in a decentralized, technically feasible manner. This includes the simplification of the combined decentralized MeOH-synthesis process by enabling future producers to access commercially relevant reactor configurations and catalyst technologies on a small, decentralized but effective scale. Building on previous developments, an integrated system was therefore designed for atmospheric, single-stage reforming of biogas to SynGas, followed by MeOH synthesis with product condensation and gas recycling. The drawbacks of SMR of biogas were addressed by implementing an ATR unit, which uses pure O_2 for partial oxidation of Biogas. Through this, auxiliary firing of feed gas for temperature control in the reforming unit is avoided, using the entire biogenic carbon feedstock for later conversion to liquid MeOH product. Additionally, this opens up synergistic effects: As the resulting high COR SynGas does not contain enough H_2 for effective conversion to MeOH (SN « 2), pure O_2 for injection in the ATR unit and pure H_2 for addition into the raw SynGas can be produced in a single electrolysis unit, opening up further possibilities for application of the technology as energy regenerative energy storage medium. A plant for testing and demonstrating this approach was therefore designed and commissioned.

In the designed pilot-plant, biogas- or sewage-gas-derived CH_4 and CO_2, together with H_2O vapor and O_2, are fed to an ATR unit equipped with robust noble-metal catalysts. System heat demand and reaction temperature are provided by partial oxidation of CH_4 to CO and H_2. Pure O_2 is injected to drive this reaction, and the resulting reformate heat is recovered in a combined heat exchanger for feed-water vaporization and biogas preheating.

For reforming of sewage gas, the feed is fed through an activated-carbon filter for sulfur removal before entering a three-way valve, enabling flexible operation with either raw sewage gas or synthetic feed gas from cylinder bundles. Feed gas is supplied via a cooled double-membrane pump (KNF N2400 ST13.E). An additional activated-carbon filter removes residual sulfur and siloxanes, while H_2S is continuously monitored (ExTox ET-4D). Mains water is distributed to both the ATR and MeOH systems; part is demineralized, collected, and vaporized in HEX 950 before mixing with preheated biogas in ATR. In the reformer pre-chamber, O_2 is radially injected to ensure homogeneous mixing prior to entering the catalytic section. A 0.7 L Pt-washcoated monolithic catalyst (Interkat, Germany) converts the biogas to CO_2-rich SynGas. The ATR is fully insulated by a micro-porous mantle surrounding both mixing and catalytic zones. The process is fully autothermal during steady-state operation, requiring external heating only during startup.

Reformate is then cooled in a condenser to remove product water and routed via a three-way valve for either direct MeOH-system supply or isolated ATR operation.

For SynGas conversion, a dedicated MeOH-synthesis unit with tubular, quasi-isothermal reactors with thermal jackets, heated by and oil thermostat unit is used. SynGas from the ATR is fed to a gas-mixing line, where

H_2, CO, and CO_2 can be dosed via mass-flow controllers (Bronkhorst EL-FLOW Select), enabling precise composition control during startup or standalone synthesis testing. In large-scale operation, H_2 will be supplied by electrolysis to adjust SynGas stoichiometry; in the pilot system, H_2 cylinders were used.
The mixed gas is compressed to 25 bar using a three-stage piston compressor (HAUG WTEGX 60/35/20), the system limit being defined by EU Pressure Equipment Directive 2014/68/EU. Compressed SynGas is passed through a gas mixer and pulsation dampener, then preheated in two serial heat exchangers before entering the parallel tubular reactors. These stainless-steel reactors (ID: 54.5 mm; AD: 88.9 mm; active length: 1250 mm) are filled with 2.048 kg of catalyst and supported by a grid plate, with glass wool used in the headspaces for gas distribution and particle retention. Reactor effluent is cooled in a stainless-steel condensation unit consisting of a counter current heat exchanger (CC-HEX) and a water-cooled condenser. Liquid product is collected, and uncondensed gas is returned through the CC-HEX and transported to the gas mixer via a high-pressure recycle pump (Fink CHEM+TEC Z04-13). System pressure and off-gas flow are controlled by a proportional membrane valve (Samson EB 8091) and off-gas is withdrawn upstream of the recycle pump. Thermal management is provided by a thermostat unit (Huber Unistat TR401 wHT, 8 kW heating, 10 kW cooling). Reactors are operated isothermally via counter current jacket cooling and recovered heat is reused for SynGas preheating. A basic flow-sheet of the demonstrated process is given in figure 3.4. Additional Images of the pilot plant user interface for plant control in WinCC and a foto of the pilot plant setup are given in figures 3.5 and 3.6 respectively.

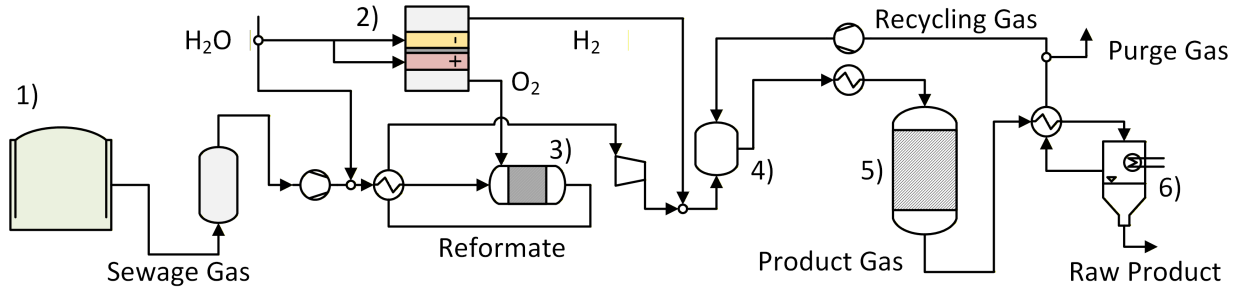

Figure 3.4.: Basic sketch of the designed biogas-to-methanol plant 1) Biogas / Sewage Gas Plant 2) Electrolysis Unit 3) Reformer 4) Gas Mixer 5) Methanol Reactors 6) raw product separator.

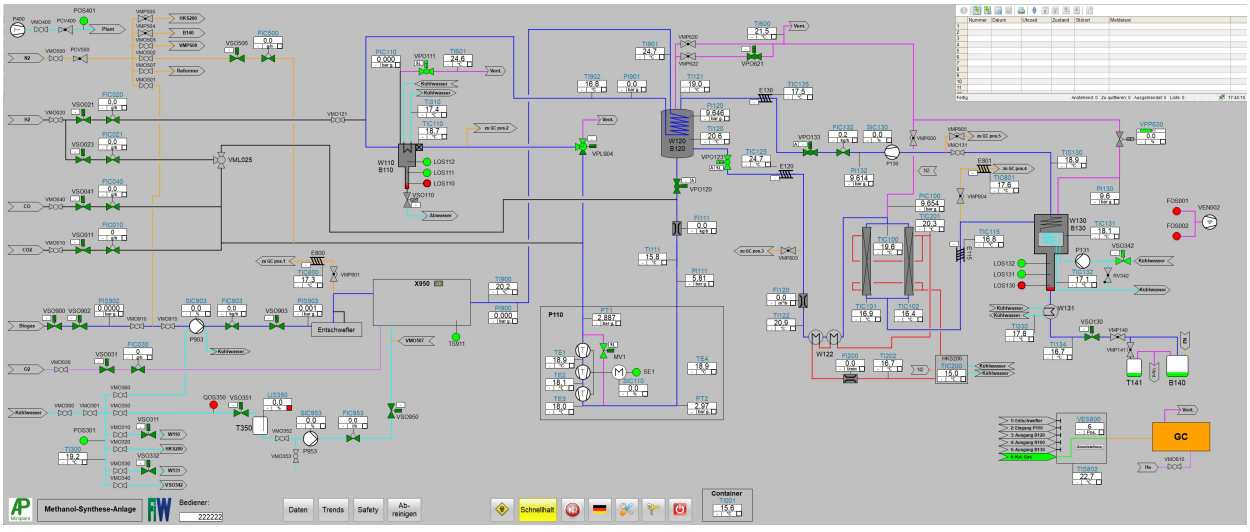

Figure 3.5.: Image of the pilot plant control user interface implemented in WinCC.

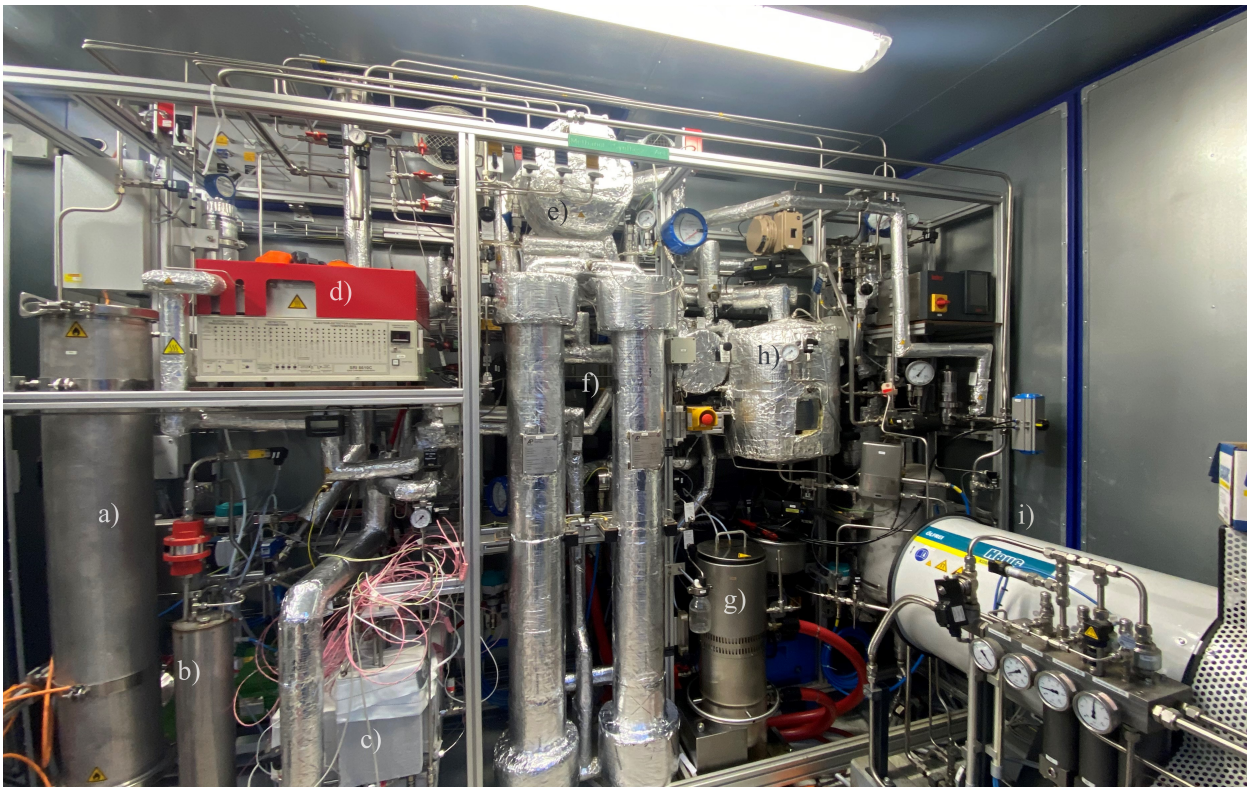

Figure 3.6.: Foto of the pilot plant setup. a) Activated carbon filter b) Siloxane filter c) Reformer in insulation enclosure d) Gas chromatography unit e) Heat exchanger for make up gas preheating f) Double reactor setup g) Oil thermostat heater/cooler h) Gas buffering/make up gas mixing i) Three stage gas compressor.

References

[1] Kang Xiao et al. “For Better Industrial Cu/ZnO/Al2O3 Methanol Synthesis Catalyst: A Compositional Study”. In: *Catalysis Letters* 147.6 (2017), pp. 1581–1591. ISSN: 1011-372X. DOI: 10.1007/s10562-017-2022-8.

[2] Sumpan Gesmanee and Wanida Koo-amornpattana. “Catalytic hydrogenation of CO2 for methanol production in fixed-bed reactor using Cu-Zn supported on gamma-Al2O3”. In: *Energy Procedia* 138 (2017), pp. 739–744. ISSN: 18766102. DOI: 10.1016/j.egypro.2017.10.211.

[3] G. H. Graaf, E. J. Stamhuis, and A.A.C.M. Beenackers. “Kinetics of low-pressure methanol synthesis”. In: *Chemical Engineering Science* 43.12 (1988), pp. 3185–3195. ISSN: 00092509. DOI: 10.1016/0009-2509(88)85127-3.

[4] F. Nestler et al. “Kinetic modelling of methanol synthesis over commercial catalysts: A critical assessment”. In: *Chemical Engineering Journal* 394 (2020), p. 124881. ISSN: 13858947. DOI: 10.1016/j.cej.2020.124881.

[5] Filippo Bisotti et al. “Impact of Kinetic Models on Methanol Synthesis Reactor Predictions: In Silico Assessment and Comparison with Industrial Data”. In: *Industrial & Engineering Chemistry Research* 61.5 (2022), pp. 2206–2226. ISSN: 0888-5885. DOI: 10.1021/acs.iecr.1c04476.

[6] Serena Poto et al. “Kinetic modelling of the methanol synthesis from CO2 and H2 over a CuO/CeO2/ZrO2 catalyst: The role of CO2 and CO hydrogenation”. In: *Chemical Engineering Journal* 435 (2022), p. 134946. ISSN: 13858947. DOI: 10.1016/j.cej.2022.134946.

4. Results of the Catalyst Screening

Based on recent literature, thirteen catalyst compositions were selected for evaluation in a broad catalyst screening campaign. Herein, CZA based catalyst were used, with alumina acting as carrier and as catalyst in catalyst-support interactions. Ceria, zirconia, yttria, magnesia, calcium oxide and tungsten were identified as high potential catalyst promoters for application in enhanced CZA-catalyst formulations. Initial catalyst screening was carried out based solely on catalyst performance in converting CO_2 and CO to MeOH. The relation of performance to physio-chemical catalyst properties were not taken into account at this stage. All materials were prepared using Al_2O_3 spheres as the support, onto which a wash coat containing 20 wt% of the active catalyst phase was applied. Table 4.1 shows the catalyst formulations developed along the screening process, with citations added, where choice of catalyst formulations was based on recent literature sources.

Table 4.1.: Target composition of reference and synthesized catalysts (mol.%)

Catalyst	**CuO**	**ZnO**	**Al_2O_3**	**MgO**	**Y_2O_3**	**ZrO_2**	**CeO_2**	**WO_3**	**CaO**	Sources
Ref-Kat	63.5	25.0	10.0	1.5						
Kat 1[a]	68.0	25.0	7.0							[1]
Kat 2[b]	63.5	25.0	10.0	1.5						[2]
Kat 3[a]	68.0	25.0			7.0					[3]
Kat 4[a]	67.0	25.0				8.0				[4]
Kat 5[a]	62.0	24.0				4.0	10.0			[5]
Kat 6[a]	57.0	23.0					20.0			[6]
Kat 7[b]	62.0	24.0				4.0	10.0			[2, 5]
Kat 8[a]	50.0	19.0				12.0	16.0		3.0	[2]
Kat 9[b]	51.0	20.0				12.0	17.0			
Kat 10[c]	62.0	24.0				4.0	10.0			
Kat 11[c]	51.0	20.0				12.0	17.0			
Kat 12[c]	45.0	18.0					25.0	12.0		
Kat 13[c]	48.0	19.0				13.0	14.0	6.0		[7]

[a] γ-Al_2O_3; [b] Basic Al_2O_3; [c] θ-Al_2O_3

To investigate the influence of surface basicity on catalytic performance, different pH-modification strategies were employed. Some samples (KAT 2, KAT 7, KAT 9) were subjected to an alkaline activation step prior to coating, while others were modified through the addition of alkaline promoters directly to the catalyst formulation (KAT 2, KAT 3, KAT 8). The catalysts were first compared under conditions representative of a CO_2-only SynGas, applying moderate pressures and temperatures. Complementary tests were then conducted using mixed carbon oxide SynGas, always under hydrogen-rich conditions (super stoichiometric H_2 content). This guaranteed constant reduction of the catalytically active phase containing CuO and ZnO in all tested formulations and ensured fair representation of true catalyst performance, not risking mechanistically suboptimal effects due to lack of active site H_2-coverage.

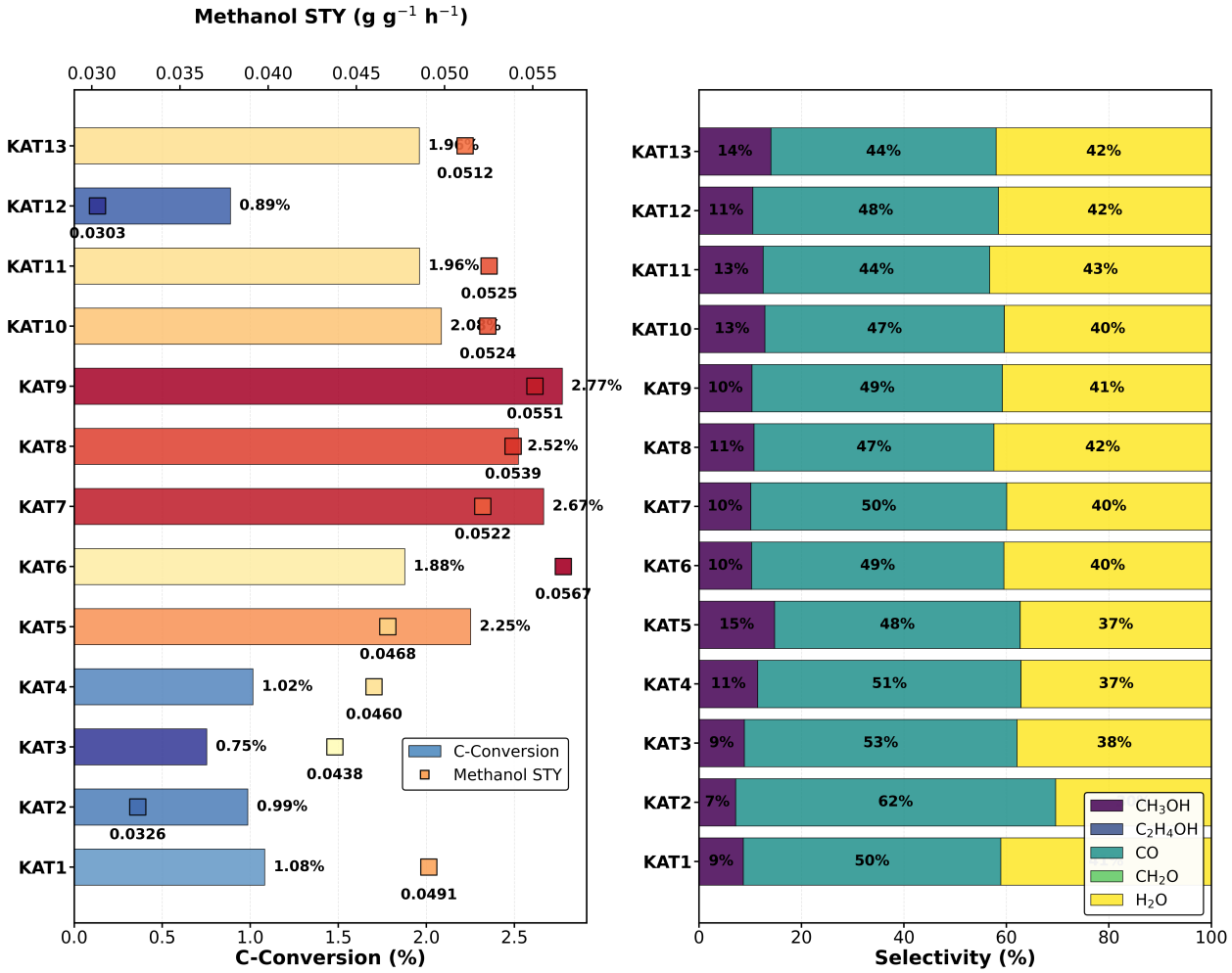

Figure 4.1.: Results of the catalyst screening applying CO_2-only SynGas. MeOH STY and CO_2 conversion (left) and selectivity towards MeOH, CO, Ethanol, Formaldehyde and Water (right). All tests conducted at SN = 3, 25 bar reactor pressure, 250 °C reactor temperature and GHSV of 10.000 h^{-1}.

Figure 4.1 summarizes the comparative performance of all catalysts using pure CO_2 as the carbon source. The left panel reports the X_C and MeOH STY for each sample, while the right panel compares the selectivity for each sample towards the main products in CO_2 hydrogenation (CO, MeOH, and H_2O). MeOH STY herein refers to the performance relative to total catalyst bulk weight, of which only 20% are classified as catalytically active. Catalysts KAT 1 – KAT 4, all based on Cu/ZnO-type formulations (Cu/ZnO, Cu/ZnO/Al_2O_3, Cu/ZnO/Al_2O_3/MgO) including variants with alkaline pre-treatment of the support, exhibit comparatively low conversion levels and low selectivity towards MeOH formation. Instead, these samples show high selectivity towards CO and H_2O. This behavior is unexpected, as the reference Cu/ZnO/Al_2O_3 catalyst typically provides acceptable activity in CO_2-rich feeds, although usually not as effective as under CO-based SynGas. Alkaline activation of the support (Catalyst 2) does not improve CO_2 conversion compared to the untreated Cu/ZnO/Al_2O_3 formulation. In contrast, catalysts containing ZrO_2, CeO_2, or combinations thereof demonstrate significantly improved performance. Catalysts 7 (CeO_2–ZrO_2), 8 (CeO_2–ZrO_2 with CaO promoter), and 9 (CeO_2–ZrO_2 with increased loading) all outperform the remaining samples. Catalysts 7 and 9 provide the highest X_C, whereas Catalyst 8 exhibits slightly lower conversion but an enhanced selectivity towards MeOH, suggesting a beneficial effect of CaO addition on product distribution. In addition, catalysts supported on θ-Al_2O_3 (Catalysts 10–13) and those promoted with tungsten or yttria (Catalysts 3,

12, and 13) do not reach the activity levels of the CeO_2–ZrO_2 formulations, although they still outperform the Cu/ZnO-based catalysts. The θ-alumina supported samples exhibit slightly enhanced MeOH selectivity, indicating beneficial support–active phase interactions as well as structural features of θ-Al_2O_3 that favor MeOH formation through stabilized adsorption of CO_2 and its intermediates. Nevertheless, the overall conversion achieved by these catalysts remains below that of Catalysts KAT 7 – KAT 9 under CO_2-only SynGas conditions, underscoring the strong synergistic role of CeO_2 and ZrO_2 in promoting CO_2-activation and MeOH synthesis. The comparison of catalyst performance under CO_2-only conditions with mixed carbon oxide (COR 0.81 and COR 0.66) feed conditions shows that KAT 5 is the only formulation exhibiting a simultaneous increase in both carbon conversion and MeOH space–time yield (STY) when CO is introduced into the feed. All other catalysts perform similarly or less effectively under mixed-feed conditions, indicating that the majority of formulations benefit primarily from CO_2-activation rather than CO conversion pathways. Catalysts KAT 7 to KAT 9 maintain comparatively high and nearly identical performance levels, with KAT 9 displaying a marginally superior STY and conversion. These trends are attributed to the activity of the applied promoters, the respective production protocols, and alkali-induced activation mechanisms that enhance CO_2 adsorption. Conversely, CO adsorption and its subsequent conversion appear to be less influenced, or in some cases negatively affected, by the same promotional strategies. Catalysts containing CeO_2 and ZrO_2 continue to show strong performance, even at moderate reaction conditions of 20 bar and 250 °C. In contrast, KAT 12 exhibits the lowest activity, X_C reaching values below 1 % consistently. The results for KAT 5, which is moderately promoted with both CeO_2 and ZrO_2, highlight the beneficial effect of these promoters not only for CO_2- hydrogenation but also for mixed CO/CO_2 SynGas conversion. Even in washcoated configurations with an overall catalyst loading of only 20 wt%, the CeO_2–ZrO_2-enhanced system demonstrates improved adsorption and activation of both CO_2 and CO, underlining the robustness of this promotional strategy. The performance screening of the 13 tested catalyst samples in mixed carbon-oxide SynGas streams is shown in figure 4.2.

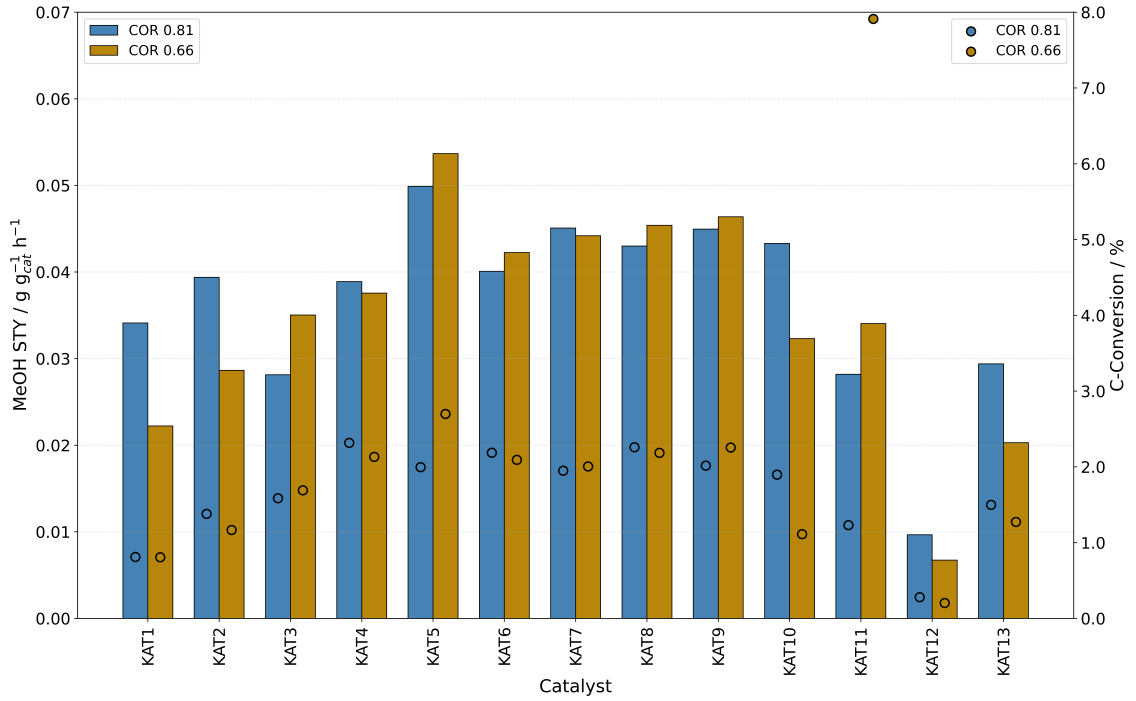

Figure 4.2.: Results of the catalyst screening applying lower COR SynGas. All tests conducted at SN = 3, 20 bar reactor pressure, 250 °C reactor temperature and GHSV of 10.000 h^{-1}

Overall, the catalyst screening confirms that unpromoted or weakly promoted Cu/ZnO formulations exhibit only mediocre performance, particularly in CO_2-only SynGas streams. This observation is consistent with previously reported studies. While promoter addition can enhance catalytic activity, both the choice of promoter and the promoter ratios play decisive roles in the resulting performance. In this context, CeO_2 and ZrO_2 were found to improve catalyst behavior in CO_2-only SynGas and also to enhance CO conversion in mixed carbon oxide feeds.

ZrO_2 promotion alone provides only modest improvements compared to binary or ternary CZA formulations. In contrast, CeO_2 promotion significantly boosts CO_2 conversion by nearly 75% in CO_2-only SynGas. The CeO_2-only promoted catalyst (KAT 6) also exhibited the highest MeOH STY in the screening tests. Contrary to expectations and earlier publications, the quaternary Cu/ZnO/CeO_2/WO_3 formulation performed poorly in CO_2 conversion, not surpassing the activity of CZA or MgO-promoted catalysts thereof.

Catalysts promoted simultaneously with CeO_2 and ZrO_2 and supported on γ-Al_2O_3 consistently demonstrated strong performance. The highest CO_2 conversion was achieved with a CeO_2/ZrO_2-promoted catalyst featuring a 0.75 ZrO_2/CeO_2 ratio. Additional surface pH adjustment through CaO incorporation slightly improved STY over the quaternary Cu/ZnO/CeO_2/ZrO_2 catalyst, though with a minor reduction in overall CO_2 conversion. All of these formulations also performed well under mixed CO/CO_2 SynGas conditions.

Based on these findings, catalysts 8 and 9 were selected for further, detailed investigation. To systematically correlate physio-chemical properties and their evolution through promotion with catalytic performance, a stepwise promotion strategy was employed. The base binary Cu/ZnO (KAT 1) catalyst was modified sequentially by adding individual promoters, first CeO_2 (KAT 5), then ZrO_2 (KAT 9), and finally CaO (KAT 8), without altering the underlying molar ratios of the previous formulations in the promotion sequence. This approach yielded four catalysts that were extensively tested under diverse operating conditions for a comprehensive performance assessment. Their physio-chemical properties were characterized in detail, enabling direct correlation with observed reaction metrics. The full characterization, performance analysis, and subsequent kinetic and mechanistic studies were published in two journal articles.

Furthermore, the deployment of catalyst 8 (KAT 8, CuO/ZnO/CeO_2/ZrO_2/CaO) in a novel pilot plant for the regenerative production of MeOH from biogas was documented in a third publication. The following chapters present these articles as previously published.

References

[1] Sumpan Gesmanee and Wanida Koo-amornpattana. “Catalytic hydrogenation of CO2 for methanol production in fixed-bed reactor using Cu-Zn supported on gamma-Al2O3”. In: *Energy Procedia* 138 (2017), pp. 739–744. ISSN: 18766102. DOI: 10.1016/j.egypro.2017.10.211.

[2] Venkata D.B.C. Dasireddy, Strah Štefančič Neja, and Likozar Blaž. “Correlation between synthesis pH, structure and Cu/MgO/Al2O3 heterogeneous catalyst activity and selectivity in CO2 hydrogenation to methanol”. In: *Journal of CO2 Utilization* 28 (2018), pp. 189–199. ISSN: 22129820. DOI: 10.1016/j.jcou.2018.09.002.

[3] Peng Gao et al. “Yttrium oxide modified Cu/ZnO/Al 2 O 3 catalysts via hydrotalcite-like precursors for CO 2 hydrogenation to methanol”. In: *Catalysis Science & Technology* 5.9 (2015), pp. 4365–4377. ISSN: 2044-4753. DOI: 10.1039/c5cy00372e.

[4] Kongzhai Li and Jingguang G. Chen. “CO 2 Hydrogenation to Methanol over ZrO 2 -Containing Catalysts: Insights into ZrO 2 Induced Synergy”. In: *ACS Catalysis* 9.9 (2019), pp. 7840–7861. ISSN: 2155-5435. DOI: 10.1021/acscatal.9b01943{\#}.

[5] Maxim Zabilskiy et al. “Methanol synthesis over Cu/CeO 2 –ZrO 2 catalysts: the key role of multiple active components”. In: *Catalysis Science & Technology* 11.1 (2021), pp. 349–358. ISSN: 2044-4753. DOI: 10.1039/d0cy01762k.

[6] Junxin Guo et al. “Synthesis of oxygen vacancies enriched Cu/ZnO/CeO 2 for CO 2 hydrogenation to methanol”. In: *Greenhouse Gases: Science and Technology* 11.6 (2021), pp. 1171–1179. ISSN: 2152-3878. DOI: 10.1002/ghg.2102.

[7] Yong Yan et al. “CO2 hydrogenation to methanol on tungsten-doped Cu/CeO2 catalysts”. In: *Applied Catalysis B: Environmental* 306 (2022), p. 121098. ISSN: 09263373. DOI: 10.1016/j.apcatb.2022.121098.

5. CO_2-to-Methanol over Cu/ZnO Infiltration Composites

This chapter presents the article *CO_2-Hydrogenation to Methanol over CuO/ZnO Based Infiltration Composite Catalyst Spheres*, as published in *ChemCatChem*. The work reports the development, characterization, and catalytic evaluation of CuO/ZnO-based infiltration composite catalyst spheres for CO_2 hydrogenation to MeOH. The article is reproduced here in its original form to provide the full experimental details, results, and discussion as appeared in the journal publication.

Declaration of contributions:

- *Carl Fritsch* conceptualization of study, methodology, formal analysis, investigation (catalyst performance), data curation, project administration, funding acquisition, resources, supervision, validation, visualization, original draft
- *Jürgen Dornseiffer* methodology, manufacturing of catalyst samples, data curation, review
- *Jule Blankenstein* formal analysis, investigation (catalyst performance), data curation, review
- *Michael Noyong* investigation (physio-chemical properties), review
- *Christian Groteklaes* investigation (catalyst performance), review
- *Ulrich Simon* investigation (physio-chemical properties), review

Original Publication
Fritsch, C.; Dornseiffer, J.; Blankenstein, J.; Noyong, M.; Groteklaes, C.; Simon, U.
CO_2-Hydrogenation to Methanol over CuO/ZnO Based Infiltration Composite Catalyst Spheres, ChemCatChem 2024, 16, e202400731, doi.org/10.1002/cctc.202400731

Abstract

Multiple active component catalysts for efficient conversion of CO_2 to Methanol (MeOH) are synthesized through coating γ-Al_2O_3 carrier spheres by incipient wetness impregnation method (IWI). The well-known bimetallic Copper Oxide/Zinc Oxide (CuO/ZnO) complex is promoted in three steps, first by Cerium Oxide (CeO_2), then additionally with Zirconium Oxide (ZrO_2) and finally with Calcium Oxide (CaO) resulting in four carrier catalysts with high surface area and catalyst pore volume. Quaternary and quinary carrier catalysts promoted with moderate CeO_2, ZrO_2 in the quaternary (20 % CZCZ) and additionally with CaO (20 %CZCZC) in the quinary catalysts demonstrate high CO_2 conversion ratios (16.2 % and 18.7 %) and space time yields (0.51 and 0.47 $g_{MeOH}\ h^{-1}\ g_{Catalyst}^{-1}$) at 5 MPa and 250 °C. The high conversion ratios (X_{CO2}) and good methanol space-time-yields (STY_{MeOH}) are attributed to enhanced copper dispersion and several multi metal oxide component interactions essential to enhance CO_2 activation and conversion through the catalytic systems as well as very high overall surface area. Compared to related studies, the carrier catalysts show superior conversion rates, proving the effectiveness of the introduced multi-component carrier catalyst and extending the understanding of infiltrate composites as possible large-scale application alternatives to precipitated MeOH catalyst systems.

5.1. Introduction

It is widely accepted that CO_2-concentration in the earth's atmosphere is a primary driving factor for anthropogenic climate change. To mitigate possible effects of CO_2-emissions into the atmosphere, CO_2 capture and utilization (CCU) has gained attention in research and first larger scale applications have been established in the past years. Furthermore, the recovery of CO_2 from regenerative sources such as biogas, sewage gas, thermal biomass treatment or from bio waste treatment processes, promises to open possibilities for substitution of fossil carbon products through biogenic alternatives. Methanol (MeOH) is one of the most commonly used petrochemical products and base chemicals. Commercially, it is produced from natural gas through a multistage process comprising of synthesis gas production by steam reforming of the feed gas and subsequent catalytic generation of MeOH of the carbon monoxide-rich gas [1]. Alternatively, MeOH can be produced directly through hydrogenation of CO_2. Catalyst development to increase activity and selectivity of known catalyst complexes towards MeOH in the hydrogenation of CO_2 has thus attracted great interest in the past years. Industrial MeOH catalysts are mostly based upon ternary metal oxide mixtures, with CuO being the main active component. ZnO and Al_2O_3 are widely regarded as the most efficient additional components for CO conversion to MeOH and are thus used in most commercial fossil MeOH applications [2, 3, 4, 5]. As the ternary commercial catalysts show low activity, mediocre selectivity towards MeOH in CO_2 hydrogenation and limited long-term stability, a wide range of possible metal oxide promoters and catalyst supports for more efficient conversion have been tested in recent studies [6, 7, 8]. Herein, some key factors for improved CO_2 adsorption and conversion have been identified: good Cu species dispersion, creation of large boundary metal interfaces and provision of oxygen vacancies are some of the most prominent, with certain metal promoters being able to induce all of the described promotional effects. Among others, CeO_2 has been shown to provide essential active sites for CO_2 adsorption, providing both active Cu-metal interfaces and creating oxygen surface vacancies, both of which have been proven to improve CO_2 conversion in CuO-ZnO catalyst [9, 10, 11, 12]. Furthermore, CeO_2 has advanced redox ability, is very stable and exhibits inverse valence transformation ($Ce^{4+} \rightarrow Ce^{3+}$) thus providing an acting point for oxygen-containing bonds [13].

ZrO_2 has been in the focus of MeOH-catalyst development for some years now. It has been proven to substantially increase Cu-species dispersion and provide further vacancies for improved adsorption [14, 15, 16, 17, 18, 19, 20, 21]. Furthermore alkaline and alkaline earth metals such as K or Mg have been shown to strongly promote dispersion in Cu-based MeOH catalysts and provide surface alkalinity, which has been shown to improve CO_2-activation capacity [22, 23, 24, 25, 26]. Many studies have also investigated the reciprocal effects of the combination of several catalyst metal oxides and catalyst supports, with emphasis on the unique synergistic effects of CuO and ZnO for hydrogenation of CO and CO_2 [27, 28, 29, 30, 31]. But examination of synergistic effects for several active components in CuO-based ternary, quaternary or quinary catalyst structures have shown promising results in enhancing MeOH selectivity, improving catalyst long term stability and increasing conversion ratios. Zablinksy et al. (2021) reported, that CeO_2/ZrO_2 interplay on ternary catalysts played a vital role in conversion efficiency and MeOH selectivity [32]. Poto et al. (2022) showed, that CuO/ZrO_2/CeO_2 catalysts were highly efficient for hydrogenation of CO_2 and ZrO_2/CeO_2 interplay was able to increase selectivity for MeOH compared to commercial CuO/ZnO/Al_2O_3 catalysts [33]. Further positive synergistic effects in ternary and quaternary catalyst structures containing ZrO_2, CeO_2 or both for CO_2 hydrogenation have also been reported in studies published recently [34, 35, 36, 37]. Most industrial catalysts and many studied catalyst in research are produced by co-precipitation of the catalytically active metal oxides[2, 4, 24].

In recent years, various approaches for catalyst production have been discussed for simplified catalyst sample manufacturing based around impregnation techniques for carrier catalysts. Samples produced by the IWI method promise an increase in catalyst surface area and sufficient dispersion of catalytically active components on the catalyst surface, while reducing catalyst production cost and technical complexity in catalyst manufacturing. While Al_2O_3 has long been a prominent carrier material, different approaches for its use have been reported in recent studies: Bansode et al. (2013) [22] introduced γ-Al_2O_3 spheres as carrier for the catalyst, while testing alkaline earth metal oxide promoters for enhanced CO_2 conversion and Ren et al. (2015) [24] extended upon their work. Both studies showed promising results, concluding that γ-Al_2O_3 is a suitable carrier for catalytically active multi metal oxide combinations and tested carrier catalysts were able to deliver high conversion ratios and good MeOH selectivity. This plays a vital role in formulating high performance catalyst compositions for future commercial applications of CO_2-to-MeOH.

In the herein presented work, findings from aforementioned studies are combined in an attempt to extend upon existing work and further deepen the understanding for catalyst performance in CuO/ZnO based ternary, quaternary and quinary catalyst structures. To investigate the effects of CeO_2 and ZrO_2 promotion of binary CuO/ZnO catalyst and to further study the effects of earth alkaline catalyst promotion such as CaO, four carrier catalysts for efficient hydrogenation of CO_2 to MeOH are prepared as infiltration composites by IWI. Highly porous alumina support spheres are coated with 20 wt % of the different catalyst metal oxide compounds. The resulting catalyst are tested for activity and selectivity towards CO_2 hydrogenation to MeOH. γ-Al_2O_3 spheres were used as catalyst support to guarantee a uniform and comparable catalyst bed for each sample during activity measurements. To highlight synergistic effects for multiple active catalyst materials, a base catalyst CuO-ZnO on alumina was used for further incremental promotion of the proven binary catalytic system. While maintaining molar ratios for CuO and ZnO we added CeO_2, ZrO_2 and CaO in promotional steps, thus preparing four different catalyst samples for physio-chemical characterization and catalyst screening towards performance of CO_2-hydrogention to MeOH. For comparison a commercial CuO/ZnO/Al_2O_3 catalyst containing 63.5 wt % CuO, 25.0 wt % ZnO, 10.0 wt % Al_2O_3 and 1.5 wt % MgO was also tested as a reference. All catalyst samples were subjected to different physio-chemical analyses. Brunauer-Emmett-Teller (BET), surface area and pore size distribution were determined. For analysis of surface topography and elemental distribution on the catalyst surface, scanning electron microscopy (SEM) with integrated energy dispersive X-ray spectroscopy (EDX) was applied. X-Ray diffraction (XRD) was used for determination of the phase composition. Surface acidity was determined by ammonia temperature programmed desorption (NH_3-TPD), while reducibility was probed by hydrogen temperature programmed reduction (H_2-TPR).

5.2. Results and Discussion

5.2.1. Results Sample Characterization

For better understanding of the possible catalytic interface involved in CO_2 hydrogenation, analyses of specific BET surface areas, pore size distribution and pore volume were carried out for all samples (Abbreviation protocol and manufacturing protocols for all herein tested samples are described in experimental section). Calculated catalytic surface areas (A_{BET}), total average pore volume (V_{TOT}) and average pore diameter (D_{Pore}) of the coated catalysts, the uncoated Al_2O_3 carrier spheres and a crushed and sieved reference catalyst sample are listed in table 5.1.

Table 5.1.: Specific surface areas (A_{BET}) and corresponding pore volumes of the catalysts in comparison to the supporting Al_2O_3 spheres and the reference.

Sample	A_{BET} $m^2 \cdot g^{-1}$	V_{TOT} $cm^3 \cdot g^{-1}$	D_{Pore} nm
Reference	76	0.18	8.85
γ-Al_2O_3	151	0.48	–
20 % CZ[a]	132	0.36	10.71
20 % CZC[a]	122	0.34	11.30
20 % CZCZ[a]	129	0.37	11.37
20 % CZczc[a]	125	0.36	11.55

[a] 20 %w catalyst coating on 800 μm carrier spheres.

The uncoated alumina spheres exhibit the highest specific surface area and the highest specific pore volume in this comparison. Through catalyst coating, overall A_{BET} and V_{TOT} are consistently reduced through the different stages of catalyst promotion, although the measured surface areas of presented catalyst samples stay inside a range of 10 %, overall surface area deviation is therefore limited. Compared to uncoated Al_2O_3, A_{BET} of 20 % CZCZC is reduced by 17 % and D_{Pore} by 25 %. All coated catalysts exhibit inter comparable average pore diameters derived from BET-measurements. Compared to the industrial pellet catalyst, catalytic boundary area is increased by up to 65 % and total average pore volume by up to 100 %. For better understanding of the presented measurements, adsorption isotherms for the carrier and each catalyst are given in the supplementary materials (figures A.1–A.5).

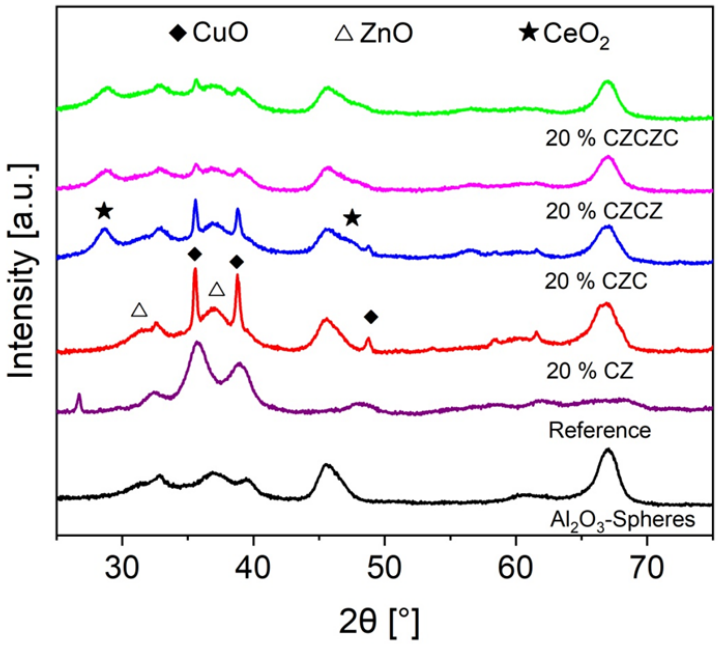

Figure 5.1.: Powder X-ray diffraction patterns of the different catalysts in comparison to the reference and the used alumina spheres. The diamond icon is used for identification of distinctive Cu-diffraction peaks, while star and triangle identify CeO_2 and ZnO respectively.

To determine the phase composition on the sample surfaces, the catalysts were analyzed by powder X-ray diffraction according to the protocol described in the experimental section. Figure 5.1 exhibits the resulting diffractograms of the infiltration composite in comparison to the reference and the alumina spheres used as support material. In general, the catalysts exhibit a comparable typical nanocrystalline diffraction pattern with

very broad wave-like peaks. The few pronounced peaks from the 2Θ positions at 35.5°, 38.7° and 48.7° for the pure CuO/ZnO catalyst (20 % CZ) can be assigned to CuO with a monoclinic structure, which become smaller and broader in intensity with increasing promoter doping. This indicates a decreasing CuO particle size and thus a higher specific catalytic interface in the same direction. An average crystallite size of the copper oxide in the 20 % CZ catalyst was determined to be 30 to 40 nm using the Scherrer formula on the full width at half maximum (FWHM) of the main peak at 2Θ = 35.5°, whereas a CuO particle size of approx. 12 nm is determined for the industrial reference catalyst.

ZnO as the second main component of all herein presented catalyst samples can be identified via the broad peaks at 2Θ = 32.5° and 2Θ = 36.3°, which are, however, superimposed by the γ-Al_2O_3 of the support material. Furthermore, the broad diffraction peak at 2Θ = 28.6° could be assigned to CeO_2 in the catalysts containing ceria. The crystalline phase of the ZrO_2 in the 20 % CZCZ and 20 % CZCZC catalysts and the Al_2O_3 in the industrial catalyst could not be detected. Solely the peak at 2Θ = 26.6° of the reference could be identified as graphite (JCPDS 26-1079), which is added to the catalyst powder as an additive for molding during the extrusion process.

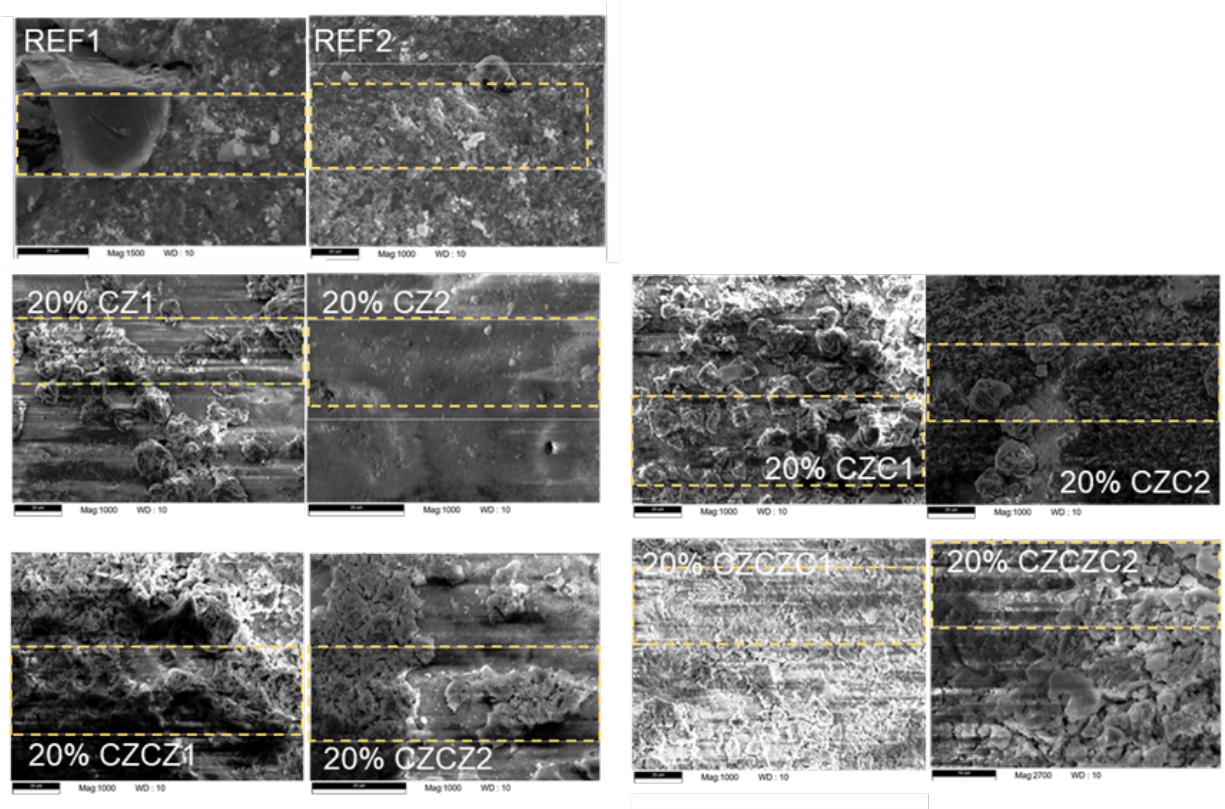

Figure 5.2.: Highly magnified SEM-images of the catalyst surfaces. Two SEM-images for each catalyst sample are used, to demonstrate the inhomogeneous catalyst structures, both in the reference and in the carrier catalysts. Image sections used for EDX analyses are marked by yellow boxes. Corresponding EDX mappings are presented in figure 5.3.

Another significant aspect of physical catalyst properties is the morphology of the catalyst surface and the elemental distribution within the multi-metal-oxides on the catalyst surfaces. Figure 5.2 shows the SEM images of all catalyst samples whereas figure 5.3 reveals the corresponding element mappings of the observed area by EDX analysis. For each catalyst sample, two images and mapping overlays are shown for demonstration of the heterogeneous character of the produced carrier catalysts with areas where the

multi-metal oxides are located and catalyst regions dominated more by Al_2O_3-carrier surface material. As can be deducted from figure 5.2, the surface morphology of the coated catalyst samples changes through increasing level of promotion from more coarsely grained, flake-shaped particles to structures based on very small flake particles. The reference catalyst shows an even, homogeneous distribution of small particles, except for comparatively large bulk carbon structures, as can be clearly seen in the maps shown in figure 5.3, where elemental carbon is marked in red color for the dispersion maps from EDX analyses. This adds to the XRD findings, confirming the presence of graphite particles in the commercial catalyst, presumably stemming from manufacturing. The images of all carrier catalysts show homogeneous portions with macroporous rough crystallite particles formed in bulbous formations on the surface.

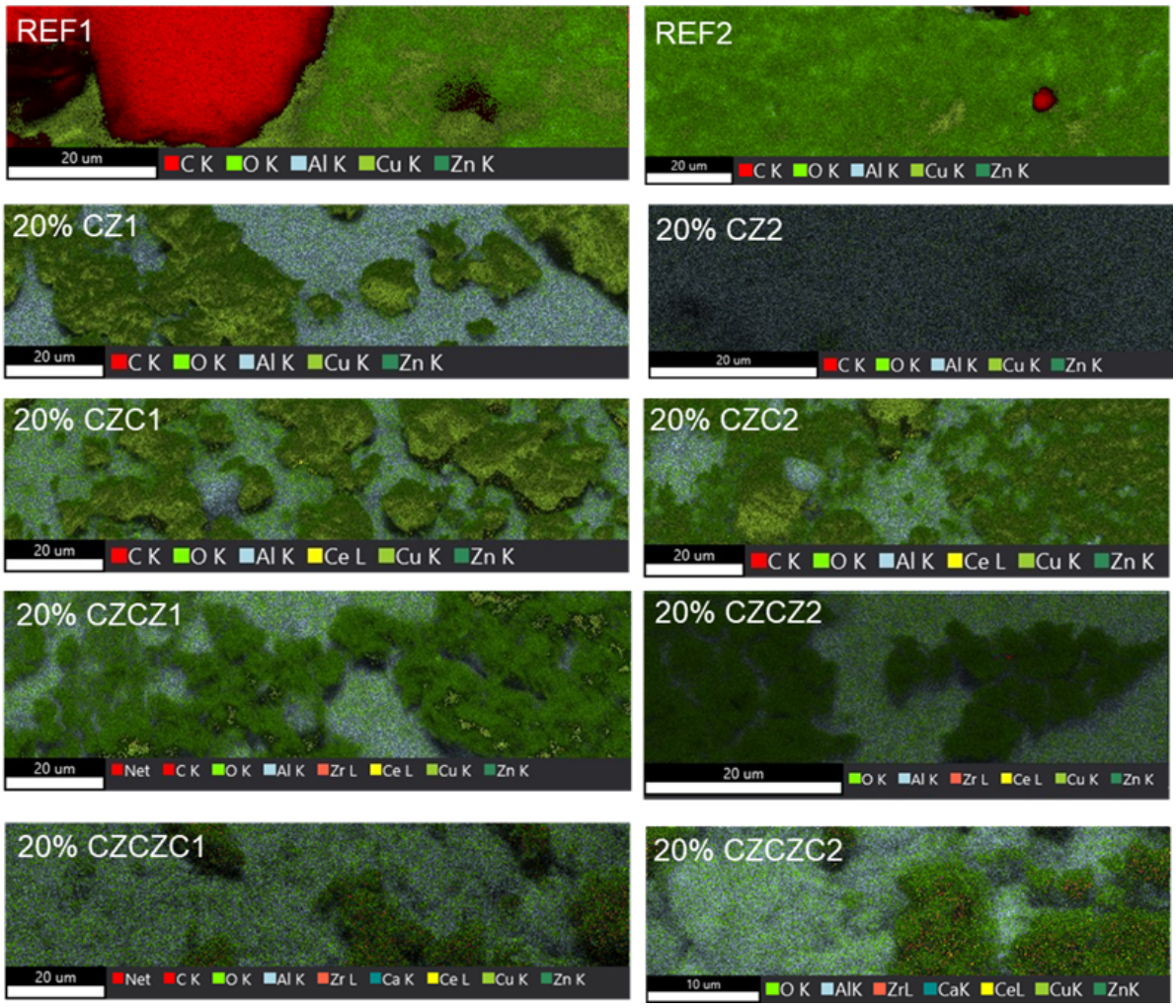

Figure 5.3.: EDX mapping overlays for all metal components in the herein presented catalyst samples. Each mapping corresponds to an image section presented in figure 5.2.

The structural manifestation of the formations changes with increasing catalyst promotion, which is attributed to the change in metal oxide structure with the addition of ZrO_2 to the catalyst surface. EDX analysis of the shown images confirm very sufficient Cu and Zn dispersion around the porous catalyst structures. Distribution of metal oxides proposed in the production protocol for the carrier catalyst (see materials section for production protocol) is confirmed by EDX analyses of the image sections depicted in figure 5.2. Additional single-element mappings further validate the even dispersion of metal oxide additives on the carrier surfaces (Supplementary materials/Appendix figures A.16–A.25). Graphs and distribution tables for elemental analysis

of the image sections are given as supplementary materials in figures A.6–A.15 and Tables A.1–A.10. Overall ZrO_2, CeO_2 and CaO loading is close to the calculated theoretical composition and elemental distribution is hereby confirmed. While multi-metal-oxide formation with CuO, CeO_2 and ZrO_2 in the coating process can be an issue for metal dispersion on the catalyst surface, this cannot be confirmed based upon the EDX images shown in figure 5.3 [38]. Especially the images for 20 % CZCZC show very even distribution of ZrO_2 and CeO_2 particles on the catalyst surface, indicating small particle sizes and good overall dispersion in the catalyst coating.

TPR tests were conducted for all catalyst samples and the reference catalyst for determination of H_2-reducibility and for investigation of possible catalyst activity. Figure 5.4 shows TCD signal intensity for the measurements conducted for the TPR reactor outlet gases of the tested samples. All samples except for 20 % CZ exhibit three overlapping reduction peaks for H_2 consumption. Onset reduction temperature is around 98 °C for the reference catalyst, whereas the samples tested in this work exhibit a prolonged reduction onset with H_2 consumption starting at around 150 °C for the carrier catalyst samples.

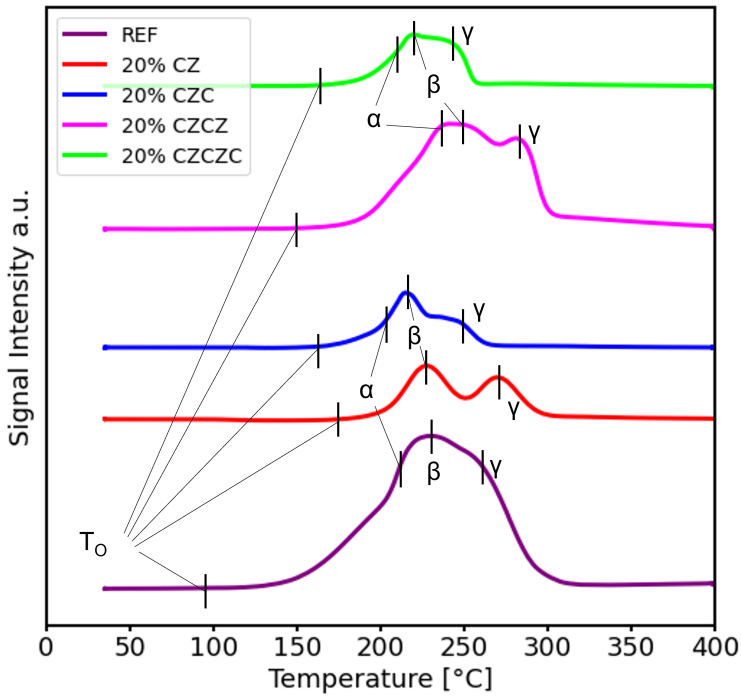

Figure 5.4.: H_2-TPR profiles of the catalysts compare to the industrial reference. TO marks onset reduction temperature. α, β and γ are used for marking the three distinctive reduction peaks. T_o - Onset reduction for first reduced, small and widely dispersed CuO particles, α - Onset reduction peak at around 190-220 °C, β - Main reduction peak at around 200-225 °C, γ - Shoulder peak at around 240-280 °C caused by more strongly interacted CuO species

For the reference, the first minor reduction peak follows at around 210 °C (α). This primary reduction peak is found in 20 % CZC, 20 % CZCZ and 20 % CZCZC as well, but it is clearly most pronounced in the reference catalyst. This weakly pronounced primary peak is strongly integrated with the more strongly pronounced second peak at around 225 °C (β) and a shoulder peak at around 265 °C (γ) for the reference catalyst. Calculated peak positions are given in Table 5.2. As only CeO_2, CuO and ZnO can be reduced in the measured temperature range, the reduction peaks can mostly be attributed to the reduction of different CuO species or interacted CuO [11, 39]. α can be associated with CuO bulk reduction of isolated CuO species or composite metal oxides, while higher reduction temperatures can be attributed to CuO that is strongly

interacted with other metal oxide species, thus inducing hard reducibility of Cu^{2+} species. It is noteworthy that the reference catalyst shows the lowest reduction temperatures of all tested samples, although not by substantial margins. This indicates CuO being less strongly interacted and generally more evenly dispersed by particle size, which is expected in precipitated solid catalysts. As the degree of catalyst promotion through CeO_2, ZrO_2 and CaO increases from 20 % CZ to 20 % CZCZC, both β and γ decrease in height and width substantially. This indicates that both bulk CuO and well-dispersed, weakly interacted Cu species decrease in prevalence and catalyst surface distribution. The 20 % CZC catalyst structure exhibits the lowest reducibility, with CeO_2-addition not improving reducibility of the catalyst sample over 20 % CZ. The addition of ZrO_2 in 20 % CZCZ greatly increases overall reduction properties over 20 % CZC and 20 % CZ, with reduction onset temperature being lowered and all overlapping reduction peaks increasing in height and width. 20 % CZCZ exhibits the highest specific H_2 consumption among all carrier catalysts, with a total H_2 consumption of 0.038 g_{H_2} $g_{\text{active component}}^{-1}$ referring to the 20 % active component in the compound catalyst. Especially the first reduction peak α increases in surface area, indicating the ability of ZrO_2 to disperse other metal oxide species on the carrier surface and produce more evenly distributed metal oxide pores. ZrO_2 additionally seems to increase reducibility of CuO and CeO_2, with overall H_2 consumption increased threefold over 20 % CZC. Addition of CaO decreases overall reducibility compared to 20 % CZCZ. This is attributed to the metal oxide species being interacted in more complex manners than in the ternary and quaternary catalyst samples 20 % CZC and 20 % CZCZ. Overall, these complex interactions lead to reduction temperatures for both α and β being raised slightly with increasing catalyst promotion, indicating that both CuO species are incorporated into more complex metal oxide compound structures, making them harder to reduce within the tested temperature window.

Table 5.2.: Onset catalyst reduction temperature (T_o) and temperature peaks for the three distinctive reduction peaks for each catalyst (α, β, γ).

Catalyst	T_o [°C]	α [°C]	β [°C]	γ [°C]	H_2 consumption [$g/g_{\text{active cat mass}}$]
Reference	98	219	232	261	0.0649
20 % CZ	176	–	226	272	0.0150
20 % CZC	160	206	217	248	0.0129
20 % CZCZ	140	239	254	283	0.0380
20 % CZCZC	163	218	219	242	0.0125

CO_2 hydrogenation to MeOH often depends on catalyst basic sites for CO_2-adsoprtion on the catalyst surface [25]. At the same time, it has been reported, that catalyst acid sites stemming from different alumina species can lead to formation of C_2+ molecules from SynGas or from MeOH itself, as applied in MeOH conversion to other chemicals [27]. Furthermore, earth alkali modified MeOH catalysts often present good options for the synthesis of higher alcohols or the reduction of surface acid sites in catalysts, thus the addition of CaO to the promoted catalysts in this work [40, 41].

To investigate the acidity of the tested catalysts, NH_3-TPD analyses were carried out in a temperature range from 50 °C to 500 °C, results are given in figure 5.5. The tested samples all show overall low acidity, the magnitude of the desorption plot is increased for better recognizability of progression over temperature. All catalysts exhibit two distinctive desorption peaks, one at low temperatures of around 120 °C to 150 °C and one at around 240 °C to 270 °C, which correspond to weak Brønsted acid sites for the lower temperatures and stronger Lewis acid sites for high temperatures.

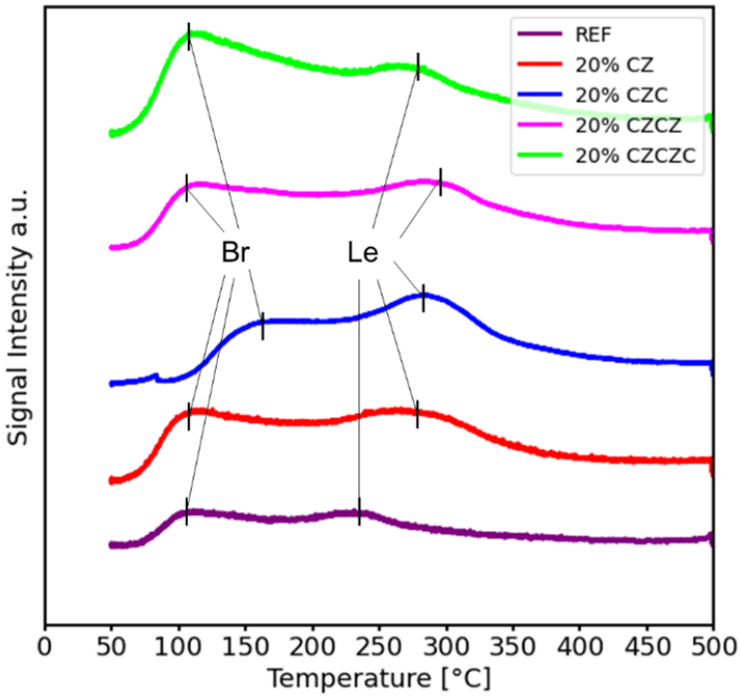

Figure 5.5.: NH_3-TPD profiles of the catalysts compare to the industrial reference. Magnitude for TCD signal is increased fivefold for better identifiability of desorption peaks. Br: Brønsted acid cites for weakly acidic surface acid components, Le: Lewis acid cites – more strongly interacted with NH_3 in testing

The reference catalyst shows the least pronounced peaks, indicating low acidity. Increasing promotion of the tested catalyst samples in this work leads to increased catalyst acidity, although the binary catalyst 20 % CZ also exhibits increased acidity over the reference. The increase in surface acidity can have a number of reasons. The overall baseline increase over the reference is attributed to the formation of intrinsic acidic alumina species on the catalyst carrier spheres and acidic sites at the metal oxide interfaces between carrier and coating [42, 43]. Additionally, both CeO_2 and ZrO_2 form highly acidic species, especially in interference with other metal oxides [44, 45, 46]. This can be observed through the results of NH_3-TPD, as 20 % CZC and 20 % CZCZ show largely increased desorption peaks, both in height and in width compared to the unpromoted 20 % CZ and reference catalysts.

20 % CZCZC shows the steepest desorption peaks, both for Brønsted and for Lewis acid-cites. This is a contradiction to the goal of acid cite compensation through addition of CaO as metal oxide promoter. It is thereby suggested, that CaO is not effective in compensating the acidity of the alumina catalyst carrier acidity. In future work, TPD measurements for acidic gases or NMR-analyses will be added for better understanding of the acid-alkaline-interplay for the presented catalysts.

5.2.2. Catalyst Performance

Catalyst performance was determined for different synthesis pressures, gas hourly space velocities (GHSV) and reactor temperatures using a custom laboratory catalyst test bench equipped with a 70 ml tubular reactor as shown in figure 5.8 and described in further detail in the experimental section. Product gas composition was determined by an online gas chromatography unit (GC), while off-gas composition was determined by inline gas measurements. For typical performance testing, 35 min test protocols were conducted. Temperature, gas composition, pressure and flow rate were set and the catalyst was treated on stream for 10 min or until

normalization of online temperature, pressure and off-gas composition measurements were observed. This was followed by a 20 min timed test run for determination of conversion performance. GC measurements were initiated after the 20 min steady-state run.

Experiments for CO_2 conversion proficiency were carried out with a constant H_2/CO_2 mixture at three different gas space velocities of 8,000 h^{-1}, 10,000 h^{-1} and 12,000 h^{-1}, three pressures of 2, 3.5 and 5 MPa, and three temperatures at 225 °C, 250 °C and 275 °C. The CO_2 to H_2 ratio was set to hyper-stoichiometric conditions using the stoichiometric number (SN), calculated according to Equation (38) and typically set to 3:

$$S_N = \frac{n_{H_2,\text{Inlet}} - n_{CO_2,\text{Inlet}}}{n_{CO_2,\text{Inlet}} + n_{CO_2,\text{Inlet}}} \tag{5.1}$$

Catalyst performance was evaluated through calculation of CO_2 conversion (X_{CO2}), product selectivity for MeOH, H_2O, CO, CH_4, DME (S_i) and MeOH-production rate STY_{MeOH} rate according to following equations 39, 40, 41:

$$X_{CO_2} = \frac{n_{CO_2,\text{in}} - n_{CO_2,\text{out}}}{n_{CO_2,\text{in}}} \tag{5.2}$$

$$S_i = \frac{n_{\text{MeOH,out}} + n_{\text{CO,out}} + n_{H_2O,\text{out}}}{n_{H_2O,\text{out}} + n_{\text{CO,out}} + n_{H_2O,\text{out}} + n_{CH_4,\text{out}} + 2n_{\text{DME,out}}} \tag{5.3}$$

$$STY_{\text{MeOH}} = \frac{\dot{m}_{\text{MeOH,out}}}{\dot{m}_{\text{catalyst}}} \tag{5.4}$$

X_{CO2} and STY_{MeOH} for different reactor pressures at 250°C reactor temperature and H_2/CO_2 ratio of 3 are shown in figure 5.6.

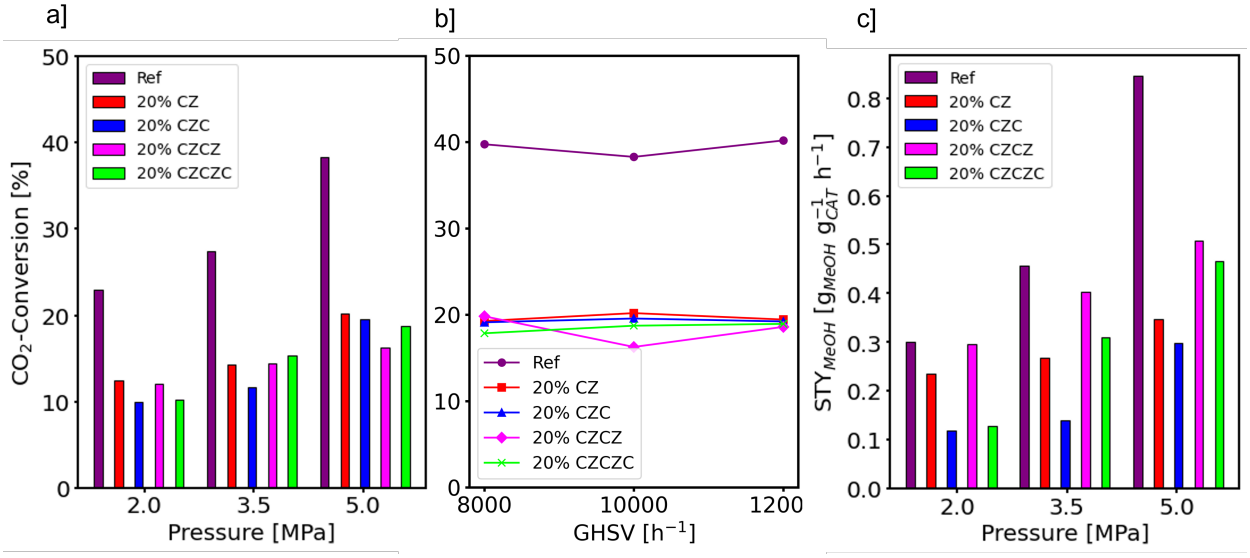

Figure 5.6.: a] CO_2 conversion over reactor pressure for the catalyst samples at 250°C reactor temperature, GHSV at 10,000 h^{-1} b] CO_2 conversion over GHSV at 250°C reactor temperature and 5 MPa reactor pressure, c] methanol production rate over reactor pressure for the catalyst samples at 250 °C reactor temperature, GHSV at 10,000 h^{-1} and gas composition SN = 3 for H_2/CO_2

Unsurprisingly, X_{CO2} increases significantly for all tested catalyst samples with increasing reaction pressure, where the industrial reference exhibits the highest X_{CO2} rates and STY_{MeOH} across the presented pressure

range. For the infiltration composite catalyst, increasing catalyst promotion leads to overall increases in activity concerning X_{CO2} and MeOH-production rate compared to the binary CuO/ZnO carrier catalysts. X_{CO2} for the base catalyst 20 % CZ was 12 % at 2 MPa and increased to 14 and 20.1 % for 3.5 and 5.0 MPa respectively. This demonstrates the high effectiveness of $CuO/ZnO/Al_2O_3$ catalysts in low pressure MeOH synthesis. The addition of CeO_2 over the base CuO/ZnO catalyst initially reduces conversion and production rates for all tested pressures. This result is rather unexpected, as existing literature suggests a beneficial impact for CeO_2 towards CO_2 adsorption and hydrogenation through generation of highly active lattice oxygen and oxygen vacancies in the ternary $CuO/ZnO/CeO_2$ catalyst structure and aids in higher dispersion levels for CuO and ZnO [47, 48, 49]. Further addition of ZrO_2 significantly increases activity levels of the tested catalysts above the previous ternary composition and achieves conversion rates comparable or superior to the binary CuO/ZnO catalyst.

This demonstrates the importance of multiple active components in the hydrogenation of CO_2. Especially the ternary interfaces between CeO_2, ZrO_2 and CuO have been shown to produce highly active catalyst compounds [32, 33, 37]. The increase in catalytic activity can be attributed to widely dispersed multi-metal oxide interfaces which unite active centers for CO_2 adsorption – Cu^0 species, oxygen vacancies and lattice oxygen in supported CeO_2 and ZrO_2 and ZnO – and H_2 adsorption – widely accepted to be located in reduced Cu and Zn catalyst surface species [24, 47, 50].

CaO-addition to the effective $CuO/ZnO/CeO_2/ZrO_2$ catalyst structure further improves conversion rates at 3.5 and 5.0 MPa slightly. The CaO promoted catalyst achieves a maximum of 18 % X_{CO2} and an hourly MeOH-production rate of 0.46 $g_{MeOH}\ g_{Cat}^{-1}\ h^{-1}$ at 5.0 MPa. Total MeOH-production rates for 20 % CZCZC are reduced slightly compared to 20 % CZCZ, which can be attributed to less CO_2 being converted to MeOH and more being converted to byproducts of the hydrogenation, primarily CO through RWGS. This contradicts previous research, which indicates that certain levels of alkali and alkali earth catalyst promotion are able to reduce RWGS selectivity substantially [24, 22, 23, 51]. This also indicates that multi-metal oxide interplay can induce inverse synthesis effects, depending on used catalyst metals and metal ratios for catalyst loading. This again is in line with previous studies that investigated metal oxide and metal support interactions [12, 21, 35, 37].

Results for X_{CO2} and STY_{MeOH} for varied synthesis temperatures and for production selectivity of MeOH, CO, CH_4 and DME at 3.5 MPa are given in figure 5.7 a) and b) respectively. High synthesis temperatures generally lead to high conversion rates but also facilitate increased reduction of CO_2 to CO and H_2O via RWGS. For all tested catalysts CO is the main carbon byproduct in CO_2 hydrogenation. Extending on the findings from figure 5.7, the reference catalyst shows the highest conversion ratios of CO_2 and subsequently exhibits the highest MeOH-production rates across the tested temperature range.

20 % CZ and 20 % CZC exhibit both the lowest conversion ratios as well as the highest selectivity values for CO_2-reduction to CO. This is clearly reflected in the lowest space time yields for MeOH, 0.24 $g_{MeOH}\ g_{Cat}^{-1}\ h^{-1}$ and 0.31 $g_{MeOH}\ g_{Cat}^{-1}\ h^{-1}$ respectively at 3.5 MPa and 275 °C. The impregnation catalysts show overall low activity for the lower two of the tested temperatures. This indicates that catalyst activity of the composites is generally low for synthesis temperatures beneath 250 °C.

The addition of ZrO_2 and CaO to 20 % CZC increases selectivity for MeOH and leads to an increase in production rates. As CO_2 hydrogenation follows one of multiple possible pathways, this can be attributed to a number of mechanistic effects.

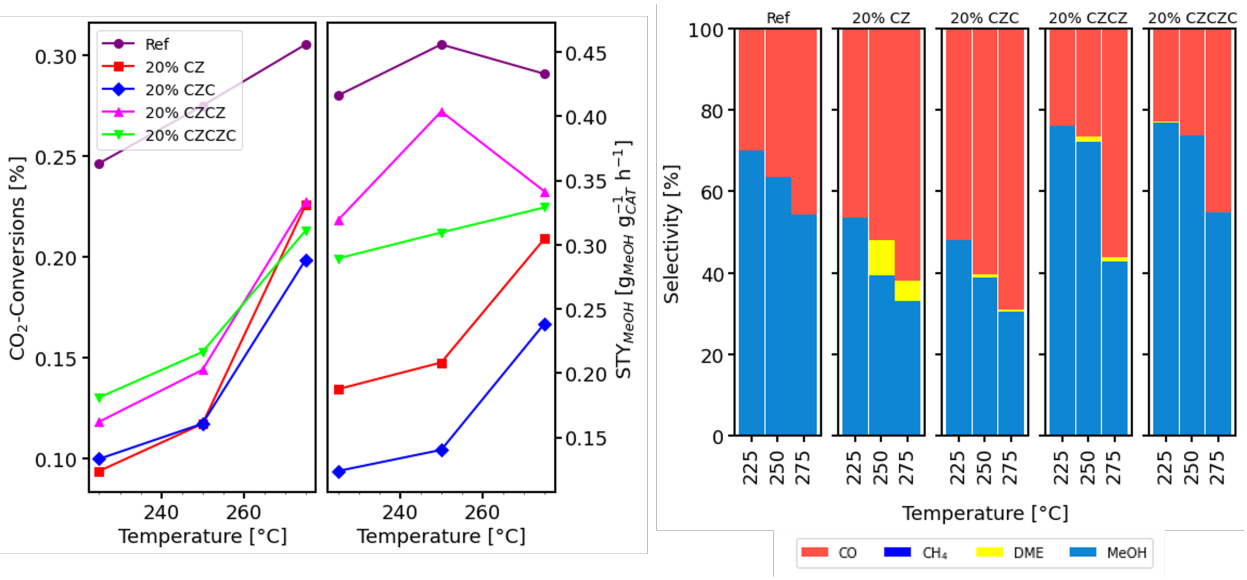

Figure 5.7.: a] CO_2 conversion and Methanol STY for different reactor temperatures b] Selectivity for MeOH, CO, CH_4 and DME generation at different temperatures. Catalyst performance was tested at 3.5 MPa reaction pressure, GHSV of 10,000 h^{-1} and H_2/CO_2 of SN = 3.

The promotion of the ternary 20 % CZC catalyst with ZrO_2 facilitates the hydrogenation through the formate or carbonate pathways, which are generally associated with stable CO_2 adsorption on oxygen vacancies or lattice oxygen in ZnO, CeO_2 and ZrO_2, on the surface of Cu-species with adsorbed H_2 as formate or on active interface sites between CuO and catalyst promoters or catalyst support [10, 11, 21, 52, 53]. This reaction mechanism does not contain CO as adsorbed intermediate and thus does not hazard the premature desorption of CO and H_2O. Furthermore, ZrO_2 and CaO strongly enhance the wide dispersion of Cu-species on the carrier surface and thus facilitate wide availability of active sites for both dissociative H_2 and CO_2 adsorption. This enables efficient reaction of adsorbed reactants and inhibits desorption of reduced CO without further interaction with topologically closely adsorbed H.

This also corresponds to the TPD and TPR results (see Figure 5.4 and 5.5), which suggest that dispersion of CuO is considerably increased by catalyst promotion through ZrO_2 and CaO in 20 % CZCZ and 20 % CZCZC respectively. These findings also confirm results from the abovementioned studies preliminarily, suggesting positive effects of low amounts of earth alkaline catalyst promotion towards effective dispersion of CuO and ZnO and thus optimized CO_2-activation for adsorption and further hydrogenation [22].

Maximum space-time yield for the infiltration composite catalysts is achieved by 20 % CZCZ at 5.0 MPa, 250 °C and a GHSV for feed gas of 10,000 h^{-1} at 0.507 $g_{MeOH}\ g_{Cat}^{-1}\ h^{-1}$. 20 % CZCZC achieves a maximum production rate of 0.50 $g_{MeOH}\ g_{Cat}^{-1}\ h^{-1}$ with 19.9 % X_{CO2} at 5 MPa, GHSV of 12,000 h^{-1} and 275 °C reactor temperature. For comparison, the reference catalyst achieves a maximum production rate of 1.14 $g_{MeOH}\ g_{Cat}^{-1}\ h^{-1}$ at 5.0 MPa and 250 °C reactor temperature. These findings are very similar to existing literature and thus partially confirm experiment reproducibility [2, 4]. None of the tested samples show high selectivity towards the reduction of CO_2 to CH_4 (see figure 5.7 b). The only notable formation of CH_4 is recorded at expected high reactor temperatures for the reference commercial catalyst. 20 % CZ, 20 % CZC, and 20 % CZCZ facilitate minor production of DME, especially the binary 20 % CZ catalyst shows selectivity towards MeOH dehydration to DME with DME-selectivity of 8.6 % at 250 °C and 3.5 MPa. Reaction conditions with the best recorded STY_{MeOH} and CO_2-turnover for the coated catalyst in comparison to the reference are given in Table 5.3.

Best STY_{MeOH} results are shown for each catalyst sample with corresponding reactor conditions for the achieved performance. In general, all catalysts expectedly exhibit the highest conversion ratios and production rates at high reactor pressure. Depending on overall catalyst selectivity, maximum production rates are either found at 250 °C or 275 °C reactor temperature. As the conversion rates consistently increase with rising reactor temperatures, the selectivity becomes the defining factor for STY_{MeOH}. As can be taken from figure 5.7 b], CO-selectivity is the defining factor for conversion efficiency as RWGS is the most relevant competing reaction to CO_2 hydrogenation to MeOH. The generation of CO has wider implications for industrial catalyst deployment. As single pass operation is only applied by a minority of industrial MeOH processes, it has to be assumed that mixed carbon oxide streams will prevail in industrial CO_2-to-MeOH process applications, as CO produced through RWGS is recycled and mixed with CO_2-based synthesis gas [2].

Table 5.3.: Conditions with best methanol space time yield (STY) and CO_2 turnover for the coated catalyst in comparison with the reference.

Catalyst	X_{CO_2} [%]	STY [$g_{MeOH}\ g_{cat}^{-1}\ h^{-1}$]	GHSV [h^{-1}]	Temp. [°C]	Pres. [MPa]
Reference	37.8	1.14	12,000	250	5
20 % CZ	22.2	0.45	10,000	275	5
20 % CZC	24.2	0.37	12,000	275	5
20 % CZCZ	16.2	0.51	10,000	250	5
20 % CZCZC	19.9	0.50	12,000	275	5

This necessitates more in-depth investigation of catalyst performance for varying carbon-oxide-ratios. Concerning space velocity, no clear conclusions can be made based upon the presented results as depicted in Figure 5.6 b]. All catalysts tend to produce better results at the higher gas hourly velocities of 10,000 h^{-1} and above.

Finally, the catalyst performance results are also compared to a variety of recent studies that have investigated the same catalyst tuning approaches for more efficient X_{CO2} and better selectivity for MeOH. In addition, commercial catalysts taken from corresponding patents are also listed for benchmark purposes. The evaluation criterion was the X_{CO2} and the STY_{MeOH}. The results for the study comparison are presented in Table 5.4. Where available, GHSV, pressure and reactor temperature are added for classification of presented data. If necessary and possible, based upon available study data, GHSV values are converted to h^{-1}. Where different catalyst samples are investigated in the presented studies, maximum values for each sample are used for the comparison presented here.

Most of the catalysts are produced through precipitation, although it is also clear that impregnation is a viable production method, especially for sample catalysts. Seven of the studies use catalysts produced by some form of impregnation. It is notable that many studies chose GHSV values that were considerably lower than those presented in the study on hand, namely [11, 14, 25, 26]. This does not seem to have a negative effect on productivity, which suggests that GHSV used by the cited commercial applications – from which the herein tested GHSV were adapted – have effects that could not be replicated in this work. Further testing is needed for determination of the effects of space velocities in this laboratory work.

Catalyst samples from this work perform very well in comparison to other tested catalyst samples from literature. 20 % CZCZ shows the highest STY_{MeOH} compared to other selected studies. In part, this can be attributed to the high synthesis pressures used in the test protocols for the presented work. Comparison to other studies that tested reactor pressures up to 5 MPa still shows that the catalysts tested herein show superior yield and conversion ratios. The effective surface interplay between ZrO_2 and CeO_2 is thus confirmed. High

surface area γ-Al_2O_3 carrier spheres seem to further boost conversion efficiency. Compared to [32, 33], we were able to achieve enhanced STY_{MeOH} in this work, proving the potential of the supported catalyst and further highlighting the role of ZnO in the conversion of CO_2 to MeOH. Concerning metal oxide promoters for conversion of CO_2 to MeOH, ZrO_2 seems to be widely regarded as the most promising in prolonging active catalyst stability and in delivering active sites for efficient CO_2-activation. Other additives that have not been used in production of the catalysts for this study include Gallium (Ga), Indium (In), Tungsten (W), Nickel (Ni), Platinum (Pt) and Gold (Au) [54, 55, 56]. While Ni, In and Pt catalyst supports have shown promising results in converting CO_2 to MeOH, in this application Al_2O_3 proves to be a better choice for large scale utilization due to its wide availability and low price.

Table 5.4.: Comparison of catalyst performance with literature data.

Catalyst	Sample Manufacturing	GHSV [h^{-1}]	Pressure [MPa]	Temperature [°C]	X_{CO2} [%]	STY [$g_{MeOH}\ g_{cat}^{-1} h^{-1}$]	Ref.
Recent Advances in Research							
Cu/ZrO_2	Deposition-Precipitation	10,000	3.00	299	16.00	–	[50]
In/ZrO_2	Impregnation	12,000	3.00	301	12.50	0.160	[47]
Cu/ZrO_2	Impregnation-Sol-Gel	20,000	3.00	250	1.00	0.144[a]	[19]
Cu-ZnO-ZrO_2	Precipitation-Reduction	4,600	5.00	263	23.00	0.210	[57]
Cu-ZnO-ZrO_2	Impregnation-Sol-Gel	8,600	3.00	250	19.20	0.376	[14]
CuO-ZnO-ZrO_2	Reverse-Co-Precipitation	–	2.00	240	14.00	0.219	[18]
CuO-Ga_2O_3/ZrO_2	Impregnation-Sol-Gel	20,000	3.00	250	1.18	0.136[a]	[19]
Cu-ZnO-ZrO_2-Al_2O_3	Co-Precipitation	12,000	3.00	250	15.00	0.009	[15]
In/CeO_2	Impregnation	12,000	3.00	301	10.20	0.008	[47]
Cu/CeO_2	Deposition-Precipitation	10,000	3.00	300	13.20	–	[50]
Cu/CeO_2	Hydrothermal	–	3.00	250	–	0.096	[48]
CuO/$CeWO_x$	Impregnation	3,000	3.50	250	13.00	0.394	[49]
CuO-ZnO-CeO_2	Reverse-Co-Precipitation	5,000	4.00	240	15.00	0.162	[11]
CuO-ZnO-CeO_2	Co-Precipitation	48,500	3.00	250	12.30	0.106	[12]
Cu-MgO-Al_2O_3	Co-Precipitation	2,000	2.00	200	4.80	–	[25]
CuO-ZnO-Al_2O_3-K	Co-Precipitation	2,400	3.00	240	14.00	0.390[a]	[26]
CuO-CeO_2-ZrO_2	Gel-Co-Precipitation	7,500–24,000	3.00	240	19.00	0.192	[33]
CuO/CeO_2-ZrO_2	Co-Precipitation	–	5.00	260	8.00	0.180	[32]
Cu-CeO_2-ZrO_2	Co-Precipitation	15,500	5.00	250	3.60	0.076	[58]
Cu-ZnO-ZrO_2-MgO/Al_2O_3	Impregnation	1,500–5,000	2.00	250	12.12	0.031	[24]
This Work							
CuO-ZnO-Al_2O_3	Co-Precipitation	10,000	5.00	250	38.20	0.840	This Work
CuO-ZnO-CeO_2/Al_2O_3	Impregnation	10,000	5.00	250	10.90	0.139	This Work
CuO-ZnO-CeO_2/Al_2O_3	Impregnation	10,000	5.00	250	12.30	0.239	This Work
CuO-ZnO-CeO_2-ZrO_2/Al_2O_3	Impregnation	10,000	5.00	250	16.20	0.507	This Work
CuO-ZnO-CeO_2-ZrO_2-CaO/Al_2O_3	Impregnation	10,000	5.00	250	16.70	0.463	This Work
Commercial CO-based Methanol Catalysts							
CuO-ZnO-Al_2O_3 (Süd Chemie)	Co-Precipitation	10,000	5.00	250	–	1.1	[2, 59]
CuO-ZnO-Al_2O_3 (BASF)	Co-Precipitation	10,000	5.00	230	–	1.43	[2, 60]
CuO-ZnO-Al_2O_3 (ICI)	Co-Precipitation	3,600	5.00	240	–	0.43	[2, 61]
Commercial CO_2-based Methanol Catalysts							
CuO-ZnO-Al_2O_3-ZnO-SiO_2 (NIRE)	Co-Precipitation	10,000	5.00	250	–	0.76	[2, 62]

5.3. Conclusions

A series of infiltration composite catalysts with 20 wt.% active components coating were prepared by the IWI method on γ-Al_2O_3 carrier spheres. The catalysts were based on CuO/ZnO and promoted with CeO_2, ZrO_2 and CaO, which were identified as possible enhancements for the direct hydrogenation of CO_2 to MeOH from literature. The IWI method was applied as a simple method for the customized and application-specific production of catalyst samples. X_{CO2}, STY_{MeOH} and selectivity towards MeOH, CO, CH_4 and DME were determined in a laboratory test bench at different space velocities, temperatures and pressures and compared to the performance of an industrial Cu-based MeOH catalyst. Special focus was put on the conversion of CO_2 to CO and H_2O through RWGS, as it is the main competing reaction in most Cu-based MeOH catalysts.
The binary catalyst complex CuO/ZnO on Al_2O_3 carrier spheres reached a maximum conversion rate of 22.2% with STY_{MeOH} of 0.45 $g_{MeOH}\ g_{Cat}^{-1}\ h^{-1}$ without additional promotion. The promoted ternary catalyst complex with added CeO_2 was not able to improve catalytic performance over 20% CZ. Catalyst promotion toward the quaternary CuO/ZnO/CeO_2/ZrO_2 and the quinary CuO/ZnO/CeO_2/ZrO_2/CaO complexes, however, was able to improve STY_{MeOH} by 13% and 11%, respectively, over the binary catalyst formula.
These findings are attributed to extremely high Cu species dispersion on the catalyst. This is supported by the presented XRD, EDX, BET, TPR and TPD results, which suggest an increase in metal species dispersion in the quaternary and quinary catalyst samples and very high surface areas in the supported catalysts. Low ZrO_2, CeO_2 and CaO loading is confirmed by EDX mappings over SEM images and elemental analysis of the catalyst samples. Formation of multi metal oxide compounds on the catalyst surface can mostly be ruled out by means of EDX mapping analyses, where ZrO_2 and CeO_2 dispersion over the image mappings is confirmed and the formation of conglomerates of metal oxides cannot be observed. Much rather do the images suggest that ZrO_2 and CeO_2 express their catalytic qualities through interplay with ZnO and CuO on the catalyst surface. This is reached while retaining very high surface areas of more than 120 $m^2\ g^{-1}$ and similar average pore sizes to the binary carrier catalyst 20% CZ of around $cm^3\ g^{-1}$.
Total reducibility of the coated catalysts is reduced slightly compared to the commercial catalyst in the tested temperature range. This is expected due to considerably lowered CuO loading of the coated catalyst samples. The quaternary catalyst formula exhibits the highest H_2 consumption of all the tested coated catalyst spheres. This is attributed to the special role of ZrO_2 in providing an effective surface structure for H_2 adsorption through generation of highly reducible CuO and CeO_2 species on the catalyst surface.
The results show the possible importance of multi metal oxide interplay in inhibiting the desorption of CO in the direct hydrogenation of CO_2, a key hurdle in developing effective catalysts for the efficient conversion of CO_2 to MeOH. Especially ZrO_2 is herein confirmed as an effective promoter in MeOH-synthesis catalysts, and its role in interaction with other catalytically active metal oxide components is further underlined.
Based upon this work, further testing will be conducted towards the conversion of mixed carbon oxide streams to MeOH. As the main competing reaction to the hydrogenation of CO_2 to MeOH is the formation of CO through RWGS, substantial amounts of CO from previous reactor passes are to be expected in industrial applications with gas recycling, no matter the selectivity of applied catalysts.
This puts special focus on both the selectivity towards carbon conversion to MeOH and the efficiency of the used catalysts in converting both CO and CO_2 to MeOH. Further work will focus on the MeOH production from mixed carbon oxide synthesis gas streams and the mechanics of the competing synthesis paths as a consequence. The effects of recycling the product gas streams will be evaluated in pilot scale application to further study these effects. Furthermore, coated composite catalysts are proven to deliver very good synthesis

results in comparison to co-precipitated samples. In addition, the simple preparation method by IWI allows the production of catalyst bodies in a wide range of different geometries with very high catalytic surface areas. Especially spherical catalyst structures are able to optimize catalyst beds regarding homogeneity, heat exchange, feed flow and gas diffusion to the active sites for single tube reactors but also for multi-pipe reactor setups and industrial applications of these.

5.4. Experimental

5.4.1. Catalyst Preparation

The infiltration composite catalysts were obtained through impregnation of high surface area aluminum-oxide (Al_2O_3) spheres with the selected metal oxide mixtures. γ-Al_2O_3 spheres (SASOL, Hamburg, Germany) with a nominal diameter of 800 μm were used as base for the further production process and loaded with 20 wt.% of each catalyst composition, respectively. Water absorption capacity of the carrier was determined through prolonged water bath immersion at 0.64 g_{H2O} $g_{Al2O3}{}^{-1}$.
The highly efficient, proven CuO–ZnO mixture was used as base for all composite samples [30]. Molar ratio of CuO and ZnO was set to 2.6 : 1 for all produced composites, which corresponds to the molar ratio used in the industrial reference catalyst Huton HUC-98 (derived from Süd Chemie Methanol Catalysts [59]).
Four carrier catalysts were produced with different molar ratios of added cerium oxide (CeO_2), zirconium oxide (ZrO_2) and calcium oxide (CaO) using IWI [63].
Highly water-soluble metal nitrate precursors were used for the catalyst coatings, specifically $Cu(NO_3)_2 \cdot 3\ H_2O$ (Carl Roth GmbH, Karlsruhe, Germany), $Zn(NO_3)_2 \cdot 4\ H_2O$ (Carl Roth GmbH, Karlsruhe, Germany), $ZrO(NO_3)_2 \cdot 2.5\ H_2O$ (Alfa Aesar GmbH, Kandel, Germany), $Ce(NO_3)_3 \cdot 6\ H_2O$ (Alfa Aesar GmbH, Kandel, Germany) and $Ca(NO_3)_2 \cdot 4\ H_2O$ (Alfa Aesar GmbH, Kandel, Germany).
To prepare the infiltration composite spheres with a catalyst content of 20 wt.%, the nitrate salts of the respective metals were first weighed into a beaker according to their molar proportions in the catalyst (table 5.5), filled with water to a total volume of 25.6 ml and dissolved by constant stirring.

Table 5.5.: Molar composition of the catalyst fractions within the infiltration composites.

Sample	CuO mol-%	ZnO mol-%	CeO_2 mol-%	ZrO_2 mol-%	CaO mol-%
CuO/ZnO[a] (20 % CZ)	72.2	27.8	–	–	–
CuO/ZnO/CeO_2[a] (20 % CZC)	65	25	10	–	–
CuO/ZnO/CeO_2/ZrO_2[a] (20 % CZCZ)	57.8	22.2	10	10	–
CuO/ZnO/CeO_2/ZrO_2/CaO[a] (20 % CZCZC)	54.2	20.8	10	10	5

[a] As coating for 20 wt % on γ-Al_2O_3-spheres (800 μm).

In each case, 50 g of catalyst spheres with 20 wt.% CuO/ZnO (abbreviated as 20% CZ), CuO/ZnO/CeO_2 (abbreviated as 20% CZC), CuO/ZnO/CeO_2/ZrO_2 (abbreviated as 20% CZCZ) and CuO/ZnO/CeO_2/ZrO_2/CaO (abbreviated as 20% CZCZC) were obtained. The reference was obtained from industrial 6 mm catalyst

pellets by crushing and sieving to a fraction between 800–900 μm diameter for comparability and reactor occupancy similar to the produced carrier catalyst samples.

5.4.2. Sample Characterization

Analyses of specific Brunauer-Emmett-Teller (BET) surface areas, pore size distribution and pore volume were carried out on an automated surface area analyzer (Micromeritics ASAP 2060) for each presented catalyst sample. Samples were tested for N_2-adsorption and desorption isotherms at -196 C. For pretreatment, samples were evacuated for 2 h at room temperature. The resulting adsorption isotherms are plotted in the supplementary materials (appendix) to this manuscript.
XRD was performed using Empyrean (Malvern Panalytical B.V., Netherlands) with CuKα radiation at 45 kV and 40 mA. XRD data were collected in a Bragg-Brentano geometry in the 2Θ range of 10°–90° with $\Delta 2\Theta \sim 0.026°$ and a counting time of 250 s/step using a 255-channel PIXcel linear detector.
For topographic analysis of the sample surfaces, scanning electron microscopy (SEM) images were taken of the catalyst surfaces using a JEOL JSM-IT800 microscopy unit. Additionally, Energy Dispersive X-ray Spectroscopy (EDX) was conducted in-situ using an EDAX Octane Elect Super system (70 mm^2 chip). SEM- and EDX-analyses were conducted at room temperature; samples were loaded unreduced.
For determination of catalyst redox properties, H_2-TPR of the samples was conducted. Experiments were carried out at ambient pressure on the automated Micromeritics 2950 MicroActive. For each TPR-measurement run, typically about 100 mg of every catalyst sample was tested in an auto-flow quartz reactor. Samples were pretreated in-situ at 200 °C for 30 minutes in helium. Afterwards, reduction was conducted with 5 % H_2 in Argon at 10 °C/min from 35 °C to 600 °C. Measurements of consumed H_2 were carried out using a TCD detector.
For specification of catalyst surface acid sites, NH_3-TPD was performed for every catalyst sample on the same device. Catalyst preparation was carried out according to the aforementioned preparation and pretreatment protocol. The catalyst samples were treated with 10 % NH_3 in helium carrier gas until the quartz reactor effluent TCD measurement returned to a stable baseline indicating full adsorption of ammonia to the different surface acid sites. Samples were flushed with helium from 50 °C to 500 °C at a heating rate of 10 °C per minute. Desorbed ammonia was measured using TCD of the reactor outlet.

5.4.3. Catalyst Performance

Catalyst performance was determined using a laboratory test bench (figure 5.8) equipped with a single tubular reactor with 70 ml dedicated catalyst volume and 25 mm inner diameter. All gases were supplied through high-pressure cylinders. Gas dosing and control of total volume flow were implemented by high-pressure bandwidth mass flow controllers (Bronkhorst El-Flow C200 Series for CO and H_2 and Bronkhorst mini CORI-Flow for CO_2). Reactor pressure was controlled through a proportional flow valve and a pressure control valve at the end of the total pressurized gas section and pressure regulators for each gas dosing section. Reactor temperature was controlled in counter-flow configuration using a thermo-oil-cryostat. Product gas composition at reactor outlet was determined by an online gas chromatography unit (Shimadzu GC2030 AT) with column – Rt-U-Bond Plot, 30 m $\times$ 0.53 mm – and mol sieve SH MSieve 5 A, 30 m $\times$ 0.53 mm – in serial configuration and TCD. Helium was used as carrier gas.
The liquid samples were collected in a high-pressure flash after condensation in a cooling section and drawn into containers through a solenoid back-pressure valve. Liquid samples were additionally analysed for their

composition and by-product contents ex-situ on a HPLC unit (Shimadzu LCMS-2020).
Finally, dry off-gas was expanded and total dry gas mass flow rate was measured. Off-gas composition was determined using inline CO_2- and H_2-measurements (BlueSense BCP-CO_2 and BCP-H_2) and an online unit for additional redundant measurement of CO_2- and CO-content (Emerson NGA2000).
For testing catalyst performance, 70 ml of each sample were gauged by volume and then weighed. Catalyst was filled into the reactor and excess volume was topped with quartz wool as filling agent and additional gas dispersion. Each catalyst sample was reduced in 100 % H_2 flow. For reduction, reactor temperature was programmed from 50 °C to 300 °C in 10 °C increments every 10 min. Molar flow rates and mass flow rates for the reactor exit gas were determined by assuming conservation of mass from dosed gases and calculating product gas molar weight. Total mass flow rates ($\dot{m}_{\mathrm{TOT}}$) were calculated by summing dosed masses from MFCs through Equation (5.5), product gas mixture molar mass was determined through Equation (5.6) (M_{Product}).

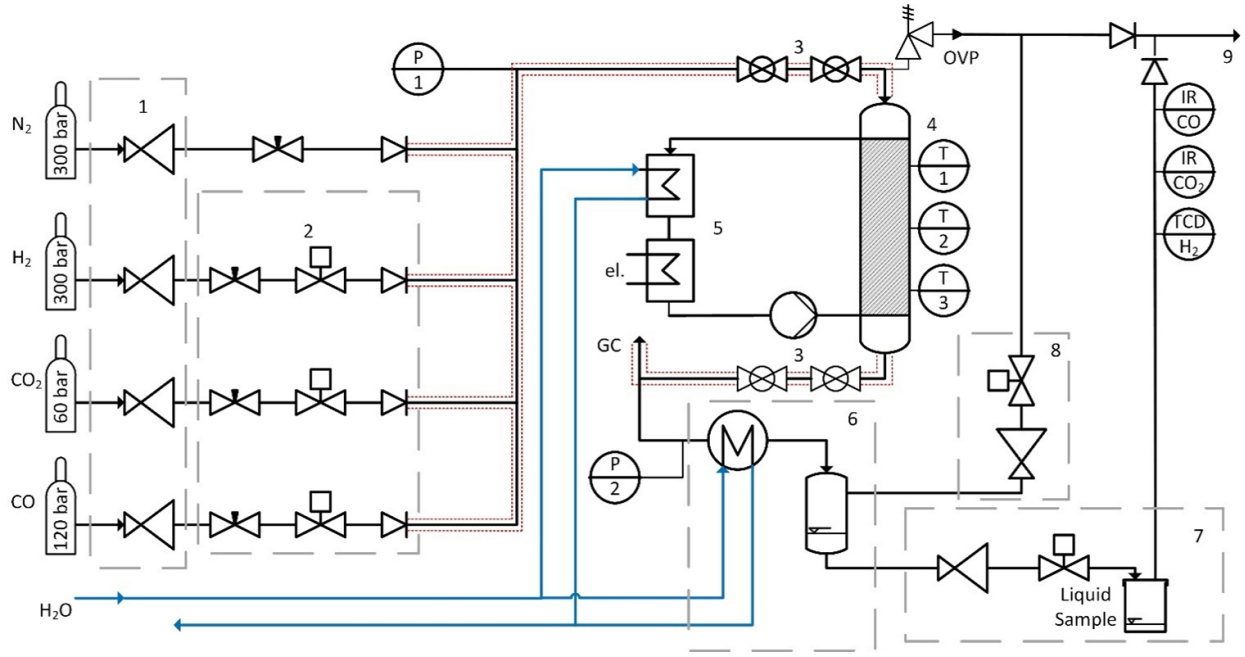

Figure 5.8.: Schematic of the lab test bench for catalyst sample performance. 1: Pressure control valves 2: Mass flow control (MFC) and check valves 3: Double valve coupling for reactor removal 4: Reactor with three temperature measurements 5: Electro-thermal oil heating/cooling 6: Product cooling and flash 7: Liquid sample 8: Flow control and expansion valve 9: Exhaust.

Total product flow rate was calculated through Equation (5.7) ($\dot{n}_{\mathrm{Product}}$):

$$\dot{m}_{\mathrm{TOT}} = \dot{m}_{\mathrm{CO2}} + \dot{m}_{\mathrm{H2}} + \dot{m}_{\mathrm{CO}} \tag{5.5}$$

$$M_{\mathrm{Product}} = \sum_{i=1}^{n} y_{\mathrm{product,\,i}} \cdot M_i \tag{5.6}$$

$$\dot{n}_{\mathrm{Product}} = \frac{\dot{m}_{\mathrm{TOT}}}{M_{\mathrm{Product}}} \tag{5.7}$$

y_{Product} was derived from GC measurements of product gas composition. Each experiment was carried out once with 5 experiments per sample being repeated threefold for demonstration of repeatability.

References

[1] Guanfu Liu, Helena Hagelin-Weaver, and Bruce Welt. "A Concise Review of Catalytic Synthesis of Methanol from Synthesis Gas". In: *Waste* 1.1 (2023), pp. 228–248. DOI: 10.3390/waste1010015.

[2] Vincent Dieterich et al. "Power-to-liquid via synthesis of methanol, DME or Fischer–Tropsch-fuels: a review". In: *Energy & Environmental Science* 13.10 (2020), pp. 3207–3252. ISSN: 1754-5692. DOI: 10.1039/D0EE01187H.

[3] Arena F. et al. "Synthesis, characterization and activity pattern of Cu–ZnO/ZrO2 catalysts in the hydrogenation of carbon dioxide to methanol". In: *Journal of Catalysis* 249.2 (2007), pp. 185–194. ISSN: 00219517. DOI: 10.1016/j.jcat.2007.04.003.

[4] Holger Ruland et al. "CO 2 Hydrogenation with Cu/ZnO/Al 2 O 3 : A Benchmark Study". In: *ChemCatChem* 12.12 (2020), pp. 3216–3222. ISSN: 1867-3880. DOI: 10.1002/cctc.202000195.

[5] Ubong J. Etim, Yibing Song, and Ziyi Zhong. "Improving the Cu/ZnO-Based Catalysts for Carbon Dioxide Hydrogenation to Methanol, and the Use of Methanol As a Renewable Energy Storage Media". In: *Frontiers in Energy Research* 8 (2020). DOI: 10.3389/fenrg.2020.545431.

[6] Menghao Ren et al. "Catalytic Hydrogenation of CO2 to Methanol: A Review". In: *Catalysts* 12.4 (2022), p. 403. DOI: 10.3390/catal12040403.

[7] Cássia S. Santana et al. "Influence of Al, Cr, Ga, or Zr as promoters on the performance of Cu/ZnO catalyst for CO2 hydrogenation to methanol". In: *Molecular Catalysis* 528 (2022), p. 112512. ISSN: 24688231. DOI: 10.1016/j.mcat.2022.112512.

[8] Poonam Sharma et al. "Recent advances in hydrogenation of CO 2 into hydrocarbons via methanol intermediate over heterogeneous catalysts". In: *Catalysis Science & Technology* 11.5 (2021), pp. 1665–1697. ISSN: 2044-4753. DOI: 10.1039/D0CY01913E.

[9] Xiaosong Hu et al. "The Synergistic Effect of CuZnCeO x in Controlling the Formation of Methanol and CO from CO 2 Hydrogenation". In: *ChemCatChem* 10.19 (2018), pp. 4438–4449. ISSN: 1867-3880. DOI: 10.1002/cctc.201800668.

[10] Feng Jiang et al. "Insights into the Influence of CeO 2 Crystal Facet on CO 2 Hydrogenation to Methanol over Pd/CeO 2 Catalysts". In: *ACS Catalysis* 10.19 (2020), pp. 11493–11509. ISSN: 2155-5435. DOI: 10.1021/acscatal.0c03324.

[11] Zhao Luo et al. "Synthesis of oxygen vacancies enriched Cu/ZnO/CeO2 for CO2 hydrogenation to methanol". In: *Greenhouse Gases - Science and Technology* 11 (2021), pp. 171–1179. DOI: 10.1002/ghg.2102.

[12] Rajan Singh, Kaushik Kundu, and Kamal K. Pant. "CO2 hydrogenation to methanol over Cu-ZnO-CeO2 catalyst: Reaction structure–activity relationship, optimizing Ce and Zn ratio, and kinetic study". In: *Chemical Engineering Journal* 479 (2024), p. 147783. ISSN: 13858947. DOI: 10.1016/j.cej.2023.147783.

[13] Mengdong Nie et al. "Effect of Mn content in CuO/MnCeO x catalysts on CO 2 hydrogenation for methanol synthesis". In: *Reaction Chemistry & Engineering* 8.6 (2023), pp. 1383–1394. DOI: 10.1039/D3RE00022B.

[14] Mauro Mureddo, Francesca Ferrara, and Alberto Pettinau. "Highly efficient CuO/ZnO/ZrO2@SBA-15 nanocatalysts for methanol synthesis from the catalytic hydrogenation of CO2". In: *Applied Catalysis B: Environmental* 258 (2019), p. 117941. ISSN: 09263373. DOI: 10.1016/j.apcatb.2019.117941. URL: https://www.sciencedirect.com/science/article/pii/S0926337319306873.

[15] Heondo Jeong, Churl Hee CHo, and Taw Hwan Kim. "Effect of Zr and pH in the preparation of Cu/ZnO catalysts for the methanol synthesis by CO2 hydrogenation". In: *Reaction Kinetics, Mechanisms and Catalysis* 106 (2012), pp. 435–443. DOI: 10.1007/s11144-012-0441-5. URL: https://link.springer.com/article/10.1007/s11144-012-0441-5.

[16] Kim Larmier et al. "CO2 -to-Methanol Hydrogenation on Zirconia-Supported Copper Nanoparticles: Reaction Intermediates and the Role of the Metal-Support Interface". In: *Angewandte Chemie (International ed. in English)* 56.9 (2017), pp. 2318–2323. DOI: 10.1002/anie.201610166.

[17] Jiahui Yu et al. "Cu-ZrO2 catalysts with highly dispersed Cu nanoclusters derived from ZrO2@ HKUST-1 composites for the enhanced CO2 hydrogenation to methanol". In: *Chemical Engineering Journal* 419 (2021), p. 129656. ISSN: 13858947. DOI: 10.1016/j.cej.2021.129656.

[18] Thongthai Witoon et al. "Tuning of catalytic CO2 hydrogenation by changing composition of CuO–ZnO–ZrO2 catalysts". In: *Energy Conversion and Management* 118 (2016), pp. 21–31. ISSN: 01968904. DOI: 10.1016/j.enconman.2016.03.075.

[19] Esteban L. Fornero et al. "Performance of ternary Cu–Ga2O3–ZrO2 catalysts in the synthesis of methanol using CO2-rich gas mixtures". In: *Catalysis Today* 213 (2013), pp. 163–170. ISSN: 09205861. DOI: 10.1016/j.cattod.2013.03.012.

[20] Xiaoying Mao et al. "The lattice oxygen determines the methanol selectivity in CO 2 hydrogenation over ZnZrO x catalysts". In: *Catalysis Science & Technology* 14.2 (2024), pp. 419–430. ISSN: 2044-4753. DOI: 10.1039/D3CY01471A.

[21] Kristian Stangeland et al. "Tuning the interfacial sites between copper and metal oxides (Zn, Zr, In) for CO2 hydrogenation to methanol". In: *Chemical Engineering Science* 238 (2021), p. 116603. ISSN: 00092509. DOI: 10.1016/j.ces.2021.116603.

[22] Atul Bansode et al. "Impact of K and Ba promoters on CO 2 hydrogenation over Cu/Al 2 O 3 catalysts at high pressure". In: *Catalysis Science & Technology* 3.3 (2013), pp. 767–778. ISSN: 2044-4753. DOI: 10.1039/c2cy20604h.

[23] Paweł Kowalik, Wiesław Próchniak, and Tadeusz Borowiecki. "The effect of alkali metals doping on properties of Cu/ZnO/Al2O3 catalyst for water gas shift". In: *Catalysis Today* 176.1 (2011), pp. 144–148. ISSN: 09205861. DOI: 10.1016/j.cattod.2011.01.028.

[24] Hong Ren et al. "Methanol synthesis from CO2 hydrogenation over Cu/g-Al2O3 catalysts modified by ZnO, ZrO2 and MgO". In: *Journal of Industrial and Engineering Chemistry* 28 (2015), pp. 261–267. ISSN: 1226086X. DOI: 10.1016/j.jiec.2015.03.001.

[25] Venkata D.B.C. Dasireddy, Strah Štefančič Neja, and Likozar Blaž. "Correlation between synthesis pH, structure and Cu/MgO/Al2O3 heterogeneous catalyst activity and selectivity in CO2 hydrogenation to methanol". In: *Journal of CO2 Utilization* 28 (2018), pp. 189–199. ISSN: 22129820. DOI: 10.1016/j.jcou.2018.09.002.

[26] Nagaraju Pasupulety et al. “A study on highly active Cu-Zn-Al-K catalyst for CO2 hydrogenation to methanol”. In: *Arabian Journal of Chemistry* 14.2 (2021), p. 102951. ISSN: 18785352. DOI: 10.1016/j.arabjc.2020.102951.

[27] Kang Xiao et al. “For Better Industrial Cu/ZnO/Al2O3 Methanol Synthesis Catalyst: A Compositional Study”. In: *Catalysis Letters* 147.6 (2017), pp. 1581–1591. ISSN: 1011-372X. DOI: 10.1007/s10562-017-2022-8.

[28] Felix Studt et al. “The Mechanism of CO and CO 2 Hydrogenation to Methanol over Cu–Based Catalysts”. In: *ChemCatChem* 7.7 (2015), pp. 1105–1111. ISSN: 1867-3880. DOI: 10.1002/cctc.201500123.

[29] Ivan Orozco et al. “Understanding Methanol Synthesis on Inverse ZnO/CuO x /Cu Catalysts: Stability of CH 3 O Species and Dynamic Nature of the Surface”. In: *The Journal of Physical Chemistry C* 125.12 (2021), pp. 6673–6683. ISSN: 1932-7447. DOI: 10.1021/acs.jpcc.1c00392.

[30] Maxim Zabilskiy et al. “The unique interplay between copper and zinc during catalytic carbon dioxide hydrogenation to methanol”. In: *Nat Commun* 11 (2020), p. 2409. DOI: 10.1038/s41467-020-16342-1. URL: https://www.nature.com/articles/s41467-020-16342-1#article-info.

[31] David Kordus et al. “Shape-Dependent CO2 Hydrogenation to Methanol over Cu2O Nanocubes Supported on ZnO”. In: *Journal of the American Chemical Society* 145.5 (2023), pp. 3016–3030. ISSN: 0002-7863. DOI: 10.1021/jacs.2c11540.

[32] Maxim Zabilskiy et al. “Methanol synthesis over Cu/CeO 2 –ZrO 2 catalysts: the key role of multiple active components”. In: *Catalysis Science & Technology* 11.1 (2021), pp. 349–358. ISSN: 2044-4753. DOI: 10.1039/d0cy01762k.

[33] Serena Poto et al. “Kinetic modelling of the methanol synthesis from CO2 and H2 over a CuO/CeO2/ZrO2 catalyst: The role of CO2 and CO hydrogenation”. In: *Chemical Engineering Journal* 435 (2022), p. 134946. ISSN: 13858947. DOI: 10.1016/j.cej.2022.134946.

[34] Libo Yao et al. “Synergy between active sites of Cu-In-Zr-O catalyst in CO2 hydrogenation to methanol”. In: *Journal of Catalysis* 372 (2019), pp. 74–85. ISSN: 00219517. DOI: 10.1016/j.jcat.2019.02.021.

[35] Thanaree Phongamwong et al. “CO 2 hydrogenation to methanol over CuO–ZnO–ZrO 2 –SiO 2 catalysts: Effects of SiO 2 contents”. In: *Chemical Engineering Journal* 316 (2017), pp. 692–703. ISSN: 13858947. DOI: 10.1016/j.cej.2017.02.010.

[36] Giuseppe Bonura et al. “Role of the ceria promoter and carrier on the functionality of Cu-based catalysts in the CO2-to-methanol hydrogenation reaction”. In: *Catalysis Today* 171.1 (2011), pp. 251–256. ISSN: 09205861. DOI: 10.1016/j.cattod.2011.04.038.

[37] Zhisheng Shi, Qingqing Tan, and Dongfang Wu. “Ternary copper-cerium-zirconium mixed metal oxide catalyst for direct CO2 hydrogenation to methanol”. In: *Materials Chemistry and Physics* 219 (2018), pp. 263–272. ISSN: 02540584. DOI: 10.1016/j.matchemphys.2018.08.038.

[38] Tafadzwa Precious Mabate et al. “Metal oxides and their roles in heterogeneous catalysis: special emphasis on synthesis protocols, intrinsic properties, and their influence in transfer hydrogenation reactions”. In: *SN Applied Sciences* 5.7 (2023). ISSN: 2523-3963. DOI: 10.1007/s42452-023-05416-6.

[39] Chunjie Haung et al. “Catalytic Hydrogenation of CO2 to Methanol: Study of Synergistic Effect on Adsorption Properties of CO2 and H2 in CuO/ZnO/ZrO2 System”. In: *Catalysts* 5 (2015), pp. 1846–1861. DOI: 10.3390/catal5041846.

[40] J. C. Slaa, J. G. van Ommen, and J.R.H. Ross. “The synthesis of higher alcohols using modified Cu/ZnO/Al2O3 catalysts”. In: *Catalysis Today* 15.1 (1992), pp. 129–148. ISSN: 09205861. DOI: 10.1016/0920-5861(92)80125-7.

[41] Pio Forzatti, Enrico Tronconi, and Italo Pasquon. “Higher Alcohol Synthesis”. In: *Catalysis Reviews* 33.1-2 (1991), pp. 109–168. ISSN: 0161-4940. DOI: 10.1080/01614949108020298. URL: https://www.tandfonline.com/doi/abs/10.1080/01614949108020298.

[42] Euiseob Yang et al. “Acidic effect of porous alumina as supports for Pt nanoparticle catalysts in n -hexane reforming”. In: *Catalysis Science & Technology* 8.13 (2018), pp. 3295–3303. ISSN: 2044-4753. DOI: 10.1039/C8CY00776D.

[43] Herman Pines and Werner O. Haag. “Alumina: Catalyst and Support. I. Alumina, its Intrinsic Acidity and Catalytic Activity”. In: *Journal of the American Chemical Society* 82.10 (1960), pp. 2471–2483. ISSN: 0002-7863. DOI: 10.1021/ja01495a021.

[44] Muthu Gnanamani et al. “Effect of pretreatment conditions on acidity and dehydration activity of CeO 2 -MeO x catalysts”. In: *Applied Catalysis A: General* 602 (2020), p. 117722. ISSN: 0926860X. DOI: 10.1016/j.apcata.2020.117722.

[45] Tiia Viinikainen et al. “Acidic and basic surface sites of zirconia-based biomass gasification gas clean-up catalysts”. In: *Applied Catalysis A: General* 362.1-2 (2009), pp. 169–177. ISSN: 0926860X. DOI: 10.1016/j.apcata.2009.04.037.

[46] Kozo Tanabe. “Surface and catalytic properties of ZrO2”. In: *Materials Chemistry and Physics* 13.3-4 (1985), pp. 347–364. ISSN: 02540584. DOI: 10.1016/0254-0584(85)90064-1.

[47] Poonam Sharma et al. “Role of ZrO2 and CeO2 support on the In2O3 catalyst activity for CO2 hydrogenation”. In: *Fuel* 331 (2023), p. 125878. ISSN: 00162361. DOI: 10.1016/j.fuel.2022.125878.

[48] Jiadong Zhu et al. “Mechanism and Nature of Active Sites for Methanol Synthesis from CO/CO2 on Cu/CeO2”. In: *ACS Catalysis* 10.19 (2020), pp. 11532–11544. ISSN: 2155-5435. DOI: 10.1021/acscatal.0c02909.

[49] Yong Yan et al. “CO2 hydrogenation to methanol on tungsten-doped Cu/CeO2 catalysts”. In: *Applied Catalysis B: Environmental* 306 (2022), p. 121098. ISSN: 09263373. DOI: 10.1016/j.apcatb.2022.121098.

[50] Weiwei Wang et al. “CO2 hydrogenation to methanol over Cu/CeO2 and Cu/ZrO2 catalysts: Tuning methanol selectivity via metal-support interaction”. In: *Journal of Energy Chemistry* 40 (2020), pp. 22–30. ISSN: 20954956. DOI: 10.1016/j.jechem.2019.03.001.

[51] Wenjia Liao, Wenjie Liao, and Ping Liu. “Methanol Synthesis from CO2 Hydrogenation over a Potassium-Promoted Cu x O/Cu(111) (x $\leq$ 2) Model Surface: Rationalizing the Potential of Potassium in Catalysis”. In: *ACS Catalysis* 10.10 (2020), pp. 5723–5733. ISSN: 2155-5435. DOI: 10.1021/acscatal.9b05226. URL: https://pubs.acs.org/doi/abs/10.1021/acscatal.9b05226.

[52] Noerma Azhari et al. “Methanol synthesis from CO2: A mechanistic overview”. In: *Results in Engineering* 16 (2016), p. 100711. ISSN: 25901230. DOI: 10.1016/j.rineng.2022.100711. URL: https://www.sciencedirect.com/science/article/pii/S2590123022003814.

[53] Suhas G. Jadhav et al. “Catalytic carbon dioxide hydrogenation to methanol: A review of recent studies”. In: *Chemical Engineering Research and Design* 92.11 (2014), pp. 2557–2567. ISSN: 02638762. DOI: 10.1016/j.cherd.2014.03.005.

[54] Oliver Martin et al. “Zinc-Rich Copper Catalysts Promoted by Gold for Methanol Synthesis”. In: *ACS Catalysis* 5.9 (2015), pp. 5607–5616. ISSN: 2155-5435. DOI: 10.1021/acscatal.5b00877.

[55] Kaihang Sun et al. “A highly active Pt/In 2 O 3 catalyst for CO 2 hydrogenation to methanol with enhanced stability”. In: *Green Chemistry* 22.15 (2020), pp. 5059–5066. ISSN: 1463-9262. DOI: 10.1039/D0GC01597K.

[56] Nora K. Zimmerli et al. “Structure and Role of a Ga-Promoter in Ni-Based Catalysts for the Selective Hydrogenation of CO2 to Methanol”. In: *JACS Au* 4.1 (2024), pp. 237–252. DOI: 10.1021/jacsau.3c00677.

[57] Xiaosu Dong et al. “CO2 hydrogenation to methanol over Cu/ZnO/ZrO2 catalysts prepared by precipitation-reduction method”. In: *Applied Catalysis B: Environmental* 191 (2016), pp. 8–17. ISSN: 09263373.

[58] Yerrayya Attada et al. “Dual experimental and computational approach to elucidate the effect of Ga on Cu/CeO2–ZrO2 catalyst for CO2 hydrogenation”. In: *Journal of CO2 Utilization* 65 (2022), p. 102251. ISSN: 22129820. DOI: 10.1016/j.jcou.2022.102251.

[59] Michael Schneider, Karl Kochloefl, and Jürgen Ladebeck. “Katalysator für die Methanolsynthese”. EP0125689A2. 1984. URL: https://worldwide.espacenet.com/patent/search/family/006199062/publication/EP0125689A2?q=0125689.

[60] Franz Bröcker et al. “Preparation of methanol synthesis catalyst comprising zinc, copper and aluminum”. US4436833A. 1984. URL: https://worldwide.espacenet.com/patent/search/family/006053171/publication/US4436833A?q=4436833.

[61] John Gallagher and John Kidd. “Methanol Synthesis”. GB1159035A. 1966. URL: https://worldwide.espacenet.com/patent/search/family/026262693/publication/GB1159035A?q=1159035.

[62] Takeuchi Masami et al. “Copper-based catalyst and method for production thereof”. US6048820A. 1998. URL: https://worldwide.espacenet.com/patent/search/family/026396807/publication/US6048820A?q=6048820.

[63] Krijn de Jong. *Synthesis of Solid Catalysts*. Hoboken: Wiley VCH, 2009. URL: https://onlinelibrary.wiley.com/doi/book/10.1002/9783527626854.

6. Industrial Methanol Synthesis over Cu/ZnO Infiltration Composites

This chapter presents the article *CO_2- and CO-Conversion to Methanol over Promoted CuO/ZnO-based Infiltration Composite Catalyst Spheres – Characterization, Experimentals and Comparative Reaction Kinetics*, which has been published in *Applied Catalysis A: General*.

In the previously published article, the carrier-based catalyst formulations were shown to exhibit high effectiveness in converting CO_2 to MeOH under single-pass reactor operation, performing very well when compared with selected recent literature. Structural, compositional, and chemical analysis verified that the surface loading matched the initial catalyst design, while also identifying potential challenges associated with surface acidity and quantifying the reducibility of the applied prototype catalysts. It was further demonstrated that CO formation represented a major obstacle for industrial deployment of these catalyst systems. At the single-pass carbon conversions typically below 20%, it became clear that mixed carbon-oxide feed streams would need to be examined to meaningfully evaluate the catalysts under industrially relevant operating conditions. In addition, the physio-chemical properties determined for the materials could not be directly correlated with their catalytic performance. These limitations were addressed in the second publication.

The article reported in this chapter presents the comprehensive extension of characterization methods and catalytic evaluation of the four previously reported CuO/ZnO-based infiltration composite catalyst spheres. The experimental scope and depth of analysis was significantly enhanced beyond the earlier study. Performance evaluation was expanded to include a broader and extensive data set involving mixed carbon-oxide feed streams, enabling a more detailed assessment of catalyst behavior under industrially relevant process conditions. In addition, a systematic analysis of temperature- and pressure-dependent reaction equilibria is included, which is essential for determining realistic steady-state equilibrium gas compositions encountered in commercial catalyst operation.

The characterization methodology was substantially advanced, incorporating essential physio-chemical techniques such as XPS and high-resolution STEM analysis as well as TPD-experiments for CO_2 and H_2, thereby enabling direct quantitative correlations between catalyst structure, chemical properties, and catalytic performance. The catalyst manufacturing protocol was critically evaluated to highlight surface-coverage achieved through IWI and possible shortcomings later discussed.

Furthermore, a kinetic comparison for all catalyst formulations was presented, supported by an effective parameter-fitting workflow made available as open-source software alongside the publication. The resulting kinetic parameters were employed to assess promoter effects on key model constants within the examined reaction network, and mechanistic implications were discussed with respect to changes in the rate-determining steps and overall reaction pathways induced by promoter species.

Declaration of contributions:

- *Carl Fritsch* conceptualization of study, methodology, formal analysis, investigation (catalyst performance, kinetic model, equilibria, evaluation of characterization methods), data curation, project

administration, funding acquisition, resources, supervision, validation, visualization, original draft

- *Andreas Serwe* formal analysis, investigation (catalyst performance, kinetic model, equilibria), data curation
- *Sven Jovanovic* investigation (Raman Spectroscopy), review
- *Hariprasad Ranganathan* investigation (TPD Analysis), review
- *Marcus Hans* investigation (FIB Lamellae, SEM), review
- *Andreas Hutzler* investigation (HAADF-STEM), review
- *Jürgen Dornseiffer* methodology, manufacturing of catalyst samples, data curation, review
- *Nikolay Kornienko* investigation (TPD), resources, review

Original Publication

Fritsch, C.; Serwe, A.; Jovanovic, S.; Hariprasad, R.; Hans, M.; Hutzler, A.; Dornseiffer, J.; Kornienko, N. CO_2- and CO Conversion to Methanol over promoted CuO/ZnO-based Infiltration Composite Catalyst Spheres - Characterization, Experimentals and Comparative Reaction Kinetics, Applied Catalysis A: General 2026, 10.1016/j.apcata.2025.120675

Abstract

Zirconia (ZrO_2)-, Ceria (CeO_2)-, and Calcium (CaO)-promoted Copper oxide (CuO) Zinc oxide (ZnO) catalysts supported on γ-alumina spheres are synthesized via incipient wetness impregnation (IWI) and characterized using transmission electron microscopy (TEM), Raman spectroscopy, X-ray Photoelectron Spectroscopy (XPS) , and CO_2/H_2-TPD. Catalytic performance is evaluated for carbon oxide hydrogenation to methanol (MeOH) in mixed carbon oxide synthesis gas, examining both CO and CO_2 conversion pathways and MeOH space-time yields (STY). Temperature- and pressure-dependent reaction equilibria for MeOH formation from CO and CO_2, as well as the reverse water-gas shift reaction (RWGS) are investigated to demonstrate promoter effects on surface reaction mechanisms and conversion efficiency towards MeOH and H_2O. Reaction kinetics are optimized using a previously formulated re-parametrized two-site Langmuir-Hinshelwood-Hougen-Watson (LHHW) model for each catalyst system, providing comparative kinetic parameters for the binary, ternary, quaternary, and quinary catalyst formulations. The kinetic models demonstrate good numerical agreement with experimental data for the promoted catalyst samples. Although CO-rich streams produce the highest MeOH-production rates in all samples, the promotion through ZrO_2 and CeO_2 significantly improved both CO and CO_2 conversion (X_C) compared to the binary CuO / ZnO catalyst formulation.

6.1. Introduction

The direct conversion of CO_2 to carbon-based platform chemicals and fuel substitutes promises to become a key technology for the mitigation of industrial carbon emissions and thus plays a vital role in reducing anthropogenic climate impact. In recent years, process development for efficient conversion technologies and advances in materials science for enhanced catalytic activation of the low-reactivity CO_2-molecule for hydrogenation to chemical products have become prevalent in respective research fields, with some initial industrial applications being demonstrated commercially lately [1, 2, 3]. In this context, it is widely accepted that methanol (MeOH) is a very promising potential product derived from CO_2 [4]. Well established production processes, a large international infrastructure, and wide applications as both alternative fuel and as a platform chemical as well as comparatively easy adaption of commercial, fossil production processes towards substitutional CO_2-introduction as reactant, have led to the beginning commercialization of a regenerative, CO_2-based MeOH-production network [3]. While process ramp-up is underway, some essential developmental issues prevail in the industrialization of the commercial CO_2 hydrogenation to MeOH on a catalytic level:

- commercial $CuO/ZnO/Al_2O_3$ (CZA)-catalysts show reduced activity towards the hydrogenation of CO_2 compared to commercial, fossil derived CO-based reactant streams [5];
- reduced activity can be attributed to the catalytically idle CO_2 being harder to activate over CZA than CO, which is far more prevalent in fossil derived SynGas. This necessitates the introduction of different, more aggressive catalyst active sites for the efficient activation and hydrogenation of CO_2 or the application of alternative catalyst technologies, improving active catalyst surface area [6, 7];
- the stoichiometric co-production of H_2O in the hydrogenation of CO_2 can lead to premature deactivation of CZA-catalysts, requiring stabilizing agents for long term stability [3, 8];
- the exact mechanisms contributing to both CO- and CO_2 hydrogenation are still disputed, making it hard to securely apply catalyst adaptions and optimizations on a molecular level for enhanced conversion of CO_2 and optimized long term catalyst stability [8, 9, 10];
- while the hydrogenation of CO_2, the underlying mechanisms and the selectivity towards MeOH production of developed and optimized catalyst formulas are the focus of many recent studies, the reduction of CO_2 to CO and H_2O via reverse water gas shift reaction (RWGS) and its effects on possible commercial application of presented catalysts are often not considered in detail. As single reactor-pass carbon conversion ratios (X_C) do not facilitate once-through reactor operation in MeOH-production processes, the unavoidable formation of CO and its reintroduction into the reactor through gas recycling should be considered for catalyst development. Thus, mixed carbon-oxide synthesis gas streams and the interplay between CO and CO_2 in the formation of MeOH should be considered, when developing new catalyst formulas and assessing conversion effectiveness [11, 12, 13].
- this requires either complex in-situ reaction characterization through methods such as in-situ Diffuse reflectance infrared Fourier transform spectroscopy (DRIFTS) analysis, the application of complex testing facilities, which allow for controlled gas recycling in laboratory environments or the application of kinetics to be able to truly assess application potentials of tested catalyst formulas [14, 15, 16]

Many recent studies have thus introduced different metal-oxides as both catalyst promoters in CZA or as carriers and primary active components in bimetallic, ternary, quaternary or quinary catalyst formulas for

enhanced hydrogenation of CO_2 to MeOH [5]. Herein, especially cerium-oxide (CeO_2) and zirconium-oxide (ZrO_2) have been identified as very efficient catalysts for the activation of CO_2 and its subsequent hydrogenation to MeOH [15, 17, 18, 19, 20]. The ability of Ceria to form oxygen vacancies on catalyst surfaces allows it to produce active centers for the effective adsorption of CO_2 [21]. Furthermore it can exhibit positive influences in lowering the Cu-crystallite sizes through improved dispersion, thus also improving surface-coverage with active centers for both CO- and H_2 adsorption [20, 22]. Therefore, the use of ceria in MeOH catalysts is able to improve both surface Cu^+ formation as well as lowering required activation energies for CO_2-activation and subsequent hydrogenation, additionally being able to produce basic active sites for improved adsorption of acidic CO_2 [20, 23]. Through these effects CeO_2 is also able to produce strengthened bonds between metallic Cu and adsorbed CO, inhibiting premature CO desorption and thus preventing CO_2-reduction to CO and H_2O through RWGS [24, 25].

In a comparable manner, ZrO_2 has been shown to positively effect hydrogenation of CO_2, increasing catalyst stability due to its slight hydrophobic character and improving dispersion of metal-oxide interfaces that act as active centers in heterogeneous MeOH catalysts [17, 19, 26]. Additionally ZrO_2 can strengthen the binding of reaction intermediates, thus inhibiting CO formation from CO_2 and improving selectivity towards MeOH [17, 27, 28]. Alkaline earth metals have also shown to be able to enhance conversion ratios, when added to CZA, with calcium oxide (CaO) and magnesium oxide (MgO) showing improved CO_2 conversion over CZA-samples, especially at high reaction temperatures [29, 30].

Multi-metal-oxide interactions in promoted catalysts can enhance the promotional effects of individual additives, improving the conversion efficiencies of multicomponent catalyst formulations compared to single-promoter systems [31, 32]. Building on recent developments in direct CO_2 hydrogenation to MeOH, we previously introduced four novel carrier catalyst samples designed for efficient CO_2-to-MeOH conversion [11]. These samples were prepared as infiltration composites by coating γ-Al_2O_3 spheres with CuO/ZnO (20% CZ) and successively adding CeO_2 (20% CZC), ZrO_2 (20% CZCZ), and CaO (20% CZCZC), yielding four catalysts with systematically varied metal-oxide promotion.

All catalysts exhibited high selectivity toward CO formation in super-stoichiometric CO_2-only feed streams. This observation raises the question of how these materials perform under more realistic industrial conditions, where recycled CO affects the steady-state equilibria of CO- and CO_2 hydrogenation as well as RWGS. The present study therefore investigates the promotional effects of CeO_2, ZrO_2, and CaO in CZA-based catalyst systems under mixed carbon-oxide synthesis conditions. The systematic examination of CO/CO_2-ratios herein represents an aspect often overlooked in CO_2-to-MeOH studies [10].

A further novelty here lies in the use of γ-Al_2O_3 carrier spheres, which allows a substantial reduction of active-material usage while potentially retaining catalytic performance compared to co-precipitated catalysts [33]. The use of structured γ-Al_2O_3 carriers offers a scalable route for preparing thin, uniform catalyst washcoats with reduced metal loading, helping to minimize diffusional limitations and improve heat transfer—factors often insufficiently controlled in conventional MeOH-synthesis catalyst testing. This design facilitates systematic evaluation of intrinsic kinetic behavior and promoter interactions on the coated catalyst surface.

We combine advanced characterization (CO_2/H_2-TPD, Raman, TEM, XPS) with kinetic parameter optimization using a tubular fixed-bed reactor model, establishing direct links between promoter-induced structural and electronic modifications and their impact on kinetic parameters. The analysis of step-wise promotional effects on H_2 and CO_2 adsorption enables isolation of single metal-oxide contributions within multi-metal combinations. Such integration of physico-chemical characterization with quantitative kinetic modeling

remains uncommon, especially for multi-promoted CZA catalysts.
Through kinetic parameter optimization for each catalyst, we clarify how CeO_2, ZrO_2, and CaO influence CO and CO_2 conversion to MeOH under industrially relevant conditions. Our results further provide mathematical confirmation that CO-to-MeOH conversion can be excluded from the reaction network under the investigated conditions. Overall, this study expands the kinetic knowledge base for highly promoted CZA catalysts and delivers a methodological foundation for efficient, parallelized kinetic parameter optimization in complex multi-promoter systems.

6.2. Experimental Section

6.2.1. Catalyst preparation

Catalyst samples were manufactured by coating high surface area 800µm diameter γ-Al_2O_3 spheres (SASOL, Hamburg Germany) through incipient wetness imprgenation method (IWI). In a first step, the maximum adsorption capacity of the carrier for water was determined, yielding an average water-adsorption capacity of 0.64 g_{H2O} g_{Al2O3}^{-1}. Metal nitrate precursors were used for compounding the individual coating for the spheres [11]:

- $Cu(NO_3)_2 \cdot 3\ H_2O$ (Carl Roth GmbH, Karlsruhe Germany)
- $Zn(NO_3)_2 \cdot 4\ H_2O$ (Carl Roth GmbH, Karlsruhe Germany)
- $ZrO(NO_3)_2 \cdot 2.5\ H_2O$ (Alfa Aesar GmbH, Kandel Germany)
- $Ce(NO_3)_3 \cdot 6\ H_2O$ (Alfa Aesar GmbH, Kandel Germany)
- $Ca(NO_3)_2 \cdot 4\ H_2O$ (Alfa Aesar GmbH, Kandel Germany)

To prepare 50 g of the infiltration composite spheres with a catalyst loading of 20 $\%_{wt}$ catalytically active coating, the nitrate salts of the respective metals were first weighed into a beaker according to their molar proportions in the catalyst (Table 6.1).

Table 6.1.: Catalyst composition for the tested samples.

Sample	CuO	ZnO	CeO_2 (mol%)	ZrO_2	CaO
CZA (Ref)	68.0	28.0	(Al_2O_3 - rest)	–	–
20% CZ	72.2	27.8	–	–	–
20% CZC	65.0	25.0	20.0	–	–
20% CZCZ	57.8	22.2	10.0	10.0	–
20% CZCZC	54.2	20.8	10.0	10.0	5.0

The compositions were chosen, so that the molar ratio between CuO and ZnO did not change throughout the chosen promotional catalyst compositions according to previously reported optimal ratios in CZA-based catalyst designs [34]. The beaker was filled with water to a total volume of 25.6 ml and the nitrate salts were dissolved under constant stirring. The solutions were mixed with 40 g of the alumina spheres in a porcelain bowl and mixed until the liquid was completely absorbed by the carrier spheres. The resulting homogeneous

loaded wet composites were dried for 4 hours at 100 °C and calcined for 1 hour at 350 °C at a heating rate of 2 °C per minute. In each case, 50 g of catalyst spheres with 20 $\%_{wt}$ CuO/ZnO (20% CZ), CuO/ZnO/CeO_2 (20% CZC), CuO/ZnO/CeO_2/ZrO_2 (20% CZCZ) and CuO/ZnO/CeO_2/ZrO_2/CaO (20% CZCZC) were obtained. An industrial precipitated CZA reference sample was crushed and sieved to 800 - 900 µm diameter from 6 mm catalyst pellets. A more detailed catalyst preparation protocol can be found elsewhere [11].

6.2.2. Physical characterization of the samples

Samples surface structure, composition and chemical state were investigated using Raman-Spectroscopy (RS), XPS and High-Angle Annular Dark-Field scanning transmission electron microscopy (HAADF-STEM). Catalyst samples were investigated calcined in their unreduced state after production and drying. Representative Raman-spectra of each unreduced catalyst loaded Al_2O_3 carrier sphere were recorded with a WITec alpha 300 R Raman microscope (Ulm, Germany) using a 532 nm excitation laser at a laser power of 7 mW and a 50x magnification Zeiss objective. The microscope utilizes the WITec ultra high throughput spectrometer UHTS 300 VIS-NIR and a 1200 g/mm grating. For each spectrum, 120 accumulations at a integration time of 0.5 seconds were recorded. All spectra were baseline corrected using the spheres algorithm of the WITec Project SIX software (Ulm, Germany).

For TEM-investigation of the samples in their oxidized state, Focused Ion Beam (FIB)-Lamellae were fabricated from the surface of the catalyst spheres at a depth of approx. 8-9 µm. A detailed account of the lamellae manufacturing process is given in the supplementary materials. Lamellae were investigated through HAADF-STEM and energy-dispersive X-ray spectroscopy (STEM-EDXS) on a Talos F200i (Thermo Fisher Scientific) using high tension of 200 kV. Fast Fourier Transformation (FFT) and Inverse fast Fourier Transformation (IFFT) were used for indexing lattice spacing of specific metal-oxide structures of the carrier and its coating based upon the STEM-images. For FFT- and IFFT- analysis, STEM images were processed in the ImageJ environment and automatic FFT- and IFFT- analysis was carried out [35]. Lattice spacing was then derived from FFT plots. A more detailed account of image processing for FFT and IFFT analysis is given in the supplementary materials.

For investigation of Cu- and Zn-species distribution on the unreduced samples as well as identifying catalyst promoter species on the surface, XPS for each catalyst sample was carried out on a Phi5000 VersaProbe II (ULVAC-Phi Inc., USA) using a monochromatic Al K-α source at 1.486 keV. X-ray was set to 50 W and 15 KV for analysis of a 200µm spot on the respective catalyst surfaces. General XPS-surveys were recorded at 187.5 eV pass energy at 0.8 eV and 100 ms per step. Details were recorded for CuO and Cu(OH) in the range of 925 eV to 955 eV and Zn-species in the range of 1010 eV to 1060 eV.

Binding energy for CO_2 and H_2 was probed through TPD-experiments. H_2-TPD was carried out on a Micromeritics 2950 MicroActive (Norcorss, USA). Typically, around 100 µg of sample was used. Samples were dried at 100 °C for at least 3 hours in an Ar environment and then loaded into a quartz reactor. Samples were then reduced under a 5% H_2 in Ar gas flow from 20 °C - 300 °C. We have reported reduction profiles for H_2-temperatures programmed reduction analysis (TPR) previously elsewhere [11].

After reduction, the reduced samples were cooled and then flushed with 5% H_2 in Ar gas flow from 20 °C to 250 °C at a heating rate of 10°C/min. Samples were returned to atmospheric pressure and temperature and the gas flow was changed to He. Desorption was then carried out until 700 °C was reached at a heating rate of 10 °C/min and reactor effluent gas was measured using a thermal conductivity detector (TCD). A baseline

correction of the recorded values was applied for further handling of the recorded data.

The H_2-TPD data was used to determine the copper surface area, copper dispersion, and the degree of reduction for each sample, based upon the previously introduced methodologies by Fichtl et al. (2014), Muhler et al. (1992) and de Carvalho et al. (2002) [36, 37, 38]. The total amount of desorbed H_2 ($n_{H_2,\text{desorbed}}$) was obtained by integrating the TPD-signal between 30–360 °C and applying the calibration factor. This represents the temperature range usually associated with activity of metallic, reduced Cu in Cu-based catalysts. Assuming a 1:1 stoichiometry between H atoms and Cu surface atoms, the number of exposed copper atoms can be expressed as:

$$n_{\text{Cu,surface}} = 2 \cdot n_{H_2,\text{desorbed}}. \tag{6.1}$$

The corresponding copper surface area A_{Cu} is calculated from the known surface atom density of polycrystalline copper ($\rho_{\text{Cu}} = 1.47 \times 10^{19}$ atoms m^{-2}) [36]:

$$A_{\text{Cu}} = \frac{n_{\text{Cu,surface}} \cdot N_A}{\rho_{\text{Cu}}}. \tag{6.2}$$

Normalization to the active catalyst mass (m_{cat}) obtains the specific copper surface area in m^2 g^{-1} catalyst:

$$A_{\text{Cu}}^{\text{spec}} = \frac{A_{\text{Cu}}}{m_{\text{cat}}}. \tag{6.3}$$

The copper dispersion D is further more defined as the ratio of surface copper atoms to the total number of copper atoms in the sample:

$$D = \frac{n_{\text{Cu,surface}}}{n_{\text{Cu,total}}}, \tag{6.4}$$

where the total number of copper atoms is obtained from the sample mass, the copper loading (w_{Cu}), and the molar mass of copper M_{Cu}:

$$n_{\text{Cu,total}} = \frac{w_{\text{Cu}}}{100} \cdot m_{\text{cat}} \cdot \frac{N_A}{M_{\text{Cu}}}, \tag{6.5}$$

Here, N_A is the Avogadro constant, which relates the number of atoms or molecules to the amount of substance in moles, with a value of approximately $6.022 \times 10^{23}\,\text{mol}^{-1}$.

The degree of reduction (DOR) quantifies the fraction of reduced copper relative to the theoretical maximum and is given by:

$$\text{DOR}\,(\%) = \frac{n_{H_2,\text{desorbed}}}{0.5 \cdot n_{\text{Cu,total}}} \times 100. \tag{6.6}$$

Desorption experiments for CO_2 were carried out on a ChemBET Pulsar TPD/TPR-instrument (Anton Paar QuantaTec, Boynton Beach, USA). Around 500 mg of each sample were dried in a U-shaped quartz tube at 120 °C overnight in Ar. Then, the samples were installed in the Pulsar instrument and heat-treated at 200 °C (rapid heating in 5 min) for 60 min and subsequently cooled to 50 °C under He-flow for drying. CO_2 adsorption was started at 50 °C under 5% CO_2/He gas flow for 90 Minutes. Then, the gas was switched to He to remove unadsorbed CO_2 for 30 min. Finally, the TPD was performed from 50 – 600 °C under He with a heating rate of 5 °C/min while the signals were monitored by TCD in the reactor effluent.

6.2.3. Activity Testing

Sample activity towards hydrogenation of CO and CO_2 as well as reaction equilibria were measured on a custom catalyst test bench with a 70 ml heated stainless steel tubular reactor. The test bench was equipped with gas-dosing mass flow controllers (MFCs) for CO, CO_2 and H_2 as well as pressure controllers and back pressure valves for control of reactor pressure. The reactor was heated or cooled through a tempered oil thermostat according to a threefold temperature measurement through thermocouples inside the catalyst bed. Reactor effluent composition was measured through a gas chromatography unit (GC, Shimadzu Nexis GC-2030) on a double column configuration with Rt-U-Bond Plot, 30 m x 0.53 mm and mol sieve SH MSieve 5A – 30 m x 0.53 mm through TCD-measurements of the sample.

Product gas was cooled and liquid components condensed in a counter current product cooling column with off-gas being depressurized and run through an off-gas analysis chain with inline CO_2- and H_2-measurements (BlueSense BCP- CO2 and BCP-H2) as well as online measurement of CO_2- and CO-content (Emerson NGA2000). A schematic of the test bench is given in figure 6.1. We have reported a more detailed P&ID and description of the reactor setup previously elsewhere [11]. For testing towards conversion activity in mixed carbon-oxide synthesis gas streams, typically 70 ml of catalyst sample were filled into the tubular reactor, with glass wool used as dispersion medium on the top and bottom of the reactor. The samples were reduced with pure H_2-flow at 0.5 MPa and 5 l/min H_2 flow. For reduction, temperature was increased in 10 °C increments every 10 minutes until 300 °C was reached. The temperature was then set to the desired reaction temperature and the gas composition and reaction pressure were set using the back pressure controller and the thermostat. Reaction conditions – gas hourly space velocity (GHSV - 8.000 h^{-1} - 12.000 h^{-1}, pressure (2.0 - 5.0 MPa) , temperature (225 °C - 275 °C) and gas composition (stoichiometric number SN = 3.0, carbon-oxide-ratio COR: 0.3 - 1) – were changed at random, with SN and COR calculated as follows:

$$SN = \frac{\dot{n}_{H_2,in} - \dot{n}_{CO_2,in}}{\dot{n}_{CO_2,in} + \dot{n}_{CO,in}} \tag{6.7}$$

$$COR = \frac{\dot{n}_{CO_2,in}}{\dot{n}_{CO_2,in} + \dot{n}_{CO,in}} \tag{6.8}$$

Tests results for $COR = 1$ using only CO_2 are taken from previously reported results [11]. A comprehensive list of all test conditions tested for all catalyst samples is given in supplementary tables B.1 - B.4. For assessment of sample performance, steady state reaction protocols were applied, where reaction conditions were adjusted and a 15 minute timer was set for the reactor system to reach a steady reaction state. Afterwards, 20 minute steady state reaction runs for each parameter combination were carried out. The GC measurements were started at the end of the steady state run, ensuring the measured reactor effluent composition fairly represented a continuous reaction conditions. Selected tests were repeated threefold for each catalyst to ensure recorded results were replicable and represented steady state conditions consistently.

For performance review under the tested conditions, conversion of CO_2 (X_{CO_2}), overall carbon conversion (X_C), MeOH-production rates (STY_{MeOH}) and MeOH selectivity (S_{MeOH}) were calculated.

$$X_{CO_2} = \frac{\dot{n}_{CO_2,in} - \dot{n}_{CO_2,out}}{\dot{n}_{CO_2,in}} \tag{6.9}$$

$$X_C = \frac{\dot{n}_{CO_2,in} + \dot{n}_{CO,in} - \dot{n}_{CO_2,out} - \dot{n}_{CO,out}}{\dot{n}_{CO_2,in} + \dot{n}_{CO,in}} \tag{6.10}$$

$$S_{MeOH} = \frac{\dot{n}_{MeOH,out}}{\sum \dot{n}_{products,out}} \tag{6.11}$$

$$STY_{MeOH} = \frac{\dot{m}_{MeOH}}{m_{Catalyst}} \tag{6.12}$$

$\dot{m}_{MeOH}$ was derived from the GC-measurements under the assumption of conservation of mass and the calculation of overall molar mass of the reactor effluent product. Total mass ($\dot{m}_{tot}$) was calculated from the total mass input, set through the mass flow controllers of the test plant. The product mass flow was then calculated:

$$\dot{m}_i = y_i \frac{\dot{m}_{tot}}{M_{tot}} M_i \tag{6.13}$$

with

$$M_{tot} = \sum y_i M_i \tag{6.14}$$

where y_i corresponds to the molar fractions for each gas species and M_i corresponds to the specific molar mass for each species respectively. Reaction equilibria were measured for each catalyst sample at three different temperatures (225 °C, 250 °C and 275 °C) and three reaction pressures (2.0 MPa, 3.5 MPa and 5.0 MPa) retaining a set SN of 3.0 for guaranteed surface-coverage with hydrogen and a set industrial GHSV of 10.000 h^{-1}. Measurements were started at COR = 1 and reactor effluent COR was measured using the IR-detectors at the reactor exit. COR was taken from the IR-measurements and set as input gas composition while retaining the COR and GHSV mentioned above. After each adaption of influent gas composition, normalization of effluent measurements or at least 10 minutes are timed as an indicator of steady-state reaction conditions on the catalyst surface. Once steady state has been reached, a new influent gas composition was set. This was repeated until the change in effluent COR was too small for the thermal gas dosing units to be able to reproduce the COR-change (0,05 Nl/min). After the final iteration of the influent gas changes, GC-measurements were started for the steady-state CO- and CO_2-conversion equilibria.

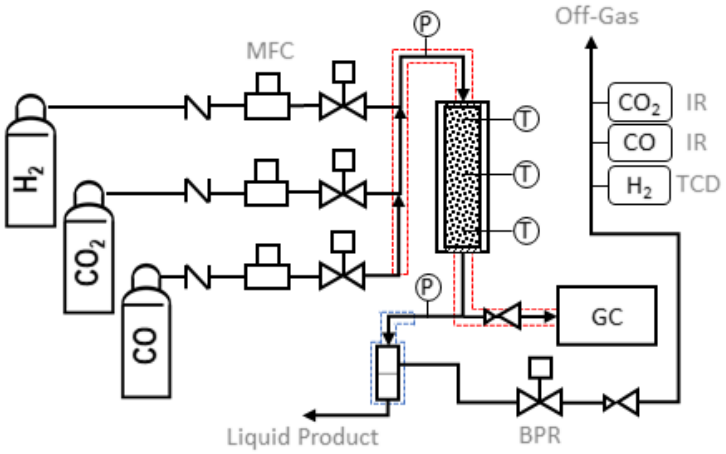

Figure 6.1.: Basic Setup for catalyst activity testing and kinetic performance measurements.

6.2.4. Reaction Kinetics

The rigorous mechanisms and kinetics of MeOH formation in CZA-catalysts are still widely disputed [12, 39, 31, 40]. Additionally, promotion of CZA leads to a change in surface activity, the creation of new, different or adapted active sites for reactant and product adsorption and thus to the change of kinetic parameters in mathematical representation of the reaction mechanisms. This facilitates the generation of new kinetic models for new catalyst formulas or the adaption of existing mechanistic models to fit test data for new catalyst compositions. Several competing kinetic models for the calculation of MeOH reactions exist, that have been widely adapted for the use of changed catalyst formulas and are able to reproduce test results for novel MeOH catalysts well [31, 41, 42, 43]. Meanwhile, most available kinetic models are based upon the Langmuir-Hinshelwood-Hougon-Watson model, which takes into account the availability of active centers in the catalyst and provides a numerical approach to the description of different species competing for the same active centers in the catalyst [44]. Herein, most existing models use single-site (SS), double-site (DS) or three-site (TS) adsorption terms (AT) for the mathematical representation of the underlying reaction mechanisms.

Here H_2, CO_2 and CO all compete for the same active sites in SS-AT, H_2 and CO/CO_2 are assigned to different sites in DS-AT and H_2, CO_2 and CO all adsorb on different neighboring acting points in TS-AT. More in-depth reviews of existing models for the calculation of MeOH-synthesis processes, the synthesis of new models for novel catalyst test data and their applications have been reported elsewhere in great detail [31, 42, 44, 45, 46]. From existing models, the DS-AT model proposed by Graaf et al. (1988) [47] has shown to reproduce CZA-test data very well. Thus, it has been applied in diverse research work concerning both the modeling of MeOH-synthesis processes and the refit of the model to different kinetic data from enhanced CZA investigations but also to adapted catalyst formulas [16]. Several studies have found that parameter refitting for the Graaf-model yields mathematically superior results compared to refits carried out for other models, even in application with CeO_2 and ZrO_2 promoted CZA based catalysts [31, 41]. Compared to many other models, the Graaf-model utilizes kinetic equations ((6.15) - (6.17)/(6.28) - (6.30)) for both CO_2 and CO hydrogenation to MeOH, making it a fitting candidate for tests conducted in mixed carbon oxide streams and model application towards the conversion of CO and CO_2 to MeOH and byproducts.

$$CO_2 + 3H_2 \rightleftharpoons CH_3OH + H_2O \quad \Delta_r H^O = -49.4 \frac{kJ}{mol} \tag{6.15}$$

$$CO + 2H_2 \rightleftharpoons CH_3OH \quad \Delta_r H^O = -90.5 \frac{kJ}{mol} \tag{6.16}$$

$$CO_2 + H_2 \rightleftharpoons CO + H_2O \quad \Delta_r H^O = 41.1 \frac{kJ}{mol} \tag{6.17}$$

Based upon the cited studies, the Graaf-model is herein applied for adapting and refitting optimized reaction kinetics for all four presented catalyst samples. For a deepened understanding of the mechanisms contributing to CO_2 conversion to CO and MeOH and the interplay between CO and CO_2 in the formation of both MeOH and H_2O in the multi-metal-oxide catalyst formulas, a kinetic parameter-set was fitted to the existing model using a custom python script, optimizing the model parameters the parameters inside a pseudohomogeneous plug-flow-reactor (PFR) model to the test result data.

Mass Transfer Limitations

In heterogeneous catalysis at high temperatures and high reaction rates, mass transfer limitations can occur that influence the outcome of kinetic tests. Kinetic tests can lead to inaccurate results if not corrected for possible mass transfer limitations [16].
Thus, external and internal limitations of mass transfer and diffusion have to be taken into account in optimizing reaction kinetics [42]. The Weisz-parameter is a good measure to approximate the effect of diffusion limitation in catalyzed reaction setups [48]. It is defined as follows:

$$\Phi_{\mathrm{WP}} = \frac{r_{\mathrm{obs}} \cdot R_p^2}{D_{\mathrm{eff}} \cdot C_{\mathrm{surface}}} \tag{6.18}$$

with r_{obs} being the observed or measured reaction rate of a single species involved in the reaction. The effective diffusivity of a single species under certain reaction conditions D_{eff} is defined as

$$D_{\mathrm{eff}} = \frac{\varepsilon}{\tau} \cdot \frac{D_{AB} \cdot D_K}{D_{AB} + D_K} \tag{6.19}$$

with the binary diffusivity D_{AB} being defined as

$$D_{AB} = \frac{1.00 \times 10^{-3} \cdot T^{1.75} \cdot \sqrt{\frac{1}{M_A} + \frac{1}{M_B}}}{P \cdot [(\Sigma v_A)^{1/3} + (\Sigma v_B)^{1/3}]^2} \tag{6.20}$$

and the Knudsen diffusivity D_{KN} being defined as

$$D_K = \frac{2}{3} \cdot r_{\mathrm{pore}} \cdot \sqrt{\frac{8RT}{\pi M}} \tag{6.21}$$

In this instance, r_{pore} represents the measured average pore volume of the applied catalyst, τ represents the tortuosity of a catalyst, ε refers to the void fraction of a catalyst type, and $C_{surface}$ refers to the effective concentration of the investigated reaction species in the reactor. For calculation of Φ_{WP} textural properties of the catalyst and additional properties of the alumina-carriers like τ where taken from previous studies [11, 49]. In many instances, internal mass transfer limitations are neglected in kinetic modeling, if Φ_{WP} assumes values below 0.1 for most test conditions [46].
For testing the reaction setup towards external mass transfer limitation, the Mears criterion is often applied. The dimensionless Mears criterion number is herein defined as:

$$\mathrm{Mears} = \frac{r_{\mathrm{obs}} \cdot d_p \cdot \rho_b}{k_c \cdot C_{\mathrm{surface}}} \tag{6.22}$$

Here, the species concentration on the catalyst surface is calculated from the ideal gas law:

$$C_{\mathrm{surface}} = \frac{P_i}{RT} \tag{6.23}$$

The mass transfer coefficient k_c is furthermore defined as:

$$k_c = \frac{\mathrm{Sh} \cdot D_{AB}}{d_p} \tag{6.24}$$

The Sherwood number Sh is calculated from

$$\mathrm{Sh} = 2 + 0.6 \cdot \mathrm{Re}^{0.5} \cdot \mathrm{Sc}^{0.33} \tag{6.25}$$

with the Reynolds number Re and the Schmidt number being defined as

$$\mathrm{Re} = \frac{\rho_g \cdot u_s \cdot d_p}{\mu_g} \tag{6.26}$$

$$\mathrm{Sc} = \frac{\mu_g}{\rho_g \cdot D_{AB}} \tag{6.27}$$

In kinetic modeling, external mass transfer limitations and their influence on the kinetic reactor model are often times neglected if the Mears criterion does not assume values above 0.15 for most of the reaction conditions. In these cases, the reaction is kinetically controlled and intrinsic reaction rates are slow enough for diffusion and mass transfer between solid and gas phases in the reactor not to limit the rates [42, 46]. In this work we tested the reaction conditions for both the Weisz- and the Mears-criterion, looking at internal and external mass transfer and diffusion limitations. CO_2, H_2, MeOH and H_2O were tested for limitations for all catalyst samples in all applied reaction conditions.

Kinetic Model Deduction

The Graaf-model is based around a two-site adsorption mechanism, where CO and CO_2 compete for one type of active site in the catalyst compound and H_2 and H_2O adsorb on a second. In the kinetic model, rate equations are used for CO- and CO_2 hydrogenation towards MeOH generation and a third for RWGS. The rate equations use adsorption and kinetic constants, to which the kinetic parameters of the model are fitted based on the tests conducted in the laboratory reactor setup. Graaf et al. (1988) based their set of reactions on three macroscopic reactions occurring simultaneously, each made up of several different elementary reaction steps, from which they derived their kinetic expressions. The reaction complex for each of the three reactions included in the mechanisms is given in table 6.2 [46, 47].

The original model suggests four possible steps for CO hydrogenation, two steps in CO_2-reduction to CO and H_2O through RWGS and six possible steps for the hydrogenation of CO_2 to MeOH and H_2O [47]. The latter corresponds to the formate pathway of CO_2 hydrogenation to MeOH, which is accepted to account for most of the CO_2 being converted in $CuO/ZnO/Al_2O_3$ catalysts, especially in high COR environments [44, 50]. Additionally, initial hydrogenation steps for both CO and CO_2 in MeOH synthesis as well as adsorption and desorption processes on the catalyst surface do not seem to influence kinetic rates much [51]. Therefore, adsorption, initial hydrogenation of adsorbed carbon oxide species and desorption of prodcuts are emitted as possible reaction steps in the later optimization of parameters, thus also reducing calculation time and streamlining the multi-stage fitting procedure. Thus, this study concentrates on fitting an optimal model based upon the reaction steps A2-A4, B1-B2 and C2-C5. For CO_2 hydrogenation, this represents the Formate-reaction pathway, although multiple steps of the formulated mathematical model can account for other reaction steps in carbon-oxide hydrogenation to MeOH. One of the major limitations in the model proposed by Graaf et al. therefore lies in the composition of the driving force terms, as they can mathematically represent different reaction intermediates, also containing some found in alternative reaction pathways [52].

Table 6.2.: Mechanism on the catalyst surface with kinetic model driving forces

Step	Reaction	Driving Force
Adsorption		
1	$CO + s1 \rightleftharpoons CO^{(s1)}$	-
2	$CO_2 + s1 \rightleftharpoons CO_2^{(s1)}$	-
3	$H_2 + 2s2 \rightleftharpoons 2H^{(s2)}$	-
4	$H_2O + s2 \rightleftharpoons H_2O^{(s2)}$	-
CO-hydrogenation pathway		
A1	$CO^{(s1)} + H^{(s2)} \rightleftharpoons HCO^{(s1)} + s2$	$p_{CO} \cdot p_{H_2} - \frac{p_{CH_3OH}}{p_{H_2}^2 \cdot K_{eq,3}}$
A2	$HCO^{(s1)} + H^{(s2)} \rightleftharpoons H_2CO^{(s1)} + s2$	$p_{CO} \cdot p_{H_2}^2 - \frac{p_{CH_3OH}}{p_{H_2} \cdot K_{eq,3}}$
A3	$H_2CO^{(s1)} + H^{(s2)} \rightleftharpoons H_3CO^{(s1)} + s2$	$p_{CO} \cdot p_{H_2}^3 - \frac{p_{CH_3OH}}{K_{eq,3}}$
A4	$H_3CO^{(s1)} + H^{(s2)} \rightleftharpoons H_3COH + s1 + s2$	$p_{CO} \cdot p_{H_2}^4 - \frac{p_{CH_3OH} \cdot p_{H_2}}{K_{eq,3}}$
Reverse water-gas shift (rWGS) pathway		
B1	$CO_2^{(s1)} + H^{(s2)} \rightleftharpoons HCOO^{(s1)} + s2$	$p_{CO_2} \cdot p_{H_2} - \frac{p_{H_2O} \cdot p_{CO}}{p_{H_2} \cdot K_{eq,2}}$
B2	$HCOO^{(s1)} + H^{(s2)} \rightleftharpoons CO^{(s1)} + H_2O^{(s2)}$	$p_{CO_2} \cdot p_{H_2}^2 - \frac{p_{H_2O} \cdot p_{CO}}{K_{eq,2}}$
CO_2-hydrogenation pathway		
C1	$CO_2^{(s1)} + H^{(s2)} \rightleftharpoons HCOO^{(s1)} + s2$	$p_{CO_2} \cdot p_{H_2} - \frac{p_{CH_3OH} \cdot p_{H_2O}}{p_{H_2}^3 \cdot K_{eq,1}}$
C2	$HCOO^{(s1)} + H^{(s2)} \rightleftharpoons H_2COO^{(s1)} + s2$	$p_{CO_2} \cdot p_{H_2}^2 - \frac{p_{CH_3OH} \cdot p_{H_2O}}{p_{H_2}^2 \cdot K_{eq,1}}$
C3	$H_2COO^{(s1)} + H^{(s2)} \rightleftharpoons H_3COO^{(s1)} + s2$	$p_{CO_2} \cdot p_{H_2}^3 - \frac{p_{CH_3OH} \cdot p_{H_2O}}{p_{H_2} \cdot K_{eq,1}}$
C4	$H_3COO^{(s1)} + H^{(s2)} \rightleftharpoons H_3CO^{(s1)} + H_2O^{(s2)}$	$p_{CO_2} \cdot p_{H_2}^4 - \frac{p_{CH_3OH} \cdot p_{H_2O}}{K_{eq,1}}$
C5	$H_3CO^{(s1)} + H^{(s2)} \rightleftharpoons H_4CO^{(s1)} + s2$	$p_{CO_2} \cdot p_{H_2}^5 - \frac{p_{CH_3OH} \cdot p_{H_2O} \cdot p_{H_2}}{K_{eq,1}}$
C6	$H_4CO^{(s1)} + H^{(s2)} \rightleftharpoons H_3COH + s1 + s2$	$p_{CO_2} \cdot p_{H_2}^6 - \frac{p_{CH_3OH} \cdot p_{H_2O} \cdot p_{H_2}^2}{K_{eq,1}}$

Overall, model deduction from the proposed reaction steps yields a possible 24 different rate equation combinations, that are differentiable by their driving force (DF) groups, with equilibrium constants taken from the recent update by Graaf et al. (2016) [53]. This constitutes a second limitation of the proposed model, as reaction equilibrium constants are assumed to be equal to those of pure precipitated CZA-catalyts. The entire model can be constructed in principle as follows:

$$r_{CO} = k_{CO} \cdot K_{CO} \cdot \frac{DF_{CO,A_i}}{Denominator} \tag{6.28}$$

$$r_{RWGS} = k_{CO_2} \cdot K_{CO_2} \cdot \frac{DF_{RWGS,B_i}}{Denominator} \tag{6.29}$$

$$r_{RWGS} = k_{CO_2} \cdot K_{CO_2} \cdot \frac{DF_{CO_2,C_i}}{Denominator} \tag{6.30}$$

with the denominator compounded from two terms – one each for each represented active site in kinetic modeling:

$$Demoninator = (1 + K_{CO}\, p_{CO} + K_{CO_2}\, p_{CO_2})(p_{H_2}^{0,5} + \frac{K_{H_2O}}{K_{H_2}^{0,5}}\, p_{H_2O}) \tag{6.31}$$

Inside the kinetic model, the adsorption constants are described though the Van't Hoff approach:

$$K_{ads,i} = e^{\frac{\Delta S_{i,ads}}{R}} e^{\frac{\Delta H_{i,ads}}{RT}} \tag{6.32}$$

The exponential relation between standard adsorption entropy and reaction temperature is herein fixed to a single parameter, leading to the following expression for the kinetic adsorption terms for the kinetic model in this work containing a single pre-exponential factor and the calculated adsorption enthalpy:

$$K_{ads,i} = a_i e^{\frac{\Delta H_{i,ads}}{RT}} \tag{6.33}$$

Kinetic constants are expressed through the Arrhenius approach, leading to following representation as kinetic isotherms containing the activation energy of each reaction step and a pre-exponential factor as fitting parameters:

$$k_i = b_i e^{\frac{Ea_i}{RT}} \tag{6.34}$$

The kinetic model can then be written as a compound of three rate equations, with its dependency on species concentration in the reactor represented by species partial pressures. Exponential weighting of the H_2 partial pressure additionally depends on the chosen reaction step, which correlates directly to the pending $H*$-species involved in the outstanding reaction steps towards product formation. In their original work from 1988, Graaf et al. found the following rate equations to represent the reaction complex in the CZA-catalyst most accurately, corresponding to H_2CO* hydrogenation as RDS in MeOH formation from CO, $HCOO*$ hydrogenation as RDS in RWGS and H_2COO* hydrogenation in MeOH formation from CO_2. AS low pressures and low temperatures are applied in this work, partial pressures are applied instead of fugacities, as applied in the original model formulation, thus avoiding calculation of computationally complex thermodynamic models in model discrimination and parameters optimization [47].

$$r_{MeOH,CO} = k_1 K_{CO} \left(p_{CO}\, p_{H_2}^{1,5} - \frac{p_{MeOH}}{p_{H_2}^{0,5} K_{eq,1}} \right) D^{-1} \tag{6.35}$$

$$r_{RWGS} = k_2 K_{CO_2} \left(p_{CO_2}\, p_{H_2} - \frac{p_{H_2O}\, p_{CO}}{K_{eq,2}} \right) D^{-1} \tag{6.36}$$

$$r_{MeOH,CO_2} = k_3 K_{CO_2} \left(p_{CO_2}\, p_{H_2}^{1,5} - \frac{p_{H_2O}\, p_{MeOH}}{p_{H_2}^{1,5} K_{eq,3}} \right) D^{-1} \tag{6.37}$$

The denominator for each of the rate equations is identical, as both active center interactions described by the denominator, are involved in all three reactions. It can be expressed as follows, where the adsorption constants for H_2 and H_2O are compounded into one value fitted through a single Arrhenius isotherm.

$$D = (1 + K_{CO}\, p_{CO} + K_{CO_2}\, p_{CO_2})(p_{H_2}^{0,5} + \frac{K_{H_2O}}{K_{H_2}^{0,5}}\, p_{H_2O}) \tag{6.38}$$

The exact composition of the driving force group is deducted from the scheme of elementary reaction steps given in table 6.2.

Reactor Modeling

The 1D PFR-model is implemented as follows:

Mass balance

$$-u_s \frac{dc_i}{dz} + \rho_{cb} \sum_{n=1}^{n_r} r_{ij} = 0 \tag{6.39}$$

Energy balance

$$-u_s c_p \frac{d\rho_g T}{dz} = \rho_g \sum_{n=1}^{n_r} (-\Delta H_i)_j r_j + \frac{4U}{D_t}(T_w - T) \tag{6.40}$$

Here, u_s represents the superficial gas velocity, c_i represents the concentration of species i along the 1D z-axis of the reactor, ρ_c represents the bulk catalyst density and r_{ij} represents the reaction rates of the three competing reaction which the parameters are fitted to during the optimization. Furthermore, u_s is updated along the z-axis of the reactor according to the gas density change through consumption of reactants and production of MeOH, H_2O and CO. ρ_g, D_t, T and T_w represent the apparent density of the gas along the z-axis of the reactor model, the diameter of the reactor tube and local reactor temperature and reactor wall temperature for the heat loss term. As the temperature is kept at quasi isothermal conditions, the loss term can be omitted for the energy balance. Reaction enthalpies $-\Delta H_{ij}$ are considered to be constant and are taken from [45]. For calculating the reaction rates based upon the reactor model and optimizing the kinetic parameters towards a good numerical fit to the test data, the differential equations for the z-axis resolved energy and mass balances inside the reactor are solved using pythons `solve_ivp` function and its BDF-solver.

Parameter Optimization

A custom python script, which is described in more detail in the supplementary materials (Appendix B), is used to fit the kinetic parameters of the Graaf-model to the herein recorded test data based upon the reactor model adapted to represent the tubular reactor used in this study. A base objective function for minimizing the root mean squared error (RMSE) of calculated reactor effluent partial pressures of the product species MeOH and H_2O is used for optimizing the 13 fitting variables from the original Graaf-model.

$$\begin{aligned} F_{obj} = \sum [& q_{MeOH} \left(\frac{p_{MeOH,\,calc} - p_{MeOH,\,exp}}{p_{MeOH,\,exp}}\right)^2 - \\ & q_{H_2O} \left(\frac{p_{H_2O,\,calc} - p_{H_2O,\,exp}}{p_{H_2O,\,exp}}\right)^2] \end{aligned} \tag{6.41}$$

Here q_{MeOH} and q_{H_2O} are weighting factors for weighting $MeOH$- and H_2O-reactor exit partial pressures inside the objective function. Alternative approaches for construction of the objective function, where the model was optimized towards different combinations of effluent species partial pressures or holistic approaches utilizing the entire composition of the reactor effluent in the minimization function were also tested. After evaluation of base-line model performance for different variations of the objective function through WPI (refer to supplementary materials - statistical analysis), the approach minimizing only residuals for the two product H_2O and MeOH was chosen, due to its superior performance in estimating product partial pressures. As most models yielded the least optimal results in calculating H_2O-partial pressures in the reactor effluent, weighting factors were introduced for better control of the

optimization results towards optimizing R^2 for H_2O estimation. q_{MeOH} was usually set to 1 while q_{H_2O} was commonly set to 3, as H_2O-production rates from RWGS and CO_2 hydrogenation played an essential role in the quality of the model fit and yielded the highest amount of uncertainty in model deduction. While adapting the Graaf-model towards the herein presented test data, it was discovered, that the original model did not accommodate well for the calculation of tubular reactors in all reaction conditions, with conversion rates often assuming unlikely values at reactor entry and reaching reaction and concentration equilibria very quickly or oscillating strongly due to the very abrupt changes in local concentration differentials along the z-axis of the reactor. As very abrupt reactor concentration differentials are unlikely in a real-world application, the herein tested objective function was expanded to include penalties (P) for oscillating concentration profiles and very abrupt changes in reactant concentration along the z-profile [16]:

$$P = \begin{cases} \sum_{i \in \{\mathrm{MeOH,H_2O}\}} 0.1 \times F_{osc,\,i} & \text{if } F_{osc,\,i} > 1 \\ 0 & \text{otherwise} \end{cases} \tag{6.42}$$

with the oscillation-function being defined as

$$F_{osc,\,i} = \sum_{z=0}^{Z} H(|\mathrm{sgn}(\frac{dC_i}{dz}(z+1)) - \mathrm{sgn}(\frac{dC_i}{dz}(z))|) \tag{6.43}$$

and with the Heaviside-step function (H) for detection of concentration-profiles oscillations defined as

$$H(x) = \begin{cases} 1 & \text{if } x > 0 \\ 0 & \text{if } x \leq 0 \end{cases} \tag{6.44}$$

For optimization of the reaction parameters, a multi-strategy, parallel programming optimization script was implemented. As all three reactions - CO_2 hydrogenation, CO hydrogenation and RWGS - are based upon a selection of possible rate-determining steps (RDS) inside the proposed reaction mechanisms for the three considered reactions, a total of multiple combinations of these rate determining steps is possible for the overall reaction set. Thus, a parallel approach to optimization is applied, where all possible combinations of RDS for the three reactions involved in the complex can be solved simultaneously. The full overview over the reaction steps considered in this work is given in table 6.2. The script used for optimization is published in a repository alongside this work [54].

End results of optimization problems can rely heavily on the initial guess [31, 42]. To ensure optimization results were independent of the initial guess required by pythons fmin-function, multiple initial optimization runs with limited optimization iterations were carried out for every possible rate model. Each initial strategy was defined by the use of a different set of initial guess parameters. The initial guesses used were the original parameters reported by Graaf et al. (1988) and Poto et al. (2022) [31, 47]. Additionally, a third strategy was run with the initial guess randomized inside feasible parameter bounds. After completion of the preliminary strategies, the resulting parameters were compared and the initial guess yielding the best short-term optimization results was chosen for full optimization of the parameters.

Minimization of the objective function and penalties was carried out in a two-stage process, where the objective- and penalty function was minimized using the downhill-simplex-algorithm from pythons fmin-

library. After initial optimization of a parameter set, the optimized kinetic parameter where handed over to a second optimization run using a limited memory Broyden–Fletcher–Goldfarb–Shannon (L-BFSG-S) algorithm for parameter refinement. Both the downhill-simplex-algorithm, as well as the L-BSFG-S algorithm are constrained optimization procedures. Optimizer constraints were applied for both the rough as well as the detailed optimization run with an optimization timeout set to 15.000 iterations inside each optimized rank. The constraints were chosen liberally, with upper limits for $\Delta H_{i,ads}$ and lower limits for $\Delta H_{i,ads}$ that inhibit the calculation of physically unfeasible models. A table containing the list of constraints is given in supplementary table B.6. The statistical analysis of the optimization results is described in detail in the Supplementary Materials. The confidence intervals of the estimated kinetic parameters were determined a-posteriori from the finite-difference approximation of the Hessian matrix of the objective function. A full description of the calculation for 95% confidence intervals is given in the supplementary materials (appendix B).

Model Sensitivity

To quantify the individual and interactive effects of kinetic parameters on reactor performance across different CO_2/CO ratios (COR), we employed Sobol-global sensitivity analysis using Python's SALib sensitivity analysis package. The Sobol approach herein decomposes the total variance of model outputs into contributions from individual model parameters and their respective interactions with each other using a variance based (ANOVA) approach and applying Monte Carlo principles for generation of a numerical model space for analysis of the parameter contributions [55]. In our sensitivity analysis, the first-order sensitivity index, S_i, represents the main effect of variable model parameter X_i on a chosen model output value. It represents the probabilistic fraction of model output that can be attributed directly to the variation of the input parameter in question [56]:

$$S_i = \frac{V_{X_i}[E_{X_{\sim i}}(Y|X_i)]}{V(Y)} \tag{6.45}$$

where V_{X_i} denotes the variance of an output value over parameter X_i, $E_{X_{\sim i}}$ is the expected value over all parameters except X_i derived from the construction of the Monte Carlo sample space of the kinetic model, and $V(Y)$ is the total variance of the model output value Y.
The total order sensitivity index, S_{T_i}, captures both main- or first-order effects and all interactive effects of higher order that involve the parameter X_i. Thus, it represents a summary the direct effect of parameter variation X_i has on model output variance and interactive effects including X_i have on the model variance:

$$S_{T_i} = \frac{E_{X_{\sim i}}[V_{X_i}(Y|X_{\sim i})]}{V(Y)} = 1 - \frac{V_{X_{\sim i}}[E_{X_i}(Y|X_{\sim i})]}{V(Y)} \tag{6.46}$$

The interaction effect is quantified as $S_{int_i} = S_{T_i} - S_i$, representing the additional variance contribution from the interaction of the parameters. To assess parameter importance across multiple model outputs and operating conditions as well as all fitting parameters, we computed summary statistics for each of the parameters first:

- the average main effect, $\overline{S_i} = \frac{1}{n_{outputs}} \sum_{j=1}^{n_{outputs}} S_{i,j}$
- the maximum main effect across all outputs, $S_{i,max} = \max_j(S_{i,j})$
- the minimum main effect, $S_{i,min} = \min_j(S_{i,j})$

Values of $S_i > 0.01$ indicate parameters with significant individual influence, while large differences between S_{T_i} and S_i suggest strong parameter coupling effects [56]. Parameters exhibiting high $S_{i,max}$ values are critical for at least one model output, whereas those with consistently high $\overline{S_i}$ values are important across all reactor performance metrics.
This analysis enables identification of critical kinetic parameters whose accurate determination are essential for reliable reactor predictions, particularly when SynGas-composition varies across different COR operating conditions in MeOH synthesis. These indices allow the identification of the most influential kinetic parameters affecting MeOH and H_2O formation, and side reactions in the reactor [57].
For further evaluation of model sensitivity towards the applied kinetic fitting parameters in the Graaf-base model, parameters are then ranked by their average impact on model results and the identified cross-sensitivities. Larger values herein represent large individual and compounded effects of selected model parameters towards selected kinetic model output variables. For detailed evaluation of the overall model sensitivity towards selected kinetic parameters, MeOH production, CO_2 conversion, H_2O production and overall MeOH selectivity were chosen as model output variables.

6.3. Results

6.3.1. Material characterization

Physical surface characterization by Raman, XPS and HAADF-STEM

Results from TEM-analysis are given in figure 6.2, Raman- and XPS-analysis are given in figure 6.3. Cross sections of 2 μm deep FIB-lamellae if the produced catalyst spheres can be seen in the top row of figures with magnified images and metal concentration profiles added in the mid row of figures. As is expected the highly promoted catalyst samples show a less uniform distribution of metal mesh alignment. All strongly magnified images (5 nm) show clear agglomerates of metal oxides over the Al_2O_3-carrier in separated groups, which is clearly marked by the alteration of metal grid orientation in these agglomerates. This is most clearly shown in 20% CZCZC, where the highest level of catalyst promotion leads to the formation of widely dispersed metal oxide accumulations. The accumulations do not span more than a few nm in diameter. This leads to the formation of plentiful multiple metal oxide interfaces, which have been shown to act as active centers for the adsorption of CO_2 and CO in MeOH synthesis and thus enhance activation of both carbon oxides for further hydrogenation, especially in CeO_2/ZrO_2-promotion and in CZA-catalysts [58, 59].
Based upon the HAADF STEM-images, integrated STEM-EDXS line profiles were plotted for analysis of the penetration of the catalytically active metal oxide species into the alumina-carrier. The profiles are given in figure 6.2 d1)-d4). Additionally, images of Cu und Zn penetration are given in figure 6.2 b1)-b4). As alumina is used as carrier, all profiles show a quite even profiles for alumina. Concerning Cu and Zn, which were used as a binary active catalyst complex in all four samples, a slight decline in signal intensity can be observed in the first 200-300 nm of the catalyst surface, with 20% CZCZ and 20% CZCZC showing the strongest agglomeration of Cu on the outer carrier surface with signal intensity and thus the elemental concentration of Cu decreasing the strongest in comparison to 20% CZ and 20% CZC. In 20% CZC a Ce deposit is clearly visible in both the 200 nm magnification spectrum-image and the concentration profile, with Ce-concentration high at the outer surface of the carrier sphere and decreasing to near zero towards the bottom of the line profile. At the same time, Cu and Zn concentration do not change much over the evaluated line,

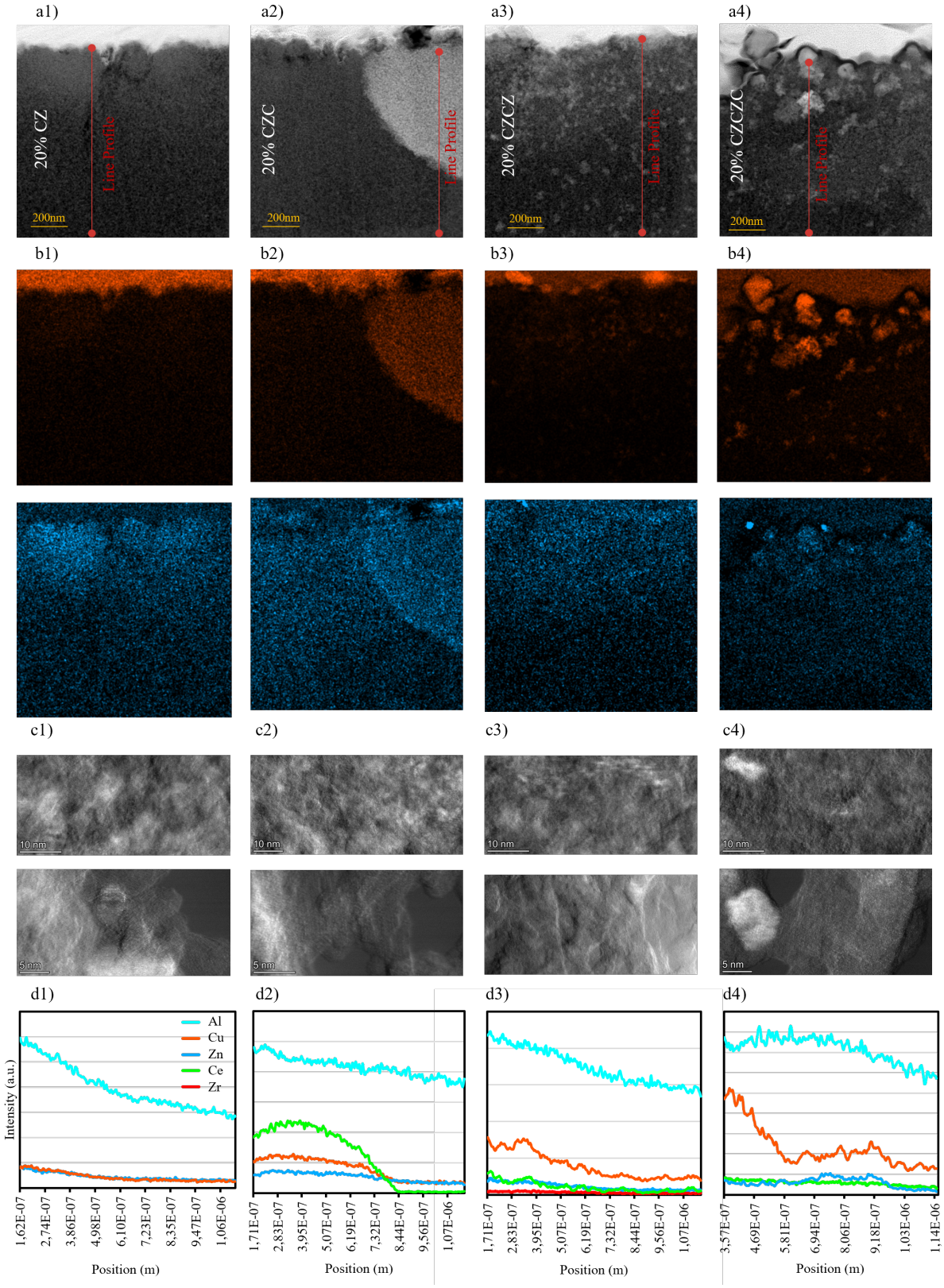

Figure 6.2.: Detail HAADF-STEM-images of the FIB-Lamellae cross sections for all four herein presented infiltration composite catalysts. a1-a4) HAADF-STEM-images of the catalyst cross sections at 200 nm b1-b4) STEM-EDX-spectrum mappings for Cu ad Zn c1-c4) 10 nm and 5 nm magnification of the lamellae cross sections d1-d4) Integrated STEM-EDXS line profiles for the detected elements over the 2 µm FIB lamellae radial cross sections.

indication good infiltration of the active catalyst components into the porous carrier. This implies somewhat inconsistent infiltration in some parts of the 20% CZC catalyst. In 20% CZCZC Zr could not be detected along the plotted line profile. Additional HAADF STEM-characterization and enhanced EDX-evaluation of the spectrum-images are presented in the supplementary materials. FFT and IFFT is performed for analysis for different metal oxide species forming in the coating process of IWI. An example analysis of different metal oxide phases in 20% CZCZC is given in figure B.11 in the supplementary files (Appendix). The analysis indicates the formation of different metal oxide phases on the carrier, indicating good metal oxide distribution and multi metal oxide interfaces and catalyst carrier boundaries, which have been shown to act as active centers in H_2 and CO_2 adsorption [60, 61].

Figure 6.3 a1)-a3) shows Raman-spectra of the unreduced catalyst surfaces for all samples presented here and the reference sample, as well as reference spectra for all applied metal oxide compounds except CaO [62]

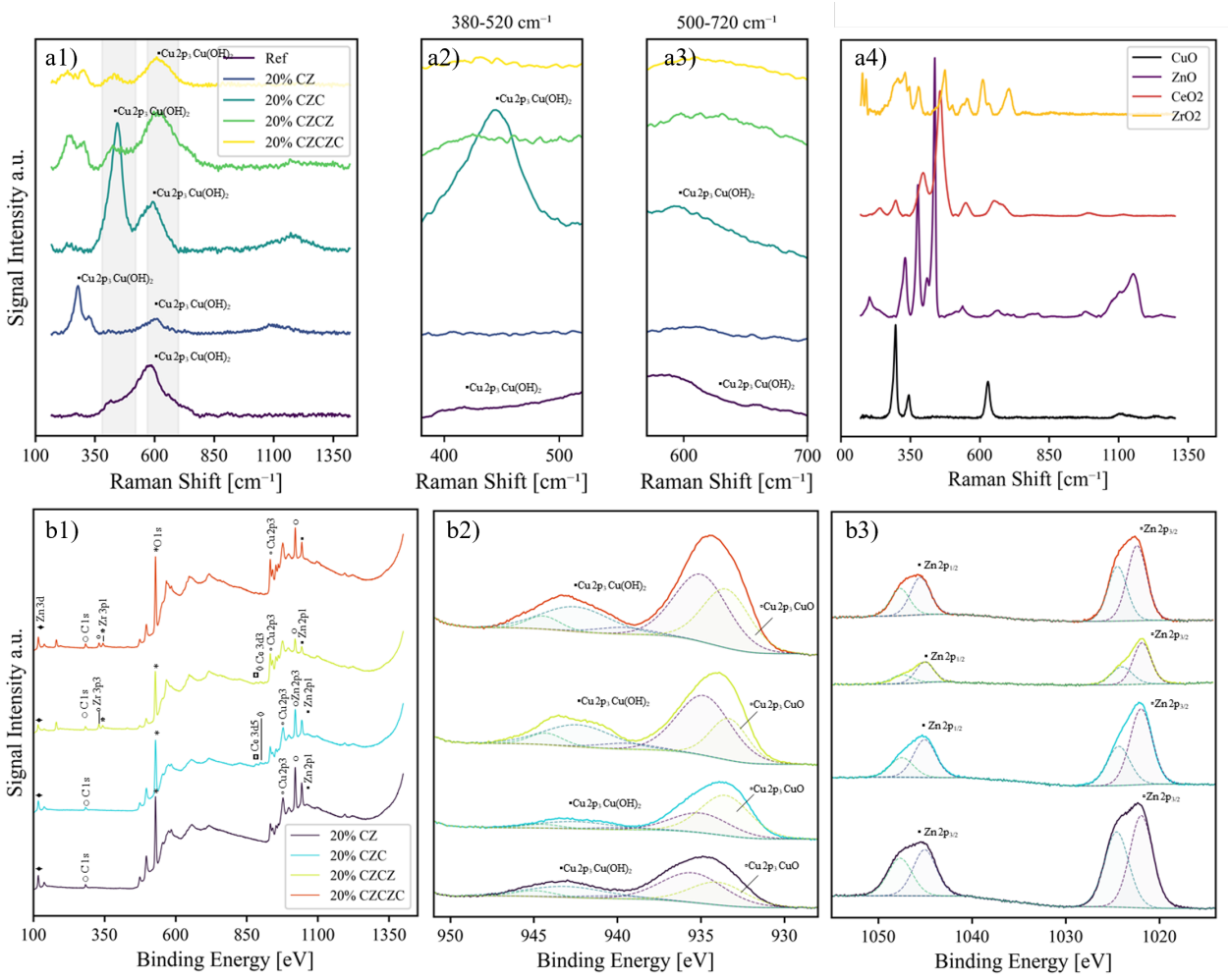

Figure 6.3.: Raman and XPS surface characterization of the catalyst samples: a1)-a3) Raman surveys for 100-1350 cm^{-1} shift (a1) and for 380-520 cm^{-1} (a2) and 500-720 cm^{-1} shift respectively (a3). Reference Raman-spectra for the individual metal oxides used in the infiltration composites (a4). b1)-b3) XPS survey spectrum for all four infiltration composite catalysts (b1). Detailed spectra for 950-930 eV (b2 - CuO) and 1060-1010 eV (b3 - ZnO).

The reference CZA-catalyst shows compounded peaks, which is dominated by Cu2p at around 600 cm^{-1}. All carrier samples show both peaks for $Cu2p_3$ at 300 and 600 cm^{-1} except for 20% CZC, where the spectrum is dominated by large peak at 450 cm^{-1}, which is attributed to ZnO and CeO_2 forming a compounded overlapping

peak, which is significantly less pronounced in all other samples. As is expected, 20% CZCZ and 20% CZCZC show the most diffuse shift patterns, with more metal oxide interacting in spectral measurements. Nonetheless, Cu2p3 is clearly distinguishable in all samples. To further identify the chemical states of metals on the catalyst surfaces and possible effects the promotional steps have on surface CuO and ZnO, we performed XPS analysis for each of the multi metal oxide catalyst samples. XPS spectra of the unreduced sample surfaces are given in figure 6.3 b1)-b3).

The survey spectrum exhibits all expected peaks, with O1s being most pronounced in 20% CZCZC. The O1s peak is located at 530 eV, which indicates that the detected O-species are bound in fully oxidized metal oxide matrices [63]. The C(1s) signals are most likely caused by the absorption of organic carbon contaminants. Detail plots for Cu2p and for Zn2p are additionally observed, to identify the effect additional promotion of the catalyst complexes may have on the chemical state of the highly active ZnO and CuO species on the catalyst surfaces. Cu2p can be fitted to two distinctive gaussian curves for Cu^0 and Cu^{2+}. All catalyst show similar amounts of Cu^0 and Cu^{2+}, with 20% CZC showing higher availability of Cu^0 and 20% CZCZ and 20% CZCZC showing slightly higher contents of Cu^{2+} in comparison. Cu^0 has been shown to act as an active center for dissociative H_2 adsorption in CuO-based catalyst [64]. This in turn indicates slightly higher availability of hydrogen active centers in 20% CZC compared to the other samples.

On the other hand, Cu^{2+} has been shown to be reduced by CO, acting as active center for the adsorption and enhancing conversion efficiency in CO hydrogenation to MeOH [65]. The spectra of Zn2p all show strong spin orbit coupling, with two distinctive peaks exhibiting for Zn-species, both of which are compounded. Pure ZnO usually shows two peaks at 1025 eV and 1048 eV, which is most closely reproduced by 20% CZ and 20% CZCZC [66]. The Zn2p peaks of 20% CZ appearing at 1021 eV are compounded with the peak showing at higher binding energy suggesting that identified Zn is present in its Zn_{2+} valence state and the second peak exhibiting at slightly lower binding energy usually being attributed to Zn_0[67]. Through its promotion with CeO_2, binding energy of Zn^0 shifts downward to around 1020.9 eV. This suggests, that electrons shift to ZnO in metal oxide interaction [68]. This in turn is indicative of more strongly interacted metal oxide activity in 20% CZC and 20% CZCZ, with binding energies in Cu2p also slightly shifted downward. Both Cu2p and Zn2p binding energies shift back upward in 20% CZCZC, which is in line with an enlarged O1s peak, oxygen in metal oxide matrices often acting as electron scavengers in complex metal-metal-oxide interactions [69]. Alternatively, the shift could be explained through other catalyst surface effects such as the formation of defects or fundamental surface restructuring through the addition of further catalyst promoters. The formation of different coordination around Zn and Cu can also be the cause of the observed shift upwards [70].

Adsorption properties for CO_2 and H_2

H_2- and CO_2-desorption measurement results are given in figure 6.4. The adsorption efficiency of CO_2 is, among other factors, dependent on the surface basicity of the catalyst samples [61]. Herein, the carrier-samples all present three compounded desorption peaks, representing weak, medium, and strong basic sites on the surface [71]. The weakest site, with desorption starting at around 100 °C, is associated with the hydroxy group [71]. This seems to be the most relevant basic active site, considering the temperatures usually associated with industrial MeOH synthesis [61, 72].

Additionally, CO_2 adsorbed in weak basic sites has been shown to facilitate the formation of formate species, which represents the most commonly referred to intermediate in the efficient conversion of CO_2 to MeOH [73]. 20% CZ presents the most prominent weak basic site desorption peak. CZA-promotion through

20% CZC and 20% CZCZ reduces peak area under 300°C, indicating that the addition of CeO_2 and ZrO_2 strengthens these sites, with the weak basic sites being nearly entirely inhibited through the addition of ZrO_2 and peak are shifting to more strongly interacted sites at higher desorption temperatures. CaO presents strengthened basic sites for the entire range, confirming the principal assumption that CaO-addition can impact the catalyst surface basicity and therefore improve the catalysts ability to adsorb CO_2, thus optimizing conversion potential. The measurements also confirm previous studies' findings, in that CaO seems to improve high temperature adsorption properties of catalyst, with 20% CZCZC showing high peak ares over 350 °C. The reference catalyst presents a single, large, compounded desorption peak above 300 °C associated with monodentate carbonates coming from oxygen-anions of low-coordination, which are less relevant to CO_2 adsorption under the herein tested reaction conditions [73]. All carrier catalysts present an additional, high-temperature desorption peak. This peak is also shared with the Ceria-promoted CZA-catalyst sample 20% CZC and with the CaO-added sample 20% CZCZC, although the latter two do not present the desorption peak in the same magnitude as the reference.

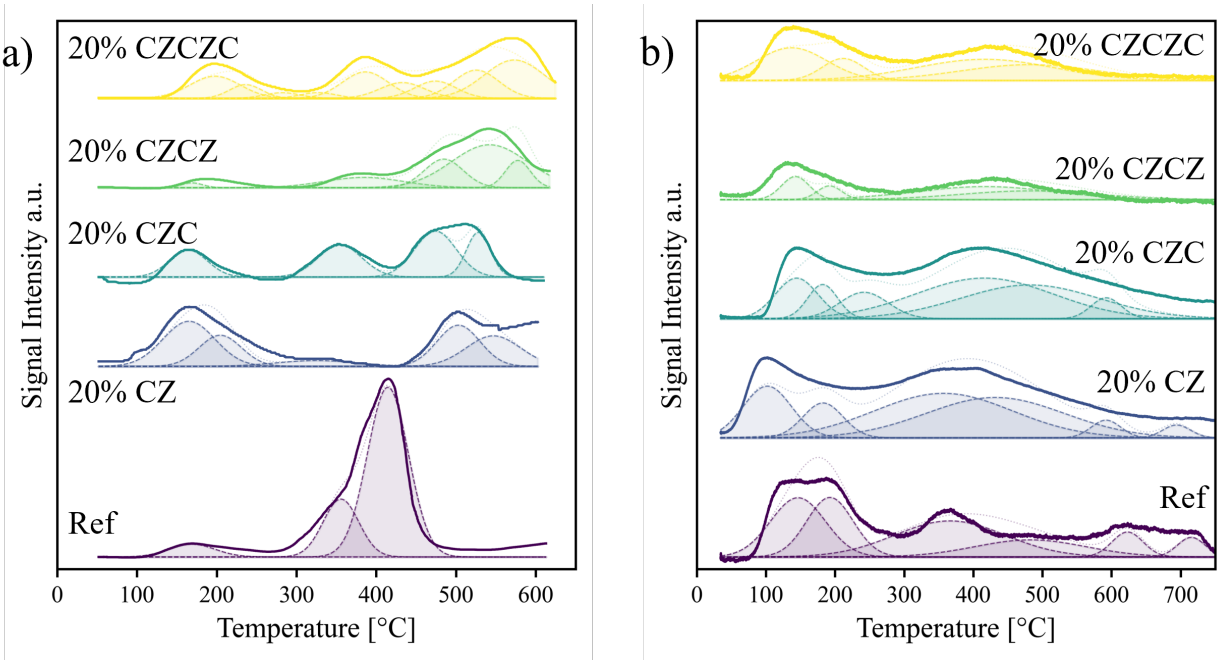

Figure 6.4.: a) CO_2-desorption measurements for the carrier and reference catalysts b) H_2-desorption curves

Results for quantitative analysis of CO_2-desorption properties are given in table 6.3. The reference CZA-catalyst shows the highest total adsorption amount, with catalytically active mass higher around five-fold compared to the prototype samples though. From the promoted catalysts, the ZrO_2-CeO_2-sample shows the highest CO_2-adsorption capacity, consuming 23.6 µmol CO_2 per gram of total active catalyst weight. Maximum desorption peak temperature is highest for 20% CZCZC, indicating that CO_2 can be stably adsorbed on the CaO-promoted sample.

All carrier catalysts exhibit two distinct desorption peaks for hydrogen-desorption with desorption spanning a significant temperature range from about 30 °C to about 720 °C. The first, lower temperature desorption peak starting significantly below 100 °C for all catalyst samples can be associated with the desorption of atomic hydrogen bound to Cu-species in the catalysts [74].

Table 6.3.: CO_2-TPD analysis results for supported copper catalysts. Catalyst masses for 20% CZ - 20% CZCZC are reduced to weight of coating (20% of total catalyst weight)

Sample	Sample Mass (g)	Total CO_2 (μmol)	Total CO_2 (μg)	CO_2 per g catalyst (μmol/g)	CO_2 per g catalyst (μg/g)	Peak T (°C)
REF	0.6600	12.34	542.98	18.69	822.70	415.2
20% CZ	0.1160	1.58	69.50	13.61	599.15	504.5
20% CZC	0.1200	1.68	74.01	14.01	616.77	512.9
20% CZCZ	0.1060	2.36	103.81	22.25	979.30	539.4
20% CZCZC	0.1100	1.45	63.91	13.20	581.02	561.9

This peak decreases through the promotional steps presented for the samples in this work, strongly correlating to the overall Cu-content of the samples. The second desorption peak indicates more strongly interacted H_2. This peak is very broad and strongly compounded for all herein tested samples, indicating wide dispersion and varying interaction of the associated active sites in the catalyst samples [75]. The reference catalyst is the only investigated sample, that shows a less distributed desorption peak, with strong H_2 desorption between 300 and 400 °C and a small compounded desorption peak at very high temperatures starting at 600 °C. The more strongly interacted H_2 can be attributed to several different active centers for H_2 adsorption, which are partially attributed to bulk Cu or to partially reduced ZnO, where dissociative adsorption of H_2 can be assumed [74]. This is in line with the decreasing Cu- and Zn-content in the promoted catalysts, which show reduced desorption peak area compared to the binary 20% CZ carrier catalyst sample. From H_2-TPD measurements, metallic copper surface area was determined for the desorption behavior between 300 and 620 K.

Table 6.4.: H_2-TPD Part 1: H_2-TPD experimental results for the catalyst samples

Sample	Mass (g)	Cu (wt%)	H_2 des. (μmol)	Cu sites/g cat. (μmol/g)	Cu area/g cat. (m^2/g)	BET area [11] (m^2/g)
REF	0.167	45.3	21.3	127.5	5.26	76
20% CZ	0.104	11.5	53.5	514.4	21.22	132
20% CZC	0.114	9.3	61.2	536.8	22.14	122
20% CZCZ	0.174	7.8	24.2	139.1	5.74	129
20% CZCZC	0.128	7.5	29.8	232.8	9.60	125

Table 6.5.: H_2-TPD Part 2: Derived parameters from H_2-TPD analysis

Sample	Reduction (%)	Dispersion (-)	Particle size (nm)
REF	1.8	0.018	57.7
20% CZ	28.4	0.284	3.6
20% CZC	36.7	0.367	2.8
20% CZCZ	11.3	0.113	9.1
20% CZCZC	19.7	0.197	5.2

The results for the determination of reduced, metallic Cu surface area for the herein presented catalyst samples as well as the reference CZA-catalyst are given in table 6.4. Desorbed amounts of H_2 are high in the herein measured desorption graphs, but generally in line with other recent related studies [12, 33]. Metallic Cu surface area after reduction is highest for 20% CZ and 20% CZC, with 20% CZCZ showing an unusual dip in adsorption activity for H_2. The high H_2-adsorption amount in 20% CZ, 20% CZC and 20% CZCZC

demonstrate the benefits of IWI-coated catalyst spheres, enabling high surface-coverage and over all good accessibility of metallic Cu species on the catalyst surface, even surpassing the accessible reduced Cu surface area in the commercial CZA-sample. High metallic Cu surface area in 20% CZC is attributed to CeO_2s ability to enhance Cu-dispersion in metal-oxide surface interaction [76]. Results of the quantitative H_2-desorption analysis are given in tables 6.4 and 6.5. Additionally BET surface area of the samples is used for determination of average particle size and theoretical carrier utilization area [11]. Average particle size is small (3.6 and 2.8 nm) for 20% CZ and 20% CZC with particle sizes assuming much larger values for 20% CZCZ. This does not correlate with the assumption, that high Cu-particle dispersion necessarily leads to enhanced conversion of carbon oxides, as 20% CZCZ performs the highest conversion rations and STY_{MeOH} of the herein introduced catalyst samples [48]. This must be attributed to multi-metal-oxide effects in CO_2-catalysis, which counteract particle sizes but are still abel to enhance conversion in 20% CZCZ significantly [18].

6.3.2. Catalyst Performance in Mixed Carbon-Oxide Synthesis Gas

Carbon-conversion equilibria over the promoted carrier catalyst samples

In industrial catalyst application, SynGas streams will be recycled for most commercial MeOH applications. Even in process applications based upon the direct conversion of CO_2 to MeOH, gas compositions inside the synthesis gas loop will therefore contain a mixture of CO_2, CO and H_2. When applying high recycle ratios in reduced X_C-applications for regenerative MeOH synthesis, the gas composition inside the synthesis loop will gradually develop towards a steady state. Here, the mixed process gas containing fresh SynGas and recycled product gas injected into the reactor will assume a gas composition closer to the conversion equilibrium of CO and CO_2 towards MeOH, H_2O and CO through RWGS respectively. The conversion efficiency in this steady state is therefore a valuable measure for the catalyst performance under industrial conditions. The development of the influent-effluent COR for all carrier catalyst samples is plotted in Figure 6.5. The respective curves end in COR-equilibria, where reactant COR equals effluent COR, indicating conversion equilibrium of both CO_2 and CO. Additionally, performance evaluations for the determined equilibria are given for each tested temperature.

As is expected, higher reactor temperatures generally lead to a higher conversion rate of CO_2 to CO via RWGS. This leads to effluent COR being lower at high temperatures across all tested pressures for the catalyst samples. It is notable, that 20% CZ exhibits the highest RWGS reaction rates of all carrier catalysts, with reaction equilibrium being reached at $93\%_{vol}$ CO_2 at 225 °C, $83\%_{vol}$ at 250 °C and $66\%_{vol}$ at 275 °C reactor temperatures for a set reactor pressure of 20 bar. 20% CZCZ generally exhibits the lowest CO-production rates across the tested temperature and pressure ranges, with $99\%_{vol}$ CO_2 for the reaction equilibrium at 225 °C and 20 bar reaction pressure, barely shifting any of the introduced CO_2 to CO. This is also reflected in the determined performance at reaction equilibrium, with 20% CZCZ showing the highest STY_{MeOH} across the tested temperature and pressure ranges for its respective conversion equilibria, highlighting the effectiveness of ZrO_2 and CeO_2 as promoters in CuO/ZnO MeOH catalysts. This is also inline with comparable studies, that have investigated multiple-component catalysts for the direct conversion of CO_2 to MeOH, with ZrO_2 and CeO_2 being able to significantly improve intermediate stability and facilitate conclusive conversion without premature desorption of CO as reaction intermediate [18, 28, 72]. Comparing the individual reaction equilibria, highest STY_{MeOH} of 0.47 $g_{MeOH}/(g_{Cat}h)$ is reached by 20% CZCZ at 275 °C reactor temperature and 50 bar reaction pressure.

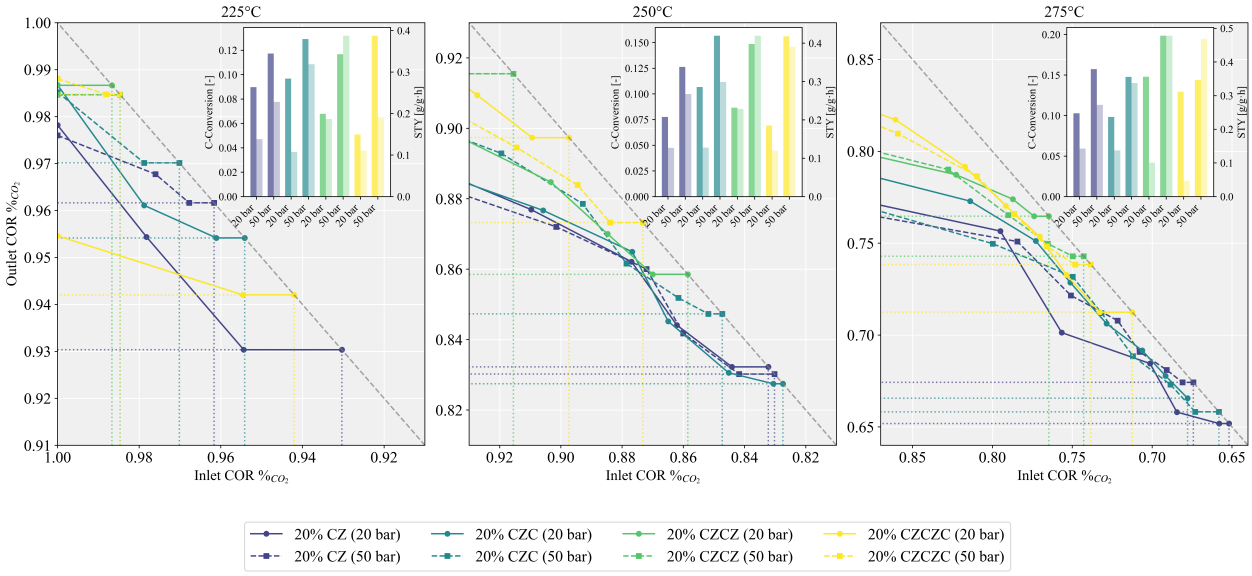

Figure 6.5.: Conversion-equilibria of the presented catalyst samples at 225 °C, 250 °C and 275 °C as well as performance figures for the determined conversion equilibria at 20 bar and 50 bar reactor pressure

Catalyst performance across varied COR

For performance evaluation of the samples and as basis for the parameter optimization of the later presented kinetic reaction model for each of the catalyst samples, a more comprehensive catalyst screening was conducted using different influent COR-compositions for different reaction pressures, temperatures and GSHV. To ensure H_2-coverage of the samples and thus to be able to eliminate insufficient H_2-coverage as a factor in kinetic analysis and performance evaluation, H_2 supply was kept super-stoichiometric ($SN = 3.0$) across all reaction conditions and their individual combinations. The results for catalyst performance at 35 bar reactor pressure in different SynGas COR are given in figure 6.6. As has been reported before for CO_2-only reaction conditions, 20% CZCZC shows the highest X_C across all tested gas compositions [11]. However, 20% CZCZ performs slightly better for single reactor pass STY_{MeOH}. All catalysts show the overall highest X_C either at reaction conditions containing no CO in the reactant feed gas or at the lowest influent gas COR. High X_{CO_2} at high COR can easily be attributed to the partial conversion of CO_2 to CO through RWGS.

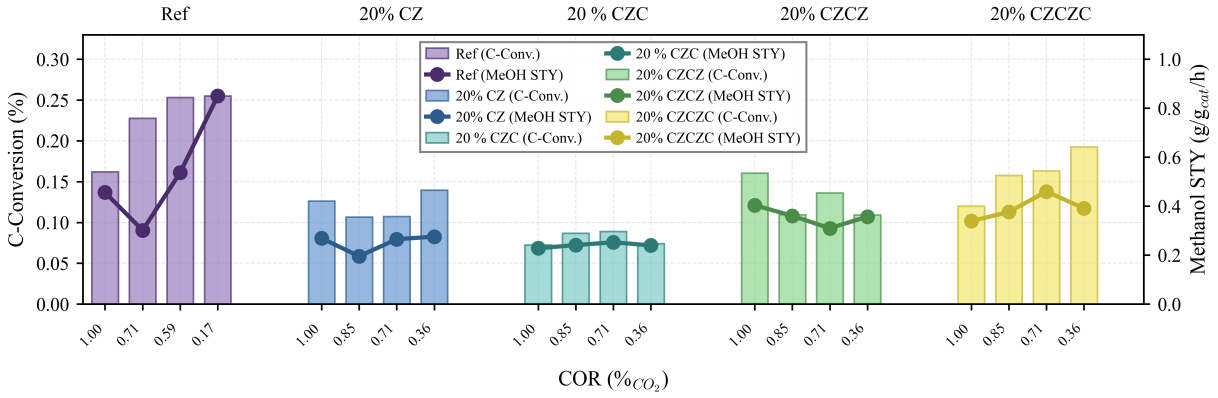

Figure 6.6.: Conversion performance of the Samples under different COR influent compositions (35 bar reactor pressure, 250 °C reactor temperature, 10.000 h^{-1} GHSV).

By implication, high STY_{MeOH} at low COR can be attributed to good direct conversion of CO to MeOH, with the lower CO_2-content in SynGas causing less CO-byproduction and more of the available carbon being converted directly to MeOH. The high selectivity of 20% CZCZ under CO_2-only synthesis conditions with lower conversion and higher STY_{MeOH} cannot be explained at this point, as it contradicts the otherwise uniform correlation between X_C and STY_{MeOH}. Highest overall tested X_C and STY_{MeOH} are reached by the industrial reference catalyst at low COR and high pressure, as is common in industrial applications for conventional, fossil MeOH synthesis.

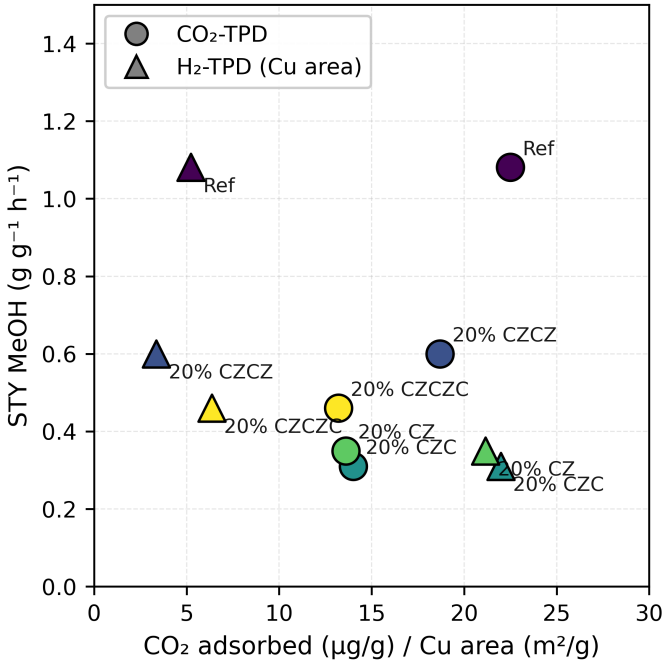

Figure 6.7.: Correlation of metallic Cu surface area and CO_2-adsorption properties to catalyst performance measured at COR = 0.71, p = 50 bar, T = 250 °C and GHSV = 10,000 h^{-1}.

Catalyst performance in mixed carbon oxide synthesis gas conditions (COR = 0.71) is additionally correlated to the results of CO_2-adsorptions properties and metallic Cu surface area derived from H_2-TPD. Results are given in figure 6.7. Astonishingly, Cu-surface area shows inversely proportional correlation to the measured STY_{MeOH} of the catalyst samples. This suggests, that H_2 adsorption does not represent an inhibiting factor in the herein tested samples. Considering these results, testing the catalysts exclusively at stoichiometric or super stoichiometric conditions can be seen as a limitation of the presented work, as over supply with H_2 might have masked shortcomings in active site H_2-coverage for the wash coated catalyst samples. Furthermore, catalyst performance correlates more clearly with CO_2-adsorption efficacy, suggesting that effective coverage of all active sites with CO_2 plays a more prominent role in ensuring neighboring reactant adsorption and subsequent catalyzed formation of MeOH or its intermediates. Nonetheless, the reference precipitated catalyst performs the best, with both the highest specific copper surface area and the highest capacity for CO_2 adsorption.

Overall best performance results of the herein presented catalyst samples as well as a comprehensive comparison to recent, adjacent literature is given in table 6.6. The results indicate that the coated CZA-based samples examined here, exhibit X_C levels that are within the same general range as those reported for Cu-based systems tested under comparable reaction conditions.

Notably, the CZA-reference catalyst achieved 39.1% carbon conversion at 250 °C and 50 bar, which substan-

tially exceeds the performance of most literature catalysts tested under less demanding conditions. Nonetheless, the coated carrier samples perform well in comparison to recent literature. For instance, Cu/Al_2O_3 and Cu/TiO_2 systems reported by Nielsen (12.1% and 10.0% respectively) underperformed the present work by factors of 3.2× and 3.9×, although applying TiO_2, a promising promoter in CO_2 hydrogenation. Direct comparison with promoter-modified systems further illustrates the effectiveness of the CZA-formulation. 20% CZCZC achieved 26.5% conversion under identical conditions to the reference (250 °C, 50 bar), surpassing the ceria-coated Cu/CeO_2 system [5.5%, Zhu et al. (2020)] by 4.8×, and substantially outperforming the Pd/ZrO_2 [Makhmutov et al.(2025)] and Pd/CeO_2ZrO_2 catalysts (6.0% and 7.0%, respectively) despite the latter being tested at similar pressures and temperatures. When compared to other studies applying similar operating conditions, the present four-component CZA-catalyst (26.5%) approaches or matches several literature benchmarks: $CuCeO_2/ZrO_2$ [20.5%, Poto et al. (2022) at 260 °C] and $Cu/ZnO/ZrO_2CeO_2$ [22.8%, Ban et al. (2015) at 230 °C]. This highlights the effectiveness of CeO_2 and ZrO_2 mixtures in MeOH formation from CO_2.

Table 6.6.: Comparison of catalyst performance with selected literature values.

Catalyst	**COR**	**SN**	**T (°C)**	**p (bar)**	**X_C (%)**	**Source**
CZA (ref)	0.71	3.0	250	50	39.1	This work
$CuZnO/Al_2O_3$	0.71	3.0	250	50	17.5	This work
$CuZnOCeO_2/Al_2O_3$	0.71	3.0	250	50	18.9	This work
$CuZnOCeO_2ZrO_2/Al_2O_3$	0.71	3.0	250	50	21.8	This work
$CuZnOCeO_2ZrO_2CaO/Al_2O_3$	0.71	3.0	250	50	26.5	This work
Cu/Al_2O_3	0.83	6.5	225	20	12.1	[10]
Cu/TiO_2	0.83	6.5	225	20	10.0	[10]
Raney Cu	0.83	6.5	225	20	8.1	[10]
Cu/CeO_2	0.75	2.0	250	30	5.5 (calc)	[12]
Pd/ZrO_2	0.80	2.25	200	50	6.0	[15]
Pd/CeO_2ZrO_2	0.80	2.25	200	50	7.0	[15]
$CuCeO_2/ZrO_2$	1.00	2.0	260	30	20.5	[31]
$ZnO–ZrO_2$	0.50	2.0	240	50	7.8	[77]
$CuCeO_2ZrO_2$	1.00	2.0	280	30	10.5	[78]
CuZnO	0.67	2.0	230	40	8.0	[79]
CuZnO-MLa	0.27	2.0	240	30	22.6	[80]
$Cu/ZnO/Al_2O_3$	0.50	2.0	230	30	10.0 (calc)	[81]
Cu/MgO	0.57	2.0	230	30	0.6 (calc)	[81]
Cu/ZnO	1.0	2.0	230	20	5.5	[82]
CuMgO/ZSM	0.13	4.0	210	30	21.4 (calc)	[83]
CZA-MgO	0.16	2.5	240	30	12.0	[84]
CZA-ZrO_2	0.16	2.5	240	30	23.2	[84]
$CuMgOCeO_2$	0.14	1.9	240	50	50.7	[85]
$Cu/Ce_{0.2}Zr_{0.8}O_2$	1.00	2.0	280	30	5.7	[86]
$Cu/ZnO/ZrO_2CeO_2$	1.00	2.0	230	30	22.8	[87]
Cu/$CeZrO_2$-MO	1.00	2.0	240	30	4.7	[88]
$CuZnOZrO_2$	1.00	2.0	240	30	17.4	[89]
$CuCeO_2/TiO_2$	1.00	2.0	260	8	1.8	[90]
$CuCeO_2/SiO_2$	1.00	2.0	260	8	3.8	[90]
CZA-Th	0.25	2.0	225	40	44.5	[91]
CrPd/ZnO	0.25	2.0	325	51	20.0 (calc)	[92]
$CuZnOGa_2O$	1.0	1.8	240	40	27.0	[93]

Several aspects appear relevant to understanding the observed performance trends: the geometry and nature of the carrier (γ-Al_2O_3 washcoated spheres), and the composition and application mode of the promoters (CeO_2, ZrO_2, CaO). Structured γ-Al_2O_3 supports and thin washcoating are often employed in scale-up or structured catalyst configurations. Such arrangements may allow for reduced metal loading per reactor volume while retaining a high external surface area and potentially beneficial transport characteristics, such as lower macropore diffusion resistance and improved heat transfer [49]. Under these circumstances, thinly coated microspheres can exhibit apparent reaction rates comparable to bulk catalysts despite containing less Cu overall. This leads to over all higher ratios between $X_C/w_{Catalyst}$.

This may partly account for the high carbon conversion rates measured for the present samples, where effective utilization of the active phase and efficient mass transfer could contribute to the achieved high performance. These structural factors might therefore offer particular advantages in systems where process intensification, reduced metal use or fast and simple production of multiple samples using a standardized effective manufacturing protocol are targeted [10]. Finally, variations in mixed CO/CO_2 feed composition (COR) appear to influence X_C dynamics greatly relative to pure CO_2-hydrogenation tests. The presence of CO in the feed may affect reaction pathways through altered CO_2-activation behavior and a modified balance between RWGS and MeOH synthesis. In addition, CO-rich mixtures may mitigate water accumulation by engaging the WGS equilibrium, potentially reducing inhibition effects at higher conversions. Literature comparisons illustrate that the influence of co-fed CO can either enhance or suppress MeOH formation, depending on COR, pressure, and conversion level [10, 77].

Notably, the present work employs a consistent COR of 0.71 across all compared formulations, whereas gathered literature comparisons span a wide range (0.13–1.00), making direct performance attribution to promoters, carriers and the interactions thereof challenging. For instance, systems with lower COR values such as CZA-Th [0.25 COR, 44.5% at 225 °C, 40 bar; Vergara et al. (2023)] or $CuMgOCeO_2$ [0.14 COR, 50.7% at 240 °C, 50 bar; Pandey et al. (2025)] achieve exceptional conversions, suggesting that CO enrichment relative to CO_2 may provide additional thermodynamic or kinetic advantages. In this context, the present data, which systematically vary COR under otherwise consistent structural and compositional conditions, provide a coherent baseline for exploration of beneficial interactions noted for each promoter under mixed SynGas environments. Additional performance comparison metrics can be found for CO_2-only SynGas streams elsewhere [11].

Concerning the chemical equilibria recorded in this work, 20% CZ shows the lowest COR for equilibrium conversion at approx. 0.83 for 250 °C reactor temperature, requiring the highest amounts of CO in the reactor make up gas for balanced reactant conversion. This equates to a CO_2/CO ratio of about 4:1, which is considerably higher in comparison to previously reported equilibrium values for CZA-catalyst systems, where equilibrium conversion has been reported at COR of 10-35% [10, 53]. This showcases the influence of promoters and support structure on the reaction mechanism and equilibrium. CeO_2 and ZrO_2 promoters added to Cu/ZnO catalysts strongly enhance CO_2-activation and hydrogenation. This is mainly due to their oxygen storage capacity and the stabilization of formate intermediates formed during MeOH synthesis. These promoters shift the reaction equilibrium toward the CO_2-hydrogenation pathway, resulting in a lower CO/CO_2 ratio required to reach equilibrium conversion [10, 40]. The promoters, along with the highly porous alumina support, suppress the CO-hydrogenation pathway relative to the CO_2 pathway much more effectively than in unpromoted Cu/ZnO catalysts. This suppression reduces the competitiveness of CO as a reactant, causing equilibrium to be established at lower partial pressures of CO, thus lowering the CO/CO_2 ratio at equilibrium.

Furthermore, CeO_2 and ZrO_2 are known to enhance the water-gas shift (WGS) reaction, which converts CO and H_2O to CO_2 and H_2. This catalytic promotion can enhance conversion of CO to CO_2 dynamically increasing the relative concentration of CO_2 in the steady state reaction environment. As a result, the CO/C_2 ratio at equilibrium is further reduced in the promoted catalyst formulations 20% CZC, 20% CZCZ and 20% CZCZC [12].

6.3.3. Results of the Parameter Fitting

For parameter fitting, no major mass transfer limitations were assumed on the basis of the extensive test for limitations described above. Table 6.7 shows average transfer coefficients and Weisz- as well as Mears-parameters for each of the catalysts for CO_2, H_2O and MeOH, which are most prone to experience transfer limitations on a molecular level [6]. The reported values were calculated as mean averages from determining the coefficients for every individual test conducted in a first optimization run. A full report of the transfer limitations for every test run is given in the supplementary materials (Appendix B, tables B.7-B.11). As can be seen, average Mears criteria are very low on average. External diffusion limitations were therefore excluded from reactor model in the fitting process. Concerning internal mass transfer limitations, only MeOH shows values above 0.1 for the herein introduced catalyst samples. As H_2, CO, CO_2 and H_2O did not show major inhibiting mass transfer behavior, and transfer limitation of the MeOH product were limited in most test conditions applied in this study, all transfer limitations were omitted in further parameter optimization.

Table 6.7.: Mass transfer analysis results for the catalyst samples.

Sample	CO_2		MeOH		H_2O		Mears
	Φ_{WP} (-)	D_K ($\times 10^{-6}$)	Φ_{WP} (-)	D_K ($\times 10^{-6}$)	Φ_{WP} (-)	D_K ($\times 10^{-6}$)	(-)
20% CZ	0.054	1.80	0.138	2.11	0.098	2.81	2.1e-04
20% CZC	0.053	1.90	0.139	2.22	0.098	2.97	2.2e-04
20% CZCZ	0.060	1.92	0.128	2.25	0.091	3.00	2.3e-04
20% CZCZC	0.064	1.94	0.134	2.27	0.094	3.03	2.5e-04

The parameters fitted to the Graaf-model with the chosen combinations of rate determining steps and some statistical indicators towards model fit are given in Table 6.8. Additionally, a short list of comparable studies that have refitted the Graaf-kinetics to other applications using adapted CZA-catalyst formulas is given in table 6.9 [31, 42, 47, 94]. The reported studies underline the meaningfulness of the calculated values from the herein tested catalyst samples, with activation energies lower - following reduced activity of the reported samples compared to the industrial CZA-catalyst. As reported by Graaf et al. and many other recent studies investigating the kinetics of MeOH synthesis over CuO / ZnO-based catalyst formulas, the optimization performed in this work yields the mathematical exclusion of the formation of MeOH through hydrogenation of CO [10, 31, 42, 46, 47]. This is represented by the fact, that calculated rates for CO hydrogenation assume near zero values in reactor calculation based upon the herein presented models. CO hydrogenation can thus be neglected in future analysis of the model fit presented in this work.
Nonetheless, the model combination given in Table 6.9 shows the optimized full model combination, including step A - *CO* hydrogenation, for comparability to related studies.

Here, the chosen optimized rate-determining step changes from one promotional step to another, with the model fit minimizing CO hydrogenation depending on the test results.

For the binary CuO/ZnO carrier catalyst, the optimization yields the best combination of models for the A3B2C3 model, which was also kinetically chosen by Graaf et al. (1988) for their industrial catalyst model using the same active phases.

Promotion of the binary catalyst changes the rate determining steps, with CeO_2 addition altering the RDS for MeOH generation through CO_2 hydrogenation, which is expectable on a molecular level, as CeO_2 is able to produce active centers for CO_2 adsorption that differ from those usually assumed to be active in CZA [20]. Here, initial hydrogenation of adsorbed CO_2 towards $HCOO*$ in the formate-pathway is favored by the CeO_2 promoted catalyst sample over the hydrogenation of H_2COO, as initially chosen in the original model by Graaf et al. (1988). Consideration of H_2COO* hydrogenation as RDS is supported by recent literature in both CZA-catalysts as well as in ZrO_2 and CeO_2-containing formulations [31]. ZrO_2-promotion changes the rate determining step of both RWGS and CO_2 hydrogenation mathematically again, with RDS in CO_2 hydrogenation returning to the initially chosen $COO*$-hydrogenation and the RDS for RWGS switching from $HCOO*$-hydrogenation towards H_2O and CO- to $COO*$ hydrogenation to $HCOO*$.

Table 6.8.: Kinetic parameters for novel 20% catalyst systems.

	20% CZ	20% CZC	20% CZCZ	20% CZCZC
Model	A3B2C3	A3B2C1	A2B1C3	A4B1C3
Rate Constants: $k = A \times e^{-E_a/RT}$				
$A_{MeOH,CO}$	1.18	32.1	8.21	0.21
$E_{a,\ MeOH,CO}$ (kJ/mol)	8.02	3.20	1.32	85.21
$A_{MeOH,\ CO_2}$	3.76×10^7	3.20×10^8	6.34×10^{10}	5.44×10^3
$E_{a,\ MeOH,\ CO_2}$ (kJ/mol)	79.3	67.5	130.8	130.8
A_{RWGS}	0.672	1.37	0.27	1.12×10^{-2}
$E_{a,RWGS}$ (kJ/mol)	27.5	8.46	25.2	29.4
Adsorption Constants: $K = B \times e^{\Delta H/RT}$				
B_{CO}	1.00×10^{-5}	1.55×10^{-2}	1.36×10^{-2}	1.12×10^{-2}
ΔH_{CO} (kJ/mol)	33.8	4.38	29.7	1.01
B_{CO_2}	2.91×10^{-7}	3.79×10^{-7}	1.70×10^{-11}	5.02×10^{-8}
ΔH_{CO_2} (kJ/mol)	57.4	30.0	114.3	66.8
B_{H_2O}	7.07×10^{-12}	1.33×10^{-11}	7.48×10^{-14}	1.21×10^{-13}
ΔH_{H_2O} (kJ/mol)	125.7	131.9	137.0	124.9
H_2: Parameters compounded with H_2O				
statistical agreement of the models predicted values with the measured data				
R^2 CO_2 ()	0.91	0.99	0.95	0.98
R^2 CO ()	0.97	0.97	0.92	0.93
R^2 MeOH ()	0.87	0.91	0.94	0.93
R^2 H_2O ()	0.97	0.92	0.91	0.91
MAPE MeOH (%)	11.56	10.11	15.38	16.51
MAPE H_2O (%)	9.21	8.41	11.12	11.76
CCC MeOH	0.85	0.94	0.81	0.83
CCC H_2O	0.91	0.96	0.84	0.82

CaO-promotion in the quinary 20% CZCZC catalyst sample does not further alter the mathematical composition of the overall model, retaining the RDS shown for 20% CZCZ, while exhibiting slightly reduced activity towards CO_2 conversion towards MeOH. The values fitted to the Graaf-model in this work assume parameter ranges that are comparable to values from similar parametrization works. On the one hand, this confirms the applicability of the presented fitting procedure, utilizing a multi initial parameter fit. In further discussion of the results, this could on the other hand also be attributed to the published optimization algorithm finding local minima close to the initial guesses taken from literature, thus providing a globally sub-optimal fit within close numerical proximity of the initial guess. Nonetheless, the models perform well in predicting CO- and CO_2 conversion as well as MeOH and H_2O-production in the test reactor, showing high overall agreement with the measured data.

Key statistical indicators are given alongside the optimized fitting parameters in table 6.8. R^2 of calculated CO, CO_2 and MeOH reactor exit partial pressures as well as MAPE and CCC of MeOH reactor exit partial pressures are shown for demonstration of model fit quality and for comparison of different approaches for statistical evaluation of modeling results. In general, the model for 20% CZC shows the best fit statistically, with R^2 for all species above 0.91 and a Mean Absolute Percentage Error (MAPE) for MeOH formation of approx. 10%, implying an average deviation of calculated values for MeOH formation of only 10% compared to the measured test data. The fitted models for 20% CZCZ and 20% CZCZC show slightly inferior statistical agreement with the measured data, but still perform well with R^2 for all species except for H_2O above 0.9 and and MAPE of approx. 15% concerning prediction efficacy towards MeOH formation. It can be argued that increased promotion of the CZA formulation alters the mechanisms of MeOH, CO, and H_2O formation more substantially, making the original assumption by Graaf et al. less applicable to the highly promoted samples and therefore leading to a slightly reduced model fit quality.

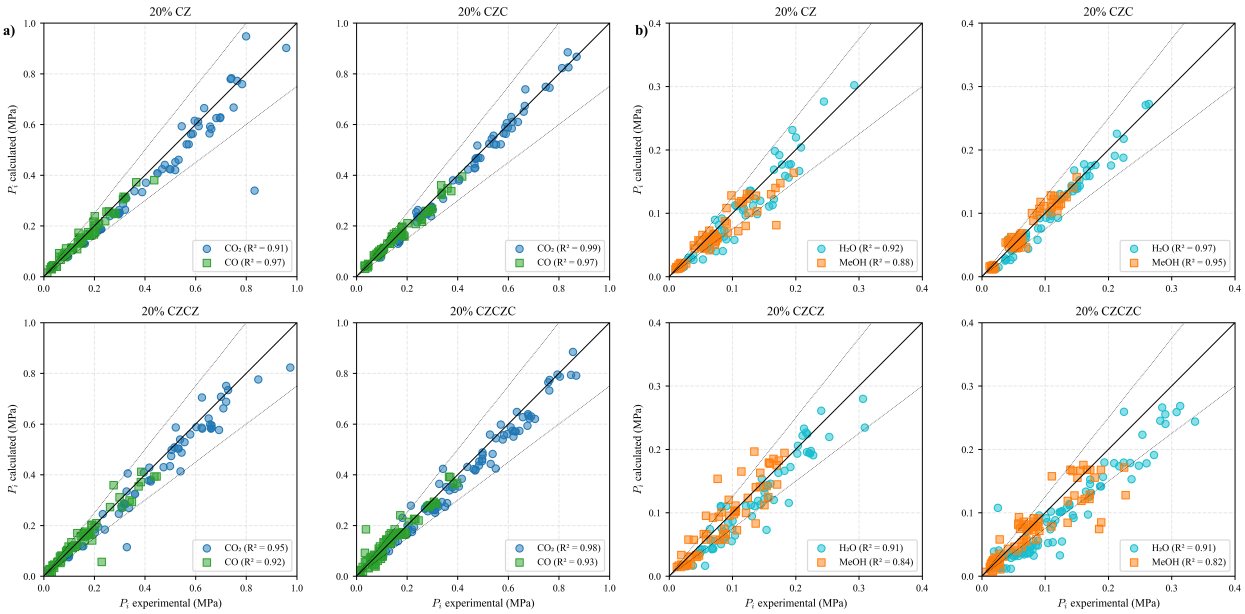

Figure 6.8.: Parity Plots for measured vs. predicted effluent partial pressures for a) CO and CO_2 and b) MeOH and H_2O in the four catalyst samples.

Calculated H_2O formation shows the lowest agreement with test data for all catalysts. This is attributed to condensation losses in the test apparatus and generally less unambiguous calibration results for GC-calibration towards H_2O in the gas phase.

Figure 6.8 shows the parity plots of CO- and CO_2- (a) as well as MeOH and H_2O- (b) reactor exit partial pressures with 25% deviation bandwidth marked inside the sub-plots.

Table 6.9.: Kinetic parameters for methanol synthesis catalysts.

	Graaf et al. [47]	Nestler et al. [42]	Poto et al. [31]	Slotboom et al. [94]
Catalyst Information				
Catalyst	$CuO/ZnO/Al_2O_3$	$CuO/ZnO/Al_2O_3$	$CuO/ZnO/CeO_2/ZrO_2$	$CuO/ZnO/Al_2O_3$
Manufacturer	Haldor Topsoe	Clariant	–	–
Type	Coprecipitation	Coprecipitation	Coprecipitation	Different data sets
Model	323	323	313	–
Rate Constants: $k = A \times e^{-E_a/RT}$				
$A_{MeOH,\,CO}$	2.69×10^7	–	7.103×10^{-1}	–
$E_{a,\,MeOH,\,CO}$ (kJ/mol)	109.9	–	33.8	–
A_{RWGS}	7.31×10^8	244.43	2.765×10^{11}	1.111×10^{10}
$E_{a,\,RWGS}$ (kJ/mol)	123.4	53.7	13.4	203.0
$A_{MeOH,\,CO_2}$	4.36×10^2	2.356×10^{-5}	1.416×10^9	7.414×10^{14}
$E_{a,\,MeOH,\,CO_2}$ (kJ/mol)	65.2	14.7	12.0	166.0
Adsorption Constants: $K = B \times e^{\Delta H/RT}$				
B_{CO}	7.99×10^{-7}	1.44×10^{-17}	3.561×10^{-3}	–
ΔH_{CO} (kJ/mol)	58.1	-0.57	-8.44	–
B_{CO_2}	1.02×10^{-7}	4.223×10^{-6}	6.173×10^{-7}	–
ΔH_{CO_2} (kJ/mol)	67.4	0	56.7	–
B_{H_2O}	4.13×10^{-11}	6.407×10^{-13}	3.521×10^{-12}	126.4 ± 66
ΔH_{H_2O} (kJ/mol)	104.5	126.8	124.2	–
H_2: Parameters compounded (Slotboom: $K_{H_2} = 1.099 \pm 0.66$)				

As can be seen, the fitted model for 20% CZC performs very well, with no estimation outliers outside of the 25% deviation areas. The 20% CZC model is able to accurately predict CO and CO_2 conversion as well as CO formation in RWGS to an R^2 of 0.99, demonstrating both the quality of the fitting procedure as well as underlining the quality of Graafs model in applications of parameter refitting for adapted MeOH-catalyst studies. Estimation of the 20% CZCZ model shows the most disarranged parity image, with single outliers being located considerably outside the 25% boundaries. For H_2O and MeOH, as with CO and CO_2 reactor exit pressures, 20% CZC shows the best statistical model fit towards the experimental data. All models show R^2 higher than 0.8 for predicting MeOH-effluent molar fractions and R^2 above 0.9 for H_2O production. Grave prediction outliers are attributed to testing inaccuracies. Model accuracy for predicting MeOH and H_2O production is significantly lower than for the calculation of carbon-oxide conversion. This is in line with multiple other recent studies and can be attributed to several factors in testing and model optimization, of which product retention in the gas probing system and enhanced measurement variance in GC calibration for liquid products are two possible reasons [42, 44].

The parametrized models for each catalyst are also tested for their performance in calculating concentration gradients in real world reactor setups. For this, the previously introduced quasi-isothermal reactor model is applied. The conversion gradients inside the reactor model are probed for each catalyst using gas compositions tested in this work, to investigate the influence each promotional step for the carrier catalysts has on the species evolution inside the reactor along the z-axis. Figure 6.9 shows the calculated concentration gradients

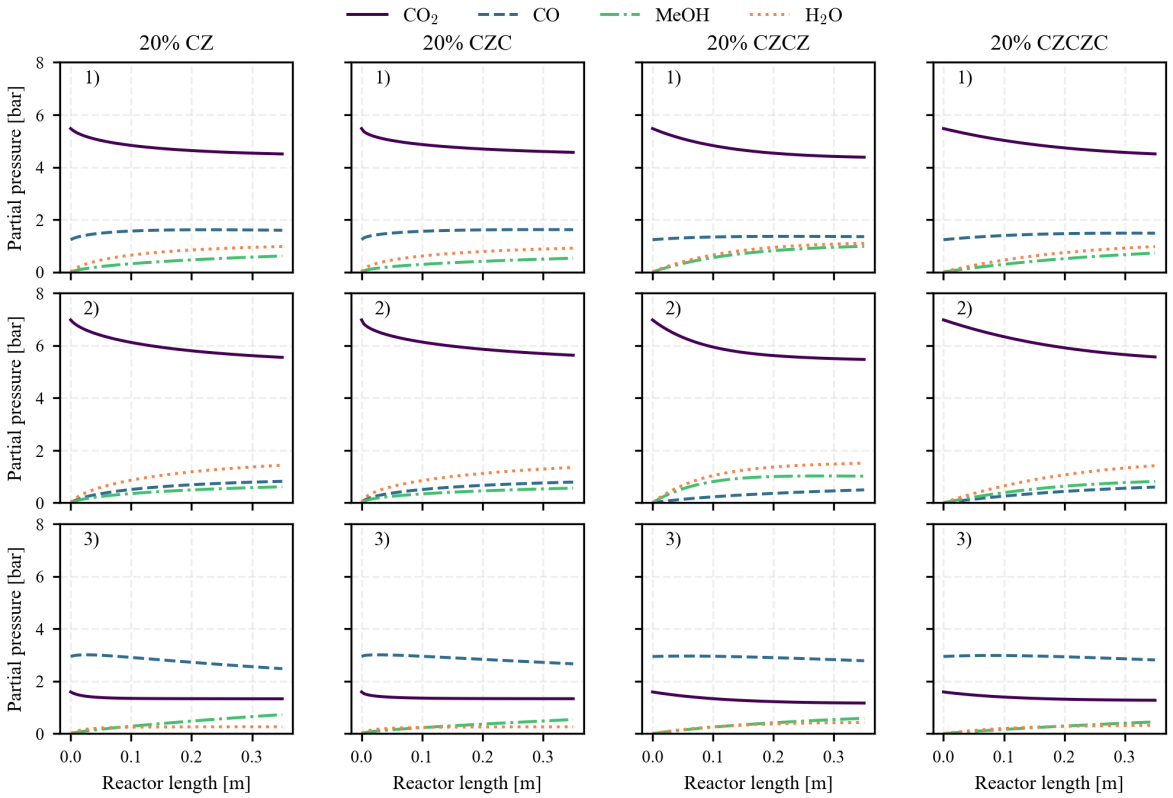

Figure 6.9.: Calculated concentration profiles inside the test reactor for three different inlet gas compositions. Top to bottom: 1) COR = 0.81, SN = 3; 2) COR = 1, SN = 3; 3) COR = 0.36, SN = 3.

inside the 0.35 m long reactor for three different reactor inlet compositions applying super stoichiometric conditions for COR = 1, COR = 0.81 and COR = 0.36. As can be taken from the subplots, educt consumption and product generation are relatively high in the first third of the reactor. 20% CZ and 20% CZC both exhibit high CO-production in the first third of the reactor, with CO-concentration reaching equilibrium fast and not changing much after about 0.1 m reactor length. Equally, CO_2 consumption is high at the beginning of the reactor, slowing down considerably after CO-concentration has reached its equilibrium. Thus, H_2O formation is high at the beginning of the reactor, being reduced as CO-concentration in the reactor reaches its equilibrium, only influenced much by the co-generation of MeOH and H_2O in CO_2 hydrogenation towards MeOH afterwards. This is in line with comparable studies, that have probed concentration profiles of the Graaf-model in tubular 1D reactor setups recently [95].

Even in the low-COR scenario, the CO-concentration in the reactor increases slightly at reactor entry, and CO consumption towards CO_2 generation and subsequent hydrogenation towards MeOH only begins after a sufficient CO-partial pressure of approx. 3 bar is reached. This is in line with the fitting results omitting CO hydrogenation for the optimized model, as all reactions pathways in the reactor are directly assigned to either WGS/RWGS or CO_2-hydrogenation reactions and CO consumption and production are not calculated through the CO-hydrogenation pathway. 20% CZCZ show significantly increased reaction rates, as already discussed in subsection 3.2. Consequently, initial CO_2 consumption is considerably higher, with species concentration for MeOH and H_2O reaching an equilibrium earlier though, barely changing after approx 50% axial reactor length. CaO-promotion in 20% CZCZC changes the model-kinetics the most. With overall smoother gradients across the reactor length. The subplots for 20% CZCZC suggest, that the reactions involved in CO_2- and CO

conversion do not reach equilibrium in the herein used reactor setup, implying that changed reactor geometries in the test setup could have contributed to increased X_C for 20% CZCZC in this work.
Sensitivity of the models towards parameter changes was investigated in order to evaluate single- and multi-parameter impact on the model results. For each model, the sensitivity of output parameters, such as X_{CO2}, STY_{MeOH}, STY_{H2O} and S_{MeOH} were tested against perturbation of single parameter classes of 10%. Table 6.10 shows the model sensitivity towards single parameters that were chosen for their high impact on model results. For each individual kinetic model, the sensitivity towards changes of 10% in the parameter values for the pre-exponential factor of MeOH formation from CO_2, activation energy for RWGS, pre-exponential, consolidated factor for the adsorption term of CO_2 and adsorption energy of CO_2 adsorption as well as the pre-exponential factor in the adsorption term for H_2O are tested under high COR conditions for SN = 2.0.

Table 6.10.: Normalized sensitivity of key model outputs towards the variation of selected model parameters. Sensitivity is given as compounded value for first order single parameters impact and higher order cross sensitivities.

Model Factor	$\mathbf{r_{MeOH}}$	$\mathbf{X_{CO_2}}$	$\mathbf{r_{H2O}}$	$\mathbf{S_{MeOH}}$
20% CZ				
$A_{MeOH,\,CO_2}$	0.2720	0.2313	0.2313	0.0910
$E_{a,\,RWGS}$	0.0093	0.4626	0.4626	0.3553
B_{CO_2}	0.2719	0.1861	0.1861	0.1258
ΔH_{CO_2}	3.0409	1.8258	1.8258	1.4235
B_{H_2O}	0.2747	0.1941	0.1941	0.1262
20% CZC				
$A_{MeOH,\,CO_2}$	0.2720	0.2313	0.2313	0.0910
A_{RWGS}	0.0039	0.0406	0.0406	0.0355
B_{CO_2}	0.2719	0.1861	0.1861	0.1258
ΔH_{CO_2}	3.0409	1.8258	1.8258	1.4235
B_{H_2O}	0.2747	0.1941	0.1941	0.1262
20% CZCZ				
$A_{MeOH,\,CO_2}$	0.0038	0.0004	0.0004	0.0035
A_{RWGS}	0.0064	0.0030	0.0030	0.0088
B_{CO_2}	0.0008	0.0002	0.0002	0.0010
ΔH_{CO_2}	0.0068	0.0018	0.0018	0.0082
B_{H_2O}	0.0000	0.0000	0.0000	0.0000
20% CZCZC				
$A_{MeOH,\,CO_2}$	0.0038	0.0004	0.0004	0.0035
A_{RWGS}	0.0064	0.0030	0.0030	0.0088
B_{CO_2}	0.0008	0.0002	0.0002	0.0010
ΔH_{CO_2}	0.0068	0.0018	0.0018	0.0082
B_{H_2O}	0.0000	0.0000	0.0000	0.0000

The models for 20% CZCZ and 20% CZCZC show high robustness towards parametric changes. This indicates low influence of the probed parameters towards the model outcome and suggests parametric uncertainty to a degree. 20% CZ and 20% CZC have more sensitive models towards most of the tested factors. This implicates more certain model fit towards these parameters and underlines the fit quality of the models fitted to the test data of 20% CZ and 20% CZC. Overall, sensitivity is moderate, suggesting more in depth review of the modeled data could be the foundation of a parameter reduction in those parameters for which the optimized models exhibit low sensitivity [44].

6.4. Conclusion

In this work, we presented a detailed performance analysis, a substantial extension of physio-chemical characterization and a parameter fitting for an existing kinetic model for four previously prepared and reported infiltration composite catalysts for the effective conversion of CO and CO_2 to MeOH. We investigated the catalysts through the analysis of radial FIB-Lamellae of the spheres, Raman- and XPS-spectra of the catalyst surfaces as well as adsorption and desorption properties for H_2- and CO_2. Physical surface properties were tested in unreduced samples, constituting a limitation of this work, but still lending valuable insights into coating efficiency of γ-alumina spheres with catalytically highly active metal oxides and their resulting surface structures. Additionally, we tested the catalyst performances in mixed carbon-oxide environments, as are expectable in industrial regenerative MeOH-synthesis with CO_2 as main carbon source and process gas recycling. The CeO_2, ZrO_2 and CaO promoted catalysts show large interfacial areas between different metal-oxide agglomerates on the γ-Al_2O_3 carrier spheres. This is indicative of the formation of active centers for both the adsorption of CO as well as CO_2. Raman- and XPS-analysis confirm the correct loading and metal-oxide ratios on the catalyst surfaces. Additionally, XPS-analysis indicated heightened dispersion and more complex metal-metal-oxide interaction on the catalyst surface, which is in line with the presented TEM-imaging. The physical findings are supported by the test results from mixed carbon-oxide SynGas testing. Here all catalyst samples perform well, with the CeO_2 and ZrO_2 promoted 20% CZCZ catalyst performing the best concerning STY_{MeOH}, showing good MeOH-production rates throughout different tested SynGas COR, pressures and reactor temperatures. This finding is especially important, as all samples were only coated with 20%w active catalyst phase with catalyst densities considerably lower than for co-precipitated commercial catalyst samples. This suggests, that only part of the active phase in precipitated catalyst samples actually contributes to the heterogeneous catalytic reactions and lays an important foundation for future development of efficient catalyst formulations. Additionally, an existing kinetic model for modeling the MeOH synthesis is re-parametrized based upon the herein presented testing result and provided open source, delivering a good and efficient approach for future kinetic work in catalysis. Mathematically, MeOH formation from CO is omitted from the numerical model, which is in line with previous findings in CO_2 hydrogenation to MeOH. An effective kinetic parameter set was determined for every sample, enabling the calculation of complex tubular reactor models and future work in scale-up for catalytic applications. The models suggests the conversion of CO_2 to MeOH via the formate route, with the hydrogenation of adsorbed $HCOO^*$s or the hydrogenation of H_2OO*-species being mathematically determined as rate determining in MeOH formation. Meanwhile, the models suggest that CO acts as H_2O scavenger, with adsorbed H_2O species necessary to activate CO on the catalyst surfaces in RWGS-reaction mechanisms. Overall, this work presents the basis for an extended understanding of how different popular MeOH-catalyst promoters interact in different formulas in carrier catalyst applications. The classic CuO/ZnO catalyst complex performs well in CO-dominated SynGas streams, CeO_2 and ZrO_2 are nonetheless able to improve conversion performance, especially in CO_2-rich synthesis gas applications.

References

[1] Vincent Dieterich et al. “Power-to-liquid via synthesis of methanol, DME or Fischer–Tropsch-fuels: a review”. In: *Energy & Environmental Science* 13.10 (2020), pp. 3207–3252. ISSN: 1754-5692. DOI: 10.1039/D0EE01187H.

[2] Maryam Ebrahimzadeh Sarvestani et al. “From catalyst development to reactor Design: A comprehensive review of methanol synthesis techniques”. In: *Energy Conversion and Management* 302 (2024), p. 118070. ISSN: 01968904. DOI: 10.1016/j.enconman.2024.118070.

[3] Trinath Biswal et al. “Conversion of carbon dioxide to methanol: A comprehensive review”. In: *Chemosphere* 298 (2022), p. 134299. DOI: 10.1016/j.chemosphere.2022.134299.

[4] Yaser Khojasteh-Salkuyeh et al. “CO2 utilization for methanol production; Part I: Process design and life cycle GHG assessment of different pathways”. In: *Journal of CO2 Utilization* 50 (2021), p. 101608. ISSN: 22129820. DOI: 10.1016/j.jcou.2021.101608.

[5] Feng Jiang et al. “Insights into the Influence of CeO 2 Crystal Facet on CO 2 Hydrogenation to Methanol over Pd/CeO 2 Catalysts”. In: *ACS Catalysis* 10.19 (2020), pp. 11493–11509. ISSN: 2155-5435. DOI: 10.1021/acscatal.0c03324.

[6] Noerma J. Azhari et al. “Methanol synthesis from CO2: A mechanistic overview”. In: *Results in Engineering* 16 (2022), p. 100711. ISSN: 25901230. DOI: 10.1016/j.rineng.2022.100711.

[7] Arik Beck et al. “The Enigma of Methanol Synthesis by Cu/ZnO/Al2O3-Based Catalysts”. In: *Chemical reviews* 124.8 (2024), pp. 4543–4678. DOI: 10.1021/acs.chemrev.3c00148.

[8] Ang Cao et al. “New insights on CO and CO2 hydrogenation for methanol synthesis: The key role of adsorbate-adsorbate interactions on Cu and the highly active MgO-Cu interface”. In: *Journal of Catalysis* 400 (2021), pp. 325–331. ISSN: 00219517. DOI: 10.1016/j.jcat.2021.06.020.

[9] L. C. Grabow and M. Mavrikakis. “Mechanism of Methanol Synthesis on Cu through CO 2 and CO Hydrogenation”. In: *ACS Catalysis* 1.4 (2011), pp. 365–384. ISSN: 2155-5435. DOI: 10.1021/cs200055d.

[10] Niels D. Nielsen, Anker D. Jensen, and Jakob M. Christensen. “The roles of CO and CO2 in high pressure methanol synthesis over Cu-based catalysts”. In: *Journal of Catalysis* 393 (2021), pp. 324–334. ISSN: 00219517. DOI: 10.1016/j.jcat.2020.11.035.

[11] Carl Fritsch et al. “CO 2 –Hydrogenation to Methanol over CuO/ZnO Based Infiltration Composite Catalyst Spheres”. In: *ChemCatChem* 16.21 (2024). ISSN: 1867-3880. DOI: 10.1002/cctc.202400731.

[12] Jiadong Zhu et al. “Mechanism and Nature of Active Sites for Methanol Synthesis from CO/CO2 on Cu/CeO2”. In: *ACS Catalysis* 10.19 (2020), pp. 11532–11544. ISSN: 2155-5435. DOI: 10.1021/acscatal.0c02909.

[13] Menghao Ren et al. “Catalytic Hydrogenation of CO2 to Methanol: A Review”. In: *Catalysts* 12.4 (2022), p. 403. DOI: 10.3390/catal12040403.

[14] Florian Nestler et al. “Experimental Validation of Methanol Synthesis from Steel Mill Gases Using a Miniplant Setup”. In: *Chemie Ingenieur Technik* 94.10 (2022), pp. 1466–1475. ISSN: 0009-286X. DOI: 10.1002/cite.202200022.

[15] Denis Makhmutov et al. “Reaction Pathways of Methanol Formation in CO 2 Hydrogenation over Pd-Based Catalysts”. In: *ACS Catalysis* 15.3 (2025), pp. 2328–2341. ISSN: 2155-5435. DOI: 10.1021/acscatal.4c07462.

[16] Filippo Bisotti et al. “Impact of Kinetic Models on Methanol Synthesis Reactor Predictions: In Silico Assessment and Comparison with Industrial Data”. In: *Industrial & Engineering Chemistry Research* 61.5 (2022), pp. 2206–2226. ISSN: 0888-5885. DOI: 10.1021/acs.iecr.1c04476.

[17] Kongzhai Li and Jingguang G. Chen. “CO 2 Hydrogenation to Methanol over ZrO 2 -Containing Catalysts: Insights into ZrO 2 Induced Synergy”. In: *ACS Catalysis* 9.9 (2019), pp. 7840–7861. ISSN: 2155-5435. DOI: 10.1021/acscatal.9b01943{\#}.

[18] Maxim Zabilskiy et al. “Methanol synthesis over Cu/CeO 2 –ZrO 2 catalysts: the key role of multiple active components”. In: *Catalysis Science & Technology* 11.1 (2021), pp. 349–358. ISSN: 2044-4753. DOI: 10.1039/d0cy01762k.

[19] Xibo Zhang et al. “Highly Dispersed ZnO Sites in a ZnO/ZrO2 Catalyst Promote the CO2-to-Methanol Reaction”. In: (2024). DOI: 10.26434/chemrxiv-2024-93gtw.

[20] Rajan Singh, Kaushik Kundu, and Kamal K. Pant. “CO2 hydrogenation to methanol over Cu-ZnO-CeO2 catalyst: Reaction structure–activity relationship, optimizing Ce and Zn ratio, and kinetic study”. In: *Chemical Engineering Journal* 479 (2024), p. 147783. ISSN: 13858947. DOI: 10.1016/j.cej.2023.147783.

[21] Runping Ye et al. “A Ce-CuZn catalyst with abundant Cu/Zn-OV-Ce active sites for CO2 hydrogenation to methanol”. In: *Nature communications* 15.1 (2024), p. 2159. DOI: 10.1038/s41467-024-46513-3.

[22] Jie Xiao et al. “Methanol Synthesis from CO 2 Hydrogenation over CuO–ZnO–TiO 2 Catalysts: The Influence of TiO 2 Content”. In: *Energy Technology* 3.1 (2015), pp. 32–39. ISSN: 2194-4288. DOI: 10.1002/ente.201402091.

[23] Leon G.A. van de Water et al. “Understanding methanol synthesis from CO/H2 feeds over Cu/CeO2 catalysts”. In: *Journal of Catalysis* 364 (2018), pp. 57–68. ISSN: 00219517. DOI: 10.1016/j.jcat.2018.04.026.

[24] Dongliang Wang et al. “Novel coal-to-methanol process with near-zero carbon emission: Pulverized coal gasification-integrated green hydrogen process”. In: *Journal of Cleaner Production* 339 (2022), p. 130500. ISSN: 09596526. DOI: 10.1016/j.jclepro.2022.130500.

[25] Wei Lin Ng et al. “Experimental work and kinetic modelling of CO2 hydrogenation to methanol on CeO2 supported In2O3 catalyst”. In: *Applied Catalysis A: General* 646 (2022), p. 118885. ISSN: 0926860X. DOI: 10.1016/j.apcata.2022.118885.

[26] Congyi Wu et al. “Inverse ZrO2/Cu as a highly efficient methanol synthesis catalyst from CO2 hydrogenation”. In: *Nature communications* 11.1 (2020), p. 5767. DOI: 10.1038/s41467-020-19634-8.

[27] Thongthai Witoon et al. “Enhanced activity, selectivity and stability of a CuO-ZnO-ZrO2 catalyst by adding graphene oxide for CO2 hydrogenation to methanol”. In: *Chemical Engineering Journal* 334 (2018), pp. 1781–1791. ISSN: 13858947. DOI: 10.1016/j.cej.2017.11.117.

[28] Xiaosu Dong et al. “CO2 hydrogenation to methanol over Cu/ZnO/ZrO2 catalysts prepared by precipitation-reduction method”. In: *Applied Catalysis B: Environmental* 191 (2016), pp. 8–17. ISSN: 09263373.

[29] Venkata D.B.C. Dasireddy, Strah Štefančič Neja, and Likozar Blaž. “Correlation between synthesis pH, structure and Cu/MgO/Al2O3 heterogeneous catalyst activity and selectivity in CO2 hydrogenation to methanol”. In: *Journal of CO2 Utilization* 28 (2018), pp. 189–199. ISSN: 22129820. DOI: 10.1016/j.jcou.2018.09.002.

[30] Chenglin Zhong et al. “Effects of alkaline-earth oxides on the performance of a CuO–ZrO 2 catalyst for methanol synthesis via CO 2 hydrogenation”. In: *RSC Advances* 5.65 (2015), pp. 52958–52965. DOI: 10.1039/C5RA06508A.

[31] Serena Poto et al. “Kinetic modelling of the methanol synthesis from CO2 and H2 over a CuO/CeO2/ZrO2 catalyst: The role of CO2 and CO hydrogenation”. In: *Chemical Engineering Journal* 435 (2022), p. 134946. ISSN: 13858947. DOI: 10.1016/j.cej.2022.134946.

[32] Fabio Salomone et al. “CO2 hydrogenation to methanol over Zr- and Ce-doped indium oxide”. In: *Catalysis Today* 423 (2023), p. 114023. ISSN: 09205861. DOI: 10.1016/j.cattod.2023.01.030.

[33] Hong Ren et al. “Methanol synthesis from CO2 hydrogenation over Cu/g-Al2O3 catalysts modified by ZnO, ZrO2 and MgO”. In: *Journal of Industrial and Engineering Chemistry* 28 (2015), pp. 261–267. ISSN: 1226086X. DOI: 10.1016/j.jiec.2015.03.001.

[34] Kang Xiao et al. “For Better Industrial Cu/ZnO/Al2O3 Methanol Synthesis Catalyst: A Compositional Study”. In: *Catalysis Letters* 147.6 (2017), pp. 1581–1591. ISSN: 1011-372X. DOI: 10.1007/s10562-017-2022-8.

[35] Caroline A. Schneider, Wayne S. Rasband, and Kevin W. Eliceiri. “NIH Image to ImageJ: 25 years of image analysis”. In: *Nature methods* 9.7 (2012), pp. 671–675. DOI: 10.1038/nmeth.2089.

[36] Matthias B. Fichtl and Olaf Hinrichsen. “On the Temperature Programmed Desorption of Hydrogen from Polycrystalline Copper”. In: *Catalysis Letters* 144.12 (2014), pp. 2114–2120. ISSN: 1011-372X. DOI: 10.1007/s10562-014-1384-4.

[37] Martin Muhler et al. “Temperature-programmed desorption of H2 as a tool to determine metal surface areas of Cu catalysts”. In: *Catalysis Letters* 14.3-4 (1992), pp. 241–249. ISSN: 1011-372X. DOI: 10.1007/BF00769661.

[38] Marta C.N Amorim de Carvalho, Fabio B. Passos, and Martin Schmal. “Quantification of metallic area of high dispersed copper on ZSM-5 catalyst by TPD of H2”. In: *Catalysis Communications* 3.11 (2002), pp. 503–509. ISSN: 15667367. DOI: 10.1016/S1566-7367(02)00195-4.

[39] Hegen Zhou et al. “Mechanism of Methanol Synthesis from CO2 Hydrogenation over Cu/g-Al2O3 Interface: Influences of Surface Hydroxylation”. In: *Catalysts* 13.9 (2023), p. 1244. DOI: 10.3390/catal13091244.

[40] Michael Bowker. “Methanol Synthesis from CO2 Hydrogenation”. In: *ChemCatChem* 11.17 (2019), pp. 4238–4246. ISSN: 1867-3880. DOI: 10.1002/cctc.201900401.

[41] Jean-François Portha et al. “Kinetics of Methanol Synthesis from Carbon Dioxide Hydrogenation over Copper–Zinc Oxide Catalysts”. In: *Industrial & Engineering Chemistry Research* 56.45 (2017), pp. 13133–13145. ISSN: 0888-5885. DOI: 10.1021/acs.iecr.7b01323.

[42] F. Nestler et al. “Kinetic modelling of methanol synthesis over commercial catalysts: A critical assessment”. In: *Chemical Engineering Journal* 394 (2020), p. 124881. ISSN: 13858947. DOI: 10.1016/j.cej.2020.124881.

[43] Łukasz Hamryszak et al. “Cu/Zn/Zr/Ga Catalyst for Utilisation of Carbon Dioxide to Methanol—Kinetic Equations”. In: *Catalysts* 12.7 (2022), p. 757. DOI: 10.3390/catal12070757.

[44] Ahmad Kouzehli, Mohammad Kazemeini, and Amirhossein Ashrafi Moghaddam. “A robust kinetic modeling of CO2 hydrogenation to methanol over an industrial copper–zinc oxide catalyst based on a single-active site mechanism”. In: *International Journal of Hydrogen Energy* 60 (2024), pp. 756–768. ISSN: 03603199. DOI: 10.1016/j.ijhydene.2024.02.176.

[45] Hye-Won Lim et al. “Modeling of the Kinetics for Methanol Synthesis using Cu/ZnO/Al 2 O 3 /ZrO 2 Catalyst: Influence of Carbon Dioxide during Hydrogenation”. In: *Industrial & Engineering Chemistry Research* 48.23 (2009), pp. 10448–10455. ISSN: 0888-5885. DOI: 10.1021/ie901081f.

[46] Nonam Park et al. “Kinetic modeling of methanol synthesis over commercial catalysts based on three-site adsorption”. In: *Fuel Processing Technology* 125 (2014), pp. 139–147. ISSN: 03783820. DOI: 10.1016/j.fuproc.2014.03.041.

[47] G. H. Graaf, E. J. Stamhuis, and A.A.C.M. Beenackers. “Kinetics of low-pressure methanol synthesis”. In: *Chemical Engineering Science* 43.12 (1988), pp. 3185–3195. ISSN: 00092509. DOI: 10.1016/0009-2509(88)85127-3.

[48] Sreetama Ghosh et al. “Experimental and kinetic modeling studies of methanol synthesis from CO2 hydrogenation using In2O3 catalyst”. In: *Chemical Engineering Journal* 416 (2021), p. 129120. ISSN: 13858947. DOI: 10.1016/j.cej.2021.129120.

[49] Li He et al. “Preparation of Pt/g-Al2O3 catalyst coating in microreactors for catalytic methane combustion”. In: *Chemical Engineering Journal* 380 (2020), p. 122424. ISSN: 13858947. DOI: 10.1016/j.cej.2019.122424.

[50] Daniel Laudenschleger, Holger Ruland, and Martin Muhler. “Identifying the nature of the active sites in methanol synthesis over Cu/ZnO/Al2O3 catalysts”. In: *Nature communications* 11.1 (2020), p. 3898. DOI: 10.1038/s41467-020-17631-5.

[51] Kyungho Lee et al. “Mechanism-Guided Catalyst Design for CO 2 Hydrogenation to Formate and Methanol”. In: *Accounts of Materials Research* 4.9 (2023), pp. 746–757. ISSN: 2643-6728. DOI: 10.1021/accountsmr.3c00075.

[52] Filippo Bisotti et al. “Century of Technology Trends in Methanol Synthesis: Any Need for Kinetics Refitting?” In: *Industrial & Engineering Chemistry Research* 60.44 (2021), pp. 16032–16053. ISSN: 0888-5885. DOI: 10.1021/acs.iecr.1c02877.

[53] Geert H. Graaf and Jozef G. M. Winkelman. “Chemical Equilibria in Methanol Synthesis Including the Water–Gas Shift Reaction: A Critical Reassessment”. In: *Industrial & Engineering Chemistry Research* 55.20 (2016), pp. 5854–5864. ISSN: 0888-5885. DOI: 10.1021/acs.iecr.6b00815.

[54] Carl Fritsch. “Open Source Python Script for optimization of reaction kinetics”. In: (2025). URL: https://github.com/Fircar/Kinetics-Optimization.

[55] Zoltán Till et al. "Reduction of lumped reaction networks based on global sensitivity analysis". In: *Chemical Engineering Journal* 375 (2019), p. 121920. ISSN: 13858947. DOI: 10.1016/j.cej.2019.121920.

[56] I.M Sobol′. "Global sensitivity indices for nonlinear mathematical models and their Monte Carlo estimates". In: *Mathematics and Computers in Simulation* 55.1-3 (2001), pp. 271–280. ISSN: 03784754. DOI: 10.1016/S0378-4754(00)00270-6.

[57] Shengqiang Lin et al. "Chemical kinetic model reduction through species-targeted global sensitivity analysis (STGSA)". In: *Combustion and Flame* 224 (2021), pp. 73–82. ISSN: 00102180. DOI: 10.1016/j.combustflame.2020.12.004.

[58] Balaji C. Dharmalingam et al. "Unravelling the role of metal-metal oxide interfaces of Cu/ZnO/ZrO2/Al2O3 catalyst for methanol synthesis from CO2: Insights from experiments and DFT-based microkinetic modeling". In: *Applied Catalysis B: Environmental* 332 (2023), p. 122743. ISSN: 09263373. DOI: 10.1016/j.apcatb.2023.122743.

[59] Robert M. Palomino et al. "Hydrogenation of CO2 on ZnO/Cu(100) and ZnO/Cu(111) Catalysts: Role of Copper Structure and Metal-Oxide Interface in Methanol Synthesis". In: *The journal of physical chemistry. B* 122.2 (2018), pp. 794–800. DOI: 10.1021/acs.jpcb.7b06901.

[60] Habib Zada, Jiafeng Yu, and Jian Sun. "Active Sites for CO2 Hydrogenation to Methanol: Mechanistic Insights and Reaction Control". In: *ChemSusChem* 18.4 (2025), e202401846. DOI: 10.1002/cssc.202401846.

[61] Jie Xiao et al. "CO2 hydrogenation to methanol over CuO ZnO TiO2ZrO2 catalyst prepared by a facile solid-state route: The significant influence of assistant complexing agents". In: *International Journal of Hydrogen Energy* 44.29 (2019), pp. 14831–14841. ISSN: 03603199. DOI: 10.1016/j.ijhydene.2019.04.051.

[62] T. Armbruster and R. Danisi, eds. *The power of databases: the RRUFF project*. Highlights in Mineralogical Crystallography. Berlin: W. De Gruyter, 2015. ISBN: 978-3-11-041704-4. URL: https://rruff.info/about/downloads/HMC1-30.pdf.

[63] M. Varga et al. "Cu–MgO Samples Prepared by Mechanochemistry for Catalytic Application". In: *Journal of Catalysis* 206.1 (2002), pp. 71–81. ISSN: 00219517. DOI: 10.1006/jcat.2001.3476.

[64] Mengdong Nie et al. "Effect of Mn content in CuO/MnCeO x catalysts on CO 2 hydrogenation for methanol synthesis". In: *Reaction Chemistry & Engineering* 8.6 (2023), pp. 1383–1394. DOI: 10.1039/D3RE00022B.

[65] H. Y. Chen et al. "Copper Sites in Copper-Exchanged ZSM-5 for CO Activation and Methanol Synthesis: XPS and FTIR Studies". In: *Inorganic chemistry* 36.7 (1997), pp. 1417–1423. DOI: 10.1021/ic9601221.

[66] Abdulrahman Syedahamed Haja Hameed et al. "Impact of alkaline metal ions Mg2+, Ca2+, Sr2+ and Ba2+ on the structural, optical, thermal and antibacterial properties of ZnO nanoparticles prepared by the co-precipitation method". In: *Journal of materials chemistry. B* 1.43 (2013), pp. 5950–5962. DOI: 10.1039/C3TB21068E.

[67] Sebastian Kuld et al. "Quantifying the promotion of Cu catalysts by ZnO for methanol synthesis". In: *Science (New York, N.Y.)* 352.6288 (2016), pp. 969–974. DOI: 10.1126/science.aaf0718.

[68] Thomas Lunkenbein et al. “Bridging the Time Gap: A Copper/Zinc Oxide/Aluminum Oxide Catalyst for Methanol Synthesis Studied under Industrially Relevant Conditions and Time Scales”. In: *Angewandte Chemie (International ed. in English)* 55.41 (2016), pp. 12708–12712. DOI: 10.1002/anie.201603368.

[69] Antonio Ruiz Puigdollers et al. “Increasing Oxide Reducibility: The Role of Metal/Oxide Interfaces in the Formation of Oxygen Vacancies”. In: *ACS Catalysis* 7.10 (2017), pp. 6493–6513. ISSN: 2155-5435. DOI: 10.1021/acscatal.7b01913.

[70] Jin Li, Michael Nolan, and Christophe Detavernier. “A step towards correct interpretation of XPS results in metal oxides: a case study aided by first-principles method in ZnO”. In: (2023). DOI: 10.26434/chemrxiv-2023-thnhv.

[71] Carlos Mendoza-Merlano et al. “Improved conversion, selectivity, and stability during CO2 methanation by the incorporation of Ce in Ni, Co, and Fe-hydrotalcite-derived catalysts”. In: *International Journal of Hydrogen Energy* 60 (2024), pp. 985–995. ISSN: 03603199. DOI: 10.1016/j.ijhydene.2024.02.149.

[72] Dawei Chen et al. “CO 2 hydrogenation to methanol over CuO–ZnO–TiO2–ZrO2: a comparison of catalysts prepared by sol–gel, solid-state reaction and solution-combustion”. In: *Journal of Sol-Gel Science and Technology* 86.3 (2018), pp. 719–730. ISSN: 0928-0707. DOI: 10.1007/s10971-018-4680-4.

[73] Yixuan Wang et al. “Unraveling the role of basic sites in the hydrogenation of CO2 to formic acid over Ni-based catalysts”. In: *Journal of Catalysis* 430 (2024), p. 115357. ISSN: 00219517. DOI: 10.1016/j.jcat.2024.115357.

[74] Peng Gao et al. “Influence of modifier (Mn, La, Ce, Zr and Y) on the performance of Cu/Zn/Al catalysts via hydrotalcite-like precursors for CO2 hydrogenation to methanol”. In: *Applied Catalysis A: General* 468 (2013), pp. 442–452. ISSN: 0926860X. DOI: 10.1016/j.apcata.2013.09.026.

[75] J. T. Miller et al. “Hydrogen Temperature-Programmed Desorption (H2 TPD) of Supported Platinum Catalysts”. In: *Journal of Catalysis* 143.2 (1993), pp. 395–408. ISSN: 00219517. DOI: 10.1006/jcat.1993.1285.

[76] Fei Chen et al. “Structure-Performance Correlations over Cu/ZnO Interface for Low-Temperature Methanol Synthesis from Syngas Containing CO2”. In: *ACS applied materials & interfaces* 13.7 (2021), pp. 8191–8205. DOI: 10.1021/acsami.0c18600.

[77] Thaylan Pinheiro Araújo et al. “Methanol Synthesis by Hydrogenation of Hybrid CO2 -CO Feeds”. In: *ChemSusChem* 14.14 (2021), pp. 2914–2923. DOI: 10.1002/cssc.202100859.

[78] Bing Han et al. “Sol-gel synthesis of Pt-Co-CeOx codierite catalyst for biogas reforming to methanol compatible syngas”. In: *Energy* 329 (2025), p. 136707. ISSN: 03605442. DOI: 10.1016/j.energy.2025.136707.

[79] Yun-Fei Shi et al. “Methanol Synthesis from CO2/CO Mixture on Cu-Zn Catalysts from Microkinetics-Guided Machine Learning Pathway Search”. In: *Journal of the American Chemical Society* 144.29 (2022), pp. 13401–13414. DOI: 10.1021/jacs.2c06044.

[80] Sonal Asthana, Komal Tripathi, and Kamal Kishore Pant. "Impact of La engineered stable phase mixed precursors on physico-chemical features of Cu- based catalysts for conversion of CO2 rich syngas to methanol". In: *Catalysis Today* 404 (2022), pp. 154–168. ISSN: 09205861. DOI: 10.1016/j.cattod.2022.02.013.

[81] Felix Studt et al. "The Mechanism of CO and CO 2 Hydrogenation to Methanol over Cu–Based Catalysts". In: *ChemCatChem* 7.7 (2015), pp. 1105–1111. ISSN: 1867-3880. DOI: 10.1002/cctc.201500123.

[82] Qaisar Maqbool et al. "Bimetallic CuPd nanoparticles supported on ZnO or graphene for CO2 and CO conversion to methane and methanol". In: *RSC sustainability* 2.11 (2024), pp. 3276–3288. DOI: 10.1039/D4SU00339J.

[83] Israf Ud Din, Mshari A. Alotaibi, and Abdulrahman I. Alharthi. "Green synthesis of methanol over zeolite based Cu nano-catalysts, effect of Mg promoter". In: *Sustainable Chemistry and Pharmacy* 16 (2020), p. 100264. ISSN: 23525541. DOI: 10.1016/j.scp.2020.100264.

[84] Woo Jin Lee et al. "The effect of metal additives in Cu/Zn/Al2O3 as a catalyst for low-pressure methanol synthesis in an oil-cooled annulus reactor". In: *Catalysis Today* 343 (2020), pp. 183–190. ISSN: 09205861. DOI: 10.1016/j.cattod.2019.03.041.

[85] Vaibhav Pandey et al. "Promotional role of methanol and CO2 in carbon dioxide-rich syngas hydrogenation over slurry reactor utilizing combustion induced Cu-based catalysts". In: *Materials Today Sustainability* 29 (2025), p. 101082. ISSN: 25892347. DOI: 10.1016/j.mtsust.2025.101082.

[86] Junyi Zuo et al. "Enhanced activity of CexZr1-xO2 solid solutions supported Cu-based catalysts for hydrogenation of CO2 to methanol". In: *Molecular Catalysis* 526 (2022), p. 112357. ISSN: 24688231. DOI: 10.1016/j.mcat.2022.112357.

[87] Hongyan Ban et al. "Influence of rare-earth elements (La, Ce, Nd and Pr) on the performance of Cu/Zn/Zr catalyst for CH3OH synthesis from CO2". In: *Catalysis Communications* 54 (2014), pp. 50–54. ISSN: 15667367. DOI: 10.1016/j.catcom.2014.05.014.

[88] Guo Wang et al. "Methanol synthesis from CO2 hydrogenation over CuO-ZnO-ZrO2-MxOy catalysts (M=Cr, Mo and W)". In: *International Journal of Hydrogen Energy* 44.8 (2019), pp. 4197–4207. ISSN: 03603199. DOI: 10.1016/j.ijhydene.2018.12.131.

[89] Chong Huang et al. "Microwave–Assisted Hydrothermal Synthesis of CuO–ZnO–ZrO 2 as Catalyst for Direct Synthesis of Methanol by Carbon Dioxide Hydrogenation". In: *Energy Technology* 5.11 (2017), pp. 2100–2107. ISSN: 2194-4288. DOI: 10.1002/ente.201700190.

[90] Tomás Vergara et al. "Combined role of Ce promotion and TiO2 support improves CO2 hydrogenation to methanol on Cu catalysts: Interplay between structure and kinetics". In: *Journal of Catalysis* 426 (2023), pp. 200–213. ISSN: 00219517. DOI: 10.1016/j.jcat.2023.07.017.

[91] Wen Ding et al. "Thorium-promoted Cu/Zn/Al syngas catalyst for methanol synthesis with enhanced activity and stability". In: *Fuel* 367 (2024), p. 131470. ISSN: 00162361. DOI: 10.1016/j.fuel.2024.131470.

[92] Qianwen Zhang, Xiaohong Li, and Kaoru Fujimoto. "Pd-promoted Cr/ZnO catalyst for synthesis of methanol from syngas". In: *Applied Catalysis A: General* 309.1 (2006), pp. 28–32. ISSN: 0926860X. DOI: 10.1016/j.apcata.2006.04.026.

[93] Molly Meng-Jung Li et al. “Enhanced CO2 hydrogenation to methanol over CuZn nanoalloy in Ga modified Cu/ZnO catalysts”. In: *Journal of Catalysis* 343 (2016), pp. 157–167. ISSN: 00219517. DOI: 10.1016/j.jcat.2016.03.020.

[94] Y. Slotboom et al. “Critical assessment of steady-state kinetic models for the synthesis of methanol over an industrial Cu/ZnO/Al2O3 catalyst”. In: *Chemical Engineering Journal* 389 (2020), p. 124181. ISSN: 13858947. DOI: 10.1016/j.cej.2020.124181.

[95] Grazia Leonzio. “Mathematical modeling of a methanol reactor by using different kinetic models”. In: *Journal of Industrial and Engineering Chemistry* 85 (2020), pp. 130–140. ISSN: 1226086X. DOI: 10.1016/j.jiec.2020.01.033.

7. Integrated H_2/O_2-Enhanced Biogas-to-Methanol Process

This chapter presents the article published as “Design, implementation and piloting of an integrated hydrogen- and oxygen-added process for conversion of biogas to methanol” in the Royal Society of Chemistry’s "Sustainable Energy & Fuels". The study addresses the growing need for renewable carbon utilization pathways by demonstrating a fully regenerative MeOH-synthesis process based on biogenic feedstocks. To this end, a novel, integrated process concept was developed that couples autothermal biogas reforming with isothermal MeOH synthesis and incorporates water electrolysis to supply both H_2 and O_2 directly to the process. This integration enables efficient use of biogenic carbon while simultaneously enhancing process flexibility and reducing external utilities demand—key requirements for future renewable, decentralized MeOH-production systems.

The work spans the complete development chain from conceptual process design to pilot-scale demonstration. A particular distinguishing feature of this study is the direct scale-up of the catalyst formulation 20% CZCZC previously designed, characterized and validated at laboratory scale. Such a continuous progression from fundamental catalyst development through to operation in a pilot-scale, industrially relevant plant is rarely executed in research. By implementing this catalyst in the biogas-to-methanol process, the study showcases not only the feasibility of the process concept but also the translational potential of rational catalyst design for real-world applications.

The integrated pilot plant was engineered, constructed, commissioned, and subsequently operated under conditions representative of industrial practice. Its performance, operational behavior, and efficiency are analyzed in detail, with particular emphasis on identifying optimization potentials for future process refinement. The results provide valuable insights into the technical viability of renewable MeOH production from organic carbon sources and offer a foundation for further scale-up and industrial deployment, both on a process and a catalyst level.

Declaration of contributions:

- *Carl Fritsch* conceptualization of study, methodology, formal analysis, investigation, data curation, project administration, funding acquisition, resources, supervision, validation, visualization, original draft
- *Jule Blankenstein* formal analysis, investigation, data curation
- *Benedikt Bender* conceptualization of study, methodology, formal analysis, investigation, review
- *Jürgen Dornseiffer* methodology, manufacturing of catalyst samples, data curation, review
- *Moritz Haep* formal analysis, investigation, data curation
- *Kristoffer Ooms* project administration, review

Original Publication

Fritsch, C.; Blankenstein, J.; Bender, B.; Dornseiffer, J.; Haep, M.; Ooms, K.
Design, Implementation and Piloting of an integrated Hydrogen- and Oxygen-added Process for Conversion of Biogas to Methanol, Sustainable Energy & Fuels 2025, 9, 6199-6215, doi.org/10.1039/D5SE00691K

Abstract

An integrated biogas-to-methanol (B2M) conversion system combining autothermal reforming (ATR) with regenerative methanol (MeOH) synthesis, integrating both oxygen (O_2) and hydrogen (H_2) from water electrolysis is designed, commissioned and investigated operationally. The pilot plant is operated under real world conditions at a wastewater treatment plant in western Germany to demonstrate the process using sewage-derived biogas and investigate its applicability and suitability for decentralized, efficient value-added bio-chemical production from renewable feedstock. The studies conducted at the test plant evaluate system effectiveness by optimizing operational parameters for both ATR (steam-to-carbon ratio [S/C], oxygen-to-fuel ratio [λ]) and the methanol (MeOH) synthesis process (stoichiometric number [SN], reaction temperature and gas space velocity [GHSV]). Additionally, stable start-up procedures are developed for reliable operation under dynamic conditions, as are expectable in industrial process application. To compare different MeOH-synthesis pathways, regenerative synthesis gas-based MeOH production is set against to direct CO_2-to-MeOH conversion. Results demonstrate that ATR of biogas produces CO_2-rich synthesis gas (SynGas) with excellent methane (CH_4) conversion and extremely low soot formation at relatively low reforming temperatures under 750 °C. Although the high CO_2-content reformate requires substantial H_2 injection for stoichiometric MeOH-synthesis SynGas conditions, the H_2-enhanced SynGas route proves superior to CO_2-only operation of the pilot plant, highlighting possible synergies in oxygen-injected ATR and MeOH-synthesis applications. The combined ATR-H_2-injection approach yields higher MeOH yields with reduced water formation and improved conversion. The findings from this study support the technical feasibility of the integrated B2M-system and provide operational foundations for economically viable decentralized MeOH production at biogas facilities and future system scale-up.

7.1. Introduction

In order to reduce anthropogenic climate impact, the transition away from fossil resources is imperative. Next to the widely discussed energy transition, this also includes the transition away from fossil-based material production. Industries that depend heavily on fossil carbon feedstock face significant challenges in their transition toward defossilization. Against this backdrop, biomass emerges as one of the most promising alternative feedstocks for reducing fossil resource dependency, offering diverse valorization pathways to create viable substitutes within existing carbon-based production systems and value chains [1]. Within this context, bio-waste assumes particular significance. Unlike conventional biomass sources, its availability remains fundamentally decoupled from production infrastructures that compete for limited land resources with sectors such as agriculture and nutrition, which themselves rely substantially on biomass availability [2]. In Germany, historical subsidy frameworks have significantly shaped the utilization of biomass and bio-waste as carbon sources, predominantly favoring fermentation, biogas production, and subsequent combustion for electricity and heat generation [3]. While this approach represents an effective biomass utilization strategy, it inherently sacrifices the renewable carbon potential, thereby precluding downstream material carbon applications unless supplemented by sophisticated carbon-capture technologies. The direct use of biogas in value-added material conversion systems therefore presents an opportunity for the efficient use of available infrastructures towards substitutional utilization of accessible, regenerative carbon sources in otherwise heavily fossil-reliant industries [4].

There are many different process routes for material biomass and bio-carbon valorization. One possible application of biomass as a substitute in historically fossil-heavy value chains is the generation of hydrogen-rich synthesis gas (SynGas). In this respect, biomass can be used as a substitute for coal in gasification-processes for generation of carbon-dioxide (CO_2) rich SynGas [5]. Alternatively, certain types of biomass can be converted to biogas through fermentation or fouling processes in order to obtain biogas, a varying mixture of CH_4 and CO_2 [6]. Biogas in turn can be used as a substitute in reforming processes, which otherwise utilize CH_4-rich natural gas for production of SynGas [7]. In this context, the production of SynGas-based fuels and chemicals offers a wide range of possibilities for material utilization of biogas and the production of renewable bio-chemicals towards the defossilization of the SynGas- and fuel-industries [8].

One of the most widely applied, SynGas-derived chemicals is methanol (MeOH) [9]. Its wide range of applications as base chemical, monomer, energy- or hydrogen-carrier and fuel or fuel-substitute makes it one of the most commonly traded petrochemical products in the world today, with about 100 Mt being produced and shipped each year [10]. The possibilities for regenerative MeOH production thus promise to assume key roles in the global transition away from fossil resources [11]. While regenerative production paths for MeOH have been the focus of many studies in recent years and some preliminary industrial-scale demonstrations have been reported upon, many technical and economical challenges still prevail on our path towards an efficient, global industrial-scale regenerative MeOH-production infrastructure [12, 13]. Economically, biogas valorization towards SynGas-production with subsequent conversion to MeOH has the potential to become a cost-effective production route for MeOH [14]. The integrated process of reforming biogas to SynGas with possible downstream applications such as MeOH synthesis has thus been reported upon often in the recent past, mainly in techno-economic, model-based assessments of possible configurations, ecological and economical aspects of process design [11, 13, 17, 18, 19, 20, 21, 22, 23, 15, 16]. While principally and technically possible, no integrated large-scale application for this process has been demonstrated commercially to this day. This can be attributed to – upon others – three factors:

1. Biogas can be converted to SynGas through reforming, but - in most cases - the resulting SynGas does not contain enough H_2 for stoichiometric conversion of CO_2 and carbon-monoxide (CO) to MeOH [11, 24, 25]. This is highly dependent on the Biogas feed composition. For effective and complete carbon conversion, process adaptions have to be made to supply the necessary H_2 to the process and bridge the stoichiometric deficit.

2. In conventional steam methane reforming (SMR), the high temperatures necessary for effective catalytic generation of SynGas are supplied through partial stream combustion of the input natural gas. As biogas contains high percentages of CO_2, the reduced heating value (HHV) results in higher amounts of input gas being combusted to generate sufficient reforming heat - some report up to 50% of the total biogas input being used for heating purposes [26, 27].

3. Biogas – especially in Germany – is produced mainly in decentralized facilities [28, 29]. This poses a number of economical challenges of scale for the allocation and efficient conversion of gas streams for industrial production of SynGas and its daughter products such as MeOH [2, 23].

To address these factors, we suggest a combined process approach for O_2-added, autothermal biogas reforming with subsequent H_2-injected conversion of the resulting SynGas to MeOH. This approach combines the commonly reported on, electricity-based E-MeOH production route with a more conventional gas-reforming-based Bio-MeOH approach. We design a system that utilizes biogas or sewage gas for autothermal reforming (ATR) to SynGas.

Here, we use pure O_2 from water electrolysis to supply the reforming unit with an oxidizing agent for catalytic partial oxidation of the CH_4 contained in the input biogas stream. While conventional SMR utilizes a partial gas stream for combustion in an auxiliary firing unit, in our autothermal approach no biogas is used for auxiliary firing and heat production. Instead, the CH_4 is oxidized partially in the catalytic reforming unit, sustaining the necessary internal heat for the reaction between CH_4 and H_2O (equation 7.1) and supplying all the necessary heat for input H_2O vaporization and reactant preheating. In this way, no regenerative carbon is lost to combustion, but is instead converted entirely to SynGas for subsequent upgrading to MeOH.

As the resulting SynGas does not have stoichiometric proportions of H_2, CO and CO_2, we take advantage of the synergies in electrolysis and use pure H_2 to inject into the SynGas, thus creating more suitable stoichiometric conditions for carbon-oxide conversion to MeOH.

We design and commission a pilot plant for demonstrating the integrated process at the waste water treatment plant (WWTP) 'Emschermündung' in western Germany with a nominal load of 4 Nm^3/h biogas feed and optimize the process operationally, featuring both independent operation of the ATR and the MeOH-synthesis loop as well as combined operation of the two thermochemical systems. We apply novel catalysts both for reforming as well as MeOH synthesis, proving the potential of the approach. In designing and operation the pilot plant, we investigate the applicability of such a combined, integrated bio-feedstock and electricity based process application under real world operational conditions, probings its suitability as a value added alternative to biogas-combustion for electricity and heat generation. In a first-time process-integration, we explore the adequacy of biogas ATR for producing SynGas for further thermochemical conversion to value added bio-products. Focusing on future demonstration and piloting of MeOH synthesis, we highlight operative aspects of synthesis operation and identify operational and efficiency shortcomings in the process, that have to be resolved for future process application and stable, effective operation of related processes. Herein, we identify challenges in start-up and steady-state operation of the system and discuss obstacles towards further scale-up and possible industrial application of the process in a decentralized environment.

7.2. State-of-the-Art, Pilot plant Design and Set-Up

ATR of biogas as well as MeOH synthesis from renewable sources have both been demonstrated separately in selected studies in the recent past, highlighting the applicability of both partial system individually and providing insights into possible system combination for regenerative MeOH-synthesis applications. Nonetheless, no combined approach of autothermal, pure oxygen-injected biogas reforming with hydrogen injected, bio-MeOH-synthesis has been reported to this date on a pilot scale. The state of the art was thus used for design and implementation of the herein reported pilot plant application of the combined process.

ATR of biogas towards H_2- or SynGas-production been demonstrated prominently by Rau et al., who built a test plant and later carried on to demonstrate the reforming process on a semi-industrial scale [30, 14]. Rau et al. (2019) used air for partial oxidation of CH_4. This introduces a large amount of nitrogen (N_2) into the system, which is counteractive at the process level for subsequent MeOH synthesis as a result of the increase in the inert gas mass and the increase in the energy demand for reforming based upon this gas introduction into the thermochemical system. For production of H_2 from the resulting SynGas, where Bio-H_2 has to be separated after reforming, this N_2 will be omitted from the product gas, as was demonstrated in the cited studies. In subsequent SynGas-applications such as MeOH synthesis, this poses an additional obstacle, where inert gas is introduced into a synthesis loop and increases energy demand for pumping, compression and system tempering in steady-state operation [31]. Considering these design limitations, ATR-processes show improved effectiveness and improved efficiency, when operated in oxygen-only environments [32]. Furthermore, autothermal reforming of synthetic biogas has been investigated in small laboratory scale applications in multiple sources, Luneau et al. (2015), Rathod & Bhale (2014), Guerrero et al. (2020) and Hou et al. (2007) proving the efficiency potential of the application [33, 34, 35, 36]. Luneau et a. showed significant catalyst deactivation at S/C 3 and λ = 0.5 after just 30 h on-stream, proving that excessive water-injection and subsequent high necessary oxygen-injection rates were able to oxidize the reforming catalysts surfaces and lead to premature deactivation of the applied catalyst formulas [33]. While proving the applicability of the process in principle, in our work we therefore aimed to reduce both water vapor injection and the reduction of λ necessary to achieve suitable reforming temperatures. Meanwhile, Rathod et al. (2014) showed that increased temperatures above 650 °C were able to significantly improve CH_4 conversion in their autothermal, dry-reforming laboratory set up with minimization of H_2O-vapor production in the process and maximization of H_2-yield, highlighting noble-metal activity in the activation and conversion of CH_4. For improved process stability, autothermal reforming with H_2O injection was chosen in this work, applying a noble-metal catalyst and reported temperature ranges with H_2O being able to additionally improve CH_4 conversion and H_2 yield through the SMR-reaction scheme (7.1) [37]. Guerrero et al. (2020) showed very high CH_4 and CO_2 conversion in their autothermal partial oxidation reactor, converting most of the injected CH_4, CO_2 and O_2 at temperatures up to 1.500 K through enabling the dry reforming reaction (2.4) [35]. While this approach is able to realize good conversion ratios, the lack of H_2O vapor and the high reforming temperatures strongly suggest co-production of soot, which acts counter actively in subsequent compression- and synthesis processes [38]. Reaction parametrization for ATR with low soot production, good CH_4 conversion and H_2-yield as well as acceptable CO_2-levels in the produced reformate were shown in an extensive equilibria-study by Nourbakhsh et al. (2018), who defined good operational spaces for oxidative SMR under atmospheric pressures [39].

Hou et al. (2007) highlighted the importance of space-velocity in CH_4-reforming under dosing of CO_2 and O_2 , leading to a reactor design accommodating for GHSV lower 54.000 h^{-1} [36].

In addition to this, Topsoe has demonstrated electrified SMR with subsequent conversion to MeOH in a

proprietary process (eSMR Methanol) [40]. Here, excess grid electricity can be used to supply the necessary heat for the reforming reaction, providing a suitable option for grid balancing. This is an alternative use of electricity integration into the thermochemical B2M-process, but it does not accommodate for the H_2-deficiency in regenerative MeOH production based upon high CO_2-contents input streams.

Meanwhile, decentralized MeOH synthesis has been demonstrated in direct CO_2 hydrogenation processes by Carbon Recycling International (CRI), who aim to produce E-MeOH on an economically viable industrial scale in several plants internationally [19]. In the large-scale research project Carbon2Chem, a demonstrator for the decentralized conversion of CO_2 from cement production processes to MeOH was operated in Oberhausen [41]. Both approaches apply CO_2-only input streams, making CO_2-removal feasible in hard to abate sectors, providing for a value-added option for effective CO_2-capture and conversion (CCU). In both cases the produces MeOH will not be regenerative in nature, utilizing fossil carbon sources for production of the C1-product.

In a comparable manner to the herein presented work, researchers from DTU Copenhagen piloted a process combining dry and wet reforming of biogas for further conversion to MeOH [42]. Here they applied their 'bio-reforming' unit, able to reform biogas through SMR to regenerative SynGas. Their bio-reforming process was able to convert CO_2 from biogas to CO and H_2, making additional injection of hydrogen optional. The two stage process requires an additional reforming unit for effective conversion of CO_2. If H_2 is additionally injected, no process-synergies for the effective integration of the O_2-product from water-electrolysis is available, reducing the system efficiency for any associated electrolysis. The process was developed concurrently to the herein presented process. Additionally, small-scale MeOH synthesis from biogas in three-phase reactors has been reported on by Schipek et al. recently [43]. Here, a complex three-phase reactor is applied, improving conversion efficiencies, but necessitating the design of an integrated system. The herein presented work aims to simplify decentralized MeOH synthesis, making commercial technologies like reactor setup and catalyst design available to possible future producers. Extending upon the existing work, we designed a system for simple, atmospheric conversion of biogas to SynGas in a single-stage ATR-unit applying robust noble-metal catalysts. SynGas is cooled and compressed for subsequent introduction into the MeOH-synthesis loop, utilizing a set of tubular isothermal fixed-bed reactors, product sequestration and gas recycling to yield regenerative raw MeOH product.

7.2.1. Design and Setup of the Autothermal Reforming Unit

For the production of SynGas from Biogas/Sewage gas, a unit for oxygen-added autothermal reforming was designed and applied. Here, CH_4 and CO_2 from sewage gas as well was H_2O vapor and O_2 are supplied to a catalytic reactor, where four main catalytic reactions take place simultaneously:

$$CH_4 + H_2O \rightleftharpoons CO + 3H_2 \quad \Delta_r H^O = 206.0 \frac{kJ}{mol} \tag{7.1}$$

$$2CH_4 + O_2 \rightleftharpoons 2CO + 4H_2 \quad \Delta_r H^O = -71.0 \frac{kJ}{mol} \tag{7.2}$$

$$CO + H_2O \rightleftharpoons CO_2 + H_2 \quad \Delta_r H^O = -41.2 \frac{kJ}{mol} \tag{7.3}$$

$$CO_2 + CH_4 \rightleftharpoons CO + 2H_2 \quad \Delta_r H^O = 247.0 \frac{kJ}{mol} \tag{7.4}$$

The thermal energy and subsequent reaction temperatures in the system are supplied through partial oxidation of CH_4 to CO and H_2 (equation 7.2). To enable this reaction, pure O_2 is supplied to the catalytic reactor, with temperatures of the resulting reformate being used in a combined heat exchanger (HEX 950) for vaporization of feed water and preheating of the sewage gas. While part of the reaction network in autothermal reforming, dry reforming (equation 7.4) can be mostly disregarded in the temperature range tested herein [14, 33]. Decomposition of CH_4 to C, Boudoard-decomposition of CO to C and CO_2 reduction were not observed in laboratory testing of the reformer and are unlikely at the temperature ranges below 700 °C [44, 45]. In the overall application of the pilot plant, sewage gas was supplied through an activated carbon filter for the elimination of sulfuric compounds, entering a three-way valve. This allowed for the operation of the system using synthetic gas from gas cylinder bundles instead of raw sewage gas. The feed gas as was pumped into the system using a double membrane pump with cooled pump bodies and heads (KNF N2400 ST13.E). Coolant was supplied in the form of mains water from the central pilot plant water supply. (Synthetic) Sewage gas was passed through an additional activated carbon filter for elimination of surplus sulfur and siloxanes, while hydrogen sulfide content was continuously monitored using a gas monitoring unit (ExTox ET-4D, Germany). Mains water was supplied centrally to both the integrated reforming unit as well as the MeOH-synthesis system. Part of the mains water was run through a demineralization unit for elimination of ions in the supplied water. Deionized water was collected and then pumped into HEX 950. Here it was vaporized, overheated and mixed with the educt sewage gas. The mixed and preheated reactants were fed into the reformer pre-chamber where O_2 was dosed through a radial injection system, ensuring thorough mixing of the input gases before entering the catalytic reforming stage. The combustible gas mixture was then fed into the catalytic reformer chamber for production of a CO_2-rich SynGas.

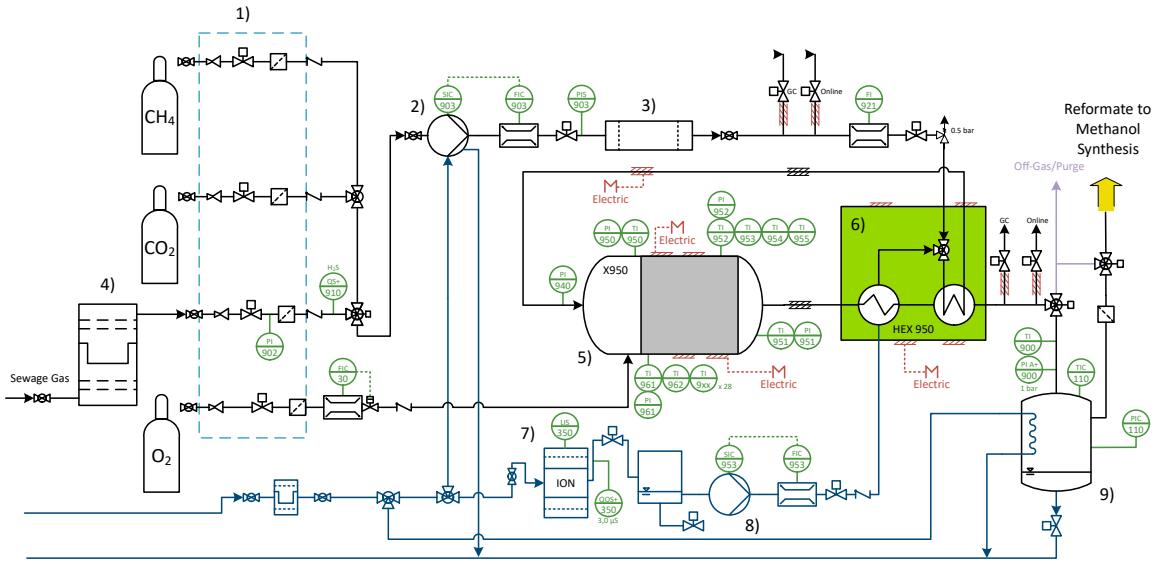

Figure 7.1.: Piping and Instrumentation Diagram (P&ID) of the Autothermal Reforming unit for oxygen-added conversion of Biogas to SynGas. 1) Gas-dosing lines for synthetic biogas and oxygen. 2) Biogas-gas pump. 3) Siloxane Filter. 4) Activated Carbon Filter. 5) Reforming Reactor with radial oxygen injection. 6) Combined heat exchanger for water evaporation and biogas preheating. 7) Feed water demineralization unit. 8) Feed water dosing pump.

A Platinum (Pt)-washcoated monolith 0.7 l carrier catalyst was used for effective conversion of Biogas to SynGas (Interkat, Germany). The reformer was insulated using a machined micro-porous mantle, encasing the tubular gas mixing stage as well as the subsequent catalyst housing. The hot SynGas was passed into HEX 950 for vaporization of feed water and preheating of the reactant biogas stream, supplying enough energy for feed overheating and maintaining stable reactor temperatures throughout, making the system truly autothermal, both concerning steady-state reactor operation and overall system energy balance. Additional heating was only required in initial system start-up. Reformate was then fed through a cooled condenser, separating product H_2O from the gas stream. SynGas was then run through a three-way valve, allowing for direct injection of the Gas into the MeOH process or separate operation of ATR and MeOH synthesis in single-system investigation or for system start-up. The reforming system is illustrated in detail in figure 7.1.

7.2.2. Design and Setup of the Methanol Synthesis System

For the effective conversion of SynGas with varying compositions, a MeOH-synthesis unit with a set of tubular reactors is applied. A P&ID of the integrated MeOH-synthesis system is given in figure 7.2.

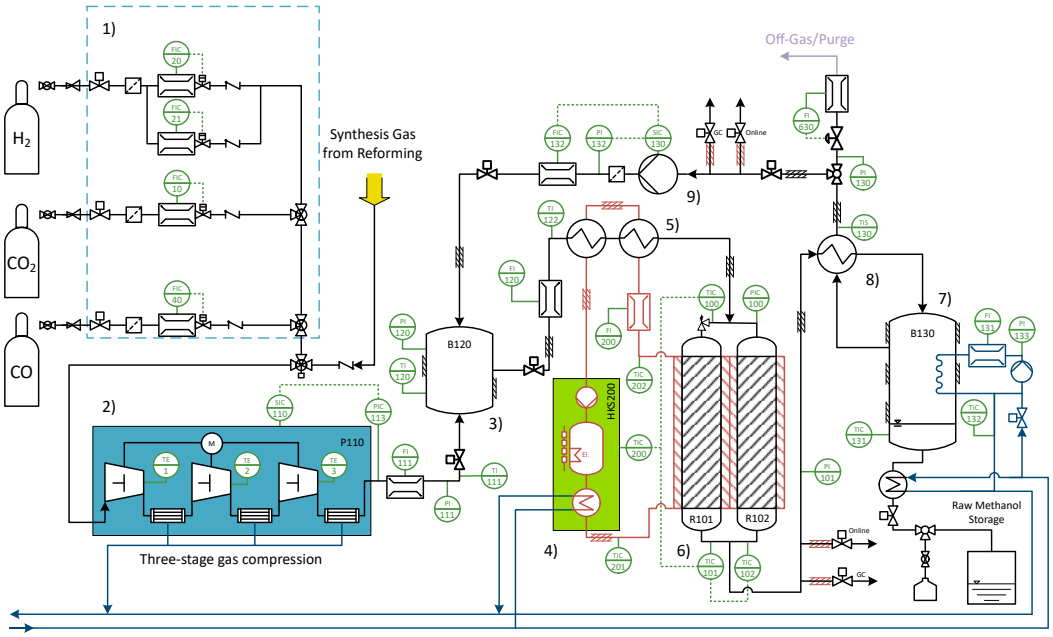

Figure 7.2.: P&ID of the Methanol Synthesis Loop for Conversion of Reformate from Autothermal Reforming. 1) Gas dosing lines for synthesis gas dosing from gas cylinders. 2) Three-stage synthesis gas compressor with intermediate stage cooling and condensation. 3) Gas mixer, combined heat exchanger and pulsation dampener for synthesis gas. 4) Thermal oil thermostat for system tempering in start-up and reactor cooling in steady-state operation. 5) Double heat-exchanger arrangement for synthesis gas pre-conditioning. 6) Double tubular quasi-isothermal methanol reactors. 7) Combined raw-product condensation and recycling gas conditioning unit. 8) Heat exchanger for product-gas cooling/recycling gas pre-heating. 9) Recycling gas compressor.

SynGas from the ATR is supplied to a gas mixing line through a three-way valve, which allows for individual system start-up as well as separate operation of the ATR and the MeOH synthesis. Here, H_2, CO and CO_2 can be dosed through thermal mass flow controllers (MFC - Bronkhorst EL-FLOW Select), which enables maximum composition control in system start-up and individual testing of the MeOH-synthesis loop. For the intended large-scale application of the herein presented system, H_2 from water electrolysis will be supplied to the SynGas for adaption of SynGas stoichiometry here. For small-scale pilot application, this was represented

by dosing H_2 from gas cylinder bundles to specification.
The mixed gas is then compressed in a three-stage piston compressor (HAUG WTEGX 60/35/20) up to 25 bar system pressure. System pressure is limited due to guidelines related to the Pressure Equipment Directive of the European Union (2014/68/EU [PED]) based upon overall system gas volume and subsequent material testing requirements [46]. The compressed and H_2-added SynGas is then fed to a gas mixer and pulsation dampener, where it is mixed with the recycled SynGas and gas pressure and flow oscillations from the piston compression are smoothened. The SynGas-mixture is then fed through two heat exchangers arranged in series for preheating before entering the parallel tubular reactors. The reactors are stainless steel reactors with 54,5 mm inner reactor diameter (ID) and 88,9 mm outer diameter (AD) including the stainless steel cooling/heating-jacket. The active reactor length is 1250 mm with a total reactor length of 1650 mm including flanges. The reactors were equipped with a metal grid base plate for support of the bulk catalyst filling. 2,048 kg of catalyst were applied to each reactor with the top and bottom headroom in the reactors being filled with glass wool for gas dispersion and particle filtering. As MeOH catalyst, a previously reported novel infiltration composite carrier catalyst coated with CuO, ZnO, CeO_2, ZrO_2 and CaO is applied [47]. Catalyst spheres had a diameter of 2,5 mm. SynGas is converted to MeOH and H_2O, with some of the entering CO_2 being converted to H_2O and CO through RWGS (cf. equation 7.3). Three general reactions takes place in converting SynGas to MeOH product, with several additional reactions yielding commonly reported on byproducts such as dimethyl ether (DME), ethanol (EtOH), formaldehyde or methane not considered or analytically recorded in this work [48]:

$$CO + 2H_2 \rightleftharpoons CH_3OH \quad \Delta_r H^O = -90.8 \frac{kJ}{mol} \tag{7.5}$$

$$CO_2 + 3H_2 \rightleftharpoons CH_3OH + H_2O \quad \Delta_r H^O = -49.5 \frac{kJ}{mol} \tag{7.6}$$

$$CO_2 + 2H_2 \rightleftharpoons CO + H_2O \quad \Delta_r H^O = 41.2 \frac{kJ}{mol} \tag{7.7}$$

The oversaturated product gas is collected from the MeOH reactors and fed into a stainless steel product condensation unit. Here, it is cooled through a counter-current gas heat exchanger (CC-HEX) and then fed to a water-cooled condenser, where liquid product is collected. Uncondensed SynGas is then fed back through the CC-HEX and fed back into the synthesis system through a high pressure recycling pump (Fink CHEM + TEC Z04-13). From there, the recycle gas stream enters the gas mixer/pulsation dampener.
System pressure and off-gas flow was controlled through a high-precision proportional membrane valve (Samson EB 8091). Off-gas was taken from the recycling stream in front of the recycling pump.
The MeOH-synthesis system was managed thermally through a thermostat system (Huber Unistat TR401 wHT) with up to 8 kW heating and 10 kW cooling performance. Reactors were cooled through countercurrent perfusion of the tubular MeOH reactors. Regenerated heat from reactor cooling was used for SynGas preheating in the serial HEX arrangement.

7.2.3. Integrated System and System Control

The integrated system was set up in a 20 ft container with initial activated carbon treatment for sewage gas, raw MeOH product collection and gas supply from gas cylinder bundles being housed in separate vessels. System control and operation was carried out from a second container with the overall decentralized

pilot plant operation being conducted on site of Emschergenossenschafts technical center on the WWTP Emschermündung in Dinslaken, Germany. The compositions of dry raw sewage gas, SynGas, MeOH-product gas, and MeOH recycle gas were measured using an integrated gas analysis tower using two Rosemount X-Stream (Emerson, USA) Continuous Gas Analyzer systems with different infrared (IR) channels for CO, CH_4 and CO_2 analysis and additional thermal conductivity (TCD) channels for H_2-analysis. Gas streams for analysis were additionally fed to a multi entry port valve for sequential analysis in a GC unit (SRI Instruments 8610C) equipped with serial columns (9' and 6' Hayesep D). Liquid samples of the raw MeOH product were analyzed for their composition ex-situ on a HPLC unit (Shimadzu LCMS-2020). Samples were taken intermittently, usually for 20-minute test durations and weighed for determination of production rates.
The system was controlled through a custom Siemens Siematic programmable logic controller and a Windows Control Center (WinCC) user interface.

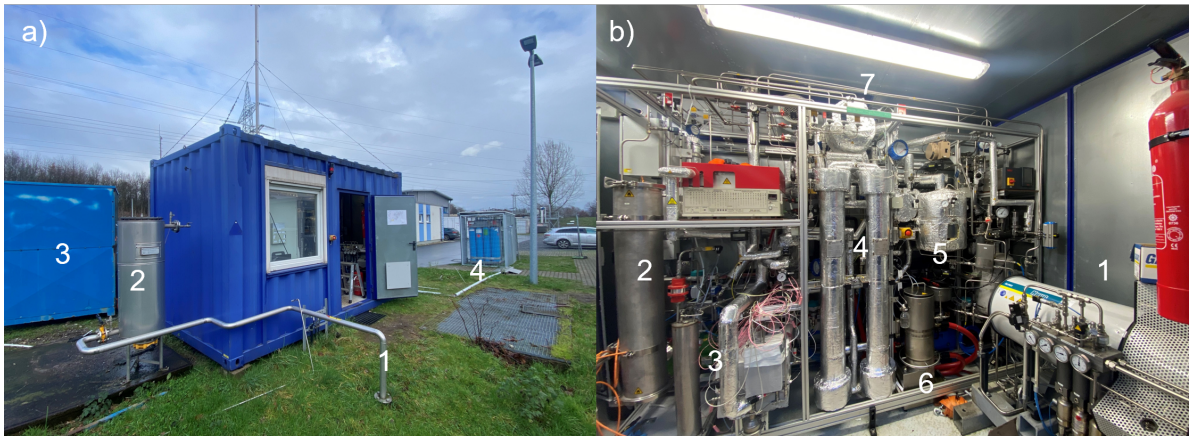

Figure 7.3.: a) Outside view of the plant in operation. 1 - Sewage gas line. 2 - Activated. charcoal filter. 3 - Gas storage for Helium and Calibration Gas (GC). 4 - Gas Storage for O_2, H_2, CO_2 and CH_4. b) Inside view of the operational process. 1 - Three-stage reformate compressor. 2 - Siloxane filter. 3 - Reforming unit encased in mantle. 4 - tubular MeOH reactors. 5 - Gas mixer/pulsation dampener. 6 - Thermostat heating and cooling unit. 7 - Heat exchanger for SynGas-preheating and energy recuperation.

7.3. Experimental

7.3.1. System Parameters and Performance Indicators

Autothermal Reforming

The ATR-process is governed by several key operating parameters that enable precise system control. The gas hourly space velocity (GHSV), defined as the normalized gas flow rate per unit catalyst bed volume, serves as a fundamental parameter for characterizing overall throughput in the ATR unit (Equation 7.8). During pilot-scale operation, GHSV is regulated via controlled introduction of biogas, O_2, and water vapor into the reformer prechamber. Both the reforming temperature and the methane conversion efficiency are modulated by strategic oxygen dosing within the reforming unit. The stoichiometric relationship between oxygen and methane in the overall process is quantified by the air-fuel ratio (λ), where $\lambda = 1$ denotes the stoichiometric oxygen requirement for complete combustion of CH_4 to CO_2 and H_2O.

The intensity of steam methane reforming in the catalytic bed of the ATR unit (equation 7.1) as well as soot production and reforming temperature are controlled through H_2O supply [49].

The steam-to-carbon-ratio (S/C) is applied for process characterization and control, describing the ratio between dosed CH_4 and H_2O steam.

$$GHSV = \frac{\dot{V}_{Gas}(Nm^3/h)}{V_{Catalyst}(m^3)} \tag{7.8}$$

$$\lambda = \frac{\dot{n}_{O_2}}{2\,\dot{n}_{CH_4}} \tag{7.9}$$

$$S/C = \frac{\dot{n}_{H_2O}}{\dot{n}_{CH_4} + \dot{n}_{CO_2}} \tag{7.10}$$

Performance of the ATR is primarily characterized through H_2-content in the produced SynGas. For characterization of the dried SynGas, the stoichiometric number (SN) for MeOH synthesis is applied. A sub-objective of the study is to minimize the necessary external H_2-injection for MeOH synthesis, the measure of the stoichiometric conditions in dried SynGas or rather the lack thereof can easily be used for a review of the ATR performance. As conversion of CO to MeOH requires less H_2 and CO-content in produced SynGas is one measure of conversion-routes inside the ATR, the resulting carbon-oxide-ratio (COR) is used as additional measure for ATR-performance as well as characterization and control of the MeOH-synthesis loop. It also represents an important measure for MeOH-system design, with conversion efficiencies and reactor sizing being heavily dependent on the ratio of injected CO and CO_2 [31].

$$SN = \frac{\dot{n}_{H_2} - \dot{n}_{CO_2}}{\dot{n}_{CO_2} + \dot{n}_{CO}} \tag{7.11}$$

$$COR = \frac{x_{CO_2}}{x_{CO_2} + x_{CO}} \tag{7.12}$$

Methanol Synthesis

In a comparable manner to the ATR, MeOH synthesis is strongly characterized by the GHSV through the MeOH reactor (equation 7.8). In contrast to the reforming unit, gas velocity is a compounded value, made up of the gas velocity through the gas recycling section and volumetric feed rate of the reformate compressor. For both streams, the normalized volumetric gas flow rate has to be determined from gas analysis and mass flow detection. As moderate temperatures and low synthesis pressures are applied in this study, ideal gas conditions are assumed for normalization of gas flow rates into the reactor. SynGas dosing and recycle ratio in the SynGas recycling loop are regulated towards high GHSV of 7.000 h^{-1} and above, which is a common parameter range in commercial MeOH synthesis [50]. In system analysis, the ratio between input SynGas stream and recycling gas stream pumped through the recycling gas loop is calculated as the recycling ratio, which describes the molar fraction of recycled gas over reformate.

Hydrogen is dosed based upon the SN-value of reformate delivered through the compressor. A minimum of SN = 2 is applied for stoichiometric SynGas composition for carbon-oxide conversion to MeOH and H_2O. For each steady state operation point of the MeOH synthesis, an additional, real SN can be derived, which combines SN from reformate dosing and SN in the recycle loop of the synthesis system.

$$r_{recy} = \frac{\sum \dot{n}_{recy,i}}{\sum \dot{n}_{reformate_i}} \tag{7.13}$$

For determination of conversion performance inside the MeOH reactor, two different measures of conversion can be applied: Single-pass reactor conversion ($X_{C_{sp}}$) is used to characterize the catalyst performance, representing the catalyst's ability to convert carbon-oxides to liquid process products in a single reactor pass. This performance metric was monitored continuously. It was calculated as the difference in molar CO- and CO_2-flux in the reactor inlet and the molar streams being recycled and purged respectively. The formation of by-products, such as Dimethylether (DME), Formaldehyde (FAD) or CH_4, which are commonly generated alongside MeOH in low pressure synthesis, is disregarded for this analysis [51, 52, 53].

A second performance indicator is the overall system carbon conversion($X_{C_{tot}}$). It represents a balanced value, indicating the amount of carbon converted to MeOH product over a defined time frame in testing. This is also used as overall system performance measure, as all carbon-reactants used in ATR are subsequently fed into the low pressure MeOH synthesis as ATR products.

$$X_{C_{sp}} = 1 - \frac{\dot{n}_{CO_2,recy} + \dot{n}_{CO_2,purge} + \dot{n}_{CO,recy} + \dot{n}_{CO,purge}}{\dot{n}_{CO_2,in} + \dot{n}_{CO,in}} \tag{7.14}$$

$$X_{C_{tot}} = \frac{n_{MeOH_{tot}}}{n_{CO_2,in,tot} + n_{CO,in,tot}} \tag{7.15}$$

For determination of overall system efficiency, the chemical efficiency was used, which can be calculated by determining the heating value (HHV) of the molar input streams, output streams and other associated process streams.

$$\eta_{ch} = \frac{\sum \dot{n}_{i,\text{product}} HHV_{i,\text{prod}}}{\sum \dot{n}_{i,\text{in}} HHV_{i,\text{in}}} \tag{7.16}$$

As both O_2 and H_2 are injected into different parts of the two-stage thermochemical process in combined system operation, performance review towards the use of both products of electrolysis was performed based upon the relation of injection requirements in O_2 addition for ATR and H_2 addition for stoichiometric MeOH synthesis. The relation between the gas injections requirements is given as a percentage of stoichiometric gas production in electrolysis, with 100 % denoting injections requirements exactly proportional to electrolysis gas production (two parts molar H_2 to one part O_2), values larger 100 % denoting excessive hydrogen demand and values lower 100% denoting excessive oxygen demand for the respective system set point:

$$\eta_{electrolysis} = \frac{\dot{n}_{demand,H_2}}{\dot{n}_{demand,O_2} * 2} * 100 \tag{7.17}$$

In a comparable manner, the relationship between H_2 produced from biogas and H_2 required from electrolysis for stoichiometric SynGas injection into the MeOH-synthesis system (SN = 2) can be described as

$$\phi_{H_2} = \frac{\dot{n}_{H_2,el}}{\dot{n}_{H_2,ATR}} \tag{7.18}$$

with values larger than 1 indicating more hydrogen in the system being supplied through the electrolysis unit and values lower 1 indicating hydrogen supply weighted towards ATR reformate.

7.3.2. System Start-Up and Determination of Steady-State

Autothermal Reforming

Startup of the ATR requires heat-up of the combined heat exchanger and the reforming reactor itself. The energy required to temper the system is supplied through electrical trace heating of the system. During system heat-up, N_2 is fed through the system for inertization. The heat supplied to the system before autothermal operation is defined by the energy requirement for full evaporation of the dosed H_2O stream and the minimal heat required for the ignition of the partial CH_4-oxidation reaction, which has been reported to be around 230 - 400 °C - depending on the applied catalyst structures [54, 55]. 400 °C was chosen as target temperature set point for reformer start-up in the piloting of the described plant. When both the reforming reactor and the combined heat exchanger reached the necessary temperatures for catalyzed CH_4-oxidation and total vaporization of the H_2O feed, H_2O was dosed into the system. Biogas-injection was started as soon as the vapor stream reached the inlet of the reforming reactor, which was indicated reliably by a temperature drop at reactor inlet - temperatures being continuously monitored throughout operation of the reformer. Cascaded feed injection in reactor start-up was necessary to avoid soot formation and keep the reactor in its defined operating window, as is common in industrial full-scale reformer operation [56]. As H_2O vapor and biogas mix at the catalyst inlet, the endothermic steam reforming reaction (equation 7.1) is triggered, which lead to a second temperature drop at reformer catalyst inlet. At this point, O_2-injection was triggered and λ was increased until a stable operating temperature was reached under constant biogas load and H_2O injection rates. For system equilibration the ATR was operated at low operating loads until stable steady state operation at $\lambda < 0.3$ and S/C =1.3 was recorded. After system equilibration, a different set-point for ATR operation was chosen and applied for system testing. Gas compositions for biogas entering the reforming unit and for dried SynGas were monitored online with S/C and λ both being calculated through the measured biogas input feed and its composition. Produced SynGas was purged in system start-up.

Methanol Synthesis

For the start-up of MeOH synthesis, the system was pressurized with pure H_2, with the purge gas valve closed and the recycling gas pump set to achieve a GHSV of around 5.000 h^{-1}. During pressurization, the reactors and SynGas heat exchanger were heated using the thermostat (HKS200 - figure 7.2). After reaching the desired system pressure, the compressor (P110 - figure 7.2) was shut of and H_2 was recycled through the system until temperature equilibration of the system was reached. After temperature equilibration in the closed H_2-synthesis loop, injection of SynGas was started (compare figure 7.4). In MeOH-synthesis-only operation, a SynGas-set point was chosen and CO- and CO_2-injection was controlled to achieve a constant SynGas stream with $3 > SN > 2$ and COR 0.5 - 1.0. P110 was then re-engaged for constant SynGas-feed into the system. In combined operation, P110 was engaged and the 3-way valve separating reforming unit and MeOH synthesis was switched to allow for SynGas pumping into the MeOH synthesis. Gas composition was monitored after P110, after reactor pass or in the recycling gas loop prior to pumping towards gas mixer. To achieve a certain SN, H_2 is dosed according to the composition of SynGas before entering the gas mixer (B120 - figure 7.2). This guaranteed optimal composition of feed SynGas but in turn lead to suboptimal SynGas compositions in recycling gas or in mixed SynGas prior to entering the reactors, which could be counteracted upon through superstoichiometric H_2-dosing towards higher SynGas SN.

7.3.3. Combined operation of ATR and MeOH Synthesis

For combined operation of the two subsystems, a system start-up according to the aforementioned protocols is carried out for each of the processes. Herein, MeOH synthesis is pressurized using pure H_2 as a medium, thus also guaranteeing full reduction of the applied catalysts before combined SynGas-operation. The separated operation of ATR and MeOH synthesis is ensured by a 3-way valve. Once equilibrated system operation at low load for ATR and H_2-only synthesis loop pressurization for MeOH synthesis are reached, the valve is switched and P110 engaged to allow for SynGas compression into the MeOH synthesis.

7.4. Results

7.4.1. System Start-Up of ATR

System Start-Up of the ATR unit was comparatively straightforward in standalone operation. Reformate composition was controllable directly through H_2O injection and adaption of λ, CO-content of the raw SynGas was directly correlated to O_2-injection. Figure 7.4 shows gas compositions in the reformer exit SynGas for dosing ramp-up of O_2 and H_2O vapor for a setpoint at 2.0 kg/h (2.4m^3/h - 68% system load). The recorded time represents actual day-time of the presented start-up protocol - the start-up procedure was started at 9:20 am, steady-state reformate conditions were reached 10 minutes later. As can be observed, CH_4 and CO_2-content of the reformer effluent reflect the composition of raw biogas at the beginning of the start-up procedure. Increased λ leads to a gradual decrease of residual CH_4 down to near total oxidation 15 minutes into the reformer start-up. The system reaches a steady state at λ = 0.3 and S/C = 1.8 after 25 minutes. A slight increase of S/C at 09:45 is clearly reflected in a slight change of reformer effluent COR, with CO dipping by about 3 percentage points through the increase in vapor injection. Equilibration of the reformer system is reached only a few minutes after the change in S/C.

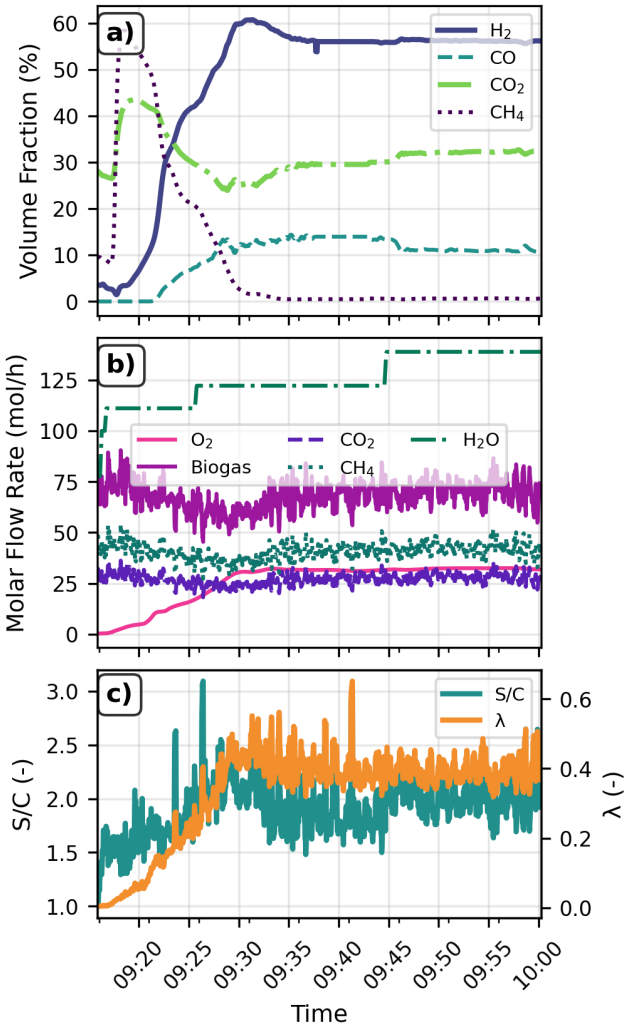

Figure 7.4.: Reformer Start-Up after preheating of the catalytic chamber and the combined heat exchanger and start of O_2-injection for autothermal operation. a) Reformate composition after reformer start-up. Steady-state gas composition is reached after 10 minutes. b) Record of feed injection into reformer for the depicted start-up procedure. c) λ and S/C for the presented start-up protocol.

7.4.2. Operation of the Biogas ATR

For identification of optimal ATR operational parameter set points, a series of tests was carried out using different S/C, λ and GHSV.

Biogas composition in the test runs reported on was approximately 60%$_{vol}$ CH_4 and 40%$_{vol}$ CO_2. Nominal capacity of the reforming unit and subsequently for the entire bio-MeOH-synthesis plant was reached at 3.5 m^3/h biogas. This translated to a space velocity of approximately of 15.000h^{-1} applying λ of 0.3 and S/C of 1.3. Depending on S/C, λ had to be set to 0.2 to 0.45 to achieve truly autothermal reforming conditions, with H_2O evaporation consuming significant amounts of the heat generated through partial CH_4-oxidation. In ATR-only tests, S/C was set at 1.3. This ensured the minimization of soot production with H_2O injection inhibiting the production of soot through carbonization [57]. Overall biogas feed and λ were set accordingly to achieve autothermal conditions and operational optimization was directed towards the optimization of COR and SN in the SynGas produced, with high SN and low COR being generally favorable for effective SynGas conversion toward MeOH over $CuO/ZnO/Al_2O_3$-based catalysts [58].

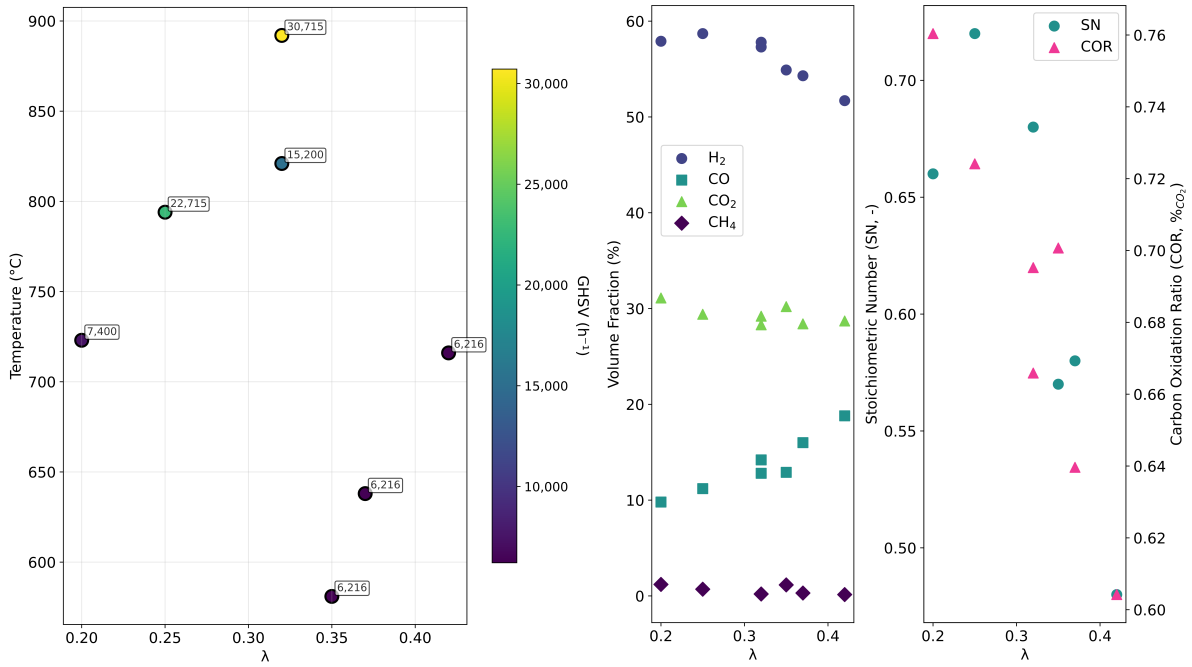

Figure 7.5.: Operational Results for separate ATR-operation under different GHSV and λ at S/C = 1.3

Figure 7.5 depicts the steady state results for the pilot ATR unit at S/C = 1.3 for varying λ and GHSV. At constant GHSV, increasing λ leads to expected higher temperatures inside the catalytic reaction chamber of the reformer as more CH_4 is oxidized. Increased feed rates and subsequent higher GHSV also lead to an increase in reaction temperature as the overall molar catalytic turnover is increased to yield higher reforming temperatures. Through change in GHSV, the load setpoint of the plant is controlled and different GHSV at set λ and S/C slightly influence the performance of the reforming unit with changing gas residence times in the catalytic reactor. An increase in GHSV at constant λ and S/C led to increased CH_4 conversion to CO, benefiting the resulting SynGas COR and SN with H_2-content in the reformate not being affected much by the reduction of gas residence time. This is in line with previous reports in autothermal and steam-methane biogas reforming [59]. At nominal load, the highest H_2-content and highest SN are reached at λ = 0.25, although CO_2-contents are significantly higher at low λ. This is attributed to the fact, that CO_2-content does

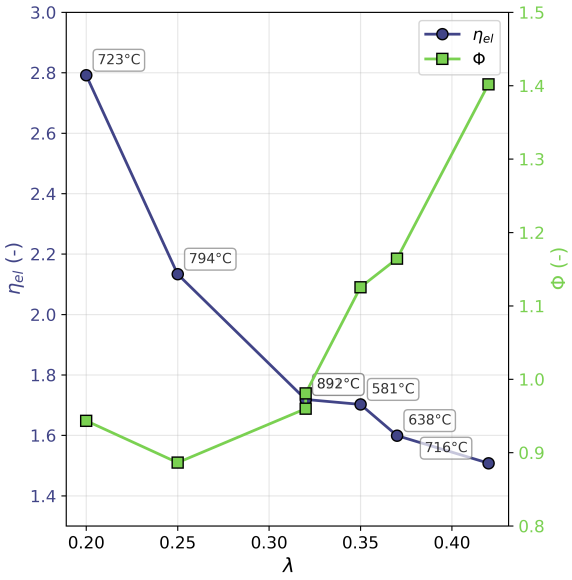

Figure 7.6.: Φ and η_{el} of the different tested operational setpoints for the ATR

not change much at all over changing λ, implying that most of the CO_2-content observed in the SynGas actually stems directly from the biogas input, not being converted but passing through the reformer inertly. The CO-content however significantly changes with increasing λ, indicating partial oxidation and contributing to COR and SN through enhancing CO-content in the SynGas. Figure 7.6 shows calculated ϕ and η_{el} for the previously mentioned λ tested in ATR-only operation. As can be taken from the figure $\lambda = 0.25$ generates SynGas with the highest H_2-content, leading to the lowest additional theoretical H_2-injection into the coupled MeOH-synthesis system. At the same time, increased λ leads to less favorable COR and higher additional H_2-demands in the MeOH-synthesis process. In industrial application this would lead to a higher demand for installed electrolysis power but to a more equalized consumption of pure H_2 and O_2 from the coupled electrolysis unit. Overall this shows, that lower λ lead to more favorable conditions for SynGas conversion to MeOH, also reducing pure O_2-demand in large scale application of the technology in combination with electrolysis.

7.4.3. Operation of MeOH-Synthesis Loop

System start-up and equilibration

As single-pass conversion ratios inside the MeOH reactors are usually considerably lower than 50%, high portions of the SynGas fed to the reactors stem from gas recycling through the recycling loop [60]. A steady-state reaction state is only reached, once the state inside the loop, or alternatively at reactor inlet has balanced out to a constant gas composition, constant temperature and constant feed rate. For investigation of the steady-state gas compositions reached in MeOH synthesis from reformed biogas, different reformate mixtures were tested towards their respective subsequent steady-state reaction compositions. Figure 7.7 shows the start-up composition development in the SynGas recycling loop for four different input gas compositions. The input gas COR dosed into the system through the compressor is given for each plot. All test compositions were tested at SN = 3. As can be taken from the figure, mixed carbon-oxide gas compositions set in for all tested input gas COR. Even in pure CO_2-dosing (COR = 1), a recycle loop COR of 0.63 is reached after equilibration of system gas compositions. This highlights the importance of mixed carbon-oxide testing

in catalyst development, as overall gas compositions in synthesis loops will always contain some amount of CO produced through RWGS. Dosing of SynGas compositions of COR around 0.64-0.68 leads to near equalization of the carbon-oxide content in the recycling gas stream, with both CO- and CO_2-content evening out at 10,5 $\%_{vol}$. The system equalization was usually reached approximately 2 hours after the change in the setpoint of the system, with the CO_2-only SynGas dosing facilitating the longest equalization times after the change of the system setpoint. This has important implications for the dynamic operation of future E-MeOH and Bio-MeOH process plants, as system setpoint or load changes do not reflect in the recycling gas composition quickly.

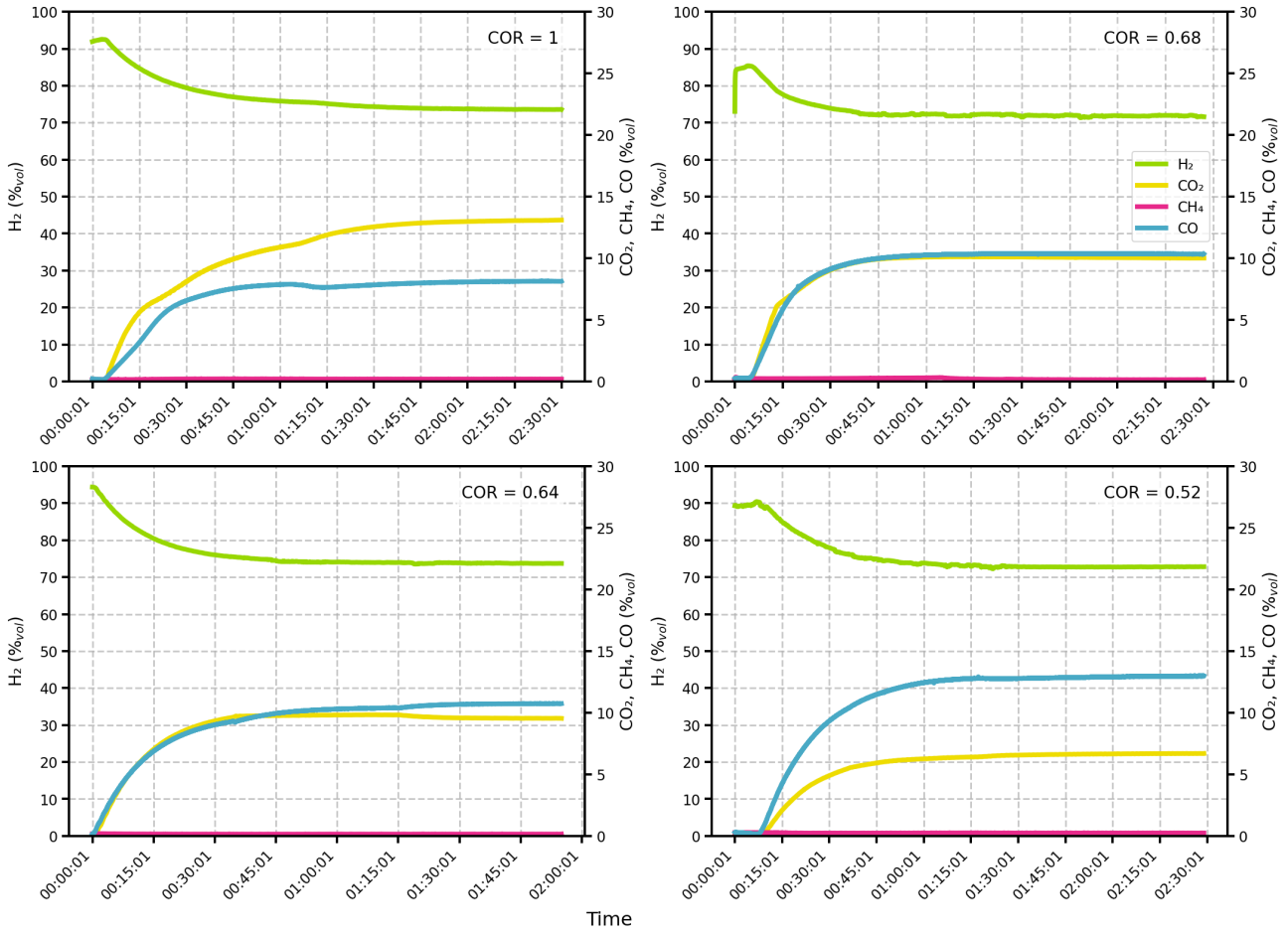

Figure 7.7.: Recycle Loop Gas Composition after System Start-Up (t = 0:00) of the Methanol Synthesis Unit. Depicted COR reflects the COR of injected SynGas into the system over the period of system start-up and equilibration. Times used in x-axes refer to test dureation from the beginning of the recording.

Steady State Operation Results

The MeOH synthesis unit was tested for conversion efficiency, equilibrium system gas compositions and methanol yields with several different input SynGas streams. In MeOH-only operation, these compositions were taken from equilibrium calculations for the ATR, yielding four probable SynGas composition concerning COR and an additional test condition for COR = 1, dosing only CO_2 and H_2, representing E-MeOH operation of the system, where pure CO_2 would be dosed from an upstream carbon-capture process such as membrane CO_2-capture or amine-washing-applications [61]. As SynGas was not expected to deliver stoichiometric

H_2-contents, SN was not considered as a factor in choosing applicable ATR-conditions for the MeOH-system-only operation runs. For each of the calculated COR, SN could be set to stoichiometric or superstoichiometric conditions through pure H_2 injection. As system pressure was limited to 20 bar, conversion ratios were expected to be low compared to industrial applications on the basis of previous laboratory results for the catalyst sample applied in this work [47]. Therefore, the investigation presented herein concentrates on the influence SynGas COR, reactor temperatures, and SN on the synthesis performance in MeOH synthesis as well as the resulting conditions in mixed SynGas streams. Increasing the reaction pressure will significantly impact equilibrium reaction conditions over the catalyst and leads to significantly improved $X_{C_{sp}}$ in steady-state system operation, with some studies showing a two-fold increase in MeOH yield over an two-fold increase of reaction pressure, depending on GHSV and reaction temperatures [62, 63].
Figure7.8 depicts different STY, $X_{C_{sp}}$ and resulting steady state reactor influent COR, calculated from SynGas COR and recycling gas COR with corresponding mass flow rates. Tests with COR 0.66 COR reformate influent show the highest overall STY and $X_{C_{sp}}$ at 250 °C and 20 bar reactor pressure and also lead to the highest SynGas COR in steady-state operation reactor entry. This can most likely be attributed to the composition being close to the the steady-state synthesis gas composition in MeOH synthesis over the herein tested quinary carrier catalyst. Through this, CO_2 is converted less readily towards CO through RWGS, making it available for MeOH generation with less of the otherwise produced CO being purged from the system in system pressure regulation. This is shown in the rightmost plot for reactor influent COR, where the average COR calculated at reactor entry is closest to raw SynGas COR at 66%. Additionally, the herein measured 0.11 $g_{MeOH}/g_{Catalyst}/h$ STY_{MeOH} quite accurately reproduces formation rates previously reported for the catalyst at 20 bar reaction pressures and comparable SynGas COR [47]. GHSV has a profound effect in MeOH generation. In laboratory set-ups, GHSV can be controlled independently of other system parameters. In pilot operation, this control is not applicable, as GSHV is directly correlated to conversion and purge ratios, which in turn are directly correlated to temperature, COR, SN and GSHV again. An overview over GHSVs influence on STY_{MeOH} is given in the supplementary files (appendix C, figure C.1).

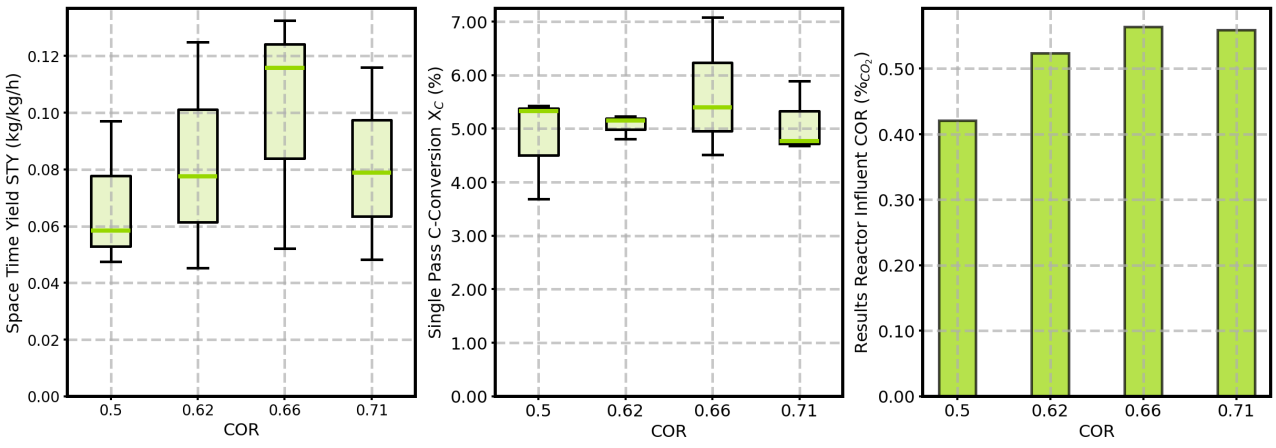

Figure 7.8.: STY_{MeOH}, $X_{C_{sp}}$ and resulting reactor influent COR for four different SynGas COR used in separate MeOH testing

In E-MeOH-operation (COR = 1), the reactor temperature has a major influence on the conversion results, as RWGS is greatly influenced by it. High temperatures facilitate higher rates for the reverse shift, resulting in a significantly lower COR in the synthesis loop and an overall shift towards H_2O production [64, 65]. As is expected and as is shown in figure 7.9, high temperatures lead to the highest overall STY, but lead

to a drop in system COR by 30 percentage points. Raw product composition is shifted from 45% MeOH contents to 35% between 225 °C and 275 °C reactor temperatures with the overall production rates increasing nearly threefold over this temperature range. This again demonstrates the importance of mixed carbon-oxide conversion efficacy of future catalyst systems towards selective conversion of CO_2 to MeOH and the inhibition of premature CO desorption in RWGS in renewable Bio- or E-MeOH processes.

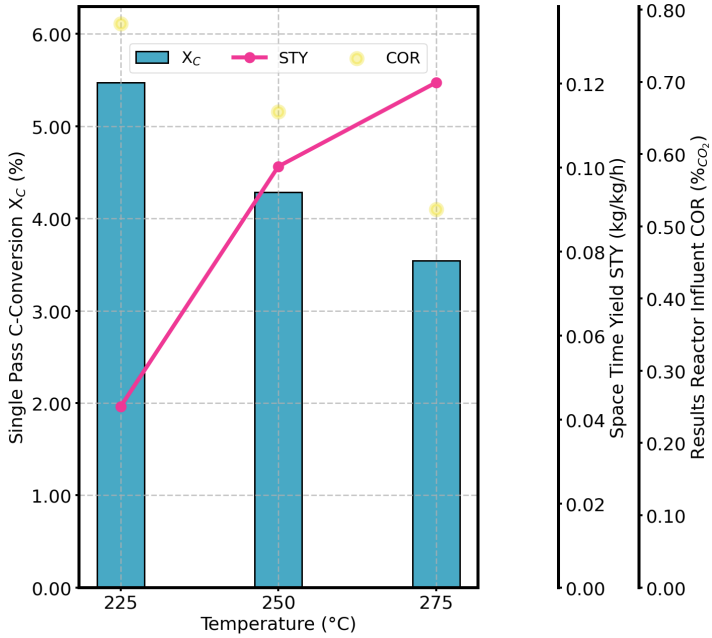

Figure 7.9.: MeOH-unit STY, $X_{C_{sp}}$ and resulting reactor influent COR in CO_2-only operation at different temperatures and SN = 2

7.4.4. Combined System Operation

Operational aspects of combined system start-up and operation

In large scale fossil MeOH-synthesis operation, start-up and shut down procedures are not commonly performed. In decentralized production of Bio-MeOH or E-MeOH, volatile plant operation according to external factors like electricity spot market price are more likely in the future and can impact operating costs or cost of production for MeOH [66, 67]. Equally, operation with or without reforming unit is possible, reacting to price changes for flexible plant operation. Likewise, small-scale and pilot plant operation facilitate more frequent start-up procedures taking into account safety measures and effective start-up times.

For combined system operation, start-up procedures of the separate thermochemical systems were carried out following the aforementioned protocols. Once a steady-state was reached in both subsystems, they were connected, switching the three-way valve separating both subsystems from purge operation to combined operation. While in principal easily attainable, pressure gradients in the gas feed line between reforming unit and compressor during the short moment of system merging were observed repeatedly. These were most probably caused by a short reduction of reformer effluent flow rate while compressor entry pressures equalized. This short adjustment period lead to a slightly increased retention time of the SynGas inside the ATR catalyst chamber. The reduced GHSV through the reforming unit in turn lead to increased residence time and slightly intensified catalytic reaction rates of CH_4 and O_2 leading to short term temperature spikes , which led to automated system shut-off in system piloting on multiple occasions [60].

Based upon these observations, a combined system start-up procedure was optimized operationally. For safety measures, both subsystems were operated at steady state, minimal load conditions, which were dictated by the minimal feed rate of the SynGas compressor, ca. 65%. Furthermore, λ was reduced to a minimum, guaranteeing a low GHSV through the reformer and inhibiting combustion that exceeds the set-point range limits of the reformer in system-merging. For future application, initial system start-up is advised to be carried out in merged process configuration to avoid the hydraulic disadvantages of valve switching between two steady-state processes. The possibilities of dynamic, economically optimized E-MeOH operation of combined systems necessitates operationally robust procedures for merging.
In steady-state system operation the low conversion performance of the applied, prototype MeOH catalyst at the limited applicable system pressures resulted in a second operational obstacle: As SynGas was not converted to liquid product at the expected rates, more of the gas inside the MeOH-synthesis loop had to be recycled. For optimal overall performance, this lead to the reduction of reformer load and the decreasing of compressor load and subsequent minimization of reformate fed into the pressurized MeOH synthesis.
As the compressor was limited in is minimum load operation (65%), more SynGas was compressed into the system, as could be converted for system pressure equilibration. In turn, gas purging had to be increased to unusual high proportions, in order to attain steady-state combined operation set points which led to the emission of excessive amount of unconverted carbon. In overall system performance assessment, this led to poor total conversion ratios in combined system testing and reduced the amount of possible system set points. In future system optimization, system pressure will be increased and a modern commercial catalyst applied. For higher conversion ratios, this will increase the range of possible SynGas feed setpoints, reduce the amount purged off-gas and improve the ratio between recycled gas and injected reformate.

Results of combined system operation

For combined system operation, the system was operationally optimized towards minimization of off-gas purging and reformer operation stability, thus providing the basis for long-term steady state operation and maximizing overall SynGas conversion towards MeOH. In system testing, four stable operational set points were found, tested and optimized. Due to the overall low conversion at the aforementioned synthesis pressures, very high recycling ratios were applied to ensure maximum overall residence time of the injected carbon-oxide species in the MeOH reactors. This lead to high GHSV through the MeOH reactors, in turn impacting the system performance with higher GHSV having to be shown to increase MeOH yield but reduce overall conversion ratios in mixed carbon-oxide SynGas streams [68].
Figure 7.10 depicts the calculated molar and energy flux inside the system for a typical steady-state set point utilizing S/C = 1.58 and λ = 0.32 in the ATR and adding H_2 to SN = 2.25. The molar flux was calculated using mass flow measurements inside the system and online gas composition measurements to determine the molar mass of the stream and the overall molar flux. Energy flux was calculated using the heating values (HHV) of the species in each molar stream depicted in the system. As can be taken from the figure, the ratio between recycling gas stream (Stream 4) and reformate input stream (Stream 3b) is 14.46, exceeding industrial application standards three- to six-fold [50]. Concerning chemical efficiency of the system, an overall efficiency of 25,29% was reached for the steady state depicted in figure 7.10. As described in subsection 4.4.1, this is due to the excessive amount of gas purging related to the minimal compressor set point for steady state operation. In the referenced steady state set point, approximately twice the energy flux was purged through H_2- and CO-content of off-gas emitted from the synthesis.

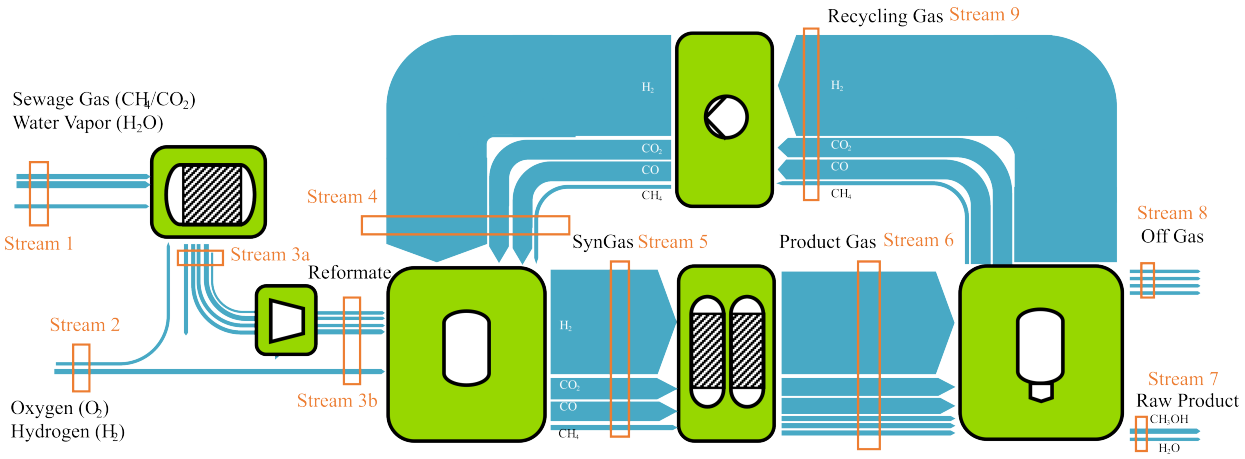

Species (-)	Stream 1 (mol/h)	Stream 2 (mol/h)	Stream 3a (mol/h)	Stream 3b (mol/h)	Stream 4 (mol/h)	Stream 5 (mol/h)	Stream 6 (mol/h)	Stream 7 (mol/h)	Stream 8 (mol/h)	Stream 9 (mol/h)
H_2		115,0	84,8	199,8	2686,1	2885,9	2791,2		105,3	2686,1
O_2		27,5								
CH_4	41,8		2,1	2,1	50,7	52,8	103,5		1,9	50,7
CO_2	27,9		46,3	46,3	517,1	563,4	534,2		20,3	517,1
CO			21,2	21,2	509,6	530,8	535,6		19,9	509,6
H_2O	111		97,2	10,3		10,3	45,7	45,7		
CH_3OH							24,3	24,3		

Species (-)	Stream 1 (kW)	Stream 2 (kW)	Stream 3a (kW)	Stream 3b (kW)	Stream 4 (kW)	Stream 5 (kW)	Stream 6 (kW)	Stream 7 (kW)	Stream 8 (kW)	Stream 9 (kW)
H_2		7,73	5,70	13,43	180,57	194,00	187,63		7,08	180,57
O_2										
CH_4	9,31		0,47	0,47	11,29	11,76	23,06		0,42	11,29
CO_2										
CO			1,67	1,67	40,06	41,73	42,10		1,56	40,06
H_2O										
CH_3OH							4,31	4,31		
Total	9,31	7,73	7,83	15,57	231,92	247,49	257,10	4,31	9,07	231,92

Figure 7.10.: Sankey Diagram of the balanced steady state system for the combined operation of ATR and MeOH synthesis with molar and energy flux given for each compounded process stream. Bar thickness correlates to molar flux.

Results for the five steady state system setpoints typically reached and optimized in combined system operation are given in table 7.1. As reformate COR and SN did not widely vary across the different reached setpoints and system loads, dosed H_2 and overall equilibrium gas compositions in the MeOH-synthesis loop did not change significantly as well. This is reflected accordingly in the recorded reformate COR and SN as well as MeOH-synthesis loop COR, which are in a range of 16% of each other when comparing the minimal and maximal set point values achieved in the system testing. The highest STY_{MeOH} is reached at the highest stable system load, which was operationally achieved at approximately 71% compressor revolutionary speed, equal to 5Nm³/h of reformate injection into the system or around 3,2 kg/h.

Table 7.1.: Performance Data for Combined Operation Series at moderate system loads

Load (%)	65	66	71	68	68
λ (–)	0.31	0.31	0.36	0.32	0.32
S/C (–)	1.39	1.36	1.49	1.58	1.42
COR_{Ref} (%)	0.72	0.65	0.62	0.67	0.66
SN_{Ref} (–)	0.61	0.58	0.62	0.57	0.58
$\eta_{electrolysis}$ (%)	187	191	160	184	185
COR_{Syn} (%)	0.57	0.51	0.49	0.51	0.53
MeOH STY (kg/kg$_{cat}$/h)	0.08	0.09	0.13	0.12	0.11
X_c (%)	31	36	39	37	35
MeOH (%wt)	33.6	37.2	39.4	38.5	38.0
H_2O (%wt)	66.4	62.8	60.6	61.5	62.0

7.5. Conclusion and Outlook

In the herein presented work, we designed, commissioned and operated a pilot plant for producing MeOH from biogas through a complex system comprising of an ATR and a MeOH-synthesis loop, utilizing pure O_2 for operation of the ATR and pure H_2 for improving SynGas stoichiometry in MeOH synthesis. The system is designed on a small but fully operational scale to represent a future system applying electrolysis for the supply of H_2 and O_2. We operate both thermochemical systems independently of each other, optimizing both subsystems towards efficient set-points independently of each other, testing the MeOH-synthesis loop additionally for its effectiveness in handling SynGas comprising of pure CO_2 and H_2. Furthermore, we introduce an operational approach for coupled system start-up and stable operation. We identify several operational hurdles in system design and stable steady-state operation and propose strategies for overcoming the identified hurdles. Overall, the herein proposed system shows high potential towards future application in decentralized material usage of biomass of biogas, while several key obstacles prevail on the path to industrialized application of the biogas-to-MeOH process, both on a pilot-scale level as well as future industrial scale levels: On the tested pilot scale of the system, back pressure gradients in ATR and MeOH-synthesis coupling lead to complications in λ-, S/C and subsequent temperature regulation in ATR. To tackle these complications, we propose a minimal load start-up operation set point to avoid temperature fluctuations in system coupling, thus laying the foundations for stable system start-up and future applications, where system load could be managed according to external factors such as electricity spot-market prices. In MeOH synthesis, low applied system pressure and overall reduced activity of the novel tested catalyst lead to decreased conversion of both CO and CO_2 towards MeOH in the reactors. This in turn leads to excessive gas purging from the system, as minimal reformate feed is limited by the operational range of the compressor P110. This leads to suboptimal setpoints in the MeOH-synthesis loop, utilizing very high recycling ratios and subsequent GHSV through the parallel MeOH reactors. Nonetheless, the presented work demonstrates the possible potential of the system under further optimization. As similar, theoretical studies have shown, minimizing the purge gas ratio and maximizing $X_{c_{sp}}$ by applying higher system pressures and utilizing MeOH catalysts of industrial efficiency, the system should be able to achieve η_{ch} of 50-60% in the future [11, 23]. Especially in Germany, where many decentralized biogas facilities are in need of value added alternatives to biogas applications as fuel for electricity and heat production, decentralized systems for material biogas conversion towards fuels of chemical substitutes can play a central role in de-fossilization of the otherwise fossil carbon reliant industries.

References

[1] Tawfik A. Saleh. "A review on the technologies for converting biomass into carbon-based materials: sustainability and economy". In: *Bioresource Technology Reports* 25 (2024), p. 101771. ISSN: 2589014X. DOI: 10.1016/j.biteb.2024.101771.

[2] Muhammad Shahbaz et al. "A comprehensive review of biomass based thermochemical conversion technologies integrated with CO2 capture and utilisation within BECCS networks". In: *Resources, Conservation and Recycling* 173 (2021), p. 105734. ISSN: 09213449. DOI: 10.1016/j.resconrec.2021.105734.

[3] Martin Dotzauer et al. *Kurzstudie zur Rolle von Biogas für ein klimaneutrales, 100 % erneuerbares Stromsystem 2035*. Ed. by DBFZ Deutsches Biomasseforschungszentrum gemeinnützige GmbH and Wuppertal Institut für Klima, Umwelt, Energie. Leipzig. URL: https://www.dbfz.de/fileadmin/user_upload/Referenzen/Studien/Kurzstudie_Biogas_2022.pdf.

[4] Naveen Chandra Joshi et al. "A concise review on waste biomass valorization through thermochemical conversion". In: *Current research in microbial sciences* 6 (2024), p. 100237. DOI: 10.1016/j.crmicr.2024.100237.

[5] R. Suresh et al. "Biomass waste as an alternative source of carbon and silicon-based absorbents for CO2 capturing application". In: *Chemosphere* 343 (2023), p. 140173. DOI: 10.1016/j.chemosphere.2023.140173.

[6] Vijayakumar Pradeshwaran, Vijayabharathi Sundaramoorthy, and Ayyadurai Saravanakumar. "A comprehensive review on biogas production from food waste: Exploring cutting-edge technologies and innovations". In: *Biomass and Bioenergy* 188 (2024), p. 107336. ISSN: 09619534. DOI: 10.1016/j.biombioe.2024.107336.

[7] Dhruv Singh, Piero Sirini, and Lidia Lombardi. "Review of Reforming Processes for the Production of Green Hydrogen from Landfill Gas". In: *Energies* 18.1 (2025), p. 15. DOI: 10.3390/en18010015.

[8] Derek T. Troiano et al. "Toward optimal use of biomass as carbon source for chemical bioproduction". In: *Current opinion in biotechnology* 81 (2023), p. 102942. DOI: 10.1016/j.copbio.2023.102942.

[9] Chundong Zhang et al. "Carbon dioxide utilization in a gas-to-methanol process combined with CO 2 /Steam-mixed reforming: Techno-economic analysis". In: *Fuel* 190 (2017), pp. 303–311. ISSN: 00162361. DOI: 10.1016/j.fuel.2016.11.008.

[10] Stefano Sollai et al. "Renewable methanol production from green hydrogen and captured CO2: A techno-economic assessment". In: *Journal of CO2 Utilization* 68 (2023), p. 102345. ISSN: 22129820. DOI: 10.1016/j.jcou.2022.102345.

[11] Stefan Bube et al. "Power and biogas to methanol – A techno-economic analysis of carbon-maximized green methanol production via two reforming approaches". In: *Energy Conversion and Management* 304 (2024), p. 118220. ISSN: 01968904. DOI: 10.1016/j.enconman.2024.118220.

[12] Sasan Dabir et al. "Feasibility Study of Biogas Reforming To Improve Energy Efficiency and To Reduce Nitrogen Oxide Emissions". In: *Industrial & Engineering Chemistry Research* 56.5 (2017), pp. 1186–1200. ISSN: 0888-5885. DOI: 10.1021/acs.iecr.6b04290.

[13] Rei-Yu Chein et al. “Analysis of methanol synthesis using CO2 hydrogenation and syngas produced from biogas-based reforming processes”. In: *Chemical Engineering Journal* 426 (2021), p. 130835. ISSN: 13858947. DOI: 10.1016/j.cej.2021.130835.

[14] F. Rau et al. “Efficiency of a pilot-plant for the autothermal reforming of biogas”. In: *International Journal of Hydrogen Energy* 44.35 (2019), pp. 19135–19140. ISSN: 03603199. DOI: 10.1016/j.ijhydene.2018.04.014.

[15] Rosa Zuloeta Bonilla and Ramchandra Bhandari. “Small-Scale Hybrid Methanol–Methane Production Based on Biogas: Stochastic Sensitivity Analysis of the Economic Sustainability”. In: *Energies* 15.24 (2022), p. 9329. DOI: 10.3390/en15249329.

[16] Emanuele Moioli and Tilman Schildhauer. “Eco-Techno-Economic Analysis of Methanol Production from Biogas and Power-to-X”. In: *Industrial & Engineering Chemistry Research* 61.21 (2022), pp. 7335–7348. ISSN: 0888-5885. DOI: 10.1021/acs.iecr.1c04682.

[17] V. Kharitonov et al. “Modelling of Methanol Production From Biogas”. In: *Latvian Journal of Physics and Technical Sciences* 60.s6 (2023), pp. 35–43. DOI: 10.2478/lpts-2023-0043.

[18] Philipp Kenkel, Timo Wassermann, and Edwin Zondervan. “Biogas Reforming as a Precursor for Integrated Algae Biorefineries: Simulation and Techno-Economic Analysis”. In: *Processes* 9.8 (2021), p. 1348. DOI: 10.3390/pr9081348.

[19] Mar Pérez-Fortes et al. “Methanol synthesis using captured CO2 as raw material: Techno-economic and environmental assessment”. In: *Applied Energy* 161 (2016), pp. 718–732. ISSN: 03062619. DOI: 10.1016/j.apenergy.2015.07.067.

[20] M. Rivarolo et al. “Feasibility study of methanol production from different renewable sources and thermo-economic analysis”. In: *International Journal of Hydrogen Energy* 41.4 (2016), pp. 2105–2116. ISSN: 03603199. DOI: 10.1016/j.ijhydene.2015.12.128.

[21] Gaetano Iaquaniello et al. “Waste-to-methanol: Process and economics assessment”. In: *Bioresource technology* 243 (2017), pp. 611–619. DOI: 10.1016/j.biortech.2017.06.172.

[22] Borja Hernández and Mariano Martín. “Optimal Process Operation for Biogas Reforming to Methanol: Effects of Dry Reforming and Biogas Composition”. In: *Industrial & Engineering Chemistry Research* 55.23 (2016), pp. 6677–6685. ISSN: 0888-5885. DOI: 10.1021/acs.iecr.6b01044.

[23] Riccardo Rinaldi et al. “Techno-economic analysis of a biogas-to-methanol process: Study of different process configurations and conditions”. In: *Journal of Cleaner Production* 393 (2023), p. 136259. ISSN: 09596526. DOI: 10.1016/j.jclepro.2023.136259.

[24] Lúcia Bollini Braga et al. “Hydrogen production by biogas steam reforming: A technical, economic and ecological analysis”. In: *Renewable and Sustainable Energy Reviews* 28 (2013), pp. 166–173. ISSN: 13640321. DOI: 10.1016/j.rser.2013.07.060.

[25] Juan Félix González, Carmen María Álvez-Medina, and Sergio Nogales-Delgado. “Biogas Steam Reforming in Wastewater Treatment Plants: Opportunities and Challenges”. In: *Energies* 16.17 (2023), p. 6343. DOI: 10.3390/en16176343.

[26] Ravindra Kumar, Anil Kumar, and Amit Pal. “Overview of hydrogen production from biogas reforming: Technological advancement”. In: *International Journal of Hydrogen Energy* 47.82 (2022), pp. 34831–34855. ISSN: 03603199. DOI: 10.1016/j.ijhydene.2022.08.059.

[27] Lukasz Szablowski, Malgorzata Wojcik, and Olaf Dybinski. "Review of steam methane reforming as a method of hydrogen production". In: *Energy* 316 (2025), p. 134540. ISSN: 03605442. DOI: 10.1016/j.energy.2025.134540.

[28] Hyunjin Park and Philipp Grundmann. "Institutional work after hype: The case of biogas in Germany". In: *Energy Research & Social Science* 119 (2025), p. 103820. ISSN: 22146296. DOI: 10.1016/j.erss.2024.103820.

[29] Wolfgang Britz and Ruth Delzeit. "The impact of German biogas production on European and global agricultural markets, land use and the environment". In: *Energy Policy* 62 (2013), pp. 1268–1275. ISSN: 03014215. DOI: 10.1016/j.enpol.2013.06.123.

[30] F. Rau et al. "Entwicklung eines autothermen Biogasreformers zur Herstellung von Wasserstoff". In: *14. Symposium Energieinnovation* (2016). URL: https://www.tugraz.at/fileadmin/user_upload/Events/Eninnov2016/files/lf/Session_B3/LF_Rau.pdf.

[31] Florian Nestler et al. "Methanol Synthesis – Industrial Challenges within a Changing Raw Material Landscape". In: *Chemie Ingenieur Technik* 90.10 (2018), pp. 1409–1418. ISSN: 0009-286X. DOI: 10.1002/cite.201800026.

[32] Stefan Rabe, Thanh-Binh Truong, and Frédéric Vogel. "Catalytic autothermal reforming of methane: Performance of a kW scale reformer using pure oxygen as oxidant". In: *Applied Catalysis A: General* 318 (2007), pp. 54–62. ISSN: 0926860X. DOI: 10.1016/j.apcata.2006.10.043.

[33] M. Luneau et al. "High-throughput assessment of catalyst stability during autothermal reforming of model biogas". In: *Catalysis Science & Technology* 5.9 (2015), pp. 4390–4397. ISSN: 2044-4753. DOI: 10.1039/C5CY00702J.

[34] Vikram Rathod and Purnanand V. Bhale. "Experimental Investigation on Biogas Reforming for Syngas Production over an Alumina based Nickel Catalyst". In: *Energy Procedia* 54 (2014), pp. 236–245. ISSN: 18766102. DOI: 10.1016/j.egypro.2014.07.267.

[35] Fabián Guerrero et al. "Syngas Production From the Reforming of Typical Biogas Compositions in an Inert Porous Media Reactor". In: *Frontiers in chemistry* 8 (2020), p. 145. ISSN: 2296-2646. DOI: 10.3389/fchem.2020.00145.

[36] Z. HOU et al. "Deactivation of Ni catalysts during methane autothermal reforming with CO2 and O2 in a fluidized-bed reactor". In: *Journal of Catalysis* 250.2 (2007), pp. 331–341. ISSN: 00219517. DOI: 10.1016/j.jcat.2007.06.023.

[37] Alessandra Di Nardo et al. "Hydrogen production via steam reforming of different fuels: thermodynamic comparison". In: *International Journal of Hydrogen Energy* 55 (2024), pp. 1143–1160. ISSN: 03603199. DOI: 10.1016/j.ijhydene.2023.11.215.

[38] R. Pérez-Hernández et al. "Hydrogen production by oxidative steam reforming of methanol over Ni/CeO2–ZrO2 catalysts". In: *International Journal of Hydrogen Energy* 36.11 (2011), pp. 6601–6608. ISSN: 03603199. DOI: 10.1016/j.ijhydene.2011.02.064.

[39] Hessamodin Nourbakhsh et al. "A thermodynamic analysis of biogas partial oxidation to synthesis gas with emphasis on soot formation". In: *International Journal of Hydrogen Energy* 43.33 (2018), pp. 15703–15719. ISSN: 03603199. DOI: 10.1016/j.ijhydene.2018.06.134.

[40] Sebastian T. Wismann et al. "Electrified methane reforming: Elucidating transient phenomena". In: *Chemical Engineering Journal* 425 (2021), p. 131509. ISSN: 13858947. DOI: 10.1016/j.cej.2021.131509.

[41] Julian Schittkowski et al. "The Carbon2Chem® Laboratory in Oberhausen – A Workplace for Lab–Scale Setups within the Cross–Industrial Project". In: *Chemie Ingenieur Technik* 94.10 (2022), pp. 1397–1404. ISSN: 0009-286X. DOI: 10.1002/cite.202200019.

[42] Philip Fosbol. *Biogas to be converted into methanol*. Ed. by DTU Chemical Engineering. Kopgenhagen, 2020. URL: https://www.dtu.dk/english/news/all-news/nyhed?id=0efd777e-fa21-4d15-af01-c50d2512e14f.

[43] Jenö Schipek et al. *Methanolherstellung aus Biogas mittels Dreiphasenreaktor: (COOMet)*. Ed. by GWF Gas. Freiberg, 2021. URL: https://gwf-gas.de/wp-content/uploads/2021/07/GE_07-08_2021_fb_Shipek.pdf.

[44] A. R. Akhunyanov et al. "Oxygen-Free Reforming of Methane into Synthesis Gas in the Presence of H2, H2O, CO, and CO2 Additives Taking into Account the Formation of Soot Particles". In: *Kinetics and Catalysis* 65.5 (2024), pp. 421–439. ISSN: 0023-1584. DOI: 10.1134/S0023158424601906.

[45] Kantilal Chouhan et al. "Simulation of steam reforming of biogas in an industrial reformer for hydrogen production". In: *International Journal of Hydrogen Energy* 46.53 (2021), pp. 26809–26824. ISSN: 03603199. DOI: 10.1016/j.ijhydene.2021.05.152.

[46] European Parliament. *Directive 2014/68/EU of the European Parliament and of the Council on the harmonisation of the laws of the Member States relating to the making available on the market of pressure equipment: Pressure Equipment Directive*. 15.05.2014.

[47] Carl Fritsch et al. "CO 2 –Hydrogenation to Methanol over CuO/ZnO Based Infiltration Composite Catalyst Spheres". In: *ChemCatChem* 16.21 (2024). ISSN: 1867-3880. DOI: 10.1002/cctc.202400731.

[48] Takuya Tsujiguchi, Takayuki Furukawa, and Nobuyoshi Nakagawa. "Effect of the impurities in crude bio-methanol on the performance of the direct methanol fuel cell". In: *Journal of Power Sources* 196.22 (2011), pp. 9339–9345. ISSN: 03787753. DOI: 10.1016/j.jpowsour.2011.08.025.

[49] Guanfu Liu, Helena Hagelin-Weaver, and Bruce Welt. "A Concise Review of Catalytic Synthesis of Methanol from Synthesis Gas". In: *Waste* 1.1 (2023), pp. 228–248. DOI: 10.3390/waste1010015.

[50] Vincent Dieterich et al. "Power-to-liquid via synthesis of methanol, DME or Fischer–Tropsch-fuels: a review". In: *Energy & Environmental Science* 13.10 (2020), pp. 3207–3252. ISSN: 1754-5692. DOI: 10.1039/D0EE01187H.

[51] Florian Nestler et al. "Methanol Synthesis from Sustainable Feedstocks – A Quantitative Side Product Analysis". In: *Chemie Ingenieur Technik* 96.9 (2024), pp. 1166–1176. ISSN: 0009-286X. DOI: 10.1002/cite.202400009.

[52] Marina Bukhtiyarova et al. "Methanol Synthesis from Industrial CO2 Sources: A Contribution to Chemical Energy Conversion". In: *Catalysis Letters* 147.2 (2017), pp. 416–427. ISSN: 1011-372X. DOI: 10.1007/s10562-016-1960-x.

[53] Dana S. Marlin, Emeric Sarron, and Ómar Sigurbjörnsson. "Process Advantages of Direct CO2 to Methanol Synthesis". In: *Frontiers in chemistry* 6 (2018), p. 446. ISSN: 2296-2646. DOI: 10.3389/fchem.2018.00446.

[54] Rakhi, Vivien Günther, and Fabian Mauss. "Insights into dry reforming of methane over nickel catalyst using a thermodynamic model". In: *Reaction Kinetics, Mechanisms and Catalysis* 136.3 (2023), pp. 1197–1210. ISSN: 1878-5190. DOI: 10.1007/s11144-023-02426-8.

[55] Yadong Wang et al. "Application of microimpinging stream reactor coupled with ultrasound in Cu/CeZrOx solid solution catalyst preparation for CO2 hydrogenation to methanol". In: *Renewable Energy* 202 (2023), pp. 834–843. ISSN: 09601481. DOI: 10.1016/j.renene.2022.11.075.

[56] European Industrial Gases Association, ed. *Safe Start Up and Shut Practices for Steam Reformers: Doc 185/20*. Brussles, 2018. URL: https://www.eiga.eu/uploads/documents/DOC185.pdf.

[57] Bartosz Hrycak et al. "Hydrogen production by the steam reforming of synthetic biogas in atmospheric-pressure microwave (915 MHz) plasma". In: *Scientific reports* 13.1 (2023), p. 2204. DOI: 10.1038/s41598-023-29433-y.

[58] Loretta Salano et al. "Integration of an Autothermal Outer Electrified Reformer Technology for Methanol Production from Biogas: Enhanced Syngas Quality Production and CO2 Capture and Utilization Assessment". In: *Processes* 12.8 (2024), p. 1598. DOI: 10.3390/pr12081598.

[59] Xianhui Zhao et al. "Biogas Reforming to Syngas: A Review". In: *iScience* 23.5 (2020), p. 101082. DOI: 10.1016/j.isci.2020.101082.

[60] Jiawei Zhong et al. "State of the art and perspectives in heterogeneous catalysis of CO2 hydrogenation to methanol". In: *Chemical Society reviews* 49.5 (2020), pp. 1385–1413. DOI: 10.1039/c9cs00614a.

[61] Mohd Hanifa et al. "A review on CO2 capture and sequestration in the construction industry: Emerging approaches and commercialised technologies". In: *Journal of CO2 Utilization* 67 (2023), p. 102292. ISSN: 22129820. DOI: 10.1016/j.jcou.2022.102292.

[62] Jerzy Skrzypek et al. "Thermodynamics and kinetics of low pressure methanol synthesis". In: *The Chemical Engineering Journal and the Biochemical Engineering Journal* 58.2 (1995), pp. 101–108. ISSN: 09230467. DOI: 10.1016/0923-0467(94)02955-5.

[63] Jean-François Portha et al. "Kinetics of Methanol Synthesis from Carbon Dioxide Hydrogenation over Copper–Zinc Oxide Catalysts". In: *Industrial & Engineering Chemistry Research* 56.45 (2017), pp. 13133–13145. ISSN: 0888-5885. DOI: 10.1021/acs.iecr.7b01323.

[64] Stavros-Alexandros Theofanidis et al. "On the Electrification of CO 2 -Based Methanol Synthesis via a Reverse Water–Gas Shift: A Comparative Techno-Economic Assessment of Thermo-Catalytic and Plasma-Assisted Routes". In: *Industrial & Engineering Chemistry Research* 63.27 (2024), pp. 12035–12052. ISSN: 0888-5885. DOI: 10.1021/acs.iecr.4c00301.

[65] Oh-Shim Joo et al. "Carbon Dioxide Hydrogenation To Form Methanol via a Reverse-Water-Gas-Shift Reaction (the CAMERE Process)". In: *Industrial & Engineering Chemistry Research* 38.5 (1999), pp. 1808–1812. ISSN: 0888-5885. DOI: 10.1021/ie9806848.

[66] Simone Mucci, Alexander Mitsos, and Dominik Bongartz. "Cost-optimal Power-to-Methanol: Flexible operation or intermediate storage?" In: *Journal of Energy Storage* 72 (2023), p. 108614. ISSN: 2352152X. DOI: 10.1016/j.est.2023.108614.

[67] Riccardo Rinaldi et al. "Techno-economic analysis of a biogas-to-methanol process: Study of different process configurations and conditions". In: *Journal of Cleaner Production* 393 (2023), p. 136259. ISSN: 09596526. DOI: 10.1016/j.jclepro.2023.136259.

[68] Jae Sung Lee et al. “Effects of space velocity on methanol synthesis from Co2/Co/H2 over Cu/ZnO/Al2O3 catalyst”. In: *Korean Journal of Chemical Engineering* 17.3 (2000), pp. 332–336. ISSN: 0256-1115. DOI: 10.1007/BF02699049.

8. Conclusion, Discussion and Outlook

8.1. Summary

This thesis set out to develop, characterize, and evaluate MeOH-synthesis catalysts tailored for the efficient conversion of CO_2-rich SynGas streams, addressing a central challenge in the transition toward sustainable chemical production. Building on an extensive assessment of the scientific literature, γ-Al_2O_3-supported Cu/ZnO formulations were selected as the basis for catalyst development in this study. While Cu/ZnO is well established for CO hydrogenation industrially, its performance in CO_2 conversion is considerably more limited, necessitating strategic promotion to enhance activity, selectivity, and stability under CO_2-rich conditions. Guided by reported advancements in promoter chemistry, thirteen distinct catalyst formulations were synthesized, incorporating variations in catalyst surface pH, promoter loading, and promoter combinations.
An initial catalyst screening confirmed the literature expectation: unpromoted Cu/ZnO/Al_2O_3 coated spheres were significantly less effective in CO_2-rich feeds than their promoted counterparts. In contrast, formulations containing CeO_2, ZrO_2, or combinations thereof exhibited distinctly improved performance, and additional CaO-induced surface basicity further enhanced X_C. These findings motivated a systematic investigation of promoter effects through a stepped promotion protocol, in which a baseline Cu/ZnO material (20% CZ) was successively modified with CeO_2 (20% CZC), ZrO_2 (20% CZCZ), and ultimately CaO (20% CZCZC). This approach enabled the isolation of individual promoter contributions and their cumulative influence on catalytic behavior.
The four resulting catalysts underwent extensive structural, textural, chemical, and electrical characterization, providing comprehensive insight into how their physico-chemical properties evolved throughout the promotion sequence. Catalytic testing under a wide range of reaction conditions, combined with equilibrium assessments, revealed significant trends in activity and apparent reaction mechanisms. Quantitative analysis through kinetic model fitting further elucidated the impact of promotion on key reaction indicators, including activation energies for carbon conversion and adsorption phenomena.
The second research track of this thesis describes the successfully established, complete process chain for conversion of biogas to regenerative MeOH. The process integrates H_2 and O_2 produced by water electrolysis, enabling a carbon-efficient and electricity-coupled route to renewable MeOH. A fully instrumented pilot test plant was designed, constructed, and commissioned for operation at a wastewater treatment facility in Germany, demonstrating the feasibility of this approach under real-world boundary conditions. The previously developed quinary-promoted catalyst formulation was successfully scaled from laboratory to pilot-scale operation, allowing the translation of catalyst development results into a demonstration-scale MeOH synthesis unit. This integration of catalyst innovation with process and plant engineering establishes a holistic foundation for future deployment of renewable MeOH-production technologies.

8.2. Discussion of Research Questions

At the start of the thesis, five research questions were laid out, relating to the development, deployment and characterization of novel carrier catalyst formulations as well as design, commissioning and operation of a pilot-plant for regenerative MeOH synthesis. All research questions could be addressed successfully in the course of the thesis: Concerning **research question 1.1** the produced catalyst samples showed markedly different behavior under CO_2-only and mixed-SynGas conditions. In pure CO_2-operation, the commercial reference catalyst achieved the highest conversion (37.8%), while the developed, promoted prototype-samples reached 16.2–24.2%, remaining below the reference but clearly outperforming the unpromoted Cu/ZnO recipe. Under CO_2-rich SynGas conditions (COR = 0.71), promotion had a significantly stronger effect: conversion increased from 17.5% for unpromoted Cu/ZnO/Al_2O_3 to 26.5% for the fully promoted CuZnO–CeO_2–ZrO_2–CaO/Al_2O_3 formulation, thereby reducing the gap to the commercial reference (39.1%) under reaction conditions close to those found in commercial, regenerative MeOH production.

The results indicate that promoter addition becomes particularly beneficial under mixed-SynGas operation. While the catalysts did not achieve superior performance compared to the commercial sample, they achieved significantly higher conversion in relation to total catalyst loading, with performance to active catalyst weight outperforming the reference catalyst significantly. Additionally, the produced and tested catalyst samples performed very well compared to other reported catalyst formulations from recent literature. This highlights the effectiveness of the assumptions made in catalyst formulation, showing that low loading with the right catalyst promoter addition will significantly enhance catalyst performance and catalyst weight to yield ratios. The high conversion ratios are attributed to very high available surface area, high distribution of surface catalyst metal-oxide species and the complex interplay of Cu, ZnO, CeO_2, and ZrO_2 in the catalytically active metal-metal-oxide mixtures.

Regarding **research question 1.2**, we were able to relate several physio-chemical properties of the produced catalyst samples to their performance in CO_2 conversion. The strongest correlation was observed for surface basicity, which increased with promoter addition and showed a clear positive relationship with CO_2 conversion. All coated samples exhibited high surface areas, yet these did not correlate linearly with catalytic activity. Similarly, the H_2-adsorption capacity of the reduced samples showed no positive influence and in some cases even an inverse trend, while the surface acidity measured by NH_3-TPD showed no meaningful correlation to catalyst performance in conversion of carbon oxides. In contrast, reducibility displayed a direct and consistent relationship with CO_2 and CO conversion for both the commercial reference catalyst and the newly developed coated samples. Furthermore, FIB-lamella investigations of the carrier surfaces combined with HAADF-STEM analysis revealed qualitative non-uniform coating penetration, indicating that future improvements in the coating and production protocols may further enhance catalyst performance through more even distribution of catalytically active species on the carrier surface.

Looking at **research question 1.3**, the adapted kinetic models expectedly and clearly quantify the mechanistic effects of promoter incorporation. Across all promoted catalysts, CO hydrogenation was consistently excluded from the optimal, mathematical reaction network, confirming that CO_2 serves as the dominant carbon source for MeOH formation in CZA-based catalyst recipes. Comparison of the fitted parameters shows that promoter addition strongly influences both CO_2 adsorption and the activation barriers of the key CO_2-conversion pathways.

CO_2 adsorption increases substantially after incorporation of CeO_2 and ZrO_2, with the pre-exponential factor B_{CO_2} rising from 2.91×10^{-7} for the unpromoted 20% CZ to 3.79×10^{-7} for 20% CZC and further to

1.70×10^{-11} for 20% CZCZ, while the adsorption enthalpy ΔH_{CO_2} decreases from 57.4 kJ/mol to 30.0 kJ/mol and 114.3 kJ/mol, respectively, reflecting the enhanced affinity of the promoted surfaces for oxidized carbon species. The activation energy for CO_2 hydrogenation increases noticeably for the ZrO_2-containing catalysts, from 79.3 kJ/mol (20% CZ) to 130.8 kJ/mol for both 20% CZCZ and 20% CZCZC, while the RWGS-activation energy decreases substantially for the CeO_2-promoted sample from 27.5 kJ/mol to 8.46 kJ/mol (20% CZC) and rises again after ZrO_2 addition to 25.2 kJ/mol (20% CZCZ). These trends indicate that CeO_2 primarily enhances CO_2-activation and RWGS turnover, whereas ZrO_2 strengthens CO_2 binding but introduces a higher barrier for direct CO_2 hydrogenation. The CaO-containing quinary catalyst shows intermediate behavior, maintaining strong CO_2 adsorption with a moderately increased RWGS-activation barrier of 29.4 kJ/mol. Overall, the kinetic models capture the mechanistic role of promoter incorporation quantitatively and provide reliable predictive capability across varying feed compositions.

In the second research track of this thesis, process development and deployment of a novel regenerative MeOH-synthesis process was investigated. In order to avoid the drawbacks associated with and previously reported for conventional steam reforming of biogas with subsequent conversion of the H_2-deficient SynGas to MeOH, **research question 2.1** was addressed as follows:

To avoid high additional energy demand for heat supply of the endothermic methane reforming process, to optimize the process concerning H_2-availability in the MeOH synthesis, and to capitalize on the synergies of regenerative electrolysis of water optimally, a novel integrated MeOH process was designed. This process approach utilizes autothermal, oxygen-integrated biogas reforming and subsequent MeOH synthesis applying the previously introduced, scaled, supported quinary catalyst sample. The process can be applied as a combination of bio-MeOH-synthesis and electricity-based synthesis, capitalizing on the benefits of both approaches while potentially minimizing the drawbacks of the overall approach. The system was designed, commissioned, and piloted in a custom demonstration plant for the integrated process.

Regrading **Research Question 2.2** catalyst performance and aforementioned performance indicators could be replicated in the process piloting. As expected, even CO_2-only SynGas dosing yielded a mixture of carbon oxides in the recycle gas loop, necessitating the conversion of both CO and CO_2 through the catalysts. This supports the research goal to develop catalysts that perform well in both CO_2-only applications as well as mixed SynGas streams. Performance was enhanced at gas compositions around COR 0.6–0.71, with a maximum production capacity of approximately 0.5 kg_{MeOH}/h reached. The developed process was piloted despite several design-misalignments and operational limitations related to the achievable ranges of key process parameters. Nevertheless, the successful demonstration establishes a solid foundation for future, more extensive process development. It provides a crucial basis for advancing decentralized, bio-based, and electricity-enhanced thermochemical processes.

8.3. Limitations

In the course of the here presented work, several shortcomings, drawbacks as well as process and protocol optimization possibilities were identified for future research. For some applied physio-chemical tests of the catalyst samples, a shortcoming was the testing under unreduced test conditions. Especially, SEM, HAADF-STEM and XPS measurements were carried out in the catalysts oxidized state. This grants insights into surface compositions of the catalyst and achieved catalyst sturcutres after calcination of the carriers, but does not lend insights into the catalyst surface structure under reaction conditions. In future work, testing protocols

will be extended to accommodate for the analysis of catalyst surface structure in reductive environments. In laboratory catalyst testing, no sub stoichiometric gas compositions concerning SN and H_2-supply were tested. While this fact ensures full reduction of the catalyst and avoids conversion limitations stemming from catalyst re-oxidation or surface H_2-deficiencies, this influences both the observed performance and the estimated kinetic parameters: High H^2-supply has shown to reduce STY specific to reactor volume compared to stoichiometric SN ranges. This can be traced back to sub optimal volumetric reactor coverage with carbon oxides, with more space being occupied by the excessive supply of H_2. Furthermore, H_2 is the reactant most unlikely to experience both internal and external mass transfer limitations. Maximum catalyst-coverage with carbon-oxide reactants is therefore imperative for maximum observed yield. Future research should extend upon the herein presented work and add substoichiometric SN conditions for an extension of the collected data-set. Performance measured under excess H_2 will further influence the mathematical optimum of the estimated kinetic parameters. The model presented in this thesis should therefore only be used for prediction of MeOH reactors applying sufficient H_2 for full carbon-oxide conversion as it will favor these systems in prediction accuracy.

Several significant drawbacks and shortcomings in process design and plant layout were identified that will serve as the basis for future development of the MeOH system. The most pressing system shortcomings were: *Reduced system pressure and thus strongly reduced conversion* – In subsequent plant operation, pressure will be increased to 30 bar reactor pressure through technical adaptation. *Misalignment of assumed conversion, purge gas, and recycle ratio* – Due to the slight misalignment of specifications, most stable steady-state setpoints could not be operated optimally. While MeOH-production rate was sufficient for a plant of this scale, better tuning of recycling ratio, purge gas ratio, and SynGas compression will significantly enhance overall carbon conversion towards near-complete conversion of the dosed SynGas. *Steady-state-only operation* – The system was only operated in steady state. Especially in electricity-integrated applications with electrolysis, system setpoints will be more dynamic according to electricity availability and price. Thus, future research will also concentrate on the dynamics of such an integrated process and how performance may vary under fluctuating system load. This places special emphasis on catalyst performance and stability, as varying reactor temperatures, changing gas compositions, and thus gradually changing concentration gradients inside the reactors challenge catalyst stability, with Cu and ZnO particle distributions potentially changing and migrating under varying reaction conditions. *System Balancing* – In pilot plant operation, composition of some process streams had to be calculated from adjacent data. For example, the composition in gas recycling and purge gas flows was calculated through balancing overall system input, and measured liquid output, assuming full condensation of the liquid MeOH/H_2O product. While it can be assumed, that most of the aforementioned product was in deed condensed and collected in the cooled high pressure flash, it has to be assumed, that some MeOH and H_2O was recycled back into the reactors. This steam content has been shown to significantly reduce catalyst activity and cause major mechanistic drawbacks in SynGas conversion over CZA based catalysts. Thus, the true performance of the catalytic system was not recorded purely, although measurements of single pass reactor conversion generally matched the performance determined in laboratory reactor operation. Future research and further development of the pilot plant should focus on the minimization of coolant temperature in the flash, to assure maximal condensation of product before gas recycling. Additionally, advanced analytics for effective inline and online measurement of recycle gas and purge gas compositions should be applied.

8.4. Outlook and Recommendations for future research

Based upon the discussed findings, several recommendations shall be made for continuation of the research initiated in this thesis.

Catalyst design and application:

While the catalysts perform well and the performance-to-loading ratio is favorable, the low density of the catalyst spheres and reduced overall volume-specific performance challenge the applicability of these catalysts in large-scale deployments as larger reactor volumes will be necessary to accommodate for industrial yields. The catalyst manufacturing protocol should therefore be adapted with slightly higher catalyst loading and a modified IWI-procedure to allow for better and more even penetration of washcoating throughout the spheres. While mass transfer was not identified as major limiting factor for the performance of the presented samples, slightly higher availability and accessibility of active sites closer to the sphere center could likely enhance catalyst performance significantly, enabling performance approaching that of commercial counterparts. Herein, the interactions of catalyst coating and carrier should also be investigated in more detail in order to better understand and thus tune the interplay of Al_2O_3 and its coatings.

Additionally, γ-alumina has been identified as an effective catalyst for the dehydration of MeOH, a second promising candidate for a regenerative carbon economy. The catalyst formulations should be tuned to enhance the conversion of MeOH to DME directly, enabling single-stage, regenerative production of DME—a process otherwise carried out based upon fossil feedstock in complex multistage thermochemical processes with lower selectivity. While the fitting procedure for the Graaf-kinetic model was effective and yielded four novel kinetic parametrization for good prediction of catalyst sample performance in reactor setups, the large number of 13 different kinetic parameters fitted to about 60-80 test runs for each sample involves some amount of uncertainty concerning the global optimality of the calculated parameter sets. The kinetic model should be simplified according to the sensitivity analysis conducted, omitting or lumping factors with low sensitivity (low certainty of optimal fit, low impact on overall model performance) and concentrating more on those factors with high sensitivity (high impact, high certainty of correct optimization). For better understanding of all mechanisms involved in the reaction complex, computational power should rather be applied in integration of additional kinetic rate equations accounting for DME- and CH_4-production on the CZA-based catalysts. This way, simpler, reduced kinetic models would be able to more accurately account for the physical mechanisms leading to formation of other hydrocarbons in MeOH synthesis.

Process Design:

The system should be implemented utilizing higher system pressures and commercial catalyst formulations with industrial conversion efficiency. This will demonstrate the overall feasibility of the approach, reaching acceptable carbon conversion ratios and STY_{MeOH} in the pilot plant. This will then lay the foundation for an in-depth energy efficiency assessment, taking into account all energy inputs necessary for the operation of the B2M process. It will also establish the basis for system scale-up to commercial scale, applying the necessary technologies for the conversion of hundreds of Nm^3/h biogas to Bio-MeOH decentralized at biogas plants.

This must also include the investigation of dynamic operational strategies that take advantage of fluctuating electricity prices. This necessitates the application of performant system and process control strategies, utilizing advanced real-time, online, and inline analytics for agile system deployment and model predictive control. Additionally, infrastructural challenges for decentralized production and further processing of the MeOH product should be assessed to enable a competitive industrial MeOH-process concept.

Appendices

A. Supplementary Materials Publication 1

CO_2-Hydrogenation to Methanol over CuO/ZnO Based Infiltration Composite Catalyst Spheres

Supporting Materials

N_2 adsorption and N_2 desorption isotherms for all presented samples

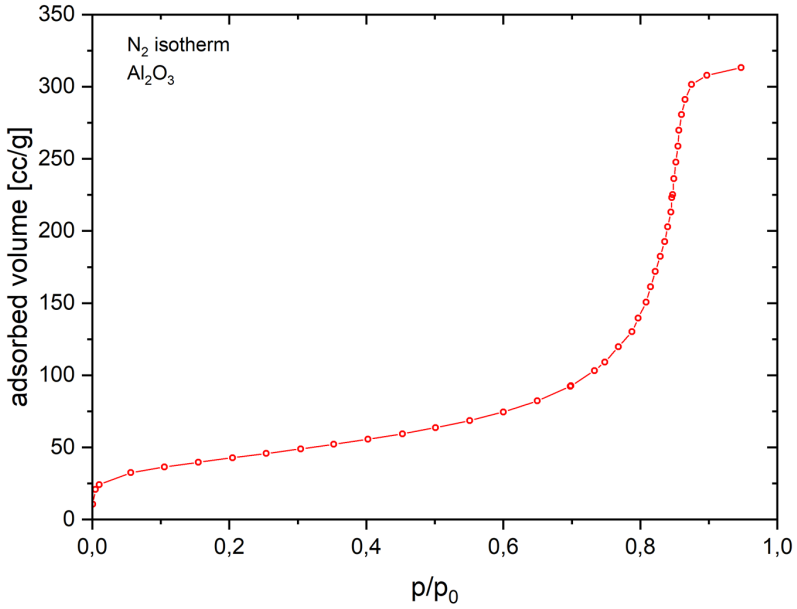

Figure A.1.: N_2-adsorption isotherm for the γ-Al_2O_3 carrier spheres

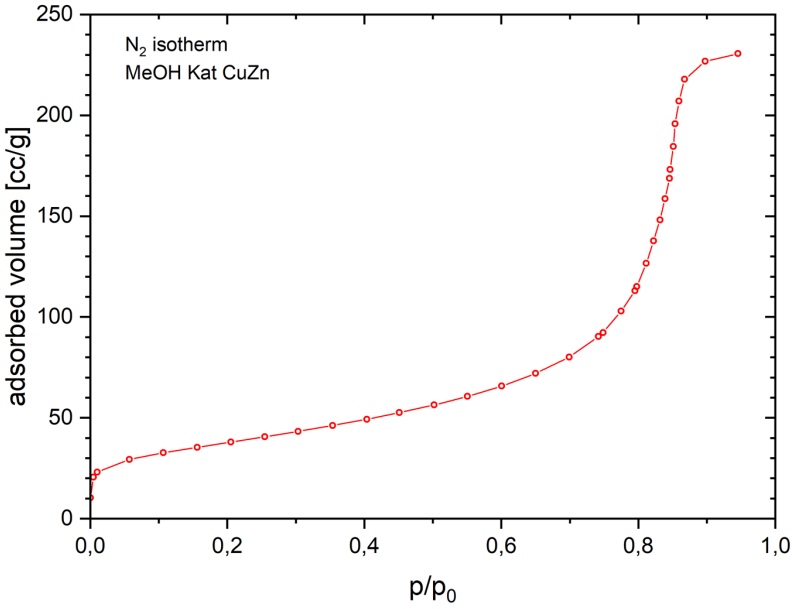

Figure A.2.: N_2-adsorption isotherm for the 20% CZ catalyst sample

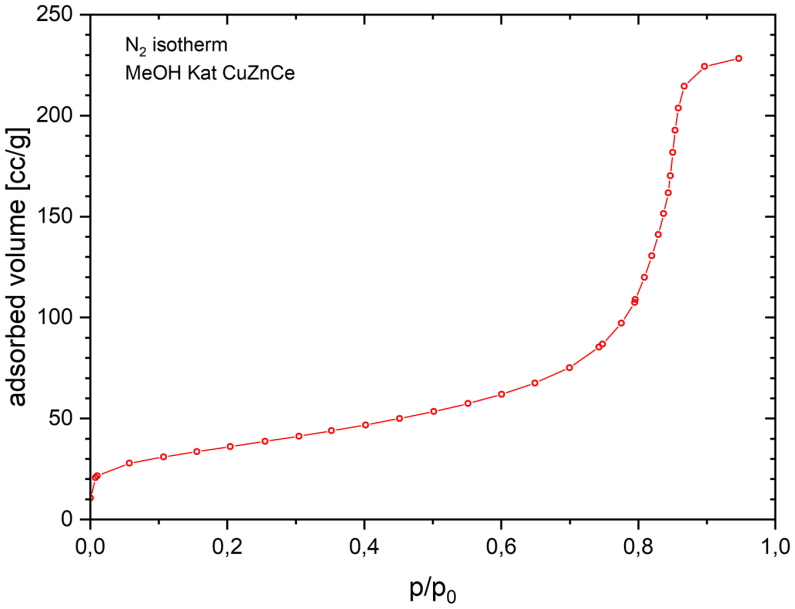

Figure A.3.: N_2-adsorption isotherm for the 20% CZC catalyst sample

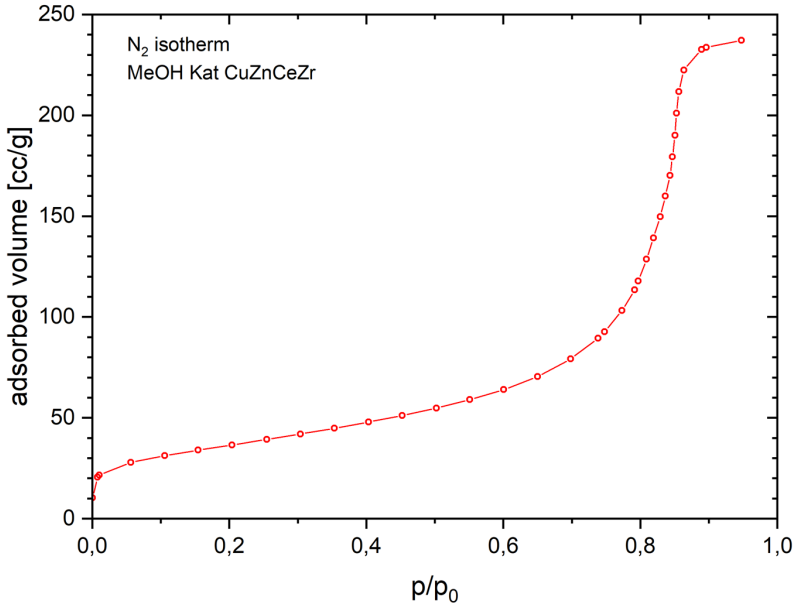

Figure A.4.: N_2-adsorption isotherm for the 20% CZCZ catalyst sample

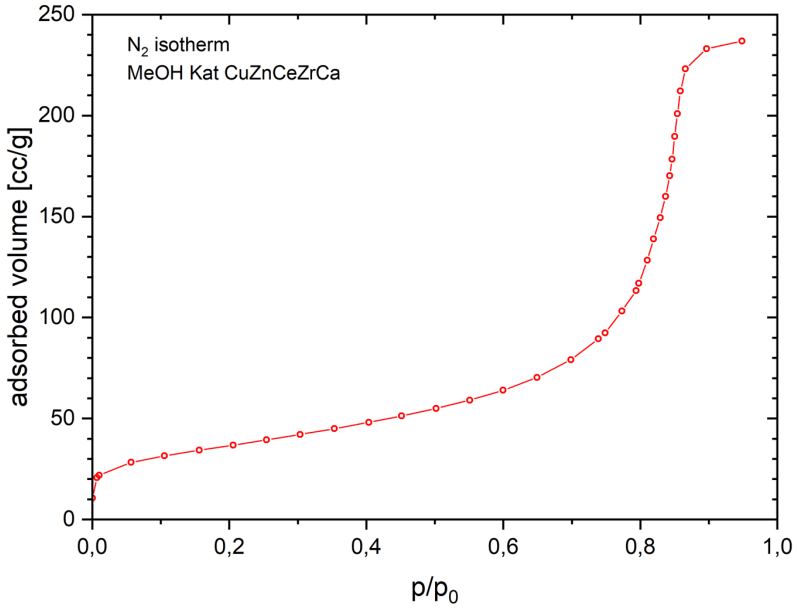

Figure A.5.: N_2-adsorption isotherm for the 20% CZCZC catalyst sample

EDX elemental analysis of image sections presented in the manuscript Reference Catalyst (REF)

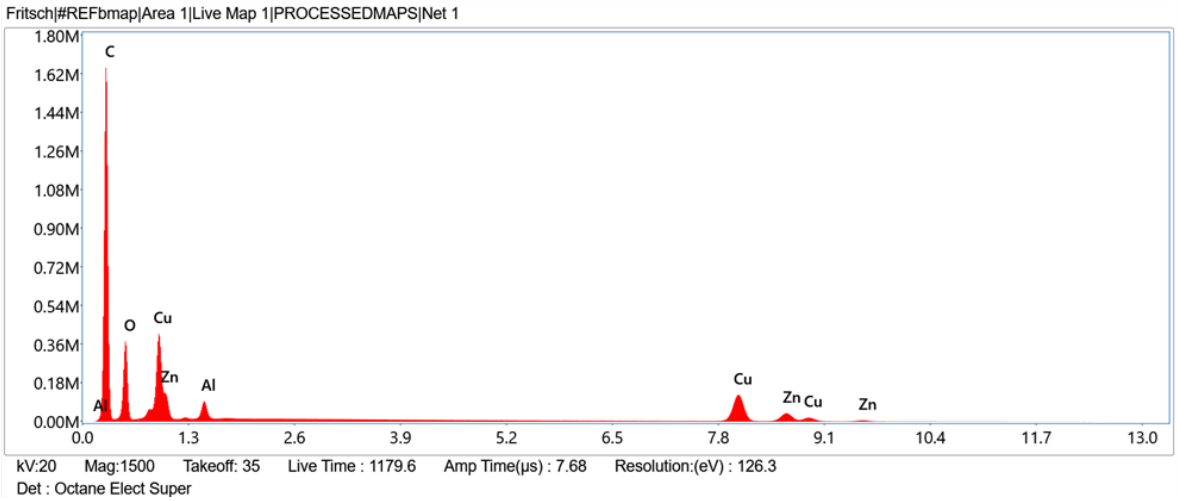

Figure A.6.: EDX-Analysis of the first SEM-image supplied for REF

Table A.1.: eZAF quantitative analysis results for elemental composition REF 1

Element	Weight (%)	MDL (%)	Atomic (%)	Error (%)	Net Int.	*R*	*A*	*F*
C K	64.2	0.01	77.5	9.7	7509.7	0.9167	0.1218	1.0000
O K	20.8	0.01	18.8	10.2	1830.4	0.9264	0.0741	1.0000
Al K	1.0	0.00	0.5	6.3	497.7	0.9438	0.4853	1.0037
Cu K	10.1	0.02	2.3	2.2	1654.1	0.9796	0.9954	1.1015
Zn K	4.0	0.02	0.9	2.4	527.0	0.9816	0.9947	1.0922

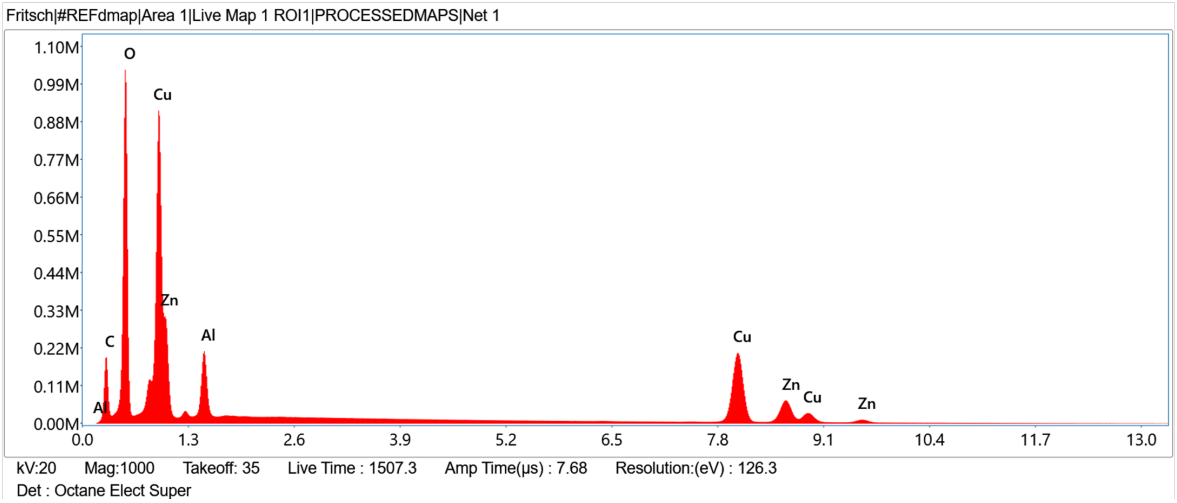

Figure A.7.: EDX-Analysis of the second SEM-image supplied for REF

Table A.2.: eZAF quantitative analysis results for elemental composition REF 2

Element	Weight (%)	MDL (%)	Atomic (%)	Error (%)	Net Int.	*R*	*A*	*F*
C K	19.5	0.03	32.8	10.4	668.8	0.8766	0.0646	1.0000
O K	41.7	0.01	52.7	9.4	4227.5	0.8891	0.1539	1.0000
Al K	5.2	0.01	3.9	7.6	1048.2	0.9123	0.3438	1.0035
Cu K	23.8	0.03	7.6	2.1	2125.0	0.9642	0.9895	1.0737
Zn K	9.9	0.03	3.1	2.2	706.2	0.9673	0.9895	1.0637

EDX elemental analysis of image sections presented in the manuscript 20% CZ (CuO/ZnO)

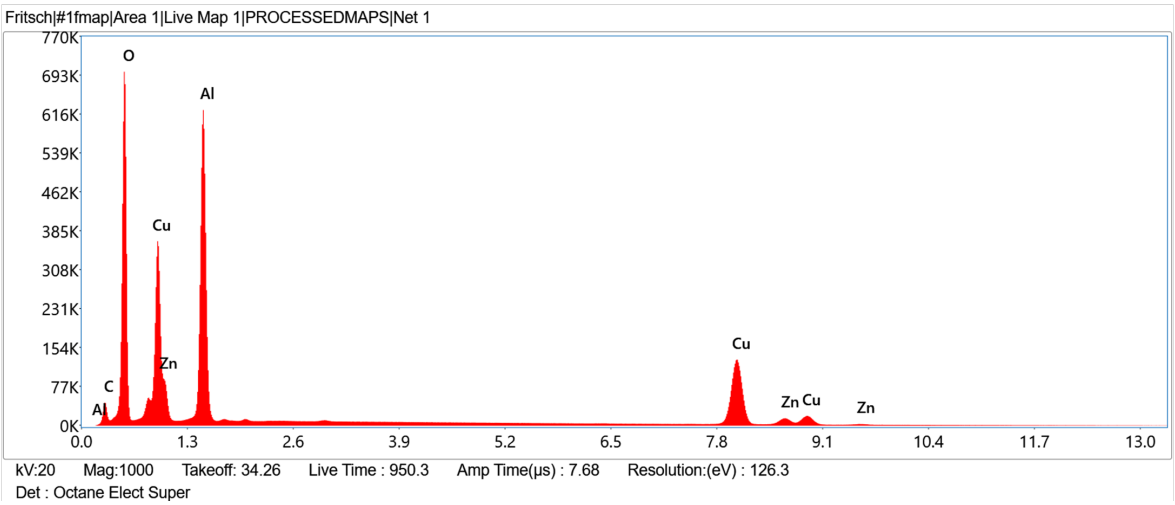

Figure A.8.: EDX-Analysis of the first SEM-image supplied for 20% CZ

Table A.3.: eZAF quantitative analysis results for elemental composition 20% CZ1

Element	Weight (%)	MDL (%)	Atomic (%)	Error (%)	Net Int.	*R*	*A*	*F*
C K	9.8	0.05	17.9	10.7	245.4	0.8764	0.0471	1.0000
O K	39.8	0.01	54.3	9.2	4503.0	0.8889	0.1723	1.0000
Al K	22.6	0.01	18.3	7.2	5088.6	0.9121	0.3830	1.0029
Cu K	24.7	0.03	8.5	2.1	2170.7	0.9641	0.9879	1.0659
Zn K	3.1	0.04	1.0	2.6	223.7	0.9672	0.9879	1.0709

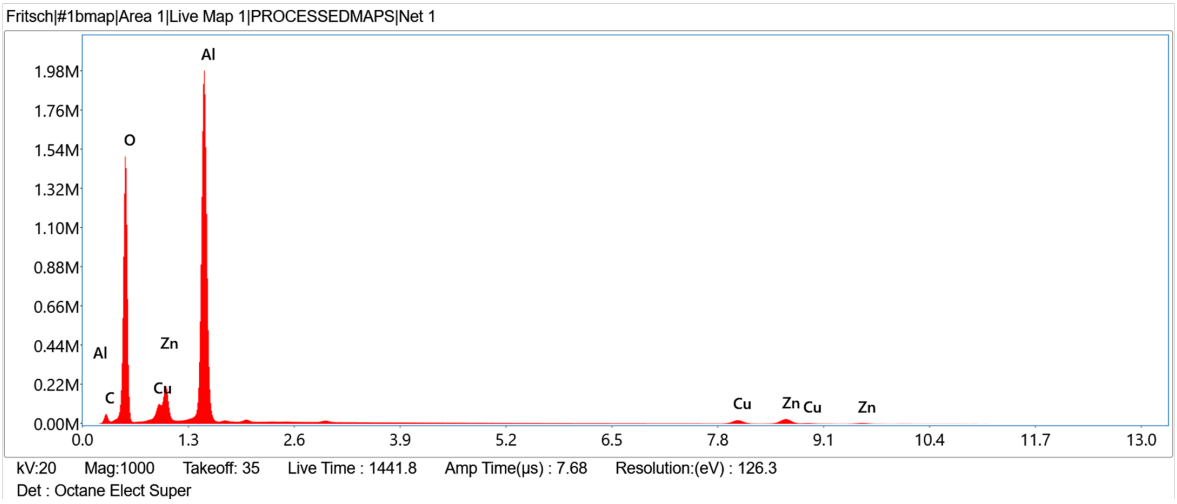

Figure A.9.: EDX-Analysis of the second SEM-image supplied for 20% CZ

Table A.4.: eZAF quantitative analysis results for elemental composition 20% CZ2

Element	Weight (%)	MDL (%)	Atomic (%)	Error (%)	Net Int.	*R*	*A*	*F*
C K	7.5	0.10	11.9	10.7	168.3	0.9032	0.0426	1.0000
O K	51.1	0.01	61.1	9.1	6223.8	0.9139	0.1861	1.0000
Al K	35.5	0.01	25.2	5.8	10756.3	0.9335	0.5183	1.0020
Cu K	2.1	0.10	0.6	2.7	199.3	0.9749	0.9896	1.1450
Zn K	3.8	0.05	1.1	2.7	287.1	0.9772	0.9917	1.1270

EDX elemental analysis of image sections presented in the manuscript 20% CZC ($CuO/ZnO/CeO_2$)

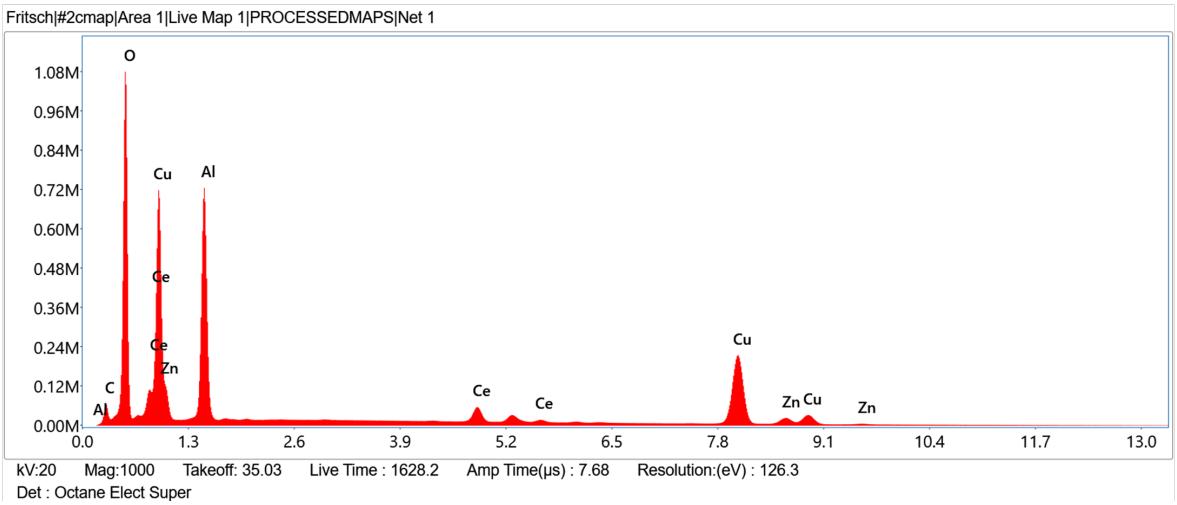

Figure A.10.: EDX-Analysis of the first SEM-image supplied for 20% CZC

Table A.5.: eZAF quantitative analysis results for elemental composition 20% CZC1

Element	Weight (%)	MDL (%)	Atomic (%)	Error (%)	Net Int.	*R*	*A*	*F*
C K	8.1	0.04	16.1	10.6	202.1	0.8584	0.0514	1.0000
O K	37.5	0.01	55.7	9.2	4091.7	0.8718	0.1813	1.0000
Al K	18.5	0.01	16.3	7.6	3446.4	0.8971	0.3440	1.0032
Cu K	25.9	0.03	9.7	2.2	2077.8	0.9559	0.9783	1.0655
Zn K	3.0	0.03	1.1	2.6	198.8	0.9597	0.9800	1.0725
Ce L	6.9	0.04	1.2	2.2	377.4	0.9384	0.9424	1.0320

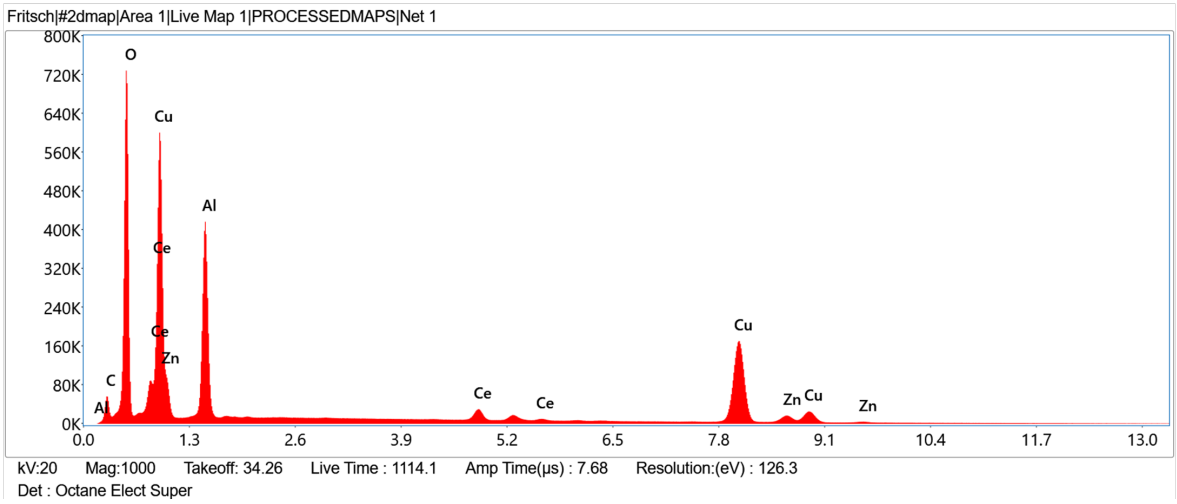

Figure A.11.: EDX-Analysis of the second SEM-image supplied for 20% CZC

Table A.6.: eZAF quantitative analysis results for elemental composition 20% CZC2

Element	Weight (%)	MDL (%)	Atomic (%)	Error (%)	Net Int.	*R*	*A*	*F*
C K	10.1	0.05	19.5	10.6	265.9	0.8608	0.0529	1.0000
O K	37.5	0.01	54.6	9.2	4077.0	0.8741	0.1751	1.0000
Al K	15.4	0.01	13.3	7.7	2899.8	0.8991	0.3373	1.0032
Cu K	29.2	0.03	10.7	2.1	2415.9	0.9570	0.9814	1.0622
Zn K	3.1	0.04	1.1	2.7	210.8	0.9607	0.9822	1.0686
Ce L	4.6	0.04	0.8	2.5	263.7	0.9399	0.9447	1.0384

EDX elemental analysis of image sections presented in the manuscript 20% CZCZ ($CuO/ZnO/CeO_2/ZrO_2$)

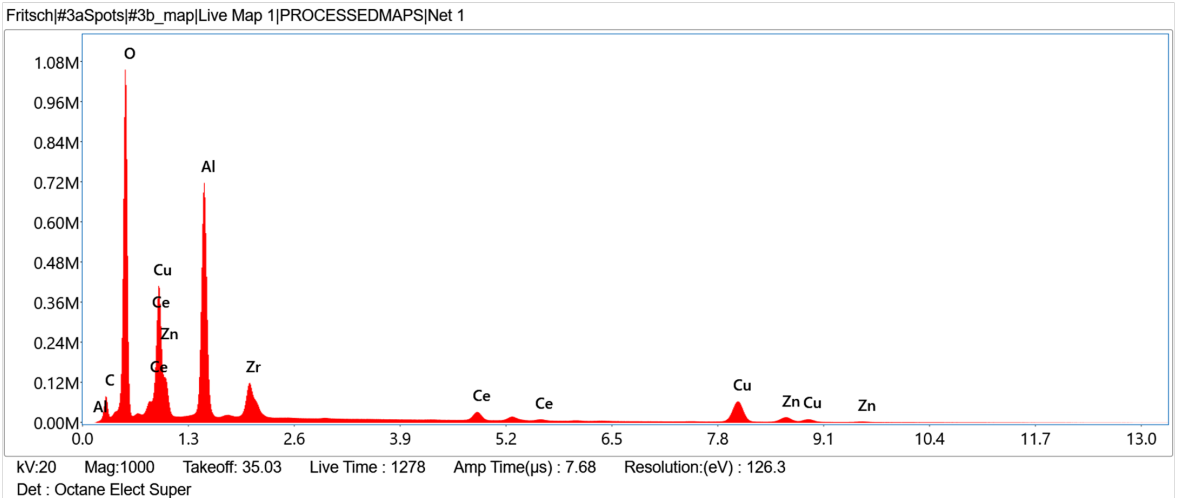

Figure A.12.: EDX-Analysis of the first SEM-image supplied for 20% CZCZ

Table A.7.: eZAF quantitative analysis results for elemental composition 20% CZCZ1

Element	Weight (%)	MDL (%)	Atomic (%)	Error (%)	Net Int.	*R*	*A*	*F*
C K	11.6	0.04	19.4	10.5	318.2	0.8811	0.0531	1.0000
O K	49.3	0.01	62.0	9.4	5054.8	0.8933	0.1599	1.0000
Al K	17.5	0.01	13.1	6.7	4338.9	0.9160	0.4298	1.0037
Cu K	8.6	0.04	2.7	2.4	758.1	0.9661	0.9826	1.1014
Zn K	2.5	0.04	0.8	2.8	183.5	0.9691	0.9854	1.1084
Zr L	6.2	0.02	1.4	5.3	723.6	0.9249	0.5841	1.0022
Ce L	4.2	0.05	0.6	2.4	240.5	0.9517	0.9463	1.0208

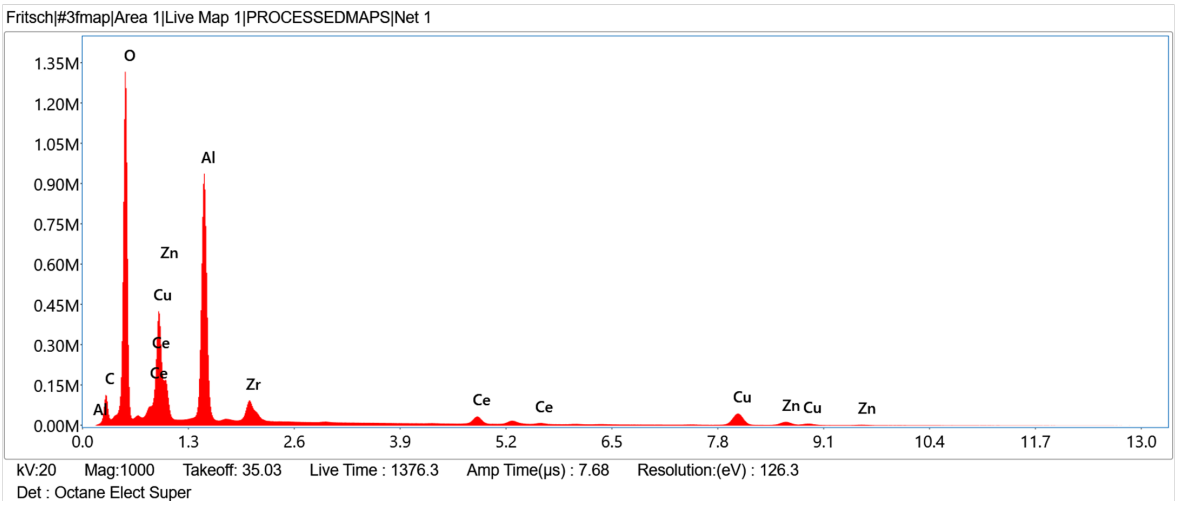

Figure A.13.: EDX-Analysis of the second SEM-image supplied for 20% CZCZ

Table A.8.: eZAF quantitative analysis results for elemental composition 20% CZCZ2

Element	Weight (%)	MDL (%)	Atomic (%)	Error (%)	Net Int.	*R*	*A*	*F*
C K	14.8	0.03	23.1	10.5	482.3	0.8924	0.0569	1.0000
O K	51.9	0.01	60.8	9.4	5903.1	0.9039	0.1601	1.0000
Al K	18.4	0.01	12.8	6.4	5363.2	0.9250	0.4582	1.0034
Cu K	5.0	0.03	1.5	2.5	493.5	0.9707	0.9846	1.1138
Zn K	1.8	0.03	0.5	2.9	144.4	0.9734	0.9872	1.1231
Zr L	4.1	0.02	0.8	5.1	537.0	0.9333	0.5994	1.0021
Ce L	4.1	0.03	0.6	2.2	264.6	0.9578	0.9530	1.0178

EDX elemental analysis of image sections presented in the manuscript 20% CZCZC ($CuO/ZnO/CeO_2/ZrO_2/CaO$)

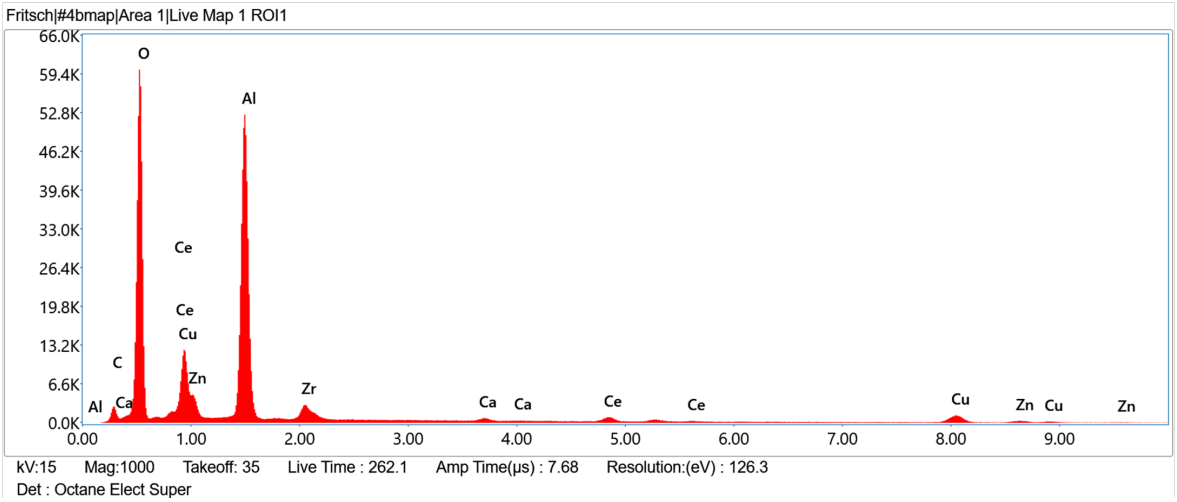

Figure A.14.: EDX-Analysis of the first SEM-image supplied for 20% CZCZC

Table A.9.: eZAF quantitative analysis results for elemental composition 20% CZCZC1

Element	Weight (%)	MDL (%)	Atomic (%)	Error (%)	Net Int.	*R*	*A*	*F*
C K	6.0	0.16	10.9	11.8	42.8	0.8785	0.0791	1.0000
O K	43.5	0.04	59.6	8.6	1339.5	0.8918	0.2812	1.0000
Al K	28.5	0.04	23.2	5.6	1523.7	0.9166	0.5831	1.0031
Ca K	0.6	0.13	0.4	6.6	22.8	0.9437	0.9146	1.0315
Cu K	9.4	0.30	3.2	5.0	69.4	0.9766	0.9900	1.0947
Zn K	3.1	0.41	1.1	9.6	17.0	0.9806	0.9918	1.0997
Zr L	3.9	0.13	0.9	6.1	80.9	0.9265	0.6740	1.0020
Ce L	5.0	0.30	0.8	8.4	35.0	0.9576	0.9655	1.0177

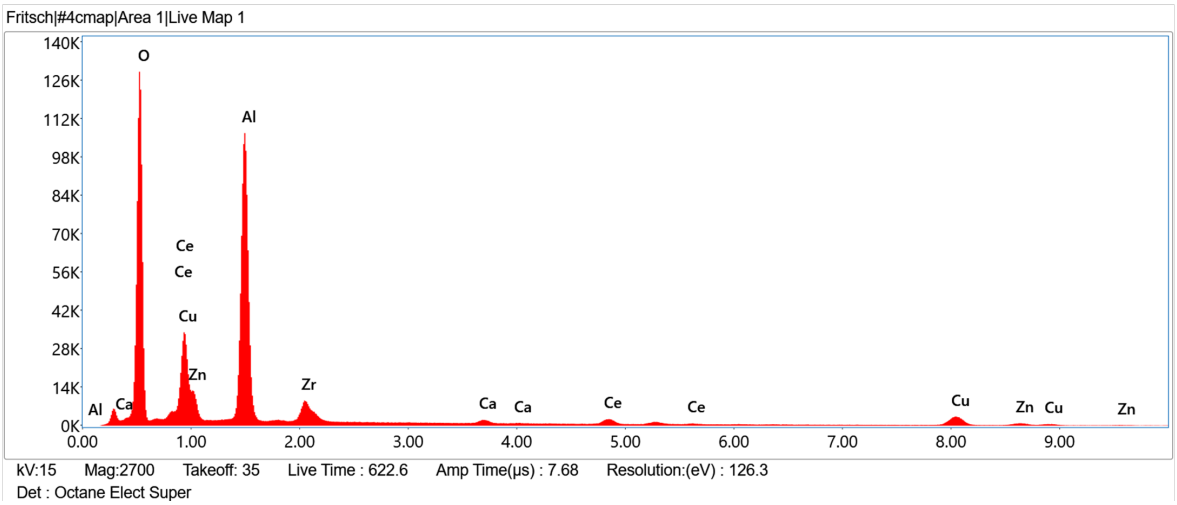

Figure A.15.: EDX-Analysis of the second SEM-image supplied for 20% CZCZC

Table A.10.: eZAF quantitative analysis results for elemental composition 20% CZCZC2

Element	Weight (%)	MDL (%)	Atomic (%)	Error (%)	Net Int.	*R*	*A*	*F*
O K	42.8	0.03	64.8	8.4	1202.9	0.8805	0.2946	1.0000
Al K	29.1	0.02	26.2	5.8	1299.2	0.9068	0.5576	1.0033
Ca K	0.7	0.10	0.4	6.6	21.6	0.9361	0.9044	1.0315
Cu K	12.1	0.29	4.6	4.2	78.0	0.9729	0.9884	1.0895
Zn K	4.0	0.40	1.5	7.0	18.7	0.9775	0.9905	1.0933
Zr L	5.9	0.14	1.6	5.8	102.3	0.9175	0.6572	1.0021
Ce L	5.5	0.25	0.9	6.3	33.6	0.9515	0.9608	1.0186

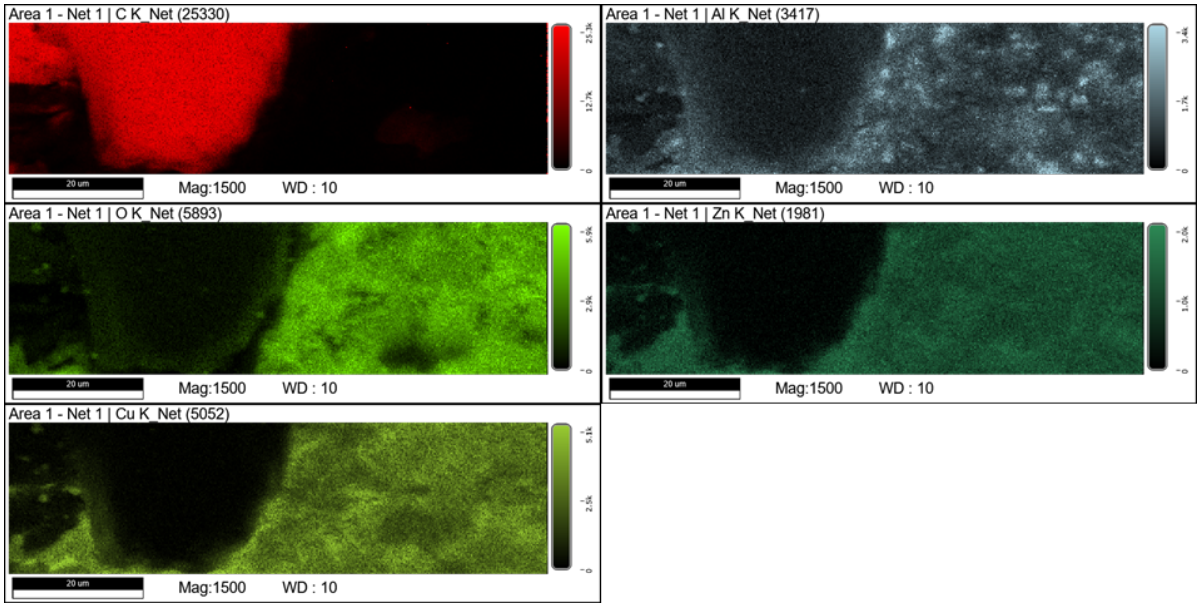

Figure A.16.: Single Element EDX Mapping for Reference Catalyst Image 1

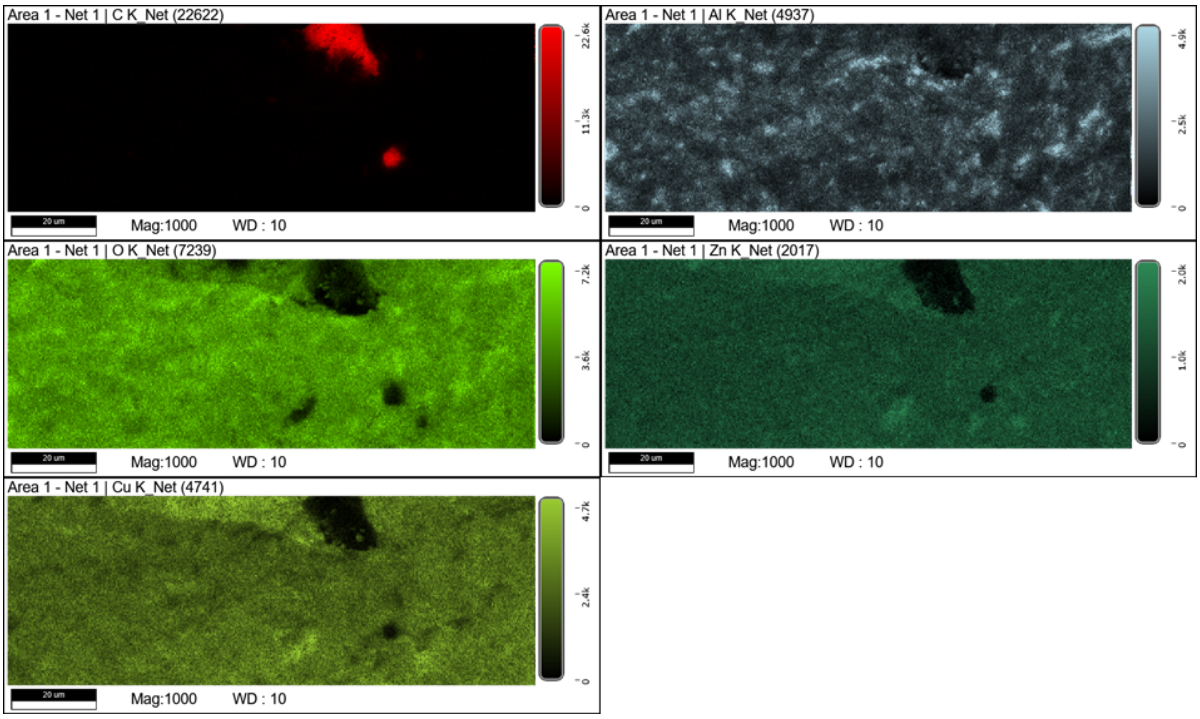

Figure A.17.: Single Element EDX Mapping for Reference Catalyst Image 2

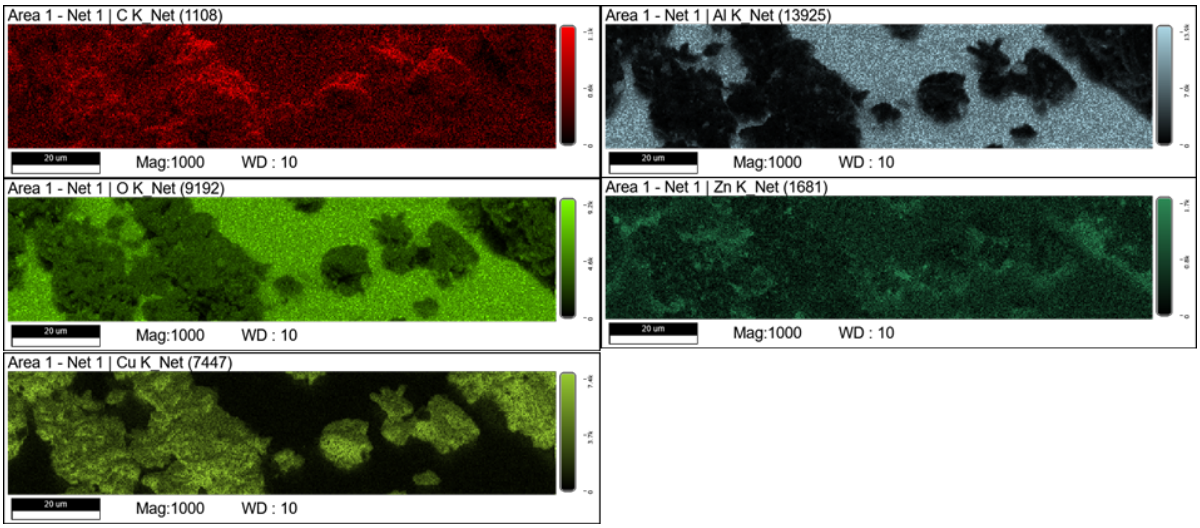

Figure A.18.: Single Element EDX Mapping for 20% CZ SEM Image 1

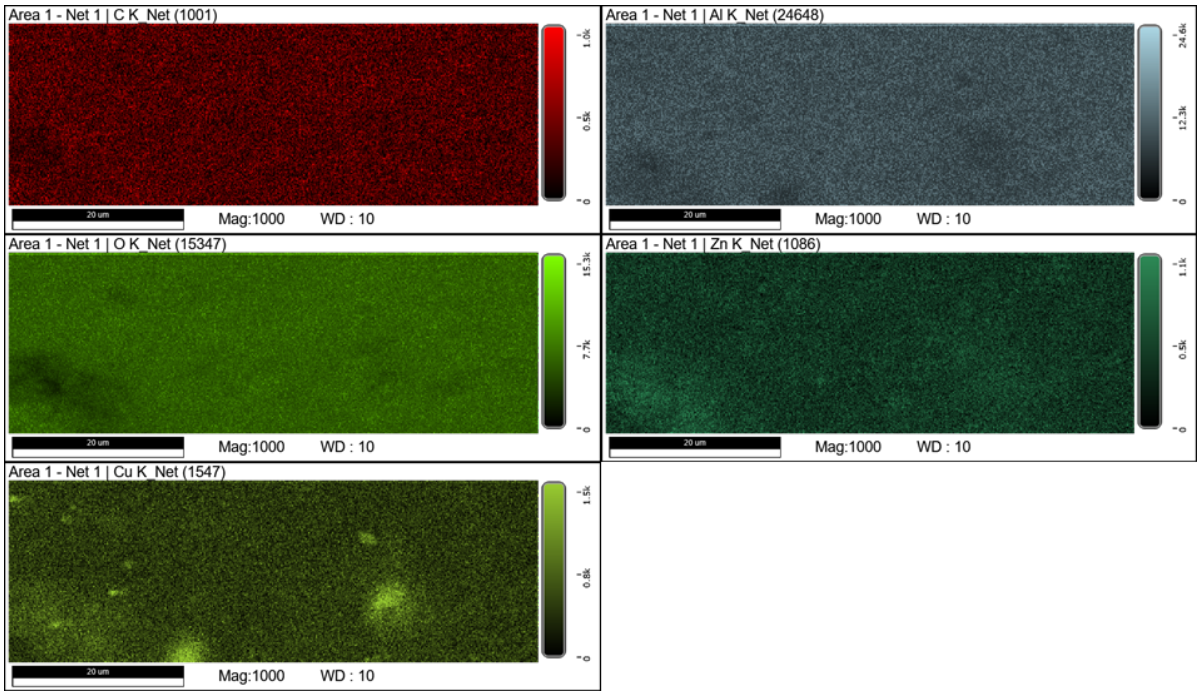

Figure A.19.: Single Element EDX Mapping for 20% CZ SEM Image 2

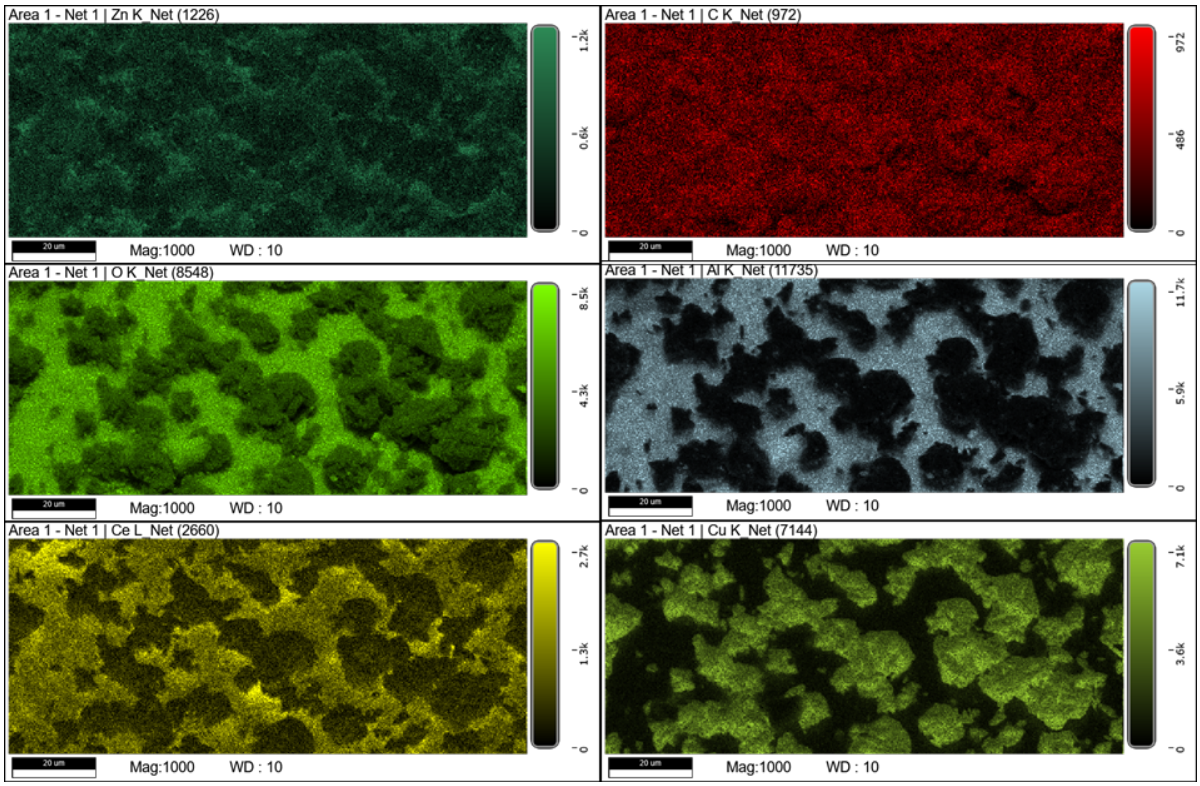

Figure A.20.: Single Element EDX Mapping for 20% CZC SEM Image 1

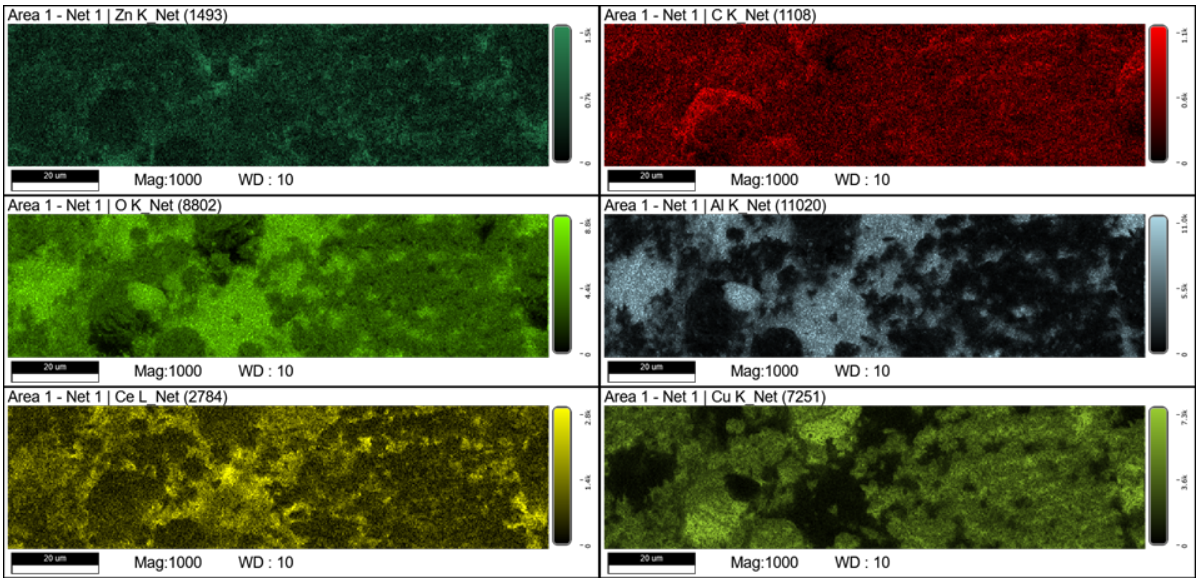

Figure A.21.: Single Element EDX Mapping for 20% CZC SEM Image 2

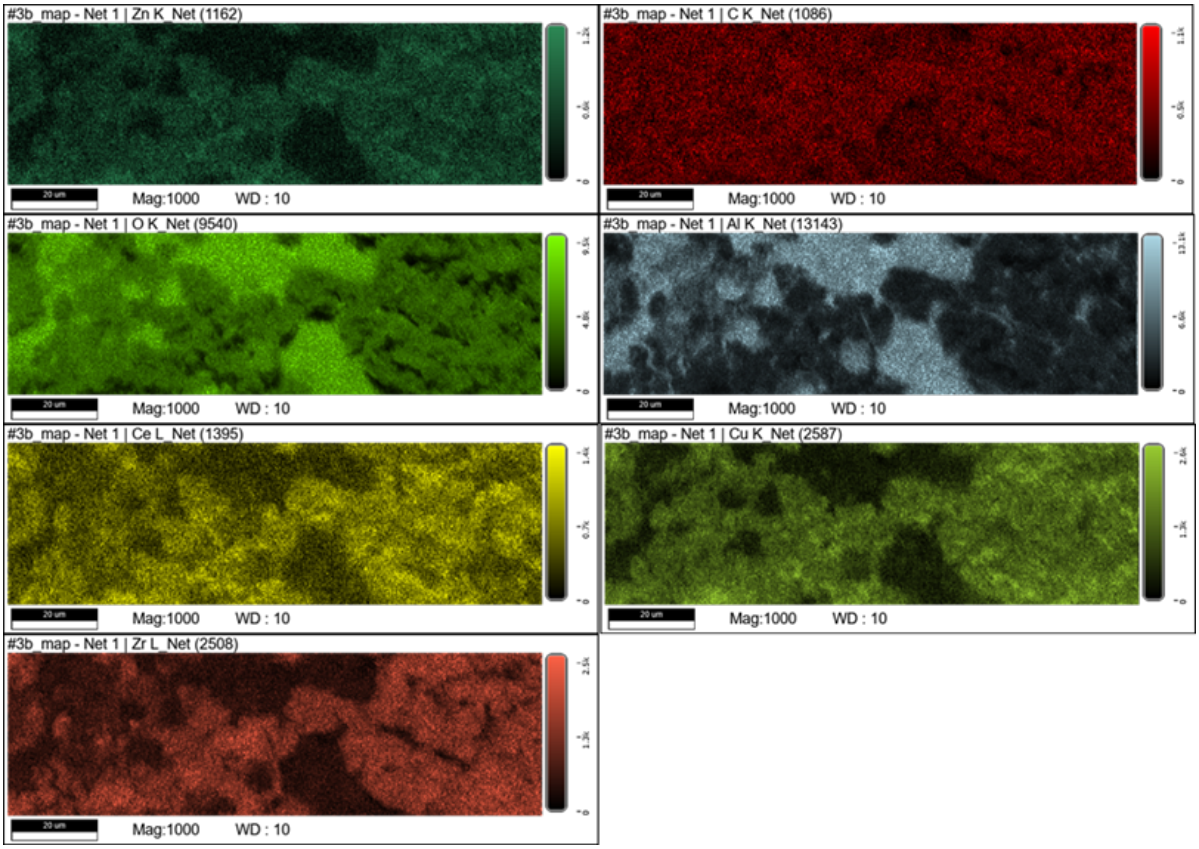

Figure A.22.: Single Element EDX Mapping for 20% CZCZ SEM Image 1

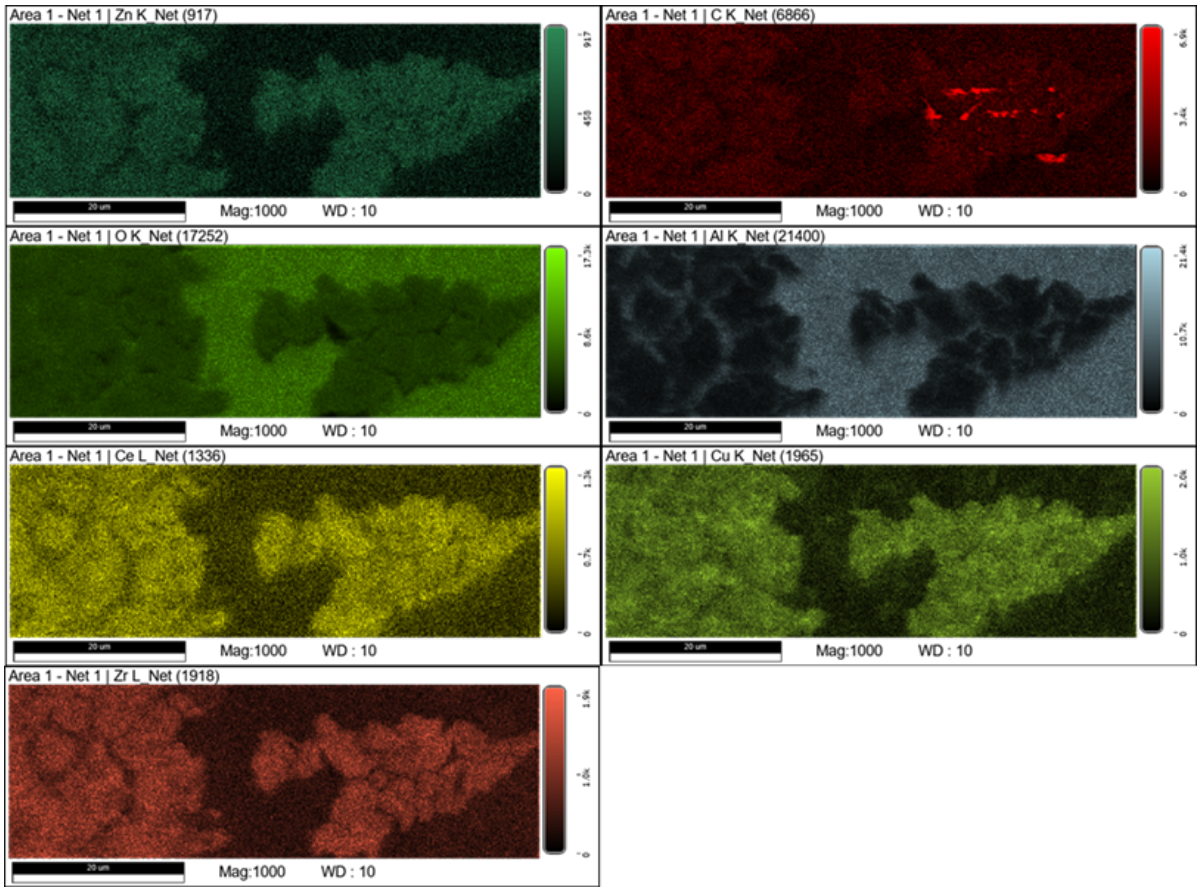

Figure A.23.: Single Element EDX Mapping for 20% CZCZ SEM Image 2

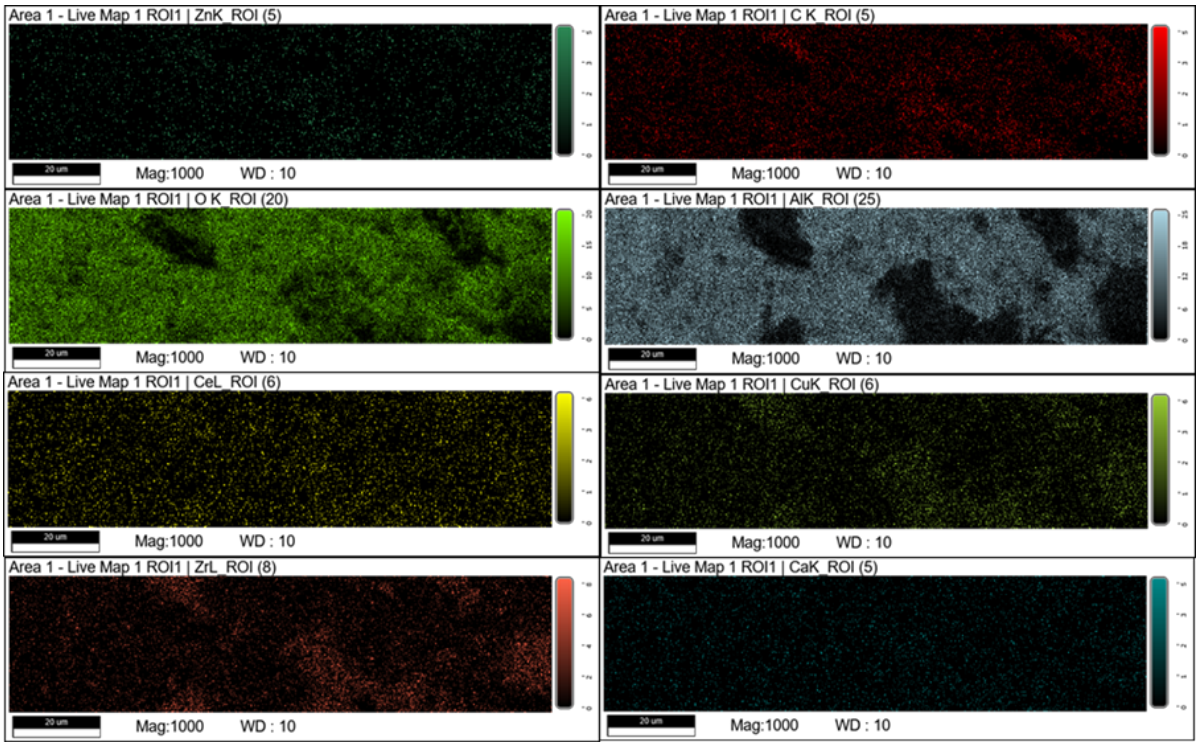

Figure A.24.: Single Element EDX Mapping for 20% CZCZC SEM Image 1

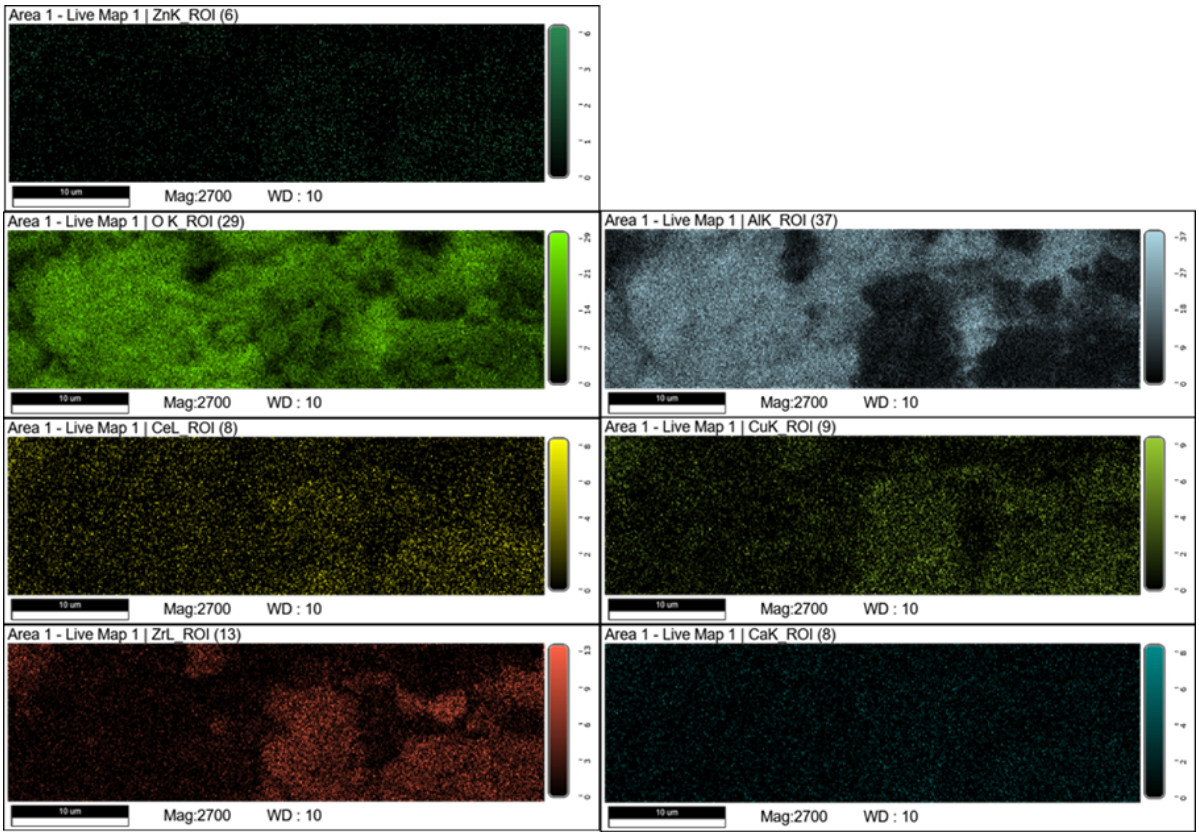

Figure A.25.: Single Element EDX Mapping for 20% CZCZC SEM Image 2

B. Supplementary Materials Publication 2

B.1. Physio-chemical Characterization

Preparation of FIB-Lamellae

Thin lamellae for transmission electron microscopy (TEM) investigations were prepared using focused ion beam (FIB) techniques in a Thermo Fisher Helios 5 Hydra UX dual-beam microscope. The spheres were mounted on a microscope stub, using silver (Ag) conductive paste. In order to enhance the electrical conductivity, the Ag paste was also partly covering the surface of the spheres, figure B.1 a) and b). Scanning electron micrographs in figure B.1 a)-d) were obtained with electron back scatter imaging.
Xenon (Xe) ions were employed and the region of interest was protected by a platinum (Pt) layer with dimensions of 10 µm length, 2 µm width and 3 µm thickness, figure B.1 e). Smooth areas of the surface were chosen in order to avoid so-called curtaining. While 12 kV acceleration voltage and 0.33 nA current were employed for Pt deposition, trench milling was done at 30 kV and 15 nA, followed by cleaning the cross-section at 4 nA, figure B.1 f). Lift-outs were attached to omniprobe copper (Cu) TEM grids and thinned to a lamella thickness of ~100 nm. Scanning transmission electron microscopy (STEM) was carried out within the dual-beam microscope at 30 kV voltage and 50 nA current, using a STEM 3+ detector in high angle annular dark field (HAADF) mode (figure B.2). In addition, mapping of the chemical composition was done by energy dispersive X-ray spectroscopy (EDX), using an EDAX Octane Elite Plus detector. Corresponding maps of Pt, aluminum (Al), oxygen (O) and Cu are displayed as well in Figure B.2.

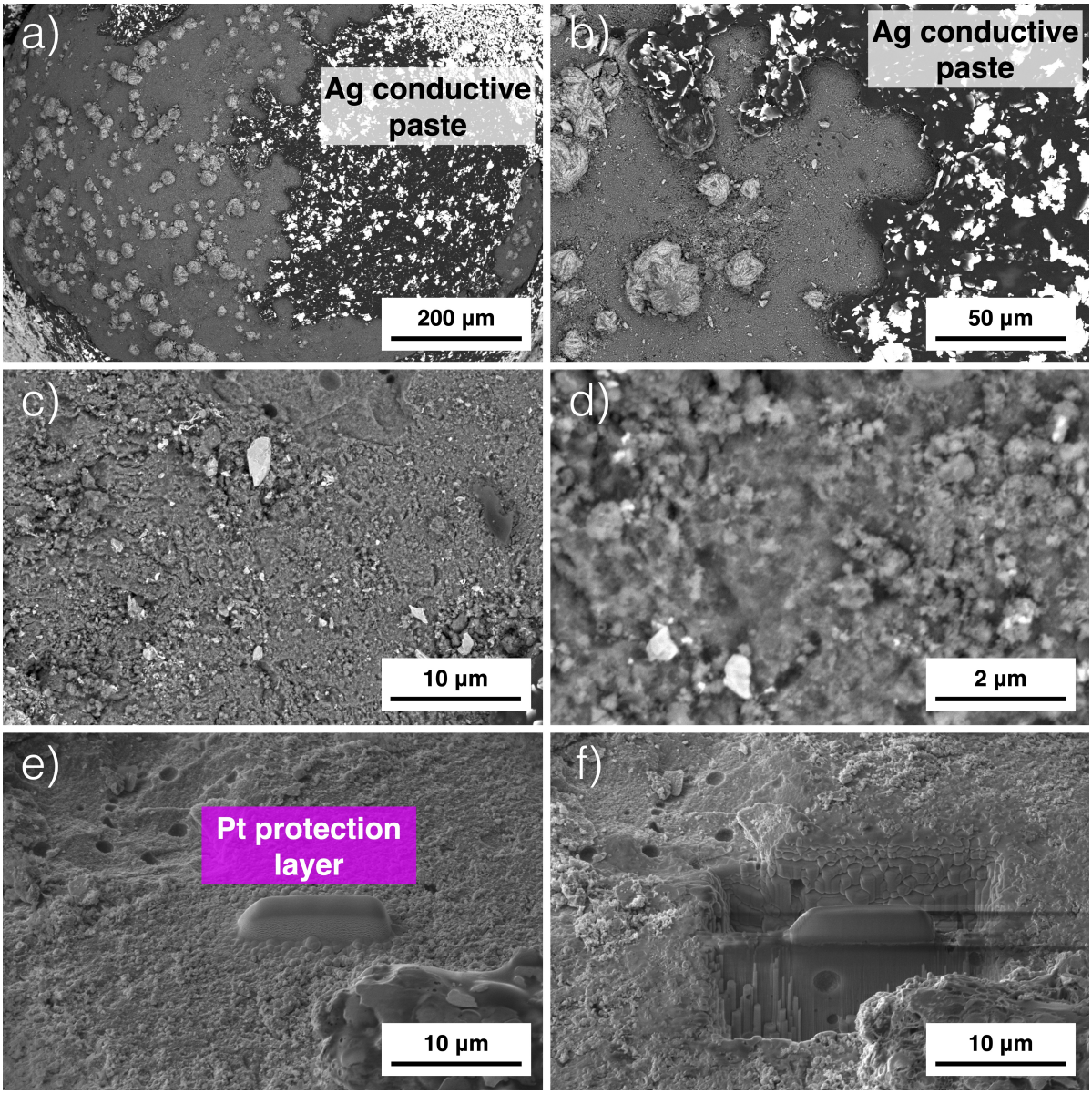

Figure B.1.: STEM-Images of 20% CZ for scoping areas suitable for FIB-milling

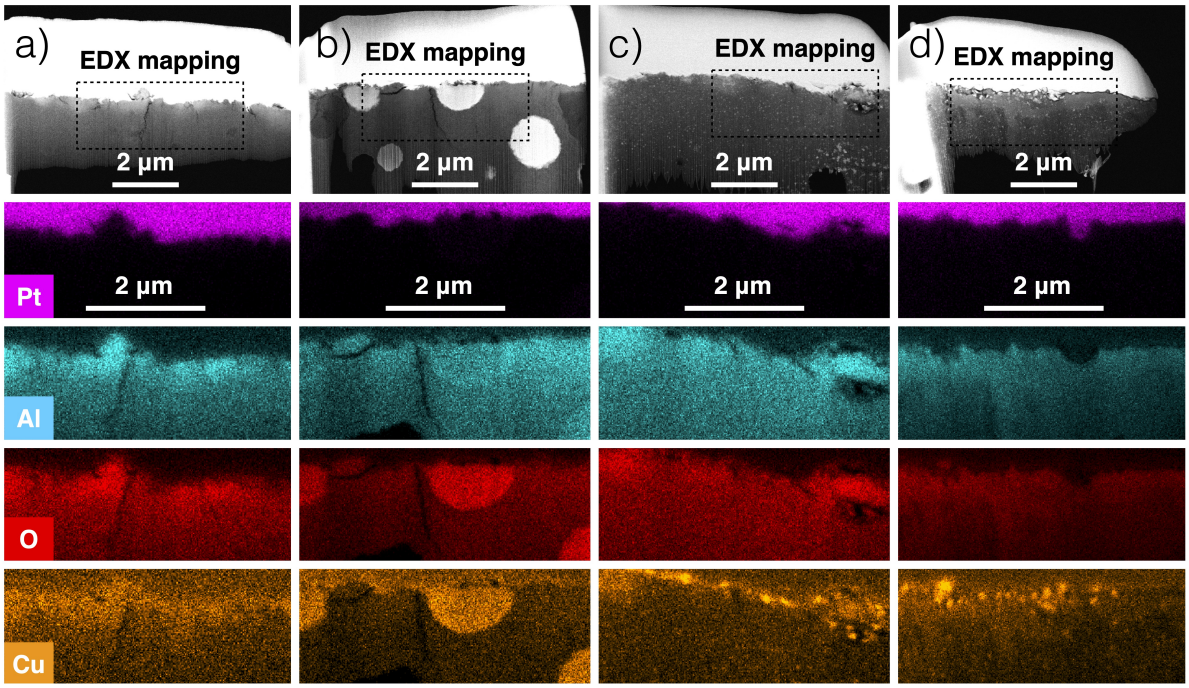

Figure B.2.: EDX-analysis of the radial lamellae cross sections for each catalyst sample. l.t.r.: 20% CZ, 20% CZC, 20% CZCZ, 20% CZCZC

TEM-Analysis

TEM-analysis was performed at multiple magnifications in several different areas. The catalyst surfaces show a heterogeneous structure, which is related to a number of different factors: In manufacturing carrier spheres using the γ-alumina oil droplet method, the spherical form of the droplets is achieved by applying oil surface tension over the formed spherical alumina. In hardening, the surface of the spheres does not form a smooth surface area around the highly porous sphere. Thus, different surface structures are formed [1, 2].

In coating the spheres through the incipient wetness method (IWI), an additional effect occurs. In precipitation of the metal oxides and the subsequent calcination of the catalyst spheres, different catalyst carrier interactions as well as metal-metal-oxide interactions lead to the formation of different metal oxide structures and agglomerates on the surface, depending on the interaction of metal in these agglomerations as well as the bulk size of the agglomerates [3, 4]. Thus, a heterogeneous surface condition can be observed in microscopic analysis of the lamellae. To account for the heterogeneous nature of the surface, several different areas on the catalyst surface were analyzed through TEM.

Figures B.3, B.4, B.5 and B.6 show HAADF STEM-images for the analyzed lamellae cross sections and according STEM-EDX-mappings of all applied metal oxides for the coatings. As can be seen, CuO penetration of the catalyst carrier spheres is least pronounced for all metal oxides. CeO_2 seems to accumulate in agglomerations of the metal oxide. ZrO_2, ZnO and CaO seem to infiltrate the catalyst carrier with the most ease, leading to very distributed penetration of the alumina carriers with these metals. This is most intensely shown in 20% CZC. The milled surface in 20% CZC exhibits a large accumulation of CuO and CeO_2, with ZnO being less strongly accumulated in this the metal oxide deposit, being rather well dispersed throughout the catalyst surface cross section.

For crystallographic analysis of the catalyst samples, images from HAADF-STEM were combined with Fast Fourier Transform (FFT) analysis. TEM images were acquired and processed following a systematic approach

to determine interplanar spacings of the constituent phases. TEM images were initially loaded into the ImageJ software. Here, contrast and brightness parameters were optimized to enhance the visibility of lattice fringes and crystalline domains. The enhancement of image contrast was crucial for distinguishing between different phases and improving the signal-to-noise ratio of the lattice information. FFT analysis was subsequently performed on selected regions of interest within the STEM images. To improve the identification of weak reflections and clarify the positions of interference maxima, the FFT images underwent further contrast and brightness adjustment. Interplanar spacings (d-spacings) were calculated from the FFT patterns using the relationship d = 1/r, where r represents the reciprocal space distance from the center of the FFT pattern to the interference spot. The reciprocal space distances were measured directly from the FFT images, and the corresponding d-spacings were computed.

For reference, a STEM image of 20% CZCZC is used for further analysis. The FFT and IFFT analysis show four different observable phases of structured metal oxide lattices. Most of the STEM image covers rather amorphous metal oxide structures. These are typically attributed to the polycrystalline γ-Al_2O_3 carrier [5]. Additionally, ZrO_2 often times forms amorphous structured when coating porous carriers [6]. The less structured surface presentation of the catalyst in the lamella cross section is thus partially attributed to ZrO_2. Cupper oxide can be found in different lattice forms on the catalyst surface, with section b indicating the presence of CuO in 020 orientation with the interplanar spacing corresponding to tenorite structures [7]. The analysis also shows an hexagonal structure which is attributed to ZnO in different orientations forming a compounded lattice of forming hexagonal interface with d-spacing indicating 100 orientation in Wurzite [8].

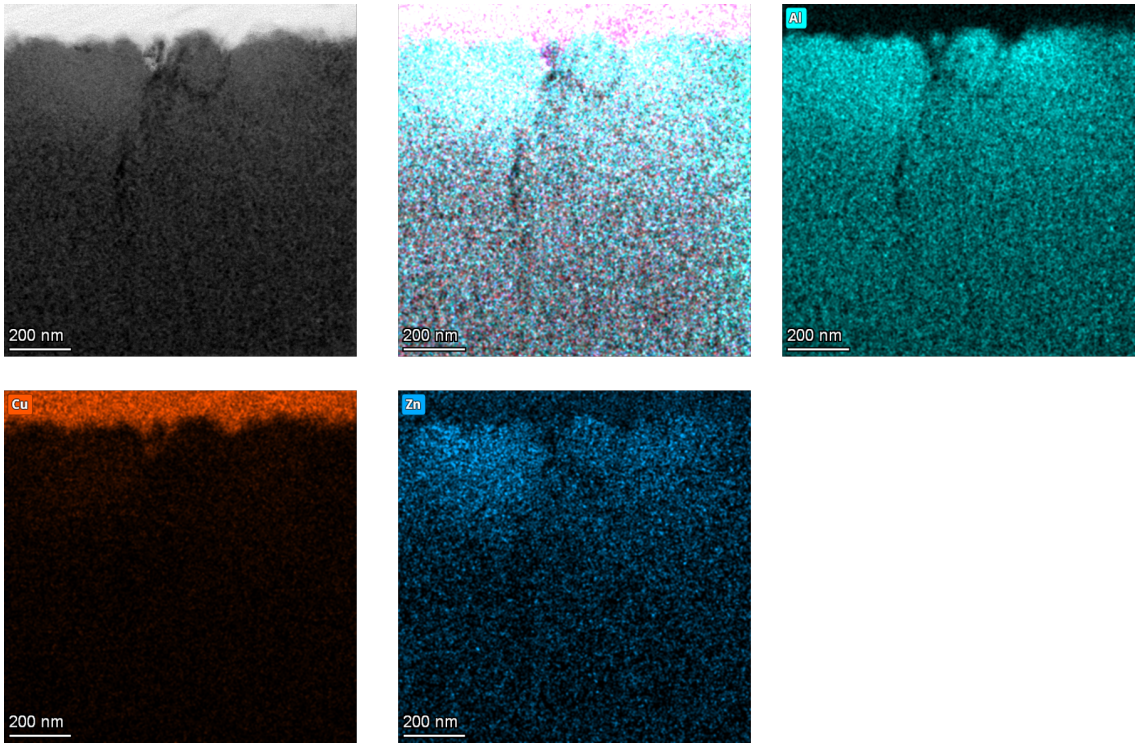

Figure B.3.: STEM EDX-analysis of the radial lamellae cross sections for 20% CZ

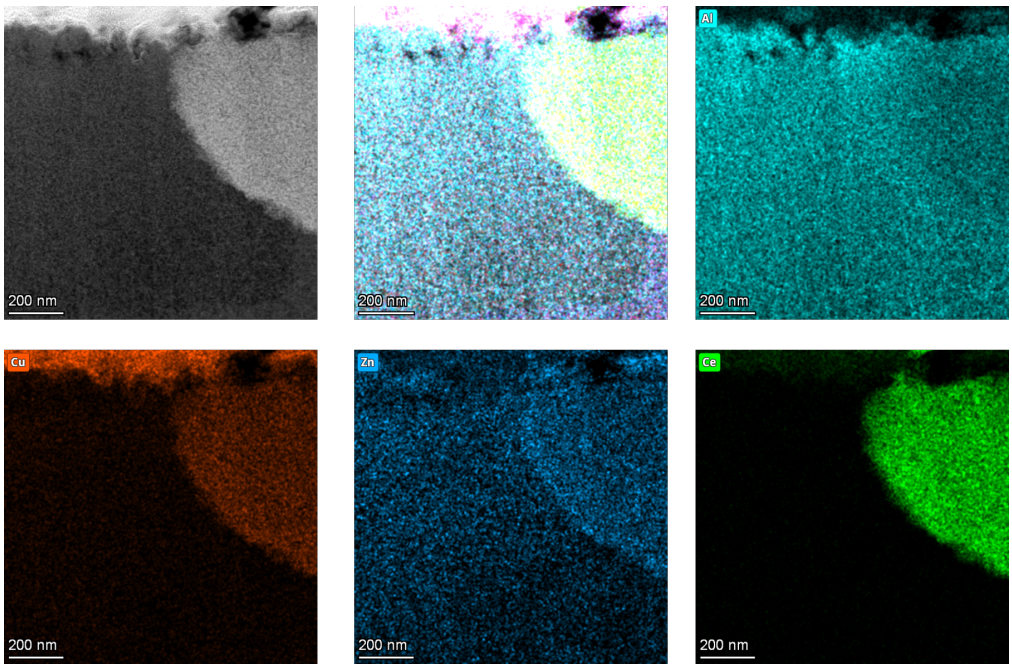

Figure B.4.: STEM EDX-analysis of the radial lamellae cross sections for 20% CZC

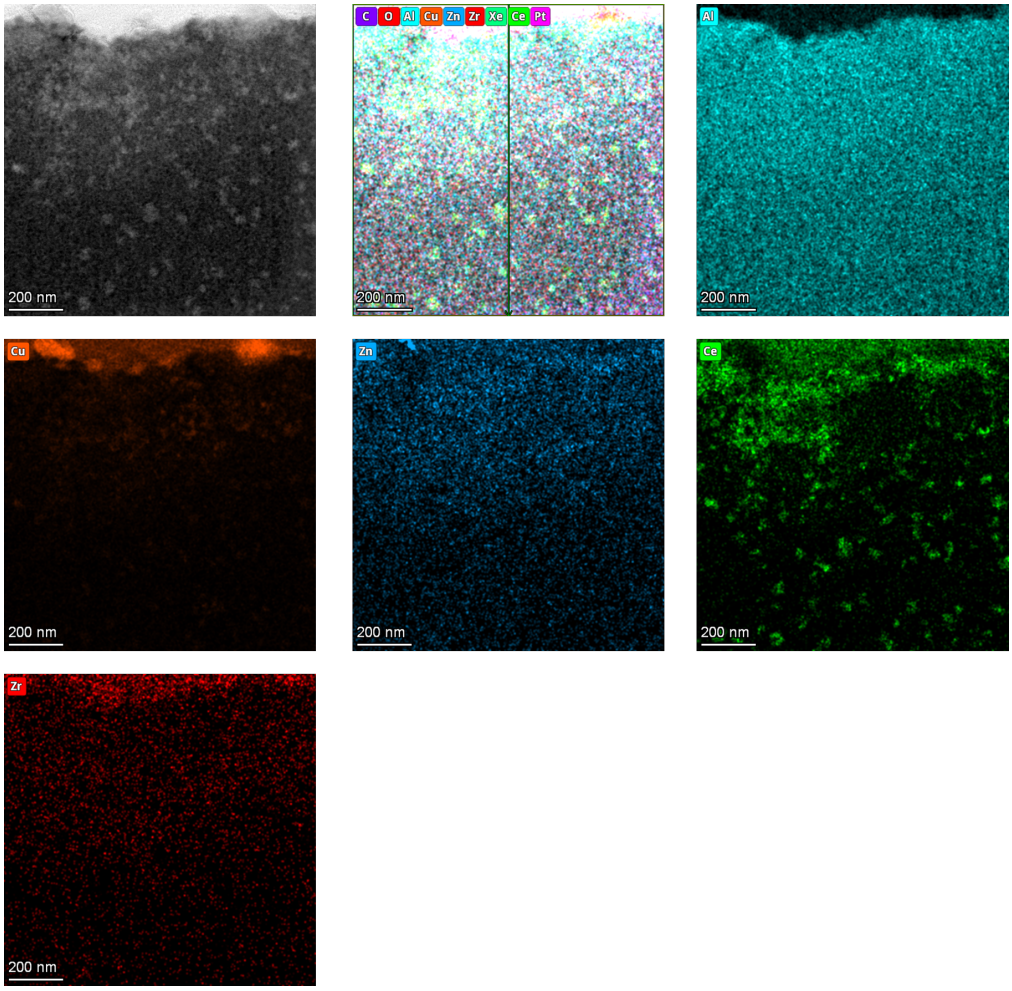

Figure B.5.: STEM EDX-analysis of the radial lamellae cross sections for 20% CZCZ

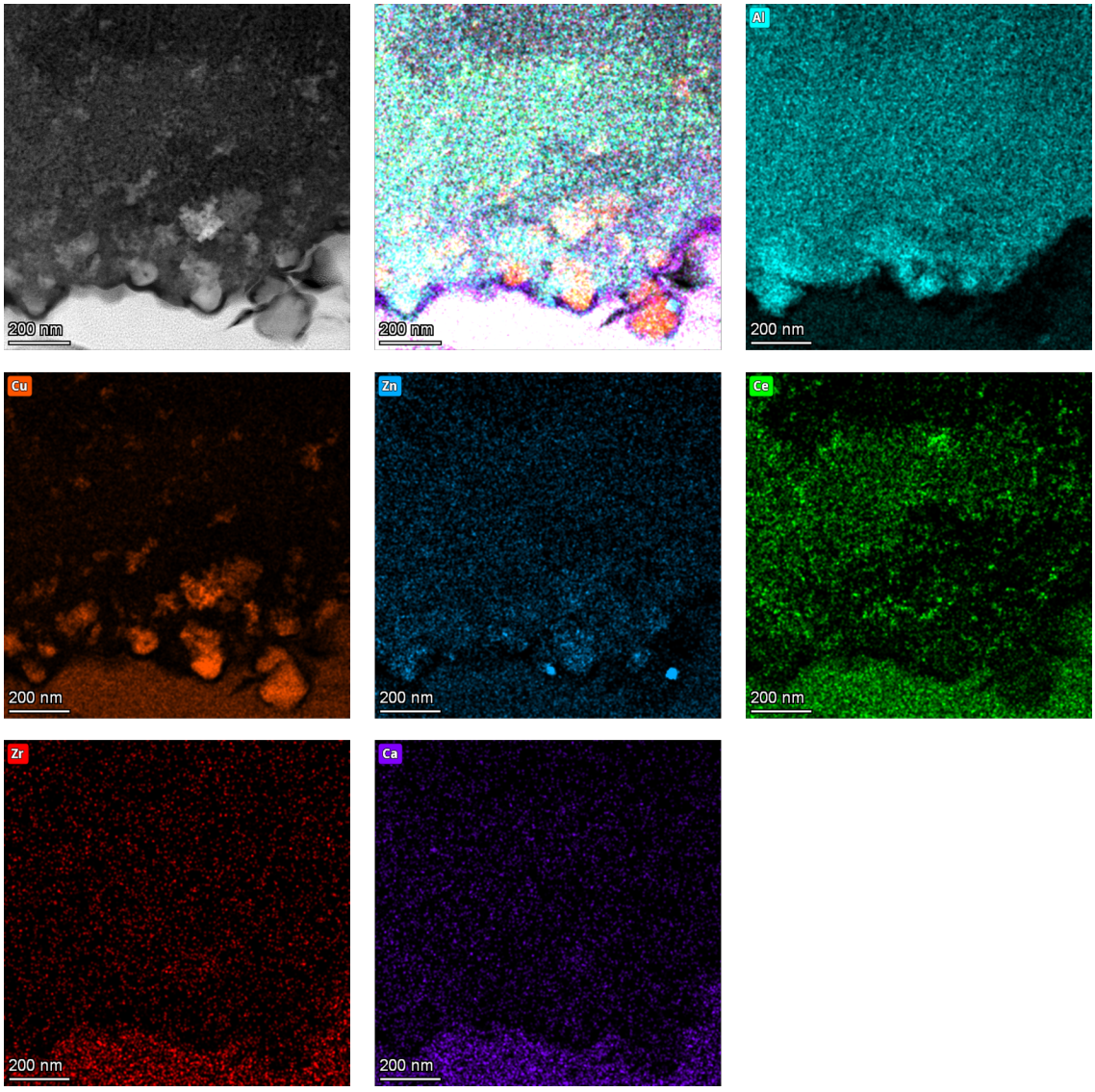

Figure B.6.: STEM EDX-analysis of the radial lamellae cross sections for 20% CZCZC

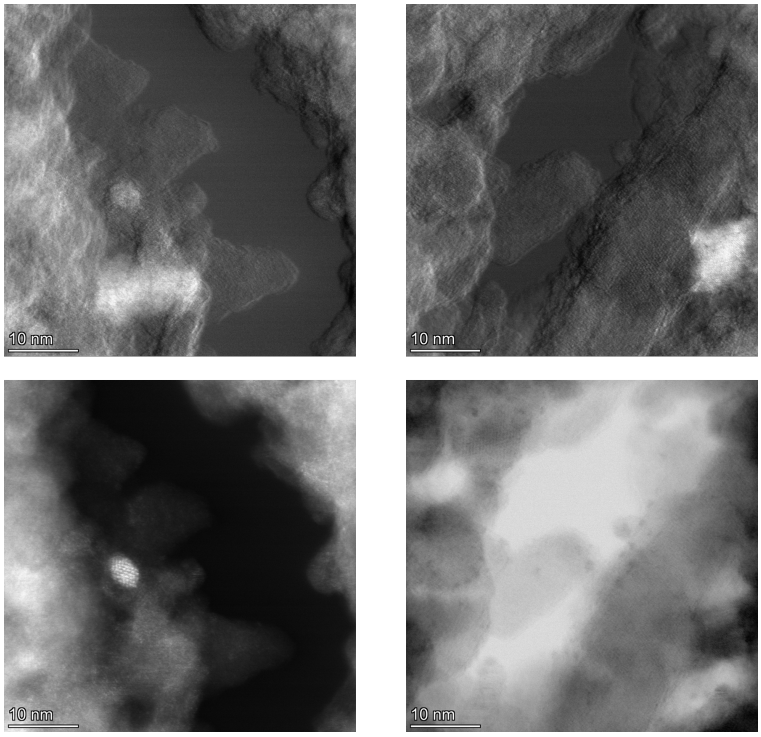

Figure B.7.: Additional bright and dark field TEM images at very high magnification of the FIB-lamella of 20% CZ

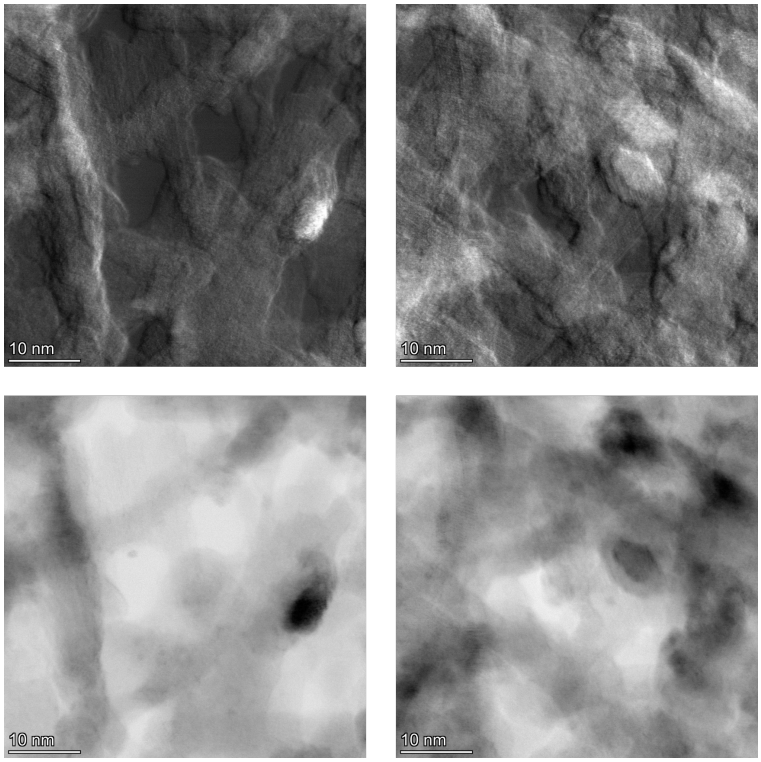

Figure B.8.: Additional bright and dark field TEM images at very high magnification of the FIB-lamella of 20% CZC

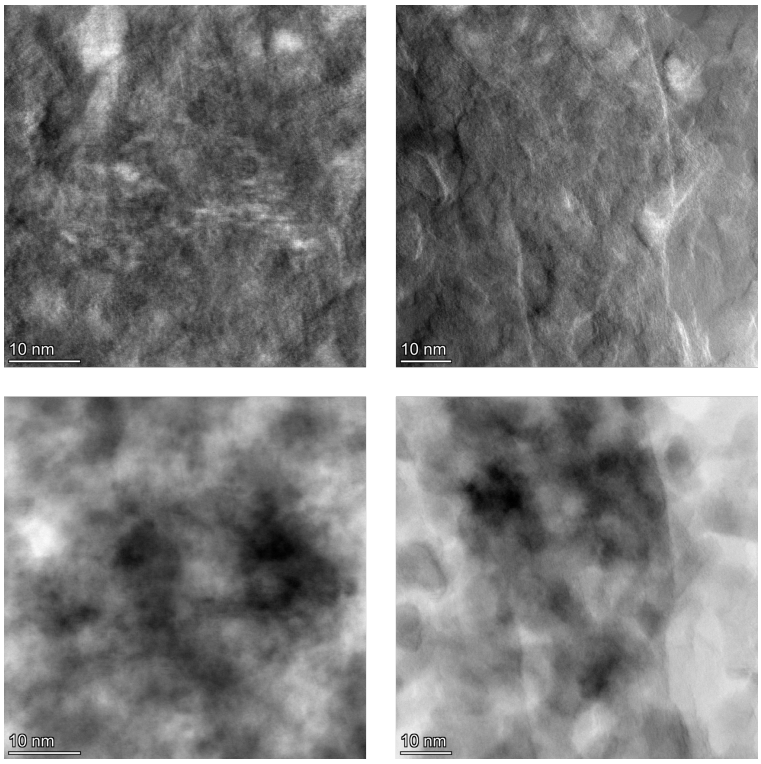

Figure B.9.: Additional bright and dark field TEM images at very high magnification of the FIB-lamella of 20% CZCZ

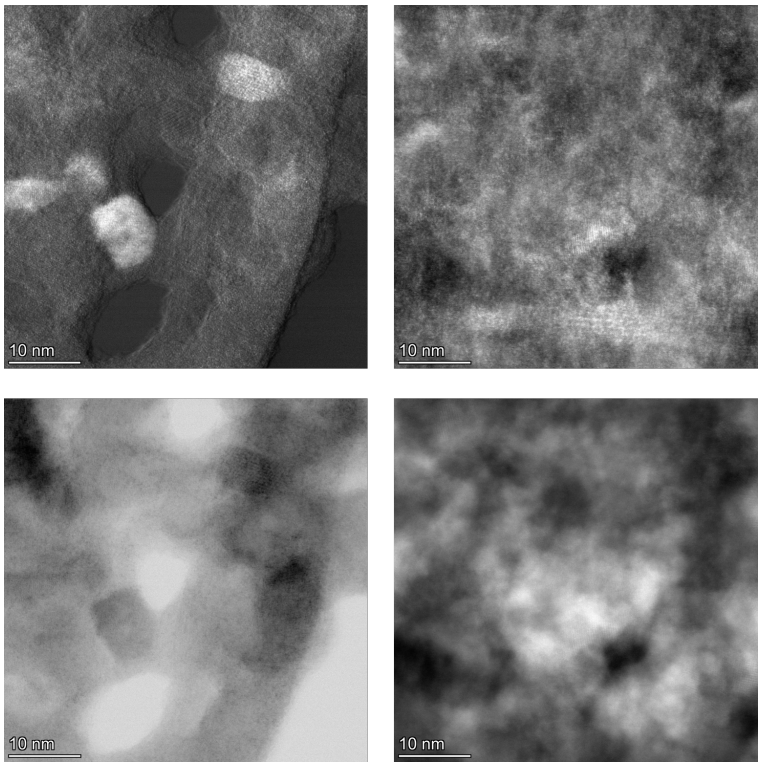

Figure B.10.: Additional bright and dark field TEM images at very high magnification of the FIB-lamella of 20% CZCZC

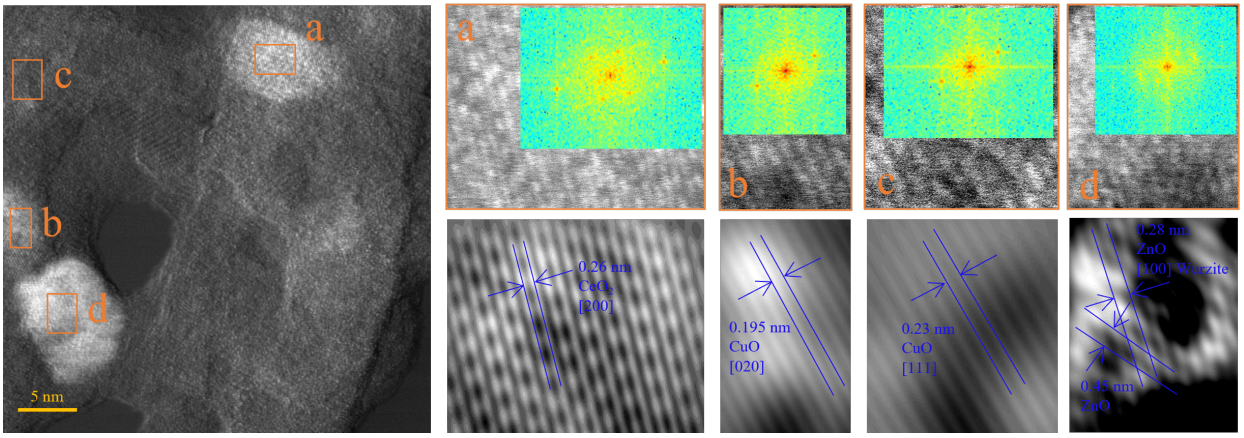

Figure B.11.: FFT and IFFT analysis of a HAADF STEM Image of the lamella of 20% CZCZC. Four different areas (Regions of Interest) are investigated.

B.2. Reaction kinetics

B.2.1. Test conditions for each catalyst

Table B.1, table B.2, table B.3 and table B.4 show the applied test conditions for each catalyst. 20% CZCZC was subjected to a slightly longer testing phase for a wider numerical basis for the conducted parameter fitting. Tests using only CO_2 in the reactant stream with COR = 1 and the stoichiometric number (SN) set at 3.0 were taken from previous studies using the same catalysts. The results of the CO_2 conversion studies have been reported elsewhere [9]. All catalysts were tested at three temperatures (225 °C, 250 °C and 275 °C), three different gas hourly space velocities (GHSV) (approx. 8.000 h^{-1}, 10.000 h^{-1}, 12.000 h^{-1}) three reactor pressures (20 bar, 35 bar, 50 bar) and four different gas compositions concerning carbon oxide ratio (COR) (1, 0.81, 0.72, 0.36). The tables contain initial gas velocity, which can be calculated from GHSV through

$$v_{\text{gas}} = \frac{\text{GHSV} \times V_{\text{reactor}}}{A_{\text{cross}} \times 3600} \tag{B.1}$$

where:

$$v_{\text{gas}} = \text{gas velocity} \quad [\text{m}\,\text{s}^{-1}] \tag{B.2}$$

$$\text{GHSV} = \text{gas hourly space velocity} \quad [\text{h}^{-1}] \tag{B.3}$$

$$V_{\text{reactor}} = \text{reactor volume} \quad [\text{m}^3] \tag{B.4}$$

$$A_{\text{cross}} = \text{reactor cross-sectional area} \quad [\text{m}^2] \tag{B.5}$$

$$3600 = \text{conversion factor from hours to seconds} \quad [\text{s}\,\text{h}^{-1}] \tag{B.6}$$

For our cylindrical reactor with diameter D = 0.02:

$$A_{\text{cross}} = \frac{\pi D^2}{4} \tag{B.7}$$

Substituting this into the velocity equation:

$$v_{\text{gas}} = \frac{\text{GHSV} \times V_{\text{reactor}}}{\frac{\pi D^2}{4} \times 3600} = \frac{4 \times \text{GHSV} \times V_{\text{reactor}}}{\pi D^2 \times 3600} \tag{B.8}$$

For a cylindrical reactor with height H, where $V_{\text{reactor}} = \frac{\pi D^2 H}{4}$:

$$v_{\text{gas}} = \frac{4 \times \text{GHSV} \times \frac{\pi D^2 H}{4}}{\pi D^2 \times 3600} = \frac{\text{GHSV} \times H}{3600} \tag{B.9}$$

This simplifies to:

$$\boxed{v_{\text{gas}} = \frac{\text{GHSV} \times H}{3600}} \tag{B.10}$$

Table B.1.: Experimental Conditions - 20% CZ Catalyst

Point	T	P	u_s	Molar Composition (%)					r_{MeOH}	r_{H_2O}	COR
	(K)	(bar)	(m/s)	H_2	CO_2	CO	H_2O	MeOH	(mol/kg/s)	(mol/kg/s)	(%)
50	498	20.0	0.0884	79.8	20.2	0.0	0.0	0.0	0.0014	0.0025	100.0
59	498	20.0	0.1029	81.5	15.7	2.8	0.0	0.0	0.0013	0.0040	84.9
7	498	35.0	0.0405	79.7	20.3	0.0	0.0	0.0	0.0012	0.0024	100.0
26	498	35.0	0.0407	81.8	14.8	3.4	0.0	0.0	0.0020	0.0019	81.3
32	498	35.0	0.0505	80.0	20.0	0.0	0.0	0.0	0.0021	0.0031	100.0
42	498	35.0	0.0506	80.0	20.0	0.0	0.0	0.0	0.0015	0.0032	100.0
33	498	35.0	0.0583	81.8	14.8	3.4	0.0	0.0	0.0026	0.0042	81.3
40	498	50.0	0.0263	90.8	9.2	0.0	0.0	0.0	0.0010	0.0015	100.0
52	498	50.0	0.0289	81.4	15.6	3.0	0.0	0.0	0.0018	0.0021	83.9
43	498	50.0	0.0370	87.2	4.6	8.2	0.0	0.0	0.0032	0.0019	35.9
53	498	50.0	0.0405	79.7	20.3	0.0	0.0	0.0	0.0023	0.0033	100.0
1	498	50.0	0.0430	78.9	21.1	0.0	0.0	0.0	0.0035	0.0045	100.0
55	523	20.0	0.0813	87.0	4.6	8.4	0.0	0.0	0.0008	0.0008	35.4
41	523	20.0	0.0892	81.9	14.6	3.5	0.0	0.0	0.0013	0.0039	80.7
9	523	20.0	0.0901	81.4	15.6	3.0	0.0	0.0	0.0011	0.0040	83.9
36	523	20.0	0.0929	80.0	20.0	0.0	0.0	0.0	0.0017	0.0044	100.0
12	523	20.0	0.0973	87.2	4.6	8.2	0.0	0.0	0.0012	0.0013	35.9
5	523	20.0	0.1072	81.8	14.8	3.4	0.0	0.0	0.0013	0.0041	81.3
18	523	20.0	0.1078	81.6	15.6	2.8	0.0	0.0	0.0014	0.0037	84.8
39	523	20.0	0.1115	80.1	19.9	0.0	0.0	0.0	0.0015	0.0050	100.0
47	523	35.0	0.0464	87.1	4.5	8.4	0.0	0.0	0.0020	0.0009	34.9
6	523	35.0	0.0511	81.7	14.8	3.5	0.0	0.0	0.0024	0.0047	70.9
14	523	35.0	0.0515	81.4	15.6	3.0	0.0	0.0	0.0019	0.0043	83.9
51	523	35.0	0.0556	87.2	4.6	8.2	0.0	0.0	0.0023	0.0015	35.9
23	523	35.0	0.0613	81.7	14.9	3.4	0.0	0.0	0.0031	0.0050	81.4
60	523	35.0	0.0637	80.1	19.9	0.0	0.0	0.0	0.0022	0.0061	100.0
10	523	35.0	0.0638	80.0	20.0	0.0	0.0	0.0	0.0023	0.0061	100.0
24	523	35.0	0.0652	77.2	20.2	2.7	0.0	0.0	0.0030	0.0054	88.2
49	523	50.0	0.0360	81.4	15.6	3.0	0.0	0.0	0.0027	0.0045	71.9
4	523	50.0	0.0358	81.7	14.8	3.5	0.0	0.0	0.0030	0.0045	80.9
8	523	50.0	0.0372	79.9	20.1	0.0	0.0	0.0	0.0032	0.0056	100.0
13	523	50.0	0.0390	87.2	4.6	8.2	0.0	0.0	0.0045	0.0017	35.9
38	523	50.0	0.0429	81.6	15.0	3.4	0.0	0.0	0.0035	0.0059	81.5
11	523	50.0	0.0432	81.6	15.6	2.8	0.0	0.0	0.0037	0.0066	84.8
31	523	50.0	0.0446	79.9	20.1	0.0	0.0	0.0	0.0032	0.0072	100.0
22	523	50.0	0.0813	87.0	4.6	8.4	0.0	0.0	0.0034	0.0017	35.4
19	548	20.0	0.0852	87.0	4.6	8.4	0.0	0.0	0.0007	0.0010	35.4
48	548	20.0	0.0937	81.7	14.8	3.5	0.0	0.0	0.0007	0.0040	80.9
27	548	20.0	0.0944	81.4	15.6	3.0	0.0	0.0	0.0011	0.0046	83.9
3	548	20.0	0.0973	80.0	20.0	0.0	0.0	0.0	0.0007	0.0057	100.0
35	548	20.0	0.1019	87.2	4.6	8.2	0.0	0.0	0.0008	0.0015	35.9
28	548	20.0	0.1128	81.4	15.2	3.4	0.0	0.0	0.0012	0.0064	71.7
15	548	20.0	0.1132	81.5	15.7	2.8	0.0	0.0	0.0011	0.0062	84.9
29	548	20.0	0.1168	80.1	19.9	0.0	0.0	0.0	0.0012	0.0060	100.0
16	548	35.0	0.0487	86.9	4.6	8.4	0.0	0.0	0.0023	0.0011	35.4
21	548	35.0	0.0535	81.6	14.9	3.5	0.0	0.0	0.0023	0.0047	81.0
17	548	35.0	0.0539	81.4	15.5	3.0	0.0	0.0	0.0022	0.0051	83.8
54	548	35.0	0.0556	80.0	20.0	0.0	0.0	0.0	0.0019	0.0071	100.0
46	548	35.0	0.0582	87.2	4.6	8.2	0.0	0.0	0.0029	0.0011	35.9
2	548	35.0	0.0642	81.7	14.9	3.4	0.0	0.0	0.0031	0.0068	81.4
34	548	35.0	0.0646	81.6	15.6	2.8	0.0	0.0	0.0029	0.0067	84.8
58	548	35.0	0.0667	80.0	20.0	0.0	0.0	0.0	0.0025	0.0086	100.0
20	548	50.0	0.0341	86.9	4.7	8.4	0.0	0.0	0.0042	0.0012	35.9
37	548	50.0	0.0385	79.8	17.3	3.0	0.0	0.0	0.0037	0.0048	75.2
56	548	50.0	0.0397	77.0	19.7	3.3	0.0	0.0	0.0047	0.0061	85.7
30	548	50.0	0.0408	87.1	4.6	8.2	0.0	0.0	0.0046	0.0016	35.9
44	548	50.0	0.0433	72.0	28.0	0.0	0.0	0.0	0.0040	0.0093	100.0
25	548	50.0	0.0450	81.8	14.8	3.4	0.0	0.0	0.0040	0.0051	81.3
57	548	50.0	0.0452	81.5	15.7	2.8	0.0	0.0	0.0037	0.0053	84.9
45	548	50.0	0.0472	79.3	20.7	0.0	0.0	0.0	0.0046	0.0082	100.0

T = temperature, P = total pressure, u_s = superficial gas velocity
r_{MeOH} = measured methanol formation rate, r_{H_2O} = measured water formation rate
COR = CO_2 conversion ratio

Table B.2.: Experimental Conditions - 20% CZC Catalyst

Point	T	P	u_s	Molar Composition (%)					r_{MeOH}	r_{H_2O}	COR
	(K)	(bar)	(m/s)	H_2	CO_2	CO	H_2O	MeOH	(mol/kg/s)	(mol/kg/s)	(%)
12	498	20.0	0.0619	87.0	5.0	8.0	0.0	0.0	0.0008	0.0007	38.5
41	523	20.0	0.0814	87.0	4.6	8.4	0.0	0.0	0.0010	0.0012	35.4
18	523	20.0	0.0896	81.7	14.8	3.5	0.0	0.0	0.0011	0.0033	80.9
59	523	20.0	0.0903	81.4	15.5	3.0	0.0	0.0	0.0010	0.0031	83.8
8	523	20.0	0.0975	87.2	4.6	8.2	0.0	0.0	0.0010	0.0014	35.9
3	523	20.0	0.1074	81.8	14.8	3.4	0.0	0.0	0.0010	0.0040	81.3
57	523	20.0	0.1080	81.6	15.6	2.8	0.0	0.0	0.0014	0.0041	84.8
20	523	20.0	0.0745	80.0	19.9	0.0	0.0	0.0	0.0010	0.0039	100.0
21	523	20.0	0.0931	80.0	20.0	0.0	0.0	0.0	0.0010	0.0041	100.0
10	523	20.0	0.1117	80.0	19.9	0.0	0.0	0.0	0.0011	0.0052	100.0
50	548	20.0	0.0853	87.1	4.5	8.4	0.0	0.0	0.0009	0.0012	34.9
47	548	20.0	0.0946	81.6	15.4	3.0	0.0	0.0	0.0010	0.0037	83.7
53	548	20.0	0.0939	81.7	14.8	3.5	0.0	0.0	0.0013	0.0057	80.9
16	548	20.0	0.1022	87.2	4.6	8.2	0.0	0.0	0.0012	0.0017	35.9
1	548	20.0	0.1125	81.8	14.8	3.4	0.0	0.0	0.0013	0.0044	81.3
26	548	20.0	0.1132	81.6	15.6	2.8	0.0	0.0	0.0013	0.0053	84.8
37	548	20.0	0.0975	80.0	20.0	0.0	0.0	0.0	0.0011	0.0060	100.0
46	548	20.0	0.1170	80.0	20.0	0.0	0.0	0.0	0.0011	0.0079	100.0
32	498	35.0	0.0507	80.0	20.0	0.0	0.0	0.0	0.0020	0.0036	100.0
13	498	35.0	0.0507	79.8	20.2	0.0	0.0	0.0	0.0022	0.0038	100.0
39	523	35.0	0.0371	87.1	4.4	8.5	0.0	0.0	0.0015	0.0009	34.1
48	523	35.0	0.0413	81.2	15.7	3.0	0.0	0.0	0.0014	0.0032	84.0
29	523	35.0	0.0425	80.0	20.0	0.0	0.0	0.0	0.0014	0.0043	100.0
23	523	35.0	0.0464	87.0	4.6	8.4	0.0	0.0	0.0012	0.0014	35.4
14	523	35.0	0.0512	81.6	14.9	3.5	0.0	0.0	0.0016	0.0038	81.0
56	523	35.0	0.0512	81.7	14.8	3.5	0.0	0.0	0.0022	0.0044	80.9
22	523	35.0	0.0516	81.3	15.6	3.0	0.0	0.0	0.0021	0.0040	83.9
34	523	35.0	0.0532	80.0	19.9	0.0	0.0	0.0	0.0020	0.0056	100.0
11	523	35.0	0.0555	87.1	4.7	8.2	0.0	0.0	0.0016	0.0014	36.4
42	523	35.0	0.0617	81.6	15.6	2.8	0.0	0.0	0.0019	0.0049	84.8
4	523	35.0	0.0639	74.9	25.1	0.0	0.0	0.0	0.0023	0.0085	100.0
25	548	35.0	0.0445	80.1	19.9	0.0	0.0	0.0	0.0021	0.0049	100.0
49	548	35.0	0.0488	87.0	4.5	8.4	0.0	0.0	0.0019	0.0011	34.9
17	548	35.0	0.0538	74.4	22.4	3.2	0.0	0.0	0.0028	0.0068	87.5
61	548	35.0	0.0557	80.0	20.0	0.0	0.0	0.0	0.0022	0.0068	100.0
43	548	35.0	0.0584	87.0	4.8	8.2	0.0	0.0	0.0024	0.0018	36.9
58	548	35.0	0.0644	75.3	21.6	3.1	0.0	0.0	0.0037	0.0086	87.4
33	548	35.0	0.0647	81.4	15.8	2.8	0.0	0.0	0.0023	0.0055	84.9
62	548	35.0	0.0648	81.6	15.6	2.8	0.0	0.0	0.0026	0.0055	84.8
45	548	35.0	0.0669	80.0	20.0	0.0	0.0	0.0	0.0026	0.0082	100.0
31	498	50.0	0.0249	87.0	4.6	8.4	0.0	0.0	0.0011	0.0008	35.4
52	498	50.0	0.0284	80.1	19.9	0.0	0.0	0.0	0.0020	0.0036	100.0
27	498	50.0	0.0355	80.0	20.0	0.0	0.0	0.0	0.0023	0.0035	100.0
5	523	50.0	0.0261	87.0	4.6	8.4	0.0	0.0	0.0022	0.0013	35.4
55	523	50.0	0.0287	81.6	14.9	3.5	0.0	0.0	0.0025	0.0038	81.0
9	523	50.0	0.0288	81.4	15.6	3.0	0.0	0.0	0.0025	0.0035	83.9
36	523	50.0	0.0325	86.6	5.3	8.2	0.0	0.0	0.0027	0.0017	39.3
15	523	50.0	0.0358	81.7	14.8	3.5	0.0	0.0	0.0032	0.0041	80.9
51	523	50.0	0.0358	83.4	13.1	3.6	0.0	0.0	0.0030	0.0037	78.4
44	523	50.0	0.0361	80.2	16.8	3.0	0.0	0.0	0.0027	0.0042	84.8
35	523	50.0	0.0372	79.0	21.0	0.0	0.0	0.0	0.0031	0.0061	100.0
19	523	50.0	0.0391	85.5	6.4	8.1	0.0	0.0	0.0029	0.0013	44.1
38	523	50.0	0.0429	84.6	11.9	3.5	0.0	0.0	0.0025	0.0043	77.3
54	523	50.0	0.0432	81.4	15.8	2.8	0.0	0.0	0.0029	0.0055	84.9
60	523	50.0	0.0477	87.1	4.4	8.5	0.0	0.0	0.0040	0.0081	34.1
2	548	50.0	0.0453	81.6	15.6	2.8	0.0	0.0	0.0039	0.0065	84.8
24	548	50.0	0.0341	86.1	5.6	8.3	0.0	0.0	0.0033	0.0013	40.3
28	548	50.0	0.0376	81.7	14.8	3.5	0.0	0.0	0.0034	0.0052	80.9
40	548	50.0	0.0390	80.0	19.9	0.0	0.0	0.0	0.0032	0.0071	100.0
6	548	50.0	0.0409	86.6	5.2	8.2	0.0	0.0	0.0037	0.0016	38.8
30	548	50.0	0.0468	80.0	20.0	0.0	0.0	0.0	0.0036	0.0086	100.0
7	548	50.0	0.0378	81.4	15.6	3.0	0.0	0.0	0.0029	0.0057	83.9

T = temperature, P = total pressure, u_s = superficial gas velocity
r_{MeOH} = measured methanol formation rate, r_{H_2O} = measured water formation rate
COR = CO_2 conversion ratio = $\%CO_2/(\%CO_2+\%CO) \times 100$

Table B.3.: Experimental Conditions - 20% CZCZ Catalyst

Point	T	P	u_s	Molar Composition (%)					r_{MeOH}	r_{H_2O}	COR
	(K)	(bar)	(m/s)	H_2	CO_2	CO	H_2O	MeOH	(mol/kg/s)	(mol/kg/s)	(%)
50	498	20.0	0.0620	87.0	4.5	8.4	0.0	0.0	0.0013	0.0013	34.9
55	523	20.0	0.0814	87.0	4.6	8.4	0.0	0.0	0.0013	0.0030	35.4
43	523	20.0	0.0812	87.2	4.6	8.2	0.0	0.0	0.0014	0.0024	36.0
25	523	20.0	0.0723	77.8	19.2	2.9	0.0	0.0	0.0012	0.0050	86.9
34	523	20.0	0.0896	81.7	14.8	3.5	0.0	0.0	0.0026	0.0040	80.9
2	523	20.0	0.0903	81.4	15.6	3.0	0.0	0.0	0.0019	0.0042	83.9
35	523	20.0	0.1081	81.6	15.6	2.8	0.0	0.0	0.0024	0.0050	84.8
36	523	20.0	0.0745	79.6	20.4	0.0	0.0	0.0	0.0022	0.0044	100.0
62	523	20.0	0.0931	80.1	19.9	0.0	0.0	0.0	0.0026	0.0052	100.0
12	523	20.0	0.1117	80.0	19.9	0.0	0.0	0.0	0.0034	0.0071	100.0
18	548	20.0	0.0853	87.0	4.6	8.4	0.0	0.0	0.0007	0.0012	35.4
21	548	20.0	0.0853	87.0	4.6	8.4	0.0	0.0	0.0011	0.0027	35.4
9	548	20.0	0.0939	81.7	14.8	3.5	0.0	0.0	0.0014	0.0047	80.9
44	548	20.0	0.0946	81.4	15.6	3.0	0.0	0.0	0.0019	0.0045	83.9
47	548	20.0	0.0946	81.4	15.5	3.0	0.0	0.0	0.0016	0.0051	83.8
15	548	20.0	0.1125	81.8	14.8	3.4	0.0	0.0	0.0025	0.0061	81.3
41	548	20.0	0.1132	81.6	15.6	2.8	0.0	0.0	0.0021	0.0075	84.8
24	548	20.0	0.1171	80.0	20.0	0.0	0.0	0.0	0.0012	0.0103	100.0
56	548	20.0	0.1171	80.0	20.0	0.0	0.0	0.0	0.0014	0.0065	100.0
49	498	35.0	0.0507	80.0	20.0	0.0	0.0	0.0	0.0046	0.0062	100.0
31	498	35.0	0.0405	80.0	20.0	0.0	0.0	0.0	0.0030	0.0043	100.0
11	523	35.0	0.0383	84.8	4.2	10.9	0.0	0.0	0.0024	0.0027	27.8
26	523	35.0	0.0410	81.8	14.7	3.5	0.0	0.0	0.0037	0.0030	80.8
5	523	35.0	0.0411	78.7	17.8	3.5	0.0	0.0	0.0023	0.0053	83.6
23	523	35.0	0.0426	75.4	24.6	0.0	0.0	0.0	0.0035	0.0050	100.0
42	523	35.0	0.0464	87.2	4.6	8.2	0.0	0.0	0.0021	0.0020	35.9
19	523	35.0	0.0512	81.7	14.8	3.5	0.0	0.0	0.0027	0.0055	80.9
16	523	35.0	0.0516	81.4	15.6	3.0	0.0	0.0	0.0035	0.0044	83.9
45	523	35.0	0.0516	81.4	15.6	3.0	0.0	0.0	0.0022	0.0051	83.9
48	523	35.0	0.0532	79.9	20.1	0.0	0.0	0.0	0.0042	0.0063	100.0
7	523	35.0	0.0618	81.6	15.6	2.8	0.0	0.0	0.0029	0.0060	84.8
60	523	35.0	0.0465	87.0	4.6	8.4	0.0	0.0	0.0012	0.0016	35.4
52	523	35.0	0.0464	87.2	4.6	8.2	0.0	0.0	0.0027	0.0020	35.9
46	523	35.0	0.0638	80.1	19.9	0.0	0.0	0.0	0.0056	0.0069	100.0
22	548	35.0	0.0557	80.0	20.0	0.0	0.0	0.0	0.0030	0.0064	100.0
6	548	35.0	0.0536	81.7	14.8	3.5	0.0	0.0	0.0022	0.0036	80.9
38	548	35.0	0.0538	78.7	17.8	3.5	0.0	0.0	0.0028	0.0055	83.6
37	548	35.0	0.0643	81.8	14.8	3.4	0.0	0.0	0.0029	0.0040	81.3
54	548	35.0	0.0644	78.9	17.9	3.2	0.0	0.0	0.0035	0.0059	84.8
39	548	35.0	0.0432	81.6	15.6	2.8	0.0	0.0	0.0051	0.0066	84.8
51	498	50.0	0.0248	87.0	4.5	8.4	0.0	0.0	0.0023	0.0034	34.9
1	498	50.0	0.0284	80.0	20.0	0.0	0.0	0.0	0.0035	0.0047	100.0
30	498	50.0	0.0355	80.0	20.0	0.0	0.0	0.0	0.0037	0.0052	100.0
13	523	50.0	0.0260	87.0	4.6	8.4	0.0	0.0	0.0026	0.0050	35.4
27	523	50.0	0.0325	87.0	4.6	8.4	0.0	0.0	0.0032	0.0020	35.4
33	523	50.0	0.0358	81.7	14.8	3.5	0.0	0.0	0.0044	0.0057	80.9
14	523	50.0	0.0361	81.4	15.6	3.0	0.0	0.0	0.0044	0.0059	83.9
20	523	50.0	0.0372	80.0	20.0	0.0	0.0	0.0	0.0049	0.0078	100.0
32	523	50.0	0.0390	87.2	4.6	8.2	0.0	0.0	0.0028	0.0017	36.0
57	523	50.0	0.0430	81.8	14.9	3.4	0.0	0.0	0.0052	0.0068	81.4
39	523	50.0	0.0432	81.6	15.6	2.8	0.0	0.0	0.0051	0.0066	84.8
3	523	50.0	0.0447	80.0	20.0	0.0	0.0	0.0	0.0054	0.0064	100.0
17	548	50.0	0.0345	79.1	13.3	7.7	0.0	0.0	0.0033	0.0045	63.4
58	548	50.0	0.0375	81.7	14.8	3.5	0.0	0.0	0.0040	0.0060	80.9
10	548	50.0	0.0378	81.3	15.6	3.0	0.0	0.0	0.0040	0.0059	83.9
29	548	50.0	0.0390	81.4	18.6	0.0	0.0	0.0	0.0026	0.0066	100.0
4	548	50.0	0.0412	81.4	10.9	7.7	0.0	0.0	0.0024	0.0041	58.6
59	548	50.0	0.0450	83.1	13.4	3.5	0.0	0.0	0.0046	0.0062	79.3
8	548	50.0	0.0453	81.5	15.7	2.8	0.0	0.0	0.0043	0.0070	84.9
40	548	50.0	0.0468	80.0	20.0	0.0	0.0	0.0	0.0043	0.0075	100.0
28	548	50.0	0.0487	87.0	4.6	8.4	0.0	0.0	0.0011	0.0017	35.4

T = temperature, P = total pressure, u_s = superficial gas velocity
r_{MeOH} = measured methanol formation rate, r_{H_2O} = measured water formation rate
COR = CO_2 conversion ratio = $\%CO_2/(\%CO_2+\%CO) \times 100$

Table B.4.: Experimental Conditions - 20% CZCZC Catalyst

Point	T	P	u_s	Molar Composition (%)					r_{MeOH}	r_{H_2O}	COR
	(K)	(bar)	(m/s)	H_2	CO_2	CO	H_2O	MeOH	(mol/kg/s)	(mol/kg/s)	(%)
2	498	20.0	0.0619	87.1	4.6	8.3	0.0	0.0	0.0010	0.0012	35.7
49	498	20.0	0.0683	81.5	14.8	3.6	0.0	0.0	0.0011	0.0024	80.4
73	498	20.0	0.0686	81.5	15.6	2.9	0.0	0.0	0.0011	0.0026	84.3
30	498	20.0	0.0710	80.0	20.0	0.0	0.0	0.0	0.0020	0.0044	100.0
3	498	20.0	0.0775	87.0	4.6	8.4	0.0	0.0	0.0007	0.0008	35.4
26	498	20.0	0.0859	81.4	15.6	3.0	0.0	0.0	0.0012	0.0023	83.9
80	498	20.0	0.0859	81.4	15.6	3.0	0.0	0.0	0.0015	0.0032	83.9
35	498	20.0	0.0853	81.6	14.8	3.5	0.0	0.0	0.0012	0.0025	80.9
52	498	20.0	0.0928	87.1	4.6	8.2	0.0	0.0	0.0009	0.0009	35.9
27	498	20.0	0.1022	81.7	14.8	3.4	0.0	0.0	0.0015	0.0032	81.3
58	498	20.0	0.1029	81.5	15.6	2.8	0.0	0.0	0.0012	0.0021	84.8
88	498	20.0	0.1063	80.0	19.9	0.0	0.0	0.0	0.0016	0.0052	100.0
69	498	35.0	0.0390	81.6	14.8	3.6	0.0	0.0	0.0026	0.0027	80.4
54	498	35.0	0.0391	81.5	15.6	2.9	0.0	0.0	0.0023	0.0031	84.3
22	498	35.0	0.0405	80.0	19.9	0.0	0.0	0.0	0.0018	0.0053	100.0
21	498	35.0	0.0442	87.0	4.6	8.4	0.0	0.0	0.0019	0.0017	35.4
32	498	35.0	0.0487	81.7	14.8	3.5	0.0	0.0	0.0032	0.0045	80.9
64	498	35.0	0.0490	81.4	15.6	3.0	0.0	0.0	0.0022	0.0056	83.9
67	498	35.0	0.0506	78.6	14.3	7.1	0.0	0.0	0.0023	0.0026	66.8
61	498	35.0	0.0506	80.0	20.0	0.0	0.0	0.0	0.0023	0.0056	100.0
14	498	35.0	0.0531	87.2	4.6	8.2	0.0	0.0	0.0019	0.0019	35.9
83	498	35.0	0.0583	81.7	14.8	3.4	0.0	0.0	0.0032	0.0049	81.3
86	498	35.0	0.0588	81.6	15.6	2.8	0.0	0.0	0.0037	0.0046	84.8
40	498	35.0	0.0608	80.0	20.0	0.0	0.0	0.0	0.0030	0.0061	100.0
56	498	40.0	0.0309	87.1	4.6	8.3	0.0	0.0	0.0020	0.0006	35.7
74	498	50.0	0.0284	80.0	19.9	0.0	0.0	0.0	0.0036	0.0057	100.0
66	523	20.0	0.0650	87.1	4.6	8.3	0.0	0.0	0.0009	0.0008	35.7
47	523	20.0	0.0718	81.6	14.8	3.6	0.0	0.0	0.0015	0.0035	80.4
65	523	20.0	0.0721	81.5	15.6	2.9	0.0	0.0	0.0012	0.0036	84.3
28	523	20.0	0.0746	80.0	20.0	0.0	0.0	0.0	0.0016	0.0046	100.0
24	523	20.0	0.0813	87.0	4.6	8.4	0.0	0.0	0.0015	0.0015	35.4
20	523	20.0	0.0895	81.7	14.8	3.5	0.0	0.0	0.0012	0.0046	80.9
79	523	20.0	0.0896	81.6	14.9	3.5	0.0	0.0	0.0011	0.0041	81.0
38	523	20.0	0.0900	81.4	15.6	3.0	0.0	0.0	0.0011	0.0039	83.9
78	523	20.0	0.0931	80.0	20.0	0.0	0.0	0.0	0.0012	0.0058	100.0
53	523	20.0	0.0934	80.4	19.6	0.0	0.0	0.0	0.0015	0.0054	100.0
76	523	20.0	0.0973	87.1	4.6	8.2	0.0	0.0	0.0011	0.0029	35.9
87	523	20.0	0.1073	81.8	14.7	3.4	0.0	0.0	0.0019	0.0039	81.2
46	523	20.0	0.1085	81.8	15.4	2.8	0.0	0.0	0.0011	0.0050	84.6
19	523	35.0	0.0411	81.5	15.6	2.9	0.0	0.0	0.0017	0.0047	84.3
85	523	35.0	0.0425	80.0	20.0	0.0	0.0	0.0	0.0022	0.0058	100.0
72	523	35.0	0.0465	86.8	4.7	8.4	0.0	0.0	0.0019	0.0056	35.9
51	523	35.0	0.0511	81.6	14.9	3.5	0.0	0.0	0.0040	0.0045	81.0
18	523	35.0	0.0515	80.9	16.0	3.0	0.0	0.0	0.0033	0.0051	84.2
4	523	35.0	0.0532	80.0	20.0	0.0	0.0	0.0	0.0029	0.0077	100.0
63	523	35.0	0.0532	80.0	19.9	0.0	0.0	0.0	0.0029	0.0075	100.0
81	523	35.0	0.0614	81.7	14.9	3.4	0.0	0.0	0.0036	0.0057	81.4
33	523	35.0	0.0622	80.8	15.6	3.5	0.0	0.0	0.0029	0.0067	81.7
62	523	35.0	0.0636	79.1	20.9	0.0	0.0	0.0	0.0037	0.0100	100.0
71	523	50.0	0.0358	81.7	14.8	3.5	0.0	0.0	0.0042	0.0069	80.9
5	523	50.0	0.0359	81.5	15.0	3.5	0.0	0.0	0.0040	0.0064	81.1
7	523	50.0	0.0361	81.4	15.6	3.0	0.0	0.0	0.0041	0.0077	83.9
82	523	50.0	0.0372	80.0	19.9	0.1	0.0	0.0	0.0035	0.0070	99.5
17	523	50.0	0.0390	87.2	4.6	8.2	0.0	0.0	0.0036	0.0052	35.9
42	523	50.0	0.0428	81.6	14.9	3.4	0.0	0.0	0.0043	0.0025	81.4
10	523	50.0	0.0446	80.0	20.0	0.0	0.0	0.0	0.0033	0.0129	100.0
9	523	50.0	0.0583	79.3	20.7	0.0	0.0	0.0	0.0040	0.0080	100.0
34	523	50.0	0.0358	81.6	14.9	3.5	0.0	0.0	0.0044	0.0049	81.0
45	523	50.0	0.0425	87.0	4.5	8.4	0.0	0.0	0.0043	0.0025	34.9
39	548	20.0	0.0758	81.5	15.6	2.9	0.0	0.0	0.0009	0.0039	84.3
48	548	20.0	0.0781	80.0	20.0	0.0	0.0	0.0	0.0010	0.0054	100.0

Table B.5.: Experimental Conditions - 20% CZCZC Catalyst (continuation)

Point	T	P	u_s	Molar Composition (%)					r_{MeOH}	r_{H_2O}	COR
	(K)	(bar)	(m/s)	H_2	CO_2	CO	H_2O	MeOH	(mol/kg/s)	(mol/kg/s)	(%)
75	548	20.0	0.0851	87.0	4.6	8.4	0.0	0.0	0.0010	0.0019	35.4
1	548	20.0	0.0939	82.0	14.4	3.5	0.0	0.0	0.0012	0.0012	80.4
77	548	20.0	0.0945	81.4	15.6	3.0	0.0	0.0	0.0011	0.0053	83.9
70	548	20.0	0.0974	78.9	21.1	0.0	0.0	0.0	0.0010	0.0078	100.0
43	548	20.0	0.1019	87.1	4.6	8.2	0.0	0.0	0.0003	0.0027	35.9
60	548	20.0	0.1126	81.1	15.4	3.4	0.0	0.0	0.0010	0.0041	81.9
12	548	20.0	0.1130	81.5	15.7	2.8	0.0	0.0	0.0011	0.0060	84.9
41	548	20.0	0.1170	80.0	20.0	0.0	0.0	0.0	0.0012	0.0066	100.0
68	548	35.0	0.0486	86.6	5.0	8.4	0.0	0.0	0.0009	0.0024	37.3
59	548	35.0	0.0537	81.3	15.2	3.5	0.0	0.0	0.0013	0.0012	81.3
50	548	35.0	0.0541	81.1	15.9	3.0	0.0	0.0	0.0030	0.0048	84.1
36	548	35.0	0.0556	79.2	20.8	0.0	0.0	0.0	0.0027	0.0074	100.0
6	548	35.0	0.0586	84.0	8.1	7.9	0.0	0.0	0.0019	0.0047	50.6
31	548	35.0	0.0642	81.7	14.8	3.4	0.0	0.0	0.0031	0.0055	81.3
8	548	35.0	0.0669	79.8	20.2	0.0	0.0	0.0	0.0031	0.0080	100.0
23	548	35.0	0.0670	83.8	16.2	0.0	0.0	0.0	0.0053	0.0067	100.0
16	523	35.0	0.0356	87.0	4.7	8.2	0.0	0.0	0.0033	0.0045	36.4
44	523	35.0	0.0512	81.7	14.8	3.5	0.0	0.0	0.0032	0.0044	80.9
13	523	50.0	0.0361	81.6	15.6	2.8	0.0	0.0	0.0019	0.0047	84.8
52	498	20.0	0.0928	87.1	4.6	8.2	0.0	0.0	0.0012	0.0008	35.9
26	498	20.0	0.0205	81.4	15.6	3.0	0.0	0.0	0.0018	0.0053	83.9
84	548	50.0	0.0341	87.0	4.6	8.4	0.0	0.0	0.0022	0.0018	35.4
15	548	50.0	0.0375	81.7	14.8	3.5	0.0	0.0	0.0041	0.0047	80.9
25	548	50.0	0.0378	81.4	15.6	3.0	0.0	0.0	0.0054	0.0069	83.9
29	548	50.0	0.0390	80.0	20.0	0.0	0.0	0.0	0.0037	0.0080	100.0
57	548	50.0	0.0409	87.2	4.6	8.2	0.0	0.0	0.0028	0.0035	35.9
55	548	50.0	0.0451	81.8	14.8	3.4	0.0	0.0	0.0043	0.0054	81.3
37	548	50.0	0.0453	81.5	15.6	2.8	0.0	0.0	0.0037	0.0059	84.8
11	548	50.0	0.0468	79.9	20.0	0.0	0.0	0.0	0.0045	0.0075	100.0

T = temperature, P = total pressure, u_s = superficial gas velocity
r_{MeOH} = measured methanol formation rate, r_{H_2O} = measured water formation rate
COR = CO_2 conversion ratio = $\%CO_2/(\%CO_2+\%CO) \times 100$

B.2.2. Constrained Optimization Problem

The estimation of kinetic parameters for complex catalytic systems presents significant mathematical challenges due to the ill-conditioning of the inverse problem and the risk of obtaining physically meaningless solutions outside of natural bounds of the physio-chemical phenomena described by the mathematical problem. Constrained optimization algorithms, including the downhill simplex (Nelder-Mead) and Limited-memory Broyden-Fletcher-Goldfarb-Shanno with box constraints (L-BFGS-B) methods, are employed in this work to ensure parameter estimates remain within physically realistic bounds while maximizing the degree of experimental data reproduction by the fitted models [10]. Mathematical constraints serve three critical functions: (1) preventing numerical instabilities arising from extreme parameter values that could cause algorithmic divergence, (2) incorporating prior physical knowledge to regularize the otherwise under-determined parameter space, and (3) ensuring thermodynamic consistency by maintaining realistic relationships between activation energies, adsorption enthalpies, and pre-exponential factors. The constraint selection methodology balances physical realism with optimization flexibility, establishing bounds based on fundamental thermodynamic principles and empirical observations from heterogeneous catalysis literature [11, 12]. Our constraint framework adopts deliberately liberal bounds to avoid imposing excessive bias on the optimization landscape while maintaining physical plausibility. The Pre-exponential factors are limited between 0 and 10^6 mol/(kg_{cat} s Pa^n), activation energies between 0 and 600 kJ/mol, and adsorption enthalpies between -600 and 0 kJ/mol, encompassing the full spectrum from strong chemisorption to activated adsorption processes. This liberal approach prevents premature convergence to local minima while ensuring that the optimum is located within a physically meaningful parameter space, thereby enhancing both the robustness of parameter estimation and the predictive capability of the resulting kinetic model and avoiding long calculation times for generation of physically meaningless models.

Table B.6.: Kinetic Parameter Constraints for Methanol Synthesis Optimization

Parameter	**Symbol**	**Lower Bound**	**Upper Bound**
Reaction Rate Pre-exponential Factors			
MeOH synthesis	A_{MeOH} ($\mathrm{mol/kg_{cat}/s/Pa^{n}}$)	1×10^{-5}	1×10^{6}
RWGS reaction	A_{RWGS} ($\mathrm{mol/kg_{cat}/s/Pa^{n}}$)	1×10^{-5}	1×10^{6}
Activation Energies			
MeOH synthesis	$E_{a,\mathrm{MeOH}}$ (kJ/mol)	0	600
RWGS reaction	$E_{a,\mathrm{RWGS}}$ (kJ/mol)	0	600
Adsorption Pre-exponential Factors (Van't Hoff)			
CO_2 adsorption	$B_{\mathrm{CO_2}}$ ($\mathrm{Pa^{-1}}$)	1×10^{-10}	1×10^{6}
H_2 adsorption	$B_{\mathrm{H_2}}$ ($\mathrm{Pa^{-1}}$)	1×10^{-10}	1×10^{6}
CO adsorption	B_{CO} ($\mathrm{Pa^{-1}}$)	1×10^{-10}	1×10^{6}
H_2O adsorption	$B_{\mathrm{H_2O}}$ ($\mathrm{Pa^{-1}}$)	1×10^{-10}	1×10^{6}
Adsorption Enthalpies			
CO_2 adsorption	$\Delta H_{\mathrm{CO_2}}$ (kJ/mol)	-600	0
H_2 adsorption	$\Delta H_{\mathrm{H_2}}$ (kJ/mol)	-600	0
CO adsorption	ΔH_{CO} (kJ/mol)	-600	0
H_2O adsorption	$\Delta H_{\mathrm{H_2O}}$ (kJ/mol)	-600	0

B.2.3. Test for mass transfer limitations

In heterogeneous catalysis at high temperatures and high reaction rates, mass transfer limitations can occur that influence the outcome of kinetic tests. Kinetic tests can lead to inaccurate results if not corrected for possible mass transfer limitations [13].

Thus, external and internal limitations of mass transfer and diffusion have to be taken into account in optimizing reaction kinetics [11]. The Weisz-parameter is a good measure to approximate the effect of diffusion limitation in catalyzed reaction setups [14]. It is defined as follows:

$$\Phi_{\mathrm{WP}} = \frac{r_{\mathrm{obs}} \cdot R_p^2}{D_{\mathrm{eff}} \cdot C_{\mathrm{surface}}} \tag{B.11}$$

with r_{obs} being the observed or measured reaction rate of a single species involved in the reaction. The effective Diffusivity of a single species under certain reaction conditions D_{eff} is defined as

$$D_{\mathrm{eff}} = \frac{\varepsilon}{\tau} \cdot \frac{D_{AB} \cdot D_K}{D_{AB} + D_K} \tag{B.12}$$

with the binary diffusivity D_{AB} being defined as

$$D_{AB} = \frac{1.00 \times 10^{-3} \cdot T^{1.75} \cdot \sqrt{\frac{1}{M_A} + \frac{1}{M_B}}}{P \cdot \left[(\Sigma v_A)^{1/3} + (\Sigma v_B)^{1/3}\right]^2} \tag{B.13}$$

and the Knudsen diffusivity D_{KN} being defined as

$$D_K = \frac{2}{3} \cdot r_{\mathrm{pore}} \cdot \sqrt{\frac{8RT}{\pi M}} \tag{B.14}$$

In this instance, r_{pore} represents the measured average pore volume of the applied catalyst, τ represents the tortuosity of a catalyst, ε refers to the void fraction of a catalyst, and $C_{surface}$ refering to the effective concentration of the investigated species in the reactor. For calculation of Φ_{WP} textural properties of the catalyst and additional properties if the alumina carriers like τ where taken from previous studies [3, 9]. In many instances, internal mass transfer limitations are neglected in kinetic modeling, if Φ_{WP} assumes values below 0.1 for most test conditions [15, 16].

For testing the reaction setup towards external mass transfer limitation, the Mears criterion is often applied. The dimensionless Mears criterion number is herein defined as:

$$\mathrm{Mears} = \frac{r_{\mathrm{obs}} \cdot d_p \cdot \rho_b}{k_c \cdot C_{\mathrm{surface}}} \tag{B.15}$$

Here the species concentration on the catalyst surface is calculated from the ideal gas law:

$$C_{\mathrm{surface}} = \frac{P_i}{RT} \tag{B.16}$$

The mass transfer coefficient k_c is furthermore defined as:

$$k_c = \frac{\mathrm{Sh} \cdot D_{AB}}{d_p} \tag{B.17}$$

The Sherwood number Sh is calculated from

$$\mathrm{Sh} = 2 + 0.6 \cdot \mathrm{Re}^{0.5} \cdot \mathrm{Sc}^{0.33} \tag{B.18}$$

with the Reynolds number Re and and the Schmidt number being defined as

$$\mathrm{Re} = \frac{\rho_g \cdot u_s \cdot d_p}{\mu_g} \tag{B.19}$$

$$\mathrm{Sc} = \frac{\mu_g}{\rho_g \cdot D_{AB}} \tag{B.20}$$

In kinetic modeling, external mass transfer limitations and their influence on the kinetic reactor model are often times neglected if the Mears criterion does not assume values above 0.15 for most of the reaction conditions. In these cases, the reaction is kinetically controlled and intrinsic reaction rates are slow enough for diffusion and mass transfer between solid and gas phases in the reactor do not limit the rates [11, 15].
In this work we tested for both the Weisz and the Mears criterion, looking at internal and external mass transfer and diffusion limitations. CO_2, H_2, MeOH and H_2O were tested for limitations for all catalysts in all reaction conditions. Tables B.7, B.8, B.9 and B.10 show the results of both external as well as internal mass transfer limitation criteria for all catalyst in respect to the species H_2, CO_2, MeOH and H_2O. None of the tested conditions show external mass transfer limitations, with the Mears criterion assuming only very low values below 0.01. For testing of internal diffusion limitations via the Weisz parameter, only MeOH and H_2O show slightly increased values above 0.1 in conditions with high productions rates at high temperatures or high pressures. Overall more than 70% of tested conditions for all catalysts show no transfer limitation in any of the species. Thus, transfer limitations are neglected in further parameter fitting.

Table B.7.: Mass Transfer Analysis - 20% CZ Catalyst

Point	H_2			CO_2			MeOH			H_2O			Mears Criterion
	Φ_{WP} (–)	D_{eff} ($\times 10^{-8}$)	D_K ($\times 10^{-6}$)	Φ_{WP} (–)	D_{eff} ($\times 10^{-8}$)	D_K ($\times 10^{-6}$)	Φ_{WP} (–)	D_{eff} ($\times 10^{-8}$)	D_K ($\times 10^{-6}$)	Φ_{WP} (–)	D_{eff} ($\times 10^{-8}$)	D_K ($\times 10^{-6}$)	(–)
Catalyst Properties: ρ_b = 872.5 kg/m³, ρ_p = 1272 kg/m³, ε = 0.314, d_p = 800 µm, d_{pore} = 10.7 nm, τ = 1.4													
1	6.8e-03	61.28	8.56	0.053	24.52	1.83	0.114	23.50	2.15	0.080	33.45	2.86	0.0002
2	7.1e-03	57.65	8.36	0.065	23.66	1.79	0.126	22.68	2.10	0.088	32.44	2.80	0.0003
3	3.7e-03	67.01	8.16	0.024	26.18	1.75	0.093	25.09	2.05	0.066	35.47	2.73	0.0001
4	6.8e-03	56.93	8.36	0.051	24.35	1.79	0.141	22.39	2.10	0.098	32.22	2.80	0.0003
5	5.0e-03	62.03	8.56	0.090	24.47	1.83	0.076	26.04	2.15	0.056	35.73	2.86	0.0002
6	6.0e-03	77.36	8.56	0.052	28.00	1.83	0.127	26.86	2.15	0.089	38.46	2.86	0.0003
7	4.5e-03	66.30	8.16	0.024	26.97	1.75	0.128	24.52	2.05	0.090	34.93	2.73	0.0002
8	5.5e-03	57.65	8.36	0.107	23.45	1.79	0.095	24.76	2.10	0.069	34.21	2.80	0.0002
9	4.5e-03	98.25	8.36	0.052	31.75	1.79	0.171	32.63	2.10	0.123	45.54	2.80	0.0002
10	4.6e-03	72.36	8.36	0.043	27.26	1.79	0.124	26.50	2.10	0.087	37.65	2.80	0.0002
11	5.7e-03	103.08	8.56	0.062	32.91	1.83	0.229	33.45	2.15	0.164	46.82	2.86	0.0003
12	4.3e-03	52.40	8.16	0.021	23.33	1.75	0.086	20.34	2.05	0.059	29.30	2.73	0.0002
13	4.6e-03	92.59	8.16	0.046	30.81	1.75	0.204	31.03	2.05	0.146	43.45	2.73	0.0002
14	1.5e-03	105.62	8.56	0.052	32.52	1.83	0.147	35.48	2.15	0.106	48.96	2.86	0.0000
15	4.2e-03	54.51	8.16	0.086	22.32	1.75	0.096	23.19	2.05	0.068	32.48	2.73	0.0001
16	9.8e-03	60.84	8.56	0.049	24.15	1.83	0.138	21.48	2.15	0.095	31.16	2.86	0.0005
17	5.8e-03	104.07	8.56	0.070	32.56	1.83	0.200	33.43	2.15	0.142	46.84	2.86	0.0003
18	6.5e-03	61.36	8.56	0.051	24.75	1.83	0.119	23.61	2.15	0.083	33.66	2.86	0.0002
19	1.7e-03	100.07	8.36	0.048	31.36	1.79	0.143	34.06	2.10	0.103	47.04	2.80	0.0000
20	5.4e-03	62.09	8.56	0.107	24.54	1.83	0.092	26.05	2.15	0.067	35.90	2.86	0.0002
21	5.2e-03	77.27	8.56	0.052	27.95	1.83	0.118	27.69	2.15	0.083	39.23	2.86	0.0002
22	3.7e-03	66.57	8.16	0.021	27.04	1.75	0.127	24.39	2.05	0.089	34.89	2.73	0.0002
23	4.1e-03	91.16	8.16	0.026	31.33	1.75	0.181	30.57	2.05	0.129	42.80	2.73	0.0001
24	6.6e-03	72.07	8.36	0.053	27.07	1.79	0.140	26.35	2.10	0.099	37.31	2.80	0.0002
25	6.2e-03	56.84	8.36	0.042	24.11	1.79	0.114	22.19	2.10	0.080	31.84	2.80	0.0003
26	2.8e-03	66.42	8.16	0.016	27.12	1.75	0.104	24.43	2.05	0.073	34.92	2.73	0.0001
27	2.6e-03	99.95	8.36	0.076	31.33	1.79	0.171	34.11	2.10	0.124	47.08	2.80	0.0001
28	3.1e-03	52.81	8.16	0.019	22.93	1.75	0.080	20.92	2.05	0.056	30.03	2.73	0.0001
29	4.6e-03	103.61	8.56	0.055	32.84	1.83	0.190	33.38	2.15	0.135	46.83	2.86	0.0003
30	6.1e-03	52.32	8.16	0.035	23.78	1.75	0.150	21.29	2.05	0.105	30.50	2.73	0.0002
31	5.9e-03	71.82	8.36	0.045	27.80	1.79	0.162	26.20	2.10	0.114	37.35	2.80	0.0003
32	9.1e-03	60.93	8.56	0.061	24.71	1.83	0.134	23.05	2.15	0.094	33.02	2.86	0.0004
33	4.7e-03	97.70	8.36	0.050	32.03	1.79	0.205	32.60	2.10	0.147	45.51	2.80	0.0002
34	2.9e-03	73.47	8.36	0.062	26.91	1.79	0.099	28.54	2.10	0.071	39.67	2.80	0.0001
35	5.6e-03	97.93	8.36	0.050	32.22	1.79	0.222	32.18	2.10	0.159	45.04	2.80	0.0002
36	5.6e-03	67.48	8.16	0.041	26.08	1.75	0.138	24.88	2.05	0.097	35.37	2.73	0.0002
37	6.6e-03	57.62	8.36	0.058	23.64	1.79	0.122	22.58	2.10	0.085	32.29	2.80	0.0003
38	6.0e-03	104.14	8.56	0.073	32.50	1.83	0.197	33.40	2.15	0.141	46.81	2.86	0.0003
39	5.9e-03	97.22	8.36	0.044	31.96	1.79	0.176	31.74	2.10	0.125	44.46	2.80	0.0002
40	4.7e-03	97.91	8.36	0.044	31.73	1.79	0.196	32.15	2.10	0.140	44.95	2.80	0.0002
41	5.6e-03	72.27	8.36	0.045	26.97	1.79	0.114	26.11	2.10	0.080	37.09	2.80	0.0002
42	2.0e-03	105.68	8.56	0.072	32.41	1.83	0.170	35.34	2.15	0.123	48.84	2.86	0.0001
43	8.4e-03	60.84	8.56	0.056	24.40	1.83	0.117	23.11	2.15	0.082	32.91	2.86	0.0003
44	5.5e-03	57.40	8.36	0.043	23.64	1.79	0.098	22.38	2.10	0.068	31.98	2.80	0.0002
45	4.3e-03	98.11	8.36	0.048	31.80	1.79	0.173	32.42	2.10	0.124	45.34	2.80	0.0002
46	5.0e-03	57.39	8.36	0.044	23.89	1.79	0.107	22.72	2.10	0.075	32.51	2.80	0.0002
47	5.3e-03	77.31	8.56	0.052	28.01	1.83	0.120	27.59	2.15	0.084	39.17	2.86	0.0002
48	3.3e-03	73.87	8.36	0.080	26.96	1.79	0.119	28.59	2.10	0.086	39.80	2.80	0.0001
49	4.5e-03	58.15	8.36	0.091	22.86	1.79	0.074	24.12	2.10	0.054	33.53	2.80	0.0001
50	3.5e-03	103.97	8.56	0.051	32.73	1.83	0.175	33.91	2.15	0.125	47.37	2.86	0.0002
51	3.9e-03	78.26	8.56	0.082	28.13	1.83	0.116	30.01	2.15	0.084	41.51	2.86	0.0001
52	6.8e-03	71.89	8.36	0.050	27.19	1.79	0.176	26.05	2.10	0.124	37.01	2.80	0.0002
53	4.7e-03	104.02	8.56	0.056	32.38	1.83	0.164	33.33	2.15	0.117	46.66	2.86	0.0002
54	1.9e-03	52.45	8.16	0.011	23.59	1.75	0.046	21.00	2.05	0.032	30.18	2.73	0.0001
55	6.0e-03	71.79	8.36	0.046	27.69	1.79	0.161	26.08	2.10	0.113	37.20	2.80	0.0003
56	7.6e-03	76.75	8.56	0.065	28.01	1.83	0.156	26.93	2.15	0.109	38.52	2.86	0.0004
57	7.3e-03	77.49	8.56	0.074	27.88	1.83	0.140	27.67	2.15	0.099	39.23	2.86	0.0003
58	3.2e-03	78.80	8.56	0.074	28.23	1.83	0.101	30.15	2.15	0.073	41.74	2.86	0.0001
59	6.2e-03	61.03	8.56	0.050	24.85	1.83	0.112	23.83	2.15	0.079	33.89	2.86	0.0002
60	7.2e-03	77.26	8.56	0.064	27.85	1.83	0.138	27.32	2.15	0.097	38.81	2.86	0.0003

Φ_{WP} = Weisz-Prater parameter, D_{eff} = effective diffusivity (m²/s), D_K = Knudsen diffusivity (m²/s)
Mears Criterion for external mass transfer limitations
Internal limitations: $\Phi_{WP} > 0.1$, External limitations: Mears > 0.15
Same point numbering as experimental conditions table
ρ_b = bulk density, ρ_p = particle density, ε = porosity, d_p = particle diameter, d_{pore} = pore diameter, τ = tortuosity

Table B.8.: Mass Transfer Analysis - 20% CZC Catalyst

Point	H_2			CO_2			MeOH			H_2O			Mears Criterion
	Φ_{WP}	D_{eff}	D_K	Φ_{WP}	D_{eff}	D_K	Φ_{WP}	D_{eff}	D_K	Φ_{WP}	D_{eff}	D_K	
	(–)	($\times 10^{-8}$)	($\times 10^{-6}$)	(–)	($\times 10^{-8}$)	($\times 10^{-6}$)	(–)	($\times 10^{-8}$)	($\times 10^{-6}$)	(–)	($\times 10^{-8}$)	($\times 10^{-6}$)	(–)
Catalyst Properties: ρ_b = 879.7 kg/m³, ρ_p = 1255 kg/m³, ε = 0.299, d_p = 800 µm, d_{pore} = 11.3 nm, τ = 1.4													
1	2.8e-03	76.21	9.04	0.062	27.66	1.93	0.096	29.29	2.27	0.069	40.78	3.02	0.0001
2	7.3e-03	74.46	9.04	0.060	27.63	1.93	0.163	26.62	2.27	0.115	37.96	3.02	0.0003
3	5.7e-03	101.95	9.04	0.084	32.34	1.93	0.178	33.65	2.27	0.127	47.08	3.02	0.0003
4	4.5e-03	55.26	8.83	0.053	23.91	1.89	0.120	23.17	2.21	0.084	33.06	2.95	0.0002
5	4.1e-03	69.56	8.83	0.030	27.11	1.89	0.104	25.23	2.21	0.073	36.17	2.95	0.0002
6	4.8e-03	95.36	8.83	0.051	31.66	1.89	0.207	32.10	2.21	0.148	44.91	2.95	0.0002
7	3.8e-03	95.43	8.83	0.040	31.60	1.89	0.168	32.03	2.21	0.120	44.84	2.95	0.0002
8	7.1e-03	101.07	9.04	0.067	32.48	1.93	0.207	32.33	2.27	0.147	45.60	3.02	0.0004
9	4.8e-03	69.72	8.83	0.041	26.91	1.89	0.124	25.95	2.21	0.087	36.90	2.95	0.0002
10	2.7e-03	69.29	8.83	0.060	26.53	1.89	0.118	27.79	2.21	0.084	38.95	2.95	0.0001
11	2.0e-03	103.33	9.04	0.064	32.34	1.93	0.145	35.22	2.27	0.105	48.64	3.02	0.0001
12	2.2e-03	97.82	8.83	0.066	31.14	1.89	0.144	33.78	2.21	0.104	46.72	2.95	0.0001
13	5.5e-03	55.04	8.83	0.047	23.40	1.89	0.105	22.33	2.21	0.074	31.84	2.95	0.0002
14	5.5e-03	69.57	8.83	0.041	27.15	1.89	0.133	25.43	2.21	0.093	36.40	2.95	0.0003
15	5.0e-03	64.38	8.62	0.031	26.53	1.84	0.137	24.41	2.16	0.096	34.79	2.88	0.0002
16	2.2e-03	71.11	8.83	0.047	26.61	1.89	0.079	28.00	2.21	0.056	39.06	2.95	0.0001
17	5.0e-03	54.71	8.83	0.038	23.87	1.89	0.115	22.19	2.21	0.080	31.80	2.95	0.0002
18	4.4e-03	54.98	8.83	0.035	23.45	1.89	0.084	22.11	2.21	0.059	31.62	2.95	0.0002
19	7.5e-03	74.64	9.04	0.067	27.87	1.93	0.162	26.84	2.27	0.114	38.36	3.02	0.0004
20	3.0e-03	55.85	8.83	0.056	22.96	1.89	0.063	23.83	2.21	0.045	33.33	2.95	0.0001
21	1.5e-03	52.57	8.62	0.030	22.11	1.84	0.066	22.46	2.16	0.047	31.85	2.88	0.0001
22	3.6e-03	56.42	8.83	0.065	23.27	1.89	0.100	23.90	2.21	0.071	33.60	2.95	0.0001
23	2.8e-03	102.65	9.04	0.085	32.27	1.93	0.171	35.08	2.27	0.124	48.47	3.02	0.0001
24	2.3e-03	97.56	8.83	0.072	31.13	1.89	0.173	33.76	2.21	0.125	46.72	2.95	0.0001
25	4.1e-03	50.55	8.62	0.025	23.18	1.84	0.094	20.56	2.16	0.065	29.64	2.88	0.0002
26	4.9e-03	100.93	9.04	0.054	32.49	1.93	0.197	33.21	2.27	0.141	46.46	3.02	0.0002
27	4.8e-03	69.82	8.83	0.045	27.12	1.89	0.151	26.08	2.21	0.106	37.17	2.95	0.0002
28	4.6e-03	64.48	8.62	0.030	26.55	1.84	0.138	24.51	2.16	0.097	34.94	2.88	0.0002
29	6.6e-03	54.57	8.83	0.041	23.69	1.89	0.117	21.31	2.21	0.081	30.74	2.95	0.0003
30	5.8e-03	101.03	9.04	0.058	32.54	1.93	0.182	32.77	2.27	0.130	46.06	3.02	0.0003
31	2.0e-03	71.54	8.83	0.048	26.59	1.89	0.098	27.76	2.21	0.070	39.00	2.95	0.0001
32	8.1e-03	58.97	9.04	0.061	24.32	1.93	0.134	22.56	2.27	0.093	32.57	3.02	0.0004
33	5.7e-03	74.54	9.04	0.055	27.82	1.93	0.148	27.17	2.27	0.104	38.64	3.02	0.0002
34	5.8e-03	54.94	8.83	0.047	23.61	1.89	0.127	22.01	2.21	0.089	31.64	2.95	0.0002
35	4.6e-03	60.95	9.04	0.079	24.26	1.93	0.093	25.28	2.27	0.067	35.15	3.02	0.0002
36	7.5e-03	69.43	8.83	0.051	27.29	1.89	0.196	24.98	2.21	0.136	35.92	2.95	0.0004
37	5.0e-03	69.93	8.83	0.046	26.82	1.89	0.121	26.05	2.21	0.085	37.03	2.95	0.0002
38	4.2e-03	95.20	8.83	0.040	31.85	1.89	0.153	31.86	2.21	0.109	44.70	2.95	0.0002
39	5.4e-03	101.22	9.04	0.067	32.50	1.93	0.209	33.39	2.27	0.149	46.72	3.02	0.0002
40	3.4e-03	69.88	8.83	0.032	27.05	1.89	0.102	26.11	2.21	0.072	37.16	2.95	0.0002
41	3.8e-03	88.67	8.83	0.038	31.52	1.89	0.173	31.91	2.21	0.124	44.65	2.95	0.0001
42	4.0e-03	95.80	8.83	0.059	31.76	1.89	0.229	32.78	2.21	0.164	45.76	2.95	0.0002
43	7.3e-03	59.22	9.04	0.066	24.01	1.93	0.122	23.10	2.27	0.086	33.06	3.02	0.0003
44	5.2e-03	94.76	8.83	0.042	32.00	1.89	0.210	31.25	2.21	0.149	43.99	2.95	0.0002
45	1.7e-03	92.28	8.62	0.046	29.90	1.84	0.113	32.31	2.16	0.081	44.73	2.88	0.0000
46	4.5e-03	55.15	8.83	0.043	23.67	1.89	0.089	22.74	2.21	0.063	32.43	2.95	0.0002
47	4.4e-03	50.22	8.62	0.024	23.31	1.84	0.115	20.35	2.16	0.079	29.35	2.88	0.0002
48	5.4e-03	74.32	9.04	0.042	27.77	1.93	0.105	26.68	2.27	0.074	38.01	3.02	0.0002
49	3.7e-03	76.07	9.04	0.082	27.65	1.93	0.116	29.25	2.27	0.083	40.77	3.02	0.0001
50	3.9e-03	69.78	8.83	0.037	27.13	1.89	0.125	26.20	2.21	0.088	37.28	2.95	0.0002
51	4.5e-03	94.68	8.83	0.035	31.96	1.89	0.174	31.23	2.21	0.124	43.94	2.95	0.0002
52	8.6e-03	54.64	8.83	0.053	23.61	1.89	0.148	21.27	2.21	0.102	30.71	2.95	0.0004
53	7.1e-03	58.94	9.04	0.051	24.20	1.93	0.110	22.45	2.27	0.076	32.38	3.02	0.0003
54	5.1e-03	55.51	8.83	0.046	23.26	1.89	0.096	22.45	2.21	0.067	31.96	2.95	0.0002
55	4.0e-03	100.99	9.04	0.047	32.57	1.93	0.174	33.41	2.27	0.124	46.71	3.02	0.0002
56	9.2e-03	74.70	9.04	0.085	27.62	1.93	0.197	27.00	2.27	0.139	38.42	3.02	0.0004
57	4.0e-03	61.08	9.04	0.070	24.25	1.93	0.080	25.34	2.27	0.058	35.17	3.02	0.0002
58	6.3e-03	74.46	9.04	0.052	27.84	1.93	0.130	26.54	2.27	0.091	37.98	3.02	0.0003
59	3.6e-03	56.39	8.83	0.063	23.49	1.89	0.112	24.15	2.21	0.080	33.86	2.95	0.0001
60	5.9e-03	74.43	9.04	0.060	28.05	1.93	0.152	27.57	2.27	0.108	39.09	3.02	0.0002
61	6.3e-03	59.19	9.04	0.057	23.98	1.93	0.101	23.20	2.27	0.070	33.11	3.02	0.0002
62	5.9e-03	59.33	9.04	0.053	24.03	1.93	0.102	22.98	2.27	0.071	33.00	3.02	0.0003

Φ_{WP} = Weisz-Prater parameter, D_{eff} = effective diffusivity (m²/s), D_K = Knudsen diffusivity (m²/s)
Mears Criterion for external mass transfer limitations
Internal limitations: $\Phi_{WP} > 0.1$, External limitations: Mears > 0.15
Same point numbering as experimental conditions table
ρ_b = bulk density, ρ_p = particle density, ε = porosity, d_p = particle diameter, d_{pore} = pore diameter, τ = tortuosity

Table B.9.: Mass Transfer Analysis - 20% CZCZ Catalyst

Point	H_2			CO_2			MeOH			H_2O			Mears Criterion
	Φ_{WP}	D_{eff}	D_K	Φ_{WP}	D_{eff}	D_K	Φ_{WP}	D_{eff}	D_K	Φ_{WP}	D_{eff}	D_K	
	(–)	($\times 10^{-8}$)	($\times 10^{-6}$)	(–)	($\times 10^{-8}$)	($\times 10^{-6}$)	(–)	($\times 10^{-8}$)	($\times 10^{-6}$)	(–)	($\times 10^{-8}$)	($\times 10^{-6}$)	(–)
Catalyst Properties: ρ_b = 849.5 kg/m³, ρ_p = 1239 kg/m³, ε = 0.314, d_p = 800 µm, d_{pore} = 11.4 nm, τ = 1.4													
1	5.1e-03	73.63	8.88	0.044	28.39	1.90	0.119	27.30	2.23	0.083	38.90	2.97	0.0002
2	5.5e-03	74.03	8.88	0.045	28.08	1.90	0.089	27.08	2.23	0.063	38.60	2.97	0.0003
3	8.0e-03	61.84	9.09	0.057	25.56	1.95	0.130	23.88	2.28	0.091	34.29	3.04	0.0003
4	4.7e-03	107.07	9.09	0.068	34.48	1.95	0.181	35.89	2.28	0.129	50.06	3.04	0.0002
5	4.2e-03	74.35	8.88	0.049	27.41	1.90	0.083	27.85	2.23	0.059	39.22	2.97	0.0001
6	2.9e-03	109.43	9.09	0.100	33.97	1.95	0.134	36.91	2.28	0.097	51.15	3.04	0.0001
7	0.011	99.99	8.88	0.065	33.21	1.90	0.190	32.61	2.23	0.136	45.76	2.97	0.0003
8	7.4e-03	78.22	9.09	0.055	28.99	1.95	0.127	28.13	2.28	0.089	39.91	3.04	0.0003
9	6.1e-03	73.56	8.88	0.046	28.16	1.90	0.110	26.95	2.23	0.077	38.39	2.97	0.0003
10	9.0e-03	57.30	8.88	0.058	24.63	1.90	0.111	23.10	2.23	0.078	32.81	2.97	0.0003
11	6.6e-03	73.18	8.88	0.048	28.08	1.90	0.115	27.24	2.23	0.081	38.50	2.97	0.0002
12	6.6e-03	73.35	8.88	0.050	28.35	1.90	0.136	27.02	2.23	0.095	38.49	2.97	0.0003
13	7.1e-03	100.33	8.88	0.057	33.22	1.90	0.185	33.41	2.23	0.132	46.74	2.97	0.0002
14	4.6e-03	60.70	8.88	0.139	23.29	1.90	0.058	24.49	2.23	0.040	34.91	2.97	0.0003
15	7.3e-03	62.48	9.09	0.075	25.68	1.95	0.115	25.25	2.28	0.081	35.79	3.04	0.0003
16	7.7e-03	106.65	9.09	0.077	34.05	1.95	0.185	34.94	2.28	0.133	48.84	3.04	0.0003
17	5.5e-03	62.23	9.09	0.044	25.88	1.95	0.103	24.03	2.28	0.071	34.69	3.04	0.0003
18	4.2e-03	78.39	9.09	0.042	29.55	1.95	0.122	29.19	2.28	0.086	41.29	3.04	0.0002
19	8.2e-03	77.95	9.09	0.050	29.11	1.95	0.139	27.29	2.28	0.097	39.00	3.04	0.0003
20	4.1e-03	62.86	9.09	0.049	25.42	1.95	0.115	24.86	2.28	0.080	35.58	3.04	0.0002
21	8.7e-03	79.29	9.09	0.070	28.55	1.95	0.097	27.71	2.28	0.068	39.68	3.04	0.0005
22	7.4e-03	72.49	8.88	0.037	28.37	1.90	0.113	26.17	2.23	0.079	37.21	2.97	0.0003
23	4.0e-03	75.11	8.88	0.098	27.69	1.90	0.111	29.37	2.23	0.080	40.95	2.97	0.0001
24	5.6e-03	106.67	9.09	0.057	34.17	1.95	0.159	34.87	2.28	0.113	48.83	3.04	0.0002
25	1.5e-03	111.97	9.09	0.050	34.37	1.95	0.134	37.29	2.28	0.097	51.53	3.04	0.0001
26	7.3e-03	77.99	9.09	0.044	29.06	1.95	0.116	27.31	2.28	0.081	39.00	3.04	0.0003
27	2.6e-03	97.23	8.67	0.067	31.45	1.86	0.106	34.04	2.17	0.077	47.08	2.90	0.0001
28	7.2e-03	62.05	9.09	0.051	25.04	1.95	0.089	23.77	2.28	0.063	33.96	3.04	0.0003
29	7.5e-03	57.74	8.88	0.054	24.35	1.90	0.095	23.13	2.23	0.067	32.91	2.97	0.0003
30	4.8e-03	100.95	8.88	0.048	33.46	1.90	0.156	33.58	2.23	0.111	47.17	2.97	0.0002
31	6.9e-03	62.01	9.09	0.053	25.38	1.95	0.097	24.22	2.28	0.068	34.55	3.04	0.0003
32	6.3e-03	78.50	9.09	0.049	28.94	1.95	0.106	28.08	2.28	0.075	39.92	3.04	0.0003
33	6.6e-03	99.87	8.88	0.041	33.31	1.90	0.132	32.75	2.23	0.094	45.92	2.97	0.0002
34	3.5e-03	59.24	8.88	0.075	24.12	1.90	0.092	25.02	2.23	0.066	35.18	2.97	0.0001
35	8.8e-03	57.78	8.88	0.065	24.31	1.90	0.114	23.11	2.23	0.080	32.90	2.97	0.0003
36	8.5e-03	57.78	8.88	0.066	24.45	1.90	0.121	23.34	2.23	0.085	33.20	2.97	0.0003
37	6.4e-03	106.45	9.09	0.058	34.33	1.95	0.172	34.41	2.28	0.122	48.39	3.04	0.0003
38	3.3e-03	75.43	8.88	0.074	27.54	1.90	0.106	28.93	2.23	0.076	40.59	2.97	0.0001
39	7.6e-03	62.12	9.09	0.061	25.46	1.95	0.117	24.25	2.28	0.082	34.68	3.04	0.0003
40	8.9e-03	68.27	8.67	0.062	27.35	1.86	0.136	26.20	2.17	0.096	37.02	2.90	0.0003
41	7.8e-03	99.82	8.88	0.048	33.33	1.90	0.160	32.68	2.23	0.114	45.84	2.97	0.0003
42	3.7e-03	55.95	8.67	0.085	22.49	1.86	0.059	23.26	2.17	0.041	33.03	2.90	0.0002
43	5.6e-03	100.52	8.88	0.050	33.22	1.90	0.160	33.58	2.23	0.114	46.97	2.97	0.0002
44	6.3e-03	53.25	8.67	0.034	23.72	1.86	0.086	21.31	2.17	0.060	30.53	2.90	0.0002
45	8.0e-03	106.98	9.09	0.083	34.03	1.95	0.187	34.77	2.28	0.133	48.76	3.04	0.0003
46	1.8e-03	82.59	9.09	0.063	29.65	1.95	0.101	31.38	2.28	0.072	43.96	3.04	0.0001
47	8.8e-03	58.19	8.88	0.073	24.18	1.90	0.137	23.01	2.23	0.096	32.96	2.97	0.0004
48	3.4e-03	103.14	8.88	0.100	32.68	1.90	0.157	35.38	2.23	0.113	49.04	2.97	0.0001
49	0.011	72.63	8.88	0.063	28.28	1.90	0.148	26.86	2.23	0.105	37.93	2.97	0.0003
50	5.7e-03	105.90	9.09	0.053	34.50	1.95	0.162	35.09	2.28	0.116	49.01	3.04	0.0002
51	2.1e-03	75.84	8.88	0.056	27.80	1.90	0.094	29.19	2.23	0.067	41.04	2.97	0.0001
52	8.1e-03	107.09	9.09	0.084	34.32	1.95	0.207	34.35	2.28	0.147	48.52	3.04	0.0005
53	5.2e-03	78.29	9.09	0.053	29.57	1.95	0.150	29.41	2.28	0.106	41.48	3.04	0.0002
54	8.5e-03	72.88	8.88	0.055	28.45	1.90	0.128	27.06	2.23	0.091	38.32	2.97	0.0003
55	6.8e-03	100.27	8.88	0.053	33.06	1.90	0.152	33.51	2.23	0.109	46.75	2.97	0.0002
56	6.9e-03	53.11	8.67	0.031	23.75	1.86	0.101	20.67	2.17	0.070	29.80	2.90	0.0003
57	5.3e-03	62.65	9.09	0.051	25.43	1.95	0.105	24.70	2.28	0.073	35.22	3.04	0.0002
58	7.5e-03	57.91	8.88	0.058	24.28	1.90	0.100	23.22	2.23	0.070	33.06	2.97	0.0003
59	5.8e-03	73.00	8.88	0.061	28.46	1.90	0.109	28.92	2.23	0.078	40.29	2.97	0.0002
60	6.4e-03	68.00	8.67	0.032	27.15	1.86	0.094	24.88	2.17	0.066	35.43	2.90	0.0002
61	4.2e-03	59.28	8.88	0.096	23.71	1.90	0.074	24.94	2.23	0.053	34.86	2.97	0.0001
62	3.5e-03	103.63	8.88	0.117	32.59	1.90	0.131	35.34	2.23	0.094	49.06	2.97	0.0001

Φ_{WP} = Weisz-Prater parameter, D_{eff} = effective diffusivity (m²/s), D_K = Knudsen diffusivity (m²/s)
Mears Criterion for external mass transfer limitations
Internal limitations: $\Phi_{WP} > 0.1$, External limitations: Mears > 0.15
Same point numbering as experimental conditions table
ρ_b = bulk density, ρ_p = particle density, ε = porosity, d_p = particle diameter, d_{pore} = pore diameter, τ = tortuosity

Table B.10.: Mass Transfer Analysis - 20% CZCZC Catalyst - Part 1

Point	H_2			CO_2			MeOH			H_2O			Mears Criterion
	Φ_{WP}	D_{eff}	D_K	Φ_{WP}	D_{eff}	D_K	Φ_{WP}	D_{eff}	D_K	Φ_{WP}	D_{eff}	D_K	
	(–)	($\times 10^{-8}$)	($\times 10^{-6}$)	(–)	($\times 10^{-8}$)	($\times 10^{-6}$)	(–)	($\times 10^{-8}$)	($\times 10^{-6}$)	(–)	($\times 10^{-8}$)	($\times 10^{-6}$)	(–)
Catalyst Properties: ρ_b = 857.7 kg/m³, ρ_p = 1241 kg/m³, ε = 0.309, d_p = 800 µm, d_{pore} = 11.5 nm, τ = 1.4													
1	9.0e-03	57.57	9.02	0.075	24.05	1.93	0.116	22.81	2.26	0.081	32.76	3.02	0.0004
2	4.2e-03	99.75	9.02	0.045	33.27	1.93	0.164	33.62	2.26	0.117	47.14	3.02	0.0002
3	1.8e-03	108.21	9.24	0.087	33.94	1.98	0.170	36.77	2.32	0.122	51.10	3.09	0.0001
4	3.9e-03	105.02	9.24	0.044	34.39	1.98	0.201	34.91	2.32	0.143	48.88	3.09	0.0002
5	1.5e-03	96.12	8.81	0.038	31.60	1.88	0.138	33.91	2.21	0.100	47.03	2.95	0.0000
6	7.2e-03	61.13	9.24	0.053	24.88	1.98	0.100	23.75	2.32	0.062	33.91	3.09	0.0002
7	5.4e-03	68.30	8.81	0.049	27.14	1.88	0.123	25.91	2.21	0.086	37.02	2.95	0.0003
8	4.8e-03	105.88	9.24	0.063	34.16	1.98	0.172	35.07	2.32	0.123	49.16	3.09	0.0002
9	4.4e-03	93.38	8.81	0.033	32.20	1.88	0.181	31.69	2.21	0.129	44.50	2.95	0.0001
10	7.4e-03	72.23	9.02	0.056	27.80	1.93	0.115	27.27	2.26	0.082	38.39	3.02	0.0002
11	6.2e-03	93.69	8.81	0.040	32.16	1.88	0.206	31.19	2.21	0.097	44.02	2.95	0.0002
12	6.2e-03	67.97	8.81	0.053	26.86	1.88	0.121	26.18	2.21	0.086	37.05	2.95	0.0002
13	4.3e-03	75.18	9.02	0.109	27.32	1.93	0.105	28.45	2.26	0.074	40.34	3.02	0.0002
14	7.0e-03	56.84	9.02	0.057	24.90	1.93	0.104	23.51	2.26	0.073	33.55	3.02	0.0003
15	2.6e-03	62.98	8.81	0.044	24.90	1.88	0.058	26.09	2.21	0.038	36.27	2.95	0.0001
16	8.6e-03	56.80	9.02	0.045	24.30	1.93	0.103	21.57	2.26	0.072	31.19	3.02	0.0004
17	5.6e-03	99.43	9.02	0.042	33.15	1.93	0.158	32.65	2.26	0.095	45.99	3.02	0.0002
18	5.8e-03	59.14	9.02	0.149	23.35	1.93	0.087	24.40	2.26	0.061	34.55	3.02	0.0002
19	4.7e-03	99.84	9.02	0.049	33.14	1.93	0.159	33.42	2.26	0.113	46.91	3.02	0.0002
20	4.2e-03	99.29	9.02	0.037	33.33	1.93	0.157	33.14	2.26	0.112	46.55	3.02	0.0002
21	3.3e-03	93.35	8.81	0.030	32.27	1.88	0.138	32.21	2.21	0.132	45.09	2.95	0.0001
22	9.8e-03	57.77	9.02	0.060	24.14	1.93	0.120	21.27	2.26	0.081	31.25	3.02	0.0006
23	2.6e-03	104.04	9.24	0.020	34.47	1.98	0.157	34.95	2.32	0.113	48.70	3.09	0.0001
24	5.7e-03	72.21	9.02	0.038	28.74	1.93	0.136	26.49	2.26	0.079	38.01	3.02	0.0003
25	2.0e-03	79.72	9.24	0.064	29.01	1.98	0.099	30.40	2.32	0.070	42.88	3.09	0.0001
26	6.9e-03	61.72	9.24	0.052	24.63	1.98	0.084	23.55	2.32	0.058	33.70	3.09	0.0003
27	3.2e-03	102.40	9.02	0.107	32.43	1.93	0.157	35.05	2.26	0.113	48.72	3.02	0.0001
28	5.4e-03	99.36	9.02	0.049	33.10	1.93	0.189	33.47	2.26	0.135	46.80	3.02	0.0002
29	5.8e-03	67.35	8.81	0.039	27.71	1.88	0.132	25.45	2.21	0.092	36.43	2.95	0.0003
30	2.2e-03	96.24	8.81	0.045	30.78	1.88	0.119	32.86	2.21	0.085	45.76	2.95	0.0001
31	5.9e-03	99.06	9.02	0.043	33.47	1.93	0.162	32.59	2.26	0.115	45.91	3.02	0.0003
32	6.6e-03	72.38	9.02	0.052	28.06	1.93	0.121	27.15	2.26	0.086	38.47	3.02	0.0002
33	6.6e-03	105.70	9.24	0.061	33.98	1.98	0.175	33.75	2.32	0.124	47.70	3.09	0.0004
34	4.1e-03	79.84	9.24	0.115	28.68	1.98	0.137	30.02	2.32	0.097	42.42	3.09	0.0002
35	7.6e-03	56.87	9.02	0.039	24.10	1.93	0.098	21.31	2.26	0.068	30.88	3.02	0.0004
36	6.5e-03	67.72	8.81	0.050	27.02	1.88	0.140	25.82	2.21	0.098	36.68	2.95	0.0002
37	3.2e-03	93.62	8.81	0.028	32.17	1.88	0.170	32.02	2.21	0.106	44.91	2.95	0.0001
38	7.9e-03	57.36	9.02	0.059	23.86	1.93	0.094	22.58	2.26	0.065	32.33	3.02	0.0003
39	1.8e-03	101.41	9.02	0.039	32.48	1.93	0.117	34.93	2.26	0.085	48.40	3.02	0.0000
40	0.010	77.01	9.24	0.078	28.67	1.98	0.125	28.39	2.32	0.089	39.90	3.09	0.0003
41	4.6e-03	100.21	9.02	0.047	32.77	1.93	0.140	33.47	2.26	0.085	46.89	3.02	0.0002
42	4.2e-03	61.93	9.24	0.106	24.74	1.98	0.052	26.20	2.32	0.068	36.38	3.09	0.0001
43	6.6e-03	58.66	9.02	0.147	22.87	1.93	0.068	24.26	2.26	0.049	33.92	3.02	0.0002
44	5.5e-03	99.21	9.02	0.048	33.62	1.93	0.177	33.06	2.26	0.126	46.55	3.02	0.0003
45	6.9e-03	53.31	8.81	0.044	23.08	1.88	0.089	21.17	2.21	0.053	30.49	2.95	0.0003
46	6.3e-03	77.06	9.24	0.046	28.87	1.98	0.113	27.94	2.32	0.080	39.64	3.09	0.0002
47	4.1e-03	94.68	8.81	0.057	31.96	1.88	0.194	33.06	2.21	0.139	46.11	2.95	0.0001
48	9.7e-03	57.26	9.02	0.061	23.67	1.93	0.107	21.92	2.26	0.075	31.53	3.02	0.0004
49	7.4e-03	56.65	9.02	0.044	23.92	1.93	0.090	22.33	2.26	0.063	31.78	3.02	0.0002
50	4.1e-03	99.72	9.02	0.040	33.00	1.93	0.143	33.26	2.26	0.102	46.66	3.02	0.0002
51	3.2e-03	93.08	8.81	0.025	32.40	1.88	0.194	32.02	2.21	0.139	44.87	2.95	0.0001
52	7.4e-03	72.54	9.02	0.055	28.33	1.93	0.129	26.67	2.26	0.090	38.13	3.02	0.0004
53	5.1e-03	106.34	9.24	0.046	34.02	1.98	0.145	33.96	2.32	0.076	47.99	3.09	0.0003
54	6.8e-03	60.79	9.24	0.047	24.92	1.98	0.092	23.74	2.32	0.064	33.76	3.09	0.0002
55	7.9e-03	61.33	9.24	0.051	25.09	1.98	0.093	23.12	2.32	0.076	33.26	3.09	0.0004
56	5.1e-03	105.76	9.24	0.066	34.23	1.98	0.203	34.99	2.32	0.145	49.07	3.09	0.0003
57	4.6e-03	67.48	8.81	0.030	26.95	1.88	0.091	25.45	2.21	0.064	36.15	2.95	0.0002
58	7.4e-03	72.94	9.02	0.062	28.08	1.93	0.133	26.84	2.26	0.093	38.37	3.02	0.0004

ρ_b = bulk density, ρ_p = particle density, ε = porosity, d_p = particle diameter, d_{pore} = pore diameter, τ = tortuosity

Table B.11.: Mass Transfer Analysis - 20% CZCZC Catalyst - Part 2

Point	H_2			CO_2			MeOH			H_2O			Mears Criterion
	Φ_{WP}	D_{eff}	D_K	Φ_{WP}	D_{eff}	D_K	Φ_{WP}	D_{eff}	D_K	Φ_{WP}	D_{eff}	D_K	
	(–)	($\times 10^{-8}$)	($\times 10^{-6}$)	(–)	($\times 10^{-8}$)	($\times 10^{-6}$)	(–)	($\times 10^{-8}$)	($\times 10^{-6}$)	(–)	($\times 10^{-8}$)	($\times 10^{-6}$)	(–)
Catalyst Properties: ρ_b = 857.7 kg/m³, ρ_p = 1241 kg/m³, ε = 0.309, d_p = 800 µm, d_{pore} = 11.5 nm, τ = 1.4													
59	7.2e-03	77.19	9.24	0.050	29.17	1.98	0.127	27.43	2.32	0.089	39.28	3.09	0.0004
60	7.6e-03	72.38	9.02	0.052	27.80	1.93	0.129	26.58	2.26	0.091	37.76	3.02	0.0003
61	4.6e-03	75.99	9.02	0.155	27.11	1.93	0.092	28.63	2.26	0.064	40.66	3.02	0.0003
62	7.9e-03	77.09	9.24	0.057	29.34	1.98	0.152	27.73	2.32	0.106	39.63	3.09	0.0004
63	3.4e-03	93.77	8.81	0.031	32.15	1.88	0.164	32.23	2.21	0.117	45.14	2.95	0.0001
64	8.2e-03	57.51	9.02	0.061	23.84	1.93	0.095	22.42	2.26	0.066	32.23	3.02	0.0004
65	3.0e-03	69.41	8.81	0.055	26.43	1.88	0.090	27.40	2.21	0.064	38.46	2.95	0.0001
66	1.8e-03	96.24	8.81	0.050	31.59	1.88	0.169	34.04	2.21	0.122	47.16	2.95	0.0000
67	3.7e-03	106.46	9.24	0.047	34.08	1.98	0.103	35.07	2.32	0.081	49.13	3.09	0.0002
68	7.2e-03	72.42	9.02	0.048	28.07	1.93	0.132	26.21	2.26	0.092	37.52	3.02	0.0003
69	3.3e-03	93.55	8.81	0.033	32.33	1.88	0.179	32.65	2.21	0.128	45.61	2.95	0.0001
70	2.4e-03	107.63	9.24	0.085	33.82	1.98	0.139	36.79	2.32	0.101	50.91	3.09	0.0001
71	8.4e-03	60.60	9.24	0.053	25.56	1.98	0.128	23.48	2.32	0.089	33.70	3.09	0.0003
72	4.8e-03	67.60	8.81	0.036	26.84	1.88	0.095	26.03	2.21	0.067	36.75	2.95	0.0001
73	7.1e-03	67.52	8.81	0.051	27.01	1.88	0.143	25.88	2.21	0.101	36.66	2.95	0.0002
74	9.5e-03	61.15	9.24	0.067	24.33	1.98	0.091	23.52	2.32	0.064	33.38	3.09	0.0003
75	6.2e-03	72.26	9.02	0.047	28.01	1.93	0.114	27.10	2.26	0.080	38.35	3.02	0.0002
76	4.5e-03	67.39	8.81	0.026	26.79	1.88	0.121	25.06	2.21	0.085	35.70	2.95	0.0001
77	5.6e-03	93.36	8.81	0.053	32.65	1.88	0.234	32.36	2.21	0.167	45.39	2.95	0.0002
78	4.6e-03	99.50	9.02	0.048	33.41	1.93	0.193	33.43	2.26	0.137	46.96	3.02	0.0002
79	2.9e-03	61.73	9.24	0.068	24.79	1.98	0.039	26.26	2.32	0.042	36.38	3.09	0.0001
80	6.8e-03	67.50	8.81	0.048	27.39	1.88	0.160	25.52	2.21	0.112	36.45	2.95	0.0003
81	4.5e-03	72.93	9.02	0.037	27.87	1.93	0.068	26.66	2.26	0.057	38.07	3.02	0.0002
82	5.0e-03	67.88	8.81	0.035	27.27	1.88	0.102	25.11	2.21	0.071	36.08	2.95	0.0003
83	9.9e-03	72.53	9.02	0.064	28.19	1.93	0.153	26.11	2.26	0.106	37.46	3.02	0.0005
84	5.9e-03	104.86	9.24	0.058	34.59	1.98	0.216	34.52	2.32	0.154	48.51	3.09	0.0003
85	6.4e-03	77.27	9.24	0.057	29.12	1.98	0.138	28.48	2.32	0.098	40.38	3.09	0.0002
86	3.0e-03	69.40	8.81	0.058	26.50	1.88	0.109	27.42	2.21	0.078	38.56	2.95	0.0001
87	3.2e-03	101.59	9.02	0.081	32.42	1.93	0.131	35.15	2.26	0.095	48.58	3.02	0.0001
88	2.1e-03	76.81	9.24	0.023	30.07	1.98	0.145	29.98	2.32	0.103	42.19	3.09	0.0001

ρ_b = bulk density, ρ_p = particle density, ε = porosity, d_p = particle diameter, d_{pore} = pore diameter, τ = tortuosity

Statistical analysis

The statistical analysis of the kinetic model is conducted using four performance indicators. The coefficient of determination (R^2) is a global statistical measure, that quantifies how much of experimental value variance can be explained by the model itself. It is defined as:

$$R^2 = 1 - \frac{\sum_{i=1}^{n}(y_i^{\text{exp}} - y_i^{\text{calc}})^2}{\sum_{i=1}^{n}(y_i^{\text{exp}} - \bar{y}^{\text{exp}})^2} \tag{B.21}$$

where y_i in this case is defined by experimental and calculated reactor exit partial pressures of the species involved in MeOH and H_2O formation. Extending on R^2 for a single species or a single variable, a combined R^2 can be used to evaluate overall model performance towards a set of different model variables and results. THe combined R^2 can be calculated as:

$$R^2_{\text{combined}} = \frac{R^2_{\text{rates}} + R^2_{\text{pressures}}}{2} \tag{B.22}$$

The Mean absolute percentage error (MAPE) expresses the average relative error expressed as a percentage. Lower values indicate better accuracy. In this work, we use it to analyze the average estimation error our model delivers when predicting effluent compositions of product gas. It is defined as:

$$\text{MAPE} = \frac{100\%}{n}\sum_{i=1}^{n}\left|\frac{y_i^{\text{exp}} - y_i^{\text{calc}}}{y_i^{\text{exp}}}\right| \tag{B.23}$$

The Concordance Correlation Coefficient (CCC) evaluates both precision (correlation) and accuracy (bias) of a mathematical model. It combines the covariance ($\sigma_{\text{exp,calc}}$) of experimental and measured values, the

variance (σ^2_{exp}) of experimental values and the variance of calculated values (σ^2_{calc}). It is defined as:

$$\text{CCC} = \frac{2\sigma_{\text{exp,calc}}}{\sigma^2_{\text{exp}} + \sigma^2_{\text{calc}} + (\bar{y}^{\text{exp}} - \bar{y}^{\text{calc}})^2} \tag{B.24}$$

where:

$$\sigma_{\text{exp,calc}} = \text{Cov}(y^{\text{exp}}, y^{\text{calc}}) \tag{B.25}$$

$$\sigma^2_{\text{exp}} = \text{Var}(y^{\text{exp}}) \tag{B.26}$$

$$\sigma^2_{\text{calc}} = \text{Var}(y^{\text{calc}}) \tag{B.27}$$

The weighted performance index (WPI) is a custom composite metric that can combine multiple performance indicators with individual weights to emphasize different aspects of model performance. This allows prioritizing what matters most for your specific application. It too combines several different metrics:

- R^2_{rates}: How well the model predicts reaction rates
- $R^2_{\text{pressures}}$: How well the model predicts exit pressures
- $(1 - \text{NRMSE}_{\text{combined}})$: Overall prediction accuracy (inverted so higher is better)

It was applied in identifying effective optimization algorithms, where R^2 was applied for calculated rates, pressures and reactor exit molar composition.

- Equal weighting: $w_1 = w_2 = w_3 = 1/3$ (balanced assessment)
- Rate-focused: $w_1 = 0.6, w_2 = 0.3, w_3 = 0.1$ (emphasize kinetics)
- Pressure-focused: $w_1 = 0.2, w_2 = 0.6, w_3 = 0.2$ (emphasize thermodynamics)
- Accuracy-focused: $w_1 = 0.3, w_2 = 0.3, w_3 = 0.4$ (emphasize overall error)

$$\text{WPI} = w_1 \cdot R^2_{\text{rates}} + w_2 \cdot R^2_{\text{pressures}} + w_3 \cdot (1 - \text{NRMSE}_{\text{combined}}) \tag{B.28}$$

where $w_1 + w_2 + w_3 = 1$ and NRMSE is the Normalized Root Mean Square Error.
The WPI was used for model discrimination in selecting good optimization strategies and superior models in comparison between rate based optimization and partial pressure based optimization strategies.
The confidence intervals of the estimated kinetic parameters were determined from the finite-difference approximation of the Hessian matrix of the objective function. After the optimization yielded the best-fit parameter vector $\hat{\xi}$, the Hessian matrix $\mathbf{H}$ was numerically estimated by finite differences of the second derivatives of the sum of squared residuals $S(\xi)$ with respect to the parameters:

$$H_{ij} \approx \frac{\partial^2 S}{\partial \xi_i \, \partial \xi_j}. \tag{B.29}$$

This approximation was obtained by perturbing each parameter θ_i around its optimal value by a small step (typically 1–5%) and recalculating $S(\theta)$ for each perturbation. The covariance matrix of the estimated parameters was then evaluated as

$$\mathbf{C}_\xi \approx 2\sigma^2 \mathbf{H}^{-1}, \tag{B.30}$$

where σ^2 denotes the variance of the residuals. The standard error of each parameter was calculated from the diagonal elements of the covariance matrix:

$$\mathrm{SE}(\xi_i) = \sqrt{C_{\xi,ii}}. \tag{B.31}$$

Assuming normally distributed residuals, the $(1-\alpha)$ confidence interval for each parameter was obtained as

$$\xi_i \pm t_{(1-\alpha/2,\nu)} \times \mathrm{SE}(\xi_i), \tag{B.32}$$

where $t_{(1-\alpha/2,\nu)}$ is the Student's t value corresponding to the confidence level $(1-\alpha)$ and ν degrees of freedom. In kinetic modeling, these confidence intervals provide a quantitative measure of the parameter identifiability and the reliability of the fit, with narrow intervals indicating well-determined parameters and wide intervals suggesting strong parameter correlations or insufficient experimental sensitivity.

B.2.4. Results of the Statistical analysis

Table B.12.: Fitted kinetic and adsorption parameters with 95% confidence bounds for 20% catalyst systems

	20% CZ	20% CZC	20% CZCZ	20% CZCZC
Model	A3B2C3	A3B2C1	A2B1C3	A4B1C3
Rate Constants: $k = A \times e^{-E_a/RT}$				
$A_{MeOH,CO}$	$1.18^{+0.11}_{-0.10}$	$32.1^{+3.41}_{-3.32}$	$8.21^{+0.79}_{-0.77}$	$0.21^{+0.18}_{-0.18}$
$E_{a,\,MeOH,CO}$ (kJ/mol)	$8.02^{+0.97}_{-0.94}$	$3.20^{+0.40}_{-0.39}$	$1.32^{+0.11}_{-0.11}$	$85.21^{+9.81}_{-0.76}$
$A_{MeOH,\,CO_2}$	$(3.76^{+0.56}_{-0.52}) \times 10^7$	$(3.20^{+0.34}_{-0.33}) \times 10^8$	$(6.34^{+0.46}_{-0.46}) \times 10^{10}$	$(5.44^{0.34}_{-0.33}) \times 10^3$
$E_{a,\,MeOH,\,CO_2}$ (kJ/mol)	$79.3^{+9.34}_{-8.96}$	$67.5^{+8.21}_{-7.86}$	$130.8^{+16.31}_{-16.24}$	$130.8^{+14.26}_{-15.35}$
A_{RWGS}	$0.672^{+0.06}_{-0.06}$	$1.37^{+0.21}_{-0.20}$	$0.27^{+0.03}_{-0.03}$	$(1.12^{+0.09}_{-0.09}) \times 10^{-2}$
$E_{a,RWGS}$ (kJ/mol)	$27.5^{+3.20}_{-3.18}$	$8.46^{+0.56}_{-0.54}$	$25.2^{+1.81}_{-1.76}$	$29.4^{+3.47}_{-3.34}$
Adsorption Constants: $K = B \times e^{\Delta H/RT}$				
B_{CO}	$(1.00^{+0.11}_{-0.09}) \times 10^{-5}$	$(1.55^{+0.08}_{-0.07}) \times 10^{-2}$	$(1.36^{+0.10}_{-0.09}) \times 10^{-2}$	$(1.12^{+0.05}_{-0.05}) \times 10^{-2}$
ΔH_{CO} (kJ/mol)	$33.8^{+1.56}_{-1.49}$	$4.38^{+0.34}_{-0.30}$	$29.7^{+1.12}_{-1.12}$	$1.01^{+0.02}_{-0.02}$
B_{CO_2}	$(2.91^{+0.18}_{-0.19}) \times 10^{-7}$	$(3.79^{+0.25}_{-0.24}) \times 10^{-7}$	$(1.70^{+0.08}_{-0.08}) \times 10^{-11}$	$(5.02^{+0.21}_{-0.20}) \times 10^{-8}$
ΔH_{CO_2} (kJ/mol)	$57.4^{+2.43}_{-2.38}$	$30.0^{+2.82}_{-2.76}$	$114.3^{+5.43}_{-5.21}$	$66.8^{+2.12}_{-2.07}$
B_{H_2O}	$(7.07^{+0.11}_{-0.11}) \times 10^{-12}$	$(1.33^{+0.09}_{-0.09}) \times 10^{-11}$	$(7.48^{+0.56}_{-0.53}) \times 10^{-14}$	$(1.21^{+0.07}_{-0.07}) \times 10^{-13}$
ΔH_{H_2O} (kJ/mol)	$125.7^{+2.74}_{-2.57}$	$131.9^{+7.23}_{-6.85}$	$137.0^{+4.26}_{-4.05}$	$124.9^{+3.21}_{-3.14}$
H_2: Parameters compounded with H_2O				

References

[1] Mohammad Abdollahi, Hossein Atashi, and Farshad Farshchi Tabrizi. “Parametric investigation of g-alumina granule preparation via the oil-drop route”. In: *Advanced Powder Technology* 28.5 (2017), pp. 1356–1371. ISSN: 09218831. DOI: 10.1016/j.apt.2017.03.004.

[2] Vahid Delavari and Mohammad Rahmani. “Numerical and experimental investigation of gamma alumina macro particle synthesis via the oil-drop method”. In: *Powder Technology* 453 (2025), p. 120635. ISSN: 00325910. DOI: 10.1016/j.powtec.2025.120635.

[3] Li He et al. “Preparation of Pt/g-Al2O3 catalyst coating in microreactors for catalytic methane combustion”. In: *Chemical Engineering Journal* 380 (2020), p. 122424. ISSN: 13858947. DOI: 10.1016/j.cej.2019.122424.

[4] Pengcheng Liu et al. “Preparation of high purity spherical g-alumina using a reduction-magnetic separation process”. In: *Journal of Physics and Chemistry of Solids* 69.4 (2008), pp. 799–804. ISSN: 00223697. DOI: 10.1016/j.jpcs.2007.09.005.

[5] Henry O. Ayoola et al. “Evaluating the accuracy of common g-Al2O3 structure models by selected area electron diffraction from high-quality crystalline g-Al2O3”. In: *Acta Materialia* 182 (2020), pp. 257–266. ISSN: 13596454. DOI: 10.1016/j.actamat.2019.10.027.

[6] Shangkun Li et al. “Methane to Methanol through Heterogeneous Catalysis and Plasma Catalysis”. In: *Catalysts* 11.5 (2021), p. 590. DOI: 10.3390/catal11050590.

[7] Mashrafi Bin Mobarak et al. “Synthesis and characterization of CuO nanoparticles utilizing waste fish scale and exploitation of XRD peak profile analysis for approximating the structural parameters”. In: *Arabian Journal of Chemistry* 15.10 (2022), p. 104117. ISSN: 18785352. DOI: 10.1016/j.arabjc.2022.104117.

[8] Hua Zhou et al. “Interfaces between hexagonal and cubic oxides and their structure alternatives”. In: *Nature communications* 8.1 (2017), p. 1474. DOI: 10.1038/s41467-017-01655-5.

[9] Carl Fritsch et al. “CO 2 –Hydrogenation to Methanol over CuO/ZnO Based Infiltration Composite Catalyst Spheres”. In: *ChemCatChem* 16.21 (2024). ISSN: 1867-3880. DOI: 10.1002/cctc.202400731.

[10] Francesca Rossi, Peter van Beek, and Toby Walsh. “Introduction”. In: 2 (), pp. 3–12. DOI: 10.1016/S1574-6526(06)80005-2.

[11] F. Nestler et al. “Kinetic modelling of methanol synthesis over commercial catalysts: A critical assessment”. In: *Chemical Engineering Journal* 394 (2020), p. 124881. ISSN: 13858947. DOI: 10.1016/j.cej.2020.124881.

[12] Y. Slotboom et al. “Critical assessment of steady-state kinetic models for the synthesis of methanol over an industrial Cu/ZnO/Al2O3 catalyst”. In: *Chemical Engineering Journal* 389 (2020), p. 124181. ISSN: 13858947. DOI: 10.1016/j.cej.2020.124181.

[13] Filippo Bisotti et al. “Impact of Kinetic Models on Methanol Synthesis Reactor Predictions: In Silico Assessment and Comparison with Industrial Data”. In: *Industrial & Engineering Chemistry Research* 61.5 (2022), pp. 2206–2226. ISSN: 0888-5885. DOI: 10.1021/acs.iecr.1c04476.

[14] Sreetama Ghosh et al. “Experimental and kinetic modeling studies of methanol synthesis from CO2 hydrogenation using In2O3 catalyst”. In: *Chemical Engineering Journal* 416 (2021), p. 129120. ISSN: 13858947. DOI: 10.1016/j.cej.2021.129120.

[15] Nonam Park et al. “Kinetic modeling of methanol synthesis over commercial catalysts based on three-site adsorption”. In: *Fuel Processing Technology* 125 (2014), pp. 139–147. ISSN: 03783820. DOI: 10.1016/j.fuproc.2014.03.041.

[16] Serena Poto et al. “Kinetic modelling of the methanol synthesis from CO2 and H2 over a CuO/CeO2/ZrO2 catalyst: The role of CO2 and CO hydrogenation”. In: *Chemical Engineering Journal* 435 (2022), p. 134946. ISSN: 13858947. DOI: 10.1016/j.cej.2022.134946.

C. Supplementary Materials Publication 3

Influence of GHSV on Methanol Synthesis performance

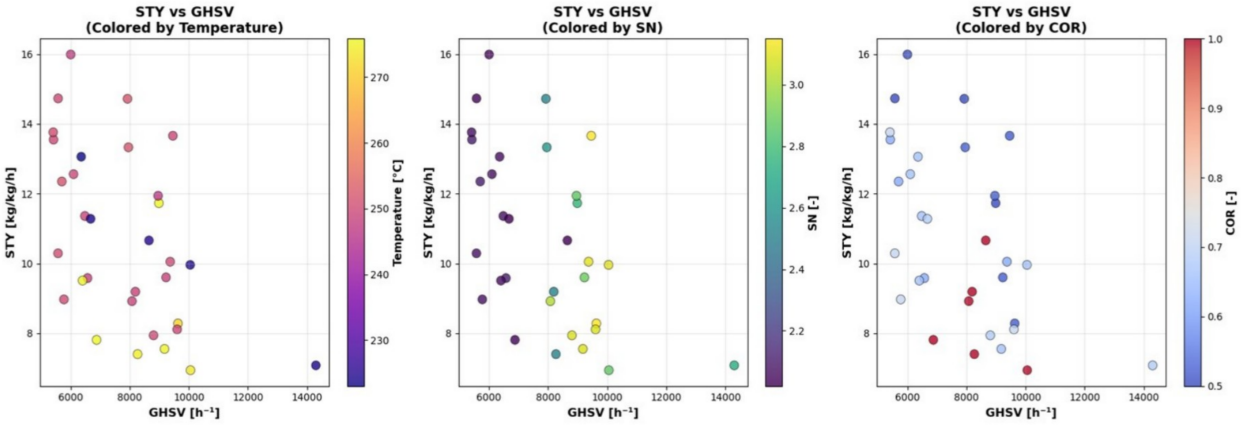

Figure C.1.: Influence on applied GHSV on Methanol Synthesis Performance

Zusammenfassung

Methanol (MeOH) gilt als vielversprechende Plattformchemikalie zur Defossilisierung kohlenstoffintensiver Sektoren – insbesondere der chemischen Industrie sowie schwer zu dekarbonisierender Bereiche des Verkehrs. Seine hohe Relevanz ergibt sich daraus, dass MeOH durch Anpassung etablierter, bislang fossilbasierter Synthesegasverfahren aus einer Vielzahl regenerativer Quellen oder direkt aus CO_2 erzeugt werden kann.
Die Nutzung regenerativer Rohstoffe sowie von CO_2 zur Herstellung von Synthesegas (SynGas) führt jedoch häufig zu hohen CO_2-Anteilen und unterstöchiometrischen Wasserstoffkonzentrationen im Prozessgas für die MeOH-Herstellung. Dies stellt besondere Anforderungen an die Prozesstechnik der regenerativen MeOH-Synthese. Kommerziell verfügbare Katalysatoren auf Basis von $CuO/ZnO/Al_2O_3$ (CZA) können diesen Betriebsbedingungen ohne Anpassungen bislang nur eingeschränkt gerecht werden.
Vor diesem Hintergrund besteht ein deutlicher Entwicklungsbedarf hinsichtlich der Weiterentwicklung klassischer CZA-Katalysatoren. Besonders vielversprechend ist die gezielte Modifikation dieser Systeme durch Additive, die eine stabilere Adsorption von CO_2 ermöglichen und zugleich eine erhöhte Toleranz gegenüber dem unvermeidbar entstehenden Reaktionsprodukt Wasser (H_2O) aufweisen. Auf dieser Basis richtet sich die Untersuchung auf die Frage, inwiefern eine gezielte Additivierung imprägnierter, CZA-basierter Katalysatoren gegenüber kommerziellen Referenzsystemen zu einer Steigerung des Kohlenstoffumsatzes beitragen kann. Darüber hinaus wird analysiert, wie sich diese Umsatzsteigerungen physiko-chemisch beschreiben lassen sowie wie sich die hergestellten Proben im mehrskaligen Einsatz für die Skalierung von Labor- auf Pilotmaßstab verhalten und welche Übertragbarkeit der labortechnischen Ergebnisse auf den pilottechnischen Betrieb besteht.
Im Rahmen dieser Arbeit wurde daher eine Serie modifizierter Katalysatorformulierungen entwickelt, bei denen das etablierte CZA-System gezielt durch ausgewählte, vielversprechende Metalloxide ergänzt wurde. Die Herstellung der Proben erfolgte mittels *incipient wetness impregnation* (IWI) auf sphärischen γ-Al_2O_3-Trägerpartikeln. Durch ein systematisches Screening unterschiedlicher Rezepturen sowie umfangreiche Charakterisierungs- und Syntheseversuchsreihen konnte eine quinäre Katalysatorzusammensetzung identifiziert werden, die sowohl eine hohe CO_2-Umsatzrate als auch eine hohe Selektivität für die MeOH-Entstehung aufweist. Aufbauend auf dieser optimierten Formulierung wurde eine weitere Katalysatorreihe hergestellt, in der der Einfluss der Additive CeO_2, ZrO_2 und CaO auf die katalytische Performance sowie die physiochemischen Katalysatoreigentschaften detailliert untersucht wurden.
Die hergestellten Proben wurden umfassend charakterisiert. Zum Einsatz kamen Rasterelektronenmikroskopie (REM), Transmissionselektronenmikroskopie (TEM), Stickstoffadsorptions-/-desorptionsanalysen mit BET-Auswertung, Röntgendiffraktometrie (XRD), Raman-Spektroskopie, Röntgenphotoelektronenspektroskopie (XPS), temperaturprogrammierte Reduktion und Desorption (H_2-TPR/TPD), temperaturprogrammierte CO_2-Desorption (CO_2-TPD) sowie temperaturprogrammierte Desorption mit Ammoniak (NH_3-TPD). Alle Katalysatorproben zeigten große mesopore Oberflächenstrukturen, sehr hohe spezifische Oberflächen, gute Metalloxidverteilung auf den Trägern sowie hohe, beladungsspezifische Reduzierbarkeit. Die Wasserstoff-Aufnahmefähigkeit war gegenüber dem Referenz-Vollkontaktkatalysator reduziert, wobei dies in Relation zu

den gemessen Umsätzen keine essenzielle Rolle spielte. Für die Aufnahmefähigkeit für CO_2 konnte hingegen eine klare positive Korrelation zur Kohenstoffkonversion festgestellt werden.
Die katalytischen Eigenschaften der Proben wurden in einem Laborreaktor sowohl unter reinen CO_2-Bedingungen als auch in CO/CO_2-haltigen Syngasgemischen untersucht, wie sie für verschiedene regenerative Anwendungen typisch sind. Bewertet wurden insbesondere die Kohlenstoff-Umsatzraten sowie die Raum-Zeit-Ausbeute von MeOH. Die Ergebnisse der Arbeiten sind in drei verschiedenen Beiträgen zu internationalen Zeitschriften präsentiert.
Witerführend wurden anschließend die Reaktionsgleichgewichte des CO_2- und CO-Umsatzes zu MeOH und H_2 bestimmt, um die Leistung der Katalysatorproben unter Bedingungen zu erproben, die dem Einsatz in industriellen Analgen möglichst nahekommen. Hierauf und auf den zuvor durchgeführten Versuchsreihen erfolgten umfassende kinetische Untersuchungen, aus denen für jede Probe ein einfaches, aber robustes kinetisches Modell entwickelt wurde. Dieses Modell ermöglicht eine präzise numerische Beschreibung der Reaktionspfade von CO und CO_2 auf den Katalysatoroberflächen aller untersuchten Formulierungen und ermöglicht Rückschlüsse über die zugrundieliegenden mechanistischen Vorgängen. Die Modelle sind gut geeignet, die Katalysatorleistung unter realen industriellen Bedingungen vorherzusagen. Die kinetischen Modelle zeigen für alle Katalysatorproben, dass CO_2 auch in CO/CO_2-Mischströmen die primäre Kohlenstoff- und Sauerstoffquelle für die Entstehung von MeOH ist, während die sekundäre oder tertiäre Hydrogenierung von Oberflächenintermediaten die ratenbestimmden Schritte für alle Proben sind.
Für die Übertragung der entwickelten Katalysatoren vom Labor auf den Demonstrationsmaßstab und den Einsatz unter Industrie-nahen Synthesebedingungen wurde weiterführend ein vollständiger Prozess zur erneuerbaren Methanolsynthese aus Biogas entwickelt. Das Biogas wird zunächst autotherm reformiert, um ein CO_2-reiches Synthesegas zu erzeugen, welches anschließend in isothermen Reaktoren katalytisch zu Rohmethanol umgesetzt wird. Da der hohe CO_2-Gehalt des reformierten Gases die Methanolsynthese über konventionelle Katalysatoren erheblich erschwert, wurde der im Labor entwickelte CuO/ZnO-basierte Trägerkatalysator mit CeO_2-, ZrO_2- und CaO-Zusatz auf pilottechnischen Maßstab übertragen und in einer eigens errichteten Demonstrationsanlage zur Pilotierung von Verfahren und Katalysatorprobe eingesetzt.
Diese Anlage wurde konzipiert, aufgebaut und in Betrieb genommen, um Biogas im integrierten Prozess zu MeOH umzusetzen. Die Pilotierung erfolgte an der Kläranlage Emschermündung unter Nutzung von Klärgas als Rohstoff und unter realitätsnahen Bedingungen bei moderatem Druck. Systematisch untersucht wurden die Auswirkungen unterschiedlicher SynGas-Zusammensetzungen und Reaktionstemperaturen auf die Produktionsleistung und Effizienz des Prototypkatalysators. Darüber hinaus wurden betriebsrelevante Aspekte einer potenziellen industriellen Skalierung des Biogas-zu-Methanol-(B2M)-Prozesses analysiert.
Damit bildet diese Arbeit den vollständigen Entwicklungsprozess in der heterogenen Katalyse ab – von der mikroskopischen Katalysatorentwicklung über die Anwendung im technischen System bis hin zur modellgestützten Skalierung auf Basis von kinetischen Modellen. Sie verdeutlicht die zentrale Rolle multi-skaliger Methoden in der modernen Prozessentwicklung und liefert eine Applikationsgrundlage auf Basis effizienter Trägerkatalysatoren für die wirtschaftlich tragfähige Integration der MeeOH-Synthese aus Biogas in eine regenerative Kohlenstoffwirtschaft.

Summary

Methanol (MeOH) is set to become a major player in the defossilization of heavily carbon-reliant industries such as the chemistry sector and hard-to-abate parts of the transportation sectors. This can mostly be attributed to the fact, that it can be readily produced from different regenerative sources through adaptation of existing fossil resources based synthesis gas (SynGas) processes. However, many of the renewable sources that MeOH can be produced from are prone to yield carbon dioxide (CO_2)-rich SynGas process streams for further conversion to MeOH, which current commercial catalysts are not always well equipped for.

In this context, some development has to be done to improve current copper oxide (CuO)/zinc oxide(ZnO)/aluminum oxide (Al_2O_3) (CZA) formulas by promoting the catalyst with metal oxides that provide more stable CO_2 adsorption and deliver greater operational resilience against water (H_2O) co-produced in MeOH synthesis based upon CO_2-rich SynGas streams. Building on this, the present thesis addresses the extent to which the targeted addition of promoters to impregnated, CZA-based catalysts can enhance carbon conversion compared to commercial reference systems. Furthermore, it investigates how such improvements in CO_2 conversion can be explained from a physio-chemical perspective, and how the synthesized catalysts perform in a multiscale context, scaling from laboratory to pilot scale, thereby assessing the transferability of laboratory findings to pilot-scale operation. A series of catalyst formulas was developed by promoting the popular CZA-complex with different promising catalyst additives. Differently promoted and chemically activated catalyst samples were produced through incipient wetness impregnation (IWI) of gamma alumina (γ-Al_2O_3) carrier spheres. Herein, a quinary formula was identified that promises to show good conversion of CO_2 to, and high selectivity for, MeOH. Based upon this quinary catalyst formulation, a furhter small batch of differently promoted catalyst samples was developed – each adding different metal oxides in promotional steps towards the quinary catalyst formulation containing 20% CuO, ZnO, CeO_2, ZrO_2, and CaO on a γ-Al_2O_3 carrier.

The produced samples underwent extensive physio-chemical characterization, catalyst testing, and deployment in a pilot-scale setup. The respective results are presented in three different contributions to international journals.

The samples are characterized extensively by applying scanning electron microscopy (SEM), transmission electron microscopy (TEM) , nitrogen (N_2)-adsorption and -desorption experiments with Brunauer-Emmett-Teller (BET) analysis, X-ray diffraction (XRD) spectroscopy, Raman spectroscopy, X-ray photoelectron spectroscopy (XPS), hydrogen (H_2) temperature-programmed reduction and desorption, CO_2 temperature-programmed desorption and ammonia (NH_3) temperature-programmed desorption. The catalysts all exhibited large mesoporous surface structures, very high specific surface areas, good metal oxide dispersion on the supports, and high loading-specific reducibility. The hydrogen uptake capacity was lower compared to the reference precipitated catalyst. However, this did not play an essential role relative to the measured conversions. In contrast, a clear positive correlation between the CO_2 uptake capacity and the carbon conversion was observed.

In a laboratory reactor setup, the samples were tested for their conversion efficiencies in both CO_2-only

SynGas streams as well as mixed carbon oxide SynGas streams extensively, which are more common in regenerative synthesis gas applications, even when using pure CO_2 as carbon source.
Reaction equilibria of CO_2 and CO towards MeOH and water (H_2O) were determined for investigation of industrially relevant SynGas compositions and their influence on catalyst conversion performance. Based upon these studies and the previously obtained, extensive performance data set a series of kinetic studies was applied. Through this a simple, robust kinetic model with good numerical fit was developed for all four promotional steps of the catalyst samples, which is able to accurately predict the reaction pathways of CO and CO_2 on the catalyst surfaces as well as predicting catalyst performance in industrial process setups.
For transfer of the laboratory test results to pilot and demonstration scale application and in addition to catalyst development, this thesis also focuses on the design and realization of a renewable process for MeOH synthesis from biogas. In this process, biogas is first autothermally reformed to produce a CO_2-rich SynGas, which is then catalytically converted to raw MeOH in isothermal reactors. The high CO_2 content of the reformed gas poses a significant challenge for MeOH synthesis over commercially available catalysts, as it limits conversion and selectivity under standard operating conditions. Therefore, the CuO/ZnO-based catalysts developed and optimized in the laboratory, promoted with CeO_2, ZrO_2, and CaO, were scaled up to pilot format and implemented in the dedicated demonstration plant.
This pilot-scale facility was designed, constructed, and commissioned to reform biogas into CO_2-rich synthesis gas and subsequently convert it catalytically into raw MeOH. The pilot operation was carried out at the wastewater treatment plant in Dinslaken, Germany, using digester gas as a renewable feedstock under mild pressures and realistic operating conditions. The study focused on the influence of different synthesis gas compositions and reaction temperatures on the production performance and efficiency of the prototype catalyst, as well as on the assessment of operational factors relevant for future industrial-scale implementation of the biogas-to-methanol (B2M) process.
This thesis thus represents the complete development chain in heterogeneous catalysis, demonstrating the importance of multi-scale methods in modern process design and providing the scientific foundation for the economic and sustainable integration of MeOH synthesis from biogas into a renewable carbon economy based on efficient supported catalysts.